AC Motor Control *and* Electric Vehicle Applications

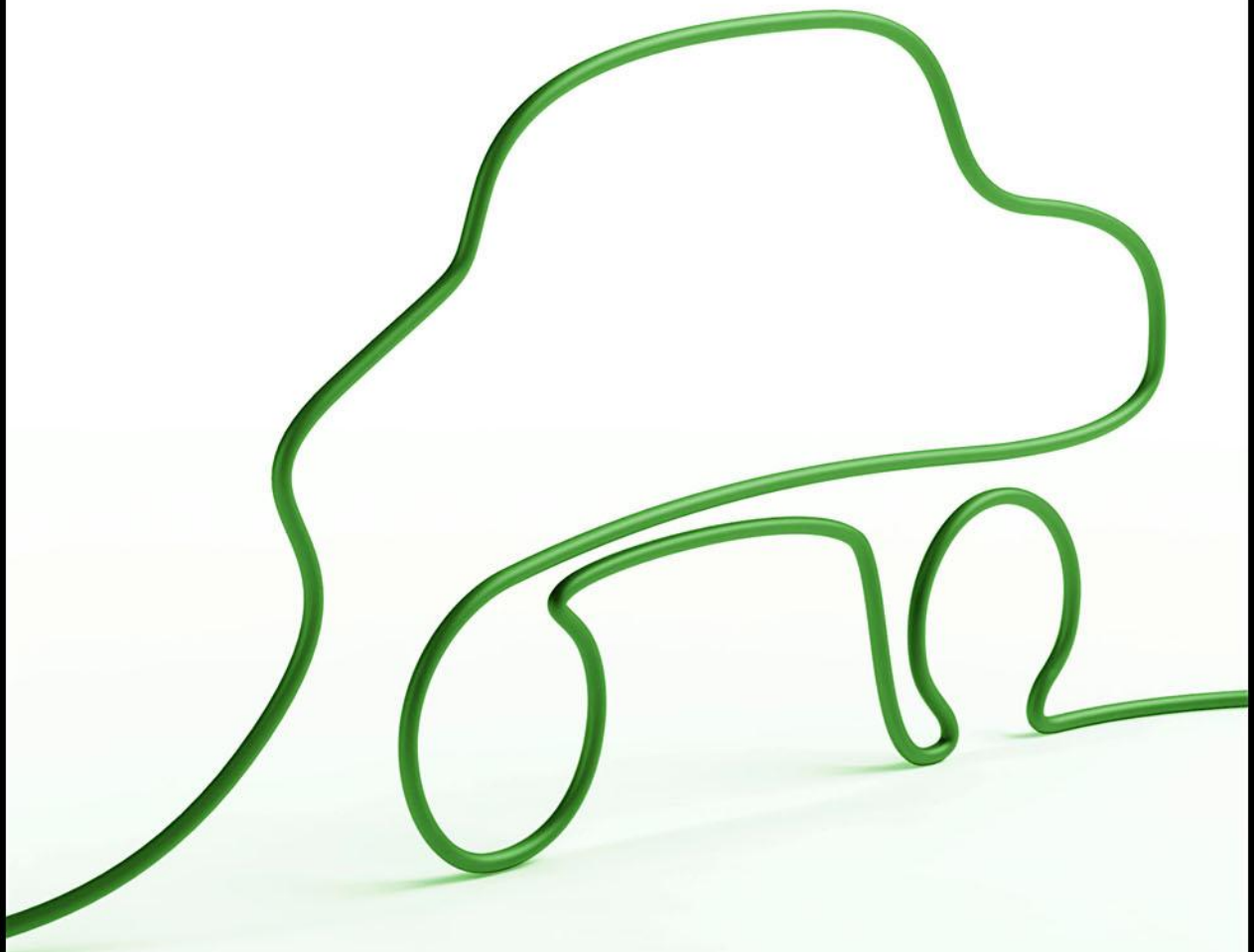

Kwang Hee Nam

CRC Press
Taylor & Francis Group

AC Motor Control *and* Electric Vehicle Applications

AC Motor Control *and* Electric Vehicle Applications

Kwang Hee Nam

CRC Press
Taylor & Francis Group
Boca Raton London New York

CRC Press is an imprint of the
Taylor & Francis Group, an **informa** business

CRC Press
Taylor & Francis Group
6000 Broken Sound Parkway NW, Suite 300
Boca Raton, FL 33487-2742

Version Date: 20131120

International Standard Book Number-13: 978-1-4398-1964-7 (eBook - PDF)

Visit the Taylor & Francis Web site at
http://www.taylorandfrancis.com

and the CRC Press Web site at
http://www.crcpress.com

Contents

Preface

The importance of motor control technology has resurfaced recently, since motor efficiency is closely linked to the reduction of greenhouse gases. Thus, the trend is to use high-efficiency motors such as permanent magnet synchronous motors (PMSMs) in home appliances such as refrigerators, air conditioners, and washing machines. Furthermore, we are now experiencing a paradigm shift in vehicle power-trains. The gasoline engine is gradually being replaced by the electric motor, as society requires clean environments, and many countries are trying to reduce their petroleum dependency. Hybrid electric vehicles (HEVs), regarded as an intermediate solution on the road to electric vehicles (EVs), are steadily increasing in proportion in the market, as the sales volume increases and the technological advances enable them to meet target costs.

Along with progress in CPU and power semiconductor performances, motor control techniques keep improving. Specifically, the remarkable integration of motor control modules (PWM, pulse counter, ADC) with a high-performance CPU core makes it easy to implement advanced, but complicated, control algorithms at a low cost. Motor-driving units are evolving toward high-efficiency, low cost, high-power density, and flexible interface with other components.

This book is written as a textbook for a graduate level course on AC motor control and electric vehicle propulsion. Not only motor control, but also some motor design perspectives are covered, such as back EMF harmonics, loss, flux saturation, reluctance torque, etc. Theoretical integrity in the AC motor modeling and control is pursued throughout the book.

In Chapter 1, basics of DC machines and control theories related to motor control are reviewed. Chapter 2 shows how the rotating magneto-motive force (MMF) is synthesized with the three-phase winding, and how the coordinate transformation maps between the *abc*-frame and the rotating *dq*-frame are defined. In Chapter 3, classical theories regarding induction motors are reviewed. From Chapter 4 to Chapter 6, dynamic modeling, field-oriented control, and some advanced control techniques for induction motors are illustrated. In Chapter 5, the benefits and simplicity of the rotor field-oriented control are stressed. Similar illustration procedures are repeated for PMSMs from Chapter 7 to Chapter 9. Chapter 9 deals with various sensorless control techniques for PMSMs including both back EMF and signal injection–based methods. In Chapter 10, the basics of PWM, inverter, and sensors are illustrated.

From Chapter 11 to 14, electric vehicle (EV) fundamentals are included. In Chapter 11, fundamentals of vehicle dynamics are covered. In Chapter 12, the concept and the benefits of electrical continuous variable transmission (eCVT) are discussed. In Chapter 13, battery EV and plug-in HEV (PHEV), including the properties and limits of batteries, are considered. In Chapter 14, some EV motor issues are discussed.

Finally, I would like to express thanks to my students, Sung Yoon Jung, Jin Seok Hong, Sung Young Kim, Ilsu Jeong, Bum Seok Lee, Sun Ho Lee, Tuan Ngo, Je Hyuk Won, Byong Jo Hyon, and Jun Woo Kim who provided me with experimental results and solutions to the problems.

All MATLAB® files found in this book are available for download from the publisher's Web site. MATLAB® is a registered trademark of The MathWorks, Inc. For product information, please contact:

The MathWorks, Inc.
3 Apple Hill Drive
Natick, MA 01760-2098 USA
Tel: 508-647-7000
Fax: 508-647-7001
E-mail: info@mathworks.com
Web: www.mathworks.com

Author

Dr. Kwang Hee Nam received his B.S. degree in chemical technology and his M.S. degree in control and instrumentation from Seoul National University in 1980 and 1982, respectively. He also earned an M.A. degree in mathematics and a Ph.D. degree in electrical engineering from the University of Texas at Austin in 1986. Since 1987, he has been at POSTECH, where he is now a professor of electrical engineering. From 1987 to 1992, he participated in the Pohang Light Source (PLS) project as a beam dynamics group leader. He performed electron beam dynamic simulation studies, and designed the magnet lattice for the PLS storage ring. He also served as the director of POSTECH Information Research Laboratories from 1998 to 1999. He is the author of over 120 publications in motor drives and power converters and received a best paper award from the Korean Institute of Electrical Engineers in 1992 and a best transaction paper award from the Industrial Electronics Society of IEEE in 2000. Dr. Nam has worked on numerous industrial projects for major Korean industries such as POSCO, Hyundai Motor Company, LG Electronics, and Doosan Infracore. Presently his research areas include sensorless control, EV propulsion systems, motor design, and EV chargers.

Chapter 1

Preliminaries for Motor Control

The DC motor offers a standard model for electro-mechanical systems, and the operational principles constitute the basics of the whole motor control theory: back EMF, torque generation, current control, torque-speed control, field-weakening, etc. The basics of DC motor and various control theories are reviewed in this chapter.

1.1 Basics of DC Machines

DC motors are popularly used since torque/speed controllers (choppers) are simple, and their costs are much lower than the inverter costs. They are still widely used in numerous areas such as in traction systems, mill drives, robots, printers, and wipers in cars. However, DC motors are inferior to AC motors in power density, efficiency, and reliability.

DC motors have two major components in the magnet circuit: field winding (or magnet) and armature winding. The DC field is generated by either field winding or permanent magnets (PMs). Armature winding is wound on a shaft. An electric motor is a machine that converts electrical oscillation into the mechanical oscillation. Although a DC source is supplied to the machine, an alternating current is developed in the armature winding by brush and commutator, i.e., the armature current polarity changes through a mechanical commutation made of brush and commutator. A picture of brush and commutator is shown in Fig. 1.1.

The basic principle of a DC motor operation is illustrated in Fig. 1.2. Fig. 1.2 (a) shows a moment of torque production with the armature coil lying in the middle of the field magnet. Fig. 1.2 (b) shows a disconnected state in which the armature winding is separated from the voltage source. Correspondingly, no force is generated. In Fig. 1.2 (c), the armature coil is re-engaged to the circuit, generating torque in the same direction. This state is the same as that in Fig. 1.2 (a) except the coil positions are switched. In some small DC machines, field winding is replaced by permanent magnets, as shown in Fig. 1.3.

Since most brushes are made of carbon, they wear out continuously. Further,

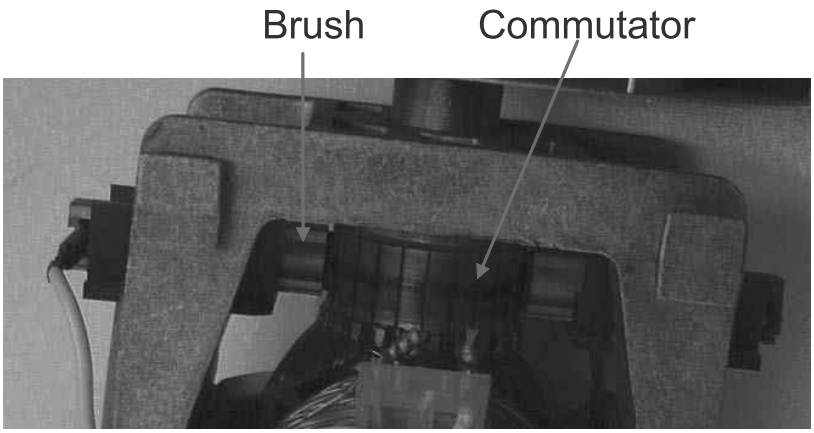

Figure 1.1: Brush and commutator of a DC machine.

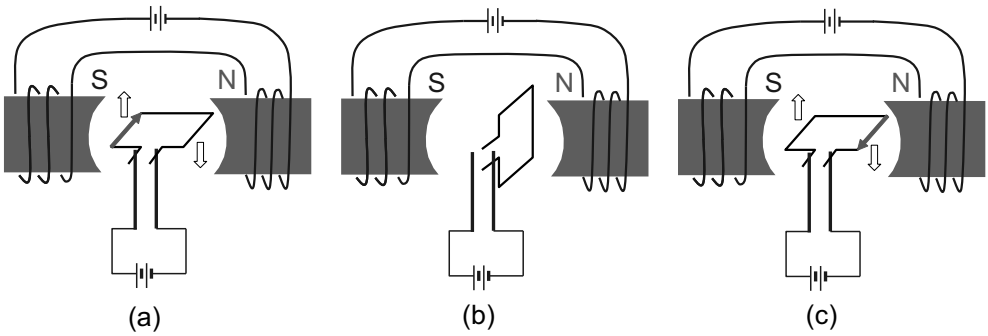

Figure 1.2: DC motor commutation and current flow: (a) maximum torque, (b) disengaged, and (c) maximum torque.

the mechanical contact causes the voltage drop, leading to an efficiency drop. DC motors require regular maintenance, since the brush and commutator wear out. As the motor size and speed increase, the commutator surface speed also increases. Further, the current density in the brush is limited and the maximum voltage on each segment of the commutator is also limited. These factors limit building a DC motor above several megawatts rating.

1.1.1 DC Machine Dynamics

In electrical rotating machines, two electromagnetic phenomena are taking place concurrently:

> **EMF generation**: When a coil rotates in a magnetic field, the flux linkage changes. According to Faraday's law, EMF is induced in the coil. It is called back EMF and described as $e_b = K_b\omega_r$, where K_b is the back EMF constant, and ω_r is the rotor angular speed.

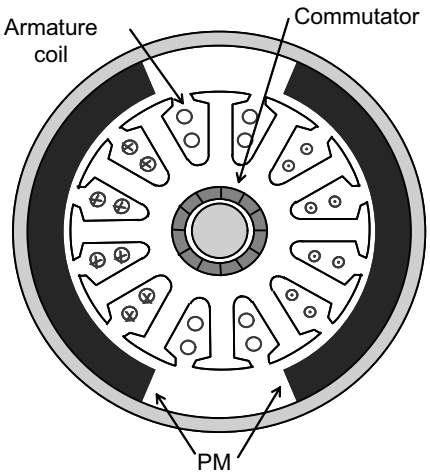

Figure 1.3: Cross section of a typical PM DC motor.

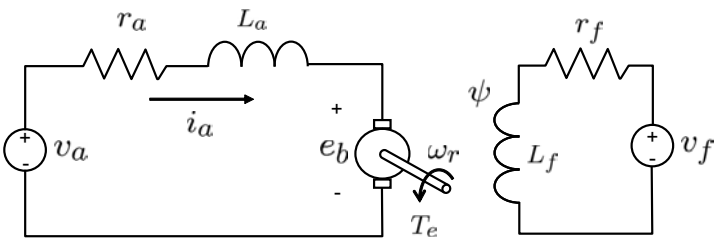

Figure 1.4: Equivalent circuit for a DC motor.

> **Torque generation**: When a current-carrying conductor is placed in a magnetic field, Lorentz force is developed on the conductor. The electromagnetic torque is expressed as $T_e = K_t i_a$, where K_t is the torque constant and i_a is armature current.

An equivalent circuit of a separately wound DC motor is shown in Fig. 1.4. Applying Kirchhoff's voltage law to the equivalent circuit, we obtain

$$v_a = r_a i_a + L_a \frac{di_a}{dt} + e_b, \tag{1.1}$$

$$e_b = K_b \omega_r, \tag{1.2}$$

$$T_e = K_t i_a \tag{1.3}$$

where v_a, i_a, r_a, and L_a are the armature voltage, current, resistance, and inductance, respectively. The back EMF constant, K_b, and torque constant, K_t, depend on the magnet flux developed by the field winding. Fig. 1.4 also shows the field winding circuit, in which the air gap flux is is denoted by ψ. Within a rated speed region, ψ is controlled to be a constant. Obviously, K_b and K_t are proportional to ψ.

Note that the electrical power of the motor is equal to $e_b i_a$, whereas the mechanical power is $T_e\,\omega_r$. From the perspective of power conversion, the electrical power and mechanical power should be the same. Neglecting the power loss by armature resistance, r_a, it follows that $T_e\omega_r = e_b i_a$. Therefore, we obtain $K_t = K_b$.

In the motoring action, a current is supplied to the armature coil from an external source, v_a. As the motor rotates, back EMF, e_b develops. But since $v_a > e_b$, the current flows into the motor ($i_a > 0$), and torque is developed on the shaft. In contrast in the generation mode, an external torque forces the machine shaft to rotate, and the back EMF is higher than the armature voltage, i.e., $v_a < e_b$. Therefore, the current flows out from the machine to the external load ($i_a < 0$). At this time, an opposing torque is developed, leading to mechanical power consumption.

Exercise 1.1
Calculate K_t and K_b for the DC motor whose parameters are listed in Table 1.1.

Solution
The back EMF is equal to $e_b = v_a - r_a i_a = 240 - 16 \times 0.6 = 230.4$ V. Hence, $K_b = e_b/\omega_r = 230.4/127.8 = 1.8$Vsec/rad. Since $K_t = T_e/i_a = 28.8/16 = 1.8$Nm/A, one can check $K_t = K_b$. ■

Table 1.1: Example DC motor parameters

Power (rated)	3.73kW
Voltage (rated)	240V
Armature current (rated)	16A
Rotor speed (rated)	1220rpm (127.8 rad/sec.)
Torque (rated)	28.8Nm
Resistance, r_a	0.6Ω

Exercise 1.2
Consider a DC motor with armature voltage 125V and armature resistance $r_a = 0.4\Omega$. It is running at 1800rpm under no load condition.
a) Calculate the back EMF constant K_b.
b) When the rated armature current is 30A, calculate the rated torque.
c) Calculate the rated speed.

Solution
a) With no load condition, $i_a = 0$. Thus,

$$K_b = \frac{125\text{V}}{1800\text{rpm}} \times \frac{60\text{rpm}}{2\pi\text{rad/sec.}} = 0.663\text{Vsec/rad.}$$

b) Since $K_t = K_b$, $T_e = K_t i_a = 0.663 \times 30 = 19.89$Nm.
c) In the steady-state, $\frac{di}{dt} = 0$. Therefore, $T_e \cdot \omega_r = (v_a - r_a i_a) i_a$. Hence,

$$\omega_r = \frac{(125 - 0.4 \times 30) \times 30}{19.89} = 170.44\text{rad/sec} = 1628\text{rpm}.$$

■

1.1.2 Field-Weakening Control

The back EMF increases as the motor speed increases. The motor is designed such that back EMF e_b reaches the maximum armature voltage, v_a^{max}, at a rated speed, ω_r^{rated}, i.e., $v_a^{max} \approx K_b \omega_r^{rated}$. If the speed is higher than ω_r^{rated}, the source (armature) voltage is not high enough to accommodate the back EMF. Then, the question is how to increase the speed above the rated speed.

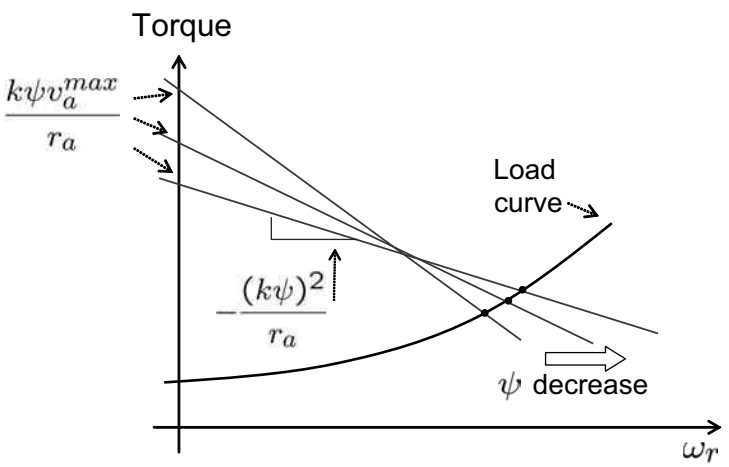

Figure 1.5: Torque curve change with respect to ψ. As ψ decreases, the operational speed increases.

In the steady-state, the armature current is constant. Thus, $L_a \frac{di_a}{dt} \approx 0$. Therefore, in the high-speed region

$$T_e = K_t i_a = K_t \frac{v_a^{max} - K_b \omega_r}{r_a} = \frac{K_t v_a^{max}}{r_a} - \frac{K_t^2}{r_a} \omega_r. \tag{1.4}$$

Note that K_t is proportional to flux, ψ, so that we let $K_t = k\psi$ for some $k > 0$. Then, (1.4) is rewritten as

$$T_e = \frac{k\psi v_a^{max}}{r_a} - \frac{k^2 \psi^2}{r_a} \omega_r. \tag{1.5}$$

Obviously, as flux ψ decreases, $k\psi v_a^{max}/r_a$ decreases; whereas the slope $-(k\psi)^2/r_a$ approaches zero. Fig. 1.5 shows three torque-speed curves for different ψ's along

with a load curve. The speed is determined at the intersection of a torque curve (1.4) and the load curve. It should be noted that the operating speed increases as ψ reduces. That is, higher speed will be obtained by decreasing the field. Therefore, higher speed is achieved by weakening the field. The field-weakening is a common technique used for increasing the speed above a rated (base) speed.

Necessity for field-weakening is seen clearly from the power relation. Power is kept constant above the rated speed. Since

$$P_e = T_e\omega_r = k\psi i_a^{rated}\omega_r,$$

the flux needs to be decreased inversely proportional to ω_r, i.e.,

$$\psi \propto \frac{1}{\omega_r}. \tag{1.6}$$

Then torque, $T_e = k\psi i_a^{rated}$ also decreases according to (1.6) as shown in Fig. 1.6.

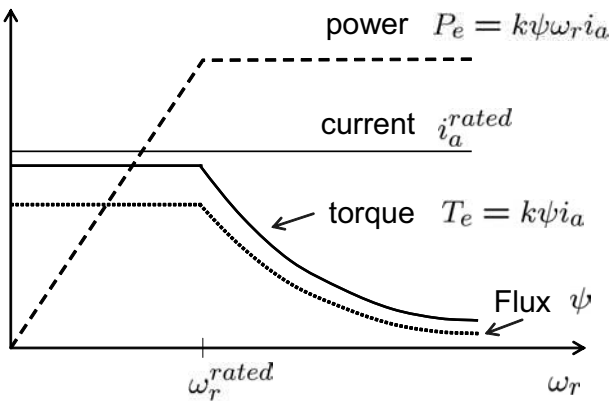

Figure 1.6: Power and torque versus speed in the field-weakening region.

Exercise 1.3

Consider a DC motor with $r_a = 0.5\Omega$, $K_t = k\psi = 0.8$Nm/A, and $K_b = 0.8$Vsec/rad.
a) Assume that the motor terminal voltage reaches $v_a^{max} = 120V$ when the motor runs at a rated speed, $\omega_r = 140$rad/sec. Calculate the rated current and rated torque.
b) Assume that a load torque, $T_L = 6$Nm, is applied and that the field is weakened for a half value, $K_t = 0.4$Vsec/rad. Determine the speed.

Solution

a)

$$\begin{aligned} i_a^{rated} &= (120 - 0.8 \times 140)/0.5 = 16\text{A}. \\ T_e &= 0.8 \times 16 = 12\text{Nm}. \end{aligned}$$

b) Using (1.4), it follows that

$$T_L = T_e = 6 = \frac{0.4 \times 120}{0.5} - \frac{0.4^2}{0.5}\omega_r.$$

Thus, $\omega_r = 281$rad/sec. ■

1.1.3 Four Quadrant Operation

Depending on the polarities of the torque and the speed, there are four operation modes:

Motoring:
Supplying positive current into the motor terminal, positive torque is developed yielding a forward motion.

Regeneration:
External torque is applied to the motor shaft against the torque that is generated by the armature current. Thus, the rotor is rotating in the reverse direction and the motor is generating electric power, while providing a braking torque to the external mechanical power source. In electric vehicles, this mode is referred to as regenerative braking.

Motoring in the reverse direction:
Supplying negative armature current, the motor rotates in the reverse direction.

Regeneration in the forward direction:
External torque is positive and larger than the negative torque that is generated by negative armature current. Electrical power is generated by the motor, while the motor is rotating in the forward direction.

1.1.4 DC Motor Dynamics and Control

The dynamics of the mechanical part is described as

$$J\frac{d\omega_r}{dt} + B\omega_r + T_L = T_e, \tag{1.7}$$

where J is the inertia of the rotating body, B is the damping coefficient, and T_L is a load torque. Combined with the electrical dynamics (1.1)-(1.3), the whole block diagram appears as shown in Fig. 1.8. Note that load torque T_L functions as a disturbance to the DC motor system, and that back EMF $K_b\omega_r$ makes a negative feedback loop.

A DC motor controller normally consists of two loops: current control loop and speed control loop. Generally both controllers utilize proportional integral (PI)

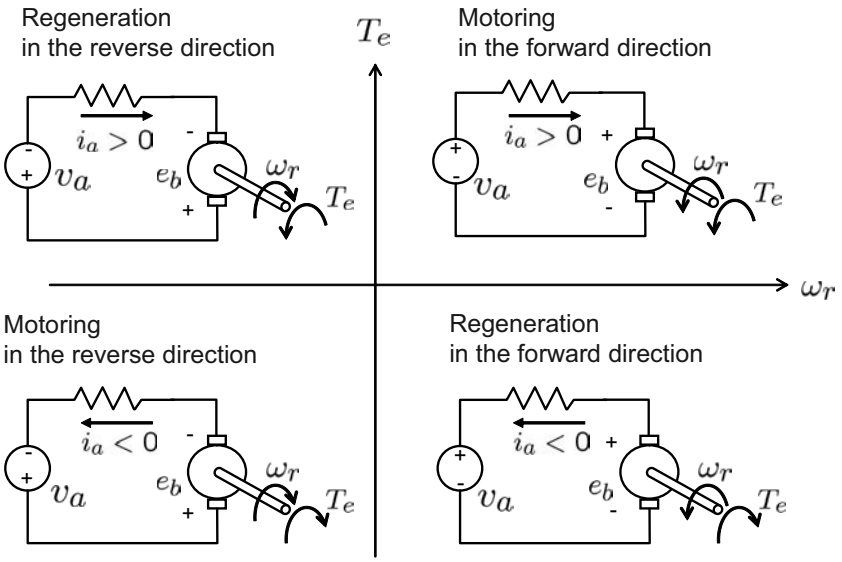

Figure 1.7: Four quadrant operation characteristics.

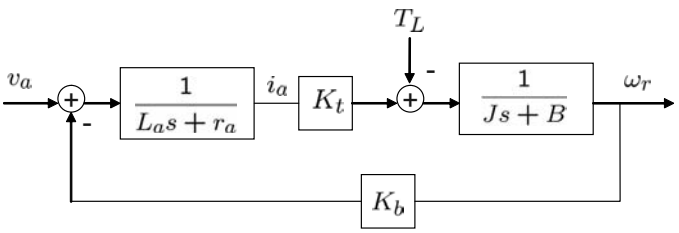

Figure 1.8: DC motor block diagram.

controllers. Since the current loop lies inside the speed loop, it is called the cascaded control structure. The overall control block diagram is shown in Fig. 1.9.

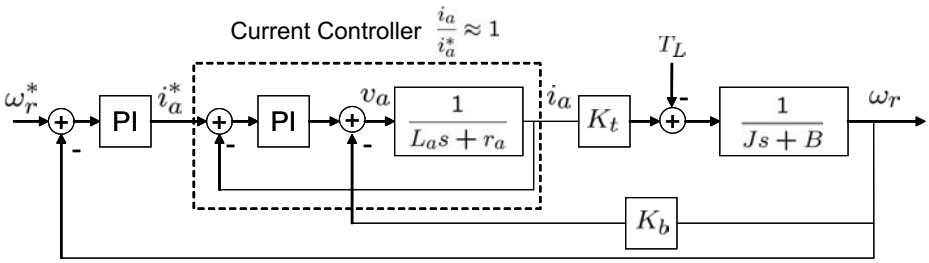

Figure 1.9: Speed and current control block diagram for DC motor.

Current Control Loop

Let the current proportional and integral gains be denoted by K_{pc} and K_{ic}, respectively. With the PI controller $K_{pc} + K_{ic}/s$, the closed-loop transfer function of the current loop is given by

$$\frac{i_a(s)}{i_a^*(s)} = \frac{K_{pc}s + K_{ic}}{L_a s^2 + (r_a + K_{pc})s + K_{ic}}, \tag{1.8}$$

where i_a^* is a current command. In choosing proportional and integral gains for current loop, small overshoot is allowed normally to shorten the rise time. The bandwidth of the current response is normally larger than that of the speed response.

Speed Control Loop

Since the current control bandwidth is larger than the speed control bandwidth, the whole current block can be treated as unity in determining speed PI gains ($K_{p\omega}$, $K_{i\omega}$). Specifically, we let $i_a(s)/i_a^*(s) = 1$ in the speed loop model. With this simplification, it follows that

$$\frac{\omega_r(s)}{\omega_r^*(s)} = \frac{K_t(K_{p\omega}s + K_{i\omega})}{Js^2 + (B + K_t K_{p\omega})s + K_t K_{i\omega}} \equiv \frac{(K_t K_{p\omega}/J)s + \omega_n^2}{s^2 + 2\zeta\omega_n s + \omega_n^2}, \tag{1.9}$$

where $\omega_n = \sqrt{K_t K_{i\omega}/J}$ is a corner frequency and $\zeta = (B + K_t K_{p\omega})/(2\sqrt{JK_t K_{i\omega}})$ is a damping coefficient. Corner frequency (or natural frequency) ω_n is determined by I-gain, $K_{i\omega}$, whereas damping coefficient ζ is a function of P-gain, $K_{p\omega}$.

1.2 Types of Controllers

The PI controllers are most widely used in the practical systems due to their tracking ability and robust properties. In this section, some basics of the PI controller and its variations are reviewed.

Consider a plant, $G(s)$ with a controller, $C(s)$, shown in Fig.1.10. One way to achieve a perfect set tracking performance is to design a precompensator such that $C(s) = G(s)^{-1}$. Then, the input, r to output, y transfer function will be unity for all frequencies. However, it cannot be a practical solution for the following reasons:

i) The plant may be in nonminimum phase, i.e., the plant has zeros in the right half plane. Then, its inverse will have poles in the right half plane. Note that a delay element of a system causes the nonminimum phase property.

ii) Normally, the plant is strictly proper, thereby its inverse contains a differentiator. Therefore, the output feedback control will not be successful since the sensed signal of the output contains noise and the noise is also differentiated. Correspondingly, it cannot have a disturbance rejection ability that can be realized via feedback.

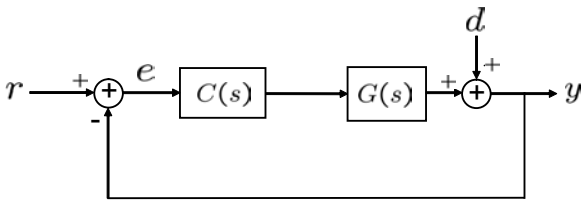

Figure 1.10: Plant with unity feedback controller.

Two important control objectives are set point tracking and disturbance rejection. For the closed-loop system, the sensitivity function is defined as

$$S \equiv \frac{y(s)}{d(s)} = \frac{1}{1+CG},$$

representing the effect of disturbance, d on output, y. Therefore, to enhance the disturbance rejection performance, the smaller S is, the better. On the other hand, the complementary sensitivity function is defined as

$$T \equiv 1 - S.$$

In this example,

$$T(s) = \frac{CG}{1+CG} = \frac{y(s)}{r(s)}.$$

That is, the complementary sensitivity function reflects the tracking performance. Therefore, it is desired to be unity.

The performance goals may be stated as $S = 0$ and $T = 1$ for all frequency bands. But, it cannot be realized due to the reasons stated above. However, the goals can be satisfied practically in a low frequency region. Bode plots of the typical sensitivity and complementary sensitivity functions are shown in Fig. 1.11. Note that $T(j\omega) \approx 0$dB and $S(j\omega)$ is far lower than 0dB in a low frequency region.

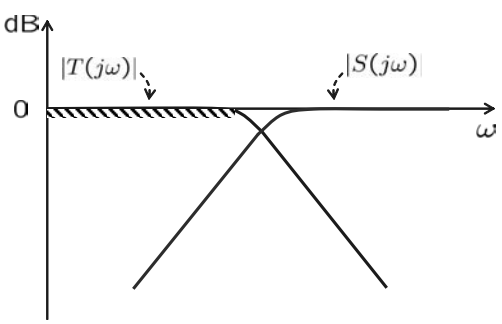

Figure 1.11: Typical sensitivity and complementary sensitivity functions.

1.2.1 Gain and Phase Margins

The phase delay is an intrinsic nature of a dynamic system, and the delay sometimes causes instability for a closed-loop system. Instability occurs in the feedback loop when two events take place at the same time: unity loop gain and 180° phase delay. A pathological example is shown Fig. 1.12: Assume that the reference command is sinusoidal and that

$$|C(j\omega)G(j\omega)| = 1 \quad \text{and} \quad \angle C(j\omega)G(j\omega) = -180^\circ,$$

i.e., the loop gain is unity and the loop delay is -180°. Then, $-y(t)$ is in phase with $r(t)$, i.e., the error is equal to $e(t) = r(t) - y(t) = 2r(t)$. Repeating the same, $e(t)$ grows indefinitely.

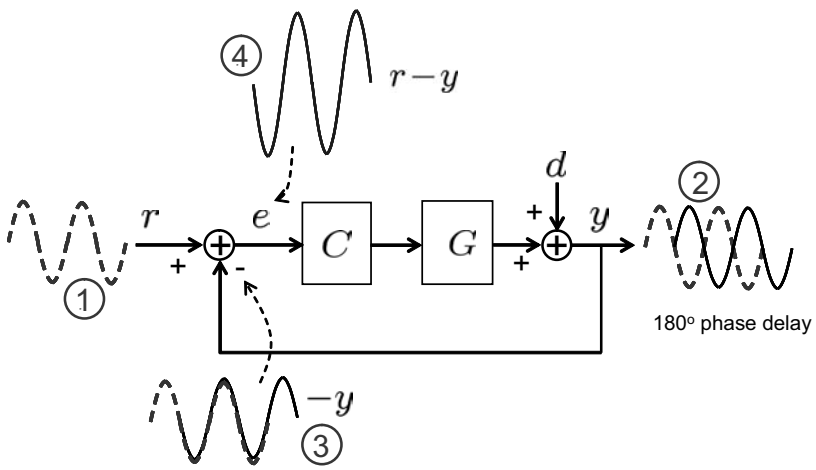

Figure 1.12: Instability mechanism when loop gain is unity and phase delay is 180°.

Phase margin and gain margin are buffers from the unstable points. The gain margin is defined by

$$A_{mg} = 20 \log_{10} \frac{1}{|C(j\omega_p)G(j\omega_p)|} \tag{1.10}$$

at ω_p where $\arg[C(j\omega_p)G(j\omega_p)] = -180^\circ$. That is, the gain margin is the difference from 0 dB to the loop gain at frequency ω_p, where the phase delay is 180°. On the other hand, the phase margin is defined by

$$\psi_{mg} = \arg[C(j\omega_g)G(j\omega_g)] + 180^\circ \tag{1.11}$$

at ω_g where $|C(j\omega_g)G(j\omega_g)| = 1$. In other words, the phase margin is the angle difference from -180° at the frequency when the loop gain has unity. Gain and phase margins are marked by arrows in the Bode plot shown in Fig. 1.13.

If a system is tuned with a high gain margin, it may be stable even under a high disturbance. However, the response is very sluggish, and as a result, it may not

satisfy certain control goals. In other words, a high gain margin may be obtained at the sacrifice of control bandwidth. But the system will become unstable in the other extreme. Hence, the controller needs to be well-tuned in the sense that agileness is balanced with stability, i.e., the system must be stable, but it should not be too relaxed. Proper selection ranges are: Gain margin = $12 \sim 20$ and Phase margin = $40^\circ \sim 60^\circ$.

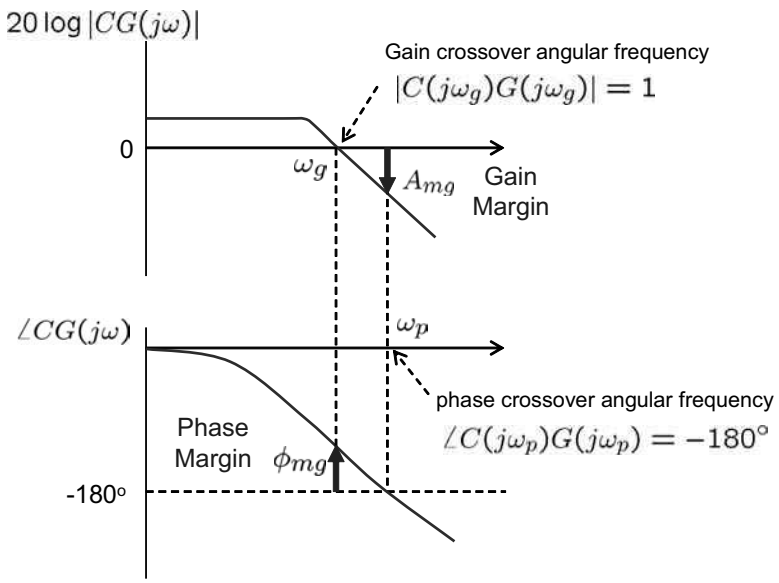

Figure 1.13: Gain and phase margins in a Bode plot.

Exercise 1.4
Suppose that $C(s) = K_p(1 + \frac{1}{s})$ and $G(s) = \frac{1}{s}$ in Fig. 1.10. Determine K_p such that the phase margin is equal to 30°.

1.2.2 PI Controller

Proportional-integral (PI) controllers are most commonly used in practice, since they have a good disturbance rejection property and are not sensitive to system parameter variation. The main virtue of I-controller is the ability of DC disturbance rejection, i.e., I-controller has the infinite gain for a DC error. For example, consider a feedback system shown in Fig. 1.10 and let $G(s) = 1/(s+\alpha)$ and $C(s) = K_p + K_i/s$. Suppose that a step disturbance $d(t) = d \cdot u_s(t - t_1)$ is applied at t_1. Then, applying the final value theorem[6],

$$\lim_{t\to\infty} e(t) = \lim_{s\to 0} sE(s)\frac{de^{-st_1}}{s} = \lim_{s\to 0} \frac{de^{-st_1}}{1 + \left(\frac{K_p s + K_i}{s}\right)\left(\frac{1}{s+\alpha}\right)} = 0.$$

That is, the steady-state error caused by a DC disturbance can be eliminated completely.

Note further that

$$K_i \int_{t_1}^{\infty} e(\tau)d\tau = d.$$

As far as $e(t) \neq 0$, the integral action takes place until the error sum is equal to the magnitude of disturbance. That is, the integral controller produces a term which cancels out the DC disturbance. Fig. 1.14 shows this integral action, in which the shaded area is equal to d. However, a very high integral gain makes the system unstable producing a large overshoot.

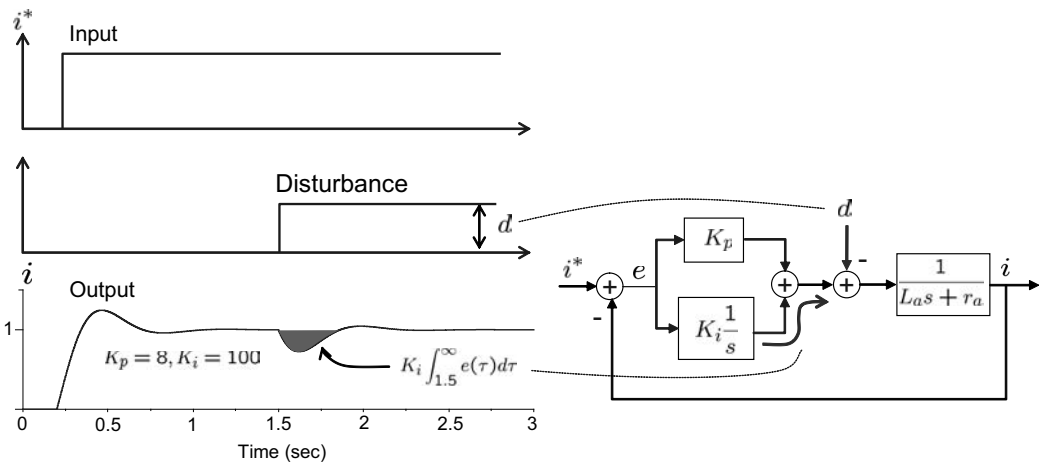

Figure 1.14: Response to a step disturbance applied at time $t = 1.5$ sec.

To classify the asymptotic behavior, system types are defined. Type m system is defined as the system of the form [6]

$$G(s) = \frac{(s + z_1)(s + z_2)\cdots}{s^m(s + p_1)(s + p_2)\cdots}.$$

The PI controller increases the system type by one. Type 1 system can reject a DC disturbance. But to reject a ramp disturbance, $d(t) = tu_s(t)$, the system type must be at least 2.

Exercise 1.5

Suppose that $C(s)G(s)$ in Fig. 1.10 is system type 2. Show that the closed-loop rejects the ramp disturbance.

Simplified Modeling of Practical Current Loop

Nowadays, most control algorithms are implemented using microcontrollers, and thereby associated delay elements are introduced in the control loop:

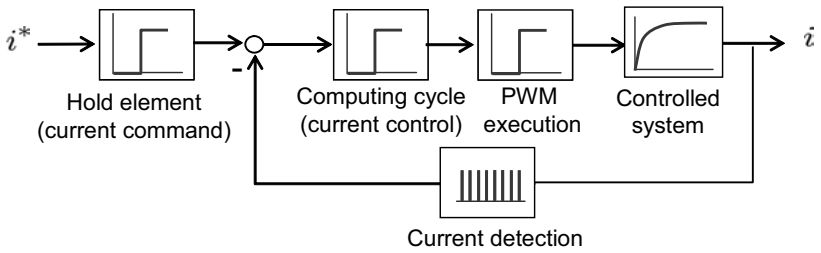

Figure 1.15: Practical current loop based on a microcontroller.

i) command holder,
ii) computing cycle time,
iii) pulse-width modulation (PWM) execution delay,
iv) value detection

The command is refreshed every sampling period. Since the command value is held until the next sampling period, the holding delay takes place, which is estimated about half of the sampling period, $T_{sa}/2$, where T_{sa} is the current sampling period. A computing cycle is required for current control and calculation of the PWM intervals. Also, there is a delay in executing the PWM. Finally, a delay is required for current sensing and A/D conversion. Fig. 1.15 shows the delay elements in the current control loop. We sum up all the delay elements in the current loop, and denote it by τ_σ. The total delay of the current loop is estimated as $\tau_\sigma = 1.5 \sim 2T_{sa}$ [2]. Note further that

$$e^{-\tau_\sigma s} = \frac{1}{e^{\tau_\sigma s}} \approx \frac{1}{1+\tau_\sigma s}\,. \tag{1.12}$$

Hence, the total delay can be represented as a a first order filter. In the speed loop, the current block is often treated as the first order system, (1.12).

1.2.3 Method of Selecting PI Gains

In this part of the section, a general guideline for selecting PI gains is presented. Fig. 1.16 (a) shows a typical motor speed control loop, and Fig. 1.16 (b) shows the Bode plot of the open-loop. Note from the PI block that K_p is speed loop proportional gain and that T_i is the integral time constant. The first order filter block $1/(1+\tau_\sigma s)$ represents the current control block.

Let $\omega_1 = \frac{1}{T_i}$ and $\omega_2 = \frac{1}{\tau_\sigma}$, and divide the whole frequency range into three parts: $[0,\ \omega_1)$, $[\omega_1,\ \omega_2)$, and $[\omega_2,\ \infty)$. Note that $[0,\ \omega_2]$ representing the current bandwidth is larger than the speed bandwidth and that $1/(1+\tau_\sigma s) \approx 1$ in $[0,\ \omega_2]$. Furthermore, in the low frequency region, $[0,\ \omega_1)$, the loop gain is approximated as $\frac{K_p}{T_i J\, s^2}$ since $K_p + \frac{K_p}{T_i\, s} \approx K_p$. However, in $[\omega_1,\ \omega_2)$ the loop gain is close to $\frac{K_p}{J\, s}$. Finally, the loop

gain is approximated as $\left(\frac{K_p}{1+\tau_\sigma s}\right)\frac{1}{Js}$. Summarizing the above, we have

$$\frac{1}{Js}\left(K_p+\frac{K_p}{T_i\,s}\right)\left(\frac{1}{1+\tau_\sigma s}\right)\approx\begin{cases}\frac{K_p}{T_iJ\,s^2} & (-40\text{dB}),\quad [0,\,\omega_1)\\ \frac{K_p}{Js} & (-20\text{dB}),\quad [\omega_1,\,\omega_2)\\ \left(\frac{K_p}{1+\tau_\sigma s}\right)\frac{1}{Js} & (-40\text{dB}),\quad [\omega_2,\,\infty)\end{cases}$$

Let $[0,\,\omega_{sc})$ be the speed bandwidth. Then, it is necessary to make $\frac{K_p}{J\omega}\approx 1$ for $\omega<\omega_{sc}$. Hence, the proportional gain should be selected as

$$K_p=J\omega_{sc}\,. \tag{1.13}$$

It is necessary to make the corner frequency ω_1 of the PI controller much less than ω_{sc}: A common rule to choose the integral time constant is

$$\omega_1=\frac{1}{T_i}=\frac{\omega_{sc}}{5}. \tag{1.14}$$

Then with the gain $K_p=J\omega_{sc}$ and $T_i=5/\omega_{sc}$, the closed-loop transfer function is

$$\frac{K_p\left(1+\frac{1}{T_is}\right)\frac{1}{Js}}{1+K_p\left(1+\frac{1}{T_is}\right)\frac{1}{Js}}=\frac{\omega_{sc}s+\frac{\omega_{sc}^2}{5}}{s^2+\omega_{sc}s+\frac{\omega_{sc}^2}{5}}\,. \tag{1.15}$$

Thus, the damping coefficient is $\zeta=\sqrt{5}/2$, and it corresponds to an overdamping.

According to ASME (American Society of Mechanical Engineers), the general guidelines for selecting PI gains are [1]:

I. Phase margin should be larger than 30°, and gain margin should be larger than 2.5 (8dB).

II. The slope of the gain plot should be −20dB/scale in the region of ω_{sc}.

III. It is desired to satisfy $\omega_{sc}-\omega_1=(\frac{1}{2}\sim\frac{1}{3})(\omega_2-\omega_{sc})$. Also, $D/E\geq 5$ needs to be satisfied, when D and E are not on the logarithmic scale. In other words, $\omega_2\geq 5\omega_1$.

IV. Point E should be less than −6dB.

V. The overshoot should be less than 200%. A proper overshoot value is 130%.

1.2.4 Integral-Proportional (IP) Controller

The integral-proportional controller (IP controller) is a variation of PI controller. The IP controller has the proportional part in the feedback path, as shown in

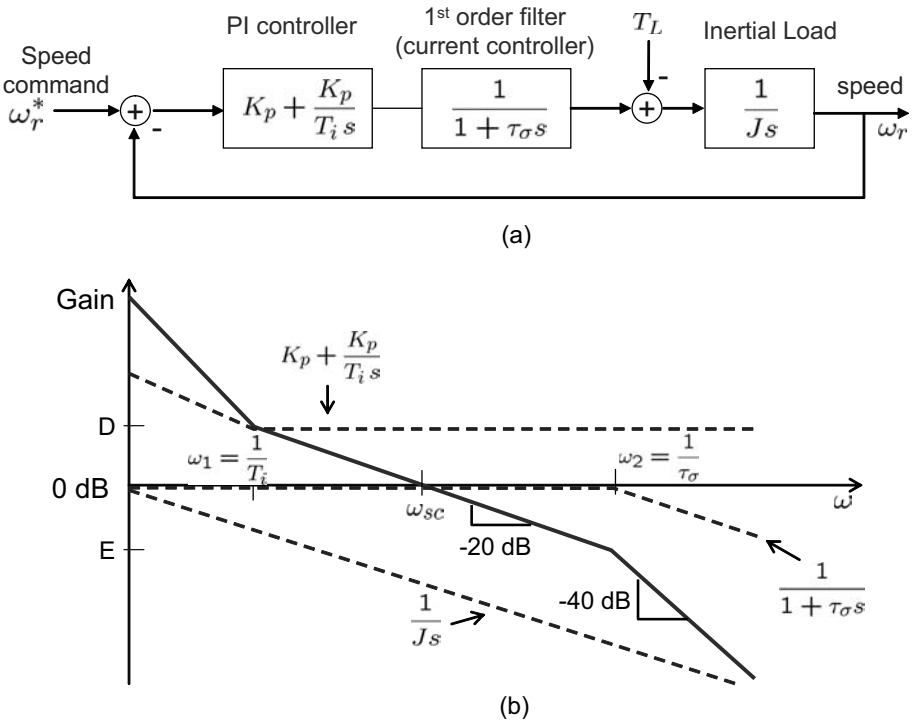

Figure 1.16: (a) Speed control loop and (b) Bode plot for the open-loop.

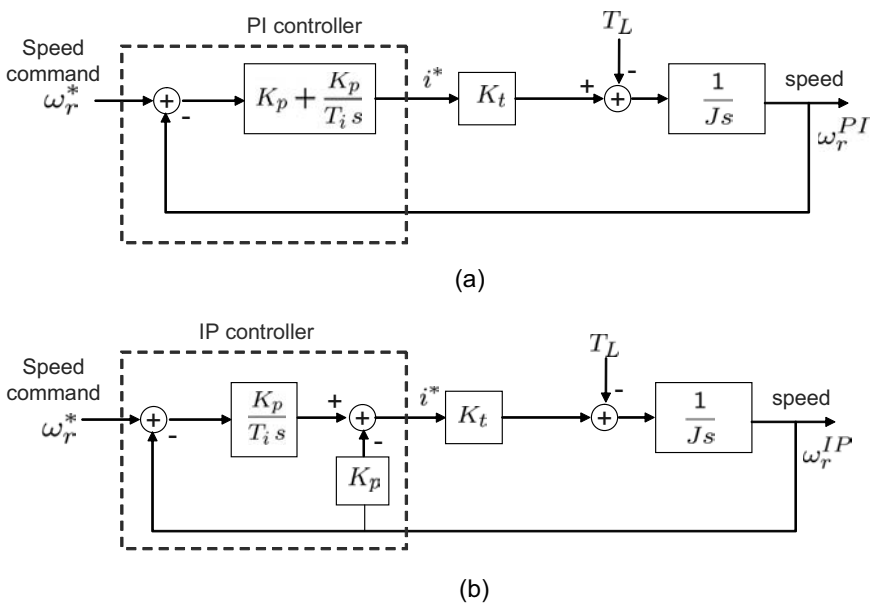

Figure 1.17: Speed control loops with (a) PI and (b) IP controllers.

Fig. 1.17 (b). The location of the integral part is the same as that of the PI controller. The transfer functions are equal to

$$\text{PI Controller} \quad \Rightarrow \quad \frac{\omega_r^{PI}(s)}{\omega^*(s)} = \frac{\frac{K_t K_p}{J}\left(s + \frac{1}{T_i}\right)}{s^2 + \frac{K_t K_p}{J}s + \frac{K_t K_p}{JT_i}} \tag{1.16}$$

$$\text{IP Controller} \quad \Rightarrow \quad \frac{\omega_r^{IP}(s)}{\omega^*(s)} = \frac{\frac{K_p K_t}{JT_i}}{s^2 + \frac{K_t K_p}{J}s + \frac{K_t K_p}{JT_i}} \,. \tag{1.17}$$

Note that both functions have the same denominator, but the numerators are different: An IP controller does not have differential operator 's', whereas a PI controller does. Let $\omega_r^{PI}(t) = \mathcal{L}^{-1}\{\omega_r^{PI}(s)\}$ and $\omega_r^{IP}(t) = \mathcal{L}^{-1}\{\omega_r^{IP}(s)\}$, where $\mathcal{L}^{-1}$ is the inverse Laplace operator. Then,

$$\omega_r^{PI}(t) = \omega_r^{IP}(t) + T_i \dot{\omega}_r^{IP}(t).$$

That is, the derivative, $\dot{\omega}_r^{IP}$, of the IP controller output appears additionally in the output of the PI controller. Therefore, PI controllers make a larger overshoot or undershoot during the transition than IP controllers. This fact is observed when we compare the controller outputs: The PI controller produces a higher current command, i^*, than an IP controller for the step input. Fig. 1.18 shows the speed responses and current commands when PI and IP controllers are utilized with the same K_p and T_i. Note that ω_r^{PI} has an overshoot, but ω_r^{IP} does not. Note also from Fig. 1.18 (b) that the current command level i^* of the PI controller is about five times larger than that of the IP controller. Hence, to avoid a possible current peaking, IP controllers are preferred in the speed loop of practical systems.

Exercise 1.6
Obtain the transfer functions from the disturbance to the output $\frac{\omega(s)}{T_L(s)}$ for the PI and IP cases shown in Fig. 1.17.

1.2.5 PI Controller with Reference Model

In the previous section, it is shown that the integral action is required to eliminate a DC offset in the output caused by a possible disturbance. But, with the use of an integral controller the system order increases. The order increase causes more phase delay, resulting in a narrow phase margin for a given control bandwidth. In this section, we consider the PI controller with reference model which implements the disturbance rejection capability without increasing the system order between the reference input and output.

PI with Reference Model

A control block diagram of the PI controller with reference model is shown in Fig. 1.19 [2]. Note that the current loop is modeled as $1/(1 + \tau_\sigma s)$. The block

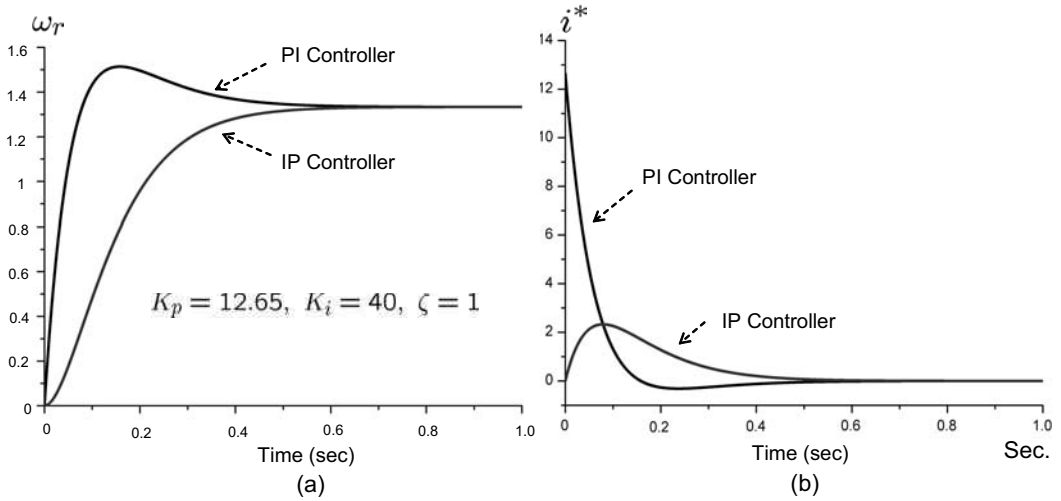

Figure 1.18: (a) Speed responses and (b) current commands for the PI and IP controllers shown in Fig. 1.17.

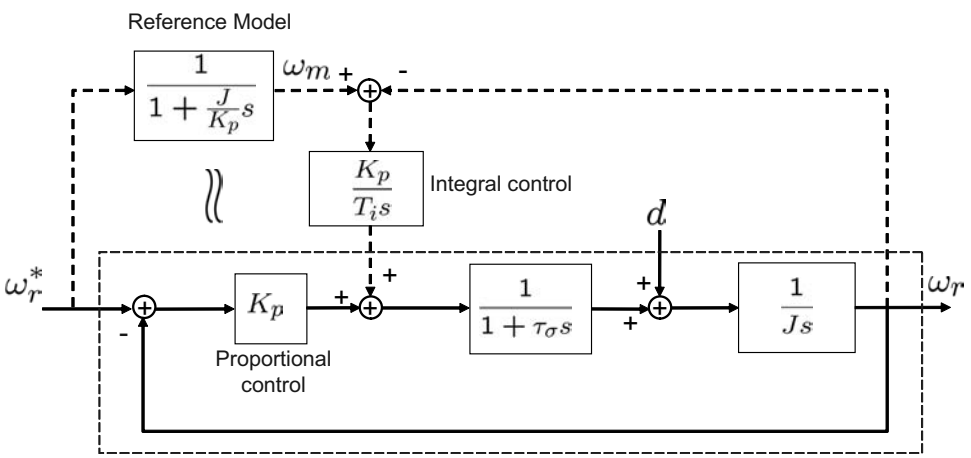

Figure 1.19: PI controller with reference model.

diagram consists of two parts: The bottom part shows the tracking control loop, whereas the upper part shows the disturbance rejection part. It should be noted that the integral controller is not involved in the tracking part. Instead, just a P-gain, K_p, appears. As a result, the closed-loop transfer function of $\omega_r(s)/\omega_r^*(s)$ appears

as a second-order system:

$$\frac{\omega_r(s)}{\omega_r^*(s)} = \frac{1}{\frac{J\tau_\sigma}{K_p}s^2 + \frac{J}{K_p}s + 1} \tag{1.18}$$

$$\approx \frac{1}{\frac{J}{K_p}s + 1} \tag{1.19}$$

Furthermore, the second-order system can be reduced further as a first order model in a low frequency area. The reduced order model, (1.19) is used as a reference model representing the tracking part. Both the model and the real plant receive the same speed command, ω_r^*. Since the same input, ω_r^*, is applied to both plant and reference model, their outputs are expected to be the same, i.e., $\omega_r \approx \omega_m$. But if the disturbance is present, they cannot be the same. On the other hand, $\omega_m - \omega_r$ carries information of disturbance, d. To compensate the disturbance, integral action is taken on the error, $\omega_m - \omega_r$. In the steady-state, it follows that

$$\frac{K_p}{T_i}\int_0^t (\omega_m(\tau) - \omega_r(\tau))d\tau = d,$$

but the integral action does not affect the tracking part. The disturbance compensation loop is denoted by dotted lines in Fig. 1.19.

The transfer function from the disturbance to the output is a 3^{rd}-order function:

$$\frac{\omega_r(s)}{d(s)} = \frac{\frac{T_i}{K_p}s(\tau_\sigma + 1)}{\frac{\tau_\sigma T_i J}{K_p}s^3 + \frac{T_i J}{K_p}s^2 + T_i s + 1}\,. \tag{1.20}$$

This result is the same as that of the conventional PI controller. But the difference lies in the tracking part: The tracking part is a second-order with the reference model, whereas it is a 3^{rd}-order with the conventional PI controller. They are compared in Table 1.2

Fig. 1.20 shows the Bode plots of $\omega_r(s)/\omega_r^*(s)$ in Table 1.2. In the simulation, we let $J = 0.015$, $\tau_\sigma = 0.000548$, $K_p = 13.69$, and $T_i = 0.0022$. One can see that the PI controller with reference model has less phase delay than the conventional PI. Fig. 1.21 shows that the conventional PI controller makes a larger overshoot in the step responses for the same gain. It is due to the presence of a zero in the conventional PI controller.

Double Ratio Rule

Based on a damping optimum of the closed control loop, gain selection based on the double ratio rules were developed [2]. Consider a closed-loop system

$$H(s) = \frac{y(s)}{u(s)} = \frac{b_n s^n + b_{n-1}s^{n-1} + \cdots + b_1 s + b_0}{a_n s^n + a_{n-1}s^{n-1} + \cdots + a_1 s + a_0}$$

Table 1.2: Comparision of transfer functions

	PI with reference model	Conventional PI
$\frac{\omega_r(s)}{\omega_r^*(s)}$	$\frac{1}{\frac{J\tau_\sigma}{K_p}s^2 + \frac{J}{K_p}s + 1}$	$\frac{T_i s + 1}{\frac{\tau_\sigma T_i J}{K_p}s^3 + \frac{T_i J}{K_p}s^2 + T_i s + 1}$
$\frac{\omega_r(s)}{d(s)}$	$\frac{\frac{T_i}{K_p}s(\tau_\sigma + 1)}{\frac{\tau_\sigma T_i J}{K_p}s^3 + \frac{T_i J}{K_p}s^2 + T_i s + 1}$	$\frac{\frac{T_i}{K_p}s(\tau_\sigma + 1)}{\frac{\tau_\sigma T_i J}{K_p}s^3 + \frac{T_i J}{K_p}s^2 + T_i s + 1}$

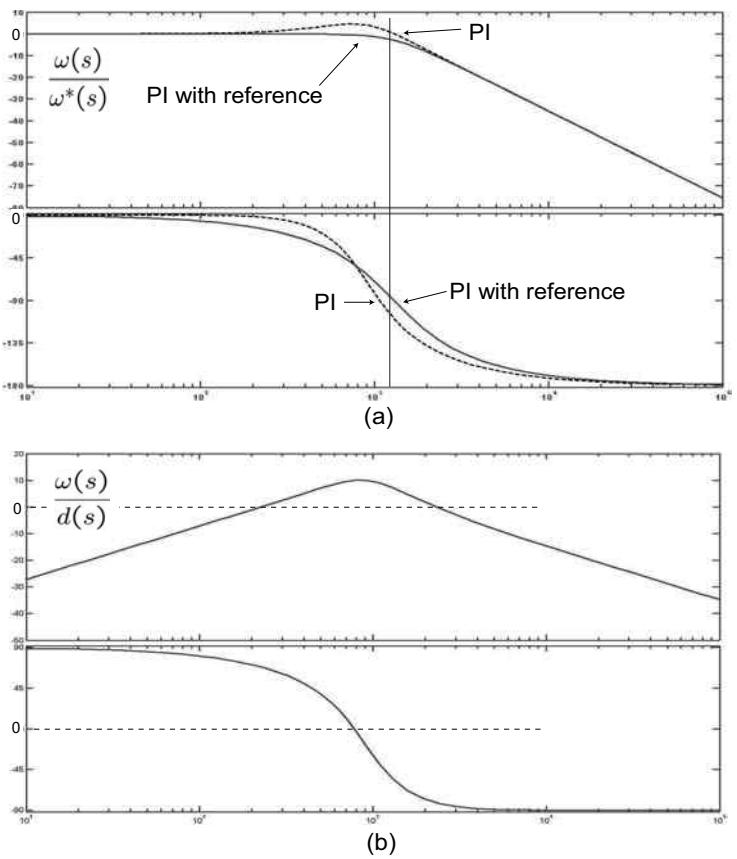

Figure 1.20: Bode plots of the systems with the PI controller with reference model and the conventional PI controller: (a) for tracking and (b) for disturbance rejection.

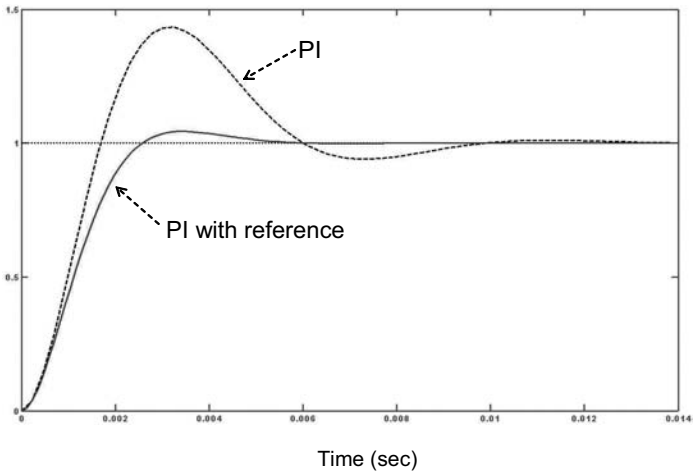

Figure 1.21: Step responses with the PI controller with reference model and the conventional PI controller for the same gains.

Make a sequence of coefficients ratios:

$$\frac{a_n}{a_{n-1}}, \frac{a_{n-1}}{a_{n-2}}, \frac{a_{n-2}}{a_{n-3}}, \cdots, \frac{a_1}{a_0}$$

Choose the coefficients such that the ratios between adjacent components are less than or equal to 1/2:

$$\frac{\frac{a_k}{a_{k-1}}}{\frac{a_{k-1}}{a_{k-2}}} = \frac{a_k a_{k-2}}{a_{k-1}^2} \leq \frac{1}{2}, \quad \text{for} \quad 2 \leq k \leq n. \tag{1.21}$$

This pole allocation method leads to a good command and disturbance response without extensive calculation. This method results in a robust response, i.e., it makes the system less susceptible to parameter variation.

For example, consider a second-order system, $1/(a_2 s^2 + a_1 s + a_0)$. Applying the double ratio rule, (1.21), we obtain $a_2 = \frac{a_1^2}{2a_0}$. Then the denominator is equal to

$$\frac{a_1^2}{2a_0}\left[s^2 + 2\left(\frac{a_0}{a_1}\right)s + 2\left(\frac{a_0}{a_1}\right)^2\right] = \frac{a_1^2}{2a_0}\left[s^2 + 2\cdot\frac{1}{\sqrt{2}}\left(\frac{\sqrt{2}a_0}{a_1}\right)s + \left(\frac{\sqrt{2}a_0}{a_1}\right)^2\right]$$

Therefore, the double ratio rule leads to the damping coefficient being $\zeta = \frac{1}{\sqrt{2}} = 0.707$.

Now we apply the double ratio rule to (1.20). Then

$$\frac{\frac{\tau_\sigma T_i^2 J}{K_p}}{\left(\frac{T_i J}{K_p}\right)^2} = \frac{K_p \tau_\sigma}{J} \leq \frac{1}{2}$$
$$\frac{\frac{T_i J}{K_p} \cdot 1}{T_i^2} = \frac{J}{K_p T_i} \leq \frac{1}{2}$$

These lead to gain selection:

$$K_p = \frac{J}{2\tau_\sigma} \tag{1.22}$$
$$T_i = \frac{2J}{K_p} = 4\tau_\sigma\,. \tag{1.23}$$

Note that the integral gain is equal to

$$K_i = \frac{K_p}{T_i} = \frac{J}{8\tau_\sigma^2}. \tag{1.24}$$

This tells us that as the delay increases, both the proportional and integral gains should be reduced. On the other hand, both gains can be increased as the inertia increases. After applying the optimal gains (1.22) and (1.23), the transfer functions turn out to be

$$\frac{\omega_r(s)}{\omega_r^*(s)} = \frac{1}{2\tau_\sigma^2 s^2 + 2\tau_\sigma s + 1} \tag{1.25}$$
$$\frac{\omega_r(s)}{d(s)} = \frac{8\tau_\sigma s(\tau_\sigma s + 1)}{8\tau_\sigma^3 s^3 + 8\tau_\sigma^2 s^2 + 4\tau_\sigma s + 1} \tag{1.26}$$

Exercise 1.7
Consider system shown in Fig. 1.19. Show that the phase margin of the open loop system is 65.5^o independently of τ_σ, if we set $K_p = \frac{J}{2\tau_\sigma}$. Show also that $\zeta = 0.707$ for closed loop system.

Solution
Open loop transfer function is $H(s) = K_p \frac{1}{(1+\tau_\sigma s)Js} = \frac{1/2\tau_\sigma}{\tau_\sigma s^2 + s}$. It is necessary to find ω that satisfies $|-\tau_\sigma\omega^2 + j\omega| = \frac{1}{2\tau_\sigma}$. The solution is $\omega = \sqrt{\frac{\sqrt{2}-1}{2}}\frac{1}{\tau_\sigma} = 0.455\frac{1}{\tau_\sigma}$. Therefore,

$$\text{phase margin} = \tan^{-1}\left(\frac{1}{-\tau_\sigma\omega}\right) + 180^o = \tan^{-1}\left(\frac{1}{-0.455}\right) + 180^o = 65.5^o.$$

Damping coefficient, $\zeta = 0.707$ follows directly from the closed loop transfer function, $\frac{1/2\tau_\sigma^2}{s^2 + 1/\tau_\sigma s + 1/2\tau_\sigma^2}$. ■

This section can be summarized as

1) The PI controller with reference model does not increase the order of the transfer function from the command to the output. Thereby, it has lower phase lag and larger phase margin. On the other hand, it has the same characteristics with the conventional PI controller in the disturbance rejection.

2) The double ratio rule is a convenient optimum damping rule that can be used for determining the PI gains. The resulting PI gain tells us that we can apply higher gain when the system has lower delay. As the delay increases, the gain should be lower correspondingly. Otherwise, the system will be unstable. Similarly, we can utilize high gain for the system having a large inertia. The double ratio rule provides us a good reference for the gain selection.

1.2.6 Two Degrees of Freedom Controller

In general, PI controllers do not utilize the structure information of the plant. The internal model control (IMC), as the name stands for, employs the model of the plant inside the controller. The IMC combined with two DOF controller is shown in Fig. 1.22 [3]. The IMC utilizes a model, $\hat{G}(s)$ in the control loop, which is an estimate of the plant, $G(s)$. Both the plant and the model receive the same input, and then the outputs are compared. For the purpose of illustration, let $\hat{G}(s) = G(s)$. Due to the presence of disturbance, the outputs are not the same. The output error is fed back to the input through the feedback compensator, $Q_d(s)$. On the other hand, the IMC also has a feedforward compensator, $Q_r(s)$.

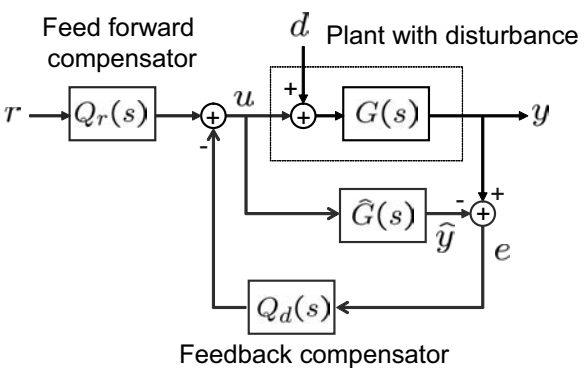

Figure 1.22: IMC structure for plant $G(s)$ with disturbance d.

The transfer function of the whole system is

$$y = \left[\frac{G(s)Q_r(s)}{1 + Q_d(s)(G(s) - \hat{G}(s))}\right] r + \left[\frac{G(s)(1 - Q_d(s)\hat{G}(s))}{1 + Q_d(s)(G(s) - \hat{G}(s))}\right] d. \tag{1.27}$$

If there is no plant model error, i.e., $G = \hat{G}$, then

$$y = G(s)Q_r(s)r + G(s)(1 - Q_d(s)G(s))d.$$

The sensitivity function S and the complementary sensitivity function T are

$$S(s) \equiv \left.\frac{y(s)}{d(s)}\right|_{r(s)=0} = G(s)(1 - Q_d(s)\hat{G}(s)), \tag{1.28}$$

$$T(s) \equiv \left.\frac{y(s)}{r(s)}\right|_{d(s)=0} = G(s)Q_r(s). \tag{1.29}$$

Note that $S(s)$ is affected by the feedback compensator $Q_d(s)$, whereas $T(s)$ is affected by the feedforward compensator $Q_r(s)$. That is, $Q_d(s)$ serves for disturbance rejection, whereas $Q_r(s)$ functions to enhance the tracking performance. Since the sensitivity function and the complementary sensitivity function can be designed independently, it is called the two DOF controller.

1.2.7 Variations of Two DOF Structures

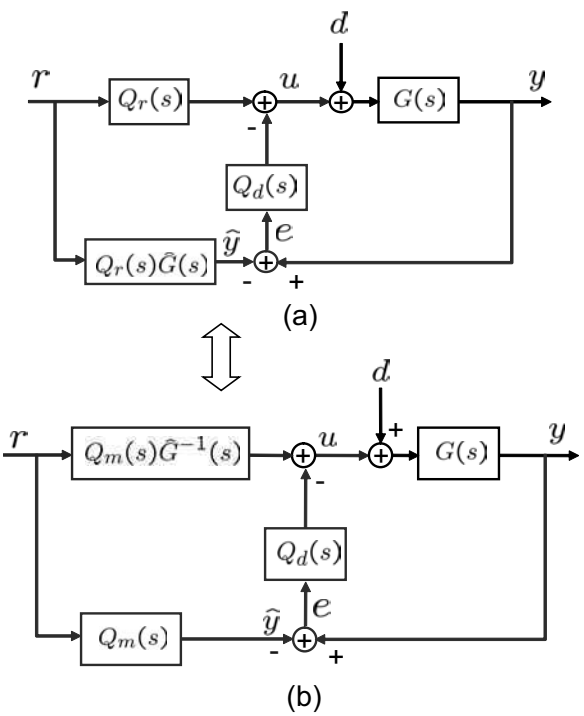

Figure 1.23: Equivalent two DOF structures when $Q_r(s) = Q_m(s)G(s)^{-1}$.

Ideal performances, $S = 0$ and $T = 1$ are obtained when $Q_d(s) = G(s)^{-1}$ and $Q_r(s) = G(s)^{-1}$. In this case, the controllers will be improper, i.e., they will contain

differentiators. Therefore, the ideal controller cannot be realized practically. Despite not being perfect, it is desired to let $S \approx 0$ and $T \approx 1$ in a low frequency range. To resolve the problem of differentiation, we put a low-pass filter $Q_m(s)$ in font of the inverse dynamics $G(s)^{-1}$, i.e.,

$$Q_r(s) = Q_m(s)G(s)^{-1}, \tag{1.30}$$

where $Q_m(s)$ is a filter that prevents improperness of $Q_r(s)$. Thus, $Q_m(s)$ is desired to have a unity gain in a low frequency region. A practical choice is

$$Q_m(s) = \frac{1}{(\tau s + 1)^n}, \tag{1.31}$$

where $1/\tau > 0$ represents a cut-off frequency and $n > 0$ is an integer. As τ gets smaller, the wider (frequency) range of unity gain is obtained. The order of the filter, n needs to be the same as the relative degree of $G(s)$. Then $Q_m(s)G(s)^{-1}$ turns out to be proper.

Variations of the IMC block diagram are shown in Fig. 1.23 [5]. Note that the IMC in Fig. 1.22 is equivalent to the one in Fig. 1.23 (a). With the feedforward compensator, (1.30), the block diagram turns out to be Fig. 1.23 (b). The controller shown in Fig. 1.23 (b) is the two DOF controller containing inverse dynamics. The role of $Q_d(s)$ is to nullify the effects of the disturbance, $d(s)$ in a low frequency region. In [4], a PI controller was selected for $Q_d(s)$.

1.2.8 Load Torque Observer

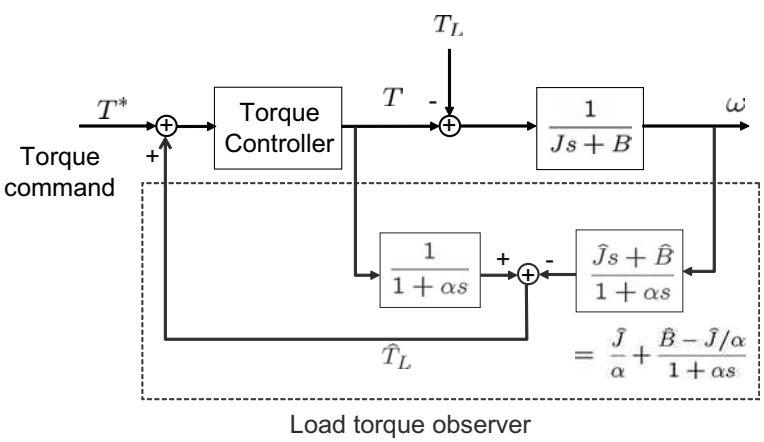

Figure 1.24: A load torque observer.

A load torque observer is often called a disturbance observer. The load torque is different from the state observer, since the disturbance is not a state variable. It is quite often used in the speed loop to reject the disturbance torque. Fig. 1.24 shows

a typical structure of the load torque observer, where the load torque, T_L, is treated as an external disturbance. The objective is to estimate the unknown load torque and feedback it to the input of the torque controller, so that the unknown load is compensated before the speed (PI) controller is activated.

In the following analysis, the load torque is assumed to be a constant. The load torque is filtered out by the plant dynamics, so that the observer has, in nature, a structure of the inverse dynamics. To circumvent the use of the differentiator, $\hat{J}s + \hat{B}$, it utilizes a low-pass filter with unity gain, $1/(1+\alpha s)$[7]. Note that the impulse response is equal to $\frac{1}{\alpha}e^{-\frac{1}{\alpha}t}u_s(t)$, where $u_s(t)$ is the unit step function. Since $\int_0^\infty \frac{1}{\alpha}e^{-\frac{1}{\alpha}t}dt = 1$ independently of α, it approaches the delta function as α decreases to zero. Therefore, practically $\frac{\hat{J}s+\hat{B}}{1+\alpha s}\omega_r(s) \approx (\hat{J}s+\hat{B})\omega_r(s)$ for a large $\alpha > 0$ while a direct differentiation is avoided:

$$\frac{\hat{J}s+\hat{B}}{1+\alpha s}\omega_r(s) = \frac{\hat{J}}{\alpha} + \frac{\hat{B}-\hat{J}/\alpha}{1+\alpha s}\omega_r(s).$$

The same low-pass filter is applied to the input, $T(s)$. Then, a torque estimate $\hat{T}_L$ is obtained as

$$\hat{T}_L = \frac{1}{1+\alpha s}T(s) - \frac{\hat{J}s+\hat{B}}{1+\alpha s}\omega(s). \tag{1.32}$$

Hong and Nam[7] put an artificial delay in the input path of the load torque (disturbance) observer for a system with measurement delay as shown in Fig. 1.25. It was shown that the observer with the artificial delay showed a better performance like a Smith predictor [8].

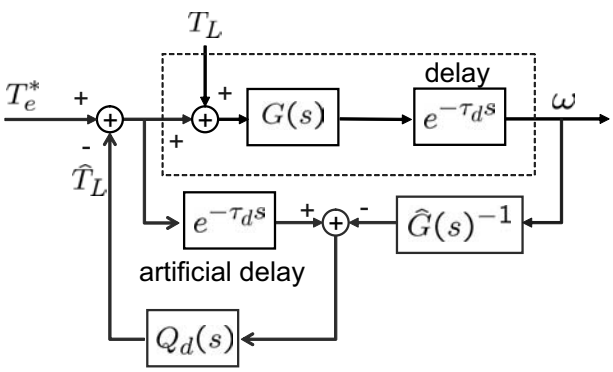

Figure 1.25: A load torque observer with an artificial delay in the input path.

1.2.9 Feedback Linearization

Consider a single input, single output nonlinear system

$$\dot{x} = f(x) + ug(x), \tag{1.33}$$
$$y = h(x), \tag{1.34}$$

where $x \in \mathbb{R}^n$, $f : \mathbb{R}^n \to \mathbb{R}^n$, $g : \mathbb{R}^n \to \mathbb{R}^n$, $h : \mathbb{R}^n \to \mathbb{R}$, $u : [0, \infty) \to \mathbb{R}^n$. Assume that f, g, and h are differentiable infinitely. Let

$$L_f h \equiv < dh, f >= \sum_{i=1}^{n} \frac{\partial h}{\partial x_i} f_i \,.$$

Correspondingly, define for $k \geq 1$

$$L_f^k h \equiv < dL_f^{k-1} h, f > \,.$$

We construct a new map $T : \mathbb{R}^n \to \mathbb{R}^n$ defined by

$$T(x) = \begin{bmatrix} h \\ L_f h \\ \vdots \\ L_f^{n-1} h \end{bmatrix} . \tag{1.35}$$

Let x_e be an equilibrium point of $f(x)$, i.e., $f(x_e) = 0$. Suppose further that the Jacobian $DT(x_e)$ has rank n, i.e.,

$$\text{rank}\,[DT(x_e)] = \text{rank} \begin{bmatrix} dh \\ dL_f h \\ \vdots \\ L_f^{n-1} h \end{bmatrix} (x_e) = n. \tag{1.36}$$

Then T is a local diffeomorphism in a neighborhood of x_e. In other words, T is a differentiable homeomorphism. When a function is one-to-one and onto, and its inverse is continuous, then the function is called homeomorphism.

We define a new coordinate system $z = T(x)$. Assume further that

$$\begin{cases} L_g L_f^k h = 0, & 0 \leq k \leq n-2. \\ L_g L_f^{n-1} h \neq 0. \end{cases} \tag{1.37}$$

Then, it follows from (1.37) that

$$\dot{z} = \begin{bmatrix} L_{f+ug} h \\ L_{f+ug} L_f h \\ \vdots \\ L_{f+ug} L_f^{n-1} h \end{bmatrix} = \begin{bmatrix} L_f h \\ L_f^2 h \\ \vdots \\ L_f^n h + u L_g L_f^{n-1} h \end{bmatrix} . \tag{1.38}$$

Now, we choose

$$u = \frac{1}{L_g L_f^{n-1} h} (v - L_f^n h). \tag{1.39}$$

Then it follows from (1.38) that

$$\dot{z} = \begin{bmatrix} z_2 \\ z_3 \\ \vdots \\ z_n \\ v \end{bmatrix} = \begin{bmatrix} 0 & 1 & 0 & \cdots & 0 \\ 0 & 0 & 1 & \cdots & 0 \\ & & & \ddots & \\ 0 & 0 & 0 & \cdots & 1 \\ 0 & 0 & 0 & \cdots & 0 \end{bmatrix} z + \begin{bmatrix} 0 \\ 0 \\ \vdots \\ 0 \\ 1 \end{bmatrix} v\,. \tag{1.40}$$

That is, through coordinate transformation (1.35) and feedback (1.39), a linear system is obtained[9]. Let $ad_f g = [f, g]$ and $ad_f^k g = [f, ad_f^{k-1} g]$, where $[f, g]$ is the Lie bracket of vector fields f and g. A necessary and sufficient condition for the existence of a function that satisfies (1.37) is

$$\begin{aligned} &\{g, ad_f g, \cdots, ad_f^{n-1} g\} && \text{are linearly independent;} \\ &\{g, ad_f g, \cdots, ad_f^{n-2} g\} && \text{are involutive,} \end{aligned}$$

where involutive means a distribution is closed under Lie bracket operation[9]. An application of feedback linearization theory to a PWM converter-inverter system is found in [10].

Bibliography

[1] R. Ordenburger, Frequency response data presentation, Standards and Design Criteria, *IEEE Trans. ASME*, No. 53-A-11, Nov. pp. 1155 – 1954.

[2] H. Gross, J. Hamann and G. Wiegartner, *Electrical Feed Drives in Automation, Basics, Computation, Dimensioning*, Publics MCD Corporate Publishing, Berlin, 2001.

[3] M. Morari and E. Zafirious, *Robust Process Control*. New Jersey: Prentice Hall, 1989, Chap. 2 – 3.

[4] N. Hur, K. Nam, and S. Won, A two degrees of freedom current control scheme for dead-time compensation, *IEEE Trans. Ind. Electron.*, Vol. 47, pp. 557 – 564, June 2000.

[5] T. Sugie and T. Yoshikawa, General solution of robust tracking problem in two-degree-of-freedom control systems, *IEEE Trans. Automat. Contr.*, Vol. AC-31, pp. 552 – 554, June 1986.

[6] B. C. Kuo and F Golnaraghi, *Automatic Control Systems,* 8th Ed., Wiley, 2003.

[7] K. Hong and K. Nam, A load torque compensation scheme under the speed measurement delay, *IEEE Trans. Ind. Electron.*, Vol. 45, no. 2, pp. 283 – 290, Apr. 1998.

[8] K. J. Astrom, C. C. Hang, and B. C. Lim, A new Smith predictor for controlling a process with an integrator and long dead-time, *IEEE Trans. Automat. Contr.*, Vol. 39, pp. 343 – 345, Feb. 1994.

[9] A. Isidori, *Nonlinear Control Systems II,* Springer, 1999.

[10] J. Jung, S. Lim, and K. Nam, A feedback linearizing control scheme for a PWM converter-inverter having a very small DC-link capacitor, *IEEE Trans. Ind. Appl.*, Vol. 35, No. 5, Sep./Oct., pp. 1124 – 1131, 1999.

Problems

1.1 Consider a DC motor with $r_a = 0.3\Omega$. Assume that voltage drop over the commutator and brush is 1V independently of the speed. The open circuit voltage is 220V at 1000rpm.

a) Calculate the back EMF coefficient, K_b.

b) Calculate current, torque, and efficiency at 950rpm.

1.2 Consider a DC motor with $r_a = 0.5\Omega$, $K_t = 0.4$ Nm/A, and $K_b = 0.4$Vsec/rad. Assume that the maximum armature voltage is $v_a^{max} = 120V$.

a) Determine the motor speed when the load torque is $T_L = 8$Nm.

b) Suppose the back EMF constant is reduced to $K_b = 0.3$Vsec/rad under the same load. Recalculate the speed.

1.3 Consider a DC motor with the following parameters: $r_a = 0.5\Omega$, $L_a = 12$ mH, $K_t = 1.8$ Nm/A, $K_b = 1.8$Vsec/rad, and $J = 0.1\text{kg}\cdot\text{m}^2$. Then the current loop transfer function with a PI controller, $K_p + K_i/s$ is

$$\frac{I_a(s)}{I_a^*(s)} = \frac{(K_p + \frac{K_i}{s})\frac{1}{L_a s + r_a}}{1 + (K_p + \frac{K_i}{s})\frac{1}{L_a s + r_a}} = \frac{\frac{K_p}{L_a}s + \frac{K_i}{L_a}}{s^2 + \frac{r_a + K_p}{L_a}s + \frac{K_i}{L_a}} = \frac{\frac{K_p}{L_a}s + \omega_n^2}{s^2 + 2\zeta\omega_n s + \omega_n^2}$$

a) Determine the proportional gain, K_p such that $\zeta\omega_n = 1000$. Also, choose K_i such that overshoot of the step response is about 10%.

b) The current loop is approximated as

$$\frac{I_a(s)}{I_a^*(s)} = \frac{\frac{K_p}{L_a\omega_n^2}s + 1}{\frac{1}{\omega_n^2}s^2 + 2\frac{\zeta}{\omega_n}s + 1} \approx \frac{1}{2\frac{\zeta}{\omega_n}s + 1}.$$

Refer to the speed loop shown in Fig. 1.16 (a) and use the approximate current model. Given $\omega_2 = 1000$rad/sec, determine the speed loop gain by utilizing (1.13), (1.14) and $\omega_{sc} - \omega_1 = \frac{1}{2}(\omega_2 - \omega_{sc})$.

c) Draw the Bode plot of the speed loop with the gains obtained in c) and determine the phase margin.

1.4 Derive (1.17).

1.5 Consider system shown in Fig. 1.19. Determine the phase margin of the open loop system if we set $K_p = \frac{J}{\tau_\sigma}$. Also, determine the damping coefficient, ζ, for the closed loop system.

1.6 Consider Fig. 1.23 (a). Let

$$\begin{bmatrix} y \\ u \end{bmatrix} = A(s) \begin{bmatrix} r \\ d \end{bmatrix} .$$

Determine $A(s) \in \mathbb{R}^{2\times 2}$.

1.7 Consider a load torque observer for the system with measurement delay shown in Fig. 1.25. Let $G(s) = \hat{G}(s) = 1/(Js + B)$ and $Q_d(s) = 1/(1 + \alpha s)$.

a) Determine the closed-loop transfer function, $\hat{T}_L(s)/T_L(s)$.
b) Repeat the same when the artificial delay is not present in the input side.
c) Approximate $e^{-\tau_d s} \approx 1 - \tau_d s$. Discuss from the stability viewpoint why the observer with the artificial delay is better compared with the ordinary one.

Chapter 2

Rotating Field Theory

In AC machines, windings are distributed in such a way that a rotating magnetic field is generated by a polyphase AC source. An ideal three-phase voltage source consists of three AC voltage sources equal in magnitude and displaced by phase angles of 120°. Apart from the efficiency in electric power transmission, the three-phase system allows for the generation of a rotating field. The flux, voltage, and current of a three-phase system are represented as vectors in the complex plane since they satisfy the balance condition, for example, $v_a + v_b + v_c = 0$ in the three-phase voltage (v_a, v_b, v_c). Transformation maps into the stationary and rotating (synchronous) dq-frames are illustrated in this chapter.

2.1 Construction of Rotating Field

A photograph of an induction motor stator is shown in Fig. 2.1. The stator is constructed by stacking punched lamination steel sheets and then winding the stator coils through the slots on the stator core. Fig. 2.2 shows the three-phase windings in a schematic view of an AC motor cross section. The axis of the a-phase current is aligned to the direction of flux generated by the a-phase current flow. Flux direction can be easily determined by applying the right-hand rule. The same rule applies to b and c phase windings. In Fig. 2.2 (b), flux directions are symbolized by the directions of coils.

Fig. 2.3 shows a cut and stretched view of the a-phase stator winding consisting of four pairs (a_1, a_1'), (a_2, a_2'), (a_3, a_3'), and (a_4, a_4'). Since the super-position law is applied, the resulting magneto motive force (MMF) resembles stairs with rotational symmetry, i.e., $\mathrm{MMF}(\theta) = -\mathrm{MMF}(\theta + \pi)$.

2.1.1 MMF Harmonics of Distributed Windings

The number of slots per phase per pole is denoted by q; the closer the MMF approaches to a sinusoidal wave, the higher q becomes. If a number of slots per phase per pole is equal to one ($q = 1$), then the corresponding MMF is a square wave as

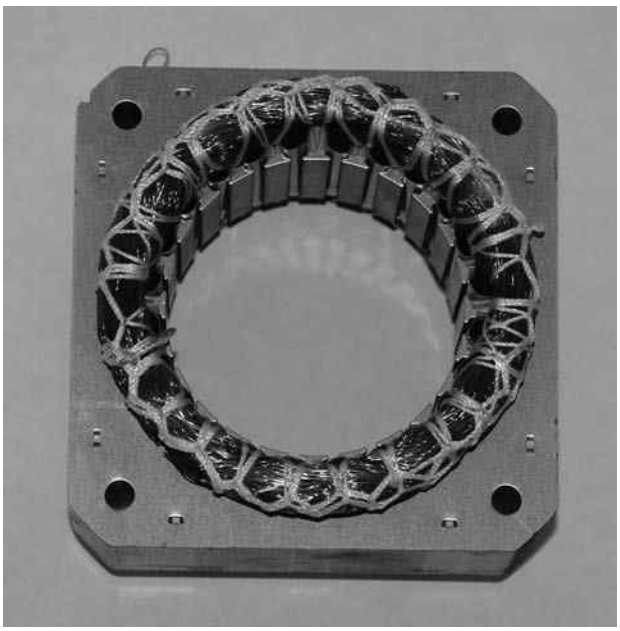

Figure 2.1: Wound stator of an induction motor.

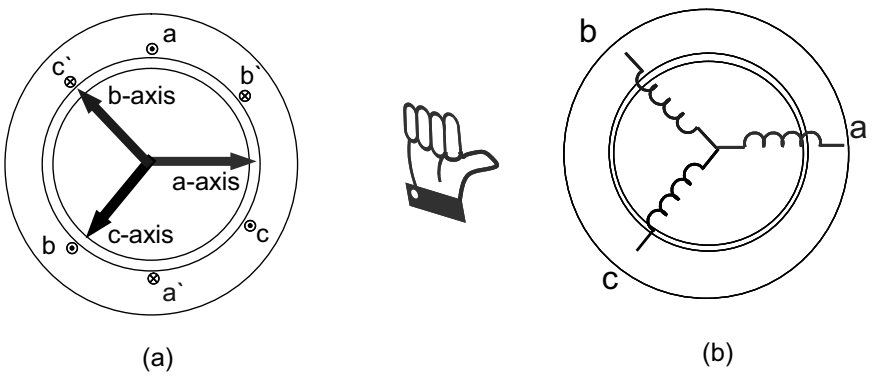

Figure 2.2: Simplified cross-sectional view of AC motor with stator phase windings.

shown in Fig. 2.4 (a). Assume that the pole pitch is τ_p and that the number of coil turns is N. According to Fourier series expansion, the square wave MMF is expressed as the infinite sum:

$$\text{MMF} = \frac{4}{\pi}\frac{IN}{2}\left(\cos\frac{\pi}{\tau_p}\theta - \frac{1}{3}\cos\frac{3\pi}{\tau_p}\theta + \frac{1}{5}\cos\frac{5\pi}{\tau_p}\theta - \frac{1}{7}\cos\frac{7\pi}{\tau_p}\theta + \cdots\right) \tag{2.1}$$

A sum up to 7th order is shown in Fig. 2.4 (b).

Fig. 2.5 shows the case of a fractional pitch winding ($W/\tau_p = 2/3$), where τ_p is

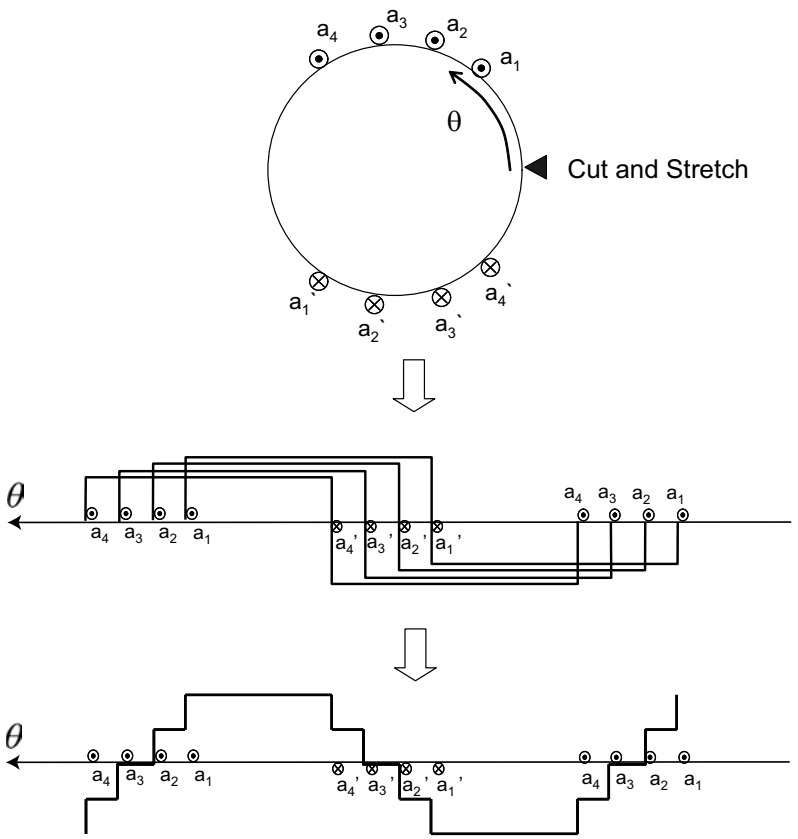

Figure 2.3: Superposition of MMFs of distributed windings.

the pole pitch and W is the coil span. Then the MMF is given by

$$\text{MMF}_{(q=2)} = \frac{NI}{2}\frac{4}{\pi}\sum_{n=1,3,5,\cdots}\frac{1}{n}k_{p(n)}\cos\frac{n\pi}{\tau_p}. \tag{2.2}$$

Note that $\frac{4}{\pi}\frac{1}{n}k_{p(n)}$ corresponds to the Fourier coefficients. Thus it should follow that

$$\begin{aligned}\frac{4}{\pi}\frac{1}{n}k_{p(n)} &\equiv \frac{2}{\pi}\int_0^{\pi}\text{MMF}(\theta)\cos(n\theta)d\theta \\ &= \frac{4}{\pi}\int_0^{\frac{W}{\tau_p}\frac{\pi}{2}}\cos(n\theta)d\theta \\ &= \frac{4}{\pi}\frac{1}{n}\sin\left(n\frac{W}{\tau_p}\frac{\pi}{2}\right).\end{aligned} \tag{2.3}$$

Therefore, it turns out that

$$k_{p(n)} = \sin\left(n\frac{W}{\tau_p}\frac{\pi}{2}\right). \tag{2.4}$$

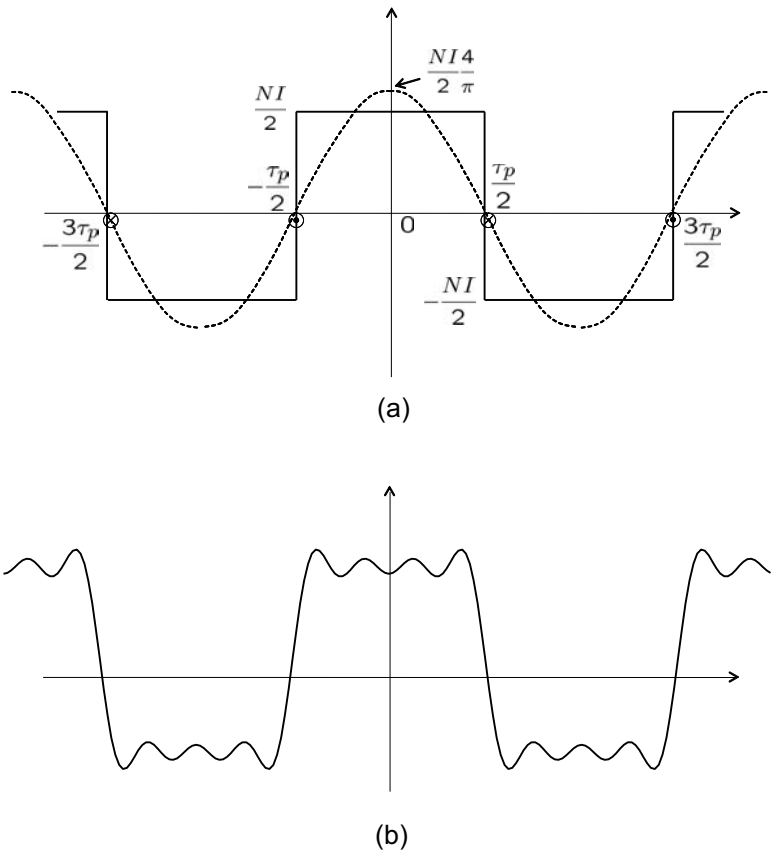

Figure 2.4: Fourier series expansion: (a) square wave MMF and its fundamental component and (b) approximation up to 7th order.

Note here that a fractional pitch factor makes the MMF shape closer to a sinusoidal wave, i.e., it helps reduce the harmonics. Specifically,

$$\left|\sin\left(n\frac{W}{\tau_p}\frac{\pi}{2}\right)\right| \leq \left|\sin\left(n\frac{\pi}{2}\right)\right| = 1.$$

At this time, the fundamental component is also reduced. For example, pitch factors for $W/\tau_p = 5/6$ for different harmonics are listed in Table 2.1. Note in that case, the 5^{th} and 7^{th} components are reduced significantly.

Table 2.1: High order pitch factors for $W/\tau_p = 5/6$.

n	1	3	5	7	9	11	13
$k_{p(n)}$	0.966	-0.707	0.259	0.259	-0.707	0.966	-0.966

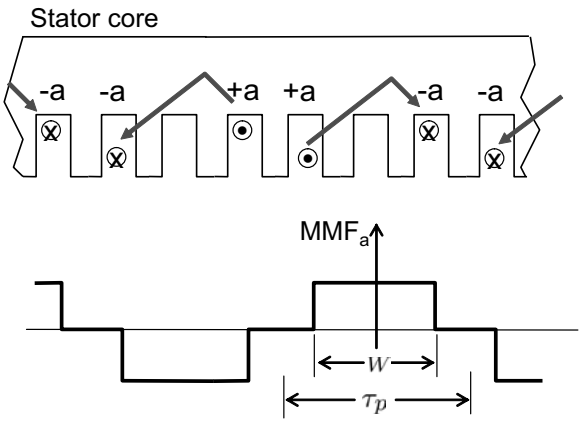

Figure 2.5: MMF for a fractional pitch winding, $W/\tau_p = 2/3$.

2.1.2 Rotating MMF Sum of Three-Phase System

Consider an extreme case in which the phase winding is distributed sinusoidally, i.e., $N_a(\theta) = \frac{N}{2}\sin\theta$, where N is the total number of turns of a phase winding. Note that the winding number is a function of θ and that the sum over a half period is equal to $\int_0^{\pi} \frac{N}{2}\sin\theta d\theta = N$. Sinusoidally distributed winding makes a perfect sinusoidal MMF, as shown in Fig. 2.6 [1]. Then, the MMF is

$$\mathrm{MMF}_a(\theta) = \frac{1}{2}\left(\int_{\theta}^{\pi+\theta} \frac{N}{2}\sin\theta d\theta\right)\cdot i_a = \frac{1}{2}Ni_a\cos\theta. \tag{2.5}$$

Since there are 120° phase displacements between the phase windings, b and c phase MMFs are derived such that

$$\mathrm{MMF}_b = \frac{1}{2}Ni_b\cos(\theta - \frac{2\pi}{3}) \tag{2.6}$$

$$\mathrm{MMF}_c = \frac{1}{2}Ni_c\cos(\theta - \frac{4\pi}{3})\,. \tag{2.7}$$

Suppose that the following balanced stator currents flow in the phase windings:

$$i_a = I\cos(\omega t), \tag{2.8}$$

$$i_b = I\cos(\omega t - \frac{2\pi}{3}), \tag{2.9}$$

$$i_c = I\cos(\omega t - \frac{4\pi}{3}). \tag{2.10}$$

Then, the total MMF is equal to

$$\mathrm{MMF}_{sum} = \mathrm{MMF}_a + \mathrm{MMF}_b + \mathrm{MMF}_c = \frac{1}{2}NI\Big[\cos\theta\cos\omega t + \cos(\theta - \frac{2\pi}{3})\cos(\omega t - \frac{2\pi}{3}) + \cos(\theta - \frac{4\pi}{3})\cos(\omega t - \frac{4\pi}{3})\Big]. \tag{2.11}$$

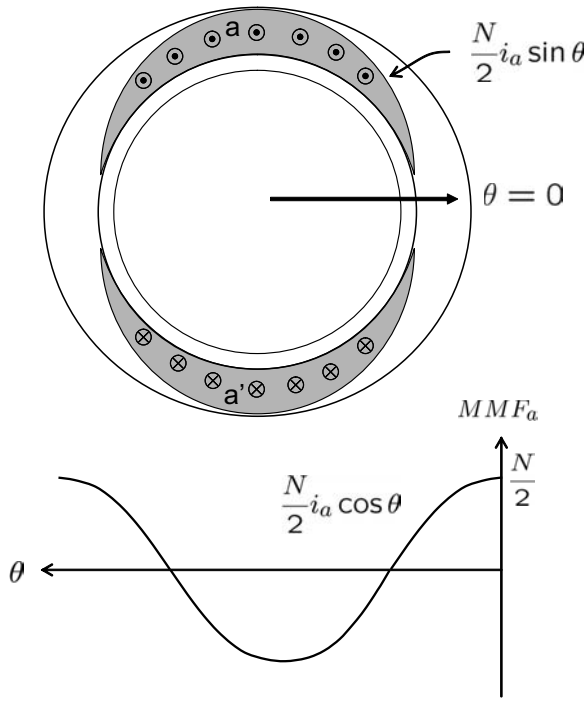

Figure 2.6: MMF made by sinusoidally distributed windings.

Utilizing the cosine law, it follows that

$$\cos\theta\cos\omega t = \frac{1}{2}\left(\cos(\theta+\omega t)+\cos(\theta-\omega t)\right),$$
$$\cos(\theta-\frac{2\pi}{3})\cos(\omega t-\frac{2\pi}{3}) = \frac{1}{2}\left(\cos(\theta+\omega t-\frac{4\pi}{3})+\cos(\theta-\omega t)\right),$$
$$\cos(\theta-\frac{4\pi}{3})\cos(\omega t-\frac{4\pi}{3}) = \frac{1}{2}\left(\cos(\theta+\omega t-\frac{8\pi}{3})+\cos(\theta-\omega t)\right).$$

Note the identity

$$\cos(\theta+\omega t)+\cos(\theta+\omega t-\frac{4\pi}{3})+\cos(\theta+\omega t-\frac{2\pi}{3}) = 0 \quad \text{for all t.}$$

This implies that the sum of the components rotating in the clockwise direction is equal to zero. Therefore, it follows that

$$\mathrm{MMF}_{sum} = \frac{3}{4} NI\cos(\theta-\omega t). \tag{2.12}$$

This is a traveling wave equation. When we set the angular position as a function of t such that $\theta = \omega t$, the MMF looks constant. This can be interpreted as the MMF is rotating at the electric angular velocity, ω. That is, a traveling MMF is obtained

by applying balanced three-phase current to sinusoidally distributed three-phase windings [1].

Exercise 2.1
Demonstrate that the MMF rotates in the reverse direction (clockwise) if we change the motor terminal connection such that $i_a = I\cos(\omega t)$, $i_b = I\cos(\omega t - \frac{4\pi}{3})$, and $i_c = I\cos(\omega t - \frac{2\pi}{3})$.

Exercise 2.2
Consider a two-phase motor as shown in Fig. 2.7. The two stator windings are distributed sinusoidally, and have 90° phase angle difference; $\text{MMF}_a = \frac{Ni_a}{2}\cos\theta$ and $\text{MMF}_b = \frac{Ni_b}{2}\sin\theta$. Find proper phase currents, i_a and i_b, as functions of time so that the rotating MMF is generated.

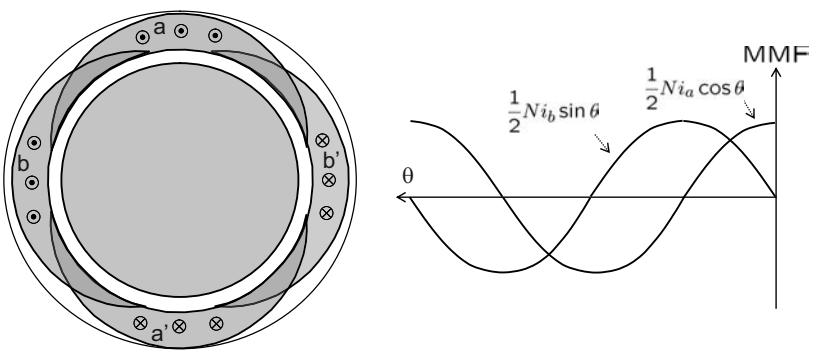

Figure 2.7: Two-phase stator windings and their MMF waveforms.

2.1.3 High-Order Space Harmonics

A perfect sinusoidal traveling MMF (2.12) is obtained only when the coil is distributed sinusoidally and when the three-phase current is also sinusoidal. But in practice, both coil distribution and current have high-order harmonics. The former is called space harmonics; the latter current (time) harmonics. In this section, MMF harmonics are considered for a non-sinusoidal coil distribution.

Consider the case of the concentrated windings ($q = 1$) shown in Fig. 2.4. Based on (2.37), it follows that

$$\text{MMF}_a = \frac{4}{\pi}\frac{Ni_a}{2}\left[\cos\frac{\pi}{\tau_p}\theta - \frac{1}{3}\cos 3\frac{\pi}{\tau_p}\theta + \frac{1}{5}\cos 5\frac{\pi}{\tau_p}\theta - \frac{1}{7}\cos 7\frac{\pi}{\tau_p}\theta\cdots\right]. \quad (2.13)$$

Since the b–phase MMF is shifted by $\frac{2\tau_p}{3}$,

$$\begin{aligned}\mathrm{MMF}_b &= \frac{4}{\pi}\frac{Ni_b}{2}\left[\cos\frac{\pi}{\tau_p}(\theta-\frac{2\tau_p}{3})-\frac{1}{3}\cos 3\frac{\pi}{\tau_p}(\theta-\frac{2\tau_p}{3})+\frac{1}{5}\cos 5\frac{\pi}{\tau_p}(\theta-\frac{2\tau_p}{3})\right.\\ &\quad\left.-\frac{1}{7}\cos 7\frac{\pi}{\tau_p}(\theta-\frac{2\tau_p}{3})+\cdots\right]. \qquad (2.14)\end{aligned}$$

Note that

$$\begin{aligned}\cos(3\frac{\pi}{\tau_p}\theta-2\pi) &= \cos(3\frac{\pi}{\tau_p}\theta)\\ \cos(5\frac{\pi}{\tau_p}\theta-\frac{10}{3}\pi) &= \cos(5\frac{\pi}{\tau_p}\theta-\frac{4\pi}{3})\\ \cos(7\frac{\pi}{\tau_p}\theta-\frac{14}{3}\pi) &= \cos(7\frac{\pi}{\tau_p}\theta-\frac{2\pi}{3}).\end{aligned}$$

Thus,

$$\begin{aligned}\mathrm{MMF}_b &= \frac{4}{\pi}\frac{Ni_b}{2}\left[\cos(\frac{\pi}{\tau_p}\theta-\frac{\pi}{3})-\frac{1}{3}\cos(3\frac{\pi}{\tau_p}\theta)+\frac{1}{5}\cos(5\frac{\pi}{\tau_p}\theta-\frac{4\pi}{3})\right.\\ &\quad\left.-\frac{1}{7}\cos(7\frac{\pi}{\tau_p}\theta-\frac{2\pi}{3})+\cdots\right]. \qquad (2.15)\end{aligned}$$

Since the c–phase MMF is shifted by $\frac{4\tau_p}{3}$,

$$\begin{aligned}\mathrm{MMF}_c &= \frac{4}{\pi}\frac{Ni_c}{2}\left[\cos(\frac{\pi}{\tau_p}\theta-\frac{4\pi}{3})-\frac{1}{3}\cos(3\frac{\pi}{\tau_p}\theta)+\frac{1}{5}\cos(5\frac{\pi}{\tau_p}\theta-\frac{2\pi}{3})\right.\\ &\quad\left.-\frac{1}{7}\cos(7\frac{\pi}{\tau_p}\theta-\frac{4\pi}{3})+\cdots\right]. \qquad (2.16)\end{aligned}$$

Suppose that balanced sinusoidal currents flow, i.e., let $i_a = I\cos\omega t$, $i_b = I\cos(\omega t-\frac{2\pi}{3})$, and $i_c = I\cos(\omega t-\frac{4\pi}{3})$. We take the sum componentwise: $\mathrm{MMF}_{sum(n)} = \mathrm{MMF}_{a(n)} + \mathrm{MMF}_{b(n)} + \mathrm{MMF}_{c(n)}$. The sum of the 3^{rd}-order components is equal to

$$\begin{aligned}\mathrm{MMF}_{sum(3)} &= -\frac{4}{3\pi}\frac{NI}{2}\left(\cos(\omega t)+\cos(\omega t-\frac{2\pi}{3})+\cos(\omega t-\frac{4\pi}{3})\right)\cos(3\frac{\pi}{\tau_p}\theta)\\ &= 0.\end{aligned}$$

The sum of the 5^{th}-order components is equal to

$$\begin{aligned}\mathrm{MMF}_{sum(5)} &= \frac{4}{5\pi}\frac{NI}{2}\left(\cos 5\frac{\pi}{\tau_p}\theta\cos\omega t+\cos(5\frac{\pi}{\tau_p}\theta-\frac{4}{3}\pi)\cos(\omega t-\frac{2\pi}{3})\right.\\ &\quad\left.+\cos(5\frac{\pi}{\tau_p}\theta-\frac{2}{3}\pi)\cos(\omega t-\frac{4\pi}{3})\right)\\ &= \frac{4}{5\pi}\frac{NI}{2}\frac{3}{2}\cos(\omega t+5\frac{\pi}{\tau_p}\theta). \qquad (2.17)\end{aligned}$$

Similarly, the sum of the 7^{th}-order components is equal to

$$\text{MMF}_{sum(7)} = -\frac{4}{7\pi}\frac{NI}{2}\frac{3}{2}\cos(\omega t - 7\frac{\pi}{\tau_p}\theta). \tag{2.18}$$

Hence, the total sum is

$$\text{MMF}_{sum} = \frac{4}{\pi}\frac{NI}{2}\frac{3}{2}\left[\cos(\omega t - \frac{\pi}{\tau_p}\theta) + \frac{1}{5}\cos(\omega t + 5\frac{\pi}{\tau_p}\theta) - \frac{1}{7}\cos(\omega t - 7\frac{\pi}{\tau_p}\theta) + \cdots\right].$$

It should be noted from (2.7), (2.17), and (2.18) that

- the 3^{rd}-order harmonic component does not appear in the three-phase system;
- the 5^{th}-order harmonic component constitutes a negative sequence in the MMF sum, i.e., it travels at the speed of $1/5\omega$ in the opposite direction (clockwise) to that of the fundamental component.
- the 7^{th}-order harmonic component constitutes a positive sequence in the MMF sum, i.e., it travels the speed of $1/7\omega$ in the same direction (counterclockwise) as that of the fundamental component.

Generalizing the above, it follows that

i) $(\nu - 1 = 6m)$ This case corresponds to $\nu = 7, 13, 19, \cdots$ and

$$\text{MMF}_{sum(\nu)} = -\frac{4NI}{\nu\pi 2}\frac{3}{2}\cos\left(\omega t - \nu\frac{\pi\theta}{\tau_p}\right). \tag{2.19}$$

These MMF components rotate in the same direction as the fundamental component.

ii) $(\nu + 1 = 6m)$ This case corresponds to $\nu = 5, 11, 17, \cdots$ and

$$\text{MMF}_{sum(\nu)} = \frac{4NI}{\nu\pi 2}\frac{3}{2}\cos\left(\omega t + \nu\frac{\pi\theta}{\tau_p}\right). \tag{2.20}$$

These MMF components rotate in the opposite direction to the fundamental component.

iii) $(\nu = 6m - 3)$ This case corresponds to $\nu = 3, 9, 15, 21\cdots$ and

$$\text{MMF}_{sum(\nu)} = 0. \tag{2.21}$$

2.2 Change of Coordinates

Geometrically a, b, and c phase windings are placed with 120° of angle difference. If a balanced three-phase current is applied to the three-phase windings, then a rotating MMF is generated. Note that *balanced* means the component sum is equal to zero at all times, while keeping 120° of phase angle difference. This makes a constraint among three variables. Thus, the balanced three-phase variables have only two degrees of freedom and can be mapped into a complex plane. The best way to construct a mapping rule from three-phase variables to the complex plane is to visualize the flux vector that would be generated in the cross-section of the motor. In other words, it is useful to assign a vector in the complex plane to a set of balanced three-phase currents, which aligns with the real flux vector, that would be generated as a consequence of current injection.

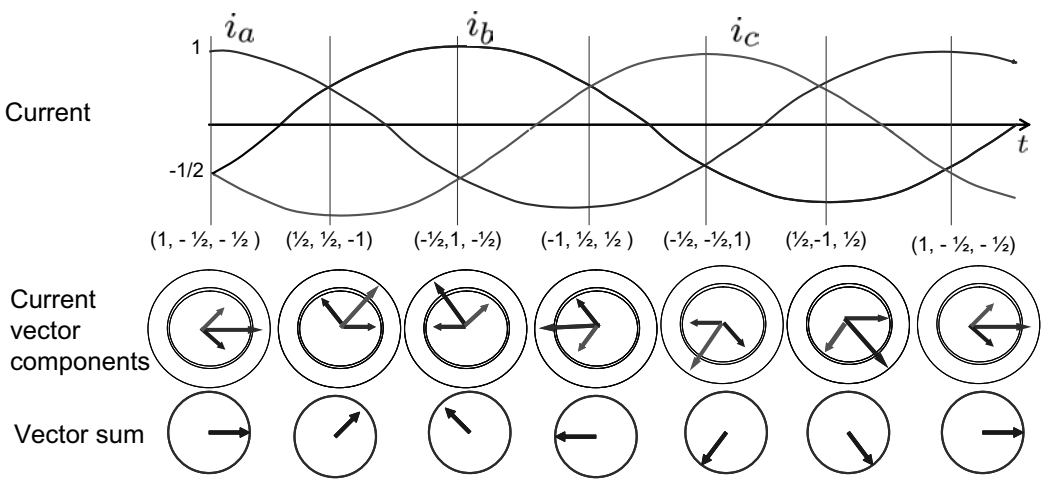

Figure 2.8: Rotation of the current vector corresponding to the balanced three-phase currents.

Fig. 2.8 shows the progressive motion of the MMF vectors when a sinusoidal three-phase current source is applied. When $(i_a, i_b, i_c) = (1, -1/2, -1/2)$, an MMF vector aligned with a–axis is obtained. Similarly, an MMF vector with 60° rotation angle is obtained when $(i_a, i_b, i_c) = (1/2, 1/2, -1)$, corresponding to $\omega t = \pi/3$. This shows graphically how a balanced three-phase source generates the rotating field.

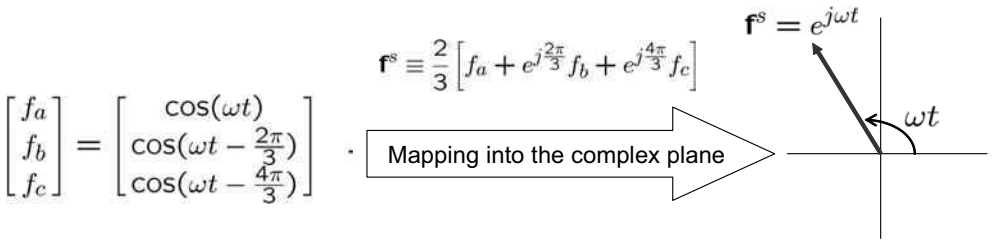

Figure 2.9: Mapping of a three-phase vector into the complex plane.

2.2.1 Mapping into the Stationary Plane

For a vector $\mathbf{f} = [f_a,\ f_b,\ f_c]^T$, we define a map from $\mathbb{R}^3$ into $\mathbb{C}$ such that [2]

$$\begin{aligned} \mathbf{f}^s = f_d^s + j f_q^s &\equiv \frac{2}{3}\left[f_a + e^{j\frac{2\pi}{3}} f_b + e^{j\frac{4\pi}{3}} f_c\right] \\ &= \frac{2}{3}(f_a - \frac{1}{2} f_b - \frac{1}{2} f_c) + j\frac{2}{3}(\frac{\sqrt{3}}{2} f_b - \frac{\sqrt{3}}{2} f_c)\,. \end{aligned} \tag{2.22}$$

Note that $\frac{2}{3}$ is multiplied to retain the peak value after mapping.

Exercise 2.3
Let $[f_a,\ f_b,\ f_c]^T = [\cos\omega t,\ \cos(\omega t - \frac{2\pi}{3}),\ \cos(\omega t - \frac{4\pi}{3})]^T$. Then, show that $\mathbf{f}^s = \cos\omega t + j\sin\omega t$.

Solution.

$$\begin{aligned} \mathbf{f}^s &\equiv \frac{2}{3}\left[\cos\omega t + e^{j\frac{2\pi}{3}}\cos(\omega t - \frac{2\pi}{3}) + e^{j\frac{4\pi}{3}}\cos(\omega t - \frac{4\pi}{3})\right] \\ &= \frac{2}{3}\left[\frac{1}{2}(e^{j\omega t} + e^{-j\omega t}) + \frac{1}{2}e^{j\frac{2\pi}{3}}(e^{j(\omega t - \frac{2\pi}{3})}) + e^{-j(\omega t - \frac{2\pi}{3})}) \right. \\ &\qquad \left. + \frac{1}{2}e^{j\frac{4\pi}{3}}(e^{j(\omega t - \frac{4\pi}{3})} + e^{-j(\omega t - \frac{4\pi}{3})})\right] \\ &= \frac{2}{3}\left[\frac{3}{2}e^{j\omega t} + \frac{1}{2}\underbrace{\left(e^{-j\omega t} + e^{-j(\omega t - \frac{4\pi}{3})} + e^{-j(\omega t - \frac{8\pi}{3})}\right)}_{=0}\right] \\ &= e^{j\omega t} = \cos\omega t + j\sin\omega t. \end{aligned} \tag{2.23}$$

Note that the positive sequence components are identical, whereas the negative sequence components are summed to be zero. ■

Equation (2.23) shows that the injection of the three-phase AC current $[\cos\omega t,\ \cos(\omega t\ -\frac{2\pi}{3}),\ \cos(\omega t - \frac{4\pi}{3})]$ creates a rotating vector $e^{j\omega t}$ in the complex plane.

Fig. 2.9 shows a schematic representation of the mapping into the stationary frame. However, it is worthwhile to note that the direction of the current sum vector is identical to the direction of $\mathbf{f}^s$ in the complex plane. That is, the direction of $\mathbf{f}^s$ is the same as that of the flux (current) vector in the cross-sectional plane of a motor. Furthermore, the peak value of the *abc* variable is the same as that of the *dq* variable. To denote the mapping into the stationary frame, the transformed variable is marked with superscript '*s*'.

The inverse map is obtained as

$$\begin{aligned} f_a &= \mathcal{R}e(\mathbf{f}^s) \\ f_b &= \mathcal{R}e(e^{j\frac{4\pi}{3}}\mathbf{f}^s) \\ f_c &= \mathcal{R}e(e^{j\frac{2\pi}{3}}\mathbf{f}^s). \end{aligned} \tag{2.24}$$

where $\mathcal{R}e(\cdot)$ means taking the real part of a variable in parentheses.

Exercise 2.4
Show that $f_a = \mathcal{R}e(\mathbf{f}^s)$.

Solution.

$$\mathbf{f}^s = \frac{2}{3}\left[f_a - \frac{1}{2}(f_b + f_c) + j\frac{\sqrt{3}}{2}(f_b - f_c)\right] = f_a + j\frac{1}{\sqrt{3}}(f_b - f_c).$$

■

Consider a three-phase current with 5^{th}-order harmonics:

$$\begin{bmatrix} i_a \\ i_b \\ i_c \end{bmatrix} = \begin{bmatrix} \cos(\omega t) \\ \cos(\omega(t - \frac{2\pi}{3\omega})) \\ \cos(\omega(t - \frac{4\pi}{3\omega})) \end{bmatrix} + \frac{1}{5}\begin{bmatrix} \cos(5\omega t) \\ \cos(5\omega(t - \frac{2\pi}{3\omega})) \\ \cos(5\omega(t - \frac{4\pi}{3\omega})) \end{bmatrix}. \tag{2.25}$$

The current vector is obtained such that

$$\begin{aligned} \mathbf{i}^s &= e^{j\omega t} + \frac{2}{3}\frac{1}{5}[\cos(5\omega t) + \cos(5\omega t - \frac{4\pi}{3})e^{j\frac{2\pi}{3}} + \cos(5\omega t - \frac{2\pi}{3})e^{j\frac{4\pi}{3}}] \\ &= e^{j\omega t} + \frac{1}{5}e^{-j5\omega t}. \end{aligned}$$

Note that the 5^{th}-order harmonic component has negative sign in the exponent, indicating it constitutes a negative sequence. That is, the 5^{th}-order harmonic makes a clockwise rotation along a small circle, while the fundamental component rotates counterclockwise. The trajectory plot is shown is Fig. 2.10 (a).

Similarly, consider a three-phase current with 7^{th}-order harmonics:

$$\begin{bmatrix} i_a \\ i_b \\ i_c \end{bmatrix} = \begin{bmatrix} \cos(\omega t) \\ \cos(\omega(t - \frac{2\pi}{3\omega})) \\ \cos(\omega(t - \frac{4\pi}{3\omega})) \end{bmatrix} - \frac{1}{7}\begin{bmatrix} \cos(7\omega t) \\ \cos(7\omega(t - \frac{2\pi}{3\omega})) \\ \cos(7\omega(t - \frac{4\pi}{3\omega})) \end{bmatrix}. \tag{2.26}$$

Then, it follows that $\mathbf{i}^s = e^{j\omega t} - \frac{1}{7}e^{j7\omega t}$. Note that the 7^{th}-order makes a counterclockwise rotation. The trajectory plot is shown Fig. 2.10 (b).

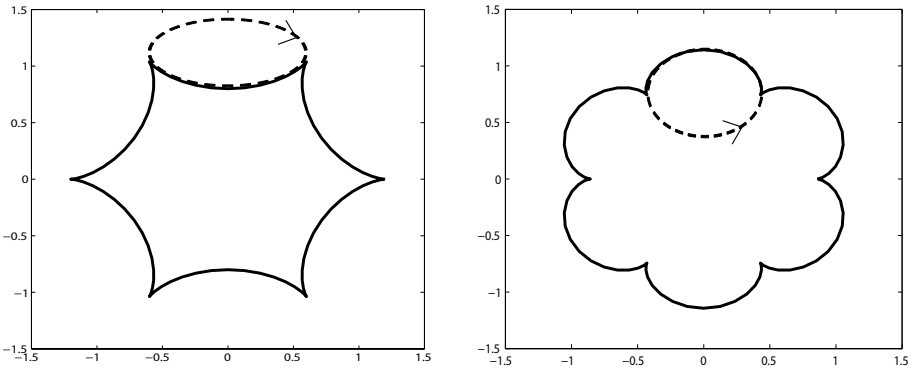

Figure 2.10: Current trajectories in the complex plane: (a) $e^{j\omega t} + \frac{1}{5}e^{-j5\omega t}$ and (b) $e^{j\omega t} - \frac{1}{7}e^{j7\omega t}$.

2.2.2 Mapping into the Rotating (Synchronous) Frame

A transformation into the rotating frame is defined by

$$\begin{aligned} \mathbf{f}^e = f_d^e + j f_q^e &\equiv e^{-j\theta}\mathbf{f}^s \\ &= e^{-j\theta}\frac{2}{3}\left[f_a(t) + e^{j\frac{2\pi}{3}} f_b(t) + e^{-j\frac{2\pi}{3}} f_c(t)\right] \\ &= \frac{2}{3}\left[e^{-j\theta} f_a(t) + e^{j(-\theta+\frac{2\pi}{3})} f_b(t) + e^{j(-\theta-\frac{2\pi}{3})} f_c(t)\right]. \end{aligned} \quad (2.27)$$

A vector representation in the rotating frame is obtained by multiplying the vector in the stationary frame by $e^{-j\theta}$. The transformation is equivalently written as

$$\begin{aligned} \mathbf{f}^e = f_d^e + j f_q^e &= \frac{2}{3}\left[f_a\cos\theta + f_b\cos(\theta - \frac{2\pi}{3}) + f_c\cos(\theta - \frac{2\pi}{3})\right] \\ &\quad -j\frac{2}{3}\left[f_a\sin\theta + f_b\sin(\theta - \frac{2\pi}{3}) + f_c\sin(\theta + \frac{2\pi}{3})\right]. \end{aligned} \quad (2.28)$$

Exercise 2.5
Let $[f_a,\, f_b,\, f_c]^T = [\cos\omega t,\, \cos(\omega t - \frac{2\pi}{3}),\, \cos(\omega t - \frac{4\pi}{3})]^T$. Show that $\mathbf{f}^e = 1$ when $\theta = \omega t$.

Solution.
Utilizing (2.23), we obtain

$$\mathbf{f}^e = e^{-j\theta}\mathbf{f}^s = e^{-j\theta}e^{j\theta} = 1.$$

■

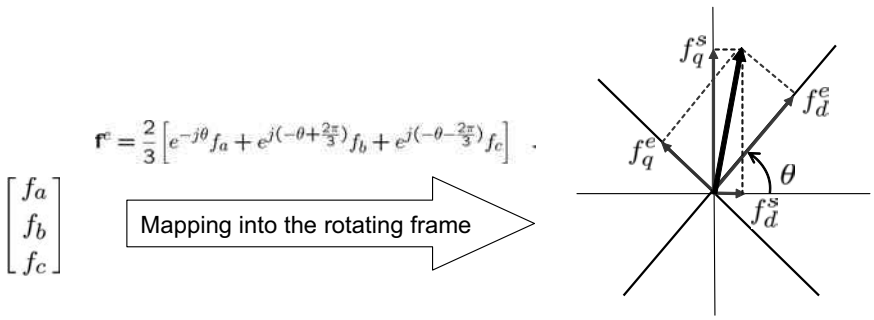

Figure 2.11: Mapping of a three-phase vector into a rotating frame.

This demonstrates that a rotating vector is seen as an invariable constant in a frame that rotates at the same speed. The rotating frame is often called a *synchronous frame* or *exciting frame*. Vectors in the rotating frame are denoted with superscript e.

2.2.3 Formulation via Matrices

Transformations into the stationary and the rotating frames can be manipulated by matrix operations. By equating the real and complex parts separately in (2.22), we obtain

$$\begin{bmatrix} f_d^s \\ f_q^s \\ f_0^s \end{bmatrix} = \frac{2}{3} \begin{bmatrix} 1 & -\frac{1}{2} & -\frac{1}{2} \\ 0 & \frac{\sqrt{3}}{2} & -\frac{\sqrt{3}}{2} \\ \frac{1}{\sqrt{2}} & \frac{1}{\sqrt{2}} & \frac{1}{\sqrt{2}} \end{bmatrix} \begin{bmatrix} f_a \\ f_b \\ f_c \end{bmatrix} . \tag{2.29}$$

Note that $f_0^s = \frac{1}{2}(f_a + f_b + f_c) = 0$ in balanced systems. Similarly, it follows from (2.28) that [1]

$$\begin{bmatrix} f_d^e \\ f_q^e \\ f_0^e \end{bmatrix} = \mathbf{T}(\theta) \begin{bmatrix} f_a \\ f_b \\ f_c \end{bmatrix} , \tag{2.30}$$

where

$$\mathbf{T}(\theta) = \frac{2}{3} \begin{bmatrix} \cos\theta & \cos(\theta - \frac{2\pi}{3}) & \cos(\theta + \frac{2\pi}{3}) \\ -\sin\theta & -\sin(\theta - \frac{2\pi}{3}) & -\sin(\theta + \frac{2\pi}{3}) \\ \frac{1}{\sqrt{2}} & \frac{1}{\sqrt{2}} & \frac{1}{\sqrt{2}} \end{bmatrix} . \tag{2.31}$$

Note that

$$\mathbf{T}(0) = \frac{2}{3} \begin{bmatrix} 1 & -\frac{1}{2} & -\frac{1}{2} \\ 0 & \frac{\sqrt{3}}{2} & -\frac{\sqrt{3}}{2} \\ \frac{1}{\sqrt{2}} & \frac{1}{\sqrt{2}} & \frac{1}{\sqrt{2}} \end{bmatrix} ,$$

which coincides with the matrix in (2.29). Note further that

$$\mathbf{T}(\theta) = \underbrace{\begin{bmatrix} \cos\theta & \sin\theta & 0 \\ -\sin\theta & \cos\theta & 0 \\ 0 & 0 & 1 \end{bmatrix}}_{=\mathbf{R}(\theta)} \frac{2}{3} \begin{bmatrix} 1 & -\frac{1}{2} & -\frac{1}{2} \\ 0 & \frac{\sqrt{3}}{2} & -\frac{\sqrt{3}}{2} \\ \frac{1}{\sqrt{2}} & \frac{1}{\sqrt{2}} & \frac{1}{\sqrt{2}} \end{bmatrix}, \tag{2.32}$$

where $\mathbf{R}(\theta)$ is a matrix which represents rotation of the coordinate frame by θ. That is, map $\mathbf{T}(\theta)$ consists of two parts: One is a map from the (a, b, c)-frame into the stationary dq-frame. The other is a map from the stationary frame into the rotating dq-frame.

The inverse map is calculated as

$$\mathbf{T}^{-1}(\theta) = \begin{bmatrix} \cos\theta & -\sin\theta & \frac{1}{\sqrt{2}} \\ \cos(\theta - \frac{2\pi}{3}) & -\sin(\theta - \frac{2\pi}{3}) & \frac{1}{\sqrt{2}} \\ \cos(\theta + \frac{2\pi}{3}) & -\sin(\theta + \frac{2\pi}{3}) & \frac{1}{\sqrt{2}} \end{bmatrix}. \tag{2.33}$$

Hence,

$$\mathbf{T}^{-1}(0) = \begin{bmatrix} 1 & 0 & \frac{1}{\sqrt{2}} \\ -\frac{1}{2} & \frac{\sqrt{3}}{2} & \frac{1}{\sqrt{2}} \\ -\frac{1}{2} & -\frac{\sqrt{3}}{2} & \frac{1}{\sqrt{2}} \end{bmatrix}.$$

Similarly to the case of forward transformation, $\mathbf{T}^{-1}$ can be decomposed as

$$\mathbf{T}^{-1}(\theta) = \begin{bmatrix} 1 & 0 & \frac{1}{\sqrt{2}} \\ -\frac{1}{2} & \frac{\sqrt{3}}{2} & \frac{1}{\sqrt{2}} \\ -\frac{1}{2} & -\frac{\sqrt{3}}{2} & \frac{1}{\sqrt{2}} \end{bmatrix} \begin{bmatrix} \cos\theta & -\sin\theta & 0 \\ \sin\theta & \cos\theta & 0 \\ 0 & 0 & 1 \end{bmatrix}.$$

It should be noted that

$$\mathbf{T}^{-1}(\theta) = \frac{3}{2}\mathbf{T}^{T}(\theta) \tag{2.34}$$

Exercise 2.6
Show that $\mathbf{R}(\theta)$ is a unitary matrix, i.e., $\mathbf{R}(\theta)^{-1} = \mathbf{R}(\theta)^{T}$.

Exercise 2.7
Determine $[v_d^s,\, v_q^s]^T$ and $[v_d^e,\, v_q^e]^T$ corresponding to $[v_a,\, v_b,\, v_c]^T$ $= \left[\cos\theta,\, \cos(\theta - \frac{2}{3}\pi),\, \cos(\theta - \frac{4}{3}\pi)\right]^T$.

Solution.

$$\begin{aligned}
\begin{bmatrix} v_d^s \\ v_q^s \end{bmatrix} &= \frac{2}{3}\begin{bmatrix} 1 & -\frac{1}{2} & -\frac{1}{2} \\ 0 & \frac{\sqrt{3}}{2} & -\frac{\sqrt{3}}{2} \end{bmatrix}\begin{bmatrix} \cos\theta \\ \cos(\theta - \frac{2\pi}{3}) \\ \cos(\theta - \frac{4\pi}{3}) \end{bmatrix} \\
&= \frac{2}{3}\begin{bmatrix} \cos\theta - \frac{1}{2}\cos(\theta - \frac{2\pi}{3}) - \frac{1}{2}\cos(\theta - \frac{4\pi}{3}) \\ \frac{\sqrt{3}}{2}\cos(\theta - \frac{2\pi}{3}) - \frac{\sqrt{3}}{2}\cos(\theta - \frac{4\pi}{3}) \end{bmatrix} = \begin{bmatrix} \cos\theta \\ \sin\theta \end{bmatrix}. \\
\begin{bmatrix} v_d^e \\ v_q^e \end{bmatrix} &= \begin{bmatrix} \cos\theta & \sin\theta \\ -\sin\theta & \cos\theta \end{bmatrix}\begin{bmatrix} \cos\theta \\ \sin\theta \end{bmatrix} = \begin{bmatrix} 1 \\ 0 \end{bmatrix}.
\end{aligned}$$

■

This is a parallel result of the complex representation in Exercise 2.5. It should be noted that the peak, not the rms, value of the phase voltage $[v_a,\, v_b,\, v_c]$ is picked up in the coordinate transformation. Formulae for coordinate changes are summarized in Table 2.2

2.2.4 Transformation of Impedance Matrices

Resistance

Consider a simple three-phase resistor load: $\mathbf{v}_{abc} = r\mathbf{i}_{abc}$, where $\mathbf{i}_{abc} = [i_a,\, i_b,\, i_c]^T$ and $\mathbf{v}_{abc} = [v_a,\, v_b,\, v_c]^T$. Let

$$\begin{aligned}
\mathbf{i}_{dq}^e &= \mathbf{T}\mathbf{i}_{abc} \\
\mathbf{v}_{dq}^e &= \mathbf{T}\mathbf{v}_{abc},
\end{aligned}$$

where $\mathbf{i}_{dq0} = [i_d,\, i_q,\, i_0]^T$ and $\mathbf{v}_{dq0} = [v_d,\, v_q,\, v_0]^T$. Then,

$$\mathbf{v}_{dq}^e = \mathbf{T}\mathbf{v}_{abc} = r\mathbf{T}\mathbf{i}_{abc} = r\mathbf{i}_{dq}^e\,.$$

The resistor, being a scalar, is invariant under the coordinate change.

Inductance

Consider flux linkage

$$\boldsymbol{\lambda}_{abc} = \mathbf{L}_{abc}\mathbf{i}_{abc}\,,$$

where $\mathbf{L}_{abc} \in \mathbb{R}^{3\times 3}$ and $\boldsymbol{\lambda}_{abc} = [\lambda_a,\, \lambda_b,\, \lambda_c]^T$. Let $\boldsymbol{\lambda}_{dq0} = [\lambda_d,\, \lambda_q,\, \lambda_0]^T$. Then,

$$\begin{aligned}
\boldsymbol{\lambda}_{dq}^e &= \mathbf{T}\boldsymbol{\lambda}_{abc} \\
&= \mathbf{T}\mathbf{L}_{abc}\mathbf{i}_{abc} \\
&= \mathbf{T}\mathbf{L}_{abc}\mathbf{T}^{-1}\mathbf{i}_{dq}^e \\
&= \mathbf{L}_{dq}\mathbf{i}_{dq}^e.
\end{aligned}$$

Table 2.2: Formulae for coordinate changes.

Forward ($abc \Rightarrow dq$)	Inverse ($dq \Rightarrow abc$)
Complex variables for the stationary frame	
$\frac{2}{3}\left[f_a(t) + e^{j\frac{2\pi}{3}} f_b(t) + e^{-j\frac{2\pi}{3}} f_c(t)\right]$	$\begin{bmatrix} f_a \\ f_b \\ f_c \end{bmatrix} = \mathcal{R}e\left(\begin{bmatrix} \mathbf{f}^{\mathrm{s}} \\ e^{j\frac{4\pi}{3}}\mathbf{f}^{\mathrm{s}} \\ e^{j\frac{2\pi}{3}}\mathbf{f}^{\mathrm{s}} \end{bmatrix}\right)$
Complex variables for the rotating frame	
$e^{-j\theta}\frac{2}{3}\left[f_a(t) + e^{j\frac{2\pi}{3}} f_b(t) + e^{-j\frac{2\pi}{3}} f_c(t)\right]$	$\begin{bmatrix} f_a \\ f_b \\ f_c \end{bmatrix} = \mathcal{R}e\left(\begin{bmatrix} e^{j\theta}\mathbf{f}^{\mathrm{s}} \\ e^{j(\theta+\frac{4\pi}{3})}\mathbf{f}^{\mathrm{s}} \\ e^{j(\theta+\frac{2\pi}{3})}\mathbf{f}^{\mathrm{s}} \end{bmatrix}\right)$
Matrices for the stationary frame	
$\frac{2}{3}\begin{bmatrix} 1 & -\frac{1}{2} & -\frac{1}{2} \\ 0 & \frac{\sqrt{3}}{2} & -\frac{\sqrt{3}}{2} \\ \frac{1}{\sqrt{2}} & \frac{1}{\sqrt{2}} & \frac{1}{\sqrt{2}} \end{bmatrix}$	$\begin{bmatrix} 1 & 0 & \frac{1}{\sqrt{2}} \\ -\frac{1}{2} & \frac{\sqrt{3}}{2} & \frac{1}{\sqrt{2}} \\ -\frac{1}{2} & -\frac{\sqrt{3}}{2} & \frac{1}{\sqrt{2}} \end{bmatrix}$
Matrices for the rotating frame	
$\frac{2}{3}\begin{bmatrix} \cos\theta & \cos(\theta-\frac{2\pi}{3}) & \cos(\theta+\frac{2\pi}{3}) \\ -\sin\theta & -\sin(\theta-\frac{2\pi}{3}) & -\sin(\theta+\frac{2\pi}{3}) \\ \frac{1}{\sqrt{2}} & \frac{1}{\sqrt{2}} & \frac{1}{\sqrt{2}} \end{bmatrix}$	$\begin{bmatrix} \cos\theta & -\sin\theta & \frac{1}{\sqrt{2}} \\ \cos(\theta-\frac{2\pi}{3}) & -\sin(\theta-\frac{2\pi}{3}) & \frac{1}{\sqrt{2}} \\ \cos(\theta+\frac{2\pi}{3}) & -\sin(\theta+\frac{2\pi}{3}) & \frac{1}{\sqrt{2}} \end{bmatrix}$

Hence, we obtain

$$\mathbf{L}_{dq} = \mathbf{T}\mathbf{L}_{abc}\mathbf{T}^{-1}\,. \tag{2.35}$$

Note that (2.35) is the similarity transformation.

Exercise 2.8
Consider a three-phase inductor shown in Fig. 2.12.

a) Specify inductance matrix, $\mathbf{L}_{abc}$.
b) Find $\mathbf{L}_{dq}$.

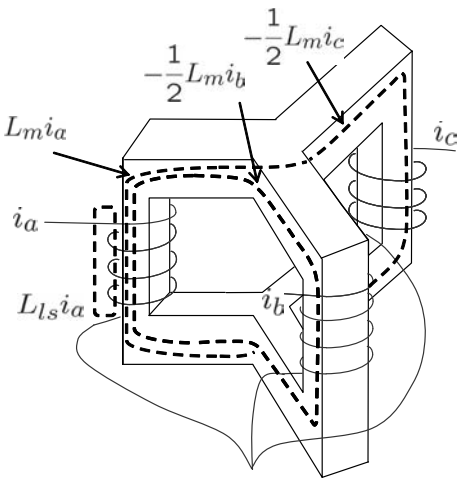

Figure 2.12: Three-phase inductor (Exercise 2.8).

Solution

a)

$$\mathbf{L}_{abc} = \begin{bmatrix} L_{ls}+L_m & -\frac{1}{2}L_m & -\frac{1}{2}L_m \\ -\frac{1}{2}L_m & L_{ls}+L_m & -\frac{1}{2}L_m \\ -\frac{1}{2}L_m & -\frac{1}{2}L_m & L_{ls}+L_m \end{bmatrix}.$$

b) $\mathbf{L}_{dq} = \mathbf{T}\mathbf{L}_{abc}\mathbf{T}^{-1}$

$$= \frac{2}{3}\begin{bmatrix} 1 & -\frac{1}{2} & -\frac{1}{2} \\ 0 & \frac{\sqrt{3}}{2} & -\frac{\sqrt{3}}{2} \\ \frac{1}{\sqrt{2}} & \frac{1}{\sqrt{2}} & \frac{1}{\sqrt{2}} \end{bmatrix} \begin{bmatrix} L_{ls}+L_m & -\frac{1}{2}L_m & -\frac{1}{2}L_m \\ -\frac{1}{2}L_m & L_{ls}+L_m & -\frac{1}{2}L_m \\ -\frac{1}{2}L_m & -\frac{1}{2}L_m & L_{ls}+L_m \end{bmatrix} \begin{bmatrix} 1 & 0 & \frac{1}{\sqrt{2}} \\ -\frac{1}{2} & \frac{\sqrt{3}}{2} & \frac{1}{\sqrt{2}} \\ -\frac{1}{2} & -\frac{\sqrt{3}}{2} & \frac{1}{\sqrt{2}} \end{bmatrix}$$

$$= \begin{bmatrix} L_{ls}+\frac{3}{2}L_m & 0 & 0 \\ 0 & L_{ls}+\frac{3}{2}L_m & 0 \\ 0 & 0 & L_{ls} \end{bmatrix}. \tag{2.36}$$

■

2.2.5 Power Relations

In the three-phase system, power is defined as the sum of individual phase powers. The voltage and current vectors are denoted by $\mathbf{v}_{abc} = [v_a, v_b, v_c]^T$ and $\mathbf{i}_{abc} = [i_a, i_b, i_c]^T$. Let $\mathbf{v}^e_{dq0} \equiv \mathbf{T}(\theta)[v_a, v_b, v_c]^T$ and $\mathbf{i}^e_{dq0} \equiv \mathbf{T}(\theta)[i_a, i_b, i_c]^T$. Then, power is

equal to

$$\begin{aligned} P &= \mathbf{v}_{abc}^T \mathbf{i}_{abc} = v_a i_a + v_b i_b + v_c i_c \\ &= (\mathbf{T}^{-1}\mathbf{v}_{dq0})^T \mathbf{T}^{-1}\mathbf{i}_{dq0} \\ &= \mathbf{v}_{dq0}^T (\mathbf{T}^{-1})^T \mathbf{T}^{-1}\mathbf{i}_{dq0} \\ &= \mathbf{v}_{dq0}^T (\frac{3}{2}\mathbf{T}^T)^T \mathbf{T}^{-1}\mathbf{i}_{dq0} \\ &= \frac{3}{2}\mathbf{v}_{dq0}^T \mathbf{i}_{dq0} \\ &= \frac{3}{2}(v_d i_d + v_q i_q + v_0 i_0) \\ &= \frac{3}{2}(v_d i_d + v_q i_q)\,. \end{aligned}$$

In the above calculation, the relation, $\mathbf{T}^{-1} = \frac{3}{2}\mathbf{T}^T$ was utilized. The last equality follows when either $v_0 = 0$ or $i_0 = 0$. Note that the factor $3/2$ is incorporated into the power equation of dq variables.

Bibliography

[1] P. C. Krause, O. Wasynczuk, and S. D. Sudhoff, *Analysis of Electric Machinery,* IEEE Press, 1995.

[2] D. W. Novotny and T. A. Lipo, *Vector Control and Dynamics of AC Drives,* Clarendon Press, Oxford 1996.

Problems

2.1 Show that Fourier series expansion of the square MMF shown in Fig. 2.13 is

$$\text{MMF} = \frac{4}{\pi}\frac{NI}{2}\left(\sin\frac{\pi}{\tau_p}\theta + \frac{1}{3}\sin\frac{3\pi}{\tau_p}\theta + \frac{1}{5}\sin\frac{5\pi}{\tau_p}\theta + \cdots\right).$$

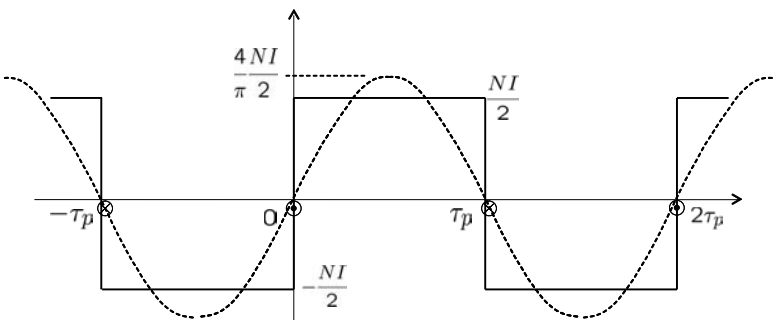

Figure 2.13: A square MMF and its fundamental component (Problem 2.1).

2.2 Consider a two arm inverter and a three-phase motor shown in Fig. 2.14. The necessary condition for the current balance among the three-phase windings is

$$\frac{v_{an} - v_{sn}}{Z} + \frac{v_{bn} - v_{sn}}{Z} - \frac{v_{sn}}{Z} = 0,$$

where Z denotes the impedance of the phase windings. Assume that c phase current is equal to $-\frac{v_{sn}}{Z} = \cos\omega t$. Find v_{an} and v_{bn} such that a rotating field is made.

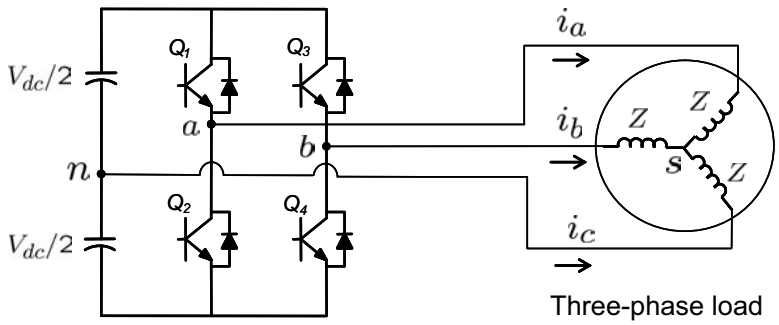

Figure 2.14: Two arm inverter for a three-phase motor (Problem 2.2).

2.3 Consider a concentrated winding configuration shown in Fig. 2.15. Assume that both side edges are identical.
a) Sketch MMF when $i_u = 0$ and $i_v = -i_w = I$.
b) The MMF have even harmonics. Determine the harmonic components for $n = 2$ and $n = 4$.

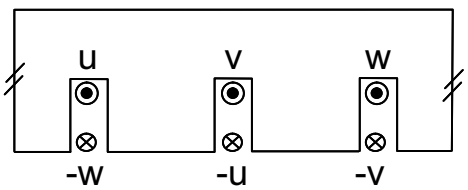

Figure 2.15: Concentrated winding (Problem 2.3).

2.4 Consider the following six-step voltages shown in Fig. 2.16. Draw $v_d^s + jv_q^s$ in the complex plane.

2.5 Transform the 5^{th} (2.25) and 7^{th} (2.26) harmonics into the synchronous frame $\theta = \omega t$. What are the common and different factors between the 5^{th} and 7^{th} harmonics in the synchronous frame?

2.6 Assume $\mathbf{U} \in \mathbb{R}^{n\times n}$ is a unitary matrix. Show that $det(\mathbf{U}) = \pm 1$, where $det(\mathbf{U})$ denotes the determinant of $\mathbf{U}$.

2.7 Consider a three-phase current with 7^{th}-order harmonics:

$$\begin{bmatrix} i_a(t) \\ i_b(t) \\ i_c(t) \end{bmatrix} = \begin{bmatrix} \cos\omega t - \frac{1}{3}\cos 3\omega t + \frac{1}{5}\cos 5\omega t - \frac{1}{7}\cos 7\omega t \\ \cos(\omega t - \frac{2\pi}{3}) - \frac{1}{3}\cos 3(\omega t - \frac{2\pi}{3}) + \frac{1}{5}\cos 5(\omega t - \frac{2\pi}{3}) - \frac{1}{7}\cos 7(\omega t - \frac{2\pi}{3}) \\ \cos(\omega t - \frac{4\pi}{3}) - \frac{1}{3}\cos 3(\omega t - \frac{4\pi}{3}) + \frac{1}{5}\cos 5(\omega t - \frac{4\pi}{3}) - \frac{1}{7}\cos 7(\omega t - \frac{4\pi}{3}) \end{bmatrix}$$

Transform the current vector into the stationary frame. Draw the trajectory utilizing MATLAB®.

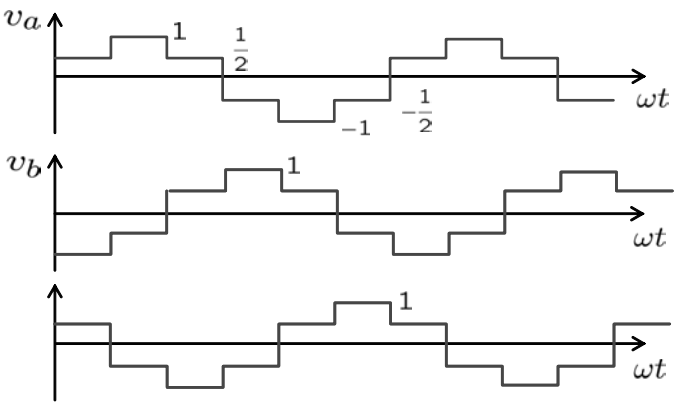

Figure 2.16: Six-step voltages (Problem 2.4).

2.8 Consider a five-phase system in which five MMFs are

$$\begin{aligned} \text{MMF}_a &= \frac{Ni_a}{2}\cos\theta, & \text{MMF}_b &= \frac{Ni_b}{2}\cos(\theta - \frac{2\pi}{5}), \\ \text{MMF}_c &= \frac{Ni_c}{2}\cos(\theta - \frac{4\pi}{5}), & \text{MMF}_d &= \frac{Ni_d}{2}\cos(\theta + \frac{4\pi}{5}), \\ \text{MMF}_e &= \frac{Ni_e}{2}\cos(\theta + \frac{2\pi}{5}). \end{aligned}$$

Obtain a current set which makes the MMF sum rotate synchronously with the electrical speed, ω, and the MMF sum.

2.9 Suppose that θ is redefined as the angle between the q–axis and the a–axis, as shown in Fig. 2.17. Based on the new definition θ, show that the transformation map is equal to

$$\mathbf{T}(\theta) = \frac{2}{3}\begin{bmatrix} \cos(\theta) & \cos(\theta - \frac{2\pi}{3}) & \cos(\theta - \frac{4\pi}{3}) \\ \sin(\theta) & \sin(\theta - \frac{2\pi}{3}) & \sin(\theta - \frac{4\pi}{3}) \\ \frac{1}{\sqrt{2}} & \frac{1}{\sqrt{2}} & \frac{1}{\sqrt{2}} \end{bmatrix}.$$

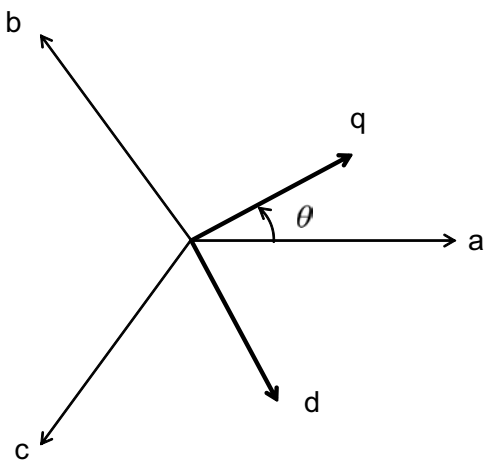

Figure 2.17: D and q axes (Problem 2.9).

Chapter 3

Induction Motor Basics

Induction motors (IMs) are commonly understood as three-phase transformers with shortened, and freely rotating secondary winding. Slip is calculated as the difference between the rotational speed of the air gap field and the shaft speed. If a load increases at a fixed frequency operation, the slip increases, which in turn induces a larger secondary current, producing higher torque. The reverse action occurs when the load decreases. This natural stabilization mechanism enables IMs to be driven by the grid lines.

IMs do not have any permanent magnets, nor brush and commutators. Hence, they are rugged, i.e., they can endure high temperatures, and are robust to mechanical shock and vibration. Induction motors are therefore widely used in many applications such as pumps, blowers, conveyer belts, cranes, elevators, refrigerators, and traction drives. In this chapter, torque-speed curves are derived, and speed control methods are illustrated.

3.1 IM Operation Principle

Torque production principles of IMs are depicted in Fig. 3.1 [1]: Assume that permanent magnets (PMs) are positioned at the top and bottom of a squirrel cage-type conductor which consists of multiple conductor bars and two end rings. The PMs represents the magnetic poles synthesized by the stator current, and the squirrel cage represents the rotor circuit. Note that the PM field is passing through the rectangles formed by conductor bars.

Assume further that the PMs are rotating in the counterclockwise direction while the cage conductor remains fixed. Consider two conductor loops at the bottom of a PM. Changes in the flux linkage induce current on the loops, opposing the flux change. That is, the current flows in a direction such that its resulting flux counteracts the variations of the PM flux linkage. Specifically, since the PM flux is decreasing in Loop 1, a clockwise loop current is induced, which adds flux to the decreasing flux. Since the PM flux is increasing in Loop 2, a counterclockwise

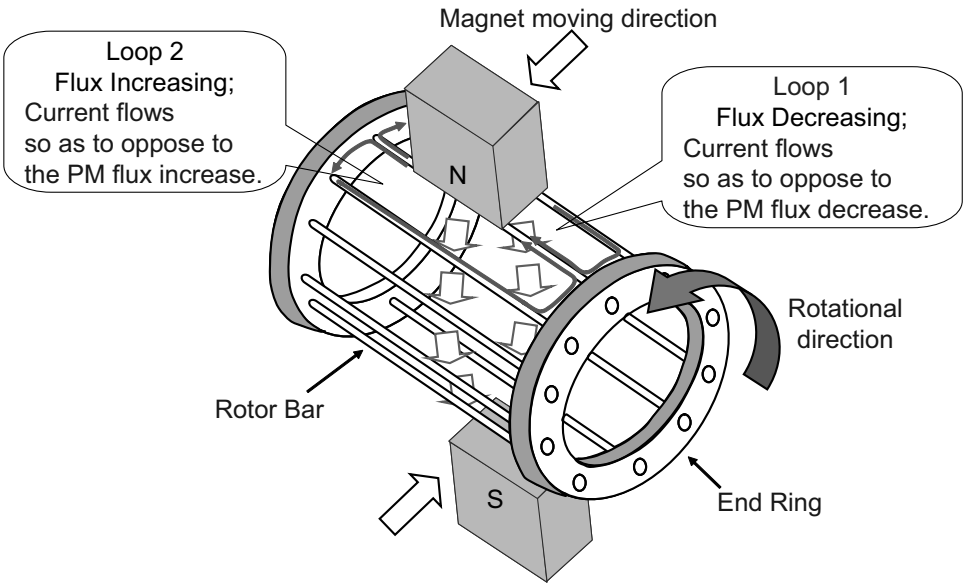

Figure 3.1: Torque production on the squirrel cage circuit.

loop current is induced, which opposes the flux increase. As a result, current flows from right to left in the center bar, between Loop 1 and Loop 2. Application of the left-hand rule shows that the Lorentz force is acting on the conductor bar to the left. That is, the bar tends to move to the left following the motion of the PM. Note that the rotor conductors are normally made of aluminum or copper, which are non-ferromagnetic materials. The above illustration gives a reasoning as to why a non-ferromagnetic material follows the motion of the PMs.

Note, however, that if the cage rotates at the same speed as the permanent magnet, flux linkage does not change, resulting in no current induction. Therefore, no torque is generated. It should be noted that the torque generated on the cage is proportional to the speed difference between the PM and the cage. In other words, the cage torque is proportional to the slip speed.

The rotating field generated by the stator winding plays the role of the moving PMs. Fig. 3.2 shows photographs of stator and rotor laminated sheets. The stator and rotor cores are made by stacking low conductive silicon steels to minimize the eddy current loss, while providing low reluctance paths for the magnet field. Through the stator slots, copper coils are wound. However, the rotor conductor bars are normally made by aluminum die casting.

Fig. 3.3 shows a photograph of an IM rotor after shaft assembly. The rotor has open slots and the casted aluminum is seen as the skewed stripes. At both ends, casted aluminum constitutes end rings with cooling fins.

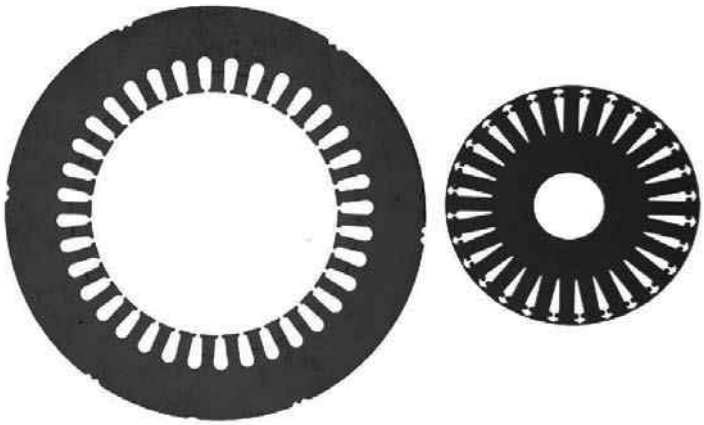

Figure 3.2: Laminated sheets for an IM: (a) stator and (b) rotor.

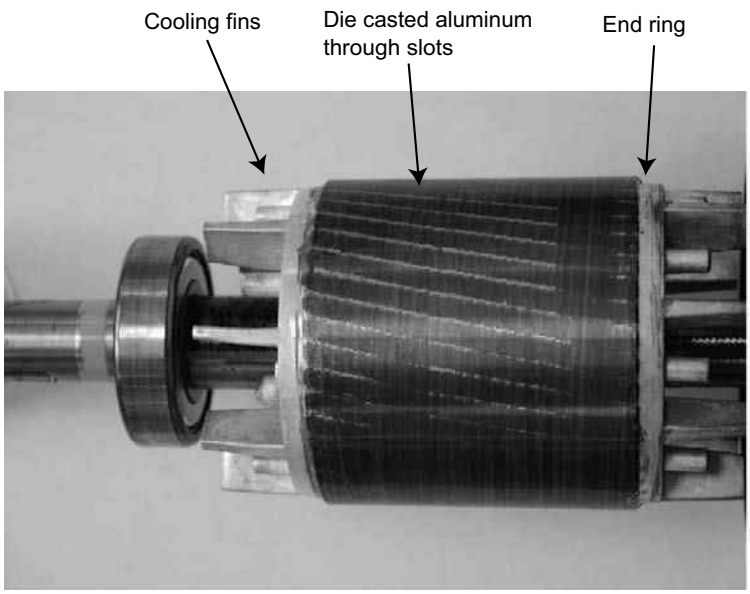

Figure 3.3: Photograph of an assembled IM rotor.

3.1.1 Equivalent Circuit

An IM can be considered as a special three-phase transformer. Induction motors have primary and secondary windings, and iron cores for flux linking as shown in Fig. 3.4. But, IMs have the following differences:

1) IMs have an air gap while transformers do not.
2) The secondary winding is always shortened.
3) The secondary winding is allowed to rotate.

Since the air gap has large reluctance, it causes a large leakage field. Thus, the leakage inductance of IMs is greater than that of transformers. Due to the voltage drop associated with the leakage field, the IM has a lower power factor than the transformer. The secondary winding is always shorted, but rotating. Thereby, infinite current increasing is prevented.

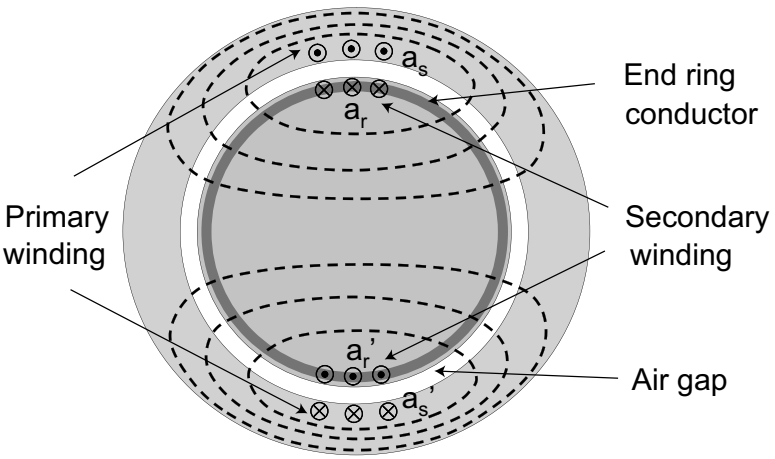

Figure 3.4: Induction motor as a rotational transformer with an air gap.

Denote by r_s, r_r, L_{ls}, L_{lr}, and L_m stator resistance, rotor resistance, stator leakage inductance, rotor leakage inductance, and magnetizing inductance, respectively. We denote by ω_r and ω_e rotor shaft and electrical speeds, respectively. In the case of the P-pole machine, the field speed seen from the rotor frame is equal to $\omega_e - (P/2)\omega_r$. The normalized speed difference is defined as the slip:

$$s = \frac{\omega_e - (P/2)\omega_r}{\omega_e}\,. \tag{3.1}$$

We denote by $\mathbf{I}_s$ and $\mathbf{I}_r$ the stator and rotor current phasors, respectively. We also denote by $\mathbf{V}_s$ the stator voltage phasor. A plausible per-phase model is shown in Fig. 3.5. It is a transformer model with the secondary circuit shorted by a slip dependent resistor, $\frac{r_r}{s}$. For zero slip, $s = 0$, the secondary circuit turns out to be open; thereby no secondary current flows.

Based on the equivalent circuit, the IM equations are derived such that

$$(r_s + j\omega_e L_{ls})\mathbf{I}_s + j\omega_e L_m(\mathbf{I}_s + \mathbf{I}_r) = \mathbf{V}_s \tag{3.2}$$

$$(\frac{r_r}{s} + j\omega_e L_{lr})\mathbf{I}_r + j\omega_e L_m(\mathbf{I}_s + \mathbf{I}_r) = 0\,. \tag{3.3}$$

The rotor equation (3.3) can be written equivalently as

$$(r_r + j(\omega_e - \frac{P}{2}\omega_r)L_{lr})\mathbf{I}_r + j(\omega_e - \frac{P}{2}\omega_r)L_m(\mathbf{I}_s + \mathbf{I}_r) = 0.$$

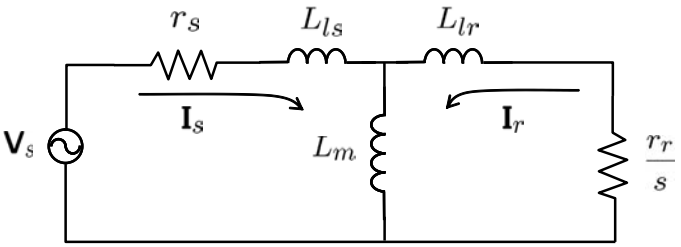

Figure 3.5: Steady state per-phase equivalent circuit of an IM.

This may be interpreted that the rotor circuit is governed by the slip frequency, $\omega_e - \frac{P}{2}\omega_r$. More rigorous IM model derivations appear in the next chapter.

The transferred power to the secondary side through the air gap is called *air gap power* and is divided into two parts:

$$P_{ag} = 3I_r^2 r_r \frac{1}{s} = \underbrace{3I_r^2 r_r}_{\text{Rotor copper loss}} + \underbrace{3I_r^2 r_r \frac{1-s}{s}}_{\text{Mechanical power}} . \tag{3.4}$$

Here, the mechanical power is counted as the air gap power, minus the copper loss.

Exercise 3.1
A three-phase, 4-pole IM draws 55kW real power from a three-phase 60Hz feeder. The copper and iron losses in the stator amount to 4kW. If the motor runs at 1740 rpm, calculate

a) the airgap power.
b) the rotor loss.
c) mechanical power.
d) the mechanical loss is 2kW. Calculate the efficiency of the motor.

Solution

a) $P_{ag} = 55 - 4 = 51$(kW).
b) $s = (1800 - 1740)/1800 = 0.033$. Thus, $3I_r^2 r_r = sP_{ag} = 1.683$(kW).
c) $P_m = (1 - s)P_{ag} = 49.3$(kW).
d) The shaft power is 49.3kW. The efficiency is equal to $49.3/55 = 0.897$.

■

3.1.2 Torque-Speed Curve

The rotor current should be calculated to obtain torque, since the IM torque is equal to

$$T_e = \frac{P_m}{\omega_r} = 3{I_r}^2 \frac{(1-s)r_r}{s\omega_r}. \tag{3.5}$$

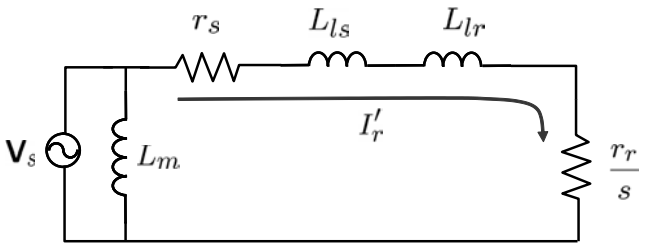

Figure 3.6: Modified equivalent circuit for IM.

To simplify the rotor current calculation, the IM equivalent circuit is often modified as shown in Fig. 3.6: The magnetizing inductance L_m is moved to the source side with the assumption that the voltage drop over the stator leakage inductance and resistance is relatively small. Note that the magnetizing inductance is much larger than the leakage inductance. Specifically, the leakage reactance $j\omega_e L_{ls}$ is about 5% of the magnetizing reactance $j\omega_e L_m$ in IMs.

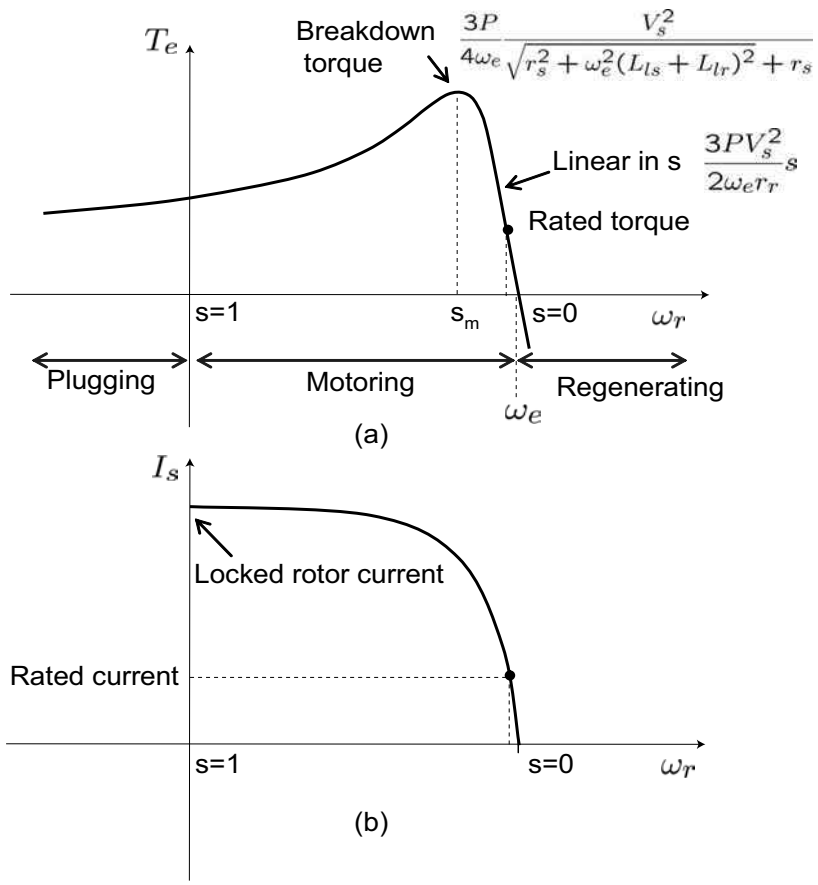

Figure 3.7: Steady state characteristics of an induction machine: (a) torque-speed curve, (b) stator current versus slip.

The rotor current, I_r' of the modified circuit is calculated as

$$I_r' = \frac{V_s}{\sqrt{\left(r_s + \frac{r_r}{s}\right)^2 + \omega_e^2 (L_{ls} + L_{lr})^2}}. \tag{3.6}$$

From the definition of the slip, it follows that $\frac{P}{2\omega_e} = \frac{1-s}{\omega_r}$. Hence, utilizing (3.5) the electromagnetic torque is calculated such that [4]

$$T_e = \frac{P}{2} \frac{3r_r}{s\omega_e} \frac{V_s^2}{\left(r_s + \frac{r_r}{s}\right)^2 + \omega_e^2 (L_{ls} + L_{lr})^2}. \tag{3.7}$$

For small slip, i.e., $s \approx 0$, torque equation (3.7) is approximated such that

$$T_e \approx \frac{P}{2} \frac{3r_r}{\omega_e s} \frac{V_s^2}{\left(\frac{r_r}{s}\right)^2} \approx \frac{3PV_s^2}{2\omega_e r_r} s. \tag{3.8}$$

In a small slip region, torque is linear in s. Hence, the torque curve appears as a straight line in the neighborhood of $s = 0$. On the other hand, when $s \approx 1$, (3.7) is approximated such that

$$T_e = \frac{P}{2} \frac{3r_r}{s\omega_e} \frac{V_s^2}{(r_s + r_r)^2 + \omega_e^2 (L_{ls} + L_{lr})^2}. \tag{3.9}$$

It is a parabola equation in s. Fig. 3.7 (a) shows a typical torque-speed curve of IM. It can be sketched as a glued curve of (3.8) and (3.9). Fig. 3.7 (b) shows that the stator current as a function of slip. Note that the current rise is steep in the neighborhood of $s = 0$. Normally, the rated slip is about $s = 0.02 \sim 0.03$. Note also that the stator current at locked state ($s = 1$) is about $6 \sim 10$ times larger than the rated current.

Exercise 3.2
A three-phase, 4-pole IM for a 440V (line-to-line) 60Hz power source has the equivalent circuit shown in Fig. 3.8 (a). A modified circuit referred to the source is also shown in Fig. 3.8 (b). Utilizing MATLAB®, draw the torque-speed curves based on the two circuits shown in Fig. 3.8 and check the differences near $s = 0$ and 1.

Solution
See Fig. 3.9. The torque is higher with the modified circuit, since $I_r' > I_r$. But the differences are small especially when $s = 0$ or 1. Hence, the modified circuit is generally used for convenience.

Exercise 3.3
An IM with a load runs at 1750 rpm when connected to a 60Hz, 220V, three-phase AC source. Calculate the shaft speed if the source voltage is increased to 250V. Assume that the load torque is constant independently of the speed.

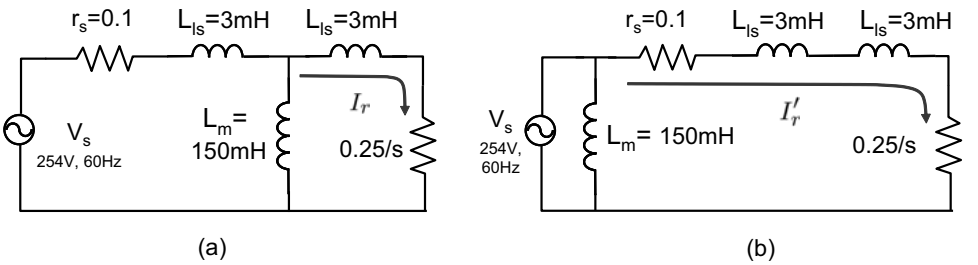

Figure 3.8: Equivalent circuits of an induction machine: (a) original equivalent circuit and (b) modified circuit (Exercise 3.2).

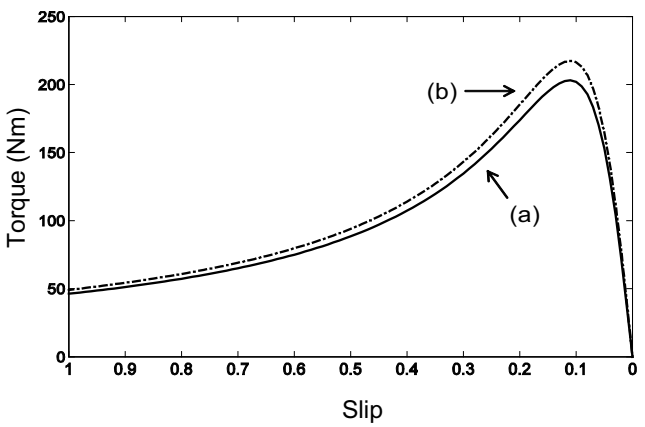

Figure 3.9: Torque-speed curves based on the equivalent circuits shown in Fig. 3.8 (Exercise 3.2).

Solution

It follows from (3.8) that the slip is inversely proportional to the square of the voltage. Hence,

$$(\text{slip at } 250) = (\text{slip at } 220)\left(\frac{220}{250}\right)^2 = 50 \times \left(\frac{220}{250}\right)^2 = 38.7\text{rpm}.$$

Hence, the operation speed is $1800 - 38.7 = 1761$rpm. ■

3.1.3 Breakdown Torque

The maximum torque is called the *breakdown torque*, since it is the torque at the boundary between the stable and unstable operations. An expression for the slip s_m that maximizes the torque may be obtained by taking the derivative of (3.7) with respect to s. The torque maximizing slip is given by

$$s_m = \frac{r_r}{\sqrt{r_s^2 + \omega_e^2 (L_{ls} + L_{lr})^2}}. \tag{3.10}$$

The breakdown torque at $s = s_m$ is

$$T_{max} = \frac{3P}{4\omega_e} \frac{V_s^2}{\sqrt{r_s^2 + \omega_e^2(L_{ls} + L_{lr})^2} + r_s}. \tag{3.11}$$

Normally, the breakdown torque of a machine is three or four times higher than the rated torque.

Fig. 3.10 (a) shows a group of torque-speed curves when r_r increases. Note from (3.10) that s_m increases with r_r, but from (3.11) that the breakdown torque is independent of r_r. That is, the breakdown torque remains the same for different rotor resistances. As is shown in Fig. 3.10 (b), the required currents are almost the same for a given torque. Since the secondary loss is $r_r I_r'^2$, the IM efficiency decreases as the rotor resistance increases. Therefore, high-efficiency IMs exhibit steep slope characteristics near zero slip, and it is necessary to reduce r_r to make a high-efficiency IM.

Exercise 3.4
A 220V (line-to-line) 60Hz, three-phase IM produces 10hp shaft power at a rated speed, 1750 rpm. The parameters of the IM are $r_s = 0.2\Omega$, $L_{ls} = L_{lr} = 2.3$mH, and L_m=34.2mH. Determine the rated torque, rotor resistance, and rotor current (I_r'). Sketch the torque-speed curve.

Solution
$T_e = P_m/\omega_r = 10 \times 746/(1750/60 \times 2\pi) = 40.7$Nm. Slip $s = 50/1800 = 0.0277$. It follows from (3.8) that

$$r_r = \frac{3PV_s^2}{2\omega_e T_e} s = \frac{3 \times 4 \times 127^2}{2 \times 377 \times 40.73} \times 0.0277 = 0.175\Omega.$$

$$I_r' = \frac{127}{\sqrt{(0.2 + 0.175/0.0277)^2 + 377^2 \times 0.0046^2}} = 18.83\text{A}.$$

■

Exercise 3.5
Consider a three-phase IM whose parameters are listed in Table 3.1. Determine the followings: 1) rated slip; 2) rated current; 3) rated power factor; 4) rated torque; 5) breakdown torque.

Solution

1) The synchronous speed is equal to 1200rpm. Thus, $s = \frac{1200-1164}{1200} = 0.03$.

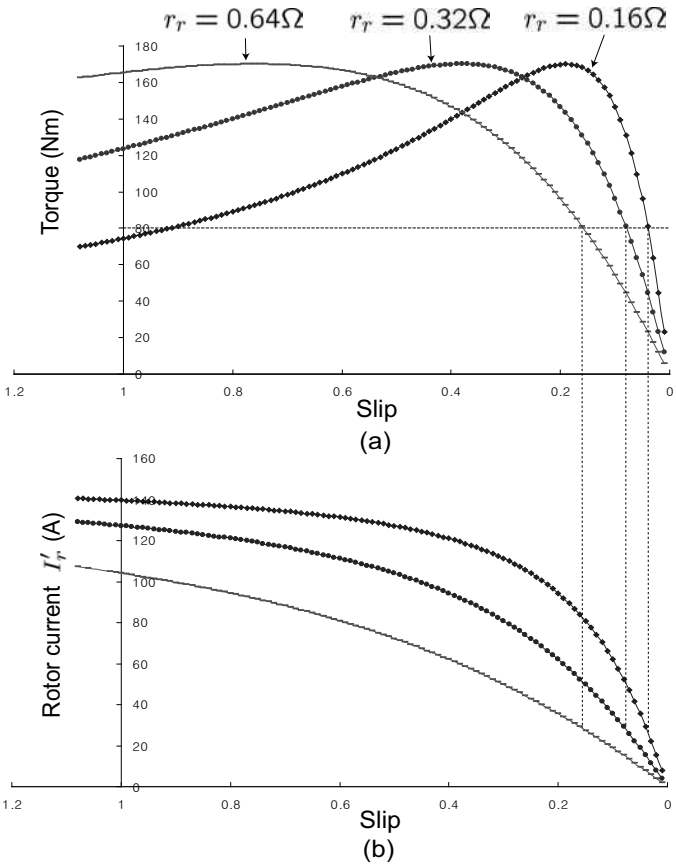

Figure 3.10: (a)Torque and (b) rotor current curves of an IM for different rotor resistances.

Table 3.1: An example IM parameters.

Rated power	10 hp (7.46 kW)
Rated stator voltage	220V
Rated frequency	60Hz
Rated speed	1164rpm
Number of poles	$P = 6$
Stator resistance, r_s	0.29 Ω
Stator leakage inductance, L_{ls}	1.38 mH
Rotor resistance r_r	0.16 Ω
Rotor leakage inductance, L_{lr}	0.717 mH
Magnetizing inductance, L_m	41 mH

2) Since $r_r/s = 0.16/0.03 = 5.33\Omega$,

$$\frac{(5.33 + j0.27)j15.46}{5.33 + j(15.46 + 0.27)} = 4.61 + j1.83.$$

Thus, the total impedance is equal to

$$(0.29 + j0.52) + (4.61 + j1.83) = 4.9 + j2.35 = 5.43\angle 25.6.$$

The phase voltage is equal to $220/\sqrt{3} = 127$V. Thus,

$$\mathbf{I}_s = \frac{127}{5.44\angle 25.7^\circ} = 23.4\angle -25.6^\circ (\text{A}).$$

3) $PF = \cos(25.6^\circ) = 0.9$ (lagging).

4)

$$\begin{aligned} I'_{r\ \text{rated}} &= \frac{127}{\sqrt{(0.29 + 5.33)^2 + (0.52 + 0.27)^2}} = 22.4\text{A} \\ T_{e\ \text{rated}} &= 3 \times \frac{3 \times 0.16}{0.03 \times 377} \times 22.3^2 = 63.3\text{Nm}. \end{aligned}$$

5)

$$T_{e\,\max} = \frac{3 \times 6}{4 \times 377} \frac{127^2}{\sqrt{0.29^2 + (0.52 + 0.27)^2} + 0.29} = 170.1\text{Nm}.$$

■

3.1.4 Stable and Unstable Regions

The operating speed is determined from the intersection of the torque-speed curve and the load curve as shown in Fig. 3.11. If the load increases, then the speed drops causing the operating point A to move to A'. As a result, slip increases with torque. Due to the increased motor torque, original point A is recovered when the additional load disappears. On the other hand if the load decreases, then the speed increases. Thus, operating point A moves to A'' with the reduction in slip and torque. If the load is returned to the original level, then the operating point returns to the original point A. Due to the tendency of the operating points to revert to the original position A the region including A, A', A'' is termed a stable region.

However, on the left-hand side of the breakdown torque, the situation is totally different. If a load increases at point B, then the speed drops. If the speed drops, the motor torque is reduced. Repeating this process, the speed finally drops to zero. Hence, a stable operation is not feasible for $s_m \leq s \leq 1$; thereby the region is called an unstable region. The stability of an operating point can be determined by the slopes of the motor and the load torque curves, i.e., if $\frac{dT_e}{d\omega_r} - \frac{dT_L}{d\omega_r} < 0$, then the point is stable, and otherwise unstable, where T_L is the load torque.

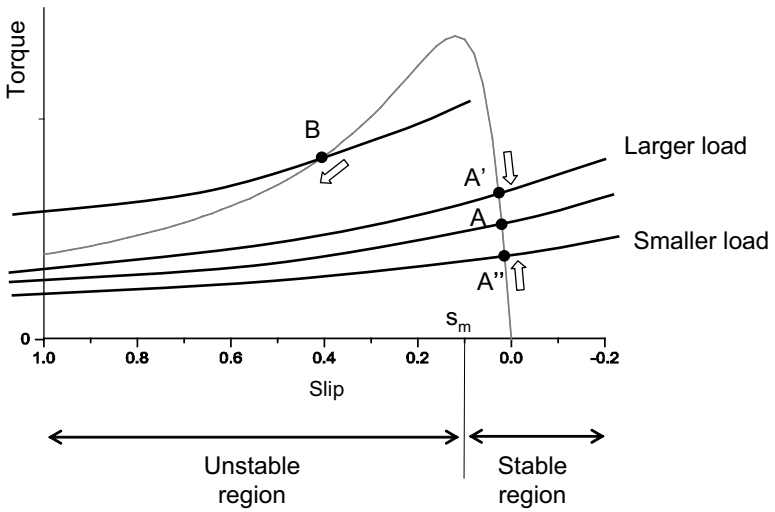

Figure 3.11: Stable and unstable regions.

3.1.5 Parasitic Torques

It was shown in the previous section that high-order MMF harmonics are generated due to the slotted structures of the stator winding. Recall from Chapter 2 that high-order fields caused by MMF harmonics travel at reduced speeds. The synchronous speed of harmonics is

$$\omega_{e\nu} = \frac{\omega_e}{\nu}, \tag{3.12}$$

where $\nu = -5, 7, -11, 13, -17, 19 \cdots$. The minus sign in the harmonic number signifies the negative sequence. When the rotor speed is ω_r, the slip for ν^{th} harmonic is

$$s_\nu = \frac{\omega_{e\nu} - \frac{P}{2}\omega_r}{\omega_{e\nu}} = \frac{\omega_e/\nu - (1-s)\omega_e}{\omega_e/\nu} = 1 - \nu(1-s). \tag{3.13}$$

Thus the slip which makes $s_\nu = 0$ is given by

$$s = 1 - \frac{1}{\nu}. \tag{3.14}$$

Therefore, the synchronous speeds of fifth and seventh harmonics are $s = 1.2$ and $6/7$, respectively. The 5^{th} and 7^{th} parasitic torques and their sum with the fundamental component are depicted in Fig. 3.12. If the 7^{th} harmonic torque is appreciably high, the motor sometimes crawls at a low speed [3]. To reduce such harmonic effects, slot numbers of stator and rotor should be properly selected, and the rotor core needs to be skewed.

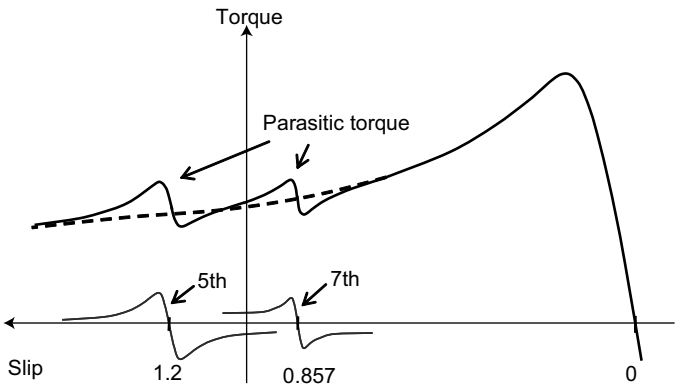

Figure 3.12: Parasitic torque caused by 5^{th} and 7^{th} MMF harmonics.

3.2 Leakage Inductance and Circle Diagram

The stator flux is desired to cross the air gap and enclose the rotor conductors (bars), building a flux linking. However, not all stator flux lines create such a flux linking between the stator and rotor windings, i.e., a small portion of flux leaks out at slots, air gap, and end turns. The presence of air gap contributes to increasing the leakage field. Typical leakage inductances are

1) slot leakage inductance.
2) zigzag leakage inductance.
3) end turn leakage inductance.

Fig. 3.13 depicts the leakage inductances. Small loops around the slots constitute slot leakage flux. The flux passing through the air gap in a zigzag pattern causes the zigzag leakage inductance. The end turn leakage inductance is caused by the flux around the end turn coils. In general, the leakage inductance proportion increases as the air gap height increases.

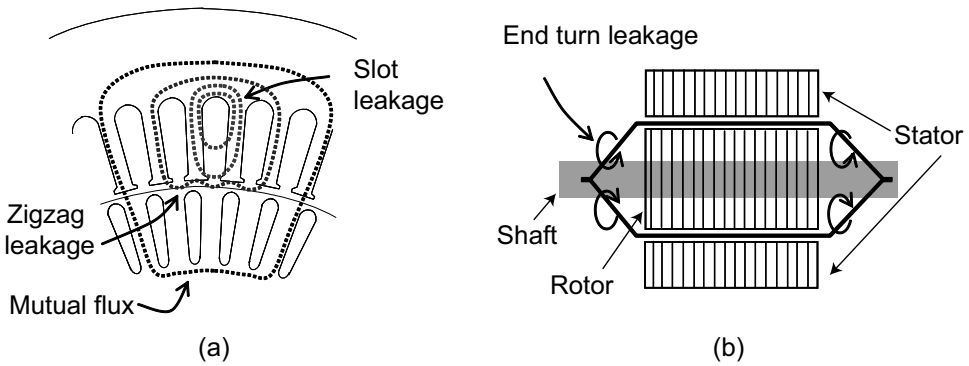

Figure 3.13: Slot, zigzag, and end-turn leakage flux: (a) front view, (b) top (side) view.

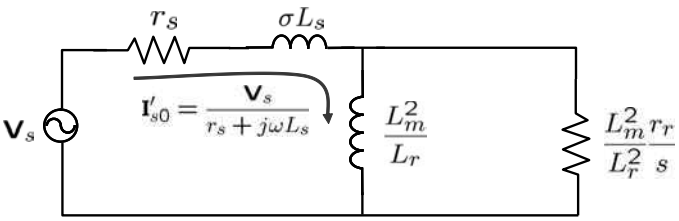

Figure 3.14: Equivalent circuit with σL_s.

Define by $L_s \equiv L_{ls} + L_m$ and $L_r \equiv L_{lr} + L_m$ the stator and rotor inductances, respectively. Then (3.2) and (3.3) are rewritten as

$$\mathbf{V}_s = (r_s + j\omega_e L_s)\mathbf{I}_s + j\omega_e L_m \mathbf{I}_r \,, \tag{3.15}$$

$$0 = (\frac{r_r}{s} + j\omega_e L_r)\mathbf{I}_r + j\omega_e L_m \mathbf{I}_s \,. \tag{3.16}$$

Let the leakage coefficient be defined by

$$\sigma = 1 - \frac{L_m^2}{L_r L_s} \,. \tag{3.17}$$

Replacing $\mathbf{I}_r$ from (3.15) by utilizing (3.16), it follows that

$$Z_s \equiv \frac{\mathbf{V}_s}{\mathbf{I}_s} = r_s + j\omega_e L_s \frac{1 + js\omega_e \sigma L_r / r_r}{1 + js\omega_e L_r / r_r}. \tag{3.18}$$

Further, (3.18) is modified as

$$\begin{aligned} Z_s &= r_s + j\omega_e \sigma L_s \frac{1/\sigma + j\omega_e s L_r / r_r}{1 + j\omega_e s L_r / r_r}, \\ &= r_s + j\omega_e \sigma L_s + \frac{(1-\sigma) j\omega_e L_s}{1 + j\omega_e s L_r / r_r}, \\ &= r_s + j\omega_e \sigma L_s + \frac{j\omega_e L_m^2 / L_r}{1 + j\omega_e s L_r / r_r}, \\ &= r_s + j\omega_e \sigma L_s + \frac{\frac{r_r}{s}\frac{L_m^2}{L_r} j\omega_e \frac{L_m^2}{L_r^2}}{\frac{r_r}{s}\frac{L_m^2}{L_r^2} + j\omega_e \frac{L_m^2}{L_r}}. \end{aligned} \tag{3.19}$$

Based on (3.19), the circuit shown in Fig. 3.5 can be transformed equivalently as shown in Fig. 3.14. Note from Fig. 3.14 that all leakage inductance appears in the stator side and that the zero slip current is equal to $\mathbf{V}_s/(r_s + j\omega_e L_s)$.

Note that if L_{lr}, $L_{ls} \ll L_m$, then

$$\sigma \approx \frac{L_{lr} + L_{ls}}{L_m}. \tag{3.20}$$

Then, the slip (3.10) yielding the maximum torque is approximated as

$$s_m = \frac{r_r}{\sqrt{r_s^2 + \omega_e^2 (L_{ls} + L_{lr})^2}} \approx \frac{r_r}{\sqrt{\omega_e^2 \sigma^2 L_m^2}} \approx \frac{r_r}{\omega_e \sigma L_r} = \frac{1}{\tau_r \omega_e \sigma}. \tag{3.21}$$

where $\tau_r = L_r / r_r$ is the rotor time constant. Let $r_s = 0$ for convenience of computation. Then, the stator current is obtained from (3.18) such that

$$\mathbf{I}_s \equiv \frac{\mathbf{V}_s}{j\omega_e L_s} \frac{1 + j\frac{s}{\sigma s_m}}{1 + j\frac{s}{s_m}}. \tag{3.22}$$

Equation (3.22) is transformed into

$$\begin{aligned} \mathbf{I}_s &= \mathbf{I}_{s0} \left[\frac{1+\sigma}{2\sigma} - \frac{1-\sigma}{2\sigma} \frac{1 - j\frac{s}{s_m}}{1 + j\frac{s}{s_m}} \right] \\ &= \mathbf{I}_{s0} \left(\frac{1+\sigma}{2\sigma} \right) + (-1) \frac{1-\sigma}{2\sigma} \mathbf{I}_{s0} \frac{|1 - j\frac{s}{s_m}|}{|1 + j\frac{s}{s_m}|} e^{j\angle \frac{1 - js/s_m}{1 + js/s_m}} \qquad (3.23) \\ &= \mathbf{I}_{s0} \left(\frac{1+\sigma}{2\sigma} \right) + \frac{1-\sigma}{2\sigma} \mathbf{I}_{s0} e^{j(\pi - 2\varphi)}, \qquad (3.24) \end{aligned}$$

where $\varphi = \tan^{-1}(s/s_m)$ and $\mathbf{I}_{s0} = \frac{\mathbf{V}_s}{j\omega_e L_s}$ is the no load current when $s = 0$ [8]. Equivalently, (3.24) is written in the polar coordinate form:

$$\mathbf{I}_s - \mathbf{I}_{s0} \left(\frac{1+\sigma}{2\sigma} \right) = \mathbf{I}_{s0} \left(\frac{1-\sigma}{2\sigma} \right) \angle(\pi - 2\varphi). \tag{3.25}$$

Note that $\mathbf{I}_{s0} = -j\frac{V_s}{\omega_e L_s} = -jI_{s0}$. The locus of $\mathbf{I}_s$ is a circle centered at $\left(0,\, jI_{s0}\frac{1+\sigma}{2\sigma}\right)$ having radius, $I_{s0}\left(\frac{1-\sigma}{2\sigma}\right)$. Based on (3.25), $\mathbf{I}_s$ can be drawn as a circle shown in Fig. 3.15, in which the horizontal axis denotes the imaginary values.

Since $\mathbf{I}_{s0}$ is drawn on the horizontal (imaginary) axis, the voltage vector, $\mathbf{V}_s$ appears on the vertical (real) axis. Therefore, the power factor (PF) angle is represented by the angle difference between the vertical axis and the current vector originating from the origin to the circle, i.e., $\phi = \angle \mathbf{V}_s - \angle \mathbf{I}_s$. Note that the minimum PF angle ϕ_{min} is attained when the current vector is tangential to the circle, and that the contact point determines the rated condition. In that case, a geometrical property of the right triangle (solid line) yields

$$\cos\phi_{min} = \frac{1-\sigma}{1+\sigma}. \tag{3.26}$$

It is also obvious that $\phi_{min} = 2\tan^{-1}\left(\frac{s_r}{s_m}\right)$, where s_r is the (rated) slip. Therefore,

$$\frac{s_r}{s_m} = \tan\frac{\phi_{min}}{2} = \frac{\sin\phi_{min}}{1 + \cos\phi_{min}} = \frac{\frac{2\sqrt{\sigma}}{1+\sigma}}{1 + \frac{1-\sigma}{1+\sigma}} \approx \sqrt{\sigma}. \tag{3.27}$$

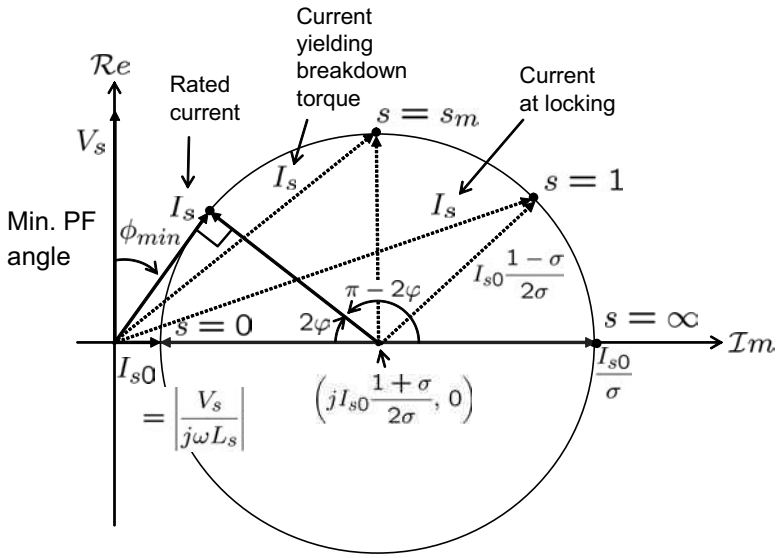

Figure 3.15: Circle (Heyland) diagram for IM with $r_s = 0$.

Applying (3.21), it follows that

$$s_r \approx \frac{1}{\tau_r \omega_e \sqrt{\sigma}}.$$

That is, the rated slip, s_r decreases as the leakage increases.

Finally, it follows from (3.22) that

$$\frac{I_s}{I_{s0}} = \frac{\sqrt{1 + \left(\frac{s_r}{\sigma s_m}\right)^2}}{\sqrt{1 + \left(\frac{s_r}{s_m}\right)^2}} \approx \frac{1}{\sqrt{\sigma}}. \tag{3.28}$$

This implies that the relative proportion of the torque producing current is inversely proportional to $\sqrt{\sigma}$ [8].

Exercise 3.6

Determine the rated current, I_s from the right triangle in the circle diagram shown in Fig. 3.15.

Solution

$$\sqrt{I_{s0}^2 \left(\frac{1+\sigma}{2\sigma}\right)^2 - I_{s0}^2 \left(\frac{1-\sigma}{2\sigma}\right)^2} = \frac{I_{s0}}{\sqrt{\sigma}}.$$

■

Exercise 3.7
Consider a three-phase IM whose parameters are listed in Table 3.1. Determine the following values or approximations:

a) leakage coefficient σ.
b) the minimum power factor.
c) rotor time constant.
d) rated slip.
e) no load current.
f) rated current.

Solution

a) $\sigma = 1 - \frac{41^2}{41.717 \times 42.38} = 0.049$.
b) $\cos\phi_{min} = \frac{1-0.049}{1+0.049} = 0.9$.
c) $\frac{41.717}{0.16} = 0.26$.
d) $s_r = \frac{1}{0.26 \times 377 \times \sqrt{0.049}} = 0.046$
e) $\frac{127}{15.98} = 7.947(\text{A})$.
f) $\frac{7.947}{\sqrt{0.049}} = 35.9(\text{A})$.

■

3.3 Slot Leakage Inductance and Current Displacement

Consider an open slot rotor shown in Fig. 3.16 (a). Assume that current I_{bar} is flowing through the rotor bar (shaded area) and that the current density, $J_{bar} = \frac{I_{bar}}{b_s h_s}$ is homogeneous over the bar cross-section, where $b_s h_s$ is the cross-sectional area. According to Ampere's law,

$$H(x) = \begin{cases} I_{bar}\frac{x}{h_s b_s}, & 0 \le x \le h_s \\ I_{bar}\frac{1}{b_{s1}}, & h_s \le x \le h_s + h_{s1} \end{cases}$$

where x is the height from the bottom of the bar and b_s is the bar width. The corresponding field density $B_x = \mu_0 H(x) = \mu_0 \frac{I_{bar}}{b_s}\frac{x}{h_s}$ increases linearly with $0 \le x \le h_s$. Note from Fig. 3.16 (a) that the bigger the flux loop is, the more current is included; thereby the field density reaches its peak at the rotor surface, as is shown in Fig. 3.16 (c).

Slot Leakage Inductance

Based on the coenergy equality,

$$W_c = \frac{1}{2}Li^2 = \frac{1}{2}\int_{vol} \mu H^2 dV,$$

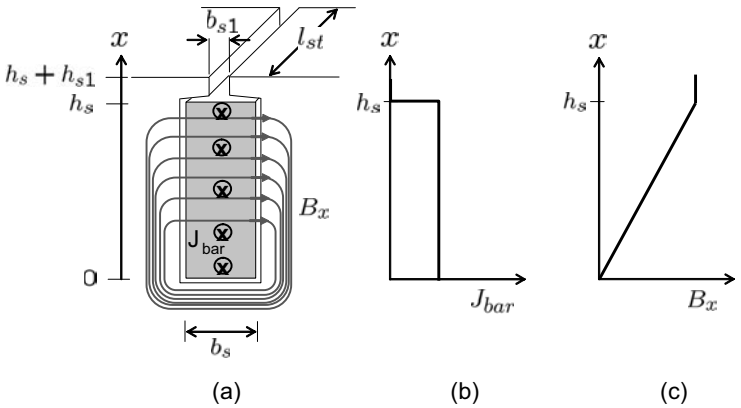

Figure 3.16: Rotor slot leakage flux for a uniform current flow (without slip): (a) slot leakage flux profile, (b) rotor bar current density, and (c) field density. [6].

the slot leakage inductance is given by

$$L_{sl} = \frac{1}{I_{bar}^2}\mu_0 \int_{vol} H^2 dV, \tag{3.29}$$

where $\int_{vol}$ is the volume integral. Then the resulting slot leakage inductance is [7]

$$\begin{aligned} L_{sl} &= \frac{1}{I_{bar}^2}\mu_0 \int_0^{h_s} H(x)^2 b_s l_{st} dx + \frac{1}{I_{bar}^2}\mu_0 \int_{h_s}^{h_s+h_{s1}} H(x)^2 b_{s1} l_{st} dx \\ &= \mu_0 l_{st}\left(\frac{h_s}{3b_s} + \frac{h_{s1}}{b_{s1}}\right). \end{aligned} \tag{3.30}$$

Current Displacement

If there is a high slip, then alternating flux passes through the rotor bar as shown in Fig. 3.17 (a). Let the flux crossing the bar from side to side be denoted by B_{sl}. This B_{sl}, alternating at a slip frequency, causes an eddy current loop I_{sl} inside the rotor bar in the direction opposing the change of the flux. Note that I_{sl} adds the current density in the upper part, while reducing the current density in the bottom part, as shown in Fig. 3.17 (a) and (b). That is, the rotor current will be pushed to the top of the bar. This is commonly known as the *skin effect*, and is often described as rotor bar current displacement. The current displacement has the effect of reducing the conduction area, i.e., increasing the rotor resistance.

Note from Fig. 3.17 (c) that the field density in the slot increases in a parabolic patten if a slip exists, i.e., it is reduced compared with the case without a slip. Therefore, the slot leakage inductance decreases with the displacement effect.

The displacement effect is described by the correction coefficient [7]:

$$K_r \equiv \frac{r_{bar}(ac)}{r_{bar}(dc)} = \xi \frac{\sinh 2\xi + \sin 2\xi}{\cosh 2\xi - \cos 2\xi}, \tag{3.31}$$

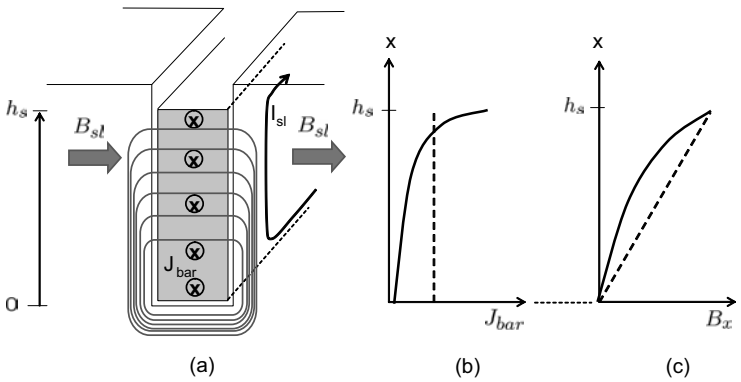

Figure 3.17: Rotor bar current displacement due to the slip field, B_{sl}: (a) slot leakage flux profile with a slip field component B_{sl}, (b) rotor bar current density, and (c) field density. [6].

where $\xi = h_{bar}/\delta$. Note that δ is the skin depth normally defined as

$$\delta = \sqrt{\frac{2}{\mu_0 \gamma \omega}},$$

where γ is the conductivity of the bar and ω is the frequency of the rotor current. At low slip frequency, current displacement is negligible. At higher slip frequencies, however, current displacement is more prominent. As is shown in Fig. 3.18, r_{bar} at 60Hz is about three times higher than r_{bar} at DC. Similarly, the slot leakage inductance changes and the correction coefficient is given by

$$K_x \equiv \frac{L_{sl}(ac)}{L_{sl}(dc)} = \frac{3(\sinh 2\xi - \sin 2\xi)}{2\xi(\cosh 2\xi - \cos 2\xi)}. \tag{3.32}$$

Fig. 3.18 shows plots of K_r and K_x as a function of ξ (slip), exhibiting a growth of the bar resistance and a decrease of the slot leakage inductance [7].

Exercise 3.8
Determine $r_{bar}(ac)/r_{bar}(dc)$ of a 3cm high copper bar when the line frequency is 60Hz and slip is 1. The copper conductivity is $\gamma = 5 \times 10^7$S/m.

Solution

$$\delta = \sqrt{2/(4\pi \times 10^{-7} \times 5 \times 10^7 \times 377)} = 9.19(\text{mm}).$$

Thus, $\xi = 30/9.19 = 3.26$. It follows from (3.31) that $r_{bar}(ac)/r_{bar}(dc) = 3.26$. That is, the rotor resistance increases 3.26 times when the slip is 1. ■

Double Cage Rotor

Fig. 3.19 shows the flux line profiles around double cage rotor slots at two extreme slip conditions: (a) high slip and (b) low slip. If the slip frequency is high, the field

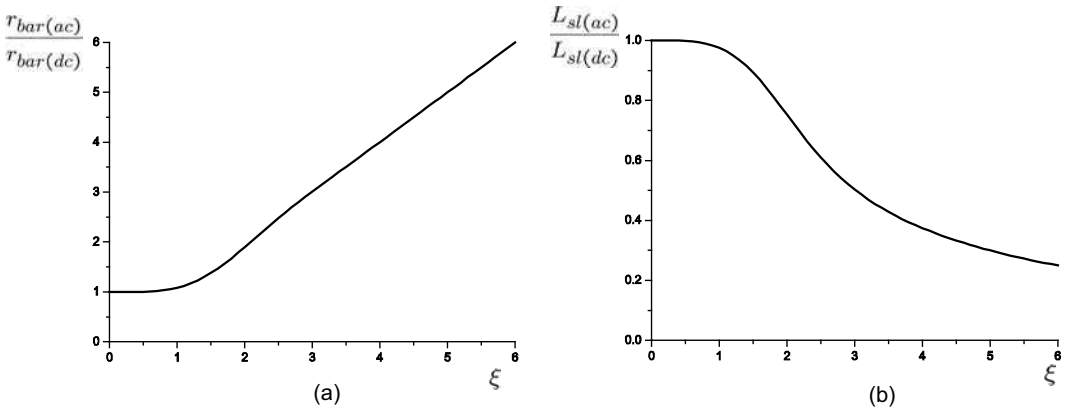

Figure 3.18: Correction coefficients reflecting displacement (skin) effect: (a) rotor bar resistance change (b) slot leakage inductance change.

cannot penetrate deeply inside the rotor core due to the skin effect. Therefore, the flux lines encircle only the upper conductors of the rotor slots. Hence, the major portion of induced current flows through the upper conductors. Since the effective conduction area is small, the rotor resistance r_{bar} is regarded high.

On the other hand, the field penetrates deeply if the slip frequency is low. The flux lines encircle both upper and lower conductors, and thereby induced current conducts both upper and lower conductors. Since large conduction area is provided, the effective rotor resistance becomes low at low slip.

Note from (3.9) that high r_{bar} is favorable for starting, since the starting torque is high with a high r_r. But, high r_r is not desirable at the normal (low slip) operation, since high r_r means low efficiency. However, the double cage rotor structure attempts to satisfy both requirements: The double cage IM has a high r_r during start and a low r_r at the rated operation.

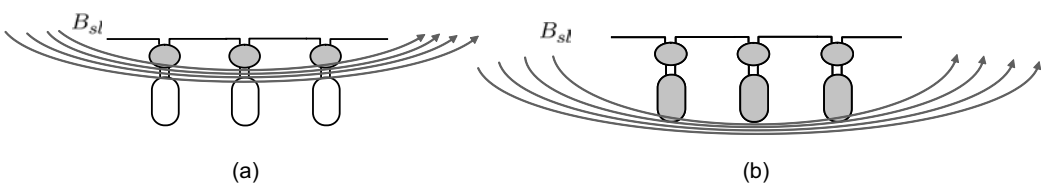

Figure 3.19: Flux lines around double cage rotor slots: (a) high slip ($r_{bar}(ac)$ is large.) and (b) low slip ($r_{bar}(ac)$ is small.).

Slot Types and NEMA Classification

The National Electrical Manufacturers Association (NEMA) of U.S.A. has classified cage-type induction machines into different categories to meet the diversified range

of applications [1]. These categories are characterized by torque-speed curves, and the most influential factor determining the torque-speed curve is the slot type.

As shown in Fig. 3.20 (a), the motor with double cage slot has high starting torque. The round slot motor has low starting torque, but has a steep slope near zero slip. Deep bar design yields medium shows performances.

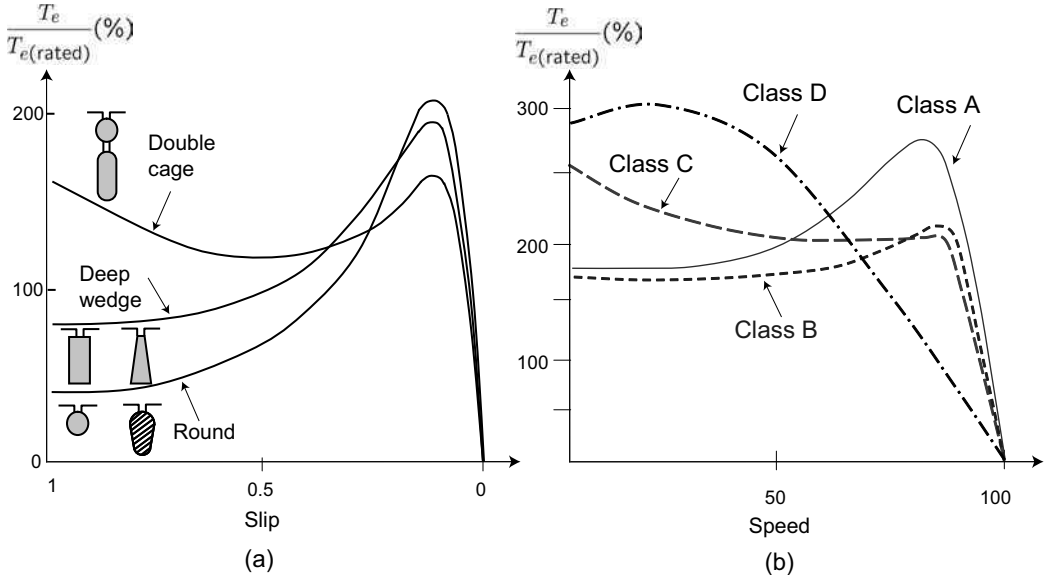

Figure 3.20: (a) Torque-speed curves for various rotor slot shapes [6] and (b) NEMA classification.

NEMA A machines are characterized by low rotor resistance; thus they have the steepest slope and a low operating slip. Therefore, they have high operating efficiency, but they have a larger starting torque with a larger starting current than general use design NEMA B machines. These characteristics result from low rotor leakage inductance and the skin effect of a mild deep bar design. NEMA A machines are suitable for inverter applications.

NEMA B machines are designed with higher rotor leakage inductance, so that the starting current is limited. The locked torque ranges from 130% to 70% of the full-load torque depending on the size. The corresponding locked-rotor current should not exceed 6.4 times the rated full-load current [1]. These general purpose motors are commonly used for constant-speed applications such as fans, centrifugal pumps, machine tools, and so forth.

NEMA C machines are designed to have a high locked rotor torque (200% of the full-load torque). To meet those starting requirements, these motors have double-cage rotor slots that have higher rotor resistance for higher slip.

NEMA D machines are designed for a wide slip range (85∼95% of synchronous speed). These machines have low efficiency, and are thereby easily overheated. Thus, they are usually designed for intermittent operation [1].

3.3.1 Line Starting

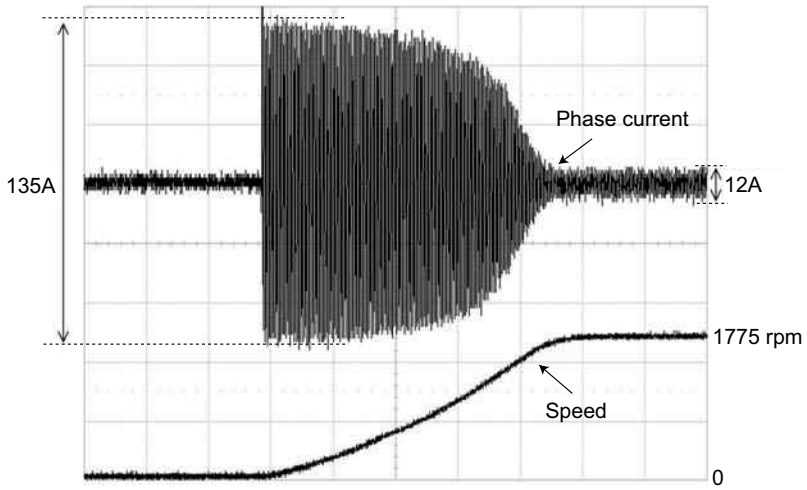

Figure 3.21: Induction motor line starting (experimental result): 4-pole, 1.5kW, 220V line-to-line.

The starting method by connecting IM directly to the power grid is called line start. Since the slip is equal to one at the time of line starting, the starting current is huge (about $6 \sim 8$ times larger than the rated current). Fig. 3.21 shows an experimental plot of line current at a line starting. The large starting current may trip the circuit breaker or blow fuses.

To avoid such problems, soft starters are utilized in the industrial sites. The soft starters are made with thyristor switches: Thyristors are connected in anti-parallel in each phase, as shown in Fig. 3.22. By changing the firing angle α of the thyristors, the rms voltage is controlled. Specifically, the rms voltage level decreases as α increases. Cases of different firing angles are shown in Fig. 3.22 (b) and (c). With the soft starter, the rms value of the motor terminal voltage can be increased gradually along with the motor shaft speed.

3.4 IM Speed Control

With the use of semiconductor switches such as IGBTs, it is possible to change the feeding voltage and frequency. A simple speed control method would be to change the voltage only. But this method has a limited effectiveness. It is better to change the voltage in accordance with the frequency.

3.4.1 Variable Voltage Control

Fig. 3.23 shows the torque-speed curves of an IM for different voltages while the frequency is fixed at 60Hz. Recall from (3.11) that the breakdown torque is propor-

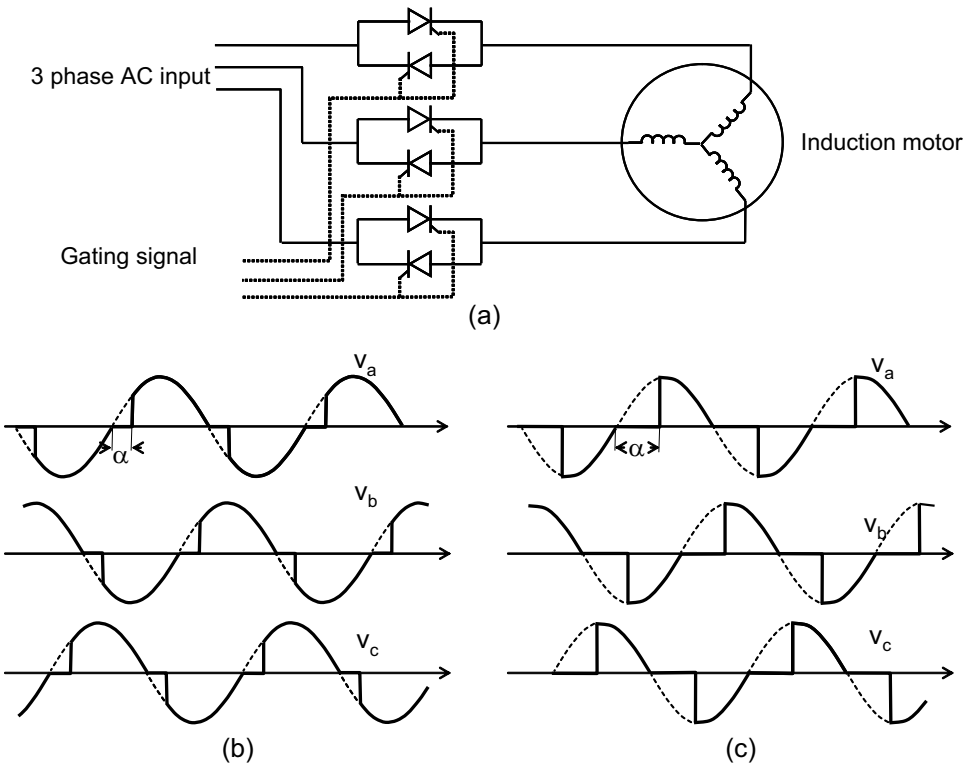

Figure 3.22: Soft starter and applied voltages: (a) soft starter circuit, (b) a large rms voltage with a small α angle, and (c) a small rms voltage with a large α angle.

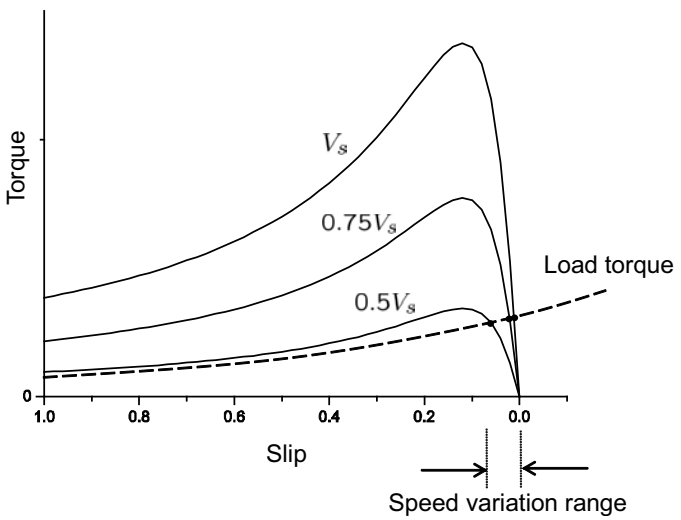

Figure 3.23: Torque-speed curves for variable voltage/fixed frequency operations.

tional to the square of the voltage. It also shows a fluidal load curve. Considering

the intersection (operation) points, one can notice that the speed control range is quite small. But with the NEMA class D machines, the speed control range can be extended. Due to their inherent low efficiency, however, class D machines are rarely used.

3.4.2 Variable Voltage Variable Frequency (VVVF) Control

With the use of inverters, it is possible to provide a variable voltage/variable frequency source to the motor. Changing the frequency means changing the synchronous speed. Note from (3.15) that the stator voltage is approximated as $\mathbf{V}_s = r_s I_s + j\omega_e(L_{ls}+L_m)\mathbf{I}_s \approx j\omega_e L_s \mathbf{I}_s = j\omega_e \boldsymbol{\lambda}_s$. Therefore, the magnitude of flux satisfies

$$\lambda_s = \frac{V_s}{\omega_e} = \frac{V_s}{2\pi f}. \tag{3.33}$$

That is, voltage to frequency ratio implies the flux. To maintain a constant flux level, the voltage should be increased when the frequency increase. In contrast, the voltage should be decreased when the frequency decreases. Otherwise, flux saturation occurs.

Torque equation (3.7) is approximated as

$$T_e = \frac{3P}{2}\left(\frac{V_s}{\omega_e}\right)^2 \frac{\omega_{sl} r_r}{r_r^2 + \omega_{sl}^2 L_{lr}^2} = \frac{3P}{2}\lambda_s^2 \frac{\omega_{sl} r_r}{r_r^2 + \omega_{sl}^2 L_{lr}^2}. \tag{3.34}$$

According to (3.34), torque just depends on the slip independently of the frequency as long as the voltage to frequency ratio (V/F) is kept constant. Hence, as shown in Fig. 3.24, the torque curves in the same shape shift in response to the different frequencies.

The motor control method keeping the V/F constant is called variable voltage/variable frequency (VVVF) method. Specifically, consider an operation point marked by "x". Note that it is impossible to operate the motor with 127V at 60Hz, since "x" is in unstable region. However with reduced voltage and frequency (25V, 12Hz), "x" is a stable operation point. Similarly, if both voltage and frequency are doubled at the same time (50V, 24Hz), another stable operation point is obtained "xx". Hence, while keeping V/F constant, it is possible to drive crane like loads requiring high start torque.

In the low-speed region, the voltage drop over the stator resistance is not negligible. For example, consider the IM in Table 3.1. Note that $r_s/\omega_e L_s = 0.048$ at 60Hz, whereas $r_s/\omega_e L_s = 0.48$ at 6Hz, i.e., the ohmic drop takes about a half of the input voltage at 6Hz. To compensate for this voltage drop, the voltage profile is boosted in a low-speed region, as shown in Fig. 3.25.

If speed information is available, it is possible to construct a slip-based feedback controller as shown in Fig. 3.25 [5]. The speed controller output is regarded as a torque command, and a required slip is calculated in proportion to the torque command. The calculated slip is added to a measured rotor speed, determining

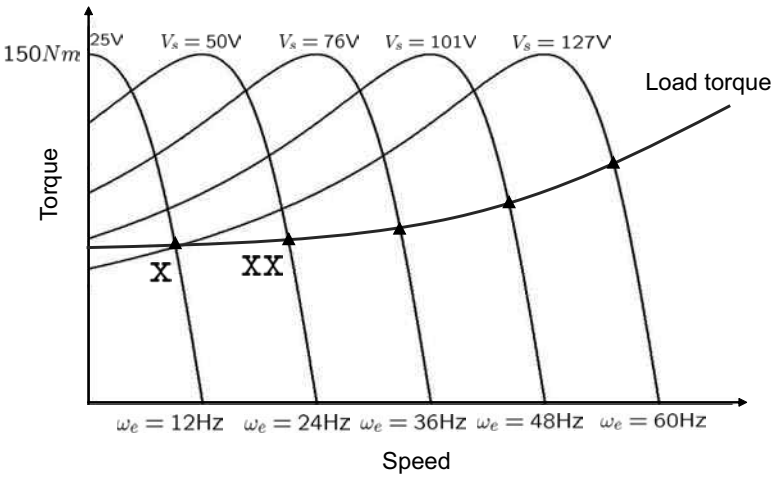

Figure 3.24: Torque-speed curves for a VVVF operation.

the electrical frequency: $\omega_e = \omega_r + \omega_{sl}$. This electrical speed is used as a command frequency to the VVVF inverter. Based on a V/F table, a voltage level is determined. VVVF inverters are widely used in many applications where precision is not essential. These applications include compressors, blowers, cranes, and transportation vehicles such as subway trains and locomotives.

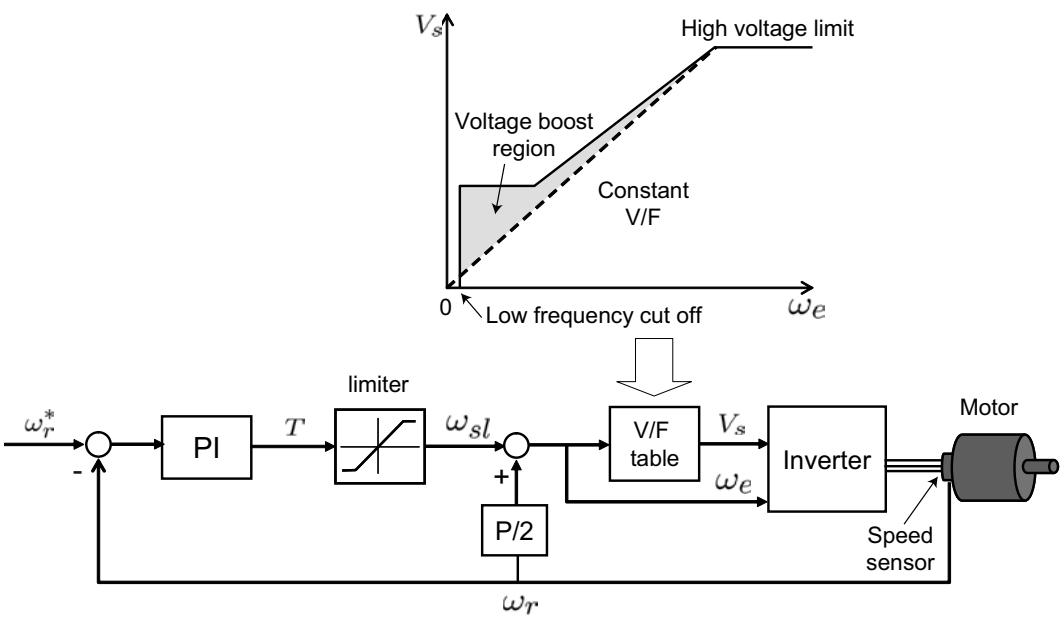

Figure 3.25: VVVF pattern and a slip-based VVVF speed controller.

Bibliography

[1] T. Wildi, *Electrical Machines, Drives, and Power Systems,* 2nd Ed., Prentice Hall, 1991.

[2] A. E. Fitzgerlad, C. Kingsley, Jr., and S. D. Umans, *Electric Machinery*, 5th Ed., McGraw Hill, New York, 2003.

[3] P.C. Sen, *Principle of Electric Machines and Power Electronics,* John Wiley & Sons, New York, 1997.

[4] B. K. Bose, *Modern Power Electronics and AC Drives,* Prentice Hall PTR, 2002.

[5] J.M.D. Murphy, *Thyristor Control of AC Motors,* Pergamon Press, 1973.

[6] A. Binder, *The squirrel cage induction machine,* http://www.ew.e-technik.tu-darmstadt.de/cms/, Lecture Note, Darmstadt University, 2008.

[7] I. Boldea and S. A. Nasar, *The Indution Machine Handbook,* CRC Press, 2002.

[8] W. Leonhard, *Control of Electrical Drives,* Springer, 1996.

Problems

3.1 Consider a 4-pole, three-phase IM with the following rated parameters: output power = 15kW, line voltage (line-to-line) = 440V, line frequency = 60Hz, and rated speed = 1748rpm. The sum of windage and friction loss is 1 kW. Calculate the air gap power and rotor copper loss.

3.2 A three-phase IM having a synchronous speed of 900rpm draws 40kVA from a three-phase feeder. The rated slip speed is 3% of the synchronous speed. The power factor is 0.9, and the total stator loss is 4kW. Calculate the torque developed by the motor.

3.3 Consider a 4-pole, three-phase IM with the following parameters: $r_s = 1.6\Omega$, $r_r = 0.996\Omega$, $L_s = 66$mH, $L_{ls} = 3.28$mH, and $L_{lr} = 3.28$mH. Assume that three-phase, 220V (line-to-line), 60Hz AC source is applied to the motor.

a) Calculate the slip yielding the breakdown torque.
b) If the rated slip is $s = s_m/2.5$, determine the rotor current, I'_r and torque using the modified equivalent circuit.
c) Determine the magnetizing current.
d) Calculate the power factor at the rated condition.

3.4 Consider a 4-pole, three-phase IM with the following parameters: $r_s = 0.1\Omega$, $r_r = 0.25\Omega$, $L_s = 150$mH, $L_{ls} = 3$mH, and $L_{lr} = 3$mH. A 440V (line-to-line), 60Hz AC source is applied to the motor. The rated slip is 3%. Determine the rated and starting torques.

3.5 Consider a 4-pole, three-phase IM with the following parameters: $r_s = 0\Omega$, $r_r = 0.25\Omega$, $L_s = 150$mH, $L_{ls} = 3$mH, and $L_{lr} = 3$mH. Assume that a 440V (line-to-line), 60Hz AC source is applied to the motor.

a) Draw a circle (Heyland) diagram.
b) Determine the rated current.
c) Determine the minimum PF angle.

3.6 Consider the thyristor voltage control circuit shown in Fig. 3.22. Assume that the source phase voltage is $V \sin \omega_e t$. Derive a relationship between the rms output voltage and the firing angle, α.

3.7 A three-phase 220V, 4-pole IM runs at 1750rpm. Suppose that the input voltage is increased to 250V. For the same load, calculate the slip and speed.

3.8 (No load test) A four pole, three-phase IM is connected to 220V(line-to-line), 60Hz line. It runs at 1750 rpm without a load. The phase current is $I_s = 2$A and the reactive power is 50W.

a) Calculate the power factor angle.
b) Calculate the stator inductance.
c) Calculate the stator resistance.

3.9 (Locked rotor test) While the IM is locked, a 90V(line-to-line), 60Hz three-phase voltage source is applied. The measured stator current is 7A, the resistance of the stator is 2.1Ω and the measured power is 800W.

a) Calculate the power factor angle.
b) Calculate the impedance.
c) Calculate the rotor resistance, r_r.
d) Assuming $L_{ls} = L_{lr}$, find the leakage impedance.

Chapter 4

Dynamic Modeling of Induction Motors

When the AC motor dynamics are described in a synchronous reference frame, they resemble the DC motor dynamics under certain conditions. Therefore, in the synchronous frame, the dq-axes currents can be interpreted as the field and torque components. The transformation maps defined in the previous chapter play a key role in deriving the dynamic models.

4.1 Voltage Equation

Time derivative of flux linkage yields a voltage equation. First, we derive stator and rotor flux linkage equations and map them into the complex plane. The voltage equations can be described either in the stationary or synchronous frames.

4.1.1 Flux Linkage

The stator flux is generated by stator and rotor currents. We will first consider the stator flux contributed by the stator current. Stator flux generated by a-phase stator current is described as a bunch of dotted lines in Fig. 4.1 (a). The innermost line that does not cross the air gap depicts leakage flux. Therefore, a-phase flux linkage produced by a-phase current is given by $\lambda_{as} = (L_{ms} + L_{ls})i_{as}$, where L_{ms} and L_{ls} denote the stator mutual and leakage inductances, respectively. On the other hand, a-phase flux produced by b-phase current is given by $\lambda_{as} = -\frac{1}{2}L_{ms}i_{as}$, since the a-phase coil and b-phase coil are separated spatially by $\frac{2\pi}{3}$ and $\cos(\frac{2\pi}{3}) = -\frac{1}{2}$. Due to the symmetry among the phases, it follows that

$$\boldsymbol{\lambda}_{abcs} = \mathbf{L}_{abcs}\mathbf{i}_{abcs}\,, \tag{4.1}$$

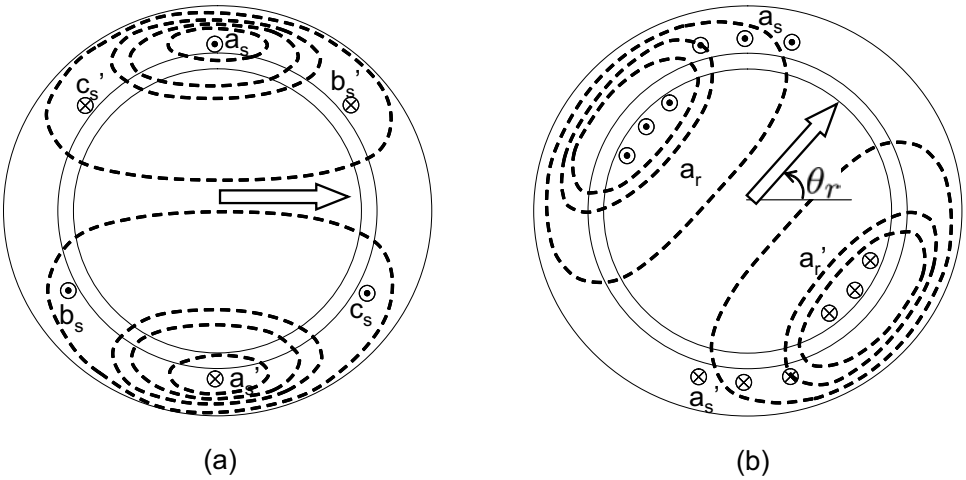

Figure 4.1: *A*-phase flux linkage (a) by *a*-phase stator current i_{as} and (b) by *a*-phase rotor current i_{ar}.

where

$$\boldsymbol{\lambda}_{abcs} = \begin{bmatrix} \lambda_{as} \\ \lambda_{bs} \\ \lambda_{cs} \end{bmatrix}, \ \mathbf{i}_{abcs} = \begin{bmatrix} i_{as} \\ i_{bs} \\ i_{cs} \end{bmatrix}, \text{ and } \mathbf{L}_{abcs} = \begin{bmatrix} L_{ms} + L_{ls} & -\frac{1}{2}L_{ms} & -\frac{1}{2}L_{ms} \\ -\frac{1}{2}L_{ms} & L_{ms} + L_{ls} & -\frac{1}{2}L_{ms} \\ -\frac{1}{2}L_{ms} & -\frac{1}{2}L_{ms} & L_{ms} + L_{ls} \end{bmatrix}.$$

The stator flux is also affected by the rotor current. However, the rotor coil position is a function of rotor angle, θ_r. Fig. 4.1 (b) shows the stator flux linkage produced by rotor current. Note that the flux linking between stator and rotor windings is maximized when $\theta_r = 0$. On the other hand, if $\theta_r = \pi/2$, the flux linking is equal to zero. For simplicity, it can be described as $\lambda_{as} = L_{ms} \cos\theta_r i_{ar}$ for *a*-phase. Since *b* and *c* phase windings are $2\pi/3$ and $4\pi/3$ apart, respectively, the stator flux contributed by the rotor current is

$$\boldsymbol{\lambda}_{abcs} = \mathbf{M}(\theta_r)\mathbf{i}_{abcr}\,, \tag{4.2}$$

where

$$\mathbf{i}_{abcr} = \begin{bmatrix} i_{ar} \\ i_{br} \\ i_{cr} \end{bmatrix} \quad \text{and} \quad \mathbf{M}(\theta_r) = L_{ms} \begin{bmatrix} \cos\theta_r & \cos(\theta_r + \frac{2\pi}{3}) & \cos(\theta_r - \frac{2\pi}{3}) \\ \cos(\theta_r - \frac{2\pi}{3}) & \cos\theta_r & \cos(\theta_r + \frac{2\pi}{3}) \\ \cos(\theta_r + \frac{2\pi}{3}) & \cos(\theta_r - \frac{2\pi}{3}) & \cos\theta_r \end{bmatrix}.$$

Complete Flux Linkage Equations

Combining (4.1) with (4.2), a complete expression of the stator flux linkage is given by

$$\boldsymbol{\lambda}_{abcs} = \mathbf{L}_{abcs}\mathbf{i}_{abcs} + \mathbf{M}(\theta_r)\mathbf{i}_{abcr}. \tag{4.3}$$

Similarly, the rotor flux linkage seen from the rotor frame is given by

$$\boldsymbol{\lambda}_{abcr} = \mathbf{M}(-\theta_r)\mathbf{i}_{abcs} + \mathbf{L}_{abcr}\mathbf{i}_{abcr}\,, \tag{4.4}$$

where

$$\boldsymbol{\lambda}_{abcr} = \begin{bmatrix}\lambda_{ar}\\ \lambda_{br}\\ \lambda_{cr}\end{bmatrix} \quad \text{and} \quad \mathbf{L}_{abcr} = \begin{bmatrix} L_{ms}+L_{lr} & -\frac{1}{2}L_{ms} & -\frac{1}{2}L_{ms}\\ -\frac{1}{2}L_{ms} & L_{ms}+L_{lr} & -\frac{1}{2}L_{ms}\\ -\frac{1}{2}L_{ms} & -\frac{1}{2}L_{ms} & L_{ms}+L_{lr}\end{bmatrix}.$$

and L_{lr} is the rotor leakage inductance. From the rotor frame, the stator current is looked behind by angle θ_r. Thus, $-\theta_r$ appears in the mutual inductance matrix, $\mathbf{M}$. Note that $\mathbf{L}_{abcr}$ is the same as $\mathbf{L}_{abcs}$ except that the stator leakage inductance L_{ls} is replaced by the rotor leakage inductance L_{lr}.

Exercise 4.1
Consider a P pole induction machine with a uniform air gap g, the rotor diameter D, and the stacking length ℓ. Assume that the number of turns per phase is N and that the number of slots per pole per phase is equal to one, i.e., $q = 1$. (Refer to the square wave MMF shown in Fig. 2.4.) Assume further that the winding factor is k_w.
a) Derive an expression for the fundamental component of air gap field density, B_{a1}, when only a-phase current, i_a flows.
b) Determine flux per pole.
c) Derive an expression for the self inductance, L_{ms} (without leakage), of a-phase winding using the result of b).

Solution
a) Expressing the MMF as a function of the angular variable θ, the fundamental component is equal to

$$\text{MMF}_a = \frac{N}{P/2}k_w\frac{1}{2}i_a\frac{4}{\pi}\cos\theta = \frac{4}{\pi}\frac{N}{P}k_w i_a\cos\theta,$$

where $4/\pi$ is the coefficient of the fundamental component of a square wave. As a similar example, refer to (2.1). Therefore, it follows that

$$B_{a1} = \mu_0\frac{1}{g}\times\text{MMF}_a = \frac{4}{\pi}\mu_0 k_w\frac{Ni_a}{gP}\cos\theta.$$

b)

$$\Phi_{pole} = \ell\int_{-\pi/2}^{\pi/2} B_{a1}\left(\frac{D}{2}\right)d\theta\frac{1}{P/2} = \frac{4}{\pi}\frac{\mu_0\ell D}{g}\frac{Nk_w}{P}i_a\frac{2}{P}.$$

c)

$$L_{ms} = \frac{P}{2}\frac{Nk_w}{P/2}\Phi_{pole}\frac{1}{i_a} = \frac{8}{\pi}\frac{\mu_0\ell D}{g}\left(\frac{Nk_w}{P}\right)^2.$$

■

Description in the Complex Plane

In this part, the flux vector $\boldsymbol{\lambda}_{abcs}$ is mapped into the complex plane using (2.22). But, the computation procedure is separated into two steps: In the first step, the mapping of (4.1) is considered. From the definition, we obtain

$$
\begin{aligned}
\boldsymbol{\lambda}^{s}_{dqs} &= \frac{2}{3}\left[\lambda_{as}(t) + e^{j\frac{2\pi}{3}}\lambda_{bs}(t) + e^{-j\frac{2\pi}{3}}\lambda_{cs}(t)\right] \\
&= \frac{2}{3}\Bigg[(L_{ms}+L_{ls})i_{as} - \frac{1}{2}L_{ms}i_{bs} - \frac{1}{2}L_{ms}i_{cs} \\
&\quad + e^{j\frac{2\pi}{3}}\Big\{-\frac{1}{2}L_{ms}i_{as} + (L_{ms}+L_{ls})i_{bs} - \frac{1}{2}L_{ms}i_{cs}\Big\} \\
&\quad + e^{-j\frac{2\pi}{3}}\Big\{-\frac{1}{2}L_{ms}i_{as} - \frac{1}{2}L_{ms}i_{bs} + (L_{ms}+L_{ls})i_{cs}\Big\}\Bigg] \\
&= \frac{2}{3}\Bigg[(\frac{3}{2}L_{ms}+L_{ls}-\frac{1}{2}L_{ms})i_{as} - \frac{1}{2}L_{ms}i_{bs} - \frac{1}{2}L_{ms}i_{cs} \\
&\quad + e^{j\frac{2\pi}{3}}\Big\{-\frac{1}{2}L_{ms}i_{as} + (\frac{3}{2}L_{ms}+L_{ls}-\frac{1}{2}L_{ms})i_{bs} - \frac{1}{2}L_{ms}i_{cs}\Big\} \\
&\quad + e^{-j\frac{2\pi}{3}}\Big\{-\frac{1}{2}L_{ms}i_{as} - \frac{1}{2}L_{ms}i_{bs} + (\frac{3}{2}L_{ms}+L_{ls}-\frac{1}{2}L_{ms})i_{cs}\Big\}\Bigg] \\
&= \frac{2}{3}\Bigg[(\frac{3}{2}L_{ms}+L_{ls})(i_{as} + e^{j\frac{2\pi}{3}}i_{bs} + e^{-j\frac{2\pi}{3}}i_{cs}) - \frac{1}{2}L_{ms}i_{as} - \frac{1}{2}L_{ms}i_{bs} - \frac{1}{2}L_{ms}i_{cs} \\
&\quad + e^{j\frac{2\pi}{3}}\Big\{-\frac{1}{2}L_{ms}i_{as} - \frac{1}{2}L_{ms}i_{bs} - \frac{1}{2}L_{ms}i_{cs}\Big\} \\
&\quad + e^{-j\frac{2\pi}{3}}\Big\{-\frac{1}{2}L_{ms}i_{as} - \frac{1}{2}L_{ms}i_{bs} - \frac{1}{2}L_{ms}i_{cs}\Big\}\Bigg] \\
&= (\frac{3}{2}L_{ms}+L_{ls})\frac{2}{3}(i_{as} + e^{j\frac{2\pi}{3}}i_{bs} + e^{-j\frac{2\pi}{3}}i_{cs}) \\
&= L_s\mathbf{i}^{s}_{dqs}\,, \qquad (4.5)
\end{aligned}
$$

where $L_s = \frac{3}{2}L_{ms} + L_{ls}$. Note that (4.5) is identical with the dq part of the matrix formalism (2.36).

Second, the contribution from the rotor current, (4.2) is mapped into the complex

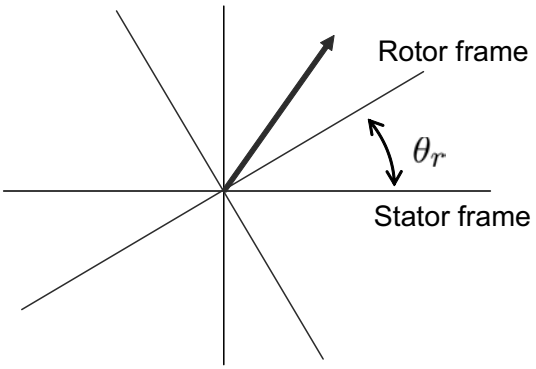

Figure 4.2: Rotor and stator frames.

plane:

$$
\begin{aligned}
\boldsymbol{\lambda}^s_{dqs} &= \frac{2}{3}\left[\lambda_{as}(t) + e^{j\frac{2\pi}{3}}\lambda_{bs}(t) + e^{-j\frac{2\pi}{3}}\lambda_{cs}(t)\right] \\
&= \frac{2}{3}L_{ms}\left[\cos\theta_r i_{ar} + \cos(\theta_r + 2\pi/3)i_{br} + \cos(\theta_r - 2\pi/3)i_{cr}\right. \\
&\quad + e^{j\frac{2\pi}{3}}\left\{\cos(\theta_r - 2\pi/3)i_{ar} + \cos\theta_r i_{br} + \cos(\theta_r + 2\pi/3)i_{cr}\right\} \\
&\quad \left. + e^{-j\frac{2\pi}{3}}\left\{\cos(\theta_r + 2\pi/3)i_{ar} + \cos(\theta_r - 2\pi/3)i_{br} + \cos\theta_r i_{cr}\right\}\right] \\
&= \frac{2}{3}\frac{1}{2}L_{ms}\left[(e^{j\theta_r} + e^{-j\theta_r})i_{ar} + (e^{j(\theta_r+\frac{2}{3}\pi)} + e^{-j(\theta_r+\frac{2}{3}\pi)})i_{br}\right. \\
&\quad + (e^{j(\theta_r-\frac{2}{3}\pi)} + e^{-j(\theta_r-\frac{2}{3}\pi)})i_{cr} + (e^{j\theta_r} + e^{-j(\theta_r-\frac{4}{3}\pi)})i_{ar} \\
&\quad + (e^{j(\theta_r+\frac{2}{3}\pi)} + e^{-j(\theta_r-\frac{2}{3}\pi)})i_{br} + (e^{j(\theta_r+\frac{4}{3}\pi)} + e^{-j\theta_r})i_{cr} \\
&\quad + (e^{j\theta_r} + e^{-j(\theta_r+\frac{4}{3}\pi)})i_{ar} + (e^{j(\theta_r-\frac{4}{3}\pi)} + e^{-j\theta_r})i_{br} \\
&\quad \left. + (e^{j(\theta_r-\frac{2}{3}\pi)} + e^{-j(\theta_r+\frac{2}{3}\pi)})i_{cr}\right] \\
&= \frac{1}{2}L_{ms}\frac{2}{3}\left[3e^{j\theta_r}i_{ar} + 3e^{j(\theta_r+\frac{2}{3}\pi)}i_{br} + 3e^{j(\theta_r-\frac{2}{3}\pi)}i_{cr}\right] \\
&= \left(\frac{3}{2}L_{ms}\right)e^{j\theta_r}\frac{2}{3}\left[i_{ar} + e^{j\frac{2}{3}\pi}i_{br} + e^{-j\frac{2}{3}\pi}i_{cr}\right] \\
&= L_m e^{j\theta_r}\mathbf{i}^r_{dqr}, \qquad (4.6)
\end{aligned}
$$

where $L_m \equiv \frac{3}{2}L_{ms}$. Note that the rotor reference frame is turned by θ_r, as depicted in Fig. 4.2. Therefore, if we look at the rotor current from the stationary frame, it is seen as $\mathbf{i}^r_{dqr}e^{j\theta_r}$.

Combining (4.5) with (4.6), we obtain the stator flux in the stationary frame as

$$\boldsymbol{\lambda}^s_{dqs} = L_s\mathbf{i}^s_{dqs} + L_m e^{j\theta_r}\mathbf{i}^r_{dqr}. \qquad (4.7)$$

In a similar manner, the rotor flux equation with reference to the rotor frame is

obtained as

$$\boldsymbol{\lambda}^r_{dqr} = L_r \mathbf{i}^r_{dqr} + L_m e^{-j\theta_r} \mathbf{i}^s_{dqs}, \tag{4.8}$$

where $L_r = \frac{3}{2}L_{ms} + L_{lr}$. Note that since the rotor frame is on $e^{j\theta_r}$, the stator current contribution is seen behind by θ_r in the rotor frame. Therefore, $e^{-j\theta_r}$ is multiplied to $\mathbf{i}^s_{dqs}$. Superscript 'r' is used to denote the quantities in the rotor frame.

Exercise 4.2
Derive (4.8) from (4.4).

4.1.2 Voltage Equations

Voltage equations for the stator and rotor are given by

$$\mathbf{v}^s_{abcs} = r_s \mathbf{i}^s_{abcs} + p\boldsymbol{\lambda}^s_{abcs}, \tag{4.9}$$
$$\mathbf{v}^r_{abcr} = r_r \mathbf{i}^r_{abcr} + p\boldsymbol{\lambda}^r_{abcr}. \tag{4.10}$$

Utilizing the mapping rule, (2.22) we obtain from (4.5) and (4.9) a stator voltage equation in the stationary dq-frame such that

$$\mathbf{v}^s_{dqs} = r_s \mathbf{i}^s_{dqs} + p\boldsymbol{\lambda}^s_{dqs}. \tag{4.11}$$

Similarly, we obtain from (4.5) and (4.10) a rotor voltage equation in the rotor dq-frame such that

$$\mathbf{v}^r_{dqr} = r_r \mathbf{i}^r_{dqr} + p\boldsymbol{\lambda}^r_{dqr}. \tag{4.12}$$

Voltage Equation in the Synchronous Frame

The synchronous frame is a rotating frame that rotates at the same speed as the electrical angular velocity, ω_e. Hence at time t, angular position of the d–axis of the synchronous frame is

$$\theta_e = \int_0^t \omega_e dt = \omega_e t.$$

Note that the electrical speed ω_e is different from the rotor speed $\frac{P}{2}\omega_r$ in induction machines, whereas they are the same in synchronous machines. Further, it is emphasized that the synchronous frame is used in both cases as a reference frame.

By multiplying $e^{-j\theta_e}$ to $\mathbf{v}^s_{dqs}$ in the stationary frame, we have a new representation $\mathbf{v}^e_{dqs}$ in the synchronous frame, i.e.,

$$\mathbf{v}^e_{dqs} = e^{-j\theta_e} \mathbf{v}^s_{dqs}, \tag{4.13}$$

where the superscript "e," meaning exciting, indicates that a variable is described in the synchronous frame.

Multiplying $e^{-j\theta_e}$ on both sides of (4.11), we have

$$\begin{aligned}\mathbf{v}^e_{dqs} = e^{-j\theta_e}\mathbf{v}^s_{dqs} &= r_s e^{-j\theta_e}\mathbf{i}^s_{dqs} + e^{-j\theta_e}p\boldsymbol{\lambda}^s_{dqs} \\ &= r_s\mathbf{i}^e_{dqs} + e^{-j\theta_e}p\boldsymbol{\lambda}^s_{dqs}. \end{aligned} \tag{4.14}$$

Note that the differential operator, p, and an operand, $e^{-j\theta_e}$, do not commute, i.e., $pe^{-j\theta_e} \neq e^{-j\theta_e}p$, since θ_e is a function of t. Therefore, a technique of inserting the identity $1 = e^{j\theta_e}e^{-j\theta_e}$ needs to be utilized [1]:

$$\begin{aligned}\mathbf{v}^e_{dqs} &= r_s\mathbf{i}^e_{dqs} + e^{-j\theta_e}pe^{j\theta_e}e^{-j\theta_e}\boldsymbol{\lambda}^s_{dqs} \\ &= r_s\mathbf{i}^e_{dqs} + e^{-j\theta_e}\left(j\omega_e e^{j\theta_e}e^{-j\theta_e}\boldsymbol{\lambda}^s_{dqs} + e^{j\theta_e}p\boldsymbol{\lambda}^e_{dqs}\right) \\ &= r_s\mathbf{i}^e_{dqs} + j\omega_e\boldsymbol{\lambda}^e_{dqs} + p\boldsymbol{\lambda}^e_{dqs}. \end{aligned} \tag{4.15}$$

Note that the additional term, $j\omega_e\boldsymbol{\lambda}^e_{dqs}$, appears in the synchronous reference frame. It originates from the transformation into a moving frame, and is known as the "*speed voltage*" or called the "*coupling voltage.*" Let $\mathbf{v}^e_{dqs} = v^e_{ds} + jv^e_{qs}$ and $\boldsymbol{\lambda}^e_{dqs} = \lambda^e_{ds} + j\lambda^e_{qs}$. Then, (4.15) is written componentwise as

$$v^e_{ds} = r_s i^e_{ds} + p\lambda^e_{ds} - \omega_e\lambda^e_{qs} \tag{4.16}$$

$$v^e_{qs} = r_s i^e_{qs} + p\lambda^e_{qs} + \omega_e\lambda^e_{ds}\,. \tag{4.17}$$

The rotor voltage equation can be transformed in the same way. But, the transforming angle is $\theta_e - \theta_r$. Multiplying both sides of (4.12) by $e^{-j(\theta_e-\theta_r)}$, we have

$$\mathbf{v}^e_{dqr} = r_r\mathbf{i}^e_{dqr} + (p + j(\omega_e - \omega_r))\boldsymbol{\lambda}^e_{dqr}. \tag{4.18}$$

Equivalently, (4.18) is expressed componentwise such that

$$v^e_{dr} = r_r i^e_{dr} + p\lambda^e_{dr} - (\omega_e - \omega_r)\lambda^e_{qr} \tag{4.19}$$

$$v^e_{qr} = r_r i^e_{qr} + p\lambda^e_{qr} + (\omega_e - \omega_r)\lambda^e_{dr}\,. \tag{4.20}$$

Comparing (4.19) and (4.20) with (4.16) and (4.17), one can see the identical structure. However, the slip speed, $\omega_e - \omega_r$ appears instead of ω_e.

Note that

$$\lambda^e_{ds} = L_s i^e_{ds} + L_m i^e_{dr} = L_{ls} i^e_{ds} + L_m(i^e_{ds} + i^e_{dr}) \tag{4.21}$$

$$\lambda^e_{qs} = L_s i^e_{qs} + L_m i^e_{qr} = L_{ls} i^e_{qs} + L_m(i^e_{qs} + i^e_{qr}) \tag{4.22}$$

$$\lambda^e_{dr} = L_r i^e_{dr} + L_m i^e_{ds} = L_{lr} i^e_{dr} + L_m(i^e_{dr} + i^e_{ds}) \tag{4.23}$$

$$\lambda^e_{qr} = L_r i^e_{qr} + L_m i^e_{qs} = L_{lr} i^e_{qr} + L_m(i^e_{qr} + i^e_{qs}) \tag{4.24}$$

and $L_s = L_{ls} + L_m$ and $L_r = L_{lr} + L_m$. Based on (4.16), (4.17), (4.19), and (4.20), an equivalent circuit for the synchronous frame model can be drawn as ig. 4.1. Note also that ω_e appears in the primary side, but the slip speed $\omega_{sl} \equiv \omega_e - \omega_r$ appears in the secondary side.

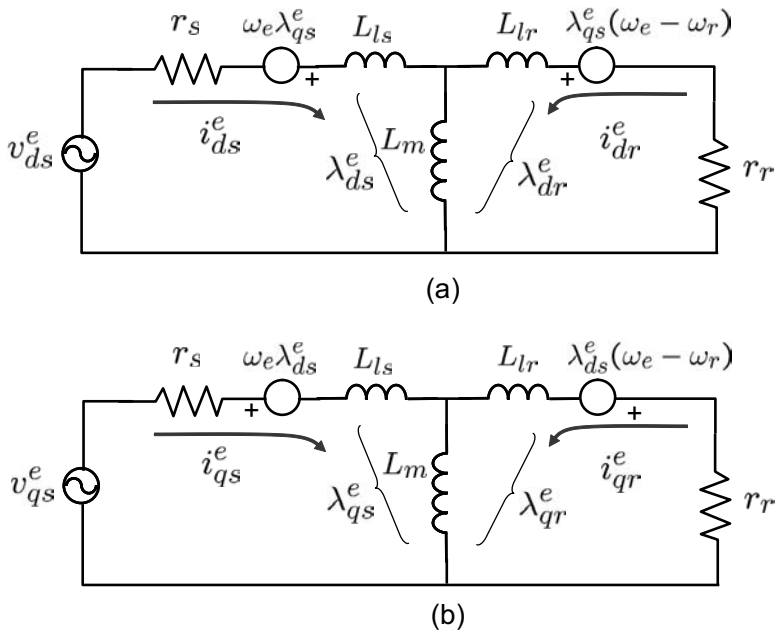

Figure 4.3: Equivalent circuit for IM in the synchronous frame: (a) d–axis and (b) q–axis.

Note that both flux and current variables appear in (4.19)−(4.17). Utilizing (4.21)−(4.24), we can express the IM synchronous model only with current variables:

$$\begin{bmatrix} v^e_{ds} \\ v^e_{qs} \\ 0 \\ 0 \end{bmatrix} = \begin{bmatrix} r_s + pL_s & -\omega_e L_s & pL_m & -\omega_e L_m \\ \omega_e L_s & r_s + pL_s & \omega_e L_m & pL_m \\ pL_m & -\omega_{sl} L_m & r_r + pL_r & -\omega_{sl} L_r \\ \omega_{sl} L_m & pL_m & \omega_{sl} L_r & r_r + pL_r \end{bmatrix} \begin{bmatrix} i^e_{ds} \\ i^e_{qs} \\ i^e_{dr} \\ i^e_{qr} \end{bmatrix}. \tag{4.25}$$

Since the rotor circuits are shorted, $v^e_{dr} = v^e_{qr} = 0$.

Voltage Equation in the Stationary Frame

Since the stator voltage equation (4.11) is already in the stationary frame, it is necessary to transform the rotor equation (4.12) into the stationary frame. Transformation can be done by multiplying $e^{-j\theta_r}$ on both sides of (4.12):

$$\mathbf{v}^s_{dqr} = r_r \mathbf{i}^s_{dqr} + (p - j\omega_r))\boldsymbol{\lambda}^s_{dqr}. \tag{4.26}$$

Similarly to (4.25), we have an IM model in the stationary frame:

$$\begin{bmatrix} v^s_{ds} \\ v^s_{qs} \\ 0 \\ 0 \end{bmatrix} = \begin{bmatrix} r_s + pL_s & 0 & pL_m & 0 \\ 0 & r_s + pL_s & 0 & pL_m \\ pL_m & \omega_r L_m & r_r + pL_r & \omega_r L_r \\ -\omega_r L_m & pL_m & -\omega_r L_r & r_r + pL_r \end{bmatrix} \begin{bmatrix} i^s_{ds} \\ i^s_{qs} \\ i^s_{dr} \\ i^s_{qr} \end{bmatrix}. \tag{4.27}$$

4.1.3 Transformation via Matrix Multiplications

In this section we will repeat the same coordinate transformation via matrix multiplications. Some mathematical preliminaries are given in the following exercises:

Exercise 4.3 [2]
Show that

$$\begin{bmatrix} \cos\theta & \sin\theta \\ -\sin\theta & \cos\theta \end{bmatrix} = e^{\mathbf{J}\theta}, \qquad \text{where} \qquad \mathbf{J} = \begin{bmatrix} 0 & 1 \\ -1 & 0 \end{bmatrix}. \tag{4.28}$$

Solution

$$e^{\mathbf{J}\theta} = \mathcal{L}^{-1}\left\{(sI - \mathbf{J})^{-1}\right\} = \mathcal{L}^{-1}\left\{\frac{1}{s^2+1}\begin{bmatrix} s & 1 \\ -1 & s \end{bmatrix}\right\} = \begin{bmatrix} \cos\theta & \sin\theta \\ -\sin\theta & \cos\theta \end{bmatrix}.$$

Note that $\mathbf{J}$ is skew symmetric, i.e., $\mathbf{J}^{-1} = \mathbf{J}^T$ and that $\mathbf{J}$ is interpreted as an operator rotating a vector 90 degrees clockwise. Hence, multiplying $\mathbf{J}$ to a vector is equivalent to multiplying $-j$ to its corresponding complex variable. ■

Exercise 4.4
Let $\theta = \omega t$ and $p = \frac{d}{dt}$. Show that

$$\mathbf{T}(\theta)p\mathbf{T}^{-1}(\theta) = \omega\begin{bmatrix} 0 & -1 & 0 \\ 1 & 0 & 0 \\ 0 & 0 & 1 \end{bmatrix}.$$

Exercise 4.5
Show that

$$e^{\mathbf{J}\theta_e} p e^{-\mathbf{J}\theta_e} = -\omega_e \mathbf{J}. \tag{4.29}$$

Solution

$$e^{\mathbf{J}\theta_e} p e^{-\mathbf{J}\theta_e} = e^{\mathbf{J}\theta_e}(-\mathbf{J})e^{-\mathbf{J}\theta_e}\frac{d\theta}{dt} = -\omega_e \mathbf{J} e^{\mathbf{J}\theta_e} e^{-\mathbf{J}\theta_e} = -\omega_e \mathbf{J}$$

Alternatively,

$$e^{\mathbf{J}\theta_e} p e^{-\mathbf{J}\theta_e} = \omega_e \begin{bmatrix} \cos\theta_e & \sin\theta_e \\ -\sin\theta_e & \cos\theta_e \end{bmatrix}\begin{bmatrix} -\sin\theta_e & -\cos\theta_e \\ \cos\theta_e & -\sin\theta_e \end{bmatrix} = \omega_e \begin{bmatrix} 0 & -1 \\ 1 & 0 \end{bmatrix} = -\omega_e \mathbf{J}.$$

■

Exercise 4.6
Show that $\mathbf{A}e^{\mathbf{A}} = e^{\mathbf{A}}\mathbf{A}$ for $\mathbf{A} \in \mathbb{R}^{n\times n}$.

From the above example, it follows that $e^{\mathbf{J}\theta_e}e^{-\mathbf{J}\theta_e} = e^{-\mathbf{J}\theta_e}e^{\mathbf{J}\theta_e} = \mathbf{I}$ and $e^{\mathbf{J}\theta_e}\mathbf{J} = \mathbf{J}e^{\mathbf{J}\theta_e}$. One can represent the complex expression, (4.7) and (4.11), as the following vector equation:

$$\begin{bmatrix} v_{ds}^s \\ v_{qs}^s \end{bmatrix} = r_s \begin{bmatrix} i_{ds}^s \\ i_{qs}^s \end{bmatrix} + L_s p \begin{bmatrix} i_{ds}^s \\ i_{qs}^s \end{bmatrix} + L_m e^{-\mathbf{J}\theta_r} p \begin{bmatrix} i_{dr}^r \\ i_{qr}^r \end{bmatrix} - \omega_r L_m \mathbf{J} e^{-\mathbf{J}\theta_r} \begin{bmatrix} i_{dr}^r \\ i_{qr}^r \end{bmatrix}. \tag{4.30}$$

Multiplying both sides of (4.30) by $e^{-\mathbf{J}\theta_e}$, we obtain

$$\begin{aligned} e^{\mathbf{J}\theta_e}\begin{bmatrix} v_{ds}^s \\ v_{qs}^s \end{bmatrix} &= r_s e^{\mathbf{J}\theta_e}\begin{bmatrix} i_{ds}^s \\ i_{qs}^s \end{bmatrix} + L_s e^{\mathbf{J}\theta_e} p\left(e^{-\mathbf{J}\theta_e}e^{\mathbf{J}\theta_e}\begin{bmatrix} i_{ds}^s \\ i_{qs}^s \end{bmatrix}\right) \\ &\quad + L_m e^{\mathbf{J}\theta_e}e^{-\mathbf{J}\theta_r} p\left(e^{\mathbf{J}\theta_r}e^{-\mathbf{J}\theta_e}e^{\mathbf{J}\theta_e}e^{-\mathbf{J}\theta_r}\begin{bmatrix} i_{dr}^r \\ i_{qr}^r \end{bmatrix}\right) - \omega_r L_m \mathbf{J} e^{\mathbf{J}\theta_e}e^{-\mathbf{J}\theta_r}\begin{bmatrix} i_{dr}^r \\ i_{qr}^r \end{bmatrix} \\ &= r_s e^{\mathbf{J}\theta_e}\begin{bmatrix} i_{ds}^s \\ i_{qs}^s \end{bmatrix} + L_s e^{\mathbf{J}\theta_e} p\left(e^{-\mathbf{J}\theta_e}\right) e^{\mathbf{J}\theta_e}\begin{bmatrix} i_{ds}^s \\ i_{qs}^s \end{bmatrix} + L_s p\left(e^{\mathbf{J}\theta_e}\begin{bmatrix} i_{ds}^s \\ i_{qs}^s \end{bmatrix}\right) \\ &\quad + L_m e^{\mathbf{J}\theta_e}e^{-\mathbf{J}\theta_r} p\left(e^{\mathbf{J}\theta_r}e^{-\mathbf{J}\theta_e}\right) e^{\mathbf{J}\theta_e}e^{-\mathbf{J}\theta_r}\begin{bmatrix} i_{dr}^r \\ i_{qr}^r \end{bmatrix} + L_m p\left(e^{\mathbf{J}\theta_e}e^{-\mathbf{J}\theta_r}\begin{bmatrix} i_{dr}^r \\ i_{qr}^r \end{bmatrix}\right) \\ &\quad - \omega_r L_m \mathbf{J} e^{\mathbf{J}\theta_e}e^{-\mathbf{J}\theta_r}\begin{bmatrix} i_{dr}^r \\ i_{qr}^r \end{bmatrix}. \end{aligned}$$

$$\begin{aligned} \begin{bmatrix} v_{ds}^e \\ v_{qs}^e \end{bmatrix} &= r_s \begin{bmatrix} i_{ds}^e \\ i_{qs}^e \end{bmatrix} - \omega_e L_s \mathbf{J}\begin{bmatrix} i_{ds}^e \\ i_{qs}^e \end{bmatrix} + L_s p\begin{bmatrix} i_{ds}^e \\ i_{qs}^e \end{bmatrix} - (\omega_e - \omega_r) L_m \mathbf{J}\begin{bmatrix} i_{dr}^e \\ i_{qr}^e \end{bmatrix} \\ &\quad + L_m p\begin{bmatrix} i_{dr}^e \\ i_{qr}^e \end{bmatrix} - \omega_r L_m \mathbf{J}\begin{bmatrix} i_{dr}^e \\ i_{qr}^e \end{bmatrix} \\ &= r_s \begin{bmatrix} i_{ds}^e \\ i_{qs}^e \end{bmatrix} + L_s(p\mathbf{I} - \omega_e \mathbf{J})\begin{bmatrix} i_{ds}^e \\ i_{qs}^e \end{bmatrix} + L_m(p\mathbf{I} - \omega_e \mathbf{J})\begin{bmatrix} i_{dr}^e \\ i_{qr}^e \end{bmatrix} \\ &= r_s \begin{bmatrix} i_{ds}^e \\ i_{qs}^e \end{bmatrix} + (p\mathbf{I} - \omega_e \mathbf{J})\begin{bmatrix} \lambda_{ds}^e \\ \lambda_{qs}^e \end{bmatrix}. \end{aligned} \tag{4.31}$$

One can see that the matrix manipulation yields the same result as (4.16) and (4.17).

4.2 IM Dynamic Models

Note that the IM models in the previous section include differential operator, p inside the matrix. To simulate IM dynamics or construct an observer for IM, we need models in the form of ordinary differential equation (ODE).

4.2.1 IM ODE Model with Current Variables

In this subsection, we derive an IM ODE model from (4.25) which is expressed with current variables in the synchronous frame. Note from the third line of (4.25) that

$$pi^e_{dr} = -\frac{1}{L_r}\left(L_m p i^e_{ds} - \omega_{sl} L_m i^e_{qs} + r_r i^e_{dr} - \omega_{sl} L_r i_{qr}\right). \tag{4.32}$$

Substituting (4.32) into the first line of (4.25), we have

$$\begin{aligned}(L_s - \frac{L_m^2}{L_r}) p i^e_{ds} \;&=\; -r_s i^e_{ds} - \frac{L_m}{L_r}\left(\omega_{sl} L_m i^e_{qs} - r_r i^e_{dr} + \omega_{sl} L_r i_{qr}\right) \\ &\quad + \omega_e L_s i^e_{qs} + \omega_e L_m i^e_{qr}. \end{aligned} \tag{4.33}$$

Recall that $\sigma \equiv 1 - L_m^2/(L_s L_r)$ is the leakage coefficient defined in the previous chapter. Thus, (4.33) is rearranged as

$$\sigma L_s p i^e_{ds} = -r_s i^e_{ds} + (\omega_e L_s - \omega_{sl}\frac{L_m^2}{L_r}) i^e_{qs} + \frac{L_m}{L_r} r_r i^e_{dr} + L_m(\omega_e - \omega_{sl}) i_{qr}.$$

Note that

$$\frac{\omega_e}{\sigma} - \frac{L_m^2}{\sigma L_s L_r}\omega_{sl} = \frac{\omega_e}{\sigma} - (\omega_e - \omega_r)\frac{L_m^2}{\sigma L_s L_r} = \frac{\omega_e}{\sigma}\left(1 - \frac{L_m^2}{L_s L_r}\right) + \omega_r \frac{L_m^2}{\sigma L_s L_r}.$$

Note on the other hand that $\omega_r \frac{L_m^2}{\sigma L_s L_r} = \frac{1-\sigma}{\sigma}\omega_r$. Therefore,

$$p i^e_{ds} = -\frac{r_s}{\sigma L_s} i^e_{ds} + (\omega_e + \omega_r \frac{1-\sigma}{\sigma}) i^e_{qs} + \frac{L_m}{\sigma L_s}\frac{r_r}{L_r} i^e_{dr} + \frac{L_m}{\sigma L_s}\omega_r i_{qr}$$

In the similar fashion, expressions for pi^e_{qs}, pi^e_{dr}, and pi^e_{qr} can be derived. Summarizing the result, we obtain an IM dynamic model in the ODE form:

$$\begin{aligned}\frac{d}{dt}\begin{bmatrix} i^e_{ds} \\ i^e_{qs} \\ i^e_{dr} \\ i^e_{qr}\end{bmatrix} \;&=\; \begin{bmatrix} -\frac{r_s}{\sigma L_s} & \omega_e + \omega_r\frac{1-\sigma}{\sigma} & \frac{L_m r_r}{\sigma L_s L_r} & \omega_r \frac{L_m}{\sigma L_s} \\ -\omega_e - \omega_r\frac{1-\sigma}{\sigma} & -\frac{r_s}{\sigma L_s} & -\omega_r \frac{L_m}{\sigma L_s} & \frac{L_m r_r}{\sigma L_s L_r} \\ \frac{L_m r_s}{\sigma L_r L_s} & -\omega_r \frac{L_m}{\sigma L_r} & -\frac{r_r}{\sigma L_r} & \omega_e - \frac{\omega_r}{\sigma} \\ \omega_r \frac{L_m}{\sigma L_r} & \frac{L_m r_s}{\sigma L_r L_s} & -\omega_e + \frac{\omega_r}{\sigma} & -\frac{r_r}{\sigma L_r}\end{bmatrix}\begin{bmatrix} i^e_{ds} \\ i^e_{qs} \\ i^e_{dr} \\ i^e_{qr}\end{bmatrix} \\ &\quad + \begin{bmatrix} \frac{1}{\sigma L_s} & 0 \\ 0 & \frac{1}{\sigma L_s} \\ -\frac{L_m}{\sigma L_r L_s} & 0 \\ 0 & -\frac{L_m}{\sigma L_r L_s}\end{bmatrix}\begin{bmatrix} v^e_{ds} \\ v^e_{qs}\end{bmatrix}. \end{aligned} \tag{4.34}$$

Equivalently, (4.34) can be expressed as

$$\frac{d}{dt}\begin{bmatrix}\mathbf{i}^e_s \\ \mathbf{i}^e_r\end{bmatrix} = \begin{bmatrix} -\frac{r_s}{\sigma L_s}\mathbf{I} + \left(\omega_e + \omega_r\frac{1-\sigma}{\sigma}\right)\mathbf{J} & \frac{L_m}{\sigma L_s}\left(\frac{1}{\tau_r}\mathbf{I} + \omega_r \mathbf{J}\right) \\ \frac{L_m}{\sigma L_r}\left(\frac{r_s}{L_s}\mathbf{I} - \omega_r \mathbf{J}\right) & -\frac{1}{\sigma\tau_r}\mathbf{I} + \left(\omega_e - \frac{\omega_r}{\sigma}\right)\mathbf{J}\end{bmatrix}\begin{bmatrix}\mathbf{i}^e_s \\ \mathbf{i}^e_r\end{bmatrix} + \begin{bmatrix}\frac{1}{\sigma L_s}\mathbf{I} \\ -\frac{L_m}{\sigma L_r L_s}\mathbf{I}\end{bmatrix}\mathbf{v}^e_s \tag{4.35}$$

where $\tau_r = L_r/r_r$ and $\mathbf{I} = \begin{bmatrix} 1 & 0 \\ 0 & 1 \end{bmatrix}$ and $\mathbf{J} = \begin{bmatrix} 0 & 1 \\ -1 & 0 \end{bmatrix}$. While checking (4.41), one needs to be careful about the sign in front of $\mathbf{J}$, since $\mathbf{J}$ here is defined differently from other literature.

4.2.2 IM ODE Model with Current-Flux Variables

For simplicity in handling the field-oriented control that appears later, it is better to select stator current and rotor flux as the state variables, instead of stator and rotor currents. It follows from (4.23) and (4.24) that the relation between the two variable sets is given as

$$\begin{bmatrix} i_{ds}^e \\ i_{qs}^e \\ i_{dr}^e \\ i_{qr}^e \end{bmatrix} = \begin{bmatrix} 1 & 0 & 0 & 0 \\ 0 & 1 & 0 & 0 \\ -\frac{L_m}{L_r} & 0 & \frac{1}{L_r} & 0 \\ 0 & -\frac{L_m}{L_r} & 0 & \frac{1}{L_r} \end{bmatrix} \begin{bmatrix} i_{ds}^e \\ i_{qs}^e \\ \lambda_{dr}^e \\ \lambda_{qr}^e \end{bmatrix}. \tag{4.36}$$

Substituting (4.36) into (4.25), it follows that

$$\begin{aligned} \begin{bmatrix} v_{ds}^e \\ v_{qs}^e \\ 0 \\ 0 \end{bmatrix} &= \begin{bmatrix} r_s + pL_s & -\omega_e L_s & pL_m & -\omega_e L_m \\ \omega_e L_s & r_s + pL_s & \omega_e L_m & pL_m \\ pL_m & -\omega_{sl} L_m & r_r + pL_r & -\omega_{sl} L_r \\ \omega_{sl} L_m & pL_m & \omega_{sl} L_r & r_r + pL_r \end{bmatrix} \begin{bmatrix} 1 & 0 & 0 & 0 \\ 0 & 1 & 0 & 0 \\ -\frac{L_m}{L_r} & 0 & \frac{1}{L_r} & 0 \\ 0 & -\frac{L_m}{L_r} & 0 & \frac{1}{L_r} \end{bmatrix} \begin{bmatrix} i_{ds}^e \\ i_{qs}^e \\ \lambda_{dr}^e \\ \lambda_{qr}^e \end{bmatrix} \\ &= \begin{bmatrix} r_s + p\sigma L_s & -\omega_e \sigma L_s & p\frac{L_m}{L_r} & -\omega_e \frac{L_m}{L_r} \\ \omega_e \sigma L_s & r_s + p\sigma L_s & \omega_e \frac{L_m}{L_r} & p\frac{L_m}{L_r} \\ -\frac{r_r L_m}{L_r} & 0 & \frac{r_r}{L_r} + p & -\omega_{sl} \\ 0 & -\frac{r_r L_m}{L_r} & \omega_{sl} & \frac{r_r}{L_r} + p \end{bmatrix} \begin{bmatrix} i_{ds}^e \\ i_{qs}^e \\ \lambda_{dr}^e \\ \lambda_{qr}^e \end{bmatrix}, \end{aligned} \tag{4.37}$$

where $\sigma \equiv 1 - L_m^2/(L_s L_r)$ is the leakage coefficient defined in the previous chapter.

Collecting the terms with differential operator on the left-hand side, we obtain

$$\begin{aligned} \begin{bmatrix} \sigma L_s & 0 & \frac{L_m}{L_r} & 0 \\ 0 & \sigma L_s & 0 & \frac{L_m}{L_r} \\ 0 & 0 & 1 & 0 \\ 0 & 0 & 0 & 1 \end{bmatrix} p \begin{bmatrix} i_{ds}^e \\ i_{qs}^e \\ \lambda_{dr}^e \\ \lambda_{qr}^e \end{bmatrix} &= \begin{bmatrix} v_{ds}^e \\ v_{qs}^e \\ 0 \\ 0 \end{bmatrix} \\ &\quad - \begin{bmatrix} r_s & -\omega_e \sigma L_s & 0 & -\omega_e \frac{L_m}{L_r} \\ \omega_e \sigma L_s & r_s & \omega_e \frac{L_m}{L_r} & 0 \\ -\frac{r_r L_m}{L_r} & 0 & \frac{r_r}{L_r} & -\omega_{sl} \\ 0 & -\frac{r_r L_m}{L_r} & \omega_{sl} & \frac{r_r}{L_r} \end{bmatrix} \begin{bmatrix} i_{ds}^e \\ i_{qs}^e \\ \lambda_{dr}^e \\ \lambda_{qr}^e \end{bmatrix}. \end{aligned} \tag{4.38}$$

In taking the inverse of the matrix in the left-hand side of (4.38), we utilize the following identity

$$\begin{bmatrix} \mathbf{A} & \mathbf{B} \\ \mathbf{0} & \mathbf{C} \end{bmatrix}^{-1} = \begin{bmatrix} \mathbf{A}^{-1} & -\mathbf{A}^{-1}\mathbf{B}\mathbf{C}^{-1} \\ \mathbf{0} & \mathbf{C}^{-1} \end{bmatrix}$$

for invertible $\mathbf{A}, \mathbf{C} \in \mathbb{R}^{n\times n}$ and $\mathbf{B},\ \mathbf{O} \in \mathbb{R}^{n\times n}$. Note that $\mathbf{0}$ denotes the zero matrix. Then,

$$\begin{bmatrix} \sigma L_s & 0 & \frac{L_m}{L_r} & 0 \\ 0 & \sigma L_s & 0 & \frac{L_m}{L_r} \\ 0 & 0 & 1 & 0 \\ 0 & 0 & 0 & 1 \end{bmatrix}^{-1} = \begin{bmatrix} \frac{1}{\sigma L_s} & 0 & -\frac{L_m}{\sigma L_r L_s} & 0 \\ 0 & \frac{1}{\sigma L_s} & 0 & -\frac{L_m}{\sigma L_r L_s} \\ 0 & 0 & 1 & 0 \\ 0 & 0 & 0 & 1 \end{bmatrix}. \tag{4.39}$$

Applying (4.39) to (4.38), we obtain

$$\frac{d}{dt}\begin{bmatrix} i^e_{ds} \\ i^e_{qs} \\ \lambda^e_{dr} \\ \lambda^e_{qr} \end{bmatrix} = \begin{bmatrix} -\frac{r_s}{\sigma L_s} - \frac{(1-\sigma)r_r}{\sigma L_r} & \omega_e & \frac{r_r L_m}{\sigma L_r^2 L_s} & \omega_r \frac{L_m}{\sigma L_s L_r} \\ -\omega_e & -\frac{r_s}{\sigma L_s} - \frac{(1-\sigma)r_r}{\sigma L_r} & -\omega_r \frac{L_m}{\sigma L_s L_r} & \frac{r_r L_m}{\sigma L_r^2 L_s} \\ \frac{r_r L_m}{L_r} & 0 & -\frac{r_r}{L_r} & \omega_{sl} \\ 0 & \frac{r_r L_m}{L_r} & -\omega_{sl} & -\frac{r_r}{L_r} \end{bmatrix} \begin{bmatrix} i^e_{ds} \\ i^e_{qs} \\ \lambda^e_{dr} \\ \lambda^e_{qr} \end{bmatrix} + \frac{1}{\sigma L_s}\begin{bmatrix} v^e_{ds} \\ v^e_{qs} \\ 0 \\ 0 \end{bmatrix}. \tag{4.40}$$

Equivalently, (4.40) can be expressed as

$$\frac{d}{dt}\begin{bmatrix} \mathbf{i}^e_s \\ \boldsymbol{\lambda}^e_r \end{bmatrix} = \begin{bmatrix} -\left(\frac{r_s}{\sigma L_s} + \frac{1-\sigma}{\sigma \tau_r}\right)\mathbf{I} + \omega_e \mathbf{J} & \frac{L_m}{\sigma L_r L_s}\left(\frac{1}{\tau_r}\mathbf{I} + \omega_r \mathbf{J}\right) \\ \frac{L_m}{\tau_r}\mathbf{I} & -\frac{1}{\tau_r}\mathbf{I} + \omega_{sl}\mathbf{J} \end{bmatrix} \begin{bmatrix} \mathbf{i}^e_s \\ \boldsymbol{\lambda}^e_r \end{bmatrix} + \frac{1}{\sigma L_s}\begin{bmatrix} \mathbf{v}^e_s \\ 0 \end{bmatrix}. \tag{4.41}$$

Similarly, the stationary frame ODE model in current-flux variables is obtained from (4.27) as

$$\frac{d}{dt}\begin{bmatrix} \mathbf{i}^s_s \\ \boldsymbol{\lambda}^s_r \end{bmatrix} = \begin{bmatrix} -\left(\frac{r_s}{\sigma L_s} + \frac{1-\sigma}{\sigma \tau_r}\right)\mathbf{I} & \frac{L_m}{\sigma L_r L_s}\left(\frac{1}{\tau_r}\mathbf{I} + \omega_r \mathbf{J}\right) \\ \frac{L_m}{\tau_r}\mathbf{I} & -\frac{1}{\tau_r}\mathbf{I} - \omega_r \mathbf{J} \end{bmatrix} \begin{bmatrix} \mathbf{i}^s_s \\ \boldsymbol{\lambda}^s_r \end{bmatrix} + \frac{1}{\sigma L_s}\begin{bmatrix} \mathbf{v}^s_s \\ 0 \end{bmatrix}. \tag{4.42}$$

Comparing (4.41) with (4.42), the IM dynamics can be generalized independently of the frame such that

$$\begin{aligned} \frac{d}{dt}\begin{bmatrix} \mathbf{i}^g_s \\ \boldsymbol{\lambda}^g_r \end{bmatrix} = & \begin{bmatrix} -\left(\frac{r_s}{\sigma L_s} + \frac{1-\sigma}{\sigma \tau_r}\right)\mathbf{I} & \frac{L_m}{\sigma L_r L_s}\frac{1}{\tau_r}\mathbf{I} \\ \frac{L_m}{\tau_r}\mathbf{I} & -\frac{1}{\tau_r}\mathbf{I} \end{bmatrix} \begin{bmatrix} \mathbf{i}^g_s \\ \boldsymbol{\lambda}^g_r \end{bmatrix} + \omega_A \begin{bmatrix} \mathbf{J} & \frac{L_m}{\sigma L_r L_s}\mathbf{J} \\ \mathbf{0} & \mathbf{0} \end{bmatrix} \begin{bmatrix} \mathbf{i}^g_s \\ \boldsymbol{\lambda}^g_r \end{bmatrix} \\ & + \omega_B \begin{bmatrix} \mathbf{0} & -\frac{L_m}{\sigma L_r L_s}\mathbf{J} \\ \mathbf{0} & \mathbf{J} \end{bmatrix} \begin{bmatrix} \mathbf{i}^g_s \\ \boldsymbol{\lambda}^g_r \end{bmatrix} + \frac{1}{\sigma L_s}\begin{bmatrix} \mathbf{v}^g_s \\ 0 \end{bmatrix}, \end{aligned} \tag{4.43}$$

where the superscript 'g' denotes the generalized frame. The equation becomes the IM model in the synchronous frame with $\omega_A = \omega_e$ and $\omega_B = \omega_{sl}$, whereas it becomes the IM model in the stationary frame with $\omega_A = 0$ and $\omega_B = -\omega_r$. Various IM dynamic equations are summarized in Table 4.1.

Table 4.1: IM dynamic equations.

Stationary frame

$$\begin{bmatrix} v_{ds}^s \\ v_{qs}^s \\ 0 \\ 0 \end{bmatrix} = \begin{bmatrix} r_s + pL_s & 0 & pL_m & 0 \\ 0 & r_s + pL_s & 0 & pL_m \\ pL_m & \omega_r L_m & r_r + pL_r & \omega_r L_r \\ -\omega_r L_m & pL_m & -\omega_r L_r & r_r + pL_r \end{bmatrix} \begin{bmatrix} i_{ds}^s \\ i_{qs}^s \\ i_{dr}^s \\ i_{qr}^s \end{bmatrix}$$

Synchronous frame

$$\begin{bmatrix} v_{ds}^e \\ v_{qs}^e \\ 0 \\ 0 \end{bmatrix} = \begin{bmatrix} r_s + pL_s & -\omega_e L_s & pL_m & -\omega_e L_m \\ \omega_e L_s & r_s + pL_s & \omega_e L_m & pL_m \\ pL_m & -\omega_{sl} L_m & r_r + pL_r & -\omega_{sl} L_r \\ \omega_{sl} L_m & pL_m & \omega_{sl} L_r & r_r + pL_r \end{bmatrix} \begin{bmatrix} i_{ds}^e \\ i_{qs}^e \\ i_{dr}^e \\ i_{qr}^e \end{bmatrix}$$

ODE with current variables (Stationary)

$$\frac{d}{dt} \begin{bmatrix} \mathbf{i}_s^s \\ \mathbf{i}_r^s \end{bmatrix} = \begin{bmatrix} -\frac{r_s}{\sigma L_s}\mathbf{I} + \omega_r \frac{1-\sigma}{\sigma}\mathbf{J} & \frac{L_m}{\sigma L_s}\left(\frac{1}{\tau_r}\mathbf{I} + \omega_r \mathbf{J}\right) \\ \frac{L_m}{\sigma L_r}\left(\frac{r_s}{L_s}\mathbf{I} - \omega_r \mathbf{J}\right) & -\frac{1}{\sigma}\left(\frac{1}{\tau_r}\mathbf{I} + \omega_r \mathbf{J}\right) \end{bmatrix} \begin{bmatrix} \mathbf{i}_s^s \\ \mathbf{i}_r^s \end{bmatrix} + \begin{bmatrix} \frac{1}{\sigma L_s}\mathbf{I} \\ -\frac{L_m}{\sigma L_r L_s}\mathbf{I} \end{bmatrix} \mathbf{v}_s^s$$

ODE with current variables (Synchronous)

$$\frac{d}{dt} \begin{bmatrix} \mathbf{i}_s^e \\ \mathbf{i}_r^e \end{bmatrix} = \begin{bmatrix} -\frac{r_s}{\sigma L_s}\mathbf{I} + \left(\omega_e + \omega_r \frac{1-\sigma}{\sigma}\right)\mathbf{J} & \frac{L_m}{\sigma L_s}\left(\frac{1}{\tau_r}\mathbf{I} + \omega_r \mathbf{J}\right) \\ \frac{L_m}{\sigma L_r}\left(\frac{r_s}{L_s}\mathbf{I} - \omega_r \mathbf{J}\right) & -\frac{1}{\sigma\tau_r}\mathbf{I} + \left(\omega_e - \frac{\omega_r}{\sigma}\right)\mathbf{J} \end{bmatrix} \begin{bmatrix} \mathbf{i}_s^e \\ \mathbf{i}_r^e \end{bmatrix} + \begin{bmatrix} \frac{1}{\sigma L_s}\mathbf{I} \\ -\frac{L_m}{\sigma L_r L_s}\mathbf{I} \end{bmatrix} \mathbf{v}_s^e$$

ODE with current-flux variables (Stationary)

$$\frac{d}{dt} \begin{bmatrix} \mathbf{i}_s^s \\ \boldsymbol{\lambda}_r^s \end{bmatrix} = \begin{bmatrix} -\left(\frac{r_s}{\sigma L_s} + \frac{1-\sigma}{\sigma\tau_r}\right)\mathbf{I} & \frac{L_m}{\sigma L_r L_s}\left(\frac{1}{\tau_r}\mathbf{I} + \omega_r \mathbf{J}\right) \\ \frac{L_m}{\tau_r}\mathbf{I} & -\frac{1}{\tau_r}\mathbf{I} - \omega_r \mathbf{J} \end{bmatrix} \begin{bmatrix} \mathbf{i}_s^s \\ \boldsymbol{\lambda}_r^s \end{bmatrix} + \frac{1}{\sigma L_s} \begin{bmatrix} \mathbf{v}_s^s \\ 0 \end{bmatrix}$$

ODE with current-flux variables (Synchronous)

$$\frac{d}{dt} \begin{bmatrix} \mathbf{i}_s^e \\ \boldsymbol{\lambda}_r^e \end{bmatrix} = \begin{bmatrix} -\left(\frac{r_s}{\sigma L_s} + \frac{1-\sigma}{\sigma\tau_r}\right)\mathbf{I} + \omega_e \mathbf{J} & \frac{L_m}{\sigma L_r L_s}\left(\frac{1}{\tau_r}\mathbf{I} + \omega_r \mathbf{J}\right) \\ \frac{L_m}{\tau_r}\mathbf{I} & -\frac{1}{\tau_r}\mathbf{I} + \omega_{sl}\mathbf{J} \end{bmatrix} \begin{bmatrix} \mathbf{i}_s^e \\ \boldsymbol{\lambda}_r^e \end{bmatrix} + \frac{1}{\sigma L_s} \begin{bmatrix} \mathbf{v}_s^e \\ 0 \end{bmatrix}$$

4.2.3 Alternative Derivations Using Complex Variables

In this section, IM dynamics are derived utilizing the complex vector notation. The stator voltage equation in the rotating reference system is

$$\mathbf{v}^e_{dqs} = r_s \mathbf{i}^e_{dqs} + \frac{d\boldsymbol{\lambda}^e_{dqs}}{dt} + j\omega_e \boldsymbol{\lambda}^e_{dqs} \tag{4.44}$$

where $r_s \mathbf{i}^e_{dqs}$ is the resistive voltage drop and r_s is the stator resistance. In the case of rotor, the slip speed $\omega_e - \omega_r$ appears in such a way that

$$0 = r_r \mathbf{i}^e_{dqr} + \frac{d\boldsymbol{\lambda}^e_{dqr}}{dt} + j(\omega_e - \omega_r)\boldsymbol{\lambda}^e_{dqr}. \tag{4.45}$$

The dynamics (4.44) and (4.45) are described in terms of four state variables: $\mathbf{i}^e_{dqs}$, $\boldsymbol{\lambda}^e_{dqs}$, $\mathbf{i}^e_{dqr}$, and $\boldsymbol{\lambda}^e_{dqr}$. In the following, the variables will be reduced to ($\mathbf{i}^e_{dqs}$, $\boldsymbol{\lambda}^e_{dqr}$) by utilizing $\boldsymbol{\lambda}^e_{dqs} = L_s \mathbf{i}^e_{dqs} + L_m \mathbf{i}^e_{dqr}$ and $\boldsymbol{\lambda}^e_{dqr} = L_m \mathbf{i}^e_{dqs} + L_r \mathbf{i}^e_{dqr}$. Then, the stator flux leakage and the rotor current are rewritten as

$$\boldsymbol{\lambda}^e_{dqs} = L_s \mathbf{i}^e_{dqs} + \frac{L_m}{L_r}(\boldsymbol{\lambda}^e_{dqr} - L_m \mathbf{i}^e_{dqs}) = \sigma L_s \mathbf{i}^e_{dqs} + k_r \boldsymbol{\lambda}^e_{dqr} \tag{4.46}$$

$$\mathbf{i}^e_{dqr} = \frac{1}{L_r}(\boldsymbol{\lambda}^e_{dqr} - L_m \mathbf{i}^e_{dqs}), \tag{4.47}$$

where $k_r = L_m/L_r$ is the coupling factor of rotor. Selecting the stator current and the rotor flux vectors as state variables, the rotor equation (4.45) leads to

$$0 = \frac{1}{\tau_r}(\boldsymbol{\lambda}^e_{dqr} - L_m \mathbf{i}^e_{dqs}) + \frac{d\boldsymbol{\lambda}^e_{dqr}}{dt} + j(\omega_e - \omega_r)\boldsymbol{\lambda}^e_{dqr},$$

where $\tau_r = L_r/r_r$ is a rotor time constant. Multiplying both sides by τ_r and rearranging, we obtain

$$\tau_r \frac{d\boldsymbol{\lambda}^e_{dqr}}{dt} + \boldsymbol{\lambda}^e_{dqr} = -j(\omega_e - \omega_r)\tau_r \boldsymbol{\lambda}^e_{dqr} + L_m \mathbf{i}^e_{dqs}. \tag{4.48}$$

Then, it follows from (4.44), (4.46), and (4.48) that

$$\begin{aligned}
\mathbf{v}^e_{dqs} &= r_s \mathbf{i}^e_{dqs} + (\frac{d}{dt} + j\omega_e)(\sigma L_s \mathbf{i}^e_{dqs} + k_r \boldsymbol{\lambda}^e_{dqr}) \\
&= r_s \mathbf{i}^e_{dqs} + \sigma L_s \frac{d\mathbf{i}^e_{dqs}}{dt} + j\omega_e \sigma L_s \mathbf{i}^e_{dqs} + k_r \frac{d\boldsymbol{\lambda}^e_{dqr}}{dt} + j\omega_e k_r \boldsymbol{\lambda}^e_{dqr} \\
&= r_s \mathbf{i}^e_{dqs} + \sigma L_s \frac{d\mathbf{i}^e_{dqs}}{dt} + j\omega_e \sigma L_s \mathbf{i}^e_{dqs} + \frac{k_r}{\tau_r}\left(-j(\omega_e - \omega_r)\tau_r \boldsymbol{\lambda}^e_{dqr} + L_m \mathbf{i}^e_{dqs} - \boldsymbol{\lambda}^e_{dqr}\right) \\
&\quad + j\omega_e k_r \boldsymbol{\lambda}^e_{dqr} \\
&= r_s \mathbf{i}^e_{dqs} + \sigma L_s \frac{d\mathbf{i}^e_{dqs}}{dt} + j\omega_e \sigma L_s \mathbf{i}^e_{dqs} + jk_r \omega_r \boldsymbol{\lambda}^e_{dqr} + r_r k_r^2 \mathbf{i}^e_{dqs} - \frac{k_r}{\tau_r}\boldsymbol{\lambda}^e_{dqr} \\
&= (r_s + k_r^2 r_r)\mathbf{i}^e_{dqs} + \sigma L_s \frac{d\mathbf{i}^e_{dqs}}{dt} + j\omega_e \sigma L_s \mathbf{i}^e_{dqs} + jk_r \omega_r \boldsymbol{\lambda}^e_{dqr} - \frac{k_r}{\tau_r}\boldsymbol{\lambda}^e_{dqr}.
\end{aligned} \tag{4.49}$$

The final stator equation is equal to

$$\tau_\sigma^{'}\frac{d\mathbf{i}_{dqs}^e}{dt}+(1+j\omega_e\tau_\sigma^{'})\mathbf{i}_{dqs}^e=-\frac{k_r}{r_\sigma\tau_r}(j\omega_r\tau_r-1)\boldsymbol{\lambda}_{dqr}^e+\frac{1}{r_\sigma}\mathbf{v}_{dqs}^e \tag{4.50}$$

where $\tau_\sigma^{'}=\sigma L_s/r_\sigma$ and $r_\sigma=r_s+k_r^2r_r$ [4]. Or, (4.49) can be rewritten as

$$\frac{d\mathbf{i}_{dqs}^e}{dt}=-\frac{r_s+k_r^2r_r}{\sigma L_s}\mathbf{i}_{dqs}^e-j\omega_e\mathbf{i}_{dqs}^e-j\frac{k_r\omega_r}{\sigma L_s}\boldsymbol{\lambda}_{dqr}^e+\frac{k_r}{\sigma L_s\tau_r}\boldsymbol{\lambda}_{dqr}^e+\frac{1}{\sigma L_s}\mathbf{v}_{dqs}^e. \tag{4.51}$$

Exercise 4.7
Show that (4.51) and (4.48) are equal to (4.40).

Exercise 4.8
Under the condition that $\lambda_{qr}=0$ and $\lambda_{dr}=\lambda_r$ in the steady-state, show that

$$i_s=\sqrt{i_{ds}^2+i_{qs}^2}=\frac{\lambda_r}{L_m}\sqrt{1+\omega_r^2\tau_r^2}\,. \tag{4.52}$$

Solution
With the assumption, it follows that $L_mi_{qs}=\omega_r\tau_r\lambda_r$ and $i_{ds}=\frac{\lambda_r}{L_m}$. Thus $i_{qs}^2=\frac{\lambda_r^2}{L_m^2}\omega_r^2\tau_r^2$ and $i_{ds}^2=\frac{\lambda_r^2}{L_m^2}$. Hence, $i_{ds}^2+i_{qs}^2=\frac{\lambda_r^2}{L_m^2}(1+\omega_r^2\tau_r^2)$. ■

4.3 Steady-State Models

A steady-state model follows straightforwardly from (4.25). The steady-state variables are denoted by capital letters, V_{dqs}, I_{dqs}, and I_{dqr}. Letting $p=0$ and substituting $s\omega_e=\omega_e-\omega_r$, it follows that

$$\begin{aligned} V_{dqs} &= r_sI_{dqs}+j\omega_e(L_sI_{dqs}+L_mI_{dqr}) && (4.53)\\ 0 &= \frac{r_s}{s}I_{dqr}+j\omega_e(L_rI_{dqr}+L_mI_{dqs})\,. && (4.54)\end{aligned}$$

Multiplying both sides (4.54) by a constant a, we have

$$\begin{aligned} 0 &= \frac{a^2r_s}{s}\frac{I_{dqr}}{a}+j\omega_e(a^2L_r\frac{I_{dqr}}{a}+aL_mI_{dqs})\,,\\ &= \frac{a^2r_s}{s}\frac{I_{dqr}}{a}+j\omega_eL_mI_{dqr}-j\omega_eL_mI_{dqr}+j\omega_e(a^2L_r\frac{I_{dqr}}{a}+aL_mI_{dqs})\,,\\ &= \frac{a^2r_s}{s}\frac{I_{dqr}}{a}+j\omega_eaL_m(\frac{I_{dqr}}{a}+I_{dqs})+j\omega_e(a^2L_r-aL_m)\frac{I_{dqr}}{a}\,. && (4.55)\end{aligned}$$

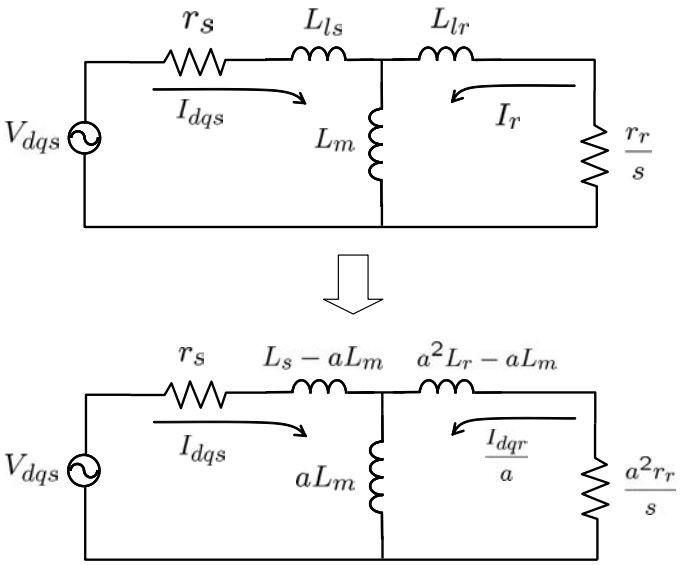

Figure 4.4: Modification of steady-state equivalent model with parameter a.

The modified equivalent circuit based on (4.55) is shown in Fig. 4.4. Note that the impedance remains the same for stator current, I_{dqs}.

Various modifications can be made with different a's. For some values of a, either rotor or stator leakage inductance disappears.

All leakage inductance in the stator
If we let $a = L_m/L_r$, then the rotor leakage inductance disappears and all the leakage inductance is located in the stator side. This equivalent circuit gives the rotor field-oriented dynamic model, which plays an important role in developing the concept of field-oriented control and will be dealt with in the next chapter.

All leakage inductance in the rotor
If we let $a = L_s/L_m$, then the stator leakage inductance disappears and all the leakage inductance is located in the rotor side.

4.4 Power and Torque Equations

Since $v^e_{ar} = v^e_{br} = v^e_{cr} = 0$, the rotor side source power is equal to zero. Thus, the electrical power applied to the motor is equal to

$$\begin{aligned} P_e = \mathbf{v}^T_{abcs}\mathbf{i}_{abcs} &= \left(\mathbf{T}(\theta_e)^{-1}\mathbf{v}^e_{dq0s}\right)^T \mathbf{T}(\theta_e)^{-1}\mathbf{i}^e_{dq0s} \\ &= \frac{3}{2}\left(\mathbf{T}(\theta_e)^T\mathbf{v}^e_{dq0s}\right)^T \mathbf{T}(\theta_e)^{-1}\mathbf{i}^e_{dq0s} \\ &= \frac{3}{2}\mathbf{v}^{eT}_{dq0s}\mathbf{i}^e_{dq0s} \end{aligned} \tag{4.56}$$

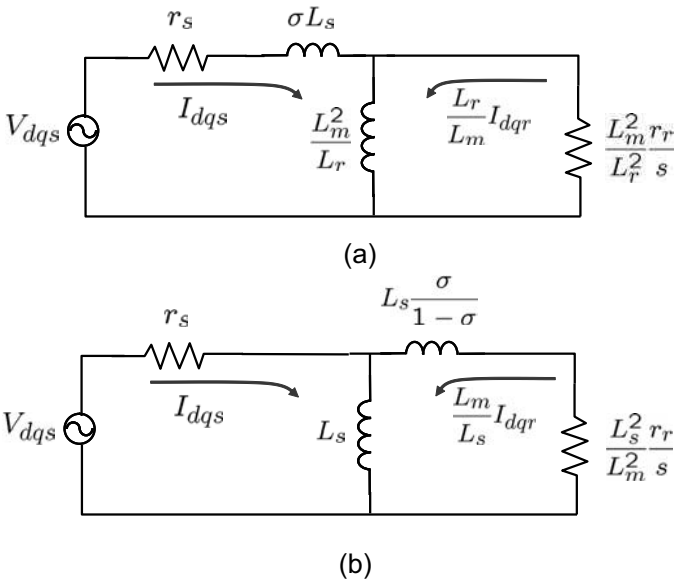

Figure 4.5: Equivalent circuits: (a) without rotor leakage inductance ($a = L_m/L_r$), (b) without stator leakage inductance ($a = L_s/L_m$).

where the last equality results from the relation $\mathbf{T}(\theta_e)^{-1} = \frac{3}{2}\mathbf{T}(\theta_e)^T$ that was shown in (2.34). The zero sequence current is assumed to be zero. We obtain from (4.56) and (4.25) that

$$\begin{aligned} P_e &= \frac{3}{2}\left(v_{ds}^e i_{ds}^e + v_{qs}^e i_{qs}^e\right) \\ &= \frac{3}{2} i_{ds}^e \left((r_s + pL_s) i_{ds}^e - \omega_e L_s i_{qs}^e + pL_m i_{dr}^e - \omega_e L_m i_{qr}^e\right) \\ &\quad + \frac{3}{2} i_{qs}^e \left(\omega_e L_s i_{ds}^e + (r_s + pL_s) i_{qs}^e \omega_e L_m i_{dr}^e + pL_m i_{qr}^e\right) \\ &= \frac{3}{2} r_s {i_{ds}^e}^2 + \frac{3}{4} L_s p {i_{ds}^e}^2 - \frac{3}{2}\omega_e L_s i_{ds}^e i_{qs}^e + \frac{3}{2} i_{ds}^e p L_m i_{dr}^e - \frac{3}{2}\omega_e L_m i_{ds}^e i_{qr}^e \\ &\quad + \frac{3}{2}\omega_e L_s i_{qs}^e i_{ds}^e + \frac{3}{2} r_s {i_{qs}^e}^2 + \frac{3}{4} L_s p {i_{qs}^e}^2 + \frac{3}{2}\omega_e L_m i_{qs}^e i_{dr}^e + \frac{3}{2} i_{qs}^e L_m p i_{qr}^e \,. \end{aligned} \tag{4.57}$$

4.4.1 Torque Equation

Note that the shaft torque of a rotating machine is obtained as a gradient of the electromagnetic power with respect to the shaft speed, i.e., $T_e = \frac{\partial P_e}{\partial \omega_r}$. Assume that the slip is constant. Then, the shaft torque follows from (4.57) such that

$$T_e = \frac{\partial P_e}{\partial \omega_r} = \frac{P}{2}\frac{\partial P_e}{\partial \omega_e} = \frac{P}{2}\frac{3}{2} L_m \left(i_{qs}^e i_{dr}^e - i_{ds}^e i_{qr}^e\right). \tag{4.58}$$

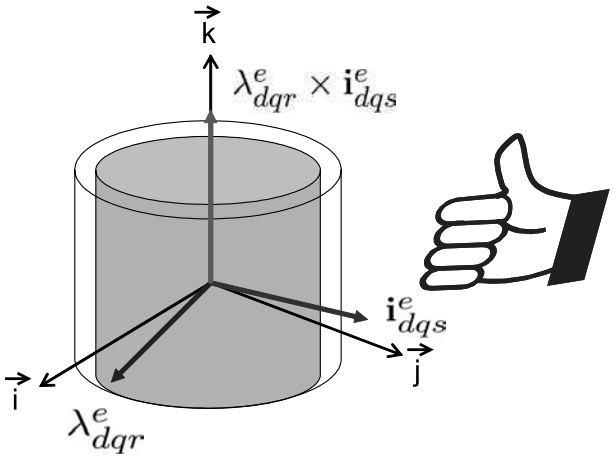

Figure 4.6: Cross product of rotor flux and stator current yields torque.

A different way of expressing (4.58) is

$$T_e = \frac{3}{2}\frac{P}{2} L_m Im\{\mathbf{i}^e_{dqs}\mathbf{i}^{e*}_{dqr}\}\,, \tag{4.59}$$

where $Im\{z\}$ implies the complex part of $z \in \mathbb{C}$.

Recall that $\boldsymbol{\lambda}_{dqr} = L_r\mathbf{i}^e_{dqr} + L_m\mathbf{i}^e_{dqs}$ and note that $Im\{\mathbf{i}^e_{dqs}\mathbf{i}^{e*}_{dqs}\} = 0$. Therefore, $Im\{\mathbf{i}^e_{dqs}\mathbf{i}^{e*}_{dqr}\} = \frac{1}{L_r} Im\{\mathbf{i}^e_{dqs}\boldsymbol{\lambda}^{e*}_{dqr}\}$. Hence, (4.59) is expressed equivalently as

$$T_e \;=\; \frac{3}{2}\frac{P}{2}\frac{L_m}{L_r} Im\{\mathbf{i}^e_{dqs}\boldsymbol{\lambda}^{e*}_{dqr}\}. \tag{4.60}$$

The other method of expressing $Im\{\mathbf{i}^e_{dqs}\boldsymbol{\lambda}^{e*}_{dqr}\}$ is the cross product of vectors. Note that

$$\begin{aligned} T_e &= \frac{3}{2}\frac{P}{2}\frac{L_m}{L_r}\left(\boldsymbol{\lambda}^e_{dqr} \times \mathbf{i}^e_{dqs}\right)_k \qquad (4.61)\\ &= \frac{3}{2}\frac{P}{2}\frac{L_m}{L_r}\left(\begin{bmatrix}\lambda^e_{dr}\\ \lambda^e_{qr}\\ 0\end{bmatrix} \times \begin{bmatrix}i^e_{ds}\\ i^e_{qs}\\ 0\end{bmatrix}\right)_k \\ &= \frac{3}{2}\frac{P}{2}\frac{L_m}{L_r}\begin{vmatrix}\overrightarrow{i} & \overrightarrow{j} & \overrightarrow{k}\\ \lambda^e_{dr} & \lambda^e_{qr} & 0\\ i^e_{ds} & i^e_{qs} & 0\end{vmatrix}_k \\ &= \frac{3}{2}\frac{P}{2}\frac{L_m}{L_r}(\lambda^e_{dr}i^e_{qs} - \lambda^e_{qr}i^e_{ds}). \qquad (4.62) \end{aligned}$$

Exercise 4.9
Using the definition $A \times B = |A| \cdot |B| \sin\theta$ for vectors A and B having an angle θ in between and utilizing (4.23), derive (4.58) from (4.61).

Bibliography

[1] P. C. Krause, O. Wasynczuk, and S. D. Sudhoff,*Analysis of Electric Machinery,* IEEE Press, 1995.

[2] C. T. Chen, *Linear System Theory and Design*, Oxford University Press, New York, 1999.

[3] D. W. Novotny and T. A. Lipo,*Vector Control and Dynamics of AC Drives,* Clarendon Press, Oxford 1996.

[4] J. Holtz, Sensorless control of induction motors, *Proc. IEEE*, Vol. 90, No. 8, pp. 1358−1394, Aug. 2002.

Problems

4.1 Show that for $\mathbf{A} \in \mathbb{R}^{n\times n}$

$$e^{\mathbf{A}t} = \mathcal{L}^{-1}\left\{(s\mathbf{I} - \mathbf{A})^{-1}\right\}, \tag{4.63}$$

where $\mathbf{I} \in \mathbb{R}^{n\times n}$ is the identity matrix, $\mathcal{L}$ denotes Laplace transformation, and s is the Laplace variable.

4.2 Show that

$$\begin{aligned}
i^e_{ds} &= \frac{1}{\sigma L_s}\left(\lambda^e_{ds} - \frac{L_m}{L_r}\lambda^e_{dr}\right)\\
i^e_{qs} &= \frac{1}{\sigma L_s}\left(\lambda^e_{qs} - \frac{L_m}{L_r}\lambda^e_{qr}\right)\\
i^e_{dr} &= \frac{1}{\sigma L_r}\left(\lambda^e_{dr} - \frac{L_m}{L_s}\lambda^e_{ds}\right)\\
i^e_{qr} &= \frac{1}{\sigma L_r}\left(\lambda^e_{qr} - \frac{L_m}{L_s}\lambda^e_{qs}\right)
\end{aligned}$$

4.3 Utilizing the results of **4.2**, derive the following from (4.15) and (4.18):

$$\frac{d}{dt}\begin{bmatrix}\lambda^e_{ds}\\ \lambda^e_{qs}\\ \lambda^e_{dr}\\ \lambda^e_{qr}\end{bmatrix} = \begin{bmatrix}-\frac{r_s}{\sigma L_s} & \omega_e & \frac{r_s L_m}{\sigma L_r L_s} & 0\\ -\omega_e & -\frac{r_s}{\sigma L_s} & 0 & \frac{r_s L_m}{\sigma L_r L_s}\\ \frac{r_s L_m}{\sigma L_r L_s} & 0 & -\frac{r_r}{\sigma L_r} & \omega_{sl}\\ 0 & \frac{r_s L_m}{\sigma L_r L_s} & -\omega_{sl} & -\frac{r_r}{\sigma L_r}\end{bmatrix}\begin{bmatrix}\lambda^e_{ds}\\ \lambda^e_{qs}\\ \lambda^e_{dr}\\ \lambda^e_{qr}\end{bmatrix} + \begin{bmatrix}v^e_{ds}\\ v^e_{qs}\\ 0\\ 0\end{bmatrix}.$$

4.4 In the stationary frame, the IM model is described as

$$\begin{bmatrix}v^s_{ds}\\ v^s_{qs}\\ 0\\ 0\end{bmatrix} = \begin{bmatrix}r_s + pL_s & 0 & pL_m & 0\\ 0 & r_s + pL_s & 0 & pL_m\\ pL_m & \omega_r L_m & r_r + pL_r & \omega_r L_r\\ -\omega_r L_m & pL_m & -\omega_r L_r & r_r + pL_r\end{bmatrix}\begin{bmatrix}i^s_{ds}\\ i^s_{qs}\\ i^s_{dr}\\ i^s_{qr}\end{bmatrix}.$$

Using the above equation, derive the following dynamic model of IM in the stationary frame:

$$\frac{d}{dt}\begin{bmatrix}i^s_{ds}\\ i^s_{qs}\\ i^s_{dr}\\ i^s_{qr}\end{bmatrix} = \begin{bmatrix}-\frac{r_s}{\sigma L_s} & \omega_r\frac{1-\sigma}{\sigma} & \frac{r_r L_m}{\sigma L_r L_s} & \omega_r\frac{L_m}{\sigma L_s}\\ -\omega_r\frac{1-\sigma}{\sigma} & -\frac{r_s}{\sigma L_s} & -\omega_r\frac{L_m}{\sigma L_s} & \frac{r_r L_m}{\sigma L_r L_s}\\ \frac{r_s L_m}{\sigma L_s L_r} & -\omega_r\frac{L_m}{\sigma L_r} & -\frac{r_r}{\sigma L_r} & -\frac{\omega_r}{\sigma}\\ \omega_r\frac{L_m}{\sigma L_r} & \frac{r_s L_m}{\sigma L_s L_r} & \frac{\omega_r}{\sigma} & -\frac{r_r}{\sigma L_r}\end{bmatrix}\begin{bmatrix}i^s_{ds}\\ i^s_{qs}\\ i^s_{dr}\\ i^s_{qr}\end{bmatrix} + \begin{bmatrix}\frac{1}{\sigma L_s} & 0\\ 0 & \frac{1}{\sigma L_s}\\ -\frac{L_m}{\sigma L_s L_r} & 0\\ 0 & -\frac{L_m}{\sigma L_s L_r}\end{bmatrix}\begin{bmatrix}v^s_{ds}\\ v^s_{qs}\end{bmatrix}.$$

4.5 Consider the steady-state voltage equations, (4.53) and (4.54):

$$\begin{aligned}\mathbf{V}_{dqs} &= r_s\mathbf{I}_{dqs} + j\omega_e\mathbf{\Lambda}_{dqs}\\ 0 &= \frac{r_r}{s}\mathbf{I}_{dqr} + j\omega_e\mathbf{\Lambda}_{dqr}.\end{aligned}$$

a) Assume that the d–axis coincides with the rotor flux. Justify the following:

$$\begin{aligned}i^e_{dr} &= 0,\\ L_m i^e_{qs} + L_r i^e_{qr} &= 0.\end{aligned}$$

b) Show that

$$\begin{aligned}\lambda^e_{qs} &= \sigma L_s i^e_{qs},\\ \lambda^e_{ds} &= \sigma L_s i^e_{ds} + \frac{L_m^2}{L_r} i^e_{ds}.\end{aligned}$$

c) Show that the voltage equations become

$$\begin{aligned} \mathbf{V}_{dqs} &= (r_s + j\omega_e \sigma L_s)\mathbf{I}_{dqs} + j\omega_e \frac{L_m^2}{L_r} i_{ds}^e \\ 0 &= \frac{r_r}{s} i_{qr}^e + j\omega_e L_m i_{ds}^e. \end{aligned}$$

d) Draw an equivalent circuit based on the equations in c).

4.6 Show that

$$\begin{aligned} \text{i)} \quad T_e &= \frac{3}{2}\frac{P}{2}(\lambda_{ds}^e i_{qs}^e - \lambda_{qs}^e i_{ds}^e), \\ \text{ii)} \quad T_e &= \frac{3}{2}\frac{P}{2}\frac{L_m}{\sigma L_s L_r}(\lambda_{dr}^e \lambda_{qs}^e - \lambda_{ds}^e \lambda_{qr}^e). \end{aligned}$$

Chapter 5

Field-Oriented Controls of Induction Motors

In AC machines, torque is expressed as the outer product of flux and current vectors. Therefore, to maximize torque the two vectors should be orthogonal. In the DC motor, the orthogonality is guaranteed by the brush and commutator action. However, in AC machines it can be achieved dynamically in the synchronous frame.

The balanced three-phase current system has two degrees of freedom. The two degrees of freedom are allocated to two different missions: One is for flux regulation, and the other for torque control. Such role decomposition is unclear in the fixed coordinate frame. But in the synchronous reference frame, the roles of dq-axes currents are naturally decomposed and the dynamics resemble those of the separately excited DC machine.

If the reference frame is aligned with the rotor flux, then the control is called *the rotor field-oriented scheme*. If the frame is aligned with the air-gap field or stator field, it is called *the air-gap field* or *stator field-oriented scheme*, respectively.

5.1 Direct versus Indirect Vector Controls

Based on the flux angle access methods, field-oriented controls are categorized as a direct or indirect method. Hall sensors or flux sensing coils may be employed to measure the rotor flux. Once the rotor flux is measured, the rotor flux angle can be calculated according to

$$\theta = \tan^{-1}\left(\frac{\lambda_{dr}^{s}}{\lambda_{qr}^{s}}\right). \tag{5.1}$$

However, installing sensors around the air gap is not an easy matter due to space limitation, armature reaction, noise, etc.

A more reasonable approach is to use current measurements and internally computed voltage values. The rotor flux is obtained indirectly from the stator flux and

stator current in such a way that

$$\begin{aligned}\lambda_{dr}^s &= \frac{L_r}{L_m}(\lambda_{ds}^s - L_s i_{ds}^e) + L_m i_{ds}^e = \frac{L_r}{L_m}(\lambda_{ds}^s - \sigma L_s i_{ds}^s),\\ \lambda_{qr}^s &= \frac{L_r}{L_m}(\lambda_{qs}^s - L_s i_{qs}^e) + L_m i_{qs}^e = \frac{L_r}{L_m}(\lambda_{qs}^s - \sigma L_s i_{qs}^s).\end{aligned}$$

Stator currents are easily measured by current sensors, and the stator fluxes are obtained by integrating $\mathbf{v}_s - r_s\mathbf{i}_s$, i.e.,

$$\lambda_{ds}^s = \int_0^t (v_{ds}^s - r_s i_{ds}^s)d\tau, \tag{5.2}$$

$$\lambda_{qs}^s = \int_0^t (v_{qs}^s - r_s i_{qs}^s)d\tau. \tag{5.3}$$

However, this approach is not reliable when a DC offset is present. On the other hand, indirect methods obtain the flux angle by exploiting the slip information calculated from the IM dynamic model.

5.2 Rotor Field-Orientated Scheme

We express (4.21) and (4.22) as

$$\lambda_{ds}^e = \left(L_s - \frac{L_m^2}{L_r}\right) i_{ds}^e + \frac{L_m}{L_r}\lambda_{dr}^e = L_s\sigma i_{ds}^e + \frac{L_m}{L_r}\lambda_{dr}^e, \tag{5.4}$$

$$\lambda_{qs}^e = \left(L_s - \frac{L_m^2}{L_r}\right) i_{qs}^e + \frac{L_m}{L_r}\lambda_{qr}^e = L_s\sigma i_{qs}^e + \frac{L_m}{L_r}\lambda_{qr}^e. \tag{5.5}$$

Utilizing (5.4) and (5.5), we obtain stator voltage equations as derived already in (4.37):

$$v_{ds}^e = (r_s + pL_s\sigma)i_{ds}^e + \frac{L_m}{L_r}p\lambda_{dr}^e - \omega_e\left(L_s\sigma i_{qs}^e + \frac{L_m}{L_r}\lambda_{qr}^e\right), \tag{5.6}$$

$$v_{qs}^e = (r_s + pL_s\sigma)i_{qs}^e + \frac{L_m}{L_r}p\lambda_{qr}^e + \omega_e\left(L_s\sigma i_{ds}^e + \frac{L_m}{L_r}\lambda_{dr}^e\right). \tag{5.7}$$

Rotor field-oriented scheme is achieved by aligning the d–axis to the rotor flux. This makes not only $\lambda_{qr}^e = 0$ but also $\dot{\lambda}_{qr}^e = 0$, as depicted in Fig. 5.1.

Stator Equation

By letting $\lambda_{qr}^e = 0$, we obtain from (5.6) and (5.7)

$$v_{ds}^e = (r_s + p\sigma L_s)i_{ds}^e - \omega_e\sigma L_s i_{qs}^e + \frac{L_m}{L_r}p\lambda_{dr}^e, \tag{5.8}$$

$$v_{qs}^e = (r_s + p\sigma L_s)i_{qs}^e + \omega_e\sigma L_s i_{ds}^e + \omega_e\frac{L_m}{L_r}\lambda_{dr}^e. \tag{5.9}$$

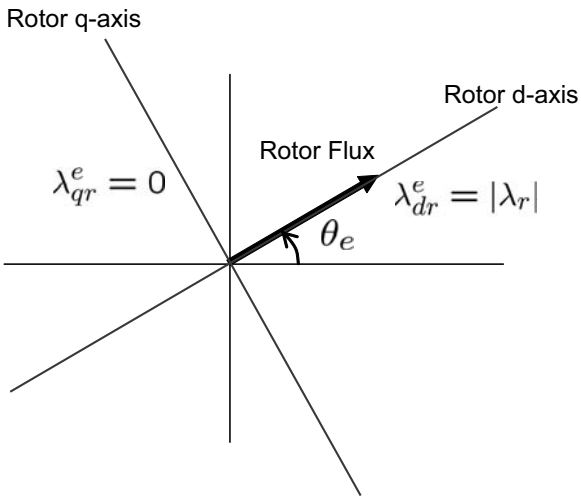

Figure 5.1: Alignment of d–axis to the rotor flux, $\boldsymbol{\lambda}^s_{dqr}$.

Note that $-\omega_e \sigma L_s i^e_{qs}$ and $\omega_e \sigma L_s i^e_{ds}$ are coupling terms between d and q axes dynamics, and that $\omega_e \frac{L_m}{L_r} \lambda^e_{dr}$ is the back EMF term.

Rotor Equation

Applying $\lambda^e_{qr} = 0$ and $\dot{\lambda}^e_{qr} = 0$ to (4.19) and (4.20), we obtain that

$$\begin{aligned} 0 &= r_r i^e_{dr} + p\lambda^e_{dr} = (r_r + L_r p) i^e_{dr} + p L_m i^e_{ds}, && (5.10) \\ 0 &= r_r i^e_{qr} + (\omega_e - \omega_r)\lambda^e_{dr}. && (5.11) \end{aligned}$$

Therefore, it follows (5.10) that

$$i^e_{dr} = -\frac{L_m p i^e_{ds}}{r_r + p L_r} \tag{5.12}$$

Utilizing (5.12), we obtain the d–axis rotor flux such that

$$\begin{aligned} \lambda^e_{dr} &= L_m i^e_{ds} + L_r i^e_{dr} \\ &= L_m i^e_{ds} - \frac{L_r L_m p i^e_{ds}}{r_r + p L_r} \\ &= \frac{L_m}{1 + p\tau_r} i^e_{ds}\,, \end{aligned} \tag{5.13}$$

where $\tau_r = \frac{L_r}{r_r}$ is the rotor time constant. In the steady-state, (5.13) reduces to

$$\lambda^e_{dr} = L_m i^e_{ds}\,. \tag{5.14}$$

Since $\lambda^e_{qr} = 0$ in the rotor field-oriented scheme, it follows that

$$0 = L_m i^e_{qs} + L_r i^e_{qr}. \tag{5.15}$$

Then, the slip equation follows from (5.11) and (5.15):

$$\omega_e - \omega_r = s\omega_e = -r_r \frac{i^e_{qr}}{\lambda_{dr}} = \frac{r_r}{L_r}\frac{L_m}{\lambda_{dr}} i^e_{qs} \,. \tag{5.16}$$

Roles of i_{ds} and i_{qs}

Comparing (5.14) with $\lambda^e_{dr} = L_m i^e_{ds} + L_r i^e_{dr}$, it is observed that $i^e_{dr} = 0$. Now, the roles of d and q axes stator currents become clear: Q-axis current, i_{qs}, is proportional to the slip and thus to torque. d–axis current, i_{ds}, is used for producing the rotor flux, λ^e_{dr}. Fig. 5.2 shows the current vectors and flux vector in the rotor field-oriented scheme. Note however that a huge q–axis rotor current flows, although λ^e_{qr} is equal to zero. This can be interpreted that i^e_{qr} flows in opposition to i^e_{qs} to counteract a possible generation of q–axis rotor flux caused by i^e_{qs}, i.e., the rotor current flows to achieve $0 = \lambda^e_{qr} = L_r i^e_{qr} + L_m i^e_{qs}$. Note also from Fig. 5.2 that the stator current, $\mathbf{i}^e_{dqs}$, leads in phase angle the rotor flux, $\boldsymbol{\lambda}^e_{dqr}$ in the vector diagram.

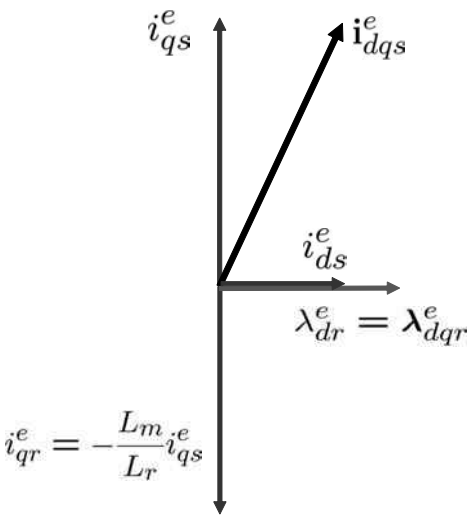

Figure 5.2: Current and flux vectors for the rotor field-oriented scheme.

Summarizing the above, the roles of currents are as follows:

1. i^e_{ds} is used solely for generating the rotor flux ⇐ (5.13).
2. $i^e_{dr} = 0$ in the steady-state can be seen by comparing (4.23) with (5.14).
3. i^e_{qs} is used for generating torque ⇐ (5.16).
4. i^e_{qr} flows in order to nullify a possible q–axis rotor flux generation caused by i^e_{qs} ⇐ (4.24).

With $\lambda_{qr}^e = 0$, the torque equation (4.62) reduces to

$$T = \frac{3P}{4}\frac{L_m}{L_r}\lambda_{dr}^e i_{qs}^e.$$

This equation is comparable to the torque equation of the DC motor. The similarities with the DC motor are:

λ_{dr}^e corresponds to the field.
i_{ds}^e corresponds to the field current.
i_{qs}^e corresponds to the armature current.

Fig. 5.3 shows the field distribution that illustrates the rotor flux generation by i_{ds}^e, torque production by stator q–axis current, and the field cancelation between i_{qs}^e and i_{qr}^e.

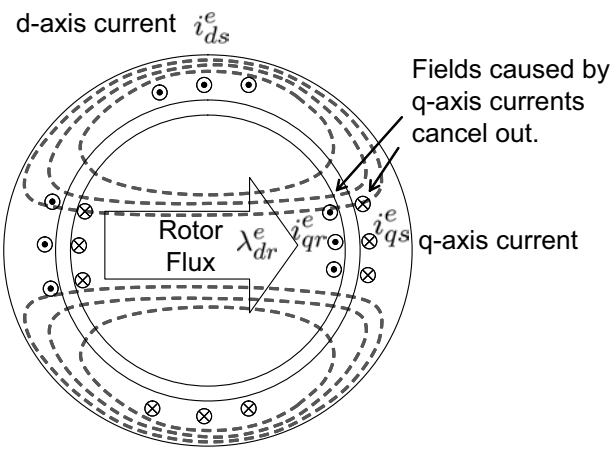

Figure 5.3: Torque production with the rotor field-oriented control: The rotor d–axis field acts on the stator q–axis current.

Vector Diagram in the Steady-State

In the steady-state, $p\lambda_{dr} = 0$ and $pi_{ds}^e = pi_{qs}^e = 0$. With the complex variables, (5.8) and (5.9) are rewritten as

$$\mathbf{v}_{dqs}^e = r_s \mathbf{i}_{dqs}^e + j\omega_e \sigma L_s \mathbf{i}_{dqs}^e + j\omega_e \frac{L_m}{L_r}\lambda_{dr}^e. \tag{5.17}$$

Based on (5.17), vector diagram for the rotor field-oriented control can be drawn as Fig. 5.4. Note that the voltage vector leads the current vector by ϕ.

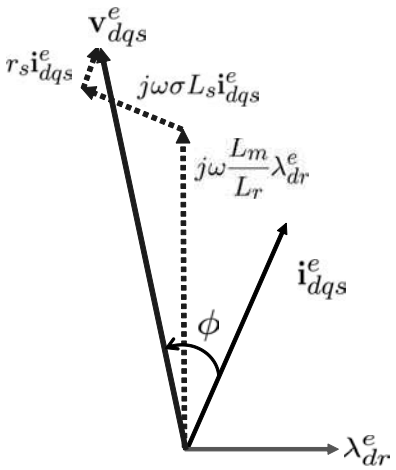

Figure 5.4: Voltage vector diagram for the rotor field-oriented control.

Block Diagram for the Rotor Field-Oriented Scheme

Substituting Laplace operator s for p, we obtain from (5.8) and (5.9) that

$$i^e_{ds} = \frac{\frac{1}{\sigma L_s}}{s+\frac{r_s}{\sigma L_s}}v^e_{ds} + \frac{1}{s+\frac{r_s}{\sigma L_s}}\omega_e i^e_{qs}, \tag{5.18}$$

$$i^e_{qs} = \frac{\frac{1}{\sigma L_s}}{s+\frac{r_s}{\sigma L_s}}\left(v^e_{qs} - \omega_e\frac{L_m}{L_r}\lambda^e_{dr}\right) - \frac{1}{s+\frac{r_s}{\sigma L_s}}\omega_e i^e_{ds}. \tag{5.19}$$

A block diagram based on the reduced model (5.18) and (5.19) is depicted in Fig. 5.5. The IM model contains just coupling terms and the back EMF.

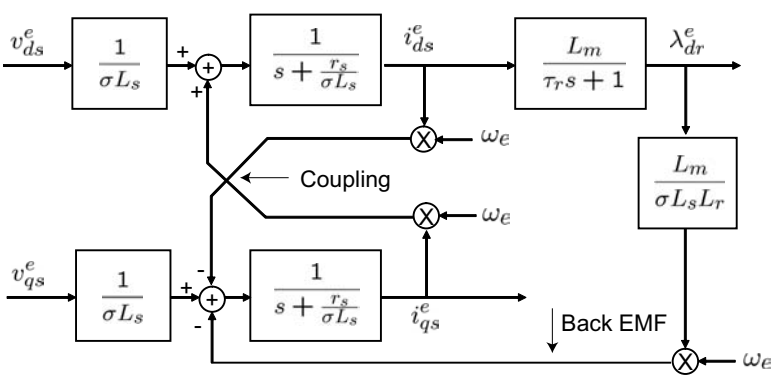

Figure 5.5: IM model under the rotor field-oriented scheme.

5.2.1 Field-Oriented Control Implementation

The IM dynamic model mimics the DC motor dynamic model in the rotor flux reference frame in which the roles of the dq-axes current are separated. Specifically, the d–axis current, functioning as the field current, should be regulated to keep a desired rotor field level. The q–axis current, functioning as the armature current, needs to be controlled for torque production in accordance with a high level controller.

Current Controller in the Synchronous Frame

For dq current regulation, it is necessary to measure the dq axis currents, and better to use PI controllers. However, to obtain dq axis currents in the synchronous (rotor field-oriented) frame, we should know the rotor flux angle, θ_e. Furthermore, the PI controllers output dq voltage commands, d_d^e and v_q^e. But, they have to be transformed into abc-frame to be used for gating the inverter switches. To summarize, the field-oriented current controller should be implemented in the synchronous frame and the rotor flux angle should be known for coordinate transformations.

Angle Estimation

The electrical angular velocity is obtained by adding slip speed to the motor shaft speed, i.e., $\omega_e = \omega_r + \omega_{sl}$. Encoders or resolvers are the most common speed sensors. The angular position θ_e of the rotor flux is obtained by integrating ω_e:

$$\theta_e = \int_0^t \omega_e dt = \int_0^t (\omega_{sl} + \omega_r) dt = \int_0^t (\frac{L_m i_{qs}^e}{\tau_r \lambda_{dr}^e} + \omega_r)\, dt. \tag{5.20}$$

Note that λ_{dr}^e is estimated by (5.13).

Decoupling Current Controller

The most common regulation method is to use PI controller with the decoupling compensation:

$$v_{ds}^e = K_p(i_{ds}^{e*} - i_{ds}^e) + K_i \int_0^t (i_{ds}^{e*} - i_{ds}^e) dt - \omega_e \sigma L_s i_{qs}^e\,, \tag{5.21}$$

$$v_{qs}^e = K_p(i_{qs}^{e*} - i_{qs}^e) + K_i \int_0^t (i_{qs}^{e*} - i_{qs}^e) dt + \omega_e \sigma L_s i_{ds}^e + \omega_e \frac{L_m}{L_r} \lambda_{dr}^e\,, \tag{5.22}$$

where K_p and K_i are proportional and integral gains, respectively. Note that the back EMF, $\omega_e \frac{L_m}{L_r} \lambda_{dr}^e$ is also compensated in the q–axis current controller, (5.22).

The d–axis current is proportional to the flux, so that d–axis current command, i_d^{e*}, is linked directly to the flux level. The q–axis current command normally comes from high level control loops, e.g. torque or speed controller.

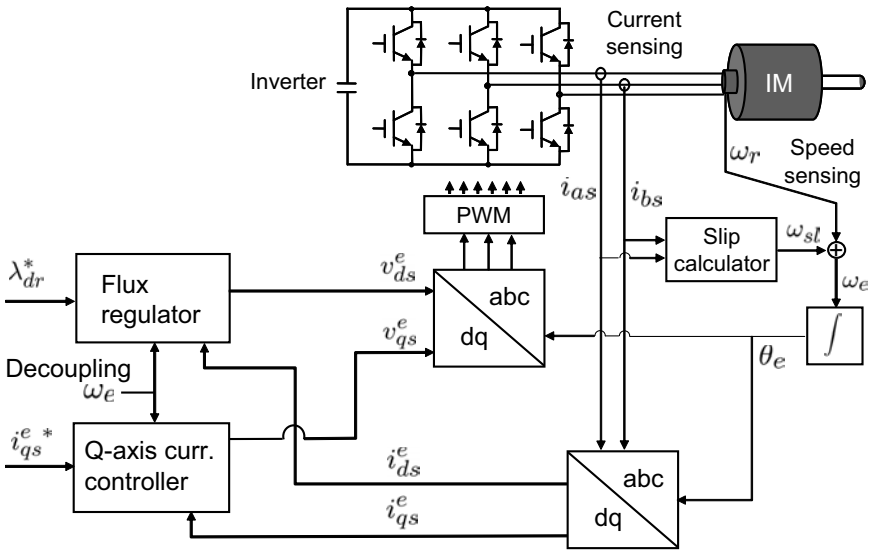

Figure 5.6: Field-oriented control block diagram involving coordinate changes.

Control Block Diagram

Block diagram for a typical field-oriented control is shown in Fig. 5.6. The field-oriented control can be illustrated with following individual steps:

1) Measure phase currents.
2) Estimate the rotor flux angle, θ_e according to (5.20).
3) Transform (i_{as}, i_{bs}) into (i^e_{ds}, i^e_{qs}) using the coordinate transformation map, $\mathbf{T}(\theta_e)$.
4) Construct dq current controllers. Apply decoupling feedback.
5) Transform the voltage vector, (v^e_{ds}, v^e_{qs}), into (v_{as}, v_{bs}, v_{cs}).
6) Convert (v_{as}, v_{bs}, v_{cs}) into on-duties of the PWM.

The above individual steps are described as sub-blocks in Fig. 5.6. Phase currents are measured by utilizing Hall sensor or shunt resistor. Since the phase current sum is equal to zero, it is normal to measure only two-phase currents, for example, (i_{as}, i_{bs}). Step 5) and 6) are practically merged into a single step (e.g. space vector modulation). It should be emphasized that the forward ($abc \rightarrow dq$) and reverse ($dq \rightarrow abc$) transformations are indispensable in the field-oriented control, and that a microcontroller performance needs to be high enough to finish all required computation within the current loop bandwidth.

A detailed control block diagram for the rotor field-oriented scheme is shown in Fig. 5.7. The current control part is based on (5.21) and (5.22), and the slip is calculated according to (5.16).

In the rated speed range, the flux level is maintained constant, but it is reduced as the speed increases (field-weakening). The field reference command, λ^{e*}_{ds} is depicted as a flattened mountain shape.

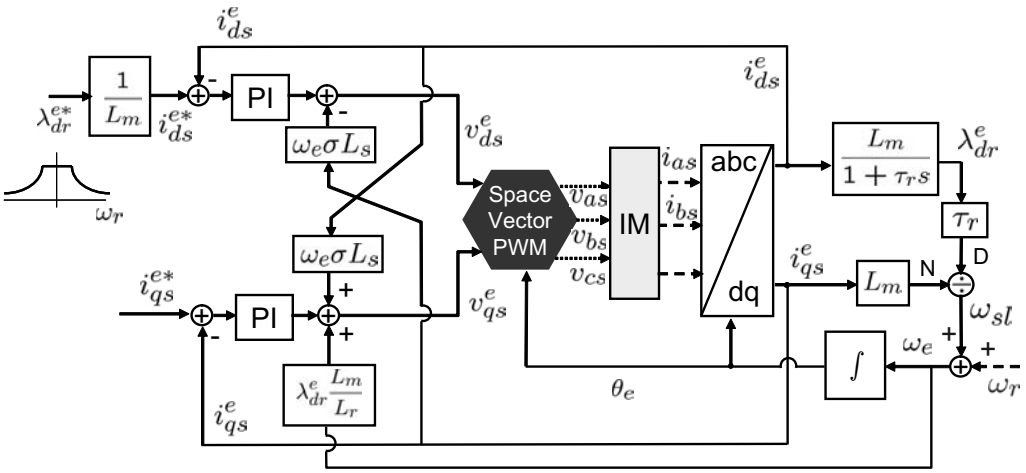

Figure 5.7: Control block based on the rotor field-oriented control scheme.

5.3 Stator Field-Oriented Scheme

The stator field-oriented scheme is the control method of aligning the d–axis of the frame with the stator flux. Thus, the q–axis stator flux is zero, i.e., $\lambda^e_{qs} = 0$. Therefore, it follows from (4.21), (4.22), (5.4), and (5.5) that

$$\lambda^e_{dr} = \frac{L_r}{L_m}(\lambda^e_{ds} - \sigma L_s i^e_{ds}), \tag{5.23}$$

$$\lambda^e_{qr} = -\frac{L_r}{L_m}\sigma L_s i^e_{qs}, \tag{5.24}$$

$$i^e_{dr} = \frac{1}{L_m}\lambda^e_{ds} - \frac{L_s}{L_m} i^e_{ds}, \tag{5.25}$$

$$i^e_{qr} = -\frac{L_s}{L_m} i^e_{qs}\,. \tag{5.26}$$

The stator flux and slip equations can be derived by substituting (5.23)−(5.26) into (4.19) and (4.20): From the rotor d–axis equation,

$$\begin{aligned} 0 &= r_r i^e_{dr} + p\lambda^e_{dr} - \omega_{sl}\lambda^e_{qr} \\ &= \frac{r_r}{L_m}(\lambda^e_{ds} - L_s i^e_{ds}) + p\frac{L_r}{L_m}(\lambda^e_{ds} - \sigma L_s i^e_{ds}) + \frac{L_r}{L_m}\omega_{sl}\sigma L_s i^e_{qs} \\ &= \frac{1}{\tau_r}(\lambda^e_{ds} - L_s i^e_{ds}) + p(\lambda^e_{ds} - \sigma L_s i^e_{ds}) + \omega_{sl}\sigma L_s i^e_{qs} \\ &= (\frac{1}{\tau_r} + p)\lambda^e_{ds} - L_s(\frac{1}{\tau_r} + p\sigma) i^e_{ds} + \omega_{sl}\sigma L_s i^e_{qs} \end{aligned}$$

we obtain

$$\lambda^e_{ds} = \frac{(\sigma p + \frac{1}{\tau_r})L_s}{p + \frac{1}{\tau_r}} i^e_{ds} - \frac{\sigma L_s i^e_{qs}}{p + \frac{1}{\tau_r}}\omega_{sl}\,. \tag{5.27}$$

From the rotor q–axis equation,

$$\begin{aligned} 0 &= r_r i^e_{qr} + p\lambda^e_{qr} + \omega_{sl}\lambda^e_{dr} \\ &= -\frac{r_r L_s}{L_m} i^e_{qs} - p\frac{L_r}{L_m}\sigma L_s i^e_{qs} + \frac{L_r}{L_m}\omega_{sl}(\lambda^e_{ds} - \sigma L_s i^e_{ds}) \\ &= -L_s i^e_{qs} - p\tau_r \sigma L_s i^e_{qs} + \tau_r \omega_{sl}(\lambda^e_{ds} - \sigma L_s i^e_{ds}) \end{aligned}$$

we obtain [1]

$$\omega_{sl} = \frac{(\frac{1}{\tau_r} + p\sigma)L_s i^e_{qs}}{\lambda^e_{ds} - \sigma L_s i^e_{ds}} = \frac{(p + \frac{1}{\sigma\tau_r})i^e_{qs}}{\frac{\lambda^e_{ds}}{\sigma L_s} - i^e_{ds}}\,. \tag{5.28}$$

Note that flux and slip equations are not decoupled in the stator field-oriented scheme. Specifically, ω_{sl} is involved for flux calculation, (5.27), and λ^e_{ds}, in turn, for slip calculation, (5.28). Further comparing (5.28) with (5.16), the stator field-oriented scheme is less advantageous than the rotor field-oriented scheme, since the former requires current differentiation. Hence, the rotor field-oriented scheme is commonly used in practical applications. The torque equation corresponding to the stator reference frame is $T_e = \frac{3}{2}\frac{P}{2}\lambda^e_{ds} i^e_{qs}$.

5.4 IM Field-Weakening Control

As the speed increases, the back EMF grows. At a rated condition, the source (inverter) voltage reaches its limit. To operate the machine above the rated speed, both torque and field have to be reduced.

5.4.1 Current and Voltage Limits

The current rating is determined mostly by the thermal capacity of the motor. Let the peak value of the maximum phase current be denoted by $I_{\max}$. Then,

$$i^{e2}_{ds} + i^{e2}_{qs} \le I^2_{\max}. \tag{5.29}$$

Thus, the current limitation is described by a circle in the (i^e_{ds}, i^e_{qs}) plane.

Let $V_{\max}$ be the peak value of the maximum phase voltage, Note that $V_{\max} = V_{DC}/\sqrt{3}$ in the space vector modulation, where V_{DC} is the DC link voltage. The voltage limit is

$$v^{e2}_{ds} + v^{e2}_{qs} \le V^2_{\max}. \tag{5.30}$$

Suppose that the machine is controlled according to the rotor field-oriented scheme, and assume that the machine is in the steady-state. The steady-state model (5.17) can be rewritten as

$$v_{ds} = r_s i^e_{ds} - \omega_e \sigma L_s i^e_{qs}\,, \tag{5.31}$$

$$v_{qs} = r_s i^e_{qs} + \omega_e L_s i^e_{ds}\,. \tag{5.32}$$

By substituting (5.31) and (5.32) into (5.30) we obtain an ellipse:

$$\left(\frac{r_s i_{qs}^e}{\omega_e} + L_s i_{ds}^e\right)^2 + \left(\frac{r_s i_{ds}^e}{\omega_e} - \sigma L_s i_{qs}^e\right)^2 \leq \frac{V_{\max}^2}{\omega_e^2}\,. \tag{5.33}$$

A further simplification is made by neglecting the stator resistance. The major effect of stator resistance appears to be a clockwise rotation of the ellipse. However, as the voltage drop over the stator resistance is relatively small in the field-weakening region, it is neglected. Then, we have

$$\frac{{i_{ds}^e}^2}{\left(\frac{V_{\max}}{\omega_e L_s}\right)^2} + \frac{{i_{qs}^e}^2}{\left(\frac{V_{\max}}{\omega_e \sigma L_s}\right)^2} \;\leq\; 1\,. \tag{5.34}$$

Note that $\frac{V_{\max}}{\omega_e L_s} \ll \frac{V_{\max}}{\omega_e \sigma L_s}$, since $\sigma \approx 0.1$. That is, the major axis lies on the i_{qs}^e-axis, whereas the minor axis lies on the i_{ds}^e-axis. Hence, (5.34) has an upright shape, as shown in Fig. 5.8. The center of the ellipse is the origin, which implies that as the frequency increases, the voltage constraint will shrink towards the origin. The machine can operate only in the intersection between the current limit circle and the voltage limit ellipse, i.e, in the overlapping area between the current circle and the voltage ellipse.

With the rotor field-oriented scheme, the torque equation is expressed as

$$T_e = \frac{3}{2}\frac{P}{2}\frac{L_m^2}{L_r} i_{ds}^e i_{qs}^e. \tag{5.35}$$

Hence, constant torque curves appear as parabolic curves. Fig. 5.8 shows the current and voltage limits with several constant torque curves.

5.4.2 Field-Weakening Control Methods

To exploit the maximum power capability of the machine, the maximum voltage and current should be utilized. Thus for the maximum power operation, the operating points need to be determined on the intersection points of the voltage and current limits. Note again that the current limit circle is invariant to the speed, whereas the voltage limit ellipse shrinks as the speed increases. Therefore, the operating points migrate along the circle to the left (Point A − Point D of Fig. 5.8). Along this migration, the torque reduces, thereby it is represented by a parabola curve in interval (A, D) of Fig. 5.9. If the speed is increased further, the voltage ellipses are separated from the circle. In that speed range, only the voltage limit is activated and the current reduces with speed. The typical profiles of voltage, current, torque, and flux in the field-weakening region are shown in Fig. 5.9.

Constant Torque Limit Region

The constant torque region indicates the speed range from zero to a rated speed. In this region, the maximum torque is limited by the maximum stator current.

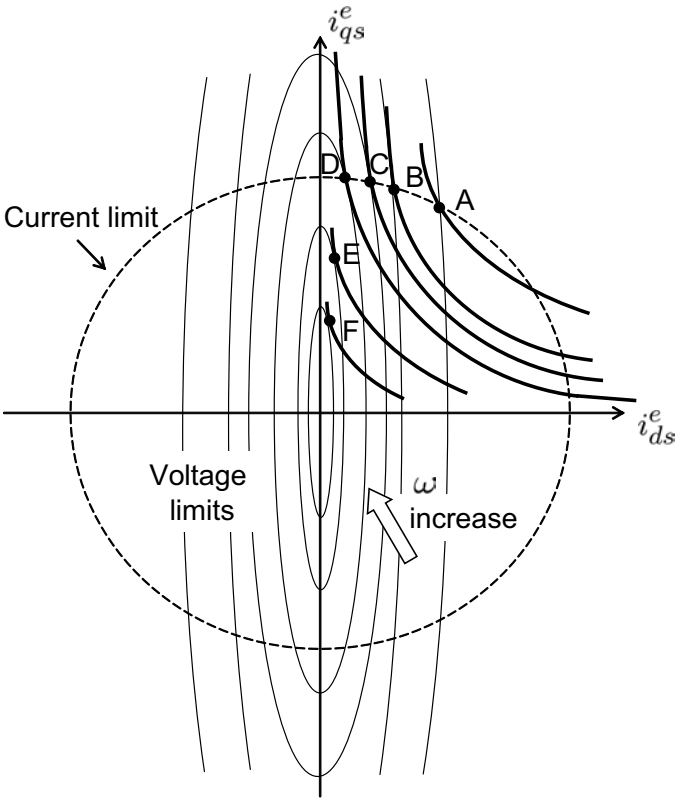

Figure 5.8: Current and speed limits with constant torque curves.

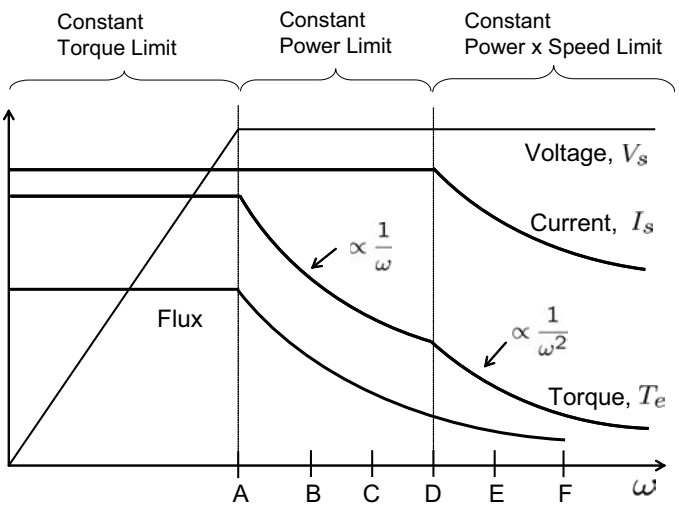

Figure 5.9: IM characteristics in constant torque and field-weakening region.

However, the power increases with the back EMF. At the rated speed, the motor terminal voltage reaches the limit.

Constant Power Limit Region

As the frequency continues to increase, the voltage ellipse shrinks while the maximum current level, $I_{\max}$, is maintained. Hence, the current vector moves along the (current) circle from A to D. At this time, the torque reduces inversely to the increase of speed, achieving constant power. Along the contour, the d–axis current reduces, incurring reduction in the d–axis rotor flux. Since the voltage and the current remain constant, power is also constant (assuming unity power factor). Thus, this region is often called *the constant power limit region*. In this region, the torque is inversely proportional to $1/\omega$.

Constant Power×Speed Limit Region

As the frequency increases further above point D, the voltage ellipse shrinks inside the current limit circle, so that the current limit is no longer activated. In this region, current also reduces. Therefore, torque reduction is accelerated. Representing torque as $T_e = ki_d^e i_q^e$,

$$i_{ds}^{e\,2} + \left(\frac{\sigma T_e}{k i_{ds}^e}\right)^2 = \left(\frac{V_{\max}}{\omega_e L_s}\right)^2.$$

Since

$$i_{ds}^{e\,2} + \left(\frac{\sigma T_e}{k i_{ds}^e}\right)^2 \geq \frac{2\sigma T_e}{k},$$

it follows that

$$\left(\frac{V_{\max}}{\omega_e L_s}\right)^2 \geq \frac{2}{k}\sigma T_e. \tag{5.36}$$

In the above derivation, inequality, $A^2 + B^2 \geq 2AB$ was utilized. Therefore, torque reduces in proportion to $1/\omega_e^2$ in this region.

5.5 Speed-Sensorless Control of IMs

To get the speed measurement, speed sensors such as encoder or resolver should be utilized. However, installing the speed sensor is sometimes difficult due to environments or cost reduction. For example, in some cranes where the distance between the motor and the inverter is several tens of meters, the use of encoder is not easy since the encoder signal attenuates and deteriorates by the environmental noise. In some home appliances, cost pressure inhibits the use of encoders. In the following, several sensorless methods are illustrated.

5.5.1 Open-Loop Stator Flux Model

It follows from the stator voltage equation (4.11) that the stator flux is obtained by integrating $\mathbf{v}^s_{dqs} - r_s\mathbf{i}^s_{dqs}$, i.e.,

$$\hat{\boldsymbol{\lambda}}^s_{dqs} = \int \left(\mathbf{v}^s_{dqs} - r_s\mathbf{i}^s_{dqs}\right) dt, \tag{5.37}$$

where $\hat{\boldsymbol{\lambda}}^s_{dqs}$ is the stator flux in the stationary frame.

However, the integrator is easily saturated by a small DC offset, so that a first order filter $\frac{\tau_0}{\tau_0 s+1} = \frac{1}{s+1/\tau_0}$ is used:

$$\tau_0 \frac{d\hat{\boldsymbol{\lambda}}^s_{dqs}}{dt} + \hat{\boldsymbol{\lambda}}^s_{dqs} = \tau_0(\mathbf{v}^s_{dqs} - r_s\mathbf{i}^s_{dqs}). \tag{5.38}$$

It is obvious the filter behaves like an integrator for frequencies higher than the corner frequency, $1/\tau_0$. It is obvious that the model becomes inaccurate when the frequency reduces to values around the corner frequency. The gain then reduces and, more importantly, the 90° phase shift of the integrator is lost. This causes an increasing error of the estimated field angle as the stator frequency reduces, which finally makes the system unstable [2]. The estimated stator flux is used for obtaining the rotor flux:

$$\hat{\boldsymbol{\lambda}}^s_{dqr} = \frac{L_r}{L_m}\left(\hat{\boldsymbol{\lambda}}^s_{dqs} - \sigma L_s\mathbf{i}^s_{dqs}\right). \tag{5.39}$$

Finally, the rotor flux angle estimate $\hat{\theta}_r$ is obtained such that

$$\hat{\theta}_r = \tan^{-1}\left(\frac{\hat{\lambda}^s_{qr}}{\hat{\lambda}^s_{dr}}\right). \tag{5.40}$$

The whole rotor flux estimation scheme is depicted graphically in Fig. 4.3. The current controller can be implemented based on the frame of $e^{j\hat{\theta}_r}$.

Another drawback of this scheme is that it is sensitive to the change of stator resistance. Stator coil resistance increases with the temperature, and the variation range is 1:2. Therefore, the estimation error due to r_s is prominent in the lower frequency area ($1 \sim 3$Hz) where $r_s|\mathbf{i}^s_{dqs}|$ is relatively large compared with $|\mathbf{v}_{dqs}|$.

5.5.2 Closed-Loop Rotor Flux Model

Two rotor flux estimates are obtained from the stator and rotor models, and an error is taken from the two flux estimates. The error is utilized for adjusting the rotor speed estimates. Since the dynamic models are used, this method is often called MRAS method [2].

In the rotor frame, the rotor voltage equation is given by

$$\mathbf{v}^r_{dqr} = r_r\mathbf{i}^r_{dqr} + \frac{d\boldsymbol{\lambda}^r_{dqr}}{dt}.$$

To transform to the stationary frame, we multiply $e^{j\theta_r}$. Then, it follows that

$$\begin{aligned} e^{j\theta_r}\mathbf{v}^r_{dqr} &= r_r e^{j\theta_r}\mathbf{i}^r_{dqr} + e^{j\theta_r}\frac{d}{dt}\left(e^{j\theta_r}e^{-j\theta_r}\boldsymbol{\lambda}^r_{dqr}\right) \\ \mathbf{v}^s_{dqr} &= r_r\mathbf{i}^s_{dqr} + j\omega_r\boldsymbol{\lambda}^s_{dqr} + \frac{d\boldsymbol{\lambda}^s_{dqr}}{dt} \\ &= \frac{r_r}{L_r}(\boldsymbol{\lambda}^s_{dqr} - L_m\mathbf{i}^s_{dqs}) + j\omega_r\boldsymbol{\lambda}^s_{dqr} + \frac{d\boldsymbol{\lambda}^s_{dqr}}{dt}. \end{aligned}$$

Therefore, the rotor flux in the stationary frame satisfies

$$\tau_r\frac{d\hat{\boldsymbol{\lambda}}^s_{dqr}}{dt} + \hat{\boldsymbol{\lambda}}^s_{dqr} = -j\omega_r\tau_r\hat{\boldsymbol{\lambda}}^s_{dqr} + L_m\hat{\boldsymbol{i}}^s_{dqs}. \tag{5.41}$$

Note that in the stationary frame the mechanical speed ω_r appears instead of ω_{sl}

We denote by $\hat{\boldsymbol{\lambda}}^R_{dqr}$, the estimate of the rotor flux obtained by utilizing (5.41), and by $\hat{\boldsymbol{\lambda}}^S_{dqr}$, the estimate of the rotor flux obtained by utilizing (5.38). Note that $\hat{\boldsymbol{\lambda}}^S_{dqr} = \hat{\boldsymbol{\lambda}}^R_{dqr}$ if both estimations are correct. If they do not match, the rotor flux estimate based on (5.41) is thought to be incorrect. The angle difference between $\hat{\boldsymbol{\lambda}}^S_{dqr}$ and $\hat{\boldsymbol{\lambda}}^R_{dqr}$ may be captured by

$$e_\lambda = \hat{\boldsymbol{\lambda}}^R_{dqr} \times \hat{\boldsymbol{\lambda}}^S_{dqr}\Big|_z = |\hat{\boldsymbol{\lambda}}^R_{dqr}|\,|\hat{\boldsymbol{\lambda}}^S_{dqr}|\sin\delta,$$

where δ is the angle between the two flux estimates. Error, e_λ is used for correcting the rotor speed estimate, $\hat{\omega}_r$. A method of updating speed estimate, $\hat{\omega}_r$, is to use the PI type controller, i.e.,

$$\hat{\omega}_r = \left(k_p + k_i\frac{1}{s}\right)e_\lambda. \tag{5.42}$$

The speed estimate is used in the rotor flux model, (5.41), making a closed-loop.

The closed-loop rotor flux model is depicted in Fig. 5.10: Two models yields two rotor flux estimates, and their angle difference is taken by utilizing the outer product. Passing the angle error through a PI regulator, a rotor speed estimate is obtained. The speed estimate is used in the rotor model, completing a closed-loop. Similarly to the above open-loop scheme, this closed-loop scheme has a fundamental limitation in the low-speed region, since it also utilizes the same integrator type estimator, (5.38).

5.5.3 Full-Order Observer

Hereforth, a rotor speed estimation method is illustrated that utilizes a full-order observer [3]. Define a stator vector by

$$\mathbf{x} = \begin{bmatrix} \mathbf{i}^e_{dqs} \\ \boldsymbol{\lambda}^e_{dqr} \end{bmatrix} \in \mathbb{R}^4.$$

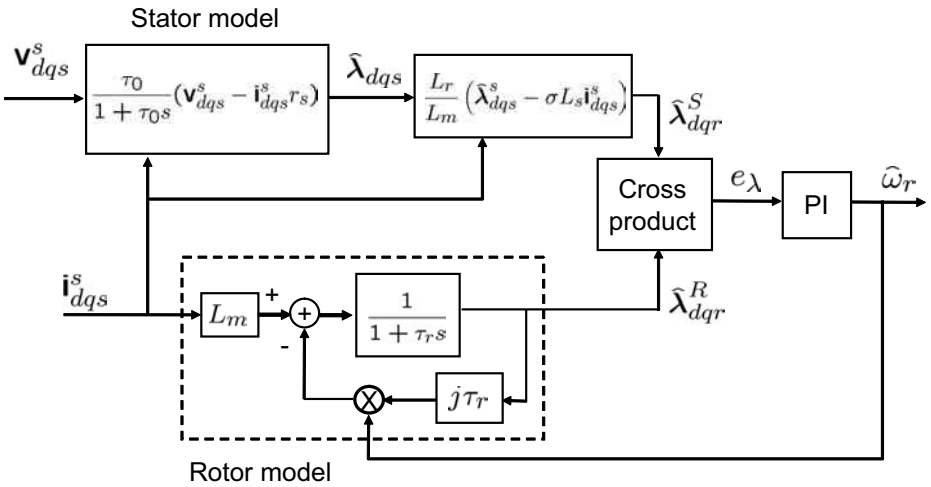

Figure 5.10: MRAS for rotor speed estimation.

Recall from (4.41) that the IM dynamics are

$$\frac{d}{dt}\mathbf{x} = \mathbf{A}(\omega_r)\mathbf{x} + \mathbf{B}\mathbf{v}^e_{dqs}, \tag{5.43}$$

$$\mathbf{i}^e_{dqs} = \mathbf{C}\mathbf{x} \tag{5.44}$$

where

$$\mathbf{A}(\omega_r) = \begin{bmatrix} -\left(\frac{r_s}{\sigma L_s} + \frac{(1-\sigma)}{\sigma\tau_r}\right)\mathbf{I} + \omega_e \mathbf{J} & \frac{L_m}{\sigma L_r L_s}\left(\frac{1}{\tau_r}\mathbf{I} + \omega_r \mathbf{J}\right) \\ \frac{L_m}{\tau_r}\mathbf{I} & -\frac{1}{\tau_r}\mathbf{I} + (\omega_e - \omega_r)\mathbf{J} \end{bmatrix},$$

$$\mathbf{B} = \begin{bmatrix} \frac{1}{\sigma L_s}\mathbf{I} \\ \mathbf{0} \end{bmatrix}, \quad \text{and} \quad \mathbf{C} = [\mathbf{I} \;\; \mathbf{0}] .$$

Note that the IM model, (5.43) and (5.44), is written in the general synchronous reference frame. However, if the reference frame is oriented to the rotor flux and ω_r is available, the electrical angular speed may be calculated according to (5.16) as $\omega_e = \omega_r + \frac{r_r}{L_r}\frac{L_m}{\lambda_{dr}} i^e_{qs}$. Therefore, ω_r is regarded as the only unknown parameter in the system matrix, $\mathbf{A}$, and we denote it by $\mathbf{A}(\omega_r)$ to show the ω_r-dependence.

An adaptive observer should be constructed to derive an estimate, $\hat{\omega}_r$ of ω_r. A full-order observer for (5.43) and (5.44) can be constructed such that

$$\frac{d}{dt}\hat{\mathbf{x}} = \mathbf{A}(\hat{\omega}_r)\hat{\mathbf{x}} + \mathbf{B}\mathbf{v}^e_{dqs} + \mathbf{G}(\mathbf{i}^e_{dqs} - \mathbf{C}\hat{\mathbf{x}}), \tag{5.45}$$

where $\mathbf{G} \in \mathbb{R}^{4\times 2}$ is an observer gain matrix. Let the observer error be defined by

$\Delta\mathbf{x} \equiv \mathbf{x} - \hat{\mathbf{x}}$. Then, the error equation turns out to be

$$\begin{aligned} \frac{d}{dt}\Delta\hat{\mathbf{x}} &= (\mathbf{A}(\omega_r) - \mathbf{GC})\Delta\mathbf{x} + (\mathbf{A}(\omega_r) - \mathbf{A}(\hat{\omega}_r))\hat{\mathbf{x}}, \\ &= (\mathbf{A}(\omega_r) - \mathbf{GC})\Delta\mathbf{x} + \Delta\omega_r \begin{bmatrix} \frac{L_m}{\sigma L_r L_s}\mathbf{J}\hat{\boldsymbol{\lambda}}^e_{dqr} \\ -\mathbf{J}\hat{\boldsymbol{\lambda}}^e_{dqr} \end{bmatrix}, \end{aligned} \tag{5.46}$$

where $\Delta\omega_r = \omega_r - \hat{\omega}_r$.

If ω_r is a constant and $(\mathbf{A}, \mathbf{C})$ is an observable pair, then there is a gain matrix $\mathbf{G} \in \mathbb{R}^{4\times 2}$ matrix such that all the eigenvalues of $(\mathbf{A} - \mathbf{GC})$ have negative real parts. Then, the convergence of the autonomous part of (5.46) is established. But in the time-varying case, the convergence argument is more complicated. Suppose that a symmetric matrix $\mathbf{Q}(t) \in \mathbb{R}^{4\times 4}$ satisfies $x^T\mathbf{Q}(t)x \geq \alpha_0 x^T x$ for all $x \in \mathbb{R}^4$, $t \geq 0$, and some $\alpha_0 > 0$. Then, $\mathbf{Q}(t)$ is called positive definite.

Lemma 1. An equilibrium, $\mathbf{0}$ of $\Delta\dot{x} = (\mathbf{A}(t) - \mathbf{GC})\Delta x$, is uniformly asymptotically stable, if and only if there exists a positive definite matrix, $\mathbf{P}(t) \in \mathbb{R}^{4\times 4}$ satisfying

$$\dot{\mathbf{P}}(t) = -(\mathbf{A}(t) - \mathbf{GC})^T\mathbf{P}(t) - \mathbf{P}(t)(\mathbf{A}(t) - \mathbf{GC}) - \mathbf{Q}(t)$$

for each bounded positive definite matrix, $\mathbf{Q}(t) \in \mathbb{R}^{4\times 4}$.

Speed Update Law Based on Full-Order Observer

Suppose that ω_r is in a small neighborhood of ω_{r0} and $|\frac{d}{dt}\omega_r|$ is bounded for all $t \geq 0$. Choose a Lyapunov function candidate such that

$$\mathcal{V} = \Delta\mathbf{x}^T\mathbf{P}(t)\Delta\mathbf{x} + \frac{1}{2\gamma}\Delta\omega_r^2 .$$

Then,

$$\dot{\mathcal{V}} = -\Delta\mathbf{x}^T\mathbf{Q}\Delta\mathbf{x} + 2\Delta\omega_r\Delta\mathbf{x}^T\mathbf{P}(t)\begin{bmatrix} \frac{L_m}{\sigma L_r L_s}\mathbf{J} \\ -\mathbf{J} \end{bmatrix}\hat{\boldsymbol{\lambda}}^e_{dqr} - \frac{1}{\gamma}\Delta\omega_r\dot{\hat{\omega}}_r \tag{5.47}$$

To make the right-hand side less than or equal to zero, it should follow that

$$2\Delta\mathbf{x}^T\mathbf{P}(t)\begin{bmatrix} \frac{L_m}{\sigma L_r L_s}\mathbf{J} \\ -\mathbf{J} \end{bmatrix}\hat{\boldsymbol{\lambda}}^e_{dqr} - \frac{1}{\gamma}\dot{\hat{\omega}}_r = 0.$$

That is,

$$\dot{\hat{\omega}}_r = 2\gamma\Delta\mathbf{x}^T\mathbf{P}(t)\begin{bmatrix} \frac{L_m}{\sigma L_r L_s}\mathbf{J} \\ -\mathbf{J} \end{bmatrix}\hat{\boldsymbol{\lambda}}^e_{dqr}. \tag{5.48}$$

Further, assume that there is no error in the rotor flux estimate, i.e., $\hat{\boldsymbol{\lambda}}^e_{dqr} = \boldsymbol{\lambda}^e_{dqr}$. Then, the third and fourth components of $\Delta\mathbf{x}$ are equal to zero. If $\mathbf{P}(t)$ is an identity matrix, (5.48) is simplified as [3]

$$\dot{\hat{\omega}}_r = \gamma'(i^e_{ds}\lambda^e_{qr} - i^e_{qs}\lambda^e_{dr}), \tag{5.49}$$

where $\gamma' > 0$ is a constant.

Remark. The speed update law, (5.48), yields

$$\dot{\mathcal{V}} = -\Delta\mathbf{x}^T\mathbf{Q}\Delta\mathbf{x} \leq 0.$$

Note that $\dot{\mathcal{V}}$ is not negative definite in the augmented space $[\Delta\mathbf{x}^T, \Delta\omega_r]^T \in \mathbb{R}^5$. Therefore, (5.48) does not guarantee asymptotic convergence. For asymptotic convergence, we may need LaSalle's theorem [4].

5.6 PI Controller in the Synchronous Frame

To implement the field-oriented control, coordinates should be changed two times: First, measured current values are transformed from the *abc* to the synchronous *dq*-frame. Then the command voltage vector is computed by the PI controllers, (5.21) and (5.22). Second, the voltage vector should be transformed back into the *abc*-frame to provide the inverter gating signals. Fig. 5.11 shows the current controller involving coordinate transformations. The question here is what the controller looks like if it is seen from the stationary frame. In this section, the PI controller established in the synchronous frame is interpreted from the view of stationary frame [5],[6].

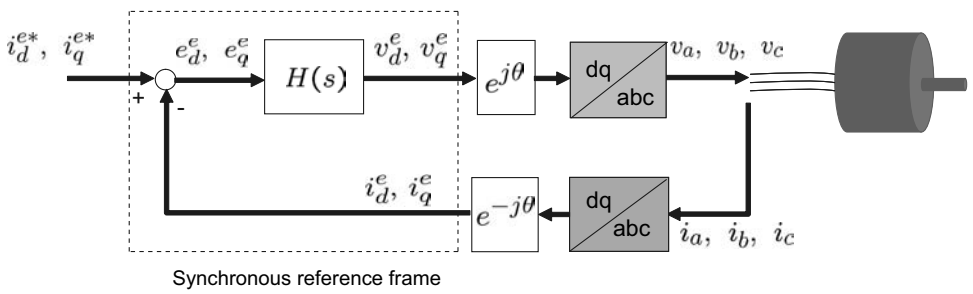

Figure 5.11: Current controller implemented in the synchronous reference.

Consider the transformation of stationary current error e_d^s, e_q^s into the error e_d^e, e_q^e in the synchronous frame:

$$\begin{bmatrix} e_d^e \\ e_q^e \end{bmatrix} = \begin{bmatrix} \cos(\omega t) & \sin(\omega t) \\ -\sin(\omega t) & \cos(\omega t) \end{bmatrix} \begin{bmatrix} e_d^s \\ e_q^s \end{bmatrix} = \begin{bmatrix} \cos(\omega t)e_d^s + \sin(\omega t)e_q^s \\ -\sin(\omega t)e_d^s + \cos(\omega t)e_q^s \end{bmatrix}.$$

The signal passes through a controller whose impulse response is $h(t)$. Then the controller outputs appear as the convolution, $h*$. Further, they are transformed back into the stationary frame:

$$\begin{bmatrix} v_d^s \\ v_q^s \end{bmatrix} = \begin{bmatrix} \cos(\omega t) & -\sin(\omega t) \\ \sin(\omega t) & \cos(\omega t) \end{bmatrix} \begin{bmatrix} h*(\cos(\omega t)e_d^s) + h*(\sin(\omega t)e_q^s) \\ -h*(\sin(\omega t)e_d^s) + h*(\cos(\omega t)e_q^s) \end{bmatrix}$$

$$= \begin{bmatrix} \cos(\omega t)[h * (\cos(\omega t)e_d^s)] + \cos(\omega t)[h * (\sin(\omega t)e_q^s)] \\ \quad + \sin(\omega t)[h * (\sin(\omega t)e_d^s)] - \sin(\omega t)[h * (\cos(\omega t)e_q^s)] \\ \\ \sin(\omega t)[h * (\cos(\omega t)e_d^s)] + \sin(\omega t)[h * (\sin(\omega t)e_q^s)] \\ \quad - \cos(\omega t)[h * (\sin(\omega t)e_d^s)] + \cos(\omega t)[h * (\cos(\omega t)e_q^s)] \end{bmatrix}. \tag{5.50}$$

For convenience of notation, we let

$$\begin{aligned} f_1(t) &= h * (\cos(\omega t)e_d^s), \\ f_2(t) &= h * (\sin(\omega t)e_d^s). \end{aligned}$$

Utilizing the fact that $\cos(\omega t) = (e^{j\omega t} + e^{-j\omega t})/2$ and $\sin(\omega t) = (e^{j\omega t} - e^{-j\omega t})/2j$, and the frequency shifting property of Laplace transformation, we obtain

$$\begin{aligned} F_1(s) &= \mathcal{L}\{h * (\cos(\omega t)e_d^s)\} = H(s) \cdot \frac{1}{2}[E_d^s(s + j\omega) + E_d^s(s - j\omega)] \\ F_2(s) &= \mathcal{L}\{h * (\sin(\omega t)e_d^s)\} = H(s) \cdot \frac{1}{2j}[E_d^s(s + j\omega) - E_d^s(s - j\omega)], \end{aligned}$$

where $H(s) = \mathcal{L}(h)$, $E_d^s(s) = \mathcal{L}(e_d^s)$, and $E_q^s(s) = \mathcal{L}(e_q^s)$. Therefore,

$$\begin{aligned} \mathcal{L}\{\cos(\omega t)[h * (\cos(\omega t)e_d^s)]\} &= \frac{1}{2}[F_1(s + j\omega) + F_1(s - j\omega)] \\ &= \frac{1}{4}[H(s + j\omega)E_d^s(s + j2\omega) + H(s + j\omega)E_d^s(s) \\ &\qquad + H(s - j\omega)E_d^s(s) + H(s - j\omega)E_d^s(s - j2\omega)] \\ \mathcal{L}\{\sin(\omega t)[h * (\sin(\omega t)e_d^s)]\} &= \frac{1}{2j}[F_2(s + j\omega) - F_2(s - j\omega)] \\ &= -\frac{1}{4}[H(s + j\omega)E_d^s(s + j2\omega) - H(s + j\omega)E_d^s(s) \\ &\qquad - H(s - j\omega)E_d^s(s) + H(s - j\omega)E_d^s(s - j2\omega)]. \end{aligned}$$

Then the d–axis part of the first component of (5.50) is equal to

$$\begin{aligned} &\mathcal{L}\{\cos(\omega t)[h * (\cos(\omega t)e_d^s)]\} + \mathcal{L}\{\sin(\omega t)[h * (\sin(\omega t)e_d^s)]\} \\ &\qquad = \frac{1}{2}[H(s + j\omega) + H(s - j\omega)]\, E_d^s(s). \end{aligned}$$

Similarly, it follows for e_q that

$$\begin{aligned} &\mathcal{L}\{\cos(\omega t)[h * (\sin(\omega t)e_d^s)]\} - \mathcal{L}\{\sin(\omega t)[h * (\cos(\omega t)e_d^s)]\} \\ &\qquad = -\frac{1}{2j}[H(s + j\omega) - H(s - j\omega)]\, E_q^s(s). \end{aligned}$$

For the I controller, $H(s) = \frac{K_i}{s}$, therefore, it follows that

$$V_d^s(s) = \mathcal{L}\{v_d^s\}$$

$$
\begin{aligned}
&= \frac{K_i}{2}\left[H(s+j\omega)+H(s-j\omega)\right]E_d^s(s) - \frac{K_i}{2j}\left[H(s+j\omega)-H(s-j\omega)\right]E_q^s(s) \\
&= \frac{K_i}{2}\left[\frac{1}{s+j\omega}+\frac{1}{s-j\omega}\right]E_d^s(s) - \frac{K_i}{2j}\left[\frac{1}{s+j\omega}-\frac{1}{s-j\omega}\right]E_q^s(s) \\
&= \frac{K_i s}{s^2+\omega^2}E_d^s(s) + \frac{K_i\omega}{s^2+\omega^2}E_q^s(s)\,.
\end{aligned}
$$

The I controller in the synchronous frame appears as a resonant controller with the rotating frequency of ω. That is, the I controller in the synchronous frame has infinite gain at DC, whereas the corresponding controller in the stationary frame has infinite gain at the rotating frequency, ω. For the PI controller $H(s) = K_p + K_i/s$, it follows that

$$
\begin{bmatrix} V_d^s(s) \\ V_q^s(s) \end{bmatrix} = \begin{bmatrix} K_p + \dfrac{K_i s}{s^2+\omega^2} & \dfrac{K_i\omega}{s^2+\omega^2} \\ -\dfrac{K_i\omega}{s^2+\omega^2} & K_p + \dfrac{K_i s}{s^2+\omega^2} \end{bmatrix} \begin{bmatrix} E_d^s(s) \\ E_q^s(s) \end{bmatrix}. \tag{5.51}
$$

The resonant controller discriminates the error signal depending on the frequency: It applies infinite gain to the spectral component of ω. That is, the integral controller is highly sensitive to the ones that would appear as constants in the synchronous frame. Fig. 5.12 shows an equivalence. The pioneering work for this transformation is shown in [6].

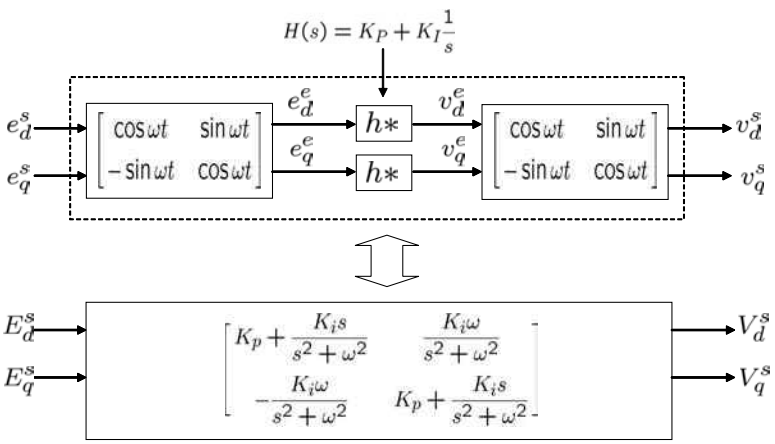

Figure 5.12: Transformation of a PI regulator in the synchronous frame into the stationary frame. Block (a) is equivalent to block (b).

Exercise 5.1
Show that

$$
V_q^s(s) = -\frac{K_i\omega}{s^2+\omega^2}E_d^s(s).
$$

Bibliography

[1] A. M. Trzynadlowski, *The Field Orientaion Principle in Control of Induction Motors*, Kluwer Academic Publishers, Boston 1994.

[2] J. Holtz, Sensorless control of induction machines − With or without signal injection? *IEEE Trans. Ind. Electron.*, Vol. 53, No. 1, pp. 7−30, Feb. 2006.

[3] H. Kubota, K. Matsuse, and T. Nakano, DSP based speed adaptive flux observer of induction motor, *IEEE Trans. Ind. Appl.*, Vol. 29, pp. 344−348, Mar./Apr. 1993.

[4] M. Vidyasagar, *Nonlinear Systems Analysis,* 2nd., Prentice Hall, 1993.

[5] D. N. Zmood, D. G. Holmes, and G. H. Bode, Frequency-domain analysis of three-phase linear current regulators, *IEEE Trans. Ind. Appl.*, vol. 37, no. 2, pp. 601−609. Mar./Apr. 2001.

[6] D.N. Zmood and D. G. Holmes, Frequency domain analysis of three-phase linear current regulators, *IEEE Trans. on Power Elec.*, vol. 18, no. 3, pp. 814−822, May 2003.

Problems

5.1 Consider an IM with the parameters

Rated power	10 hp (7.46 kW)
Rated stator voltage	220V
Rated frequency	60 Hz
Rated speed	1160rpm
Number of poles	$P = 6$
Stator resistance, r_s	0.33 Ω
Stator leakage inductance, L_{ls}	1.38 mH
Rotor resistance r_r	0.16 Ω
Rotor leakage inductance, L_{lr}	0.717 mH
Magnetizing inductance, L_m	38 mH

a) Determine the rated current if PF is 0.86 and efficiency is 0.84 at the rated condition.

b) Assume that the motor is in the steady-state with the above conditions. Suppose that the d–axis current is regulated to be $I^e_{ds} = 10$A. Calculate I_{qs} at the rated condition.

c) Calculate I_{qr} and λ_{dr}, and draw a current vector diagram.

d) Using the dq currents obtained in b), calculate the slip, s at $\omega_e = 377$rad/sec when the motor is controlled with the rotor field-oriented scheme.

e) Calculate the rated torque.

5.2 An IM is controlled with the rotor field-oriented scheme. Rotor resistance varies along with the rotor temperature, thereby rotor time constant changes. Let τ_{rn} be the nominal rotor time constant used for the field-oriented control, and let τ_r be the real rotor time constant. Assume that rotor flux, λ^e_{dr}, is the same for both cases, and denote by $\bar{i}^e_{ds}$, $\bar{i}^e_{qs}$ the stator currents in the $e^{j\bar{\theta}_e}$ frame, where $\bar{\theta}_e$ is the angle calculated based on τ_{rn}.

a) Using the slip equation, determine angle error, $\Delta\theta_e \equiv \bar{\theta}_e - \theta_e$.

b) Show that

$$\Delta \mathbf{i}^e_{dqs} \equiv \bar{\mathbf{i}}^e_{dqs} - \mathbf{i}^e_{dqs} \approx j\Delta\theta \mathbf{i}^e_{dqs}.$$

c) If $\tau_r < \tau_{rn}$, the real slip is larger than the estimated value based on τ_{rn}. Correspondingly, larger torque will be produced. Similarly if $\tau_r > \tau_{rn}$, smaller torque will be produced. Discuss the stabilizing action of the field-oriented control using the result obtained in b).

5.3 Show that

$$\boldsymbol{\lambda}^e_r = \frac{L_r}{L_m}(\lambda^e_{ds} - \sigma L_s \mathbf{i}^e_{ds}).$$

5.4 Consider equations, (5.27) and (5.28) for the stator field-oriented scheme.

a) Setting $p = 0$ and eliminating i^e_{ds}, obtain a quadratic equation in ω_{sl}.

b) Obtain a relation so that the discriminant is not negative.

c) Using $T_e = (3P/4)\lambda_{ds}^e i_{qs}^e$, calculate the upper bound of $|T_e|/|\boldsymbol{\lambda}_s|^2$.

5.5 Consider the IM in Problem **5.1**. Assume that $I_{max} = 23.3$A(rms). Calculate the maximum torque at $\omega_e = 377$rad/sec by utilizing (5.29), (5.34), and (5.35).

5.6 Derive (5.47) and (5.49).

Chapter 6

Permanent Magnet AC Motors

Permanent magnets (PMs) eliminate the use of field exciting coils and slip rings for current conduction. Due to the absence of field winding inside the rotor, PM motors have low inertia. The field strength is so high the motor volume can be reduced. Further, since there is no copper loss of the secondary winding, the PM motors have higher efficiency than induction motors. Also, permanent magnet synchronous motors (PMSMs) are advantageous in incorporating the reluctance torque in the field-weakening range, so that they can be designed to have a wide constant power speed range (CPSR). As a result, PMSMs have higher power densities than any other types of motors.

As the greenhouse effect becomes a serious concern, the efficiency of home appliances becomes more important than ever. Due to recent reduction in PM material cost and growing concern for greenhouse gases, PMSMs are widely used in home appliances such as refrigerators, air conditioners, vacuum cleaners, washers, etc. Also, hydraulic actuators in vehicles and airplanes are being replaced by PMSMs for higher fuel efficiency. Furthermore, PMSMs are popularly used as propulsion motors for hybrid electric vehicles and ships.

6.1 PMSM and BLDC Motor

Three-phase AC motors are simply described as a three-phase circuit consisting of inductors and EMF's as shown in Fig. 6.2. In the equivalent circuit, the motor terminal voltages (source voltages) are denoted by v_a, v_b, and v_c, and the back EMFs by e_a, e_b, and e_c.

PM motors can be broadly classified into two categories according to the patterns of back EMFs. One category is characterized by sinusoidal back EMF, and the other category by trapezoidal or square back EMF. The former is called *PMAC motor* or PMSM, and the latter *brushless DC motor* (BLDC motor). The back EMF patterns are shaped depending on the magnet and cavity arrangements and the coil winding structures. In the following section, it will be shown how constant

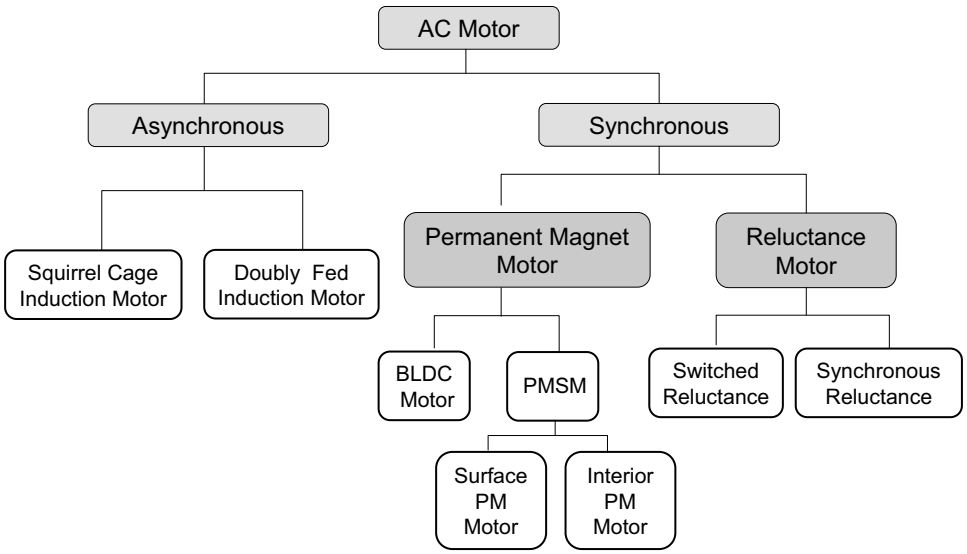

Figure 6.1: Taxonomy of AC motors.

torque is developed with AC sources.

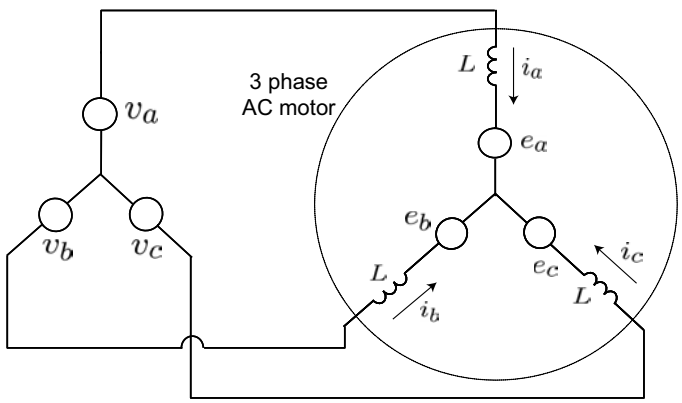

Figure 6.2: Simplified equivalent circuit of three-phase motors.

6.1.1 PMSM Torque Generation

The patterns of back EMF and current waveform can be easily understood in the light of the torque to current relationship. However, both PMSM and BLDC motors have the same design goal, which is to establish a linear relationship between torque and the phase current magnitude, independently of rotor angle. Fig. 6.3 shows how a constant power is made from a PMSM. The PMSM phase windings have balanced three-phase sinusoidal patterns: $[e_a, e_b, e_c] = [E\cos(\omega_e t), E\cos(\omega_e t - \frac{2\pi}{3}), E\cos(\omega_e t - \frac{4\pi}{3})]$. Assume that an external three-phase power source pro-

vides balanced three-phase sinusoidal currents: $[i_a,\, i_b,\, i_c] = [I\cos(\omega_e t),\ I\cos(\omega_e t - \frac{2\pi}{3}),\ I\cos(\omega_e t - \frac{4\pi}{3})]$. Then, the total electrical power is equal to

$$\begin{aligned} P_{tot} &= e_a i_a + e_b i_b + e_c i_c \\ &= EI[\cos^2(\omega_e t) + \cos^2(\omega_e t - \frac{2\pi}{3}) + \cos^2(\omega_e t - \frac{4\pi}{3})] \\ &= \frac{EI}{2}[1 + \cos 2(\omega_e t) + 1 + \cos 2(\omega_e t - \frac{2\pi}{3}) + 1 + \cos 2(\omega_e t - \frac{4\pi}{3})] \\ &= \frac{3EI}{2}. \end{aligned}$$

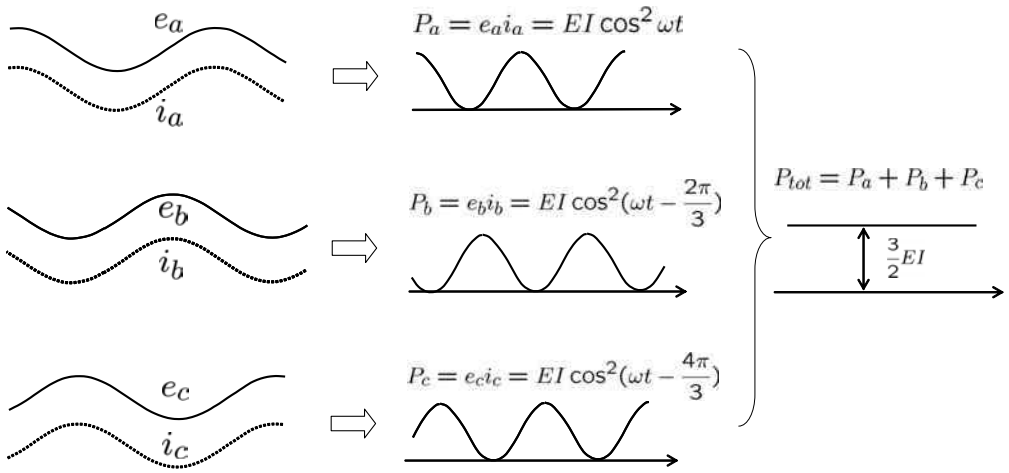

Figure 6.3: Constant power generated from three-phase sinusoidal currents and sinusoidal back EMFs.

The motor converts the electrical power, $P_{tot} = e_a i_a + e_b i_b + e_c i_c$ into the mechanical power. Thus, the shaft torque is given by dividing the power by mechanical speed:

$$T_e = \frac{P_{tot}}{\omega_r} = \frac{3EI}{2\omega_r}\,. \tag{6.1}$$

Further, since the back EMF is proportional to the rotor speed, we may let $E = k_b\omega_r$ for some constant, $k_b > 0$. Therefore, it follows from (6.1) that

$$T_e = \frac{3k_b}{2} I\,. \tag{6.2}$$

Note that the torque is proportional to only the current, like in a DC motor.

Exercise 6.1
Consider a PMSM which has the following back EMFs: $[e_a,\, e_b,\, e_c] = [E\cos(\omega_e t),$

$E\cos(\omega_e t - \frac{2\pi}{3})$, $E\cos(\omega_e t - \frac{4\pi}{3})$]. Assume that an external power source supplies balanced three-phase sinusoidal currents: $[i_a, i_b, i_c] = [I\cos(\omega_e t - \phi),\ I\cos(\omega_e t - \frac{2\pi}{3} - \phi),\ I\cos(\omega_e t - \frac{4\pi}{3} - \phi)]$. Determine the total electrical power and torque when the rotor speed is ω_r.

Solution
Electrical power is

$$P_{tot} = e_a i_a + e_b i_b + e_c i_c = \frac{3EI}{2}\cos\phi.$$

Thus torque is equal to $T_e = \frac{3EI}{2\omega_r}\cos\phi = \frac{3k_b}{2} I\cos\phi$. ■

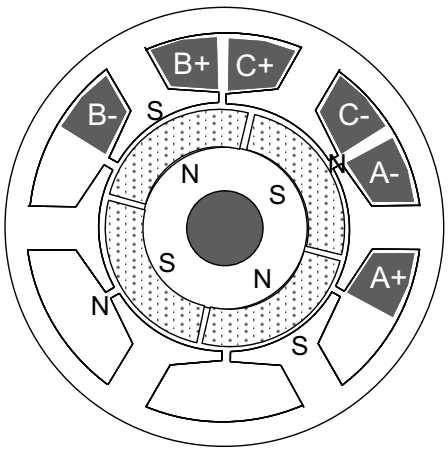

Figure 6.4: Four pole BLDC motors with 120° coil span and PMs covering 180° pole arc in electrical angle.

6.1.2 BLDC Motor Torque Generation

Fig. 6.4 shows a schematic diagram of a typical BLDC motor with 120° coil span and PMs covering 180° pole arc in electrical angle. Therefore, the back EMF exhibits a trapezoidal waveform with 120° flat top (bottom) regions. Suppose that an external power source provides a constant phase current when the corresponding back EMF maintains constant peak values over 120° periods. Further, assume that the phase current is zero elsewhere, i.e., the current is regulated to be zero during the back EMF transition. Each phase produces a square shaped periodic power which conducts for 120° per a half period. Since each phase is shifted by 120°, the sum of phase powers turns out to be constant. At each instant, one phase power is equal to zero, while the other two are EI. Hence, the torque will be proportional to the current:

$$T_e = \frac{P_{tot}}{\omega_r} = \frac{2EI}{\omega_r} = 2k_b I.$$

Fig. 6.5 shows how a constant power is made from a BLDC motor.

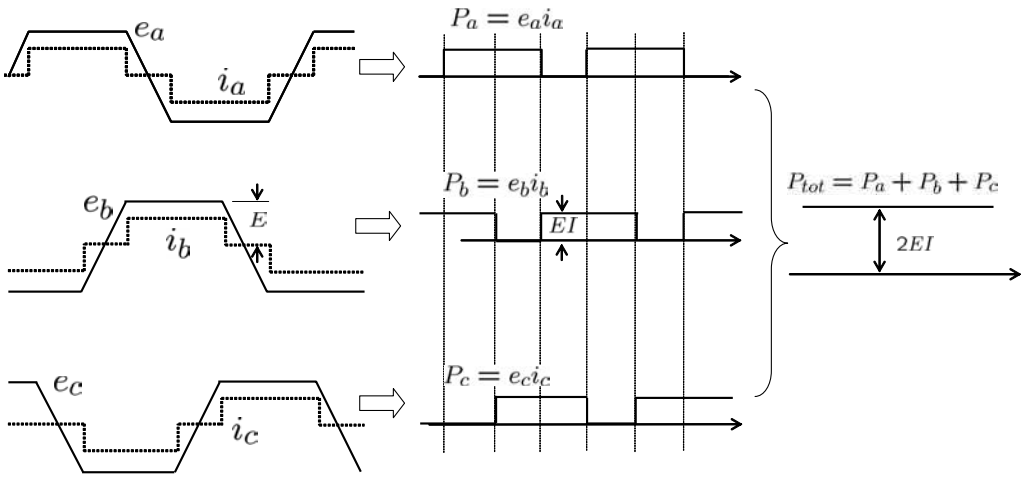

Figure 6.5: Three-phase trapezoidal back EMFs and square wave currents making a constant power.

Hall Sensors and Inverter for BLDC Motors

Fig. 6.6 shows the location of three Hall sensors in a 4-pole, 6-slot BLDC motor, and the Hall sensor signals along with phase currents. BLDC motors employ three Hall sensors, and they are displaced by 60° (120° in electrical angle). The Hall sensors are discrete type and each Hall sensor detects the radial field of PMs. As the rotor rotates 180°, three Hall sensors provide six sets of signals: (Hall A, Hall B, Hall C)=(1,1,0), (1,0,0), (1,0,1), (0,0,1), (0,1,1), and (0,1,0). Fig. 6.6 shows instances when the sensor signal transition occurs. Note for example that Hall sensor "A" detects the edge of the north pole of a PM at an instant when the phase "A" winding starts to experience constant rotor flux linkage. That is, the signal transition occurs when the back EMF starts to change from the peak values.

Exercise 6.2
Discuss why e_a is low and e_c is high in the interval of (Hall A, Hall B, Hall C)=(110).

Each set of Hall signals indicates one of six sector positions, based on which the gating signals are generated. An inverter circuit and PWM signals for a BLDC motor are shown in Fig. 6.7. The voltage level is determined by the on-duty interval of the PWM.

Torque Ripple of BLDC Motors

Normally torque ripple of BLDC motors is about $4 \sim 5\%$ in a low-speed region, while it is less than 1% in PMSMs. However, the torque ripple problem of BLDC motor

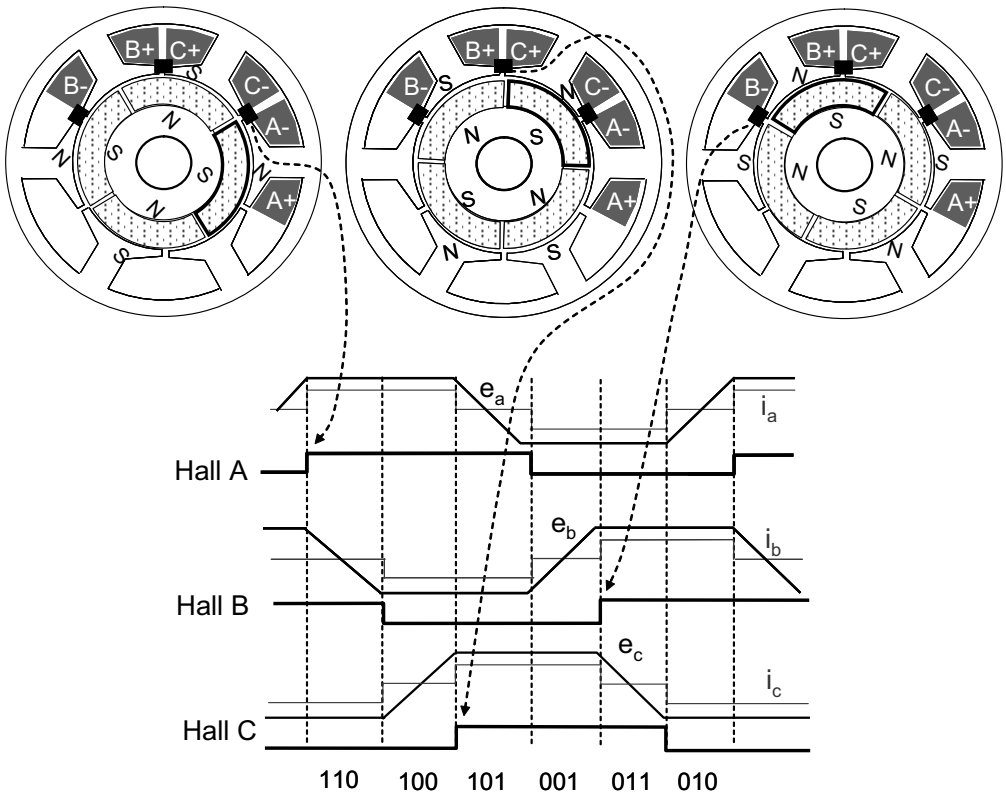

Figure 6.6: Three Hall sensor signals of a 4-pole, 6-slot BLDC motor.

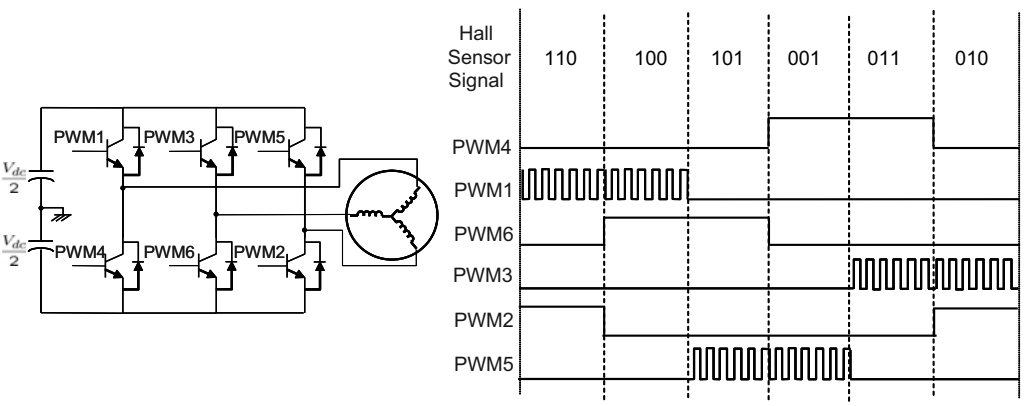

Figure 6.7: Inverter and PWM gating signals for the BLDC motor.

becomes serious as the speed increases. It is because the current cannot change sharply as shown in Fig. 6.5.

The presence of inductance limits the rate of current rise. It takes time to reach a set value I, since the current increases with a certain slope. Based on the motor model shown in Fig. 6.2, the rate of current change (for example, a-phase) is

determined by

$$\left|\frac{di_a}{dt}\right| = \frac{|\frac{V_{dc}}{2} - k_e\omega_r|}{L} \tag{6.3}$$

where k_e is the back EMF constant and V_{dc} is the inverter DC link voltage. In the low-speed region, $V_{dc}/2 \gg k_e\omega_r$ so that $|\frac{di_a}{dt}|$ is high during current change. But in the high-speed region, $V_{dc}/2 \approx k_e\omega_r$ so that $|\frac{di_a}{dt}|$ is low.

Fig. 6.8 shows schematic drawings illustrating how torque ripple is generated: The speed of column (b) is about two times higher than that of column (a). The current slope decreases as the speed (back EMF) increases. Therefore, the power profile of each phase looks more trapezoidal in the high-speed region, and their sum, $P_{tot} = e_a i_a + e_b i_b + e_c i_c$, is no more constant. It has dents which deepen as the speed increases. Fig. 6.8 (a-3) and (b-3) show the torque profiles obtained by $T_e = P_{tot}/\omega_r$. Note that the torque ripples (dents) are larger at a higher speed and that the ripples constitute 6^{th}-order harmonics. Distortion in the back EMF shape or Hall sensor position error also creates torque ripple.

6.1.3 Comparision between PMSM and BLDC Motor

PMSMs are better in speed and position accuracies than BLDC motors. Also, PMSMs do not create torque ripple like BLDC motors. But the merits of BLDC motors lie in simplicity and costwise competitiveness. BLDC motors are normally used for low cost, low power (less than 5kW) applications such as blowers, material handling equipments, home appliances, etc.. Comparisions between BLDC motors and PMSMs are listed in Table 6.1.

Table 6.1: Comparisions Between BLDC motors and PMSMs

	BLDCM	PMSM
Back EMF	Trapezoidal	Sinusoidal
Phase current	Square	Sinusoidal
Torque ripple	high	low
Position sensor	Hall sensors (inexpensive)	resolver (expensive)
Stator winding	concentrated (less copper)	distributed (more copper)
PM usage	large	relatively small
Eddy loss in PMs	large	relatively small
Control complexity	simple	complicated
Speed range	narrow	wide
Inverter price	low	high

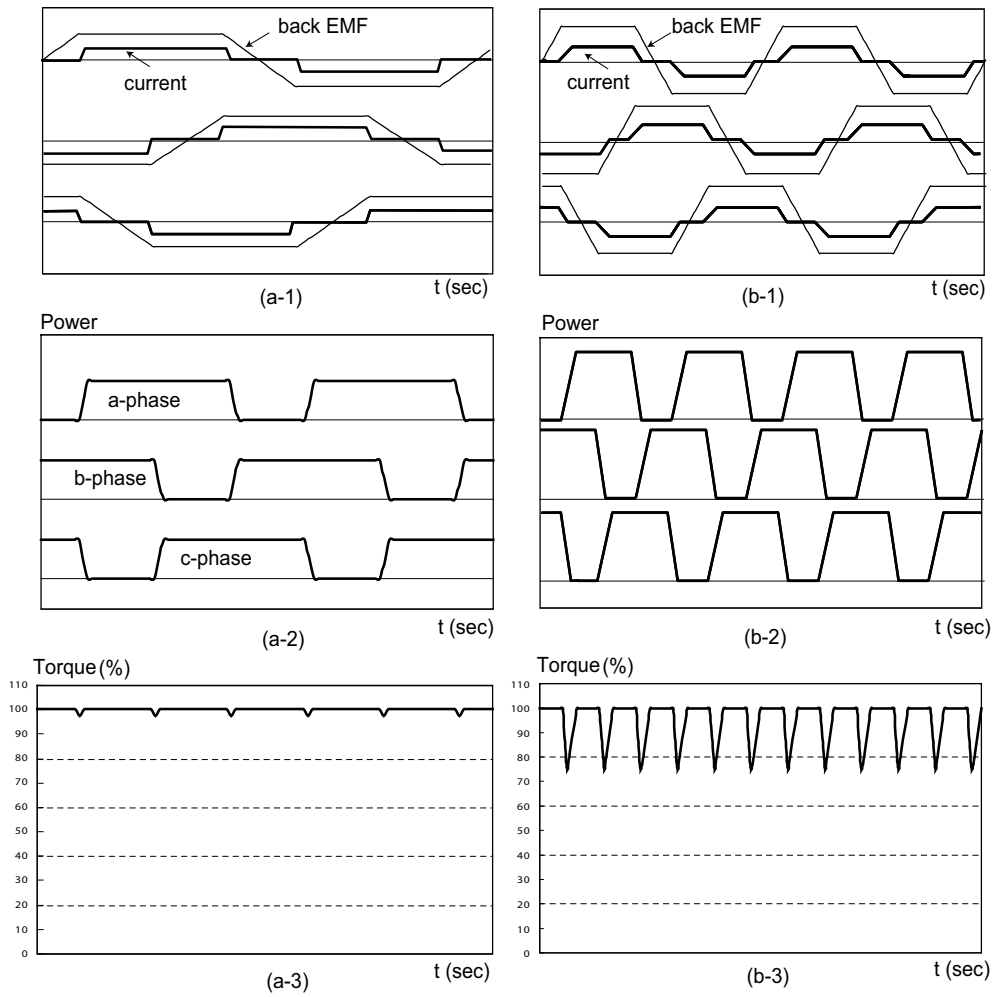

Figure 6.8: Torque ripples of a BLDC motor due to reduced $\frac{di}{dt}$ at (a) low and (b) high speeds: (a-1), (b-1) back EMFs and phase currents; (a-2), (b-2) power of each phase; (a-3), (b-3) shaft torque.

6.1.4 Types of PMSMs

Fig. 6.9 shows cross-sectional views of four pole surface mounted PMSMs and interior PMSMs. The difference is the location of PMs, which are marked by dark areas. If PMs are mounted on the surface of the rotor (Fig. 6.9(a), (b)), it is called surface mounted PMSM, in short SPMSM. If PMs are buried in the cavities of the rotor core (Fig. 6.9(c), (d)), they are called interior PMSM, in short IPMSM. In Fig. 6.9 (b), PMs are inserted on the groove of the rotor surface, which is called an inset magnet motor. The inset magnet motor, though the magnets are on the surface, has different reluctances like IPMSMs. Specifically, the q–axis inductance is larger than the d–axis inductance. With the flux-concentrating arrangement (Fig. 6.9(d)), the air gap

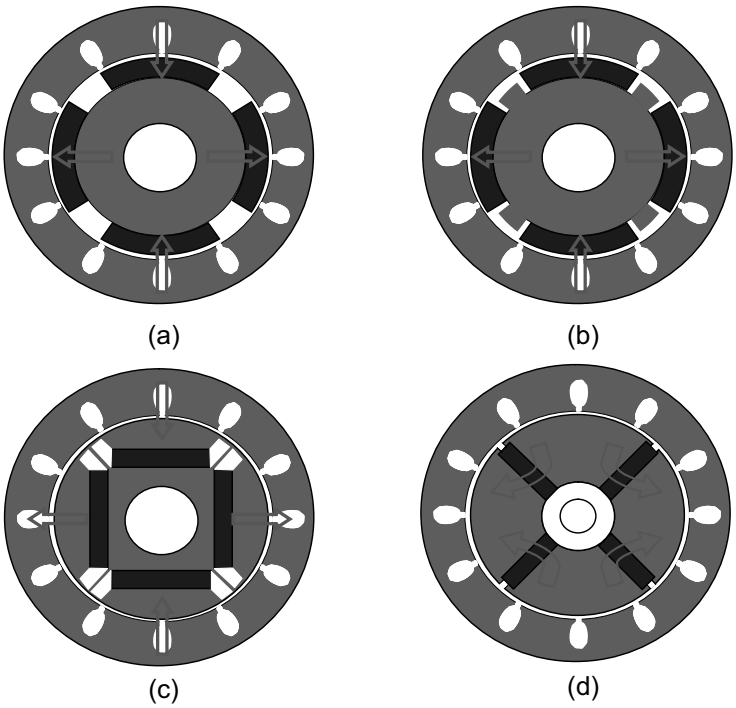

Figure 6.9: Typical PMSM structures: (a) surface magnet, (b) inset magnet, (c) interior magnet, (d) interior magnet (flux-concentration).

field density can be increased higher than that at the surface of PMs. For example, it is possible to achieve 0.8T air gap field density with 0.4T ferrite magnets if a flux-concentration arrangement is utilized. It is important to note that none ferrormagnet material (e.g. stainless steel) needs to be used at the shaft area to penalize flux flow through the center part.

A common problem in SPMSM lies in the methods of fixing PMs on the rotor surface. Glues are widely used, but they have aging effects under the stress of heat cycles and large centrifugal force. If stainless band is used for fixing and protecting PMs, then loss will take place on the surface of the stainless steel due to the eddy current caused by slot harmonics and the inverter PWM carrier. Further, the protecting devices like glass fiber or stainless steel require a larger air gap. In IPMSMs, no fixation device is required since PMs are inserted in the cavities. Further, PMs are protected from stator MMF harmonics and slot harmonics, allowing for use of cost-effective rectangular shaped magnets. Differences between SPMSM and IPMSM are listed in Table 6.2.

Table 6.2: Comparisions between SPMSM and IPMSM

	SPMSM	IPMSM
PM location	surface	cavities
PM fixation	glue or band	insertion
Field harmonics on PM	large	small
PM usage	large	relatively small
Saliency ratio	1	> 1
Reluctance torque usage	no	yes
Power density	low	high
Speed range (Field-weakening)	small	large

6.2 PMSM Dynamic Modeling

Note that the relative recoil permeabilities are ferrite: $1.05 \sim 1.15$, Nd-Fe-B : $1.04 \sim 1.11$, and Sm-Co : $1.02 \sim 1.07$ [2]. That is, the permeabilities are close to one although they can retain high residual field density. From the magnetic reluctance view point, they can be treated the same as a vacuum. Since the permeability of widely used PMs are close to unity, PMs look like air in the view of magnetic reluctance. Therefore, the reluctance profile changes whether the PMs are set on the rotor surface or in the cavities of the rotor. The reluctance variation is reflected in the L_d and L_q difference.

SPMSM Inductance

Consider a SPMSM shown in Fig. 6.10. The two diagrams represent the same motor, but with two different flux paths corresponding to the d and q phase windings. The PMs are denoted by dark arcs. The lines shown in Fig. 6.10 (a) denote d–axis flux corresponding to the d–axis current. Note that the d–axis windings are positioned along the q–axis.

Applying Ampere's law to the d–axis current and integrating along the designated loop in Fig. 6.10 (a), it follows that

$$\frac{B}{\mu_{PM}} 2h_m + \frac{B}{\mu_0} 2g + \frac{B}{\mu_{Fe}} \ell_{core} = N i_d, \tag{6.4}$$

where μ_{PM} is the permeability of the PM and ℓ_{core} is the total length of flux paths in the steel core. However, $\mu_{Fe} = 4000\mu_0$ in the case of electrical steel. Therefore, $\frac{B}{\mu_{Fe}} \ell_{core}$ is relatively small, thereby often neglected. Since $\mu_{PM} \approx \mu_0$, we obtain

$$B = \frac{\mu_0 N}{2(g + h_m)} i_d \tag{6.5}$$

Further, let A be the air gap area through which the flux crosses. In this case,

$A \approx \frac{1}{2}\pi D_r l_{st}$, where D_r and l_{st} are the diameter and stacked length of the rotor, respectively.

Note that $N\Phi = NB \times A = L_d i_d$, where N is the number of turns of the d–axis winding. Then, the d–axis inductance is

$$L_d = \frac{\mu_0 N^2 A}{2(g + h_m)} \tag{6.6}$$

The loops shown in Fig. 6.10 (b) describe the q–axis flux. Note that the flux does not pass through PMs. Applying Ampere's law, we obtain $L_q = \frac{\mu_0 N^2 A}{2(g+h_m)}$ which is the same as L_d, i.e., $L_d = L_q$.

The presence of PMs does not affect the reluctance of the flux loops. In other words, the effective air gap is uniform along the rotor circumference in SPMSMs. Therefore, $L_d = L_q$.

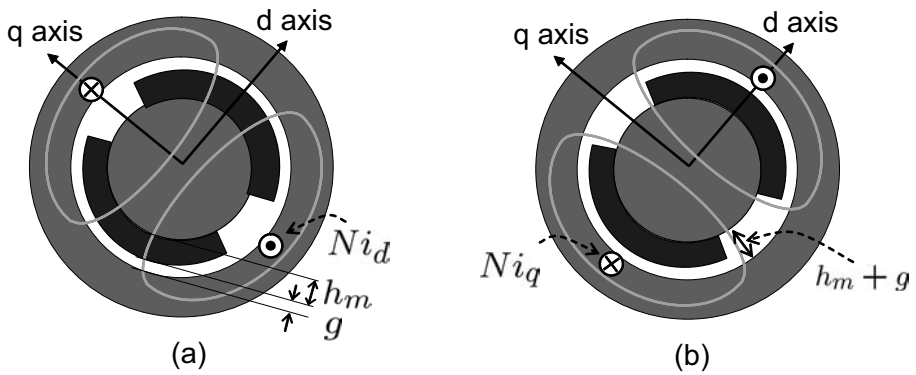

Figure 6.10: Flux paths of SPMSM: (a) d–axis flux path, (b) q–axis flux path: ($L_d = L_q$).

IPMSM Inductance

The reluctances are different depending on the flux paths in IPMSMs. According to Fig. 6.11 (a) and (b), PMs are encountered following the d–axis flux, whereas no PM is found along the q–axis flux. Hence, the d–axis reluctance is greater than that of the q–axis, i.e., the d–axis inductance is smaller than that of the q–axis. Specifically, we obtain

$$L_d = \frac{\mu_0 N^2 A}{2(g + h_m),} \tag{6.7}$$

$$L_q = \frac{\mu_0 N^2 A}{2g}. \tag{6.8}$$

Thus, $L_d < L_q$ for this type of IPMSM. This inductance asymmetry generates the reluctance torque, and the reluctance torque contributes to increasing the shaft torque with negative d–axis current. One can make an IPMSM with $L_d > L_q$, but it is rarely used.

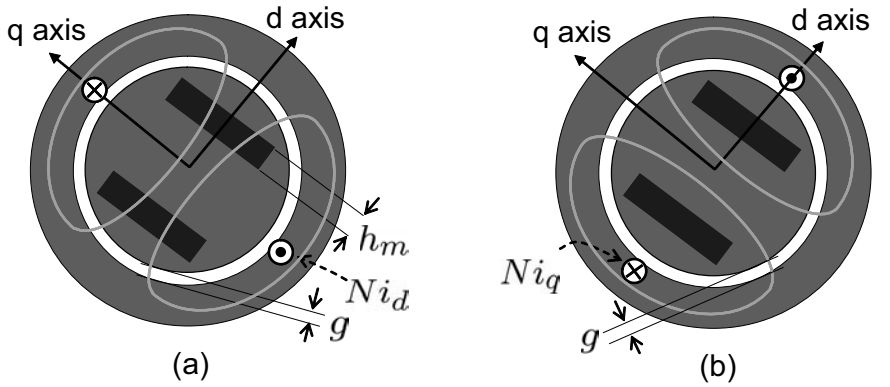

Figure 6.11: Flux paths of IPMSM: (a) d–axis flux path, (b) q–axis flux path: $(L_d < L_q)$.

6.2.1 SPMSM Voltage Equations

The dynamics in the *abc*-frame is used sometimes for computer simulation. The SPMSM voltage equation is described in *abc*-frame firstly, and then description in the *dq*-frame follows. In the synchronous motor, $\theta_e = \frac{P}{2}\theta_r$ and $\omega_e = \frac{P}{2}\omega_r$. Firstly, the theory will be developed for two-pole motors ($P = 2$). Thus, θ and ω are used without subscripts, or θ_e and ω_e are used for general case (high pole machines).

SPMSM Dynamics in the abc Frame

The first thing in deriving the dynamic model is to obtain the flux linkage of the stator winding. Two elements contribute to forming the flux linkage: the stator current and rotor flux. Note, however, that the contribution of rotor flux to a phase winding varies as the rotor rotates, i.e., the flux linkage is a function of θ. Fig. 6.12 shows how the rotor flux links to a-phase winding: Since the rotor flux linking is maximum at $\theta = 0$, (b) and zero at $\theta = \pi/2$, (c). Therefore, the fundamental components are described by cosine functions. The stator flux linkage of SPMSM is described as

$$\begin{bmatrix}\lambda_a\\ \lambda_b\\ \lambda_c\end{bmatrix} = \underbrace{\begin{bmatrix} L_{ms}+L_{ls} & -\frac{1}{2}L_{ms} & -\frac{1}{2}L_{ms}\\ -\frac{1}{2}L_{ms} & L_{ms}+L_{ls} & -\frac{1}{2}L_{ms}\\ -\frac{1}{2}L_{ms} & -\frac{1}{2}L_{ms} & L_{ms}+L_{ls}\end{bmatrix}}_{=\mathbf{L}_{abcs}} \begin{bmatrix} i_a\\ i_b\\ i_c\end{bmatrix} + \psi_m \begin{bmatrix}\cos\theta\\ \cos(\theta-2\pi/3)\\ \cos(\theta+2\pi/3)\end{bmatrix}. \quad (6.9)$$

Recall that SPMSMs are considered to have a uniform air gap from the view of the magnetic circuit of the stator windings, since the permeability of PMs is close to one. As a result, we have $\mathbf{L}_{abcs}$ which is constant independently of the rotor position.

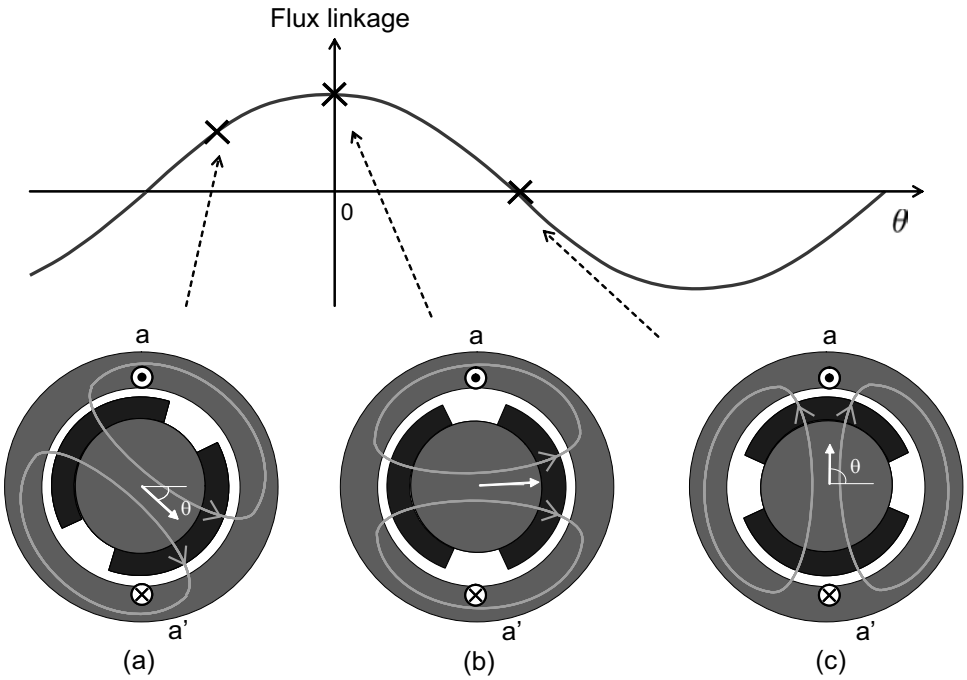

Figure 6.12: Change of rotor flux linkage to a-phase winding as the rotor rotates.

The voltage equation is given by

$$\begin{aligned}\mathbf{v}_{abc} &= r_s\mathbf{i}_{abc} + \frac{d}{dt}\boldsymbol{\lambda}_{abc} \\ &= r_s\mathbf{i}_{abc} + \mathbf{L}_{abcs}\frac{d}{dt}\mathbf{i}_{abc} - \omega\psi_m \begin{bmatrix}\sin\theta \\ \sin(\theta - 2\pi/3) \\ \sin(\theta + 2\pi/3)\end{bmatrix}. \end{aligned} \tag{6.10}$$

In the form of ordinary differential equation,

$$\frac{d}{dt}\mathbf{i}_{abc} = -r_s\mathbf{L}_{abcs}^{-1}\mathbf{i}_{abc} + \omega\psi_m\mathbf{L}_{abcs}^{-1}\begin{bmatrix}\sin\theta \\ \sin(\theta - 2\pi/3) \\ \sin(\theta + 2\pi/3)\end{bmatrix} + \mathbf{L}_{abcs}^{-1}\mathbf{v}_{abc}\,, \tag{6.11}$$

where

$$\mathbf{L}_{abcs}^{-1} = \frac{2}{L_{ms}((2+\gamma)^3 - 3(2+\gamma) - 2)}\begin{bmatrix}(2+\gamma)^2 - 1 & 3+\gamma & 3+\gamma \\ 3+\gamma & (2+\gamma)^2 - 1 & 3+\gamma \\ 3+\gamma & 3+\gamma & (2+\gamma)^2 - 1\end{bmatrix}.$$

and $\gamma = 2L_{lk}/L_{ms}$. A schematic description is shown in Fig. 6.13.

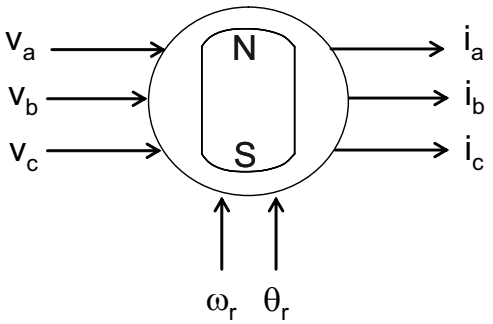

Figure 6.13: A MATLAB® simulation model for a SPMSM in the (a, b, c) frame.

SPMSM Dynamics in the Stationary d – q Frame

Using the transformation map $f^s_{dq} = \frac{2}{3}\left[f_a(t) + e^{j\frac{2\pi}{3}} f_b(t) + e^{-j\frac{2\pi}{3}} f_c(t)\right]$, $\mathbf{L}_{abcs}\mathbf{i}_{abc}$ of (6.9) yields $L_s\mathbf{i}^s_{dq}$, as was shown in (4.5). Here, the second part of (6.9) is transformed as follows:

$$\begin{aligned}
& \frac{2}{3}\psi_m\left[\cos\theta + e^{j\frac{2\pi}{3}}\cos(\theta - \frac{2\pi}{3}) + e^{-j\frac{2\pi}{3}}\cos(\theta + \frac{2\pi}{3})\right] \\
= \; & \frac{2}{3}\frac{1}{2}\psi_m\left[e^{j\theta} + e^{-j\theta} + (e^{j(\theta-\frac{2}{3}\pi)} + e^{-j(\theta-\frac{2}{3}\pi)})e^{j\frac{2\pi}{3}}\right. \\
& \qquad \left. + (e^{j(\theta+\frac{2}{3}\pi)} + e^{-j(\theta+\frac{2}{3}\pi)})e^{-j\frac{2\pi}{3}}\right] \\
= \; & \frac{2}{3}\frac{1}{2}\psi_m\left[e^{j\theta} + e^{-j\theta} + e^{j\theta} + e^{j(\theta-\frac{4}{3}\pi)} + e^{j\theta} + e^{j(\theta+\frac{4}{3}\pi)}\right] \\
= \; & \frac{2}{3}\frac{1}{2}\psi_m 3e^{j\theta} = \psi_m e^{j\theta}.
\end{aligned}$$

That is, the rotor flux vector appears as a complex vector with magnitude ψ_m and angle θ. As the angle increases, the flux vector rotates with the center at the origin. Hence, the flux linkage in the stationary dq-frame is given by

$$\boldsymbol{\lambda}^s_{dq} = L_s\mathbf{i}^s_{dq} + \psi_m e^{j\theta}, \tag{6.12}$$

$$\text{or} \quad \begin{bmatrix}\lambda^s_d \\ \lambda^s_q\end{bmatrix} = L_s\begin{bmatrix}i^s_d \\ i^s_q\end{bmatrix} + \psi_m\begin{bmatrix}\cos\theta \\ \sin\theta\end{bmatrix}, \tag{6.13}$$

where $L_s = \frac{3}{2}L_{ms} + L_{ls}$.

Then the SPMSM dynamics in the stationary dq-frame are given as follows:

$$\mathbf{v}^s_{dq} = r_s\mathbf{i}^s_{dq} + L_s\frac{d}{dt}\mathbf{i}^s_{dq} + j\omega\psi_m e^{j\theta}, \tag{6.14}$$

Or, we have in the matrix form

$$\frac{d}{dt}\begin{bmatrix}i^s_d \\ i^s_q\end{bmatrix} = -\frac{r_s}{L_s}\begin{bmatrix}i^s_d \\ i^s_q\end{bmatrix} - \frac{\psi_m\omega}{L_s}\begin{bmatrix}-\sin\theta \\ \cos\theta\end{bmatrix} + \frac{1}{L_s}\begin{bmatrix}v^s_d \\ v^s_q\end{bmatrix}. \tag{6.15}$$

SPMSM Dynamics in the Synchronous Reference Frame

We consider transforming $\boldsymbol{\lambda}^s_{dq}$ into the one in a synchronous frame via multiplication by $e^{-j\theta}$, i.e., $\boldsymbol{\lambda}^e_{dq} = e^{-j\theta}\boldsymbol{\lambda}^s_{dq}$. That is, the dynamics will be described in the coordinates which are aligned with the physical rotor and rotates at the rotor speed, ω. It follows from (6.12) that

$$\begin{aligned} \boldsymbol{\lambda}^e_{dq} &= L_s \mathbf{i}^e_{dq} + \psi_m \\ \text{or} \qquad \begin{bmatrix} \lambda^e_d \\ \lambda^e_q \end{bmatrix} &= L_s \begin{bmatrix} i^e_d \\ i^e_q \end{bmatrix} + \psi_m \begin{bmatrix} 1 \\ 0 \end{bmatrix}. \end{aligned} \tag{6.16}$$

Now, we embark on the voltage equation in the synchronous frame. The procedure of transforming the voltage equation from the stationary into the synchronous frame is given as follows:

$$\begin{aligned} e^{-j\theta}\mathbf{v}^s_{dq} &= r_s e^{-j\theta}\mathbf{i}^s_{dq} + e^{-j\theta} p e^{j\theta} e^{-j\theta}\boldsymbol{\lambda}^s_{dq} \\ \mathbf{v}^e_{dq} &= r_s \mathbf{i}^e_{dq} + e^{-j\theta} p(e^{j\theta}\boldsymbol{\lambda}^e_{dq}) \\ &= r_s \mathbf{i}^e_{dq} + e^{-j\theta} j\omega e^{j\theta}\boldsymbol{\lambda}^e_{dq} + e^{-j\theta} e^{j\theta} p\boldsymbol{\lambda}^e_{dq} \\ &= r_s \mathbf{i}^e_{dq} + j\omega\boldsymbol{\lambda}^e_{dq} + p\boldsymbol{\lambda}^e_{dq} \\ &= r_s \mathbf{i}^e_{dq} + L_s \frac{d}{dt}\mathbf{i}^e_{dq} + j\omega L_s \mathbf{i}^e_{dq} + j\omega\psi_m. \end{aligned} \tag{6.17}$$

Then, we obtain from (6.17) voltage equation for SPMSM

$$v^e_d = r_s i^e_d + L_s \frac{d}{dt} i^e_d - \omega L_s i^e_q \tag{6.18}$$

$$v^e_q = r_s i^e_q + L_s \frac{d}{dt} i^e_q + \omega L_s i^e_d + \omega\psi_m. \tag{6.19}$$

Note again that $\omega\psi_m$ is the back EMF which depends only on speed, and $\omega L_s i^e_d$ and $-\omega L_s i^e_q$ are the coupling terms which are induced while transforming into the rotating frame. In the normal differential equation form, (6.18) and (6.19) are written equivalently as [1]

$$\frac{d}{dt}\begin{bmatrix} i^e_d \\ i^e_q \end{bmatrix} = \begin{bmatrix} \frac{-r_s}{L_s} & \omega \\ -\omega & -\frac{r_s}{L_s} \end{bmatrix} \begin{bmatrix} i^e_d \\ i^e_q \end{bmatrix} - \frac{\psi_m \omega}{L_s}\begin{bmatrix} 0 \\ 1 \end{bmatrix} + \frac{1}{L_s}\begin{bmatrix} v^e_d \\ v^e_q \end{bmatrix}. \tag{6.20}$$

6.2.2 IPMSM Dynamic Model

In IPMSM, the inductance changes depending on the rotor position. The flux linkage change is described by a sinusoidal function of the rotor angle, θ.

Flux Linkage of IPMSM

Consider flux linkage of a–phase winding for different rotor positions shown in Fig. 6.14. Fig. 6.14 (a) shows different rotor positions for given flux loops of the

a–phase winding. Note that the effective air gap changes, as the rotor rotates. The effective air gap reaches its peak, when the flux lines cross the cavities at the right angle. However, it reduces to the minimum value, when the lines do not cross the cavities. A plot of the gap function, $g(\theta)$, is shown in Fig. 6.14 (a). It is a periodic function with a DC offset.

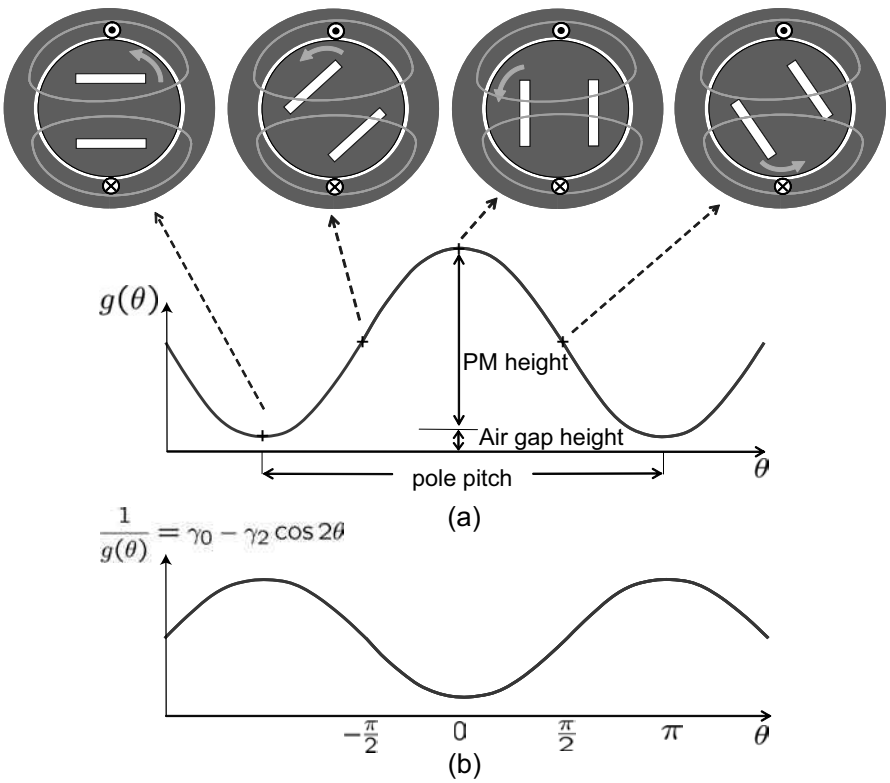

Figure 6.14: Effective air gap and its inverse as a function of θ: (a) $g(\theta)$, (b) $1/g(\theta)$.

Note on the other hand that the inductance is an inverse function of the air gap. Note from Fig. 6.14 (b) that $\frac{1}{g(\theta)}$ can be approximated as

$$\frac{1}{g(\theta)} = \gamma_0 - \gamma_2 \cos 2\theta, \tag{6.21}$$

where γ_0 and γ_2 are positive constants. This kind of approximation is also found in [1]. It is worthwhile to note the meaning of 2θ. Since the reluctance does not have polarity, it shows two periodic changes per one rotor revolution.

Utilizing (6.21), the a–phase winding inductance is equal to

$$L_a(\theta) = \mu_0 \frac{N^2 A}{2g(\theta)} = L_{ms} - L_\delta \cos 2\theta, \tag{6.22}$$

where

$$L_{ms} \equiv \mu_0 \frac{N^2 A}{2} \gamma_0, \tag{6.23}$$

$$L_{\delta} \equiv \mu_0 \frac{N^2 A}{2} \gamma_2. \tag{6.24}$$

Note that L_{ms} is the static component corresponding to the average gap length, and L_{δ} describes the reluctance component.

Extending the result to different phase windings, the stator inductance is described as

$$\overline{\mathbf{L}}_{abcs} = \mathbf{L}_{abcs} - \mathbf{L}_{rlc}(\theta), \tag{6.25}$$

where

$$\mathbf{L}_{rlc}(\theta) = L_{\delta} \begin{bmatrix} \cos 2\theta & \cos(2\theta - 2\pi/3) & \cos(2\theta + 2\pi/3) \\ \cos(2\theta - 2\pi/3) & \cos(2\theta + 2\pi/3) & \cos 2\theta \\ \cos(2\theta + 2\pi/3) & \cos 2\theta & \cos(2\theta - 2\pi/3) \end{bmatrix}. \tag{6.26}$$

Note that $\mathbf{L}_{abcs}$ is the inductance corresponding to the uniform air gap which appeared in (6.9), and that $\mathbf{L}_{rlc}(\theta)$ is something that varies along with the angle. It should be noted that (6.26) describes only the fundamental component of inductance change. The total flux linkage is

$$\begin{bmatrix} \lambda_{as} \\ \lambda_{bs} \\ \lambda_{cs} \end{bmatrix} = [\mathbf{L}_{abcs} - \mathbf{L}_{rlc}(\theta)] \begin{bmatrix} i_{as} \\ i_{bs} \\ i_{cs} \end{bmatrix} + \psi_m \begin{bmatrix} \cos\theta \\ \cos(\theta - 2\pi/3) \\ \cos(\theta + 2\pi/3) \end{bmatrix}. \tag{6.27}$$

Transformation of Reluctance Matrix

$\mathbf{L}_{rlc}$ may be called reluctance matrix, since it results in reluctance torque in the later part. Let $\Delta\boldsymbol{\lambda} = [\Delta\lambda_a, \Delta\lambda_b, \Delta\lambda_c]^T \equiv \mathbf{L}_{rlc}(\theta)\mathbf{i}_{abc}$. Using $f_{dq}^s = \frac{2}{3}\left[f_a(t) + e^{j\frac{2\pi}{3}} f_b(t) + e^{-j\frac{2\pi}{3}} f_c(t)\right]$, we consider mapping $\Delta\boldsymbol{\lambda}$ into a vector in the complex plane. The

desired vector follows from direct calculation [3]:

$$\begin{aligned}
&\frac{2}{3}\left[\Delta\lambda_a(t)+e^{j\frac{2\pi}{3}}\Delta\lambda_b(t)+e^{-j\frac{2\pi}{3}}\Delta\lambda_c(t)\right]\\
&= \frac{2}{3}\frac{1}{2}L_\delta\Big[(e^{j2\theta}+e^{-j2\theta})i_a+(e^{j(2\theta-\frac{2}{3}\pi)}+e^{-j(2\theta-\frac{2}{3}\pi)})i_b+(e^{j(2\theta+\frac{2}{3}\pi)}\\
&\quad +e^{-j(2\theta+\frac{2}{3}\pi)})i_c+e^{j\frac{2}{3}\pi}(e^{j(2\theta-\frac{2}{3}\pi)}+e^{-j(2\theta-\frac{2}{3}\pi)})i_a+e^{j\frac{2}{3}\pi}(e^{j(2\theta+\frac{2}{3}\pi)}\\
&\quad +e^{-j(2\theta+\frac{2}{3}\pi)})i_b+e^{j\frac{2}{3}\pi}(e^{j2\theta}+e^{-j2\theta})i_c+e^{-j\frac{2}{3}\pi}(e^{j(2\theta+\frac{2}{3}\pi)}+e^{-j(2\theta+\frac{2}{3}\pi)})i_a\\
&\quad +e^{-j\frac{2}{3}\pi}(e^{j2\theta}+e^{-j2\theta})i_b+e^{-j\frac{2}{3}\pi}(e^{j(2\theta-\frac{2}{3}\pi)}+e^{-j(2\theta+\frac{2}{3}\pi)})i_c\Big]\\
&= \frac{1}{2}L_\delta\frac{2}{3}\left[3e^{j2\theta}i_a+3e^{j(2\theta-\frac{2}{3}\pi)}i_b+3e^{j(2\theta+\frac{2}{3}\pi)}i_c\right]\\
&= \frac{3}{2}L_\delta e^{j2\theta}\frac{2}{3}\left[i_a+e^{-j\frac{2}{3}\pi}i_b+e^{j\frac{2}{3}\pi}i_c\right]\\
&= \frac{3}{2}L_\delta e^{j2\theta}(\mathbf{i}^s_{dq})^*\,. \qquad (6.28)
\end{aligned}$$

where $(\mathbf{i}^s_{dq})^*$ is the complex conjugate of $\mathbf{i}^s_{dq}$. Note that the computation result is remarkably simple.

It follows from (6.27) and (6.28) that the stator flux of IPMSM is described in the stationary dq coordinate such that

$$\boldsymbol{\lambda}^s_{dq}=L_s\mathbf{i}^s_{dq}-\frac{3}{2}L_\delta e^{j2\theta}(\mathbf{i}^s_{dq})^*+\psi_m e^{j\theta} \qquad (6.29)$$

or

$$\begin{bmatrix}\lambda^s_d\\ \lambda^s_q\end{bmatrix}=\begin{bmatrix}L_s-\frac{3}{2}L_\delta\cos 2\theta & -\frac{3}{2}L_\delta\sin 2\theta\\ -\frac{3}{2}L_\delta\sin 2\theta & L_s+\frac{3}{2}L_\delta\cos 2\theta\end{bmatrix}\begin{bmatrix}i^s_d\\ i^s_q\end{bmatrix}+\psi_m\begin{bmatrix}\cos\theta\\ \sin\theta\end{bmatrix}. \qquad (6.30)$$

By comparing (6.30) with (6.13), it is clear that $\frac{3}{2}L_\delta\cos 2\theta$ and $\frac{3}{2}L_\delta\sin 2\theta$ are originated from the rotor saliency.

IPMSM Dynamics in the Stationary Frame

Using (6.29), the stationary IPMSM dynamic model is obtained as

$$\begin{aligned}
\mathbf{v}^s_{dq} &= r_s\mathbf{i}^s_{dq}+\frac{d}{dt}\boldsymbol{\lambda}^s_{dq}\\
&= r_s\mathbf{i}^s_{dq}+\frac{d}{dt}(L_s\mathbf{i}^s_{dq}-\frac{3}{2}L_\delta e^{j2\theta_e}\mathbf{i}^{s*}_{dq})+j\psi_m e^{j\theta}. \qquad (6.31)
\end{aligned}$$

Rewriting (9.68) in the matrix form, it follows that

$$\begin{aligned}
\begin{bmatrix}v^s_d\\ v^s_q\end{bmatrix} &= r_s\begin{bmatrix}i^s_d\\ i^s_q\end{bmatrix}+\begin{bmatrix}L_s-\frac{3}{2}L_\delta\cos 2\theta & -\frac{3}{2}L_\delta\sin 2\theta\\ -\frac{3}{2}L_\delta\sin 2\theta & L_s+\frac{3}{2}L_\delta\cos 2\theta\end{bmatrix}\frac{d}{dt}\begin{bmatrix}i^s_d\\ i^s_q\end{bmatrix}\\
&\quad -3\omega L_\delta\begin{bmatrix}-\sin 2\theta & \cos 2\theta\\ \cos 2\theta & \sin 2\theta\end{bmatrix}\begin{bmatrix}i^s_d\\ i^s_q\end{bmatrix}+\omega\psi_m\begin{bmatrix}-\sin\theta\\ \cos\theta\end{bmatrix}. \qquad (6.32)
\end{aligned}$$

This stationary model is useful for developing a signal injection-based sensorless algorithm.

IPMSM Dynamics in the Synchronous Reference Frame

Further transforming flux (6.29) into the synchronous reference frame, we obtain

$$\begin{aligned}\boldsymbol{\lambda}^e_{dq} &= L_s e^{-j\theta}\mathbf{i}^s_{dq} - \frac{3}{2}L_\delta e^{j\theta}(\mathbf{i}^s_{dq})^* + \psi_m \\ &= L_s\mathbf{i}^e_{dq} - \frac{3}{2}L_\delta(\mathbf{i}^e_{dq})^* + \psi_m, \end{aligned} \tag{6.33}$$

or

$$\begin{bmatrix}\lambda^e_d \\ \lambda^e_q\end{bmatrix} = \begin{bmatrix}L_s - \frac{3}{2}L_\delta & 0 \\ 0 & L_s + \frac{3}{2}L_\delta\end{bmatrix}\begin{bmatrix}i^e_d \\ i^e_q\end{bmatrix} + \psi_m\begin{bmatrix}1 \\ 0\end{bmatrix}. \tag{6.34}$$

By comparing (6.34) with the expression, (6.30), in the stationary frame, it is apparent that 2θ disappears in the synchronous frame, leaving the inductance asymmetry between d and q inductances.

Note that

$$j\omega\boldsymbol{\lambda}^e_{dq} = j\omega L_s\mathbf{i}^e_{dq} - j\omega\frac{3}{2}L_\delta(\mathbf{i}^e_{dq})^* + j\omega\psi_m \tag{6.35}$$

$$p\boldsymbol{\lambda}^e_{dq} = L_s p\mathbf{i}^e_{dq} - \frac{3}{2}L_\delta(p\mathbf{i}^e_{dq})^*. \tag{6.36}$$

Substituting (6.35) and (6.36) into the voltage equation (6.17), we obtain

$$\begin{aligned} v^e_d &= r_s i^e_d + \omega\left(L_s + \frac{3}{2}L_\delta\right)i^e_q + \left(L_s - \frac{3}{2}L_\delta\right)\frac{d}{dt}i^e_d \\ v^e_q &= r_s i^e_q + \omega\left(L_s - \frac{3}{2}L_\delta\right)i^e_d + \left(L_s + \frac{3}{2}L_\delta\right)\frac{d}{dt}i^e_q + \omega\psi_m. \end{aligned}$$

Letting

$$\begin{aligned} L_d &= L_s - \frac{3}{2}L_\delta \\ L_q &= L_s + \frac{3}{2}L_\delta\,, \end{aligned}$$

we obtain the final voltage equation

$$v^e_d = r_s i^e_d + L_d\frac{di^e_d}{dt} - \omega L_q i^e_q \tag{6.37}$$

$$v^e_q = r_s i^e_q + L_q\frac{di^e_q}{dt} + \omega L_d i^e_d + \omega\psi_m\,. \tag{6.38}$$

Note again that coupling terms, $-\omega L_q i^e_q$ and $\omega L_d i^e_d$, are originated from rotating the coordinate and they make an interference between d and q dynamics. In the normal differential equation form, (6.37) and (6.38) are written equivalently as

$$\frac{d}{dt}\begin{bmatrix}i^e_d \\ i^e_q\end{bmatrix} = \begin{bmatrix}-\frac{r_s}{L_d} & \omega\frac{L_q}{L_d} \\ -\omega\frac{L_d}{L_q} & -\frac{r_s}{L_q}\end{bmatrix}\begin{bmatrix}i^e_d \\ i^e_q\end{bmatrix} - \frac{\omega\psi_m}{L_q}\begin{bmatrix}0 \\ 1\end{bmatrix} + \begin{bmatrix}\frac{1}{L_d}v^e_d \\ \frac{1}{L_q}v^e_q\end{bmatrix}. \tag{6.39}$$

Just the existence of L_δ makes a difference between L_d and L_q. Note that if $L_d = L_q$, then (6.39) turns out to be the same as (6.20).

Matrix Formalism

The same voltage equation is derived through matrix formalism. Recall that the transformation into the reference frame is achieved by multiplying by $e^{\mathbf{J}\theta}$. For example, $\mathbf{v}^e_{dq} = e^{\mathbf{J}\theta}\mathbf{v}^s_{dq}$. Recall from (4.29) that $e^{\mathbf{J}\theta}\frac{d}{dt}\left(e^{-\mathbf{J}\theta}\right) = -\omega\mathbf{J}$. With the use of (6.34), it follows that

$$\begin{aligned}
e^{\mathbf{J}\theta}\mathbf{v}^s_{dq} &= r_s e^{\mathbf{J}\theta}\mathbf{i}^s_{dq} + e^{\mathbf{J}\theta}\frac{d}{dt}\left(e^{-\mathbf{J}\theta}e^{\mathbf{J}\theta}\boldsymbol{\lambda}^s_{dq}\right), \\
\mathbf{v}^e_{dq} &= r_s\mathbf{i}^e_{dq} + e^{\mathbf{J}\theta}\frac{d}{dt}\left(e^{-\mathbf{J}\theta}\boldsymbol{\lambda}^e_{dq}\right), \\
&= r_s\mathbf{i}^e_{dq} + e^{\mathbf{J}\theta}\frac{d}{dt}\left(e^{-\mathbf{J}\theta}\right)\boldsymbol{\lambda}^e_{dq} + \frac{d}{dt}\boldsymbol{\lambda}^e_{dq}, \\
&= r_s\mathbf{i}^e_{dq} - \omega\mathbf{J}\boldsymbol{\lambda}^e_{dq} + \begin{bmatrix} L_d\frac{di^e_d}{dt} \\ L_q\frac{di^e_q}{dt}\end{bmatrix}, \\
&= r_s\mathbf{i}^e_{dq} - \omega\begin{bmatrix} L_q i^e_q \\ -L_d i^e_d - \psi_m\end{bmatrix} + \begin{bmatrix} L_d\frac{di^e_d}{dt} \\ L_q\frac{di^e_q}{dt}\end{bmatrix}.
\end{aligned} \tag{6.40}$$

Note that the result is the same as (6.39).

6.2.3 Multi-Pole PMSM Dynamics and Vector Diagram

Equations (6.37) and (6.38) describe the dynamics of a single-pole pair. Specifically, v^e_d and v^e_q are the voltages of a single-pole pair winding, and ψ_m is the flux linkage of a single rotor pole pair. Most commonly, the P-pole system is constructed by connecting $P/2$-pole pair subsystems in series. The parallel windings are rarely used due to the circulating current. Fig. 6.15 shows an example of 6-pole PMSM, in which just a-phase windings are depicted. Note that the electrical speed is equal to $\omega_e = \frac{P}{2}\omega$ in the P-pole motor, since each pole pair winding experiences $\frac{P}{2}$ periodic changes of flux linkage at each rotation.

To derive the P-pole IPSMS dynamics from the single-pole pair dynamics, we should multiply (6.37) and (6.38) by $P/2$, and replace ω by ω_e:

$$\frac{P}{2}v^e_d = \frac{P}{2}r_s i^e_d + \frac{P}{2}L_d\frac{di^e_d}{dt} - \omega_e\frac{P}{2}L_q i^e_q \tag{6.41}$$

$$\frac{P}{2}v^e_q = \frac{P}{2}r_s i^e_q + \frac{P}{2}L_q\frac{di^e_q}{dt} + \omega_e\frac{P}{2}L_d i^e_d + \omega_e\frac{P}{2}\psi_m. \tag{6.42}$$

The things that change with the series connection are voltage and impedances. Let $\tilde{v}^e_d = (P/2)v^e_d$, $\tilde{v}^e_q = (P/2)v^e_q$, $\tilde{r}_s = (P/2)r_s$, $\tilde{L}_d = (P/2)L_d$, $\tilde{L}_q = (P/2)L_q$, and $\tilde{\psi}_m = (P/2)\psi_m$. Then, we have

$$\tilde{v}^e_d = \tilde{r}_s i^e_d + \tilde{L}_d\frac{di^e_d}{dt} - \omega_e\tilde{L}_q i^e_q \tag{6.43}$$

$$\tilde{v}^e_q = \tilde{r}_s i^e_q + \tilde{L}_q\frac{di^e_q}{dt} + \omega_e\tilde{L}_d i^e_d + \omega_e\tilde{\psi}_m. \tag{6.44}$$

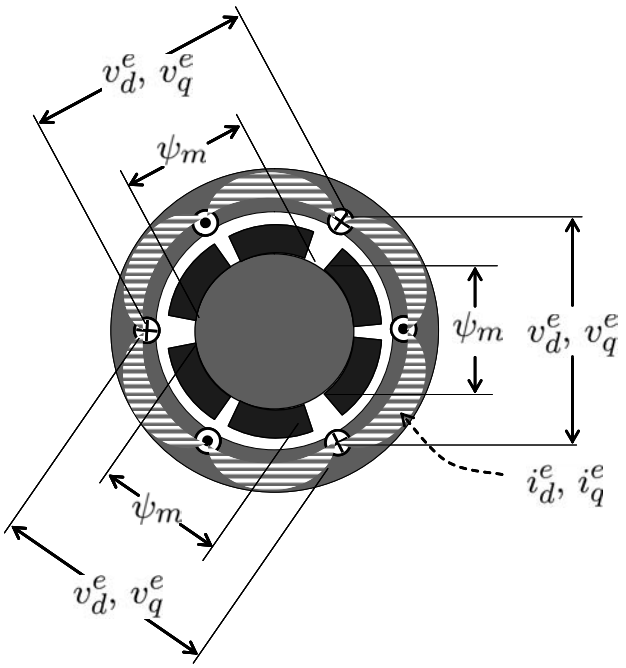

Figure 6.15: Structure of 6-pole motor showing a series connection of three equal sub-dynamics.

However, for simplicity, we will abuse the notations in the following: v_d^e, v_q^e, r_s, L_d, L_q, and ψ_m will be used even in high pole machines, instead of $\tilde{v}_d^e$, $\tilde{v}_q^e$, $\tilde{r}_s$, $\tilde{L}_d$, $\tilde{L}_q$, and $\tilde{\psi}_m$. Then, the P-pole IPMSM dynamics are given as

$$v_d^e = r_s i_d^e + L_d \frac{di_d^e}{dt} - \omega_e L_q i_q^e \tag{6.45}$$

$$v_q^e = r_s i_q^e + L_q \frac{di_q^e}{dt} + \omega_e L_d i_d^e + \omega_e \psi_m. \tag{6.46}$$

That is, the P-pole dynamics are not different from the two-pole dynamics, as far as ω_e and the parameters measured from the terminals are used. PMSM equations are summarized in Table 6.3.

Equivalent Circuit

The rotor flux linkage is equivalently expressed as a product of d–axis inductance, L_d and a virtual current, i_f, i.e.,

$$\psi_m = L_d i_f. \tag{6.47}$$

With i_f, a PMSM equivalent circuit is depicted as shown in Fig. 6.16.

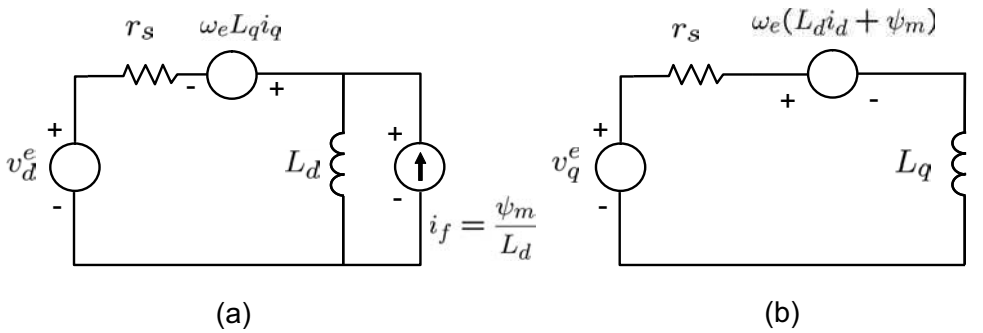

Figure 6.16: Equivalent circuit of PMSM: (a) d–axis and (b) q–axis.

Table 6.3: PMSM dynamic equations.

SPMSM in the stationary frame
$\frac{d}{dt}\begin{bmatrix} i_d^s \\ i_q^s \end{bmatrix} = -\frac{r_s}{L_s}\begin{bmatrix} i_d^s \\ i_q^s \end{bmatrix} - \frac{\psi_m \omega_e}{L_s}\begin{bmatrix} -\sin\theta_e \\ \cos\theta_e \end{bmatrix} + \frac{1}{L_s}\begin{bmatrix} v_d^s \\ v_q^s \end{bmatrix}$.
IPMSM in the stationary frame
$\begin{bmatrix} v_d^s \\ v_q^s \end{bmatrix} = r_s\begin{bmatrix} i_d^s \\ i_q^s \end{bmatrix} + \begin{bmatrix} L_s - \frac{3}{2}L_\delta\cos 2\theta_e & -\frac{3}{2}L_\delta \sin 2\theta_e \\ -\frac{3}{2}L_\delta \sin 2\theta_e & L_s + \frac{3}{2}L_\delta \cos 2\theta_e \end{bmatrix}\frac{d}{dt}\begin{bmatrix} i_d^s \\ i_q^s \end{bmatrix}$ $-3\omega_e L_\delta \begin{bmatrix} -\sin 2\theta_e & \cos 2\theta_e \\ \cos 2\theta_e & \sin 2\theta_e \end{bmatrix}\begin{bmatrix} i_d^s \\ i_q^s \end{bmatrix} + \omega_e \psi_m \begin{bmatrix} -\sin\theta_e \\ \cos\theta_e \end{bmatrix}$
SPMSM in the synchronous frame
$\frac{d}{dt}\begin{bmatrix} i_d^e \\ i_q^e \end{bmatrix} = \begin{bmatrix} \frac{-r_s}{L_s} & \omega_e \\ -\omega_e & -\frac{r_s}{L_s} \end{bmatrix}\begin{bmatrix} i_d^e \\ i_q^e \end{bmatrix} - \frac{\psi_m \omega_e}{L_s}\begin{bmatrix} 0 \\ 1 \end{bmatrix} + \frac{1}{L_s}\begin{bmatrix} v_d^e \\ v_q^e \end{bmatrix}$
IPMSM in the synchronous frame
$\frac{d}{dt}\begin{bmatrix} i_d^e \\ i_q^e \end{bmatrix} = \begin{bmatrix} -\frac{r_s}{L_d} & \omega_e \frac{L_q}{L_d} \\ -\omega_e \frac{L_d}{L_q} & -\frac{r_s}{L_q} \end{bmatrix}\begin{bmatrix} i_d^e \\ i_q^e \end{bmatrix} - \frac{\omega_e \psi_m}{L_q}\begin{bmatrix} 0 \\ 1 \end{bmatrix} + \begin{bmatrix} \frac{1}{L_d} v_d^e \\ \frac{1}{L_q} v_q^e \end{bmatrix}$

6.3 PMSM Torque Equations

Torque is obtained by the cross product of stator flux linkage $\boldsymbol{\lambda}_{dq}^e$ and stator current $\mathbf{i}_{dq}^e$. With the right-hand rule, torque is obtained in the axial direction. With the

use of orthogonal unity vectors $\overrightarrow{i}$, $\overrightarrow{j}$, and $\overrightarrow{k}$, we have

$$\begin{aligned}
T_e &= \frac{3}{2}\frac{P}{2}\left(\boldsymbol{\lambda}^e_{dq} \times \mathbf{i}^e_{dq}\right)_k \\
&= \frac{3}{2}\frac{P}{2}\left(\begin{bmatrix}\lambda^e_{ds}\\ \lambda^e_{qs}\\ 0\end{bmatrix} \times \begin{bmatrix}i^e_d\\ i^e_q\\ 0\end{bmatrix}\right)_k \\
&= \frac{3}{2}\frac{P}{2}\begin{vmatrix}\overrightarrow{i} & \overrightarrow{j} & \overrightarrow{k}\\ \lambda^e_{ds} & \lambda^e_{qs} & 0\\ i^e_d & i^e_q & 0\end{vmatrix}_k \\
&= \frac{3}{2}\frac{P}{2}(\lambda^e_{ds}i^e_q - \lambda^e_{qs}i^e_d) \\
&= \frac{3}{2}\frac{P}{2}\left[(L_d i^e_d + \psi_m)i^e_q - L_q i^e_q i^e_d\right] \\
&= \frac{3P}{4}\left[\psi_m i^e_q - (L_q - L_d)i^e_d i^e_q\right]. \qquad (6.48)
\end{aligned}$$

Note that $\psi_m i^e_q$ is the electro-magnetic torque based on the Lorentz force, whereas $-(L_q - L_d)i^e_d i^e_q$ is the reluctance torque caused by the $L_d - L_q$ asymmetry.

With the lossless model, $v^e_d = -\omega_e L_q i^e_q$ and $v^e_q = \omega_e L_d i^e_d + \omega_e \psi_m$, the total electric power is

$$\begin{aligned}
P_e &= \frac{3}{2}(v^e_q i^e_q + v^e_d i^e_d) \\
&= \frac{3}{2}\omega_e(\psi_m i^e_q + (L_d - L_q)i^e_d i^e_q) \\
&= \frac{3P}{4}\omega_r(\psi_m i^e_q + (L_d - L_q)i^e_d i^e_q). \qquad (6.49)
\end{aligned}$$

Torque is derived from the power such that $T_e = \frac{\partial P_e}{\partial \omega_r}$. Then the identical result, (6.48) follows.

Note further that the torque equation is independent of the coordinate frame.

$$T_e = \frac{3P}{4}Im(\mathbf{i}^e_{dq} \cdot \boldsymbol{\lambda}^{e\,*}_{dq}) = \frac{3P}{4}Im(\mathbf{i}^e_{dq} e^{j\theta_e} \cdot e^{-j\theta_e}\boldsymbol{\lambda}^{e\,*}_{dq}) = \frac{3P}{4}Im(\mathbf{i}^s_{dq} \cdot \boldsymbol{\lambda}^{s\,*}_{dq}).$$

In the stationary frame, the torque equation has the same form:

$$T_e = \frac{3P}{4}(\lambda^s_{ds}i^s_q - \lambda^s_{qs}i^s_d), \qquad (6.50)$$

where

$$\begin{aligned}
\lambda^s_d &= L_s i^s_d - \frac{3}{2}L_\delta(-i^s_d \cos 2\theta_e + i^s_q \sin 2\theta_e) + \psi_m \cos\theta_e, \\
\lambda^s_q &= L_s i^s_q - \frac{3}{2}L_\delta(i^s_d \sin 2\theta_e - i^s_q \cos 2\theta_e) + \psi_m \sin\theta_e.
\end{aligned}$$

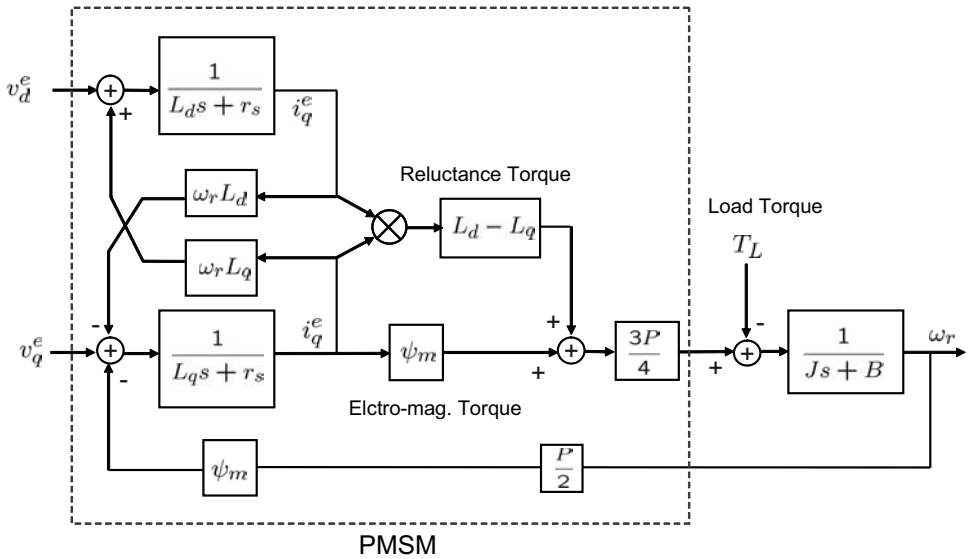

Figure 6.17: Block diagram representing the PMSM dynamics.

6.4 PMSM Block Diagram and Control

Suppose that J is the rotor inertia, and B is the friction coefficient, and T_L is a load torque. Then, the mechanical equation is given by

$$J\frac{d\omega_r}{dt} + B\omega_r = T_e - T_L\,. \tag{6.51}$$

Based on (6.39) and (6.53), the IPMSM dynamics can be depicted as shown in Fig. 6.17.

The typical control block diagram is shown in Fig. 6.18. To implement the current controller in the synchronous reference frame, the sensed current should be changed through the transformation map, abc/dq. For such transformation, the flux angle, θ_e is required, and the angle is obtained from the position sensor, e.g. absolute encoder or resolver. In case of resolver, resolver-to-digital converter (RDC) is required to convert the resolver signal into position and velocity values.

In general, current controller involves decoupling and back EMF compensation, as well as PI controllers:

$$v_d^e = (PI)(i_d^{e*} - i_d^e) - \omega L_q i_q^e\,, \tag{6.52}$$
$$v_q^e = (PI)(i_q^{e*} - i_q^e) + \omega L_d i_d^e + \omega\psi_m\,. \tag{6.53}$$

The PWM duties are determined normally by the space vector PWM method from the input voltages v_d^e and v_q^e in the reference frame.

For current sensing, Hall sensors are most widely utilized. There are two types of Hall sensors: one is voltage type, and the other is current type. The current type

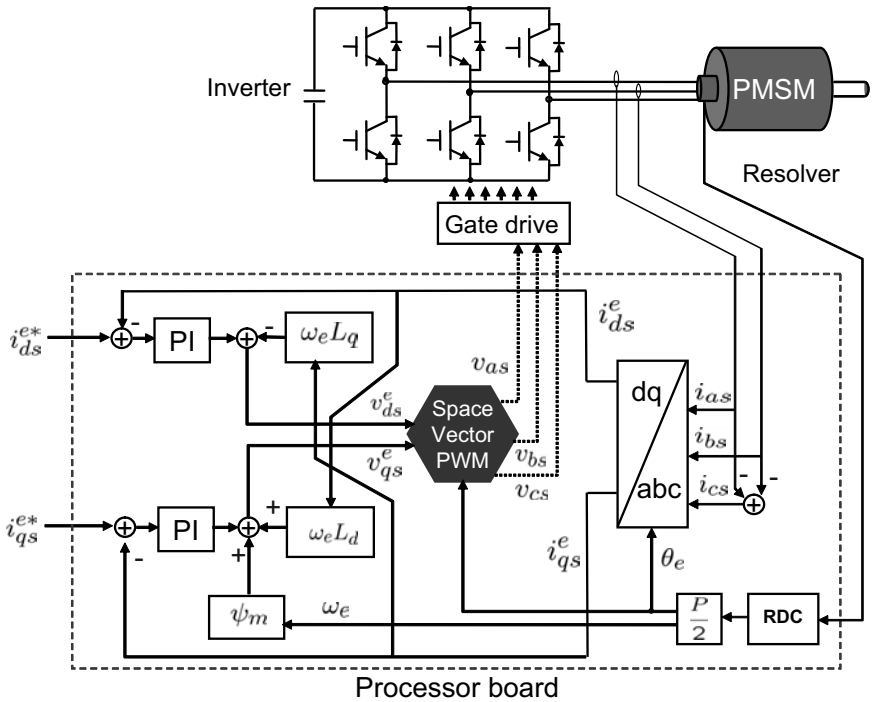

Figure 6.18: Control block diagram of PMSM using the coordinate transformation map.

Hall sensor contains a current controller inside to obtain zero flux measurement. Therefore, the linearity is superior to the voltage type Hall sensors. Or, in some home appliances where precise control is not necessary like blowers or compressors, or the system cost is critical, (speed) sensorless control is often utilized.

6.4.1 MATLAB® Simulation

Simulation parameters are listed in Table 6.4, and PI gains for current and speed controllers are $K_P = 1.07$ and $K_I = 350$ for current controller and $K_P = 20$ and $K_I = 40$ for speed controller. Fig. 6.19 shows a speed step response and the corresponding a-phase current under no load condition. Fig. 6.20 shows a speed response and the corresponding dq currents when a step load torque (212Nm) is applied at $t = 10$ sec. Fig. 6.21 shows speed and phase currents when the speed changes from 500rpm and to -500rpm.

Table 6.4: PMSM parameters for MATLAB® simulation.

Motor power	80kW	L_d	0.538mH
Rated speed	3600rpm	L_q	0.824mH
Rated torque	212Nm	r_s	6.5mΩ
Rated current	$296A_{rms}$	Flux (ψ_m)	0.162Wb
Rated voltage	176 V_{rms}	Inertia, J	$0.1kgm^2$
Number of poles	6	Damping coeff., B	0

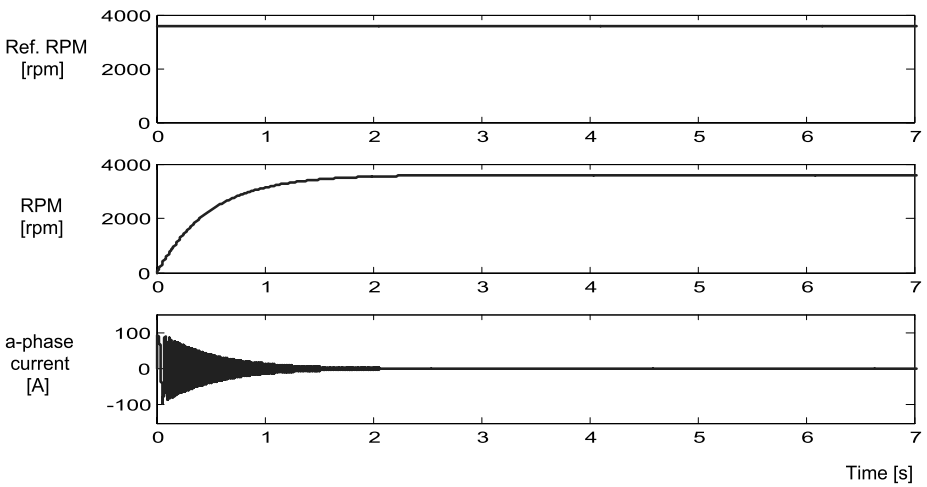

Figure 6.19: Speed response under no load condition.

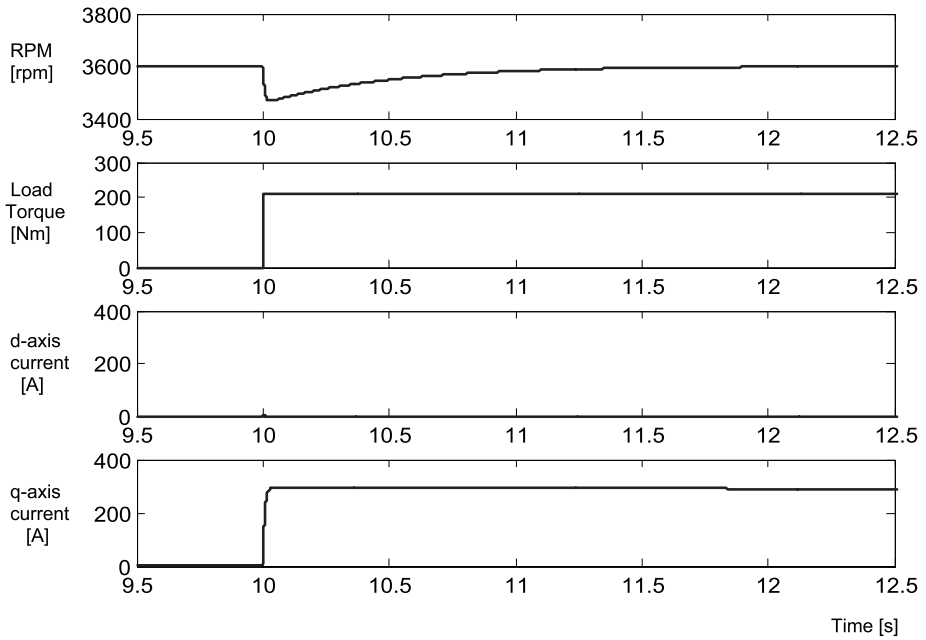

Figure 6.20: Speed and current responses to a step load torque applied at $t = 10$sec.

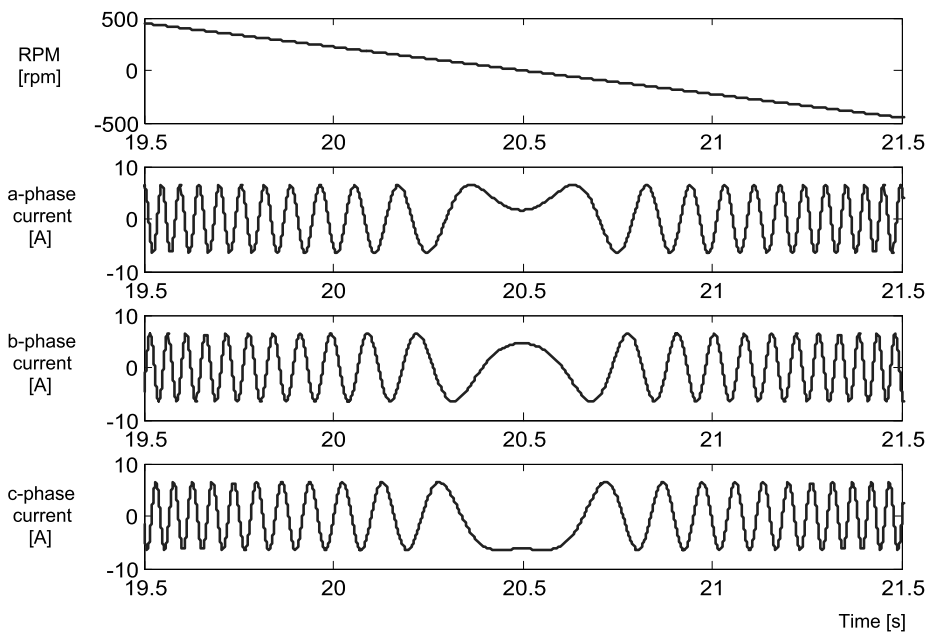

Figure 6.21: Phase currents when the speed changes from 500rpm to -500rpm.

Bibliography

[1] P. C. Krause, O. Wasynczuk, and S. D. Sudhoff, *Analysis of Electric Machinery,* IEEE Press, 1995.

[2] J. R. Hendershot and TJE Miller, *Design of Brushless Permanent-magnet Motors,* Oxford Science Publications, Oxford University Press, New York, 1994.

[3] D. W. Novotny and T. A. Lipo, *Vector Control and Dynamics of AC Drives,* Clarendon Press, Oxford 1996.

Problems

6.1 Consider a two-pole machine shown in Fig. 6.22 that has air gap height, g, average air gap-diameter, D, and stack length, L. Suppose that the stored energy in the air gap is

$$W_{fld} = \frac{\mu_0 \pi D L}{4g} \left(\mathrm{MMF}_s^2 + \mathrm{MMF}_r^2 + 2\mathrm{MMF}_s \mathrm{MMF}_r \cos\theta \right).$$

Determine the torque, T_e.

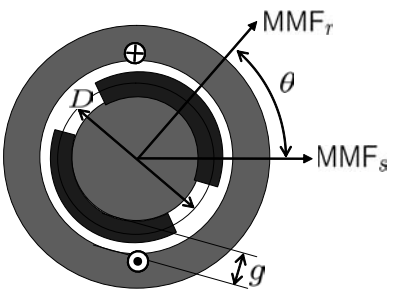

Figure 6.22: Two-pole machine (Problem 6.1)

6.2 Consider a 6-pole IPMSM section shown in Fig. 6.23. It is assumed that the rotor without a PM rotates when 40A current flows through the a-phase windings, i.e., $i_a = 40A$ and $i_b = i_c = 0$. The corresponding flux λ_{as}^s of a-phase winding is plotted in the right side.

a) Assuming that the leakage inductance is equal to zero, determine L_s and L_δ.

b) Determine L_d and L_q.

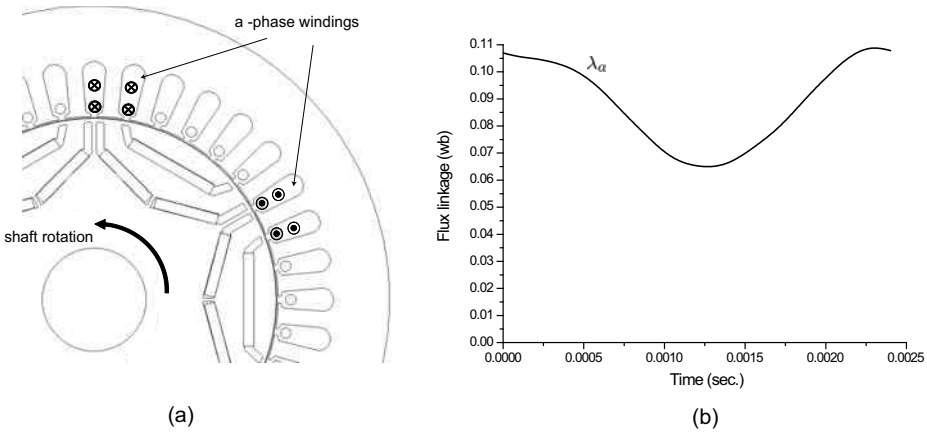

Figure 6.23: Flux linkage of a–phase winding of a 6-pole IPMSM (Problem 6.2).

6.3 Fig. 6.24 shows the back EMFs of phase windings at open terminal at 6000rpm. The number of poles is 4, and $L_d = 1.2$mH and L_q=2.3mH. Suppose that the motor is running at 6000rpm when $i_d^e = -6.6$A and $i_q^e = 37.5$A.

a) Estimate the back EMF constant, ψ_m.
b) Construct a voltage vector diagram for the lossless model.
c) Calculate torque.
d) Calculate power factor.

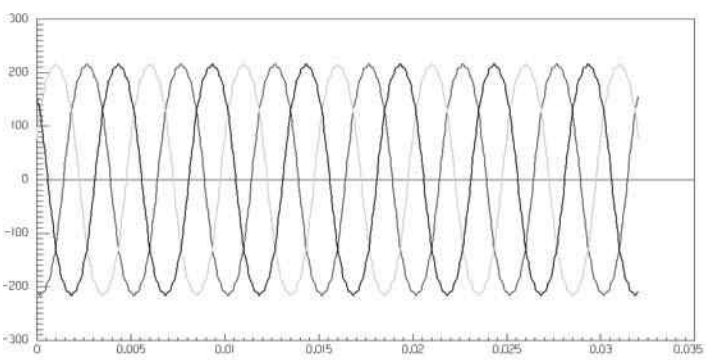

Figure 6.24: Back EMF (Problem 6.3).

6.4 Determine whether $L_q > L_d$ or $L_d > L_q$ for the PMSMs shown in Fig. 6.9.

6.5 Consider an IPMSM with the following parameters: $\frac{3}{2}L_{ms} + L_{ls} = 0.8\text{mH}$, $L_\delta = 0.1\text{mH}$, $r_s = 0.036\text{m}\Omega$, $\psi_m = 0.2229\text{V}\cdot\text{s}$. Two computation methods are shown in Fig. 6.25: one is in the synchronous frame, the other in the stationary frame. Current controller is constructed in the synchronous frame with PI gains, $K_p = 30$ and $K_i = 40$, and current commands, $(i_d^{e*}, i_q^{e*}) = (-2, 10)$. The same voltage $(v_d^e,\, v_q^e)$ is fed to the stationary frame model via coordinate transformation:

$$\begin{bmatrix} v_d^s \\ v_q^s \end{bmatrix} = \begin{bmatrix} \cos\theta & -\sin\theta \\ \sin\theta & \cos\theta \end{bmatrix} \begin{bmatrix} v_d^e \\ v_q^e \end{bmatrix}.$$

Let $\omega = 15\text{rad/sec}$. Show that mapping of $(i_d^e,\, i_q^e)$ into the stationary frame yields the same vector as $(i_d^s,\, i_q^s)$, i.e., show that the two calculation results following ①and ② are the same. Utilize M-file of MATLAB®. As for the numerical method, use the following Rounge−Kutta 4^{th} method with step size $h = 0.00001\text{sec}$:

```
function xx = rook(t,xy,h,w)
xytemp=xy;
kk1= ex45fc(t,xytemp,h,w);
kk2= ex45fc(t+h/2,xytemp+kk1*0.5*h,h,w);
kk3= ex45fc(t+h/2,xytemp+kk2*0.5*h,h,w);
kk4= ex45fc(t+h,xytemp+kk3*h,h,w);
xx = xytemp+h*(kk1+2*kk2+2*kk3+kk4)/6;
```

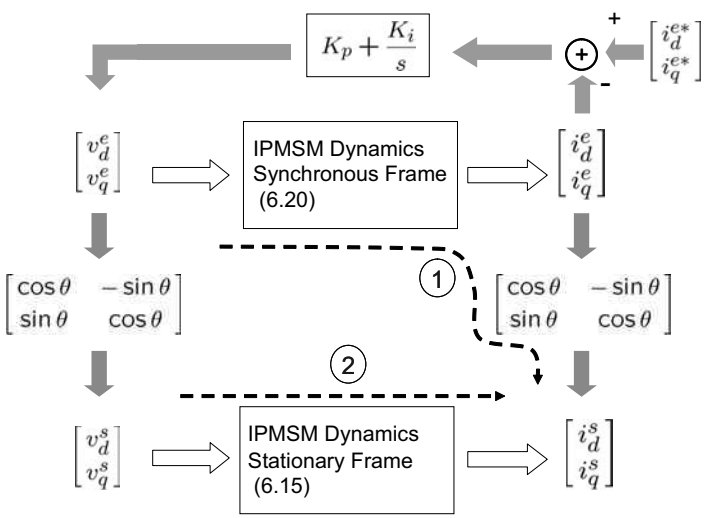

Figure 6.25: Two computation methods verifying identity of the dynamics in the synchronous and stationary frames (Problem 6.5).

Chapter 7

PMSM High-Speed Operation

The motors are designed such that its terminal voltage reaches the maximum source voltage when it operates at the base speed with the rated torque. Since the back EMF grows with the speed, the speed range can be extended only by reducing the air-gap field with negative d–axis current. The field-weakening is a technique of finding a high-speed solution within the boundary of speed limit.

The PMSM speed range is divided into two with a base speed as the pivot: The low-speed range from zero to the base speed is called the constant torque region, while the high-speed range above it is called the field-weakening region (or the constant power speed region). In the constant torque region, the performance is limited only by the allowable maximum current, since the back EMF is not high enough to hit the voltage limit.

7.1 Machine Sizing

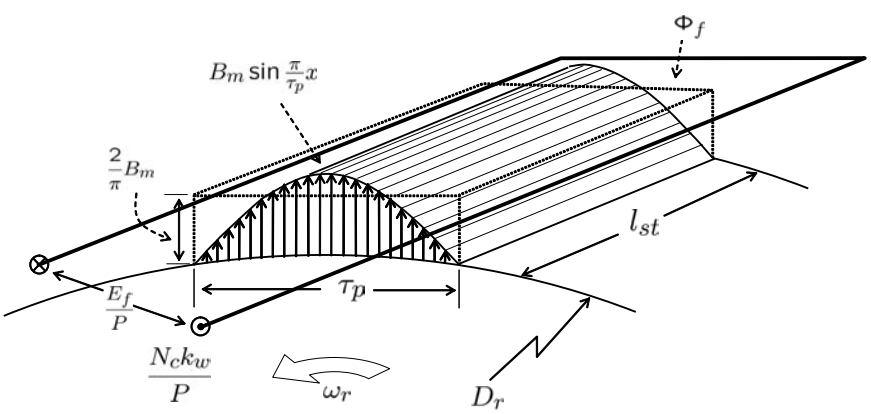

Figure 7.1: A single-pole section of a PM synchronous motor.

In this section, the relationship between the motor volume and torque is consid-

ered. Consider a single-pole section of a PM motor shown in Fig. 7.1, where τ_p is the pole arc length and l_{st} is the stack length. Assume that air gap field density by the rotor PM is sinusoidal and that the rotor is rotating at the speed of ω_r. Then the air gap field density is modeled as a traveling wave, $B_m \sin\left(\frac{\pi}{\tau_p}x - \frac{P}{2}\omega_r t\right)$. Let N_c be the number of coil turns per phase and k_w be the winding factor. Then the flux linkage of a phase winding is equal to

$$\lambda_{pole} = N_c k_w l_{st} \int_0^{\tau_p} B_m \sin\left(\frac{\pi}{\tau_p}x - \frac{P}{2}\omega_r t\right) dx \tag{7.1}$$

$$= N_c k_w l_{st} \tau_p \frac{2}{\pi} B_m \cos\frac{P}{2}\omega_r t\,. \tag{7.2}$$

From the Lenz law, the induced phase voltage is

$$e_f = -\frac{d}{dt}\lambda_{pole} = N_c k_w \Phi_f \frac{P}{2}\omega_r \sin\frac{P}{2}\omega_r t, \tag{7.3}$$

where $\Phi_f = l_{st}\tau_p \frac{2}{\pi} B_m$. Note that $\frac{2}{\pi}$ denotes the average level of $\sin x$. Therefore, the rms value of the induced voltage is equal to

$$E_f = \frac{1}{\sqrt{2}} 2\pi f_e \cdot N_c k_w \Phi_f = \sqrt{2}\pi f_e N_c k_w \Phi_f, \tag{7.4}$$

where $f_e \equiv \frac{P}{2}\frac{\omega_r}{2\pi}$ is the electrical frequency.

The electric loading is defined as the ampere-turn per circumferential length of the stator bore:

$$A_m = \frac{2mN_c\sqrt{2}I_a}{P\tau_p} = \frac{2mN_c\sqrt{2}I_a}{\pi D_r}, \tag{7.5}$$

where D_r is the diameter of the air gap, m is the number of phases, and I_a is the rms phase current. Note that $2mN_c$ is the total number of conductors in the whole slot. The electric loading is the description of a current sheet along the airgap, and it is limited by the ability of heat dissipation from the conductor bundles.

The apparent electromagnetic power crossing the air gap is equal to the product of the induced voltage and current:

$$P_{gap} = mE_f I_a = m\sqrt{2}\pi f_e N_c k_w \Phi_f \frac{A_m \pi D_r}{2\sqrt{2}mN_c}$$

$$= \frac{\pi}{2} k_w \frac{f_e}{P/2}(P\tau_p) l_{st} B_m A_m D_r$$

$$= \frac{\pi}{4} k_w D_r^2 l_{st} B_m A_m \omega_r\,. \tag{7.6}$$

In deriving the third equality, $\pi D_r = P\tau_p$ and $f_e/(P/2) = \omega_r/(2\pi)$ are utilized. Since torque is obtained as $T_e = P_{gap}/\omega_r$, it follows from (7.6) that

$$T_e = k_w B_m A_m \mathrm{Vol}_{(rotor)}\,, \tag{7.7}$$

Table 7.1: Magnetic and electric loadings.

Machine type	Magnetic loading B(T)	Electric loading A_m(A/cm)
IM ($\sim$ 10kW)	0.6$\sim$0.8	100$\sim$ 350
IM (10 $\sim$ 1000kW)	0.6$\sim$0.8	250$\sim$ 450
PMSM (air cooling, $\sim$ 10kW)	0.7	150
PMSM (water cooling, 10 $\sim$ 100kW)	0.8	$\sim$ 600

where $\text{Vol}_{(rotor)}$ denotes the rotor volume as depicted in Fig. 7.2. Here, B_m is called the magnet loading. Once a motor type and a cooling method are determined, B_m and A_m are almost fixed. Therefore, torque is proportional to the rotor volume as depicted graphically in Fig. 7.2.

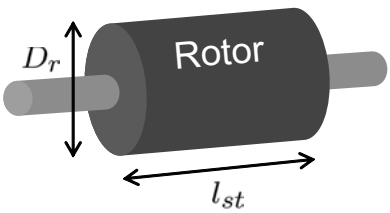

Figure 7.2: Torque is proportional to the rotor volume.

7.1.1 Electric and Magnet Loadings

To achieve a high torque density, motors are designed to use the achievable maximum electric and magnetic loadings. Ranges of electric and magnetic loadings are A_m : 150 $\sim$ 3000A/cm and B_m : 0.6 $\sim$ 1.4T. High electric loading leads to a large heat generation in the coil, or may cause PM demagnetization. Note that the coil temperature rise is determined by $A_m \times J$, where J is the coil current density. Current density of air cooled motors is $J = 3.5\text{A/mm}^2$ for continuous operation. Therefore, if the cooling method is more efficient, a higher electric loading can be used. For example, $A_m = 150$A/cm for a totally enclosed PM servo motor without a fan. But with water cooling, it can be increased to 600A/cm. Typical range of magnetic and electric loadings are listed in Table 7.1 .

7.1.2 Machine Sizes under the Same Power Rating

Since $P_{gap} = T_e\omega_r$, there are two ways of increasing the motor power: to increase the rated torque or to increase the rated speed. For the same power, rated torque decreases as the base speed increases. Since motor volume is proportional to torque,

motor volume reduces as the rated speed increases. That is, a high-speed motor has a smaller volume for a given power.

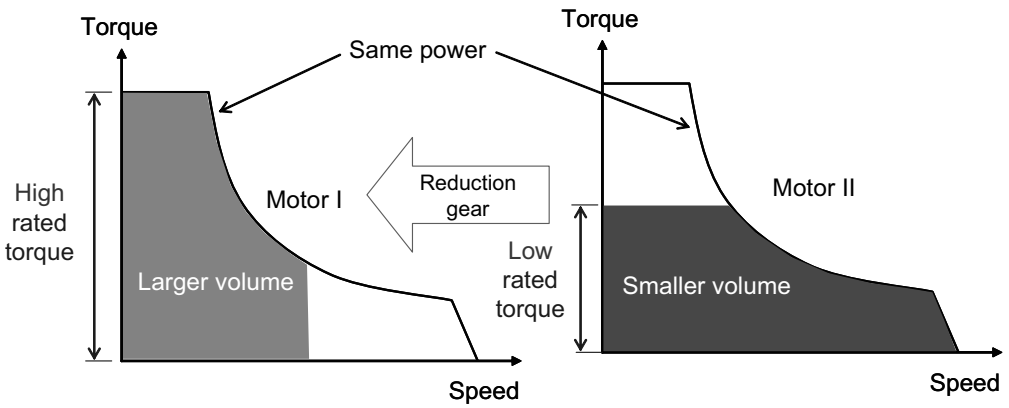

Figure 7.3: Size comparision of high and low-speed motors.

Concerning the motor size comparision, refer to Fig. 7.3, in which two motor operation regions are marked by shaded areas. Note that the two parabola curves, representing the power, are identical. That is, Motor I and Motor II have the same power ratings. There is a trade-off between the rated torque and the maximum speed. Motor I has a high starting (rated) torque but a low maximum speed, whereas Motor II has lower starting (rated) torque but a higher maximum speed. Based on (7.7), Motor I obviously has a larger volume than Motor II.

Note, however, that a high-speed motor can be fit into a desired operation range with a reduction gear. Therefore, a high-speed motor along with a reduction gear offers a reduced volume. Due to this smaller volume merit, there is a tendency to utilize high-speed motors in electric vehicles (EVs). Recently, the maximum electric vehicle (EV) motor speed reached to 13,500rpm (Prius III) [2]. Note that 13,500rpm is nearly the peak speed that roll bearings can endure in the 60kW power range.

7.2 Extending Constant Power Speed Range

Consider the PMSM dynamics:

$$v_d^e = r_s i_d^e + L_d \frac{di_d^e}{dt} - \omega_e L_q i_q^e \tag{7.8}$$

$$v_q^e = r_s i_q^e + L_q \frac{di_q^e}{dt} + \omega_e L_d i_d^e + \omega_e \psi_m. \tag{7.9}$$

Based on (7.8) and (7.9), the current and voltage vectors are depicted as shown in Fig. 7.4 (a) when $i_d < 0$ and $i_q > 0$. Note that the coupling voltage, $\omega_e L_d i_d^e$, is opposite to the back EMF when $i_d^e < 0$. Therefore, increasing i_d^e in the negative direction helps compensating the growing back EMF.

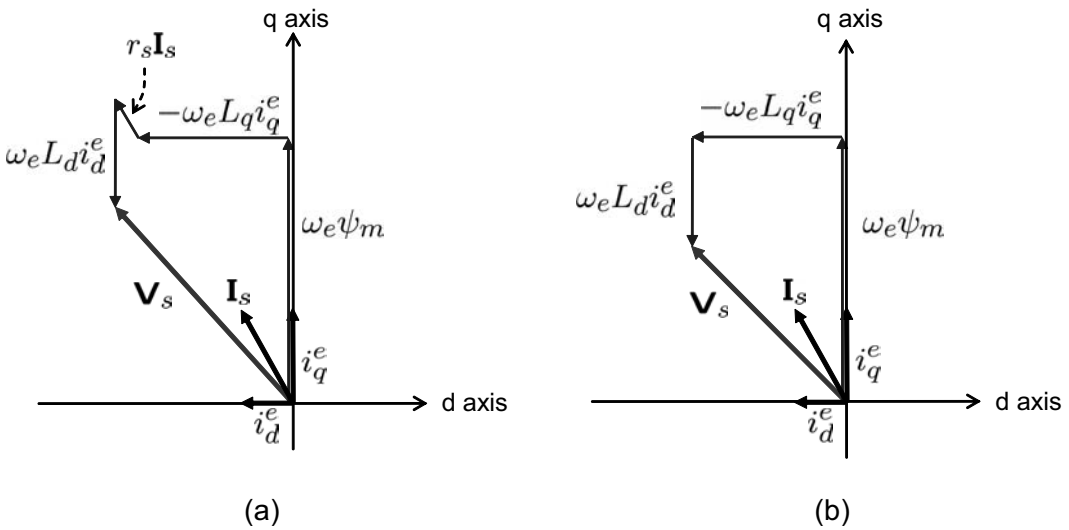

Figure 7.4: Voltage and current vectors in the (i_d^e, i_q^e) plane: (a) with r_s and (b) without r_s.

However, in high-speed region, the voltage drops over stator resistance are relatively small. Neglecting the ohmic voltage drops and assuming the steady-state condition, we have

$$v_d^e = -\omega_e L_q i_q^e \tag{7.10}$$
$$v_q^e = \omega_e L_d i_d^e + \omega_e \psi_m. \tag{7.11}$$

These equations are called lossless model. Based on (7.10) and (7.11), the vector diagram is simplified, as in Fig. 7.4 (b).

At the base speed with a rated load, the terminal voltage reaches the maximum. To increase the speed more, it is necessary to increase the d–axis current in the negative direction at the cost of reducing the q–axis current. With this method, the torque reduces, but the power is kept constant. That constant power range is called constant power speed range (CPSR). The CPSR can be extended infinitely or limited, and it is determined by the relative magnitudes between ψ_m and $L_d I_s$.

Let the magnitude of maximum voltage denoted by V_s. Then the voltage limit is described by

$$v_d^{e\,2} + v_q^{e\,2} \le V_s^2. \tag{7.12}$$

Recall from (6.47) that the rotor flux was described with a virtual current source, i.e., $\psi_m = L_d i_f$. Then, it follows from (7.10), (7.11), and (7.12) that

$$\frac{i_q^{e\,2}}{V_s^2/(\omega_e L_q)^2} + \frac{(i_d^e + i_f)^2}{V_s^2/(\omega_e L_d)^2} \le 1\,. \tag{7.13}$$

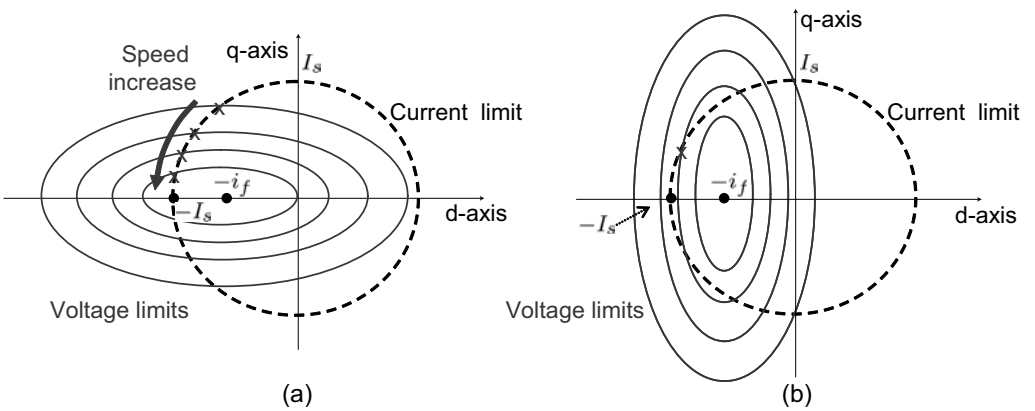

Figure 7.5: Current limit and voltage limits for various speeds in the current plane: (a) $L_d < L_q$ and (b) $L_d > L_q$.

As shown in Fig. 7.5, the voltage limit is described by a bunch of ellipses for different speeds, and the current limit by a circle in the $(i_d^e,\, i_q^e)$ plane:

$$i_d^{e\,2} + i_q^{e\,2} \leq I_s^2. \tag{7.14}$$

It is obvious from (7.13) that the ellipses shrinks to $(-i_f,\, 0)$ as the speed ω increases. Practically feasible solution pairs, $(i_d^e,\, i_q^e)$, exist within the intersecting area of the ellipses and the circle.

Consider $\omega_e L_d i_d^e$ and $\omega_e \psi_m$ in Fig. 7.7. To counteract the growing back EMF, the d–axis current is increased in the negative direction. However, one can see from the intersection points in Fig. 7.5 that the increase of i_d^e (in the negative direction) is obtained at the expense of decreasing q–axis current in the limiting case. That implies that torque needs to be reduced to provide a larger negative d–axis current.

Since i_q^e approaches zero as ω becomes large, it is obvious from voltage limit equation (7.13) that

$$(i_d^e + i_f)^2 \leq \frac{V_s^2}{(L_d \omega_e)^2}\,. \tag{7.15}$$

For sufficiently large ω, the right-hand side of (7.15) vanishes. Therefore, it should follow that $i_d^e \to -i_f$ as $\omega \to \infty$. As was observed in [4], the ability of producing power at infinite speed is determined by the criteria

$$\psi_m = L_d I_s\,. \tag{7.16}$$

Fig. 7.6 shows three cases with the voltage and current limits and power plots versus speed. Specific illustrations for the three cases are summarized in the following: [3]

i) $\psi_m > L_d I_s$: This corresponds to the case where the rotor flux linkage is larger than the maximum field that the stator current can provide. Above the rated

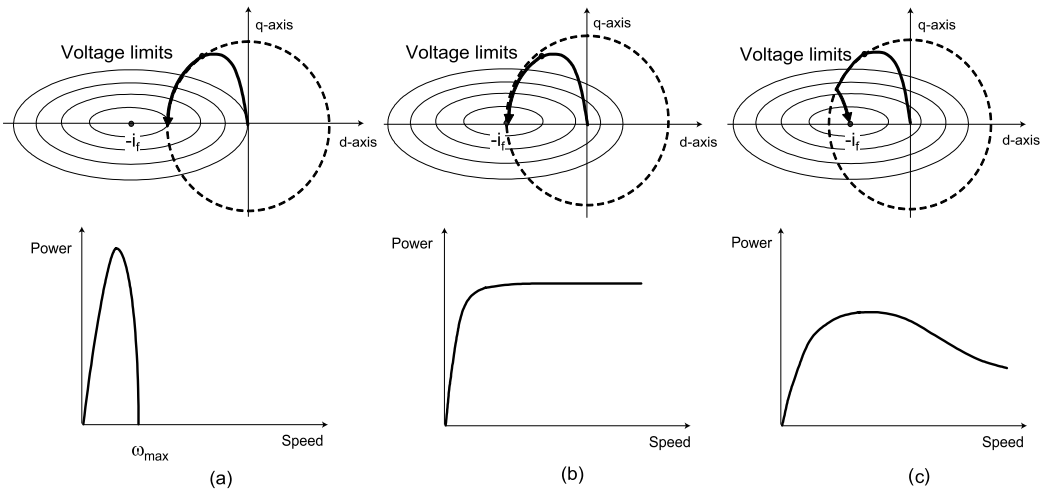

Figure 7.6: Current contours and power versus speed for three cases: (a) $\psi_m > L_d I_s$, (b) $\psi_m = L_d I_s$, and (c) $\psi_m < L_d I_s$.

speed, the power decreases to zero drastically. Since the ellipses' center, $-i_f$ lies out of the current limit, there will be no more intersection above the critical speed defined by

$$\omega_c \equiv \frac{V_s}{\psi_m - L_d I_s}\,. \tag{7.17}$$

That is, the current limit and voltage limit curves are separated for $\omega_e > \omega_c$, so that no proper solution exists.

ii) $\psi_m = L_d I_s$: This is the case where $i_f = I_s$. Since the ellipse center lies on the current limit circle, intersection always exists for any arbitrarily large ω. Thus, the constant power region can be extended to the infinite speed theoretically.

iii) $\psi_m < L_d I_s$: The constant power range will be extended to the infinite speed, too. But, the output power is low compared with the case ii).

This indicates that to expand the CPSR the strength of rotor PM should be balanced with the maximum stator current. Criteria (7.16) is an important guide line in designing the CPSR.

7.2.1 Magnetic and Reluctance Torques

If we fix the magnitude of current, then $(i_d^e,\, i_q^e)$ will be a point on a circle. With polar description, it follows that

$$i_d^e = -I_s \sin\beta, \tag{7.18}$$
$$i_q^e = I_s \cos\beta, \tag{7.19}$$

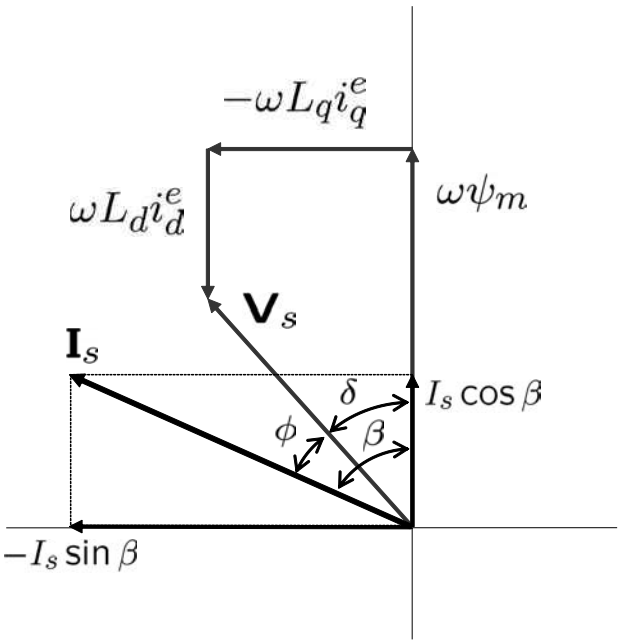

Figure 7.7: Voltage and current angles.

where $I_s = \sqrt{{i_d^e}^2 + {i_q^e}^2}$ and $\beta = \tan^{-1}(-i_d^e/i_q^e)$. Note that β is the angle between the q–axis and the current vector, as shown in Fig. 7.7. Substituting (7.18) and (7.19) into the torque equation (6.48), we have

$$\begin{aligned} T &= \frac{3P}{4}[\psi_m i_q^e - (L_q - L_d) i_d^e i_q^e] \\ &= \frac{3P}{4}[\psi_m I_s \cos\beta + \frac{1}{2}(L_q - L_d) I_s^2 \sin 2\beta]\,. \end{aligned} \tag{7.20}$$

Note that $\frac{3P}{4}\psi_m I_s \cos\beta$ is a magnetic torque that comes from the Lorentz force, whereas $\frac{3P}{4}\frac{1}{2}(L_q - L_d) I_s^2 \sin 2\beta$ is the reluctance torque originated from L_d, L_q asymmetry. Note further that the magnetic torque is a function of $\cos\beta$, while the reluctance torque is a function of $\sin 2\beta$. In order to make the reluctance torque positive when $L_q > L_d$, current angle should be larger than zero, i.e., $\beta > 0$. The corresponding torque versus current angle is shown in Fig. 7.8 (a). On the other hand, if $L_d > L_q$, the peak torque is obtained for $\beta < 0$, as shown in Fig. 7.8 (b). But, the case, $L_d > L_q$ is rare. Thus, we will consider Fig. 7.8 (a) in the following.

Further note that $\beta > 0$ implies that the d–axis current is negative. The relative magnitude of reluctance torque is not small for high β value. Even the reluctance torque component can be made higher than the magnetic torque by increasing the ratio, L_q/L_d.

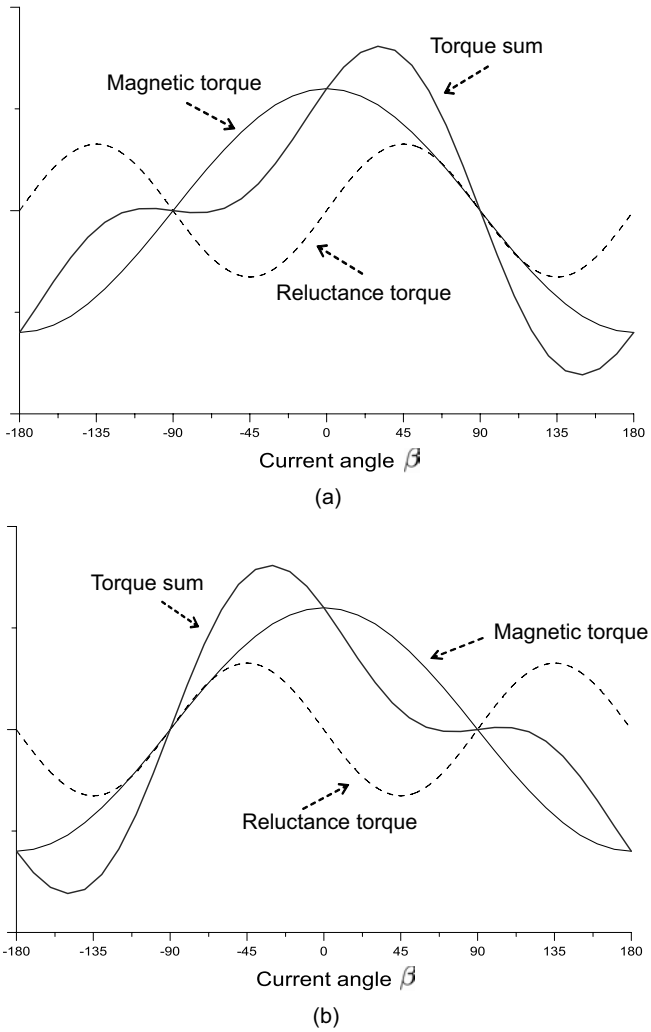

Figure 7.8: Torque sum consisting of magnetic and reluctance torque components: (a) $L_d < L_q$ and (b) $L_d > L_q$.

7.3 Current Control Methods

Since there is no reluctance torque component for SPMSMs, the torque is determined only by q–axis current. However in case of IPSMS, the reluctance torque level is decided by the d–axis current, thereby numerous combinations of (i_d^e, i_q^e) are feasible for a given torque production. Hence, several current selection methods were developed together with current and voltage constraints.

7.3.1 Q-Axis Current Control

This is a simplest control method, by letting $i_d^e = 0$ and taking advantage of a linear relationship between torque and i_q^e. For SPMSM torque control, no other option is possible except the q–axis current control. Since $i_d^e = 0$, no reluctance torque is utilized. Thus, the q–axis current control method is less efficient for IPSMSs.

7.3.2 Maximum Torque per Ampere Control

The maximum torque per ampere (MTPA) control is a method of maximizing the torque for given magnitude of current, as viewed in Fig. 7.9.

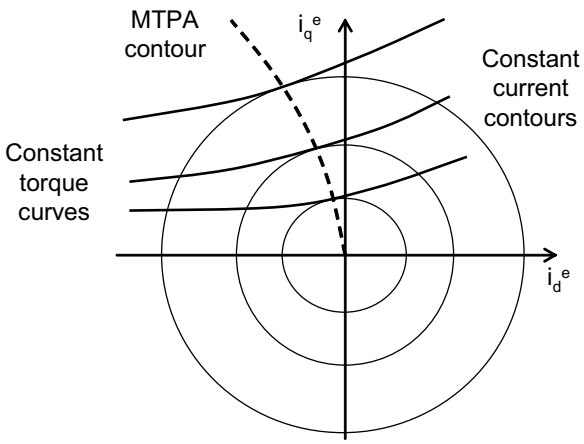

Figure 7.9: MTPA contour.

First, we let the current magnitude be fixed, and change the current angle, β, until the torque is maximized. To obtain the desired angle, we take the differentiation of T with respect to β:

$$\frac{\partial T}{\partial \beta} = \frac{3P}{4}[-\psi_m I_s \sin\beta + (L_q - L_d) I_s^2 \cos 2\beta] = 0\,.$$

Equivalently,

$$2(L_q - L_d) I_s \sin^2\beta + \psi_m \sin\beta - (L_q - L_d) I_s = 0\,.$$

Thus, we have

$$\beta = \sin^{-1}\left[\frac{-\psi_m + \sqrt{\psi_m^2 + 8(L_q - L_d)^2 I_s^2}}{4(L_q - L_d) I_s}\right]. \tag{7.21}$$

Equation (7.21) gives us the current angle for a given current magnitude I_s. Further, since $i_d = -I_s \sin\beta$, we have

$$i_d^e = \frac{1}{4(L_q - L_d)}\left(\psi_m - \sqrt{\psi_m^2 + 8 I_s^2 (L_q - L_d)^2}\right). \tag{7.22}$$

Dotted line in Fig. 7.9 is the MTPA contour when the current magnitude is increasing from zero to I_s. Note that it is the set of points, $\{(-I_s \sin\beta, I_s \cos\beta)\}$, that a torque line intersect a (current) circle tangentially as shown in Fig. 7.9. The MTPA method is widely used in many practical applications since it is simple and minimizes the copper loss. However, this approach cannot be applied above the rated speed due to the voltage limit.

Different Derivation Using Lagrangian

The MTPA is viewed as the torque maximization under the current constraints. Consider power maximization problem under the current limit (7.14):

$$\max_{i_d^e,\, i_q^e} T_e \qquad \text{under} \quad {i_d^e}^2 + {i_q^e}^2 - I_s^2 \le 0.$$

Let the Lagrangian be defined by [6]

$$L(i_d^e,\, i_q^e) = \frac{3P}{4}\left(\psi_m i_q^e + L_d(1-\xi) i_d^e i_q^e\right) + \mu_1\left({i_d^e}^2 + {i_q^e}^2 - I_s^2\right),$$

where $\xi \equiv L_q/L_d$ is the saliency ratio and μ_1 is a Lagrange coefficient. Necessary conditions for the optimality are

$$\frac{\partial L}{\partial i_d^e} = \frac{3P}{4}(1-\xi) L_d i_q^e + 2\mu_1 i_d^e = 0, \tag{7.23}$$

$$\frac{\partial L}{\partial i_q^e} = \frac{3P}{4} L_d\left(i_f + (1-\xi) i_d^e\right) + 2\mu_1 i_q^e = 0. \tag{7.24}$$

Then we obtain from (7.23) and (7.24) that

$$(1-\xi)\left({i_q^e}^2 - {i_d^e}^2\right) - i_f i_d^e = 0.$$

Since the solution is found on the boundary, we utilize the boundary equation ${i_d^e}^2 + {i_q^e}^2 - I_s^2 = 0$. Then, we have the following second-order equation:

$$2(i_d^e)^2 + \frac{i_f}{(1-\xi)} i_d^e - I_s^2 = 0.$$

Thus, the meaningful solution is given by

$$\begin{aligned} i_d^e &= \frac{1}{4(\xi-1)}\left(i_f - \sqrt{i_f^2 + 8I_s^2(\xi-1)^2}\right) \\ &= \frac{1}{4(\xi-1)L_d}\left(\psi_m - \sqrt{\psi_m^2 + 8I_s^2(\xi-1)^2 L_d^2}\right) \quad . \end{aligned} \tag{7.25}$$

This result agrees with the previous solution (7.22).

7.3.3 Maximum Power Control

Motors are designed, in general, to reach the maximum voltage at the rated speed and load conditions. Above the rated speed, the voltage limit forces to increase the current angle, meaning more d–axis current and less q–axis current. Thereby, airgap flux is weakened and torque decreases.

With the lossless motor model (7.10) and (7.11), the power is given by

$$P_e = \frac{3}{2}\left(v_q^e i_q^e + v_d^e i_d^e\right) = \frac{3}{2}\omega_e\left(\psi_m i_q^e + (L_d - L_q) i_d^e i_q^e\right) . \tag{7.26}$$

More formally, the power maximization problem in the field-weakening region is stated as follows:

$$\max_{i_d^e,\, i_q^e} P_e \qquad \text{under} \quad c_1(i_d^e,\, i_q^e) \le 0, \quad c_2(i_d^e,\, i_q^e) \le 0,$$

where

$$\begin{aligned} c_1(i_d^e,\, i_q^e) &= (i_d^e)^2 + (i_q^e)^2 - I_s^2, \\ c_2(i_d^e,\, i_q^e) &= \xi^2 (i_q^e)^2 + (i_d^e + \frac{\psi_m}{L_d})^2 - \frac{V_s^2}{\omega^2 L_d^2}. \end{aligned}$$

Note that the power maximization for a given speed is the same as the torque maximization. It is obvious from a geometric viewpoint that the maximum solution is found at an intersection point of the two curves, $c_1 = 0$ and $c_2 = 0$. Note also that the intersection point satisfies the necessary conditions of Kuhn−Tucker theorem [6]. Substituting ${i_q^e}^2 = I_s^2 - {i_d^e}^2$ into equation $c_2 = 0$, it follows that

$$0 = (1 - \xi^2){i_d^e}^2 + 2\frac{\psi_m}{L_d} i_d^e + \frac{\psi_m^2}{L_d^2} + \xi^2 I_s^2 - \frac{V^2}{\omega^2 L_d^2}.$$

Since the intersection point in the second quadrant is meaningful, we just need to consider the negative i_d^e solution. Thus, we have

$$i_d^e = \frac{1}{(\xi^2 - 1)}\left(\frac{\psi_m}{L_d} - \sqrt{\xi^2 \frac{\psi_m^2}{L_d^2} + (\xi^2 - 1)(\xi^2 I_s^2 - \frac{V^2}{\omega^2 L_d^2})}\right), \tag{7.27}$$

$$i_q^{e*} = \sqrt{I_s^2 - {i_d^{e*}}^2}. \tag{7.28}$$

Intersection points of the current limit circle and voltage limit ellipses make the loci of maximum powers versus speed. That is, the maximum power is obtained along the current limit circle $c_1(i_d^e,\, i_q^e) = 0$.

7.3.4 Maximum Torque/Flux Control

This control strategy is applicable to the last step in high-speed operation when $I_s > \psi_m/L_d$. At an extreme high speed, voltage limit shrinks to a point $(-\frac{\psi_m}{L_d}, 0)$. Correspondingly, the operation points, determined on the voltage limit curve, converge to $(-\frac{\psi_m}{L_d}, 0)$.

Let the d–axis flux denoted by $\lambda_d \equiv L_d i_d^e + \psi_m$. Then, flux equation follows from the voltage limit, (7.13):

$$(L_q i_q^e)^2 + \lambda_d^2 = (V_s/\omega_e)^2. \tag{7.29}$$

A maximum torque for a given flux level is obtained at a point where the voltage limit and torque curves intersect tangentially. Therefore, the curve consists of the tangential intersection points between the torque and voltage limit curves.

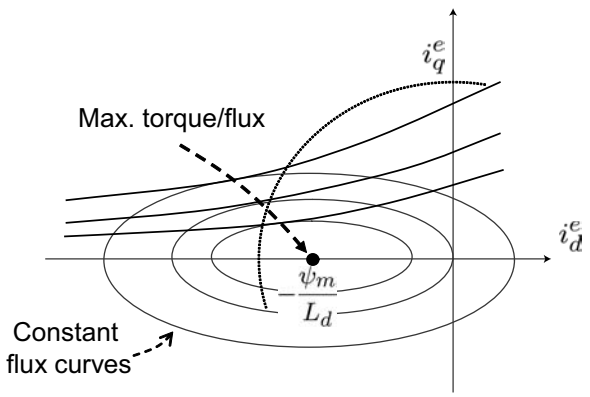

Figure 7.10: Maximum torque per flux solutions.

Substituting (7.29) into torque equation (7.20), it follows that

$$T_e^2 = \left(\frac{3P}{4}\right)^2 \left(\lambda_d - L_q \frac{\lambda_d - \psi_m}{L_d}\right)^2 \frac{(V_s/\omega_e)^2 - \lambda_d^2}{L_q^2}.$$

Taking differentiation with respect to λ_d and making it equal to zero result in [5]

$$\lambda_d = \frac{-L_q\psi_m + \sqrt{L_q^2\psi_m^2 + 8(L_d - L_q)^2(V_s/\omega_e)^2}}{4(L_d - L_q)}.$$

Therefore, the torque/flux maximizing solution is given by

$$i_d^e = \frac{\lambda_d - \psi_m}{L_d} \tag{7.30}$$

$$i_q^e = \frac{\sqrt{(V_s/\omega_e)^2 - \lambda_d^2}}{L_q}. \tag{7.31}$$

Fig. 7.10 shows the solution contour when $\psi_m - L_d I_s < 0$. In the limiting case, λ_d vanishes, i.e., $i_d^e \to -\psi_m/L_d$ and $i_q^e \to 0$ as $\omega_e \to \infty$.

Table 7.2: An example IPMSM specifications.

No. of poles	6	Power (rated)	8.8 kW
DC link voltage	300V	Base speed	2600rpm
Inductance (L_d)	3.05 mH	Current (rated)	40A
Inductance (L_q)	6.2 mH	Flux (ψ_m)	0.0948Wb

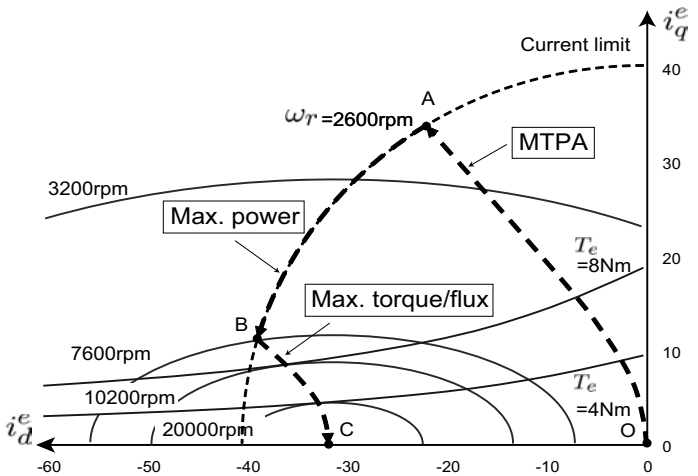

Figure 7.11: Combination of control strategies: $\overline{OA}$: MTPA, $\overline{AB}$: maximum power, and $\overline{BC}$: maximum torque/flux .

7.3.5 Combination of Control Methods

Fig. 7.11 shows a control sequence consisting of MTPA, maximum power, and maximum torque/flux contours for an IPMSM. The motor parameters are shown in Table 7.2. Within the base speed range, it is desirable to operate along the MTPA line from the efficiency view point. Beyond the base speed, the maximum power is determined along an segment, $\overline{AB}$ of the current limit circle. As the motor speed increases, the voltage limit ellipse shrinks. From point "B," the operation point follows the maximum torque/flux line, $\overline{BC}$.

Fig. 7.12 shows the corresponding torque and power plots over $\overline{AB}$ and $\overline{BC}$. In this plot, constant current, $(i_d^e, i_q^e) = (-22, 34)$, was applied from zero speed until the point "A" was reached. Note that the power reduces along the maximum torque/flux line.

7.3.6 Unity Power Factor Control

Depending upon the combination of i_d and i_q, the unity power factor (PF) can be obtained in the high-speed region. The unity PF condition is related to the use of

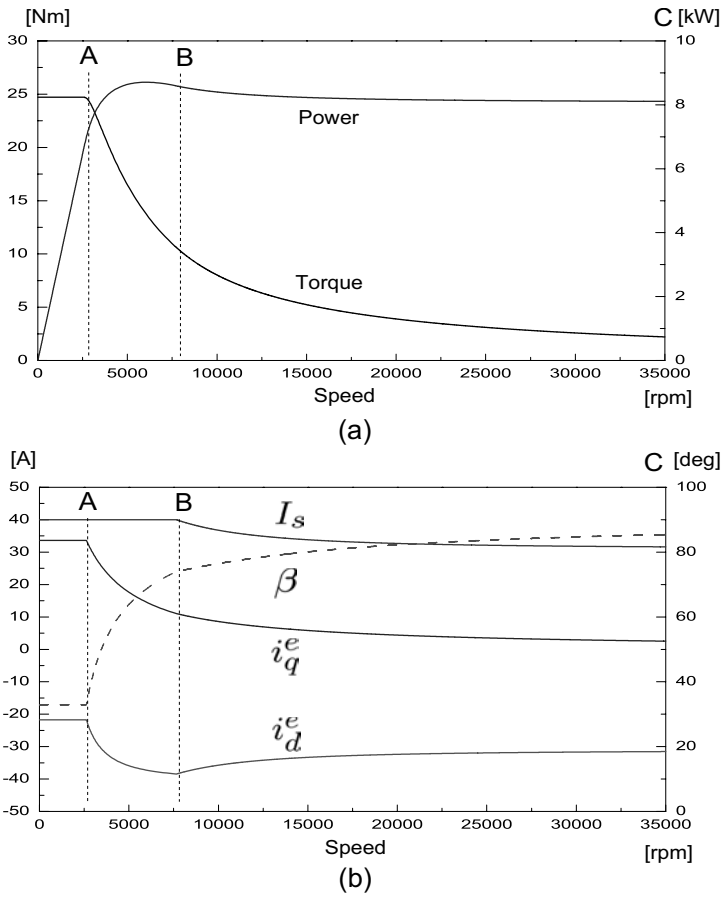

Figure 7.12: IPMSM characteristics versus speed: (a) torque and power plots and (b) current and current angle. From zero speed to "A": constant current, $\overline{AB}$: maximum power, and $\overline{BC}$: maximum torque/flux).

minimum current vector, thereby to the loss minimization problem. In the sequel, the unity PF condition is derived and interpreted geometrically.

From the geometry shown in Fig. 7.7, it follows that

$$\delta = \tan^{-1}\left(\frac{-v_d^e}{v_q^e}\right) = \tan^{-1}\left(\frac{\omega_e L_q i_q^e}{\omega_e \psi_m + \omega_e L_d i_d^e}\right) \tag{7.32}$$

$$\beta = \tan^{-1}\left(\frac{-i_d^e}{i_q^e}\right). \tag{7.33}$$

At the unity PF, current angle and voltage angle are the same, i.e., $\delta = \beta$. Therefore, it follows from (7.32) and (7.33) that

$$\frac{\xi i_q^e}{i_f + i_d^e} = \frac{-i_d^e}{i_q^e}. \tag{7.34}$$

Rearranging (7.34), unity PF condition is given by

$$\frac{{i_q^e}^2}{(\frac{i_f}{2\sqrt{\xi}})^2} + \frac{(i_d^e + \frac{i_f}{2})^2}{(\frac{i_f}{2})^2} = 1. \tag{7.35}$$

That is, the unity PF condition is described as an ellipse with center $(-\frac{i_f}{2}, 0)$ that passes through the origin and $(-i_f, 0)$. Since the minor axis is $\frac{i_f}{2\sqrt{\xi}}$, the shape of unity PF ellipse is pressed as the saliency ratio, ξ, increases.

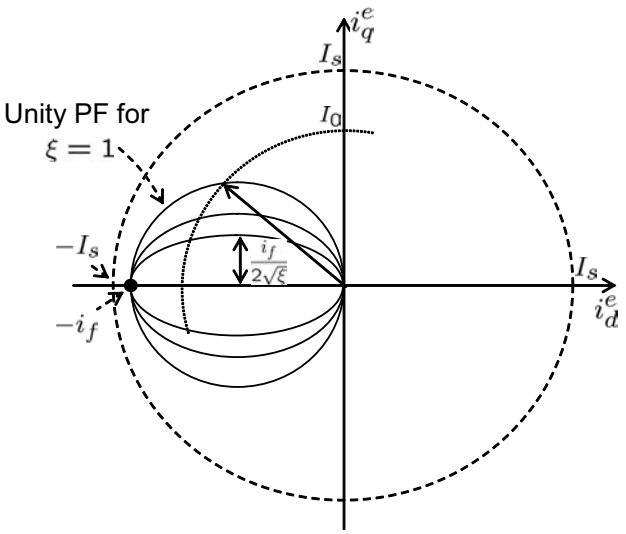

Figure 7.13: Unity PF ellipses for different saliency ratios, ξ's.

It is obvious that no unity PF solution exists when $I_0 > i_f$, Since ${i_q^e}^2 = I_0^2 - {i_d^e}^2$, we obtain from (7.34) that for $I_0 < i_f$

$$(\xi - 1){i_d^e}^2 - i_f i_d^e - \xi I_0^2 = 0\,. \tag{7.36}$$

Thus, the d–axis current at unity PF is

$$i_d^{e\,*} = \frac{i_f - \sqrt{i_f^2 + 4\xi(\xi-1)I_0^2}}{2(\xi - 1)}\,. \tag{7.37}$$

Note that $i_d^{e\,*}$ is dependent upon ψ_m/L_d, saliency, and the current magnitude.

In the following, the unity PF solution is calculated for a simple case, $\xi = 1$, where there is no saliency. When $\xi = 1$, the unity PF curve (7.35) turns out to be a circle, as shown in Fig. 7.14, The beauty of this case is that $i_d^{e\,*}$ and $i_q^{e\,*}$ are obtained directly from the geometric relationship. By applying the cosine law to the triangle ABO in Fig. 7.14, we obtain

$$\theta = \cos^{-1}\left(\frac{\frac{i_f^2}{4} + \frac{i_f^2}{4} - I_0^2}{2\,\frac{i_f}{2}\cdot\frac{i_f}{2}}\right) = \cos^{-1}\left(\frac{\frac{i_f^2}{2} - I_0^2}{\frac{i_f^2}{2}}\right)\,. \tag{7.38}$$

Note that triangle ABO is an isosceles triangle, hence the unity PF current angle is $\beta^* = \frac{\pi}{2} - \frac{\pi-\theta}{2}$. Therefore,

$$\beta^* = \frac{1}{2}\cos^{-1}\left(1 - 2\frac{I_0^2}{i_f^2}\right). \tag{7.39}$$

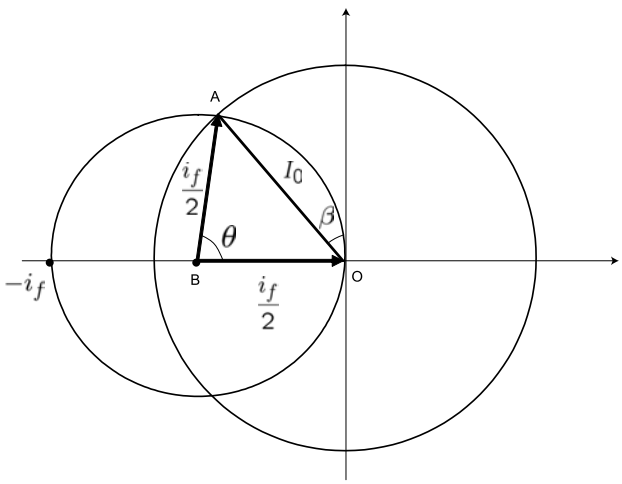

Figure 7.14: Application of the cosine law to unity PF condition when $\xi = 1$.

Exercise 7.1
Calculate the dq-axes currents yielding the unity PF when $\xi = 1$ and $I_0 < i_f$.

Solution

$$i_d^{e\,*} = -\frac{I_0^2}{i_f}, \qquad i_q^{e\,*} = I_0\sqrt{1 - \frac{I_0^2}{i_f^2}}.$$

■

Exercise 7.2
a) Determine the motor terminal voltage at point "A" ($i_d^e = -22$A, $i_q^e = 34$A, and 2600 rpm) of Fig. 7.11.
b) Calculate the power factor at "A".
c) Draw voltage and current vectors.

Solution
a) The electrical speed is $\frac{2600}{60} \times 2\pi \times 3 = 817$rad/sec.
The back EMF is equal to $\omega_e \psi_m = 817 \times 0.0948 = 77.5$V.
At the same time,

$$\begin{aligned} \omega_e L_d i_d^e &= 817 \times 0.00305 \times (-22) = -54.8\text{V} \\ \omega_e L_q i_q^e &= 817 \times 0.0062 \times 34 = 172\text{V}. \end{aligned}$$

The terminal voltage is

$$V_s = \sqrt{(\psi_m \omega_e + \omega_e L_d i_d^e)^2 + (\omega_e L_q i_q^e)^2} = \sqrt{(77.5 - 54.8)^2 + 172^2} = 173.5\text{V}.$$

b)

$$\begin{aligned} \delta &= \tan^{-1}\left(\frac{172}{77.5 - 54.8}\right) = 82.5^\circ \\ \beta &= \tan^{-1}\left(\frac{22}{34}\right) = 32.9^\circ \\ \text{PF} &= \cos(\beta - \delta) = \cos(-49.6^\circ) = 0.65. \end{aligned}$$

c) See Fig. 7.15 ■

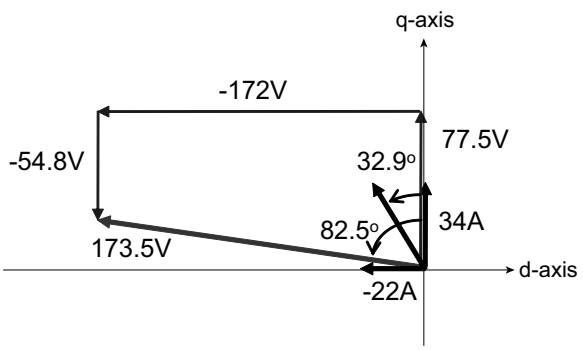

Figure 7.15: Vector diagram (Exercise 7.2).

Fig. 7.16 shows how the power profile and PF change as the strength of the rotor PM changes. The results were obtained using the IPMSM parameters listed in Table 7.2. Since $I_s = 40$A, the condition, $\psi_m = L_d I_s$ is satisfied when $\psi_m / L_d = 40$A. Note that the power is extended infinitely with the unity PF when $\psi_m / L_d = 40$A. If $\psi_m / L_d = 52$A, the power drops rapidly in high-speed region. Obviously, the strong PM field is useful for high torque in the low-speed region. Note also that the peak power is obtained near 5000rpm where the PF angle is zero.

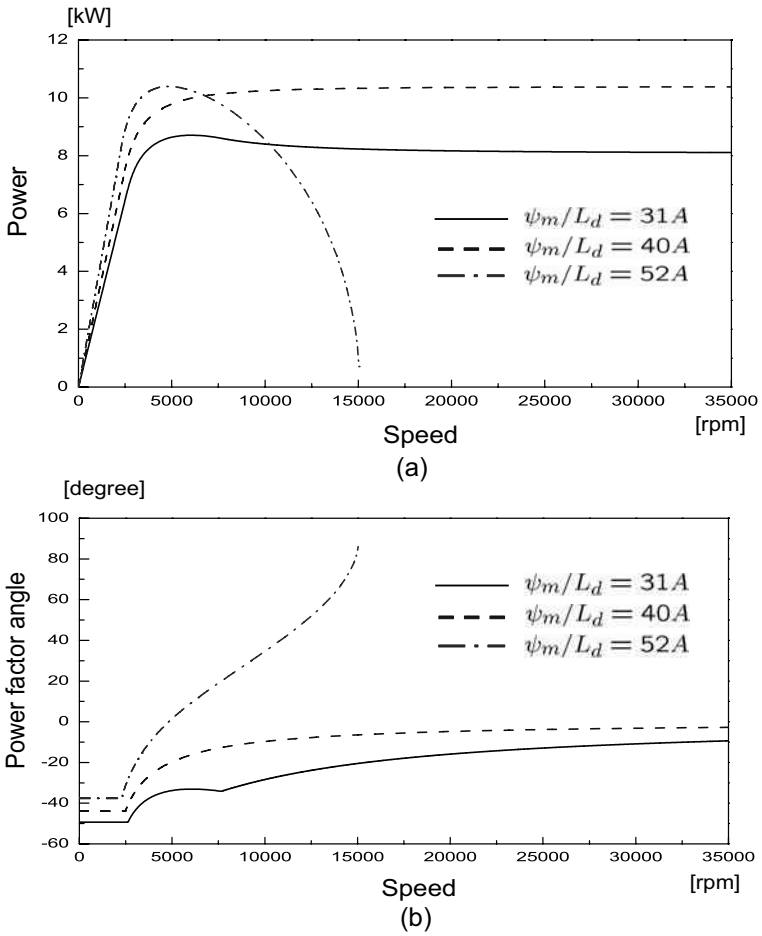

Figure 7.16: Power and PF profile change versus speed when ψ_m changes: (a) Power profile and (b) PF profile.

Exercise 7.3
a) Determine torque at point "B" ($i_d^e = -38.5$A, $i_q^e = 11$A, and 7600 rpm) of Fig. 7.11.
b) Determine also the ratio of reluctance torque to magnetic torque.
c) Calculate the power.

Solution
a)

$$\begin{aligned} T_e &= \frac{3P}{4}\left(\psi_m i_q^e + (L_d - L_q) i_d^e i_q^e\right) \\ &= \frac{18}{4}\left(0.0948 \times 11 + (-0.00315) \times (-38.5) \times 11\right) = 10.7\text{Nm}. \end{aligned}$$

b) The ratio of reluctance torque to magnetic torque = 1.28, i.e., the reluctance torque is 28% larger than the magnetic torque.
c) $P_e = 10.7 \times \frac{7600}{60} \times 2\pi = 8.5\text{kW}$. ■

7.4 Properties When $\psi_m = L_d I_s$

With constant power condition $\psi_m = L_d I_s$, voltage limit is described by an ellipse with center $(i_d^e, i_d^e) = (-I_s, 0)$.

$$\frac{(i_q^e)^2}{V_s^2/(\omega_e \xi L_d)^2} + \frac{(i_d^e + I_s)^2}{V_s^2/(\omega_e L_d)^2} \quad \leq \quad 1. \tag{7.40}$$

Hence, as ω increases, the ellipse shrinks down to the point $(-I_s, 0)$. Hence, the CPSR can be extended to infinite speed if $\psi_m = L_d I_s$.

Further, theorems like optimality can be proved easily if $\psi_m = L_d I_s$ satisfied. In this section, some properties are investigated theoretically. First we consider the Kuhn−Tucker theorem, which provides necessary conditions for the optimality under inequality constraints.

Kuhn−Tucker Theorem for Local Maxima [6]**.** Let $f : U \to \mathbb{R}$ be a C^1 function on a certain open set $U \in \mathbb{R}^n$, and let $h_i : \mathbb{R}^n \to \mathbb{R}, \quad i = 1, ..., \ell$, be C^1 functions. Suppose x^* is a local maximum of f on the set $D = U \cap \{x \in \mathbb{R}^n \mid h_i(x) \leq 0, \quad i = 1, ..., \ell\}$. Then there exist $\mu_1^*, ..., \mu_\ell^* \in \mathbb{R}$ such that

i) $\mu_i^* \leq 0$, for $i = 1, ..., \ell$;

ii) $\mu_i^* h_i(x^*) = 0$, for $i = 1, ..., \ell$;

iii) $\frac{\partial}{\partial x} f(x^*) + \sum_{i=1}^{\ell} \mu_i^* \frac{\partial}{\partial x} h_i(x_i^*) = 0$.

The coefficients $\mu_1, \cdots, \mu_\ell$ are called Kuhn−Tucker (K-T) multipliers and have the similar meaning to the Lagrangian multipliers. Note that x^* is on the boundary or interior of D. Hence, condition *ii)* states that either x^* is a point of the boundary $h_i = 0$, or an interior point ($h_i < 0$) to $h_i = 0$. In the latter case, the constraint is meaningless, and thus condition *i)* requires that the corresponding K-T multiplier be zero, i.e., $\mu_i = 0$. Therefore, it is called the complementary slackness condition. Condition *iii)* sets the first partial derivatives of f is equal to a linear combination of gradient vectors, $\frac{\partial h}{\partial x}$ of constraint functions at the Kuhn−Tucker point, x^*. ■

If $\psi_m = L_d I_s$, solution (7.27) and (7.28) reduces to

$$i_d^{e*} = \frac{1}{\xi^2 - 1} \left(I_s - \sqrt{\xi^4 I_s^2 - \frac{V^2}{\omega^2 L_d^2}(\xi^2 - 1)} \right). \tag{7.41}$$

Utilizing $i_q^{e*} = \sqrt{I_s^2 - i_d^{e*\,2}}$, it follows that

$$i_q^{e*} = \frac{1}{\xi^2 - 1}\sqrt{-2\xi^2 I_s^2 + \frac{V^2}{\omega^2 L_d^2}(\xi^2 - 1) + 2I_s\sqrt{\xi^4 I_s^2 - \frac{V^2}{\omega^2 L_d^2}(\xi^2 - 1)}}\,. \tag{7.42}$$

Solution pair (7.41) and (7.42) are the power maximizing solutions for a given speed ω.

Theorem 1. Suppose that $i_d^e \le -I_s/\sqrt{2}$, $i_q^e > 0$, and that $\xi \ge 1$. Then for a given speed ω, the intersection point (7.41) and (7.42) of curves $c_1(i_d^e,\, i_q^e) = 0$ and $c_2(i_d^e,\, i_q^e) = 0$ maximizes P_e subject to $c_1 \le 0$ and $c_2 \le 0$.

Proof. Firstly, we need to show that necessary conditions *i), ii)*, and *iii)* of the Kuhn−Tucker Theorem are satisfied: Condition *iii)* yields

$$\frac{\partial L}{\partial i_d^e} = \frac{3}{2}\omega_e(1-\xi)L_d i_q^e + 2\mu_1 i_d^e + 2\mu_2(i_d^e + I_s) = 0, \tag{7.43}$$

$$\frac{\partial L}{\partial i_q^e} = \frac{3}{2}\omega_e L_d\,(i_f + (1-\xi)i_d^e) + 2\mu_1 i_q^e + 2\mu_2\xi^2 i_q^e = 0. \tag{7.44}$$

We obtain from (7.43) and (7.44) that

$$\mu_2 = \frac{3}{2}\omega_e L_d \frac{(2i_d^2 - I_s^2)(1-\xi) + i_f i_d^e}{2i_q^e\left[(1-\xi^2)i_d^e + I_s\right]}$$

$$\mu_1 = \frac{\frac{3}{2}\omega_e(\xi - 1)L_d i_q^e - 2\mu_2(i_d^e + I_s)}{2i_d^e}.$$

Therefore, $\mu_1 < 0$ and $\mu_2 < 0$ by the assumptions, i.e., Condition *i)* follows. This implies that both constraints are effective, i.e., the maximizing solution is obtained at intersection of boundaries. Thus, the solution given by (7.41) and (7.42) is the power maximizing solution. ∎

Assumption $i_d^e \le -I_s/\sqrt{2}$ implies that current angle is larger than 45 degrees, i.e., $\beta \ge 45°$. From the numerator of μ_2 being positive we obtain a more relaxed inequality:

$$i_d^e \le \frac{i_f - \sqrt{i_f^2 + 8(\xi-1)^2 I_s^2}}{4(\xi - 1)}. \tag{7.45}$$

According to Theorem 1, maximum power versus speed moves along the intersection of the voltage and current limits. The loci may be represented by $\{\max_{c_1,\,c_2\le 0} P_e(\omega_e) \mid \omega_b \le \omega_e\}$, where ω_b is a base speed. As far as the operating point is on that loci, V_s and I_s remain the same. Hence, power depends only on the PF, and the maximum value is equal to $\frac{3}{2}V_s I_s$.

7.4.1 Maximum Power and Power Factor

With the above polar coordinate representation, power is equal to

$$\begin{aligned} P_e &= \frac{3}{2}\left(v_q^e i_q^e + v_d^e i_d^e\right) \\ &= \frac{3}{2}\left(\omega_e \psi_m I_s \cos\beta - \omega_e \frac{L_d - L_q}{2} I_s^2 \sin 2\beta\right). \end{aligned} \tag{7.46}$$

Utilizing the notion of inner product, (7.46) can be expressed equivalently as

$$P_e = \frac{3}{2}\mathbf{V_s}\cdot\mathbf{I_s} = \frac{3}{2}V_s I_s \cos\phi, \tag{7.47}$$

where $\mathbf{V_s}$ and $\mathbf{I_s}$ are stator voltage vector and current vector, respectively.

In this section, it is demonstrated that if $\psi_m = L_d I_s$, then the unity PF is obtained at infinite speed. Note from Fig. 7.7 that

$$\begin{aligned} \mathbf{V_s} &= V_s\angle\delta + 90^\circ = v_d^e + j v_q^e, \\ \mathbf{I_s} &= I_s\angle\beta + 90^\circ = i_d^e + j i_q^e, \end{aligned}$$

where current and voltage angles are denoted by β and δ, respectively.

Theorem 2. Consider lossless PMSM model (7.10) and (7.11) with current limit, $c_1(i_d^e, i_q^e) \le 0$ and voltage limit, $c_2(i_d^e, i_q^e) \le 0$. Suppose that $\psi_m = L_d I_s$. Along the power curve $\{\max_{c_1, c_2 \le 0} P_e(\omega_e) \mid \omega_b \le \omega_e\}$, PF converges to unity as speed ω goes to infinity. Correspondingly, the maximum power is obtained at infinite speed, i.e.,

$$\lim_{\omega_e \to \infty} \{\max_{c_1, c_2 \le 0} P_e(\omega_e)\} = \frac{3}{2} V_s I_s.$$

Proof. As speed increases, the voltage ellipse shrinks to the center $(-I_s, 0)$. Since the solution is given at the intersection, the current vector rotates to the negative d–axis in the second quadrant. Specifically, the current vector converges to $(-I_s, 0)$. Therefore, β approaches to 90° as $\omega_e \to \infty$. That is,

$$\lim_{\omega_e \to \infty} \mathbf{I_s} = I_s\angle 180^\circ. \tag{7.48}$$

On the other hand, it follows from (7.10) and (7.11) that

$$\begin{aligned} V_s &= \sqrt{(v_q^e)^2 + (v_d^e)^2} \\ &= \omega_e L_d I_s \sqrt{(1 - \sin\beta)^2 + \xi^2 \cos^2\beta}. \end{aligned} \tag{7.49}$$

Note that

$$\begin{aligned} \frac{V_s^2}{L_d^2 I_s^2} &= \omega^2[(1 - \sin\beta)^2 + \xi^2\cos^2\beta] \\ &= \omega^2[2(1 - \sin\beta) + (\xi^2 - 1)\cos^2\beta] \\ &= \omega^2(1 - \sin\beta)[2 + (\xi^2 - 1)(1 + \sin\beta)]. \end{aligned}$$

Hence, it follows that for a constant $\alpha > 0$

$$\lim_{\substack{\omega_e \to \infty \\ \beta \to 90^\circ}} \omega^2(1 - \sin\beta) = \frac{V_s^2}{2\xi^2 L_d^2 I_s^2} \equiv \alpha\,. \tag{7.50}$$

Utilizing (7.50), we obtain

$$\begin{aligned} \lim_{\substack{\omega_e \to \infty \\ \beta \to 90^\circ}} v_d^e &= \lim_{\substack{\omega_e \to \infty \\ \beta \to 90^\circ}} \omega_e L_q I_s \cos\beta \\ &= \lim_{\substack{\omega_e \to \infty \\ \beta \to 90^\circ}} \omega_e L_q I_s \sqrt{1 - \sin\beta}\sqrt{1 + \sin\beta} \\ &= \sqrt{2\alpha} L_q I_s = V_s\,. \end{aligned}$$

Therefore, it follows from (7.49) that $\lim_{\omega_e \to \infty} v_q^e = 0$. This, in turn, implies that voltage angle δ converges to 90°, i.e.,

$$\lim_{\substack{\omega_e \to \infty \\ \beta \to 90^\circ}} \mathbf{V_s} = V_s \angle 180^\circ. \tag{7.51}$$

Hence, unity PF at infinite speed follows from (7.48) and (7.51).

On the other hand, it follows from (7.46) and (7.50) that

$$\begin{aligned} &\lim_{\substack{\omega_e \to \infty \\ \beta \to 90^\circ}} P_e \\ = &\lim_{\substack{\omega_e \to \infty \\ \beta \to 90^\circ}} \frac{3}{2}\left[\omega_e L_d I_s^2 \cos\beta(1 - \sin\beta) + \omega_e L_q I_s^2 \sin\beta\cos\beta\right] \\ = &\lim_{\substack{\omega_e \to \infty \\ \beta \to 90^\circ}} \frac{3}{2}\left[\frac{L_d I_s^2 \cos\beta}{\omega_e}\alpha + L_q I_s^2 \omega_e \sin\beta\sqrt{1 - \sin^2\beta}\,\right] \\ = &\frac{3}{2}\sqrt{2} L_q I_s^2 \sqrt{\alpha} = \frac{3}{2} V_s I_s\,. \end{aligned}$$

■

7.5 Per Unit Model of the PMSM

The base values are chosen to give one per unit stator current and flux at one per unit speed when a rated current gives the maximum (rated) torque. The scaled values are denoted with subscript "pu". The DC link voltage of the inverter is denoted by V_{dc}. The maximum voltage is reached when the base torque is produced at the base frequency. Thus, the base voltage, V_b, is calculated as the maximum phase voltage

that can be synthesized by the inverter:

$$\begin{aligned}
\text{voltage} &: V_b = \frac{V_{dc}}{\sqrt{3}} \\
\text{current} &: I_b = \sqrt{i_{db}^2 + i_{qb}^2} \\
\text{flux linkage} &: \psi_b = \sqrt{(\psi_m + L_d i_{db})^2 + (L_q i_{qb})^2} \\
\text{frequency} &: \omega_b = \frac{V_b}{\psi_b} \\
\text{inductance} &: L_b = \frac{\psi_b}{I_b}.
\end{aligned}$$

A normalized dq model is

$$\begin{aligned}
v_{dn} = \frac{v_d}{V_b} &= -\frac{\omega_e \xi L_d i_q}{\omega_b \psi_b} = -\frac{\omega_e \xi L_d i_q}{\omega_b L_b I_b} = -\omega_n \xi L_{dn} i_{qn} \\
v_{qn} = \frac{v_q}{V_b} &= \frac{\omega_e L_d i_d + \omega_e \psi_m}{\omega_b \psi_b} = \frac{\omega_e L_d i_d}{\omega_b L_b I_b} + \frac{\omega_e \psi_m}{\omega_b \psi_b} = \omega_n L_{dn} i_{dn} + \omega_n \psi_n,
\end{aligned}$$

where

$$\begin{aligned}
\omega_n &= \frac{\omega_e}{\omega_b} \\
L_{dn} &= \frac{L_d}{L_b} = \frac{\omega_b L_d I_b}{V_b}, \quad L_{qn} = \frac{L_q}{L_b} = \frac{\omega_b L_q I_b}{V_b}, \\
v_{dn} &= \frac{v_d}{V_b}, \quad v_{qn} = \frac{v_q}{V_b}, \\
i_{dn} &= \frac{i_d}{I_b}, \quad i_{qn} = \frac{i_q}{I_b}, \\
\psi_n &= \frac{\psi_m}{\psi_b}.
\end{aligned}$$

Since $P_{en} = v_{dn} i_{dn} + v_{qn} i_{qn}$ and $T_n = P_{en}/\omega_n$, the final normalized dq model turns out to be [3]

$$v_{dn} = -\omega_n \xi L_{dn} i_{qn}, \tag{7.52}$$

$$v_{qn} = \omega_n L_{dn} i_{dn} + \omega_n \psi_n, \tag{7.53}$$

$$T_n = \psi_n i_{qn} - (\xi - 1) L_{dn} i_{dn} i_{qn}. \tag{7.54}$$

The normalized torque equation, (7.54), indicates to us that ψ_n can be traded partially with ξ. If ξ is increased, then ψ can be reduced correspondingly. That is, the use of permanent magnet can be reduced as the saliency ratio increases. Since the cost of PM material, typically neodymium or samarium-cobalt, is high, it motivates us to design high saliency ratio motors. But, due to the mechanical strength requirements and manufacturing complexity, it is not easy to increase ξ more than 3.

Exercise 7.4
Consider an "IPMSM-A" with the following parameters: 6-pole, $L_d = 3$mH, $L_q = 6.2$mH, $\psi_m = 0.146$Wb, $\omega_b = 816.8$rad/sec, and $i_{db} = -22$A, $i_{qb} = 34$A.

a) Calculate the normalized model.
b) Show that $v_{dn}^2 + v_{qn}^2 = 1$ when $\omega_n = 1$.

Solution

a)

$$\begin{aligned}
\xi &= \frac{0.0062}{0.003} = 2.07 \\
\psi_b &= \sqrt{(0.146 - 0.003 \times 22)^2 + (0.0062 \times 34)^2} = 0.225 \\
V_b &= \omega_b \psi_b = 816.8 \times 0.225 = 183.78 \\
I_b &= \sqrt{22^2 + 34^2} = 40 \\
L_{dn} &= \frac{\omega_b L_d I_b}{V_b} = \frac{816.8 \times 0.003 \times 40}{183.78} = 0.533 \\
\psi_n &= \frac{\psi_m}{\psi_b} = \frac{0.146}{0.225} = 0.649
\end{aligned}$$

$$\begin{aligned}
v_{dn} &= -1.1\omega_n i_{qn}, \\
v_{qn} &= 0.533\omega_n i_{dn} + 0.649\omega_n, \\
T_n &= 0.649 i_{qn} - 0.57 i_{dn} i_{qn}.
\end{aligned}$$

b) $v_{dn}^2 + v_{qn}^2 = (1.1 \times 0.85)^2 + (0.649 - 0.533 \times 0.55)^2 = 1.$ ■

7.5.1 Power-Speed Curve

If the rotor flux is strong such that $\psi_m > L_d I_b$, then the speed range cannot be extended indefinitely. The critical speed, ω_c, is defined by the speed at which power drops to zero. At ω_c, the q–axis current is equal to zero, while $i_b^e = I_b$. Therefore, it follows from (7.17) that at the critical speed

$$\frac{\omega_c \psi_m}{\omega_b \psi_b} - \frac{\omega_c L_d I_b}{V_b} = \frac{V_b}{V_b} \qquad \Rightarrow \qquad \psi_n - L_{dn} = \frac{1}{\omega_{cn}}, \tag{7.55}$$

where $\omega_{cn} \equiv \frac{\omega_c}{\omega_b}$. It should be noted that the critical speed is inversely proportional to $\psi_n - L_{dn}$.

Exercise 7.5
Consider "IPMSM-A" whose parameters listed in Exercise 7.4. Determine ω_c in rpm.

Solution

$$\begin{aligned} \omega_{cn} &= \frac{1}{\psi_n - L_{dn}} = \frac{1}{0.649 - 0.533} = 8.62 \\ \omega_c &= 8.62 \times 2600 = 22412\text{rpm}. \end{aligned}$$

■

Exercise 7.6
Consider "IPMSM-B" whose parameters are the same as those of "IPMSM-A" except $\psi_m = 0.16$Wb.
a) Determine ω_{cn}.
b) Plot the power curves of "IPMSM-A" and "IPMSM-B".

Solution

$$\begin{aligned} \psi_n &= \frac{0.16}{\sqrt{(0.16 - 0.003 \times 22)^2 + (0.0062 \times 34)^2}} = 0.693 \\ \omega_{cn} &= \frac{1}{\psi_n - L_{dn}} = \frac{1}{0.693 - 0.533} = 6.25 \\ \omega_{cn} &= 6.25 \times 2600 = 16250\text{rpm}. \end{aligned}$$

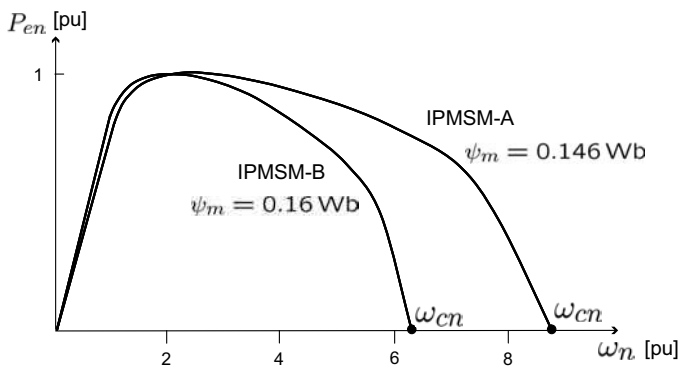

Figure 7.17: Normalized power curves for "IPMSM-A" and "IPMSM-B," (Exercise 7.6).

If the PM strength is high, the starting torque (initial power) is also high. But, the critical speed reduces as the PM strength increases. The PM strength needs to

be determined considering the usable speed range. The results can be summarized as

1. To make the critical speed, ω_{cn}, larger, the use of PM should be reduced.
2. With the increase in the saliency ratio, ξ, the use of PM can be reduced.
3. The maximum torque is almost invariant to saliency ratio, ξ.

7.6 An EV Motor Example

Table 7.3: Parameters of an IPMSM for a fuel cell EV.

Parameters [Unit]	Values
Motor power	100kW
Rated speed	2600rpm
Rated torque	300Nm
L_d	0.1mH
L_q	0.35mH
L_δ	0.083mH
r_s	26mΩ
Flux (ψ_m)	0.052Wb
Rated current	354A_{rms}
Rated voltage	102 V_{rms}
Number of poles	8
Inertia, J	0.01kg m^2
Damping coeff., B	0.001 kg/s

Fig. 7.18 shows a photograph of a 100kW IPSM motor designed for a fuel cell EV. Machine parameters are listed in Table 7.3. Fig. 7.19 shows a current contour yielding the maximum power. Fig. 7.20 shows the voltage components at three different speeds, 2600rpm, 6000rpm, and 12000rpm. Back EMF grows with speed: At 12,000rpm, it reaches 260V. However, coupling voltage $\omega_e L_d i_d^e$ with negative i_d^e cancels out most of back EMF, so that it enables torque control with a small terminal voltage (150V). Magnitudes of terminal voltage and current are the same for all three cases. At 3,600 rpm, voltage vector leads current vector. But as the speed increases, angle difference decreases, i.e., the PF approaches to unity. Fig. 7.21 shows the power and torque plots versus plot.

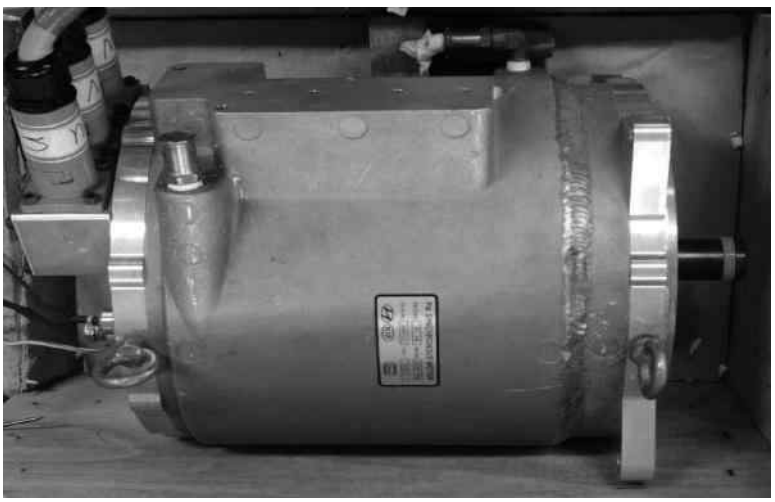

Figure 7.18: 100kW fuel cell EV motor (Hyundai Motor Company).

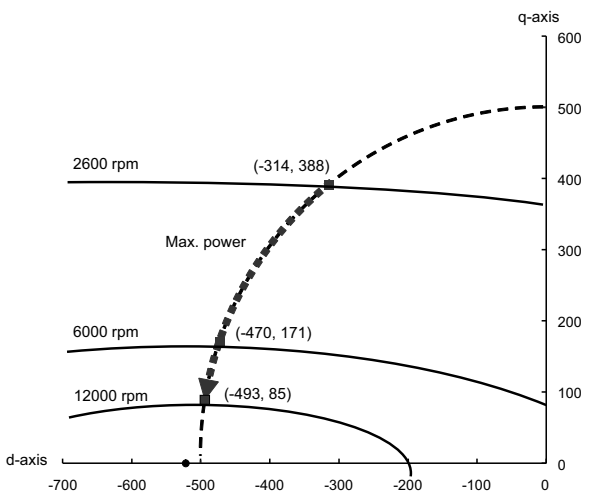

Figure 7.19: Maximum power contour in the (i_d, i_q) plane.

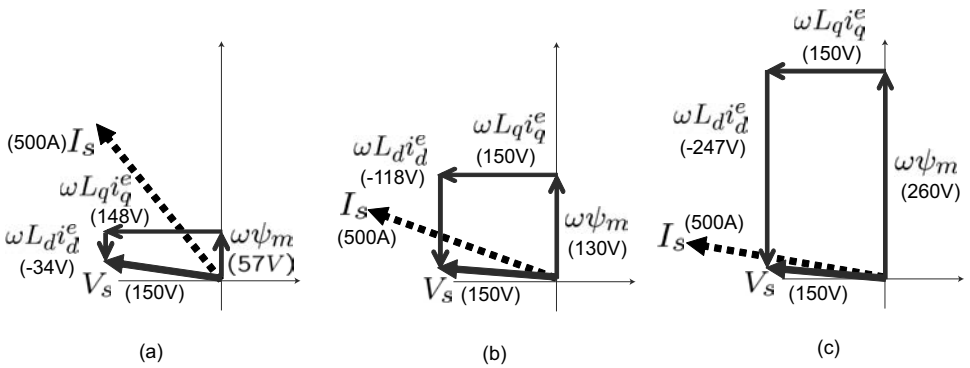

Figure 7.20: Vector diagrams showing the proportions of back EMF and coupling voltage as speed increases; (a) 3600 rpm, (b) 6000rpm, (c) 12000 rpm.

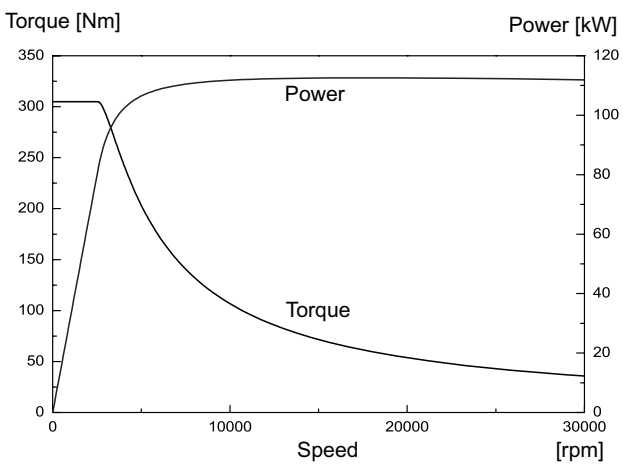

Figure 7.21: Power and torque versus speed: (a) power and (b) torque.

Bibliography

[1] A. Binder, *Permanent Magnet Synchronous Machine Design,* Lecture Note, May 2008.

[2] Y. Mizuno et al., Development of New Hybrid Transmission for Compact-Class Vehicles Proc. of SAE, Paper No. 2009-01-0726, 2009.

[3] W.L. Soong and T.J.E. Miller, Field-weakening performance of brushless synchronous AC motor drives, *IEE Proc-Electr. Power Appl.*, Vol. 141, No. 6, November 1994.

[4] D. W. Novotny and T. A. Lipo,"Vector Control and Dynamics of AC Drives," Clarendon Press, Oxford 1996.

[5] S. Morimoto, Y. Takeda, T. Hirasa, K. Taniguchi, Expansion of Operating Limits for Permanent Magnet Motor by Current Vector Control Considering Inverter Capacity, *IEEE Trans. on Ind. Appl.*, Vol. 26, No. 5, 1990.

[6] D. G. Luenberger, "Linear and Nonlinear Programming," 2nd Ed., Kluwer Academic Publisher, Norwell, 2004.

Problems

7.1 It is desired to design an IPMSM whose rated power is 36kW at the base speed, 3000 rpm. Assume that $k_w = 0.96$, $B_m = 0.8$T and $A_m = 550$A/cm. Calculate T_e and the stack length, l_{st}, when the rotor diameter is $D_r = 11$cm.

7.2 Plot the magnet and reluctance torque components versus speed above 2600 rpm for the IPMSM listed in Table 7.2. Repeat the same when $L_d = 2.2$mH.

7.3 Derive $(i_d^e,\, i_q^e)$ that yields the maximum torque while satisfying the unity power factor. Determine the values of T_e and $(i_d^e,\, i_q^e)$ for the IPMSM listed in Table 7.2.
Hint: Let the Lagrangian defined by $L(i_d^e, i_q^e) = \frac{3P}{4}(\psi_m i_q^e + L_d(1-\xi) i_d^e i_q^e) + \mu_1(\xi i_q^{e2} + i_d^{e2} + i_d^e i_f)$.

7.4 Obtain the per-unit model for the IPMSM listed in Table 7.2. Note that the base currents are $(i_{db},\, i_{qb}) = (-21.7,\, 33.6)$A.

7.5 Consider an EV motor whose parameters listed in Table 7.3. Note that the base currents are $(i_{db},\, i_{qb}) = (-314,\, 388)$A.

a) Determine the normalized model.
b) Show that $v_{dn}^2 + v_{qn}^2 = 1$ when $\omega_n = 1$.
c) Determine the critical speed, ω_{cn} and ω_c in rpm.

Chapter 8

Loss-Minimizing Control

Motor loss consists of copper loss, iron loss, stray loss, and mechanical loss. Copper loss is the Joule loss of copper winding of the stator coil. Since there is no secondary winding in PMSMs, the copper loss of a PMSM is lower than that of the corresponding induction motor [1]. The iron loss consists of hysteresis and eddy current losses. The former originates from the hysteresis band of the core, while the latter is caused by the conductivity of the core material. The hysteresis loss is higher than the eddy current loss under the base frequency. But, the eddy current loss becomes dominant in the high frequency region. The stray loss accounts for the losses of winding (high-order) space harmonics and slot harmonics. Mechanical loss includes friction and windage losses, but it is not dealt with here.

In the IPMSM, the d–axis current is used not only for field-weakening, but for generating the reluctance torque. Therefore in producing a given required torque, numerous combinations are feasible between the magnetic and the reluctance torques. However, their proportions need to be considered in the perspective of loss minimization.

8.1 Motor Losses

Hysteresis Loss

A hysteresis loop is shown in Fig. 8.1. Hysteresis loss (energy), W_h per volume Vol of a ferromagnetic material due to a current cycle is equal to the loop area, i.e.,

$$\frac{W_h}{\text{Vol}} = \oint H dB. \tag{8.1}$$

Assume that $B(t) = B_m \sin(2\pi f t)$. Then, the power loss will be proportional to the frequency, f. However, the energy loss per cycle is a nonlinear function of maximum field density B_m, since the loop area is not proportional to B_m. The hysteresis power loss can be modeled approximately for a given magnetic material by

$$P_h = k_h f B_m^n \tag{8.2}$$

where k_h and n are empirical constants. The exponent, n is usually in the range $1.8 < n < 2.2$ [1].

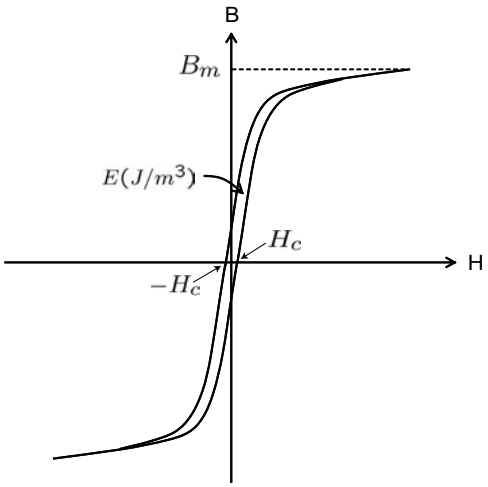

Figure 8.1: $B - H$ curve of a soft magnet material with the loop area representing the hysteresis loss.

Exercise 8.1
Consider the toroidal core with N-turn coil shown in Fig. 8.2. The core cross sectional area is A and the mean periphery is ℓ. When a voltage source, $e(t)$, is applied to the coil terminals, current, $i(t)$, flows in the coil. At this time, core field density increases from zero to B. Derive the energy loss, $W_h = A\ell \int_0^B H dB$ from $\int ei\, dt$.

Solution.

$$W_h = \int e(t)i(t)\, dt = \int i\frac{d(N\Phi)}{dt}dt = \ell \int_0^{\Phi} \frac{Ni}{\ell} d\Phi = A\ell \int_0^B H dB.$$

■

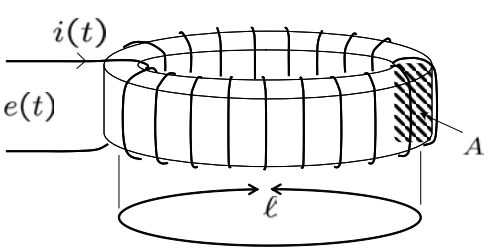

Figure 8.2: A toroidal core with N-turn coil (Exercise 8.1).

Eddy Current Loss

If a time-varying magnetic field passing through a conductive material, then it sets up around itself an electric field that opposes the change in the magnetic field. The electric field induces a loop current in the ohmic conductor. The induced current, called eddy current, results in ohmic heating. Inductive heating devices utilize this heating principle in melting metals or heating some plastic materials.

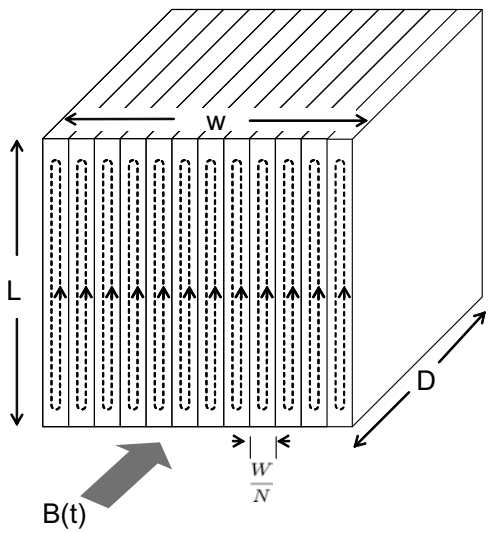

Figure 8.3: Stack of laminated metal sheets and eddy current loops.

But for motors and transformers, the eddy current implies a loss. To reduce the power loss, cores are constructed by stacking up thin steel sheets. Fig. 8.3 shows a stack of laminated metal sheets and eddy current loops. Assume that a time varying magnetic field $B(t)$ is passing and that each sheet is insulated electrically. Reacting to the time varying field, current paths are formed in the transversal planes. Since individual sheets are insulated, the current flow is confined within a thin sheet. Therefore, the current loops are hardly formed. More specifically, the loop resistance increases as the sheet width, W/N, narrows down. When $B(t) = B_m \sin(2\pi ft)$, the average eddy current loss is calculated as [4]

$$P_{ed} = \frac{\pi^2 \sigma LDW^3}{8N^2} f^2 B_m^2, \tag{8.3}$$

where σ is the conductivity of the core material. This means that the eddy current loss is reduced by a factor of $1/N^2$, when compared with that of the single block. It should also be noted that the eddy current loss is proportional to the square of the frequency, f, and to the square of the maximum field density, B_m.

In practice, $1 \sim 3.5\%$ silicon steel is used for the motor core, which has low conductivity. If the silicon content is even higher, the steel becomes more brittle and the maximum B field is reduced. Further, each sheet surface is insulated by

some organic compounds, or oxidated by phosphoric acid. Most commercial motors are made of $0.35 \sim 0.5$mm-thick silicon steel sheets.

8.2 Loss-Minimizing Control for IMs

Note from (5.35) that torque is a product of the dq-axes currents. Hence, there is a degree of freedom in choosing the levels of the current components for a torque production. Specifically, in attaining the same torque, one option is to use a large d–axis current and a small q–axis current, and the other is to use the reverse. But a proportioning method between the d and q axes currents may be considered from the perspective of minimizing the motor loss.

In the low-frequency operation, the core loss (hysteresis and eddy current loss) is lower than the copper loss. As the speed goes up, however, contribution of the core loss increases and finally becomes dominant. Hence, the loss-minimizing dq currents set varies, depending on the required torque and speed.

Numerous control schemes have been proposed by many researchers concerning the optimal choice of excitation current or flux level for a given operating point [5],[6]. The techniques allowing efficiency improvement can be divided into two categories. The first category is the so-called loss-model-based approach [5],[8], which consists of computing losses by using the machine model and selecting a flux level that minimizes these losses. The second category is the power-measure-based approach, also known as search controllers [7], in which the flux (or its equivalent variables) is decreased until the electrical input power settles down to the lowest value for a given torque and speed.

8.2.1 IM Model with Eddy Current Loss

In a high-frequency region, the eddy current loss is dominant over the hysteresis loss. The rotor iron loss is quite small compared with the stator iron loss, since the rotor flux alternates at the slip frequency. The stator core (eddy current) loss is approximated by

$$P^s_{iron} = k'_e \omega^2 \Phi^2 \approx \frac{\omega^2 \Phi^2}{1/k'_e} = \frac{\omega^2 \Phi^2}{r_m}, \tag{8.4}$$

where Φ is the air gap flux. Since $\omega\Phi$ represents the airgap voltage, $1/k'_e$ has the dimension of resistance. Letting $r_m = 1/k'_e$, the eddy current loss can described by a parallel resistor with the magnetizing inductor, L_m.

Denote the magnetizing current by

$$\mathbf{i}^s_{dqm} \;=\; i^s_{dm} + j i^s_{qm},$$

where $i^s_{dm} = i^s_{ds} + e^{j\omega_r} i^s_{dr}$ and $i^s_{qm} = i^s_{qs} + e^{j\omega_r} i^s_{qr}$. Then, the stationary IM model

(4.27) is rewritten as

$$v_{ds}^s = r_s i_{ds}^s + L_{ls}\frac{di_{ds}^s}{dt} + L_m\frac{di_{dm}^s}{dt} \tag{8.5}$$

$$v_{qs}^s = r_s i_{qs}^s + L_{ls}\frac{di_{qs}^s}{dt} + L_m\frac{di_{qm}^s}{dt} \tag{8.6}$$

$$0 = r_r i_{dr}^s + L_{lr}\frac{di_{dr}^s}{dt} + L_m\frac{di_{dm}^s}{dt} + \omega_r L_{lr} di_{qr}^s \tag{8.7}$$

$$0 = r_r i_{qr}^s + L_{lr}\frac{di_{qr}^s}{dt} + L_m\frac{di_{qm}^s}{dt} - \omega_r L_{lr} di_{dr}^s. \tag{8.8}$$

Note that the redundant variables, i_{dm}^s and i_{qm}^s are utilized in (8.5)–(8.8). Transforming (8.5)−(8.8) into the synchronous frame, we obtain

$$v_{ds}^e = r_s i_{ds}^e + L_{ls}\frac{di_{ds}^e}{dt} - \omega_e L_{ls} i_{qs}^e + v_{dm}^e, \tag{8.9}$$

$$v_{qs}^e = r_s i_{qs}^e + L_{ls}\frac{di_{qs}^e}{dt} + \omega_e L_{ls} i_{ds}^e + v_{qm}^e, \tag{8.10}$$

$$0 = r_r i_{dr}^e + L_{lr}\frac{di_{dr}^e}{dt} - \omega_{sl} L_{lr} i_{qr}^e + v_{dm}^e, \tag{8.11}$$

$$0 = r_r i_{qr}^e + L_{lr}\frac{di_{qr}^e}{dt} + \omega_{sl} L_{lr} i_{dr}^e + v_{qm}^e, \tag{8.12}$$

where

$$v_{dm}^e = L_m\frac{di_{dm}^e}{dt} - \omega_e L_m i_{qm}^e \tag{8.13}$$

$$v_{qm}^e = L_m\frac{di_{qm}^e}{dt} + \omega_e L_m i_{dm}^e. \tag{8.14}$$

The eddy current loss can be included such that

$$\mathbf{i}_{dqs}^e + \mathbf{i}_{dqr}^e = \frac{1}{r_m}\left(L_m\frac{d\mathbf{i}_{dqm}^e}{dt}\right) + \mathbf{i}_{dqm}^e. \tag{8.15}$$

Note from (8.15) that $\mathbf{i}_{dqs}^e + \mathbf{i}_{dqr}^e$ is split into two parts: the real magnetizing current and the loss current that is determined by the air gap voltage.

8.2.2 Loss Model Simplification

A problem with the previous loss model is the complexity caused by the additional current equation, (8.15). To circumvent this complexity, model simplification methods were proposed. A typical method was to ignore the leakage inductances [8]. Such simplification may be effective in a low-frequency region. However, as the velocity increases, the voltage drop over the leakage inductance becomes significant. For example, it takes 40 $\sim$ 50% of the rated voltage in a high-speed region. Therefore,

ignoring the leakage inductance will result in a significant error when calculating the loss.

Note however that $\mathbf{i}^e_{dqs} + \mathbf{i}^e_{dqr} \approx \mathbf{i}^e_{dqm}$, since the loss current is small compared with the magnetizing current, i.e., $\left|\frac{1}{r_m} L_m \frac{d\mathbf{i}^e_{dqm}}{dt}\right| \ll |\mathbf{i}^e_{dqr}|$. Lim and Nam [9] described the loss current with the use of an additional (dependent) voltage source, i.e., they let the loss current be $\overline{\mathbf{v}}_{dqm}/r_m$, where $\overline{\mathbf{v}}_{dqm} = \overline{v}_{dm} + j\overline{v}_{qm}$ is a virtual voltage source whose level is determined according to

$$\overline{v}_{dm} = L_m \frac{d(i^e_{ds} + i^e_{dr})}{dt} - \omega_e L_m \big(i^e_{qs} + i^e_{qr}\big) \tag{8.16}$$

$$\overline{v}_{qm} = L_m \frac{d(i^e_{qs} + i^e_{qr})}{dt} + \omega_e L_m \big(i^e_{ds} + i^e_{dr}\big). \tag{8.17}$$

Fig. 8.4 shows Lim and Nam's simplified IM model. Nothing is altered in the main motor part. But to reflect the iron (eddy current) loss, an additional voltage source and a resistance are introduced. However, the loss, $(v^2_{dm} + v^2_{dm})/r_m$, will be counted as the iron loss of the IM.

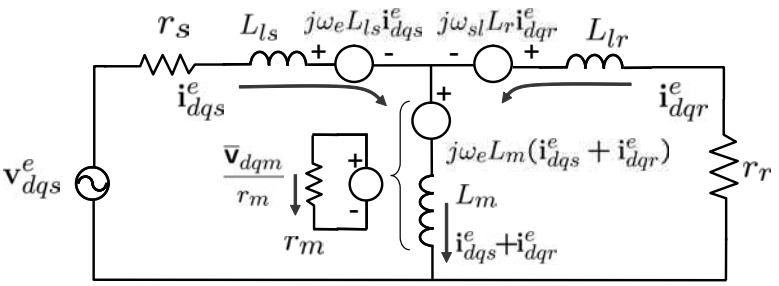

Figure 8.4: Simplified IM model with iron (eddy current) loss.

8.2.3 Loss Calculation

The rotor field-oriented scheme is realized by aligning the reference frame on the rotor flux axis. Then, $\lambda_{qr} = \dot{\lambda}_{qr} = 0$. Substituting $i^e_{dr} = (\lambda^e_{dr} - L_m i^e_{ds})/L_r$ and $i^e_{qr} = -(L_m/L_r) i^e_{qs}$ into (8.16) and (8.17), we obtain

$$\overline{v}_{dm} = \frac{L_m L_{lr}}{L_r} \frac{di^e_{ds}}{dt} + \frac{L_m}{L_r} \frac{d\lambda^e_{dr}}{dt} - \omega_e \frac{L_m L_{lr}}{L_r} i^e_{qs} \tag{8.18}$$

$$\overline{v}_{qm} = \frac{L_m L_{lr}}{L_r} \frac{di^e_{qs}}{dt} + \omega_e \frac{L_m}{L_r} (L_{lr} i^e_{ds} + \lambda^e_{dr}). \tag{8.19}$$

In the steady-state, $\frac{di^e_{ds}}{dt} = \frac{di^e_{qs}}{dt} = \frac{d\lambda^e_{dr}}{dt} = 0$. Further, $i^e_{dr} = 0$, since $\lambda^e_{dr} = L_m i^e_{ds}$. Therefore, in the steady-state we have

$$V^e_{dm} = -\omega_e \frac{L_m L_{lr}}{L_r} i^e_{qs} \tag{8.20}$$

$$V^e_{qm} = \omega_e \frac{L_m}{L_r} (L_{lr} i^e_{ds} + \lambda^e_{dr}) = \omega_e L_m i^e_{ds}. \tag{8.21}$$

Then the iron loss is equal to $({V^e_{dm}}^2 + {V^e_{qm}}^2)/r_m$. Along with the copper loss, the total motor losses are equal to

$$\begin{aligned} P_{loss} &= r_s({i^e_{ds}}^2 + {i^e_{qs}}^2) + r_r({i^e_{dr}}^2 + {i^e_{qr}}^2) + \frac{1}{r_m}({V^e_{dm}}^2 + {V^e_{qm}}^2) \\ &= r_s({i^e_{ds}}^2 + {i^e_{qs}}^2) + r_r\frac{L_m^2}{L_r^2}{i^e_{qs}}^2 + \frac{1}{r_m}\left(\omega_e^2 L_m^2(\frac{L_{lr}}{L_r})^2{i^e_{qs}}^2 + \omega_e^2 L_m^2{i^e_{ds}}^2\right) \\ &= {i^e_{ds}}^2\left(r_s + \frac{\omega_e^2 L_m^2}{r_m}\right) + {i^e_{qs}}^2\left(r_s + \frac{r_r L_m^2}{L_r^2} + \frac{\omega_e^2 L_m^2 L_{lr}^2}{r_m L_r^2}\right) \\ &= R_d(\omega_e)\cdot {i^e_{ds}}^2 + R_q(\omega_e)\cdot {i^e_{qs}}^2, \end{aligned} \tag{8.22}$$

where

$$R_d(\omega_e) = r_s + \frac{\omega_e^2 L_m^2}{r_m} \tag{8.23}$$

$$R_q(\omega_e) = r_s + \frac{r_r L_m^2}{L_r^2} + \frac{\omega_e^2 L_m^2 L_{lr}^2}{r_m L_r^2}. \tag{8.24}$$

Note that $R_d(\omega_e)$ and $R_q(\omega_e)$ are the dq-axes equivalent resistors representing the total losses.

In the rotor field orientation scheme only d–axis current contributes to generating the flux, while q–axis current makes torque. Specifically, in the q–axes, i^e_{qs} is opposite in polarity to i^e_{qr} so that $\lambda^e_{qr} = 0$. In the steady-state, it follows that $\lambda^e_{dr} = L_m i^e_{ds}$. Hence, the iron loss is mainly caused by the d–axis stator current. Comparing $R_d(\omega_e)$ and $R_q(\omega_e)$, one can notice that $R_d(\omega_e)$ is dominant over $R_q(\omega_e)$, as ω_e increases. This is because L_{lr}/L_r is very small value in (8.24). Therefore, it motivates us to reduce the d–axis current(or flux level) for the loss minimization. However, too much decrease in i^e_{ds} (or λ^e_{dr}) leads to extremely large i^e_{qs} for a desired torque production, yielding a great copper loss. Hence, a compromise between the iron loss and copper loss needs to be made for optimal operation.

8.2.4 Optimal Solution for Loss-Minimization

The electro-magnetic torque in the rotor field-oriented scheme at steady-state is given by

$$T_e = \frac{3}{2}\frac{P}{2}\frac{L_m}{L_r}\lambda^e_{dr} i^e_{qs} = K_t i^e_{ds} i^e_{qs}, \tag{8.25}$$

where $K_t = \frac{3}{2}\frac{P}{2}\frac{L_m^2}{L_r}$. As was stressed in the previous, the iron loss is closely related to the flux level, i.e., i^e_{ds}, while the copper loss is related to the i^e_{qs}. Hence, depending on the operating condition, loss-minimizing choice of i^e_{ds} and i^e_{qs} differs. In this section we consider deriving the optimal choice for (i^e_{ds}, i^e_{qs}) under voltage and current constraints based on the loss model derived in the previous.

Since there is a rated flux level for each motor, the d–axis current constraint also needs to be limited below a rated value.

$$i_{ds}^e \leq I_{dn}, \tag{8.26}$$

where I_{dn} is a rated d–axis current.

The aim is to find an optimum flux level that minimizes the loss while producing a desired torque T_e under the voltage and current constraints. Specifically, it is to minimize P_{loss} subject to equality constraint $T_e - K_t i_{ds}^e i_{qs}^e = 0$ and inequality constraints:

$$\begin{aligned} \text{Minimize} \quad P_{loss} \qquad \text{subject to} \qquad & K_t i_{ds}^e i_{qs}^e - T_e = 0, \\ & (\omega_e L_s i_{ds}^e)^2 + (\omega_e \sigma L_s i_{qs}^e)^2 \leq V_{max}^2, \\ & {i_{ds}^e}^2 + {i_{qs}^e}^2 \leq I_{max}^2, \\ & i_{ds}^e \leq I_{dn}. \end{aligned}$$

It leads us to apply the Kuhn−Tucker theorem. First, the cost function is defined by

$$\begin{aligned} J(i_{ds}^e, i_{qs}^e) &= P_{loss}(i_{ds}^e, i_{qs}^e) + \lambda_1 \cdot (K_t i_{ds}^e i_{qs}^e - T_e) \\ &+ \mu_1 \cdot \{(\omega_e L_s i_{ds}^e)^2 + (\omega_e \sigma L_s i_{qs}^e)^2 - V_{max}^2\} \\ &+ \mu_2 \cdot ({i_{ds}^e}^2 + {i_{qs}^e}^2 - I_{max}^2) + \mu_3 \cdot (i_{ds}^e - I_{dn}), \end{aligned} \tag{8.27}$$

where λ_1, $\mu_1 \geq 0$, $\mu_2 \geq 0$ and $\mu_3 \geq 0$ are the Lagrange multipliers. We define regions in (i_{ds}^e, i_{qs}^e) space such that

$$U_v = \{(i_{ds}^e, i_{qs}^e) \mid (\omega_e L_s i_{ds}^e)^2 + (\omega_e \sigma L_s i_{qs}^e)^2 \leq V_{max}^2\} \tag{8.28}$$

$$U_c = \{(i_{ds}^e, i_{qs}^e) \mid {i_{ds}^e}^2 + {i_{qs}^e}^2 \leq I_{max}^2\}, \tag{8.29}$$

$$U_d = \{(i_{ds}^e, i_{qs}^e) \mid 0 \leq i_{ds}^e \leq I_{dn}\}. \tag{8.30}$$

Note that each boundary of U_v, U_c, and U_d consists of regular points. The minimum point is found under the following conditions:

$$\frac{\partial J(i_{ds}^e, i_{qs}^e)}{\partial i_{ds}^e} = 2R_d i_{ds}^e + \lambda_1 K_t i_{qs}^e + \mu_1 2\omega_e^2 L_s^2 i_{ds}^e + \mu_2 2 i_{ds}^e + \mu_3 = 0, \tag{8.31}$$

$$\frac{\partial J(i_{ds}^e, i_{qs}^e)}{\partial i_{qs}^e} = 2R_q i_{qs}^e + \lambda_1 K_t i_{ds}^e + \mu_1 2\omega_e^2 L_s^2 \sigma^2 i_{qs}^e + \mu_2 2 i_{qs}^e = 0, \tag{8.32}$$

$$\frac{\partial J(i_{ds}^e, i_{qs}^e)}{\partial \lambda_1} = K_t i_{ds}^e i_{qs}^e - T_e = 0, \tag{8.33}$$

$$\mu_1 \cdot ((\omega_e L_s i_{ds}^e)^2 + (\sigma \omega_e L_s i_{qs}^e)^2 - V_{max}^2) = 0, \tag{8.34}$$

$$\mu_2 \cdot ({i_{ds}^e}^2 + {i_{qs}^e}^2 - I_{max}^2) = 0, \tag{8.35}$$

$$\mu_3 \cdot (i_{ds}^e - I_{dn}) = 0. \tag{8.36}$$

Conditions (8.34), (8.35), and (8.36) require that either $\mu_1 = \mu_2 = \mu_3 = 0$ when $(i^e_{ds},\, i^e_{qs})$ is in the interior, or $(i^e_{ds},\, i^e_{qs})$ is on the boundary. Depending on the location of the solution curves, the optimal solutions are classified into 4 parts [9]:

i) Interior points : $(i^e_{ds}, i^e_{qs}) \in \{U_v \cap U_c \cap U_d\}$

At an interior point, $\mu_1 = \mu_2 = \mu_3 = 0$. The solution follows straightforwardly from (8.31), (8.32), and (8.33), that is to say;

$$2R_d i^e_{ds} + \lambda_1 K_t i^e_{qs} = 0, \tag{8.37}$$
$$2R_q i^e_{qs} + \lambda_1 K_t i^e_{ds} = 0, \tag{8.38}$$
$$K_t i^e_{ds} i^e_{qs} - T_e = 0, \tag{8.39}$$

such that

$$(i^e_{ds}, i^e_{qs}) = \left(\left(\frac{R_q(\omega_e)T_e^2}{R_d(\omega_e)K_t^2}\right)^{1/4}, \quad \left(\frac{R_d(\omega_e)T_e^2}{R_q(\omega_e)K_t^2}\right)^{1/4} \right). \tag{8.40}$$

At this time, $\lambda_1 = 2\sqrt{R_d(\omega_e)R_q(\omega_e)}/K_t$.

ii) Points on the boundary $\partial\overline{U}_d$ (d–axis current limit)

We denote by $\partial\overline{U}_d$ the boundary of the closure of U_d. For points on $\partial\overline{U}_d$, $\lambda_1 \neq 0$, $\mu_3 \neq 0$ while $\mu_1 = \mu_2 = 0$. Hence, solving $\partial J/\partial i^e_{ds} = \partial J/\partial i^e_{qs} = 0$, $i^e_{ds} = I_{dn}$, and (8.33), we obtain

$$(i^e_{ds}, i^e_{qs}) = \left(I_{dn}, \quad \frac{T_e}{K_t I_{dn}} \right). \tag{8.41}$$

iii) Points on the boundary $\partial\overline{U}_c$ (Current limit)

Note that $\lambda_1 \neq 0$, $\mu_2 \neq 0$ while $\mu_1 = \mu_3 = 0$ for points on $\partial\overline{U}_c$. Solving $\partial J/\partial i^e_{ds} = \partial J/\partial i^e_{qs} = 0$, ${i^e_{ds}}^2 + {i^e_{qs}}^2 = I^2_{max}$ and (8.33), we obtain

$$(i^e_{ds}, i^e_{qs}) = \left(\frac{\sqrt{I^2_{max} - (I^4_{max} - 4T_e^2/K_t^2)^{\frac{1}{2}}}}{\sqrt{2}}, \quad \frac{\sqrt{I^2_{max} + (I^4_{max} - 4T_e^2/K_t^2)^{\frac{1}{2}}}}{\sqrt{2}} \right). \tag{8.42}$$

iv) Points on the boundary $\partial\overline{U}_v$ (Voltage limit)

Note that $\lambda_1 \neq 0$, $\mu_1 \neq 0$ while $\mu_2 = \mu_3 = 0$ for points in $\partial\overline{U}_v$. Solving $\partial J/\partial i^e_{ds} = \partial J/\partial i^e_{qs} = 0$, $(\omega_e L_s i^e_{ds})^2 + (\omega_e \sigma L_s i^e_{qs})^2 = V^2_{max}$, and (8.33), we obtain

$$(i^e_{ds}, i^e_{qs}) = \tag{8.43}$$

$$\left(\frac{\sqrt{V^2_{max} + (V^4_{max} - 4\omega_e^4\sigma^2 L_s^4 T_e^2/K_t^2)^{\frac{1}{2}}}}{\sqrt{2}\omega_e L_s}, \frac{\sqrt{V^2_{max} - (V^4_{max} - 4\omega_e^4\sigma^2 L_s^4 T_e^2/K_t^2)^{\frac{1}{2}}}}{\sqrt{2}\omega_e \sigma L_s} \right).$$

Region Separated by Different Constraints

The maximum output torque and power of the machine are ultimately limited by the allowable inverter (source) current and voltage rating. Due to the presence of the voltage and currents limits, the torque vs. speed curve is plotted as Fig. 8.5. The torque-speed plane is divided into three regions as discussed in Section 5.4. Note that ω_n is called the rated speed or the based speed, and ω_{ps} represents the boundary speed between Region II and Region III. They are calculated such that

$$\omega_n = \frac{V_{max}}{\sqrt{L_s^2 I_{dn}^2 + \sigma^2 L_s^2 (I_{max}^2 - I_{dn}^2)}} \tag{8.44}$$

$$\omega_{ps} = \sqrt{\frac{L_s^2 + \sigma^2 L_s^2}{2\sigma^2 L_s^4}} \frac{V_{max}}{I_{max}}. \tag{8.45}$$

The maximum available torques in each region are expressed such that

$$T_{m1} = K_t I_{dn} \sqrt{I_{max}^2 - I_{dn}^2}, \tag{8.46}$$

$$T_{m2} = K_t \sqrt{\frac{(V_{max}/\omega_e)^2 - (\sigma L_s I_{max})^2}{L_s^2 - \sigma^2 L_s^2}} \sqrt{\frac{(L_s I_{max})^2 - (V_{max}/\omega_e)^2}{L_s^2 - \sigma^2 L_s^2}}, \tag{8.47}$$

$$T_{m3} = K_t \frac{V_{max}}{\sqrt{2}\omega_e L_s} \frac{V_{max}}{\sqrt{2}\omega_e \sigma L_s}. \tag{8.48}$$

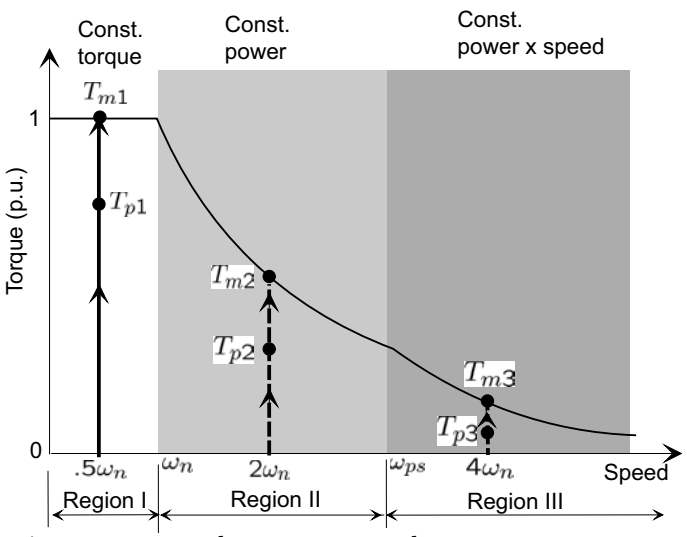

Figure 8.5: Maximum torque plot versus speed.

Fig. 8.5 represents the output (or load) torque at fixed speeds, i.e., $0.5\omega_n$, $2\omega_n$, and $4\omega_n$. The corresponding contours are shown in Fig. 8.6 (a), 8.6 (b), and 8.6 (c), respectively. In Region I, the maximum torque T_{m1} is determined by the rated dq-axes currents at the rated speed. In Region II, the maximum torque T_{m2}, being

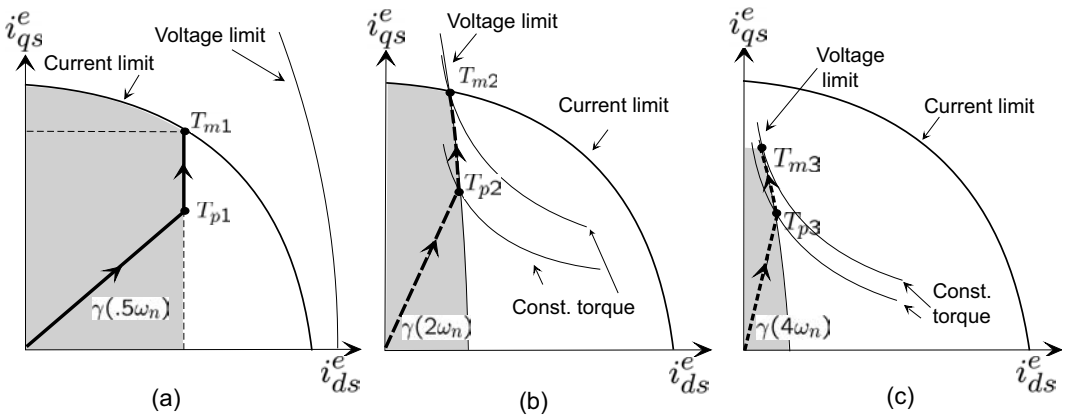

Figure 8.6: Optimal trajectories at constant speeds while the load torque increases: (a) $\omega = 0.5\omega_n$ in Region I, (b) $\omega = 2\omega_n$ in Region II, and (c) $\omega = 4\omega_n$ in Region III.

a function of ω_e, is determined by the intersecting point between the voltage limit curve and the current limit curve. As the frequency increases, the ellipse representing the voltage limit shrinks down gradually. Therefore, level of the intersecting point T_{m2}, shown in Fig. 8.6 (b), decreases with ω_e. At some high speed, the osculatory point between torque and voltage limit curves lies inside the current limit circle. This characterizes Region III. Hence, in Region III the maximum torque boundary T_{m3} has nothing to do with the current limit.

Optimal Constant Speed Contours versus Load Torque

In this section, we consider the optimal constant speed contours versus load torque in each speed region. The case differs whether the curve is in the interior or on the boundary. If an operating point in the interior of the constraint curves, the loss-minimizing current level for a given torque and speed is given by (8.40). From (8.40), the following linear relationship is obtained:

$$i^e_{ds} = \gamma(\omega_e) i^e_{qs} = \sqrt{\frac{R_q(\omega_e)}{R_d(\omega_e)}}\, i^e_{qs}, \tag{8.49}$$

where $\gamma(\omega_e) \triangleq \sqrt{R_q(\omega_e)/R_d(\omega_e)}$. This implies that the flux level needs to increase or decrease linearly with the torque. This linear relationship is shown as the linear segments of the trajectories in Fig. 8.6. Note also that the slope $\gamma(\omega_e)$ decreases as ω_e increases. However, after it hits the d–axis current constraint at T_{p1}, it stays on the d–axis current limiting boundary, $\partial\overline{U}_d$ until it reaches the boundary $\partial\overline{U}_c$ of the current limit. This states that once d–axis current reaches the rated value I_{dn}, the torque increases further only by an increase in the q–axis current. Since T_{p1} is the

crossing point, it can be found by solving (8.41) and (8.49) such that

$$T_{p1}(\omega_e) = K_t I_{dn} I_{dn} \sqrt{\frac{R_d}{R_q}} = K_t \sqrt{\frac{R_d}{R_q}} I_{dn}^2. \tag{8.50}$$

In Region II where $\omega_e > \omega_n$, the same linear relationship (8.49) between i_{ds}^e and i_{qs}^e holds if the load torque is low, i.e., in interior region. Since T_{p2} is the point where the linear curve intersects the voltage limit ellipse, it follows from (7.50), (8.25), and (8.49) that

$$T_{p2}(\omega_e) = K_t \frac{\sqrt{R_q R_d} V_{max}^2}{(R_q + R_d\sigma^2)\omega_e^2 L_s^2}. \tag{8.51}$$

The maximum torque T_{m2} is determined by the crossing points of the voltage limit curve $\partial\overline{U}_v$ and the current limit curve $\partial\overline{U}_c$. From T_{p2} to T_{m2}, the optimal trajectory of the torque at a fixed speed lies on the voltage limit ellipse (8.43). However, if ω_e increases in Region II, the values (i_{ds}^e, i_{qs}^e) of the crossing point reduce with the shrink of the ellipse. A reduction of the crossing point values corresponds to the decrease of the maximum torque T_{m2} with the speed, as shown in Fig. 8.6 (b).

In Region III, ω_e is larger than ω_{ps}. Then, the ellipse shrinks further so that the maximum torque T_{m3} given in (8.48) is determined not by the current limit curve, but only by the voltage limit curve, as shown in Fig. 8.6 (c). Eventually, the voltage limit ellipse lies inside the current limit circle completely as ω_e increases.

$$T_{p3}(\omega_e) = K_t \frac{\sqrt{R_q R_d} V_{max}^2}{(R_q + R_d\sigma^2)\omega_e^2 L_s^2}. \tag{8.52}$$

One can note from (8.48) that the product of maximum torque T_{m3} and speed squared is constant in Region III. Since the power is a product of torque and speed, the product of torque and speed squared being constant is equivalent to saying that the product of power and speed is constant. Hence, Region III is often called constant power-speed limit region.

8.2.5 Experimental Results

Table 8.1 shows parameters used in the experiment. Fig. 8.7(a) and (b) show the experimental results of torque, speed, flux, and loss when the torque command changes from 20 to 0 and from 0 to −20 N.m. Fig. 8.7(a) shows the responses of the conventional vector control without a loss minimization control. Because of the field-weakening profile, the flux level is slightly decreased from the rated flux level 0.8 Wb when the motor rotates above the rated speed (1800rpm). At steady-state with 2000rpm, the power loss of the motor is about 200W. Fig. 8.7(b) shows the responses of the proposed loss-minimizing control (LMC). The flux level is changed according to the torque and speed for the loss minimization. One can note that the significant loss reduction is observed in steady-state operation region.

Table 8.1: The parameters of the induction motor used in experiments.

Motor rating	9kW (4-pole)	Current rating	20A
Voltage rating	400V	Rated speed	1750rpm
r_s	0.399 Ω	r_r	0.3538 Ω
r_m	650 Ω	L_s	59.327 mH
L_r	60.448 mH	L_m	56.646 mH

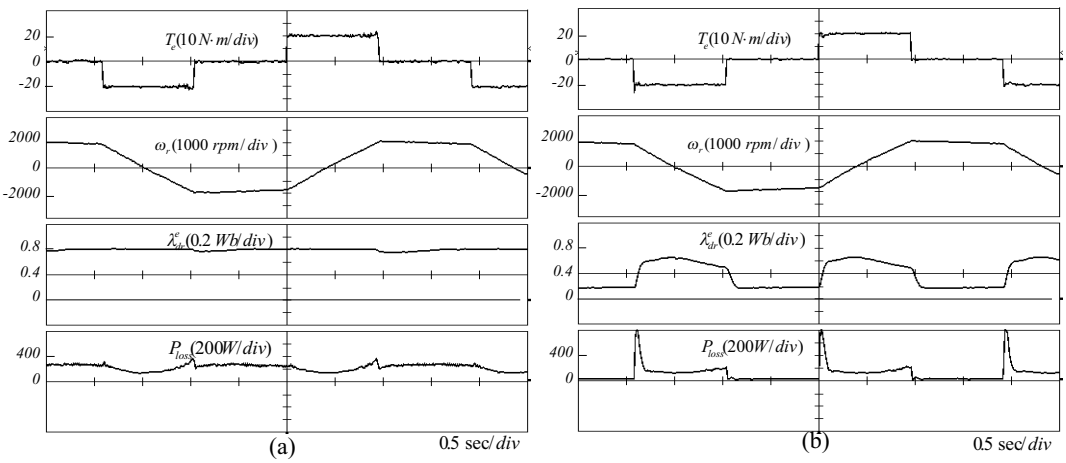

Figure 8.7: Experimental results of torque, speed, flux, and loss when the torque command changes from 20 to 0 and from 0 to −20 Nm: (a)Conventional vector controller and (b)loss minimization control.

Fig. 8.8(a) and (b) show the experimental results speed, torque, flux, and loss when the speed command is kept at 1000rpm and the load torque changes from 0 to 20 Nm. Fig. 8.8(a) shows the responses of the conventional vector control method, while Fig. 8.8(b) shows those of the proposed LMC. When the load torque is 20 Nm, the power losses of the two methods are almost the same with 230 W; however, when the load torque is zero, the loss of the proposed method is reduced about 100 W.

8.3 Loss-Minimizing Control for IPMSMs

In the IPMSMs, torque is also dependent on the d–axis current. Therefore, like induction motors, there are numerous ways of combining dq-axes currents for a constant torque production. But, the loss is different for each current set, (i_d^e, i_q^e). Hence, the LMC of an IPMSM is a control method that controls torque with the current sets that minimize the loss. The solution derivation process of the IPMSM is

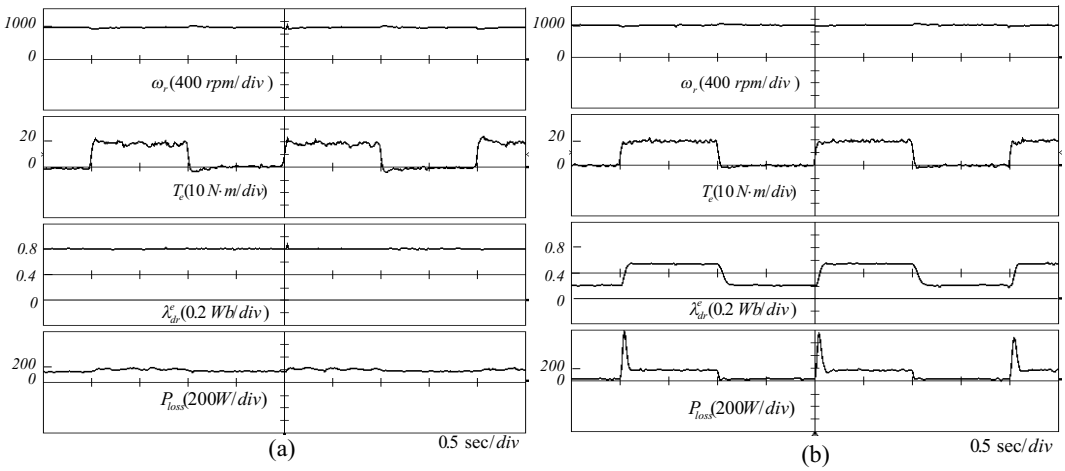

Figure 8.8: Experimental results of speed, torque, flux, and loss when the speed command is kept at 1000rpm and the load torque changes from 0 to 20 Nm: (a) conventional vector controller and (b) loss minimization control.

similar that of the induction motor. But the torque equation and voltage constraint are different. Further, negative d–axis current is utilized in the IPMSM.

Nakamura et al. [10] utilized the fact that high-efficiency is obtained at the unity power factor condition in the design of a controller for the PMSM. Morimoto et al. [11] established a loss-minimizing control based on an equivalent circuit that contained an iron loss model, as well as a copper loss model. Taking differentiation of the loss function, the d–axis current yielding the minimum loss was obtained. Bianchi et al. [14] searched the maximum torque experimentally when the current magnitude was fixed.

Gallegos-Lopez et al. [13] proposed an idea of extending maximum torque per ampere (MTPA) to the field-weakening region with a focus on automotive application. However, the iron loss was not properly considered. Cavallaro et al. [12] developed an on-line loss-minimizing algorithm based on the loss model of Morimoto [11].

In the following, a Lagrange equation is utilized in finding the loss-minimizing solution. The loss-minimizing solutions for different torque and speed are made into a look-up table, and based on that a loss-minimizing control (LMC) is developed. A similar method based on approximate analytical solutions was presented in [15].

8.3.1 PMSM Loss Equation and Flux Saturation

For the mathematical treatment, the losses are modeled as follows:

1) Copper Loss:
Copper loss is caused by the stator coil resistance r_s:

$$P_{cu} = \frac{3}{2} r_s I_s^2 = \frac{3}{2} r_s (i_d^2 + i_q^2). \tag{8.53}$$

2) Iron Loss:
Iron loss consists of hysteresis loss and eddy current loss. Here, the total iron loss is simply modeled as

$$P_{iron} = c_{fe} \omega^{\gamma} (\lambda_d^2 + \lambda_q^2), \tag{8.54}$$

where $\gamma = 1.5 \sim 1.6$ and $c_{fe} = 1.5 \sim 1.6$.
3) Stray Loss:
The stray losses are due to the higher winding space harmonics and slot harmonics. These losses take place in the surface layers of the stator and rotor adjacent to the air gap and in the volume of the teeth. The calculation of stray losses is difficult and does not guarantee a satisfactory accuracy. In practice, the stray losses are evaluated as

$$P_{str} = c_{str} \omega^2 (i_d^2 + i_q^2), \tag{8.55}$$

where c_{str} is the stray loss coefficient [3].

Summing the above losses, the total loss P_t is equal to

$$\begin{aligned} P_t &= P_{cu} + P_{iron} + P_{str} \\ &= (\frac{3}{2} r_s + c_{str} \omega^2)(i_d^2 + i_q^2) + c_{fe} \omega^{\gamma} (\lambda_d^2 + \lambda_q^2) \\ &= k_1(\omega) i_d^2 + k_2(\omega) i_q^2 + k_3(\omega) i_d + k_4(\omega) \end{aligned} \tag{8.56}$$

where

$$\begin{aligned} k_1(\omega) &= \frac{3}{2} r_s + c_{fe} \omega^{\gamma} L_d^2 + c_{str} \omega^2, \\ k_2(\omega) &= \frac{3}{2} r_s + c_{fe} \omega^{\gamma} L_q^2 + c_{str} \omega^2, \\ k_3(\omega) &= 2 c_{fe} \omega^{\gamma} L_d \psi_m, \\ k_4(\omega) &= c_{fe} \omega^{\gamma} \psi_m^2 . \end{aligned}$$

Hereforth, illustrations are made with an example electric vehicle (EV) motor. Its picture and parameters are listed in Fig. 8.9 and Table 8.2.

The stator flux is proportional to the stator current. However, as the current increases, core saturation develops gradually. Fig. 8.10 shows the measured values of fluxes by utilizing the steady-state relations:

$$\begin{aligned} \lambda_d &= \frac{1}{\omega}(v_q - r_s i_q), \\ \lambda_q &= -\frac{1}{\omega}(v_d - r_s i_q) . \end{aligned}$$

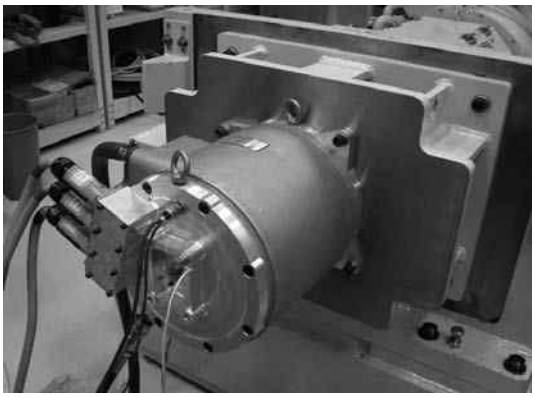

Figure 8.9: Example EV propulsion motor.

Table 8.2: Parameters and coefficients of a PMSM for FCEV

Input DC link voltage [V]	240
Maximum output power [kW]	80
Maximum torque [Nm]	220
Maximum speed [rpm]	11000
Maximum phase current [A]	400
Rated output power [kW]	40
Rated torque [Nm]	133
Rated speed [rpm]	2600
Rated phase current [A]	216
Number of pole (P)	6
Permanent magnet flux (λ_m) [Wb]	0.07
Number of stator slot	54
Switching frequency [kHz]	8
nominal d axis inductance (L_d) [uH]	375
nominal q axis inductance (L_q) [uH]	835
stator resistance (r_s) [mΩ]	29.5
coefficient of iron loss (C_{fe})	2.1×10^{-2}
coefficient of stray loss (C_{str})	6.5×10^{-9}
coefficient of q axis inductance (α)	4.85×10^{-4}

But some values corresponding to high currents ($\sqrt{i_d^2 + i_q^2} \geq 500$A) are extrapolated with the data obtained from FEM calculation. Note that almost no saturation in λ_d takes place along d–axis current. However, saturation in λ_q becomes apparent as i_q increases.

Based on the above measured values of flux linkage, the inductances are calcu-

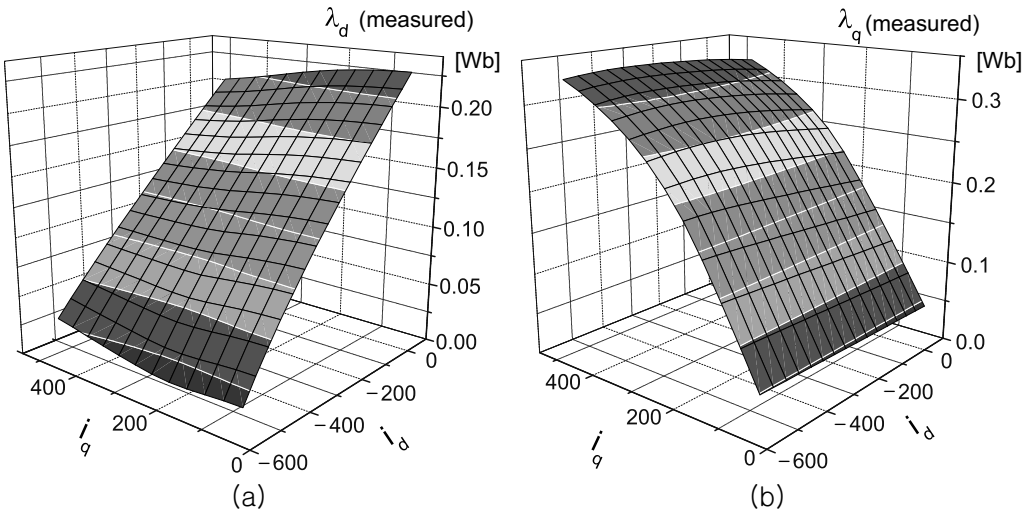

Figure 8.10: Measured stator flux linkages versus dq-axes current (a) d-axis flux linkage, (b) q-axis flux linkage.

lated via numerical differentiation:

$$\begin{aligned} L_d &= \frac{\partial \lambda_d}{\partial i_d} \approx \left.\frac{\Delta \lambda_d}{\Delta i_d}\right|_{i_q=const.}, \\ L_q &= \frac{\partial \lambda_q}{\partial i_q} \approx \left.\frac{\Delta \lambda_q}{\Delta i_q}\right|_{i_d=const.}. \end{aligned} \tag{8.57}$$

$$\begin{aligned} L_{dq} &= \frac{\partial \lambda_d}{\partial i_q} \approx \left.\frac{\Delta \lambda_d}{\Delta i_q}\right|_{i_d=const.}, \\ L_{qd} &= \frac{\partial \lambda_q}{\partial i_d} \approx \left.\frac{\Delta \lambda_q}{\Delta i_d}\right|_{i_q=const.}. \end{aligned} \tag{8.58}$$

Fig. 8.11 shows the plots of inductances versus current. Note that $L_q > L_d$ and that the cross coupling inductances, L_{dq} and L_{qd}, are small enough to be neglected. The saturation effect is noticeable in L_q as i_q increases.

To show why $L_q > L_d$ and the saturation effect is more pronounced in q–axis, FEM simulation results of an example six pole IPMSM are presented in Fig. 8.12. In the FEM simulations, PMs were not set in the cavities. Fig. 8.12 (a) shows the flux lines when only the d–axis current is excited, whereas Fig. 8.12 (b) shows the same when only the q–axis current is excited. Note that the cavities are arranged in favor of q–axis flux generation. For d–axis flux, the cavities function as barrier. Therefore, more flux lines are formed when q–axis current flows, and it substantiates $L_q > L_d$. Further, it also tells that the possibility of core saturation is higher with i_q^e.

Fig. 8.11 shows inductances versus current obtained by processing the experimental data according to (8.57). Almost no saturation is observed in L_d. As indicated in Fig. 8.11 (b), the variation in L_q is approximated by a linear function in i_q such that

$$L_q = L_{q0}(1 - \alpha i_q), \tag{8.59}$$

where $\alpha > 0$ is a constant representing the slope.

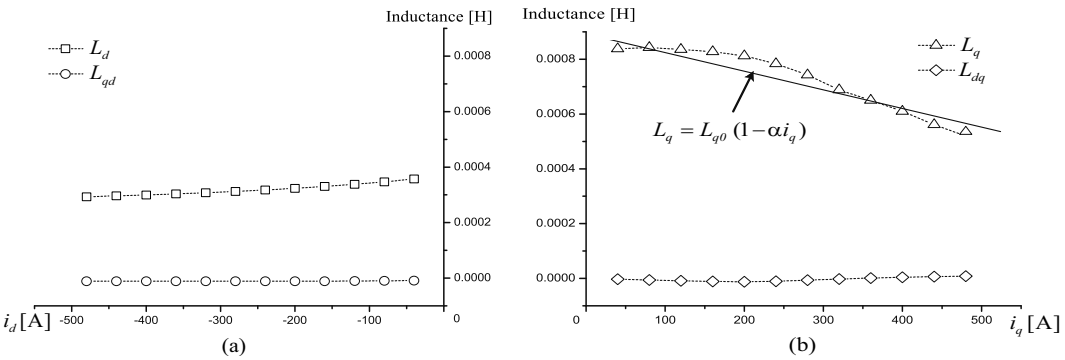

Figure 8.11: Measured values of (a) L_d and L_{qd} versus i_d when $i_q = 160$A, (b) L_q and L_{dq} versus i_q when $i_d = -160$A.

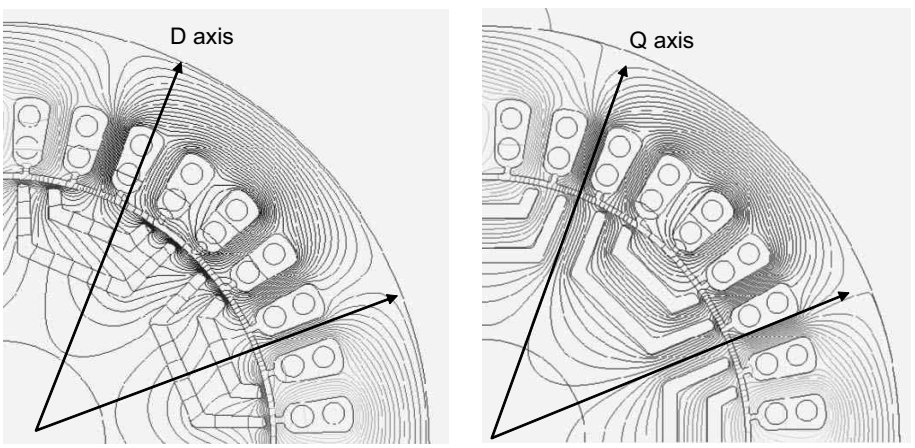

Figure 8.12: Flux lines excited by (a) i_d^e and (b) i_q^e.

8.3.2 Solution Search by Lagrange Equation

To produce a requested torque T_0 for a given speed ω, there are numerous choices for (i_d, i_q). But, we consider the loss-minimizing current set (i_d, i_q) for a given

torque value T_0 and speed ω. Further, there are voltage and current limits. The loss minimization is formulated as

$$\text{Minimize } P_t(i_d,\, i_q) = (\frac{3}{2}r_s + c_{str}\omega^2)(i_d^2 + i_q^2) + c_{fe}\omega^\gamma((L_d i_d + \psi_m)^2 + L_q^2 i_q^2)$$

$$\text{subject to} \quad \frac{3P}{4}(\psi_m i_q + (L_d - L_q) i_d i_q) - T_0 = 0, \tag{8.60}$$

$$(L_d i_d + \psi_m)^2\omega^2 + \omega^2(L_q i_q)^2 \le V_{max}^2, \tag{8.61}$$

$$i_d^2 + i_q^2 \le I_{max}^2. \tag{8.62}$$

Since the loss-minimizing control problem is an optimization under inequality constraints, one may need to apply Kuhn−Tucker theorem. However, we separate the cases depending whether the optimal solution is found on the boundary or in the interior of the constraints.

First, we just consider the optimization in the interior. Let the Lagrangian be defined by

$$L(i_d, i_q) = P_t(i_d, i_q) + \mu(T_e - T_0)$$

where μ is the Lagrangian multipliers. The necessary conditions for the existence of the optimal solution are

$$\begin{aligned}\frac{\partial L(i_d, i_q)}{\partial i_d} &= 3r_s i_d + 2c_{str}\omega^2 i_d + 2c_{fe}\omega^\gamma L_d^2 i_d \\ &\quad + 2c_{fe}\omega^\gamma L_d \psi_m + \mu\frac{3P}{4}(L_d - L_q) i_q = 0, \end{aligned} \tag{8.63}$$

$$\begin{aligned}\frac{\partial L(i_d, i_q)}{\partial i_q} &= 3r_s i_q + 2c_{str}\omega^2 i_q + 2c_{fe}\omega^\gamma L_q^2 i_q \\ &\quad + \mu\frac{3P}{4}\psi_m + \mu\frac{3P}{4}(L_d - L_q) i_d = 0. \end{aligned} \tag{8.64}$$

Eliminating μ from (8.63) and (8.64) and substituting $i_q = T_0 / \frac{3P}{4}(\psi_m + (L_d - L_q) i_d)$, we obtain a 4^{th}-order equation [15]:

$$f_{\omega,\, T_0}(i_d) = A i_d^4 + B i_d^3 + C i_d^2 + D i_d + E = 0 \tag{8.65}$$

where

$$
\begin{aligned}
A &= \frac{27P^3}{64}(L_d - L_q)^3(3r_s + 2c_{str}\omega^2 + 2c_{fe}\omega^\gamma L_d^2) \\
B &= \frac{27P^3}{64}\psi_m(L_d - L_q)^2(9r_s + 6c_{str}\omega^2 + 6c_{fe}\omega^\gamma L_d^2 \\
&\quad +2(L_d - L_q)c_{fe}\omega^\gamma L_d) \\
C &= \frac{27P^3}{64}\psi_m^2(L_d - L_q)(9r_s + 6c_{str}\omega^2 + 6c_{fe}\omega^\gamma L_d^2 \\
&\quad +6(L_d - L_q)c_{fe}\omega^\gamma L_d) \\
D &= \frac{27P^3}{64}\psi_m^3(3r_s + 2c_{str}\omega^2 + 2c_{fe}\omega^\gamma L_d^2 \\
&\quad +6(L_d - L_q)c_{fe}\omega^\gamma L_d) \\
E &= \frac{27P^3}{32}\psi_m^4 c_{fe}\omega^\gamma L_d - \frac{9P}{4}(L_d - L_q)r_s T_0^2 \\
&\quad -\frac{3P}{2}(L_d - L_q)c_{str}\omega^2 T_0^2 \\
&\quad -\frac{3P}{2}(L_d - L_q)c_{fe}\omega^\gamma L_q^2 T_0^2
\end{aligned}
$$

Note that all the coefficients $A \sim E$ contains ω, and that only E includes torque T_0.

Fig. 8.13 (a), (b), and (c) show the plots of (8.65) for different torque and speed. They are close to straight lines in the region where $i_d < 0$, so that it is easy to find the zero crossing points which were marked by "×". The second row of Fig. 8.13 shows the curves of motor losses P_t versus i_d along the constant torque lines. The loss curves were calculated by utilizing (8.56). It should be noted that P_t has the minimum values where function f crosses zero, as predicted by the necessary conditions (8.60), (8.63), and (8.64) for optimality. That is, minimum values of P_t are obtained at the i_d's satisfying $f_{\omega, T_0}(i_d) = 0$. The third row of Fig. 8.13 shows the plots of constant torque curves in the current plane with current and voltage limits. The optimal points are also marked by "×". However, as the speed increases, the voltage limit curve shrinks. As a result, some solutions located out of the voltage limit, and marked by "⋇". Those points should be replaced by the points on the boundary. That is, in such cases the solution is found on an intersection of the voltage limit ellipse and the torque parabola[13]. The solution on the boundary was marked by "⊗".

8.3.3 Construction of LMC Look-Up Table

The loss-minimizing solutions need to be prepared as a table a priori. In the following, an algorithm of generating the loss-minimizing (i_d, i_q) sets is summarized:

For a given speed ω_j, choose a feasible torque T_e^k from the torque-speed curve, where "feasible" means that a solution exists within the voltage and current limits.

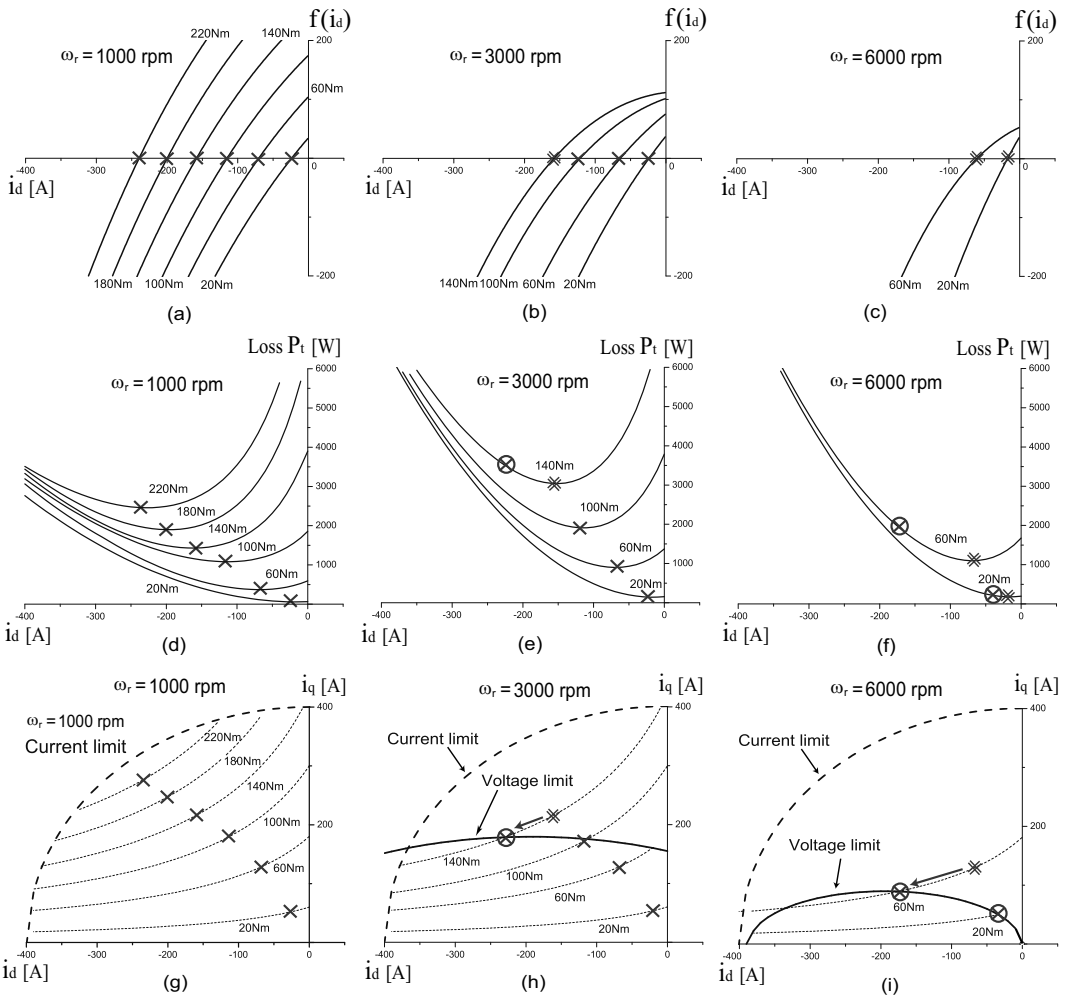

Figure 8.13: Calculated results illustrating how to find the loss-minimizing (i_d, i_q) for three different speeds: (a), (b), and (c): plot of $f(i_d)$ for different torques, (d), (e), and (f): power loss curves along constant torque contours (g), (h), and (i): constant torque contours in the (i_d, i_q) plane.

For ω_j, we denote the region inside a voltage limit by

$$U_V^j = \left\{ (i_d, i_q) \mid (L_d i_d + \psi_m)^2 + (L_q i_q)^2 \ \leq \ \frac{V_{max}^2}{\omega_j^2} \right\},$$

where $V_{max} = V_{DC}/\sqrt{3}$. A procedure for generating the LMC table consists of two parts: from the interior points and from the boundary.

A1 (From interior)

i) Calculate the coefficients $A \sim E$ of function f utilizing (ω_i, T_e^j);

ii) Plot $f(i_d)$ and find a zero crossing value, i_d^{jk};

iii) Obtain q–axis current corresponding to i_d^{jk} in such a way that $i_q^{jk} = \frac{4}{3P} T_e^k / \left(\psi_m + (L_d - L_q) i_d^{jk}\right)$;

iv) Check whether or not the current pair satisfies the voltage limit condition, i.e., check $(i_d^{jk}, i_d^{jk}) \in U_V^j$.

If the solution is outside of the voltage limit, then the solution should be extrapolated to the boundary along the constant torque curve and the optimal solution is found on an intersection point between the torque and the voltage limit curves. When there are two intersection points, the left side solution will be the optimal since it has a shorter length. A method of finding the boundary optimal solution from (i_d^{jk}, i_q^{jk}) can be summarized as:

A2 (From boundary)

i) Let $i_d^{jk'} = i_d^{jk} - \Delta i_d$;

ii) Find the corresponding q–axis current utilizing $i_q^{jk} = \frac{4}{3P} T_e^k / \left(\psi_m + (L_d - L_q) i_d^{jk}\right)$;

iii) Check whether $(i_d^{jk'}, i_d^{jk'}) \in U_V^j$. If "yes," stop. If "no," let $(i_d^{jk}, i_q^{jk}) = (i_d^{jk'}, i_q^{jk'})$, and go to Step i).

As we run (**A2**), the point moves to the left along the constant torque line T_e^j to the point where the torque line intersects the voltage limit curve.

Repeating algorithms (**A1**) and (**A2**) for all feasible (T_e^k, ω_r) under the speed and current limits, we can construct a look-up table of the optimal current pairs.

8.3.4 LMC-Based Controller and Experimental Setup

Fig. 8.14 shows a PMSM controller, which includes the LMC table. The LMC table requires torque and speed as the input variables, and provides the optimal current commands. The LMC table is made for the largest possible DC link voltage in operation. However, the table output values are checked to find whether or not they are feasible under a given DC link voltage. If it is not feasible, then the output values are adjusted according to algorithm(**A2**). Next, the table output values are used for the current commands, which minimize the motor loss for a given speed, torque, and DC link voltage. Conventional PI controllers can be used for d and q–axis current control along with decoupling and back-EMF compensation.

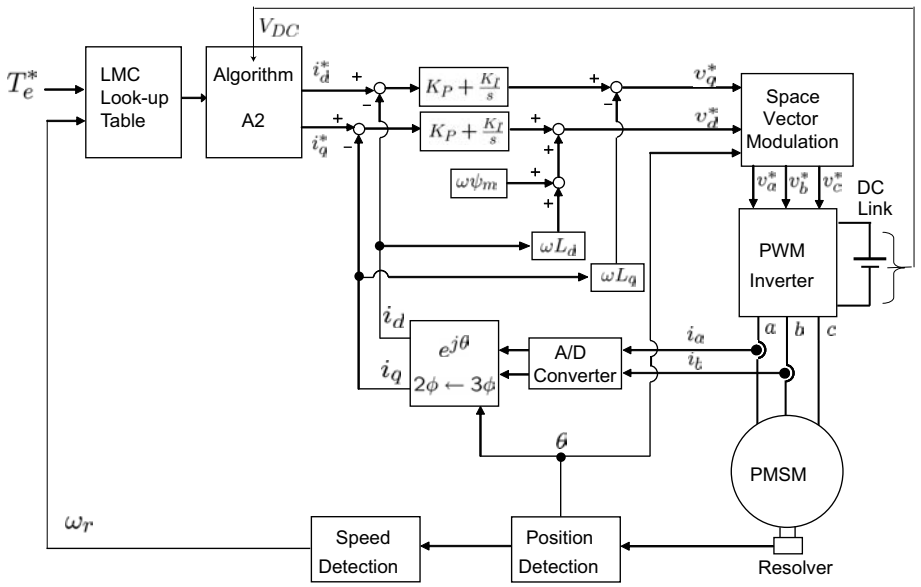

Figure 8.14: LMC structure for IPMSM.

The experimental environment is shown in Fig. 8.15. The proposed LMC were implemented utilizing a floating-point DSP (MPC5554). The PWM switching frequency was selected to be 8kHz and the dead-time 2μs. Current control routine was carried out every 125μs, and torque command was refreshed at every 1.25ms.

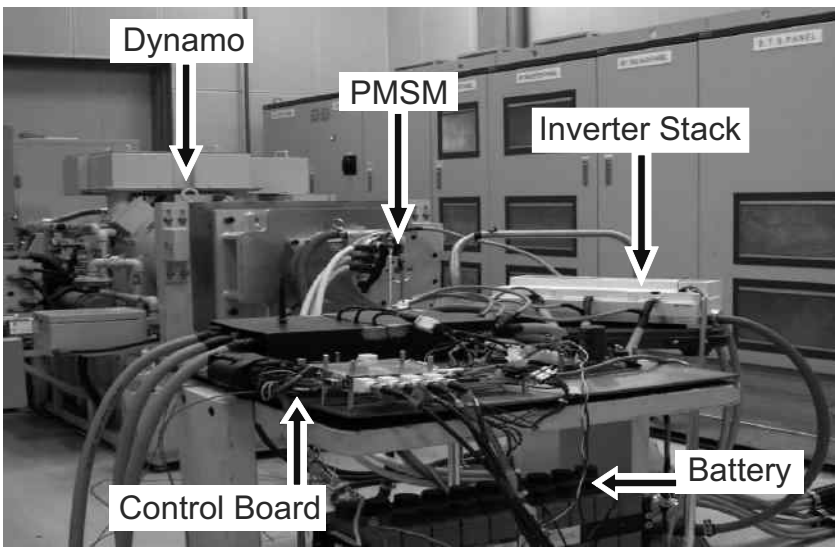

Figure 8.15: Photograph of the experimental setup.

The PMSM under test was controlled in a torque mode by an inverter with the LMC scheme, and the induction motor of the dynamo was controlled in a speed control mode. A power analyzer monitors the input power ($V_{DC} \cdot I_{DC}$) at the DC link. A torque transducer was also installed between the two motors to measure the output torque. Through multiplying a measured torque by motor speed, mechanical shaft power ($P_{out} = T_e \cdot \omega_r$) was obtained. The motor power loss was calculated according to

$$P_t = V_{DC} I_{DC} - T_e \cdot \omega_r - P_{inv}, \tag{8.66}$$

where P_{inv} is the inverter loss. Inverter loss comes from conduction and switching losses of IGBTs and diodes, i.e., $P_{inv} = P_{IGBTs} + P_{diode}$, where P_{IGBTs} and P_{diode} are the IGBT and diode losses, respectively. Based on the method proposed in [6], the IGBT and diodes losses are estimated as follows

$$P_{IGBT} = 6\left\{\frac{1}{2}DT\left(\frac{2\sqrt{2}}{\pi}I_c V_{ce}^{(on)}\right) + \frac{1}{2}E_{ts} f_{sw}\right\}, \tag{8.67}$$

$$P_{diode} = 6\left\{\frac{1}{2}(1-DT)\left(\frac{2\sqrt{2}}{\pi}I_c V_F^{(on)}\right) + \frac{1}{2}E_{rr} f_{sw}\right\}, \tag{8.68}$$

where $V_{ce}^{(on)}$ is the collector-emitter voltage during on-state, DT is an average conduction time of IGBT, I_c is the rms value of phase current, E_{ts} is the total switching loss of IGBT, $V_F^{(on)}$ is the on-drop voltage of diode, E_{rr} is the reverse recovery loss of diode, and f_{sw} is the PWM switching frequency. Note that DT is dependent on power factor ($\cos\phi$), and that the conduction times of IGBT and diode appear to be complementary. For the switching and reverse recovery losses of IGBT and diode, we utilized the data in the data sheets.

Iron loss coefficient C_{fe} was selected to be 0.021 based on FEM calculation results around the nominal operating point, and we let $\gamma = 1.5$. It was assumed that the mechanical losses such as bearing and windage losses are small enough to be negligible. As a consequence, $P_t - P_{cu} - P_{fe}$ would be close to the stray loss, P_{str}. Based on this method, the coefficient, C_{str} was selected to be 6.5×10^{-9}. This approximation corresponds to a rough estimation, $P_{str} \approx 0.03 \sim 0.05 P_{out}$ [3], of the stray loss of small motors.

8.3.5 Experimental Results

The parameters, as well as loss coefficients, c_{fe} and c_{str}, of the PMSM used in the experiment are summarized in Table 8.2. Instead of utilizing algorithms (**A1**) and (**A2**), the loss-minimizing current sets can be found by the experimental method that scans the motor losses over feasible mesh points in the current plane. Fig. 8.16 shows the loss-minimizing currents (i_d, i_q) for different speed and torque conditions found by an experimental scanning method. Fig. 8.18 shows the colored efficiency map of the motor. Efficiency ranges above 90% in most torque-speed region, but it is low in the low-speed/low-torque region.

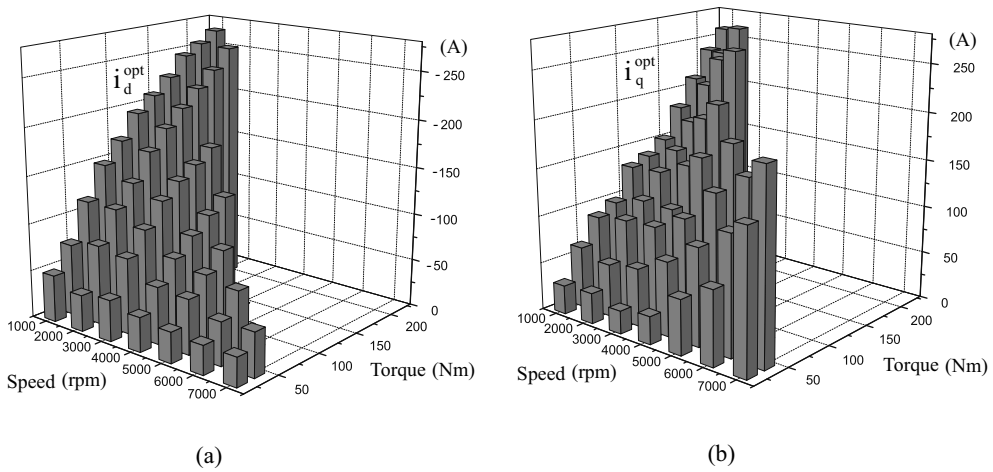

Figure 8.16: Loss-minimizing currents (i_d, i_q) for different speed and torque conditions found by an experimental scanning method.

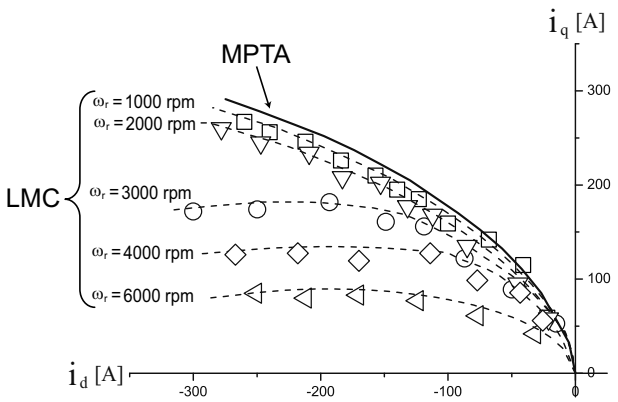

Figure 8.17: Loss-minimizing (i_d, i_q) under fixed speeds 1000, 3000, and 6000rpm, while the torque is increasing. Symbols : experimental results, dashed line : computed results.

Fig. 8.17 shows the loss-minimizing (i_d, i_q) under fixed speeds 1000∼6000rpm, while the torque is increasing. It compares the loss-minimizing data obtained from the experimental scanning method with those from algorithms (**A1**) and (**A2**) (symbols: experimental results, dashed line: computed results). This shows that the two methods yield the same results. Fig. 8.17 also shows the contour of MTPA. Note again that MTPA is independent of the speed, and thus it cannot reflect the iron loss or the stray loss, which are dependent upon the speed. The LMC results at 1000rpm are similar to those of MTPA.

Fig. 8.19 shows the plots of responses to a varying load torque at constant speed

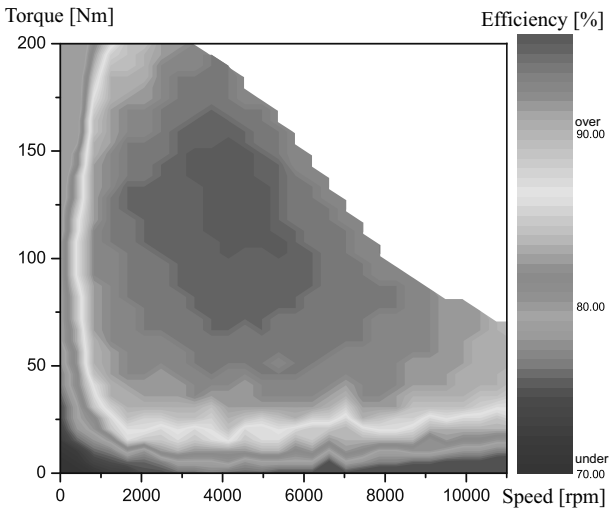

Figure 8.18: Efficiency map for the IPMSM for EV.

(2000rpm). Note that both i_d and i_q change when torque varies. It displays the plots of measured shaft power and DC link power. The LMC results were compared to those of MTPA. Note from Fig. 8.19 (c) that LMC yielded lower loss than MTPA.

Fig. 8.20 shows the responses when the operating points move along the maximum torque and maximum power contours with the LMC. Fig. 8.20 (b) shows the current contour in the d, q current plane which corresponds to speed, torque, power, and loss plots shown in Fig. 8.20 (a). During the period from the origin (start) to the point O, torque was increased rapidly to the maximum (400A). Then to meet the power rating of the inverter, the current magnitude was decreased to 300A (Point P). Then, the points followed the current limit line with the increase in speed (Point Q). Fig. 8.20 (c) shows the computed result of the current trajectory.

8.3.6 Summary

The optimal condition ended up with a 4^{th}-order polynomial in i_d. A zero crossing point of the polynomial was shown to be the loss-minimizing point. The calculated minimizing solutions were compared with the values obtained from an experimental scanning method. The two results agreed in most torque-speed range. In addition, the loss-minimizing data were made into a look-up table, and used for constructing an LMC. The proposed LMC provides the loss-minimizing current commands in all operating ranges.

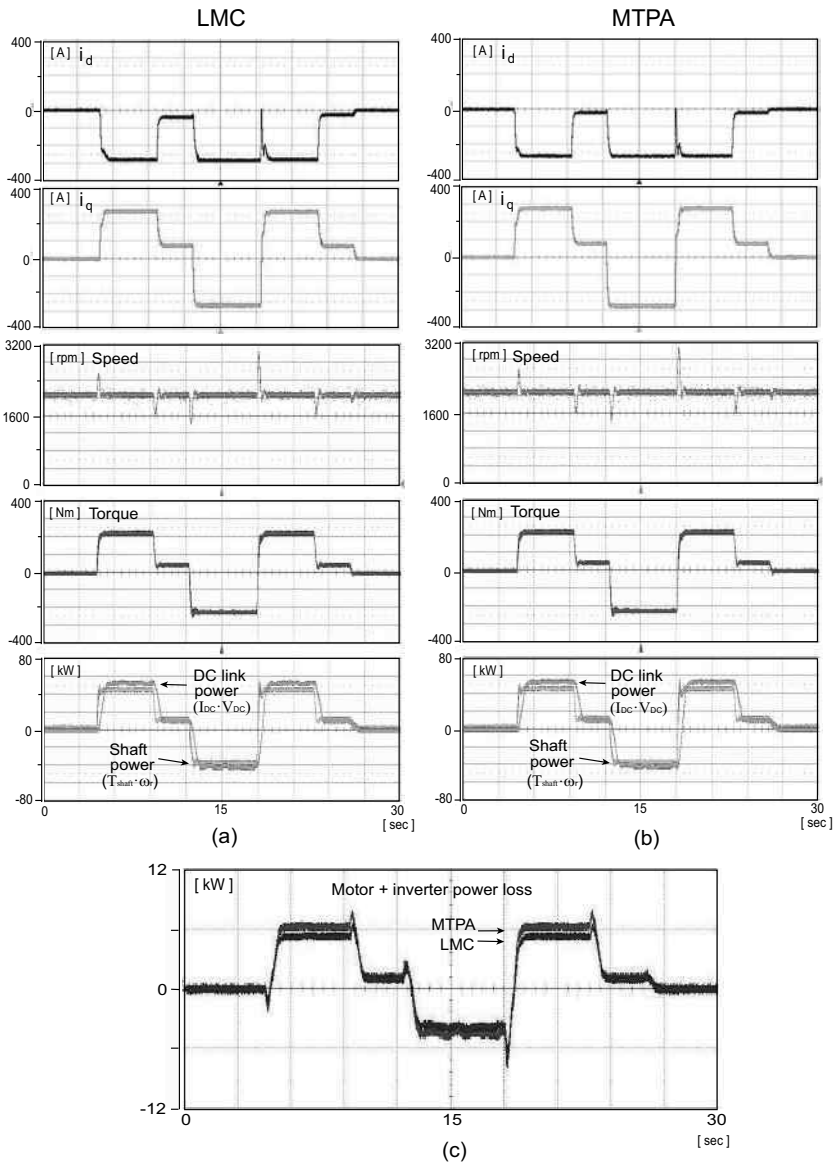

Figure 8.19: Current responses when load torque changes at 2000rpm: (a) LMC, (b) MTPA, and (c) the loss comparision.

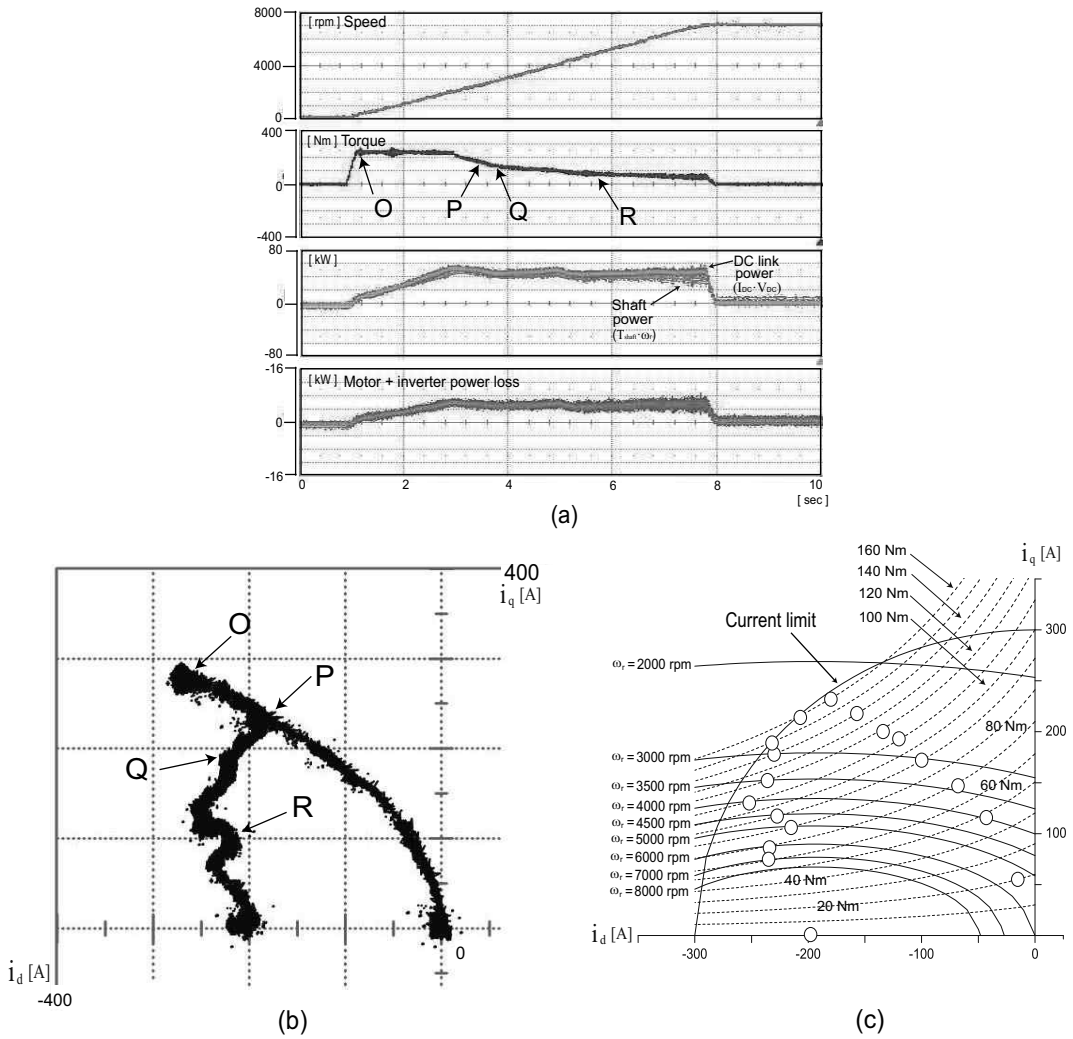

Figure 8.20: Excursion along maximum torque and maximum power contour with LMC control: (a) Speed, torque, power, and loss plots, (b) Current contour in the d, q current plane, (c) Computed current trajectory.

Bibliography

[1] C. C. Mi, G. R. Slemon, and R. Bonert, "Minimization of iron losses of permanent magnet synchronous machines," *IEEE Trans. on Energy Convers.,* vol. 20, no. 1, Mar. 2005.

[2] A. Binder, *Permanent Magnet Synchronous Machine Design,* Lecture Note, Pohang, May 2008.

[3] J. F. Gieras and M. Wing, *Permanent Magnet Motor Technonology, Design Applications*, 2nd. Ed., Marcel, Dekker, Inc., New York, 2002.

[4] M. Zahn, "Electromagnetic Field Theory, a problem solving approach" John, Wiley & Son. Inc., 1979.

[5] R.D. Lorenz and S.M. Yang, Efficiency-optimized flux trajectories for closed-cycle operation of field-orientation induction machine drives, *IEEE Trans. Ind. Appl.*, Vol. 28, No. 3, pp. 574 – 580, 1992.

[6] F. Abrahamsen, F. Blaabjerg, J.K. Pedersen, and P.B. Thoegersen, Efficiency-optimized control of medium-size induction motor drives, *IEEE Trans. Ind. Appl.*, Vol. 37, No. 6, pp.1761 – 1767, 2001.

[7] J.C. Moreira, T.A. Lipo, and V. Blasko, Simple efficiency maximizer for an adjustable frequency induction motor drive, *IEEE Trans. Ind. Appl.*, Vol. 27, No. 5, pp. 940 – 946, 1991.

[8] F. Fernandez-Bernal, A. Garcia-Cerrada, and R. Faure, Model based loss minimization for DC and AC vector-controlled motors including core saturation, *IEEE Trans. Ind. Appl.*, Vol. 36, No. 3, pp. 755 – 763, 2000.

[9] S. Lim and K. Nam, Loss-minimising control scheme for induction motors, *IEE Proc.-Electr. Power Appl.*, Vol. 151, No. 4, pp. 385 – 397, July 2004.

[10] Y. Nakamura, F. Ishibashi, and S. Hibino, "High-efficiency drive due to power factor control of a permanent magnet synchronous motor" *IEEE Trans. Power Electron.,* vol 10, Issue 2, pp. 247 – 253, Mar. 1995.

[11] S. Morimoto, Y. Tong, Y. Takeda, and T. Hirasa, "Loss minimization control of permanent magnet synchronous motor drives," *IEEE Trans. Ind. Electron.,* vol. 41, no. 5, pp. 511 – 517, Oct. 1994.

[12] C. Cavallaro, A. O. D. Tommaso, R. Miceli, A. Raciti, G. R. Galluzzo, and M. Tranpanese, "Efficiency enhancement of permanent-magnet synchronous motor drives by online loss minimization approaches," *IEEE Trans. Ind. Electron.,* vol 52, no. 4, pp. 1153 – 1160, Aug. 2005.

[13] G. Gallegos-Lopez, F. S. Gunawan, and J. E. Walters, "Optimum torque control of permanent-magnet AC machines in the field-weakened region," *IEEE Trans. Ind. Appl.,* vol. 41, no. 4, pp. 1020 – 1028, July/Aug. 2005.

[14] N. Bianchi, S. Bolognani, and M. Zigliotto, "High-performance PM synchronous motor drive for an electrical scooter," *IEEE Trans. Ind. Appl.,* vol. 19, no. 4, pp. 715 – 723, Dec. 2004.

[15] J. Lee, K. Nam, S. Choi, and S. Kwon, Loss-Minimizing Control of PMSM With the Use of Polynomial Approximations, *IEEE Trans. on Power Elec.*, Vol 24, No. 4, pp. 1071 – 1082, April, 2009.

Problems

8.1 Consider calculating the eddy current loss of the lamination stack shown in Fig. 8.3.

a) Consider a narrow loop whose area is $4xy$ shown in Fig. 8.21. Show that the EMF around the loop is equal to $v = \dfrac{4L}{W/N} x^2 \dfrac{dB}{dt}$.

b) Denote by σ the conductivity of the core material. Assume that $L \gg W/N$ and that the loop has incremental width dx. Show that the resistance of the loop is

$$r_x = \frac{4}{\sigma D} \frac{L}{W/N} \frac{x}{dx} .$$

c) Show that the dissipated power, dP_{xy} in each incremental loop is

$$dP_{xy} = \frac{4\sigma LD}{W/N} x^3 dx \left(\frac{dB}{dt} \right)^2 .$$

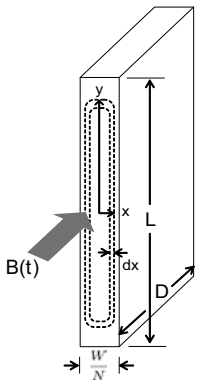

Figure 8.21: A laminated sheet (Problem 8.1).

d) Show that the power loss, P_{sheet} in each sheet is

$$P_{sheet} = \frac{L\sigma DW^3}{16N^3}\left(\frac{dB}{dt}\right)^2.$$

e) Assume further that field density is given by $B(t) = B_m \sin(2\pi ft)$, where f is a frequency. Show that the total eddy current loss of the stack is

$$P_{st} = N \times P_{sheet} = \frac{\pi^2 \sigma LDW^3}{4N^2} f^2 B_m^2 \cos^2(2\pi ft).$$

f) Show that the average value of P_{st} is equal to (8.3).

8.2 Derive (8.45) from (5.34) and (5.36).

8.3 Derive (8.47).

Chapter 9

Sensorless Control of PMSMs

Rotor position information is required for the field orientation control of PMSMs. But in some applications, installing position sensors makes problems: In some vacuum pumps, it is not possible to extend the motor shaft out of the motor housing due to the sealing problem. In crane and elevator applications, the distance between the motor and inverter is so far that the sensor signal attenuation and the noise interference make a problem. In some household appliances such as refrigerators and air conditioners, the cost pressure forces eliminate the use of speed sensors. The above problems have motivated the development of sensorless algorithms for PMSMs, and numerous works have been published.

Sensorless techniques for PMSMs are classified broadly into two types: back EMF based methods and signal injection methods. Matsui [1] pioneered back EMF based sensorless controls for PMSMs. Tomita et al.[2] introduced a disturbance observer for an EMF estimation. Corley and Lorenz [3] proposed a sensorless control that operated at zero speed with a high frequency current injection and a heterodyne filtering technique. Zhu et al.[6] introduced a sensorless control by signal injection that considered the cross-coupling magnetic saturation. Aihara et al.[7] combined a signal injection technique with a back EMF based position estimation method. A sliding mode current observer was utilized to find out the position and velocity estimates by Chen et al.[8]. The influence of measurement errors and inverter irregularities on the performance of the sensorless control was studied by Nahid-Mobarakeh et al.[9]. Xu and Rahman [10] and Liu et al.[11] used an adaptive sliding mode observer with a simple Kalman filter for the direct torque control of a PMSM. Bolognani et al.[12] applied the extended Kalman filter to a PMSM sensorless control, and studied a guideline for choosing the noise covariance matrices. Very recently, Ortega et al.[13] published a result on the application of a nonlinear observer to SPMSM. They utilized a new state variable and proposed a simple nonlinear state observer. Nonlinear state observers were utilized for for rotor position estimation in [14], [15]. It is widely recognized that the back EMF based methods perform relatively well in middle and high-speed applications. But the major drawback is that they behave poorly at standstill and in the low-speed region. Further, they are sensitive to inherent motor

torque ripple and noises. But with high-frequency signal injection methods, full torque-zero speed operation is feasible at the cost of probing signal power.

9.1 IPMSM Dynamics a Misaligned Frame

Since the exact rotor angle is not known, the field-oriented control must be constructed based on an angle estimate. The PMSM dynamics in a misaligned coordinate frame carries the additional voltage terms caused by the angle estimation error. The additional terms look like unknown nonlinear disturbances to the system. Certain types of observers are utilized to estimate the terms which contain the angle error.

Denote by $\overline{\theta}_e$ an angle estimate. The variables based on $\overline{\theta}_e$ are marked by overline's. Let

$$\Delta\theta_e = \overline{\theta}_e - \theta_e, \tag{9.1}$$

$$\Delta\omega_e = \overline{\omega}_e - \omega_e\,. \tag{9.2}$$

Fig. 9.1 shows aligned and misaligned axes and the angle error.

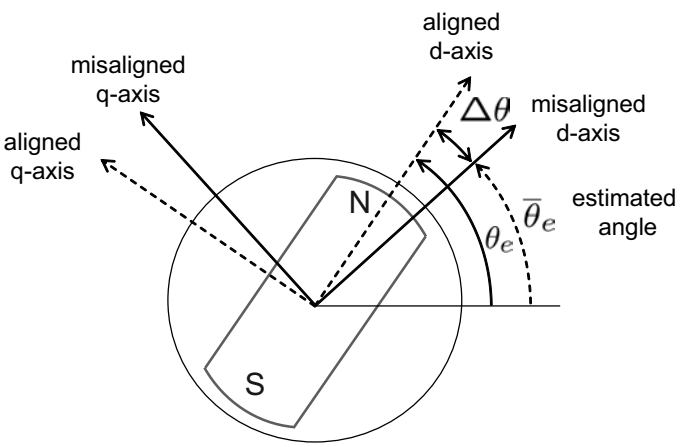

Figure 9.1: Misaligned (tilted) dq-frame.

An IPMSM model with respect to $\overline{\theta}_e$ is developed in the following. Recall from (6.29) that the flux in the stationary frame is equal to

$$\boldsymbol{\lambda}^s_{dq} = L_s\mathbf{i}^s_{dq} - \frac{3}{2}L_\delta e^{j2\theta_e}\mathbf{i}^{s*}_{dq} + \psi_m e^{j\theta_e}, \tag{9.3}$$

where $L_s = \frac{3}{2}L_{ss} + L_{ls}$. Transforming the flux (9.3) to the frame of $e^{j\overline{\theta}_e}$, we obtain

$$\overline{\boldsymbol{\lambda}}^e_{dq} \equiv e^{-j\overline{\theta}_e}\boldsymbol{\lambda}^s_{dq} = L_s e^{-j\overline{\theta}_e}\mathbf{i}^s_{dq} - \frac{3}{2}L_\delta e^{j(2\theta-\overline{\theta}_e)}(\mathbf{i}^s_{dq})^* + \psi_m e^{-j\Delta\theta_e}.$$

Defining the current in the reference frame by $\bar{\mathbf{i}}^e_{dq} = e^{-j\overline{\theta}_e}\mathbf{i}_{dq}$, we have

$$\overline{\boldsymbol{\lambda}}^e_{dq} = L_s\bar{\mathbf{i}}^e_{dq} - \frac{3}{2}L_\delta(\bar{\mathbf{i}}^e_{dq})^* e^{-j2\Delta\theta_e} + \psi_m e^{-j\Delta\theta_e}.$$

Therefore,

$$j\overline{\omega}_e\overline{\boldsymbol{\lambda}}^e_{dq} = j\overline{\omega}_e L_s\bar{\mathbf{i}}^e_{dq} - j\overline{\omega}_e\frac{3}{2}L_\delta(\bar{\mathbf{i}}^e_{dq})^* e^{-j2\Delta\theta_e} + j\overline{\omega}_e\psi_m e^{-j\Delta\theta_e} \tag{9.4}$$

$$p\overline{\boldsymbol{\lambda}}^e_{dq} = L_s p\bar{\mathbf{i}}^e_{dq} - \frac{3}{2}L_\delta(p\bar{\mathbf{i}}^e_{dq})^* e^{-j2\Delta\theta_e} + 3L_\delta j\Delta\omega_e(\bar{\mathbf{i}}^e_{dq})^* e^{-j2\Delta\theta_e} - j\Delta\omega_e\psi_m e^{-j\Delta\theta_e}. \tag{9.5}$$

Substituting (9.4) and (9.5) into (6.17), it follows that

$$\begin{aligned}\begin{bmatrix}\overline{v}^e_d\\ \overline{v}^e_q\end{bmatrix} &= r_s\begin{bmatrix}\bar{i}^e_d\\ \bar{i}^e_q\end{bmatrix} + \begin{bmatrix}L_s - \frac{3}{2}L_\delta\cos 2\Delta\theta_e & \frac{3}{2}L_\delta\sin 2\Delta\theta_e\\ \frac{3}{2}L_\delta\sin 2\Delta\theta_e & L_s + \frac{3}{2}L_\delta\cos 2\Delta\theta_e\end{bmatrix}\frac{d}{dt}\begin{bmatrix}\bar{i}^e_d\\ \bar{i}^e_q\end{bmatrix}\\ &\quad +(3\Delta\omega_e - \frac{3}{2}\overline{\omega}_e)L_\delta\begin{bmatrix}\sin 2\Delta\theta_e & \cos 2\Delta\theta_e\\ \cos 2\Delta\theta_e & -\sin 2\Delta\theta_e\end{bmatrix}\begin{bmatrix}\bar{i}^e_d\\ \bar{i}^e_q\end{bmatrix}\\ &\quad +\overline{\omega}_e L_s\begin{bmatrix}-\bar{i}^e_q\\ \bar{i}^e_d\end{bmatrix} + \omega_e\psi_m\begin{bmatrix}\sin\Delta\theta_e\\ \cos\Delta\theta_e\end{bmatrix}\end{aligned} \tag{9.6}$$

Note that the misaligned equation (9.6) is the same as the stationary IPMSM model, (6.32), if $\Delta\theta_e = -\theta$, $\Delta\omega_e = -\omega$, and $\overline{\omega}_e = 0$. That is, if the misaligned angle is equal to the rotor angle, then the synchronous IPMSM model turns out to be stationary IPMSM model.

9.1.1 Different Derivation of the Misaligned Model

Note again that

$$e^{\mathbf{J}\Delta\theta_e} = \begin{bmatrix}\cos\Delta\theta_e & \sin\Delta\theta_e\\ -\sin\Delta\theta_e & \cos\Delta\theta_e\end{bmatrix} \qquad \text{for} \qquad \mathbf{J} = \begin{bmatrix}0 & 1\\ -1 & 0\end{bmatrix}.$$

Denote the voltage and current vectors in the misaligned frame by $\overline{\mathbf{v}}^e_{dq} = e^{\mathbf{J}\Delta\theta_e}\mathbf{v}^e_{dq}$ and $\bar{\mathbf{i}}^e_{dq} = e^{\mathbf{J}\Delta\theta_e}\mathbf{i}^e_{dq}$ as in (9.34). Then, the IPMSM dynamics in the misaligned coordinate is written as

$$\overline{\mathbf{v}}^e_{dq} = e^{\mathbf{J}\Delta\theta_e}\begin{bmatrix}r_s + pL_d & -\omega_e L_q\\ \omega_e L_d & r_s + pL_q\end{bmatrix}e^{-\mathbf{J}\Delta\theta_e}\bar{\mathbf{i}}^e_{dq} + e^{\mathbf{J}\Delta\theta_e}\begin{bmatrix}0\\ \omega_e\psi_m\end{bmatrix}. \tag{9.7}$$

In some literature, the following notations are used:

$$\begin{aligned}L_{av} &\equiv \frac{L_d + L_q}{2} = L_s,\\ L_{df} &\equiv \frac{L_q - L_d}{2} = \frac{3}{2}L_\delta.\end{aligned}$$

Then,

$$
\begin{aligned}
& e^{\mathbf{J}\Delta\theta_e}\begin{bmatrix} pL_d & 0 \\ 0 & pL_q \end{bmatrix} e^{-\mathbf{J}\Delta\theta_e}\bar{\mathbf{i}}^e_{dq} \\
= \;& \Delta\omega_e \begin{bmatrix} L_{df}\sin 2\Delta\theta_e & -L_{av}+L_{df}\cos 2\Delta\theta_e \\ L_{av}+L_{df}\cos 2\Delta\theta_e & -L_{df}\sin 2\Delta\theta_e \end{bmatrix}\begin{bmatrix} \bar{i}^e_d \\ \bar{i}^e_q \end{bmatrix} \\
& + \begin{bmatrix} L_{av}-L_{df}\cos 2\Delta\theta_e & L_{df}\sin 2\Delta\theta_e \\ L_{df}\sin 2\Delta\theta_e & L_{av}+L_{df}\cos 2\Delta\theta_e \end{bmatrix}\begin{bmatrix} p\bar{i}^e_d \\ p\bar{i}^e_q \end{bmatrix}.
\end{aligned}
$$

Similarly, it follows that

$$
\begin{aligned}
& e^{\mathbf{J}\Delta\theta_e}\begin{bmatrix} 0 & -\omega_e L_q \\ \omega_e L_d & 0 \end{bmatrix} e^{-\mathbf{J}\Delta\theta_e}\bar{\mathbf{i}}^e_{dq} \\
= \;& (\overline{\omega}_e-\Delta\omega_e)\begin{bmatrix} -L_{df}\sin 2\Delta\theta_e & -L_{av}-L_{df}\cos 2\Delta\theta_e \\ L_{av}-L_{df}\cos 2\Delta\theta_e & L_{df}\sin 2\Delta\theta_e \end{bmatrix}\begin{bmatrix} \bar{i}^e_d \\ \bar{i}^e_q \end{bmatrix}.
\end{aligned}
$$

Then,

$$
\begin{aligned}
& \Delta\omega_e \begin{bmatrix} L_{df}\sin 2\Delta\theta_e & -L_{av}+L_{df}\cos 2\Delta\theta_e \\ L_{av}+L_{df}\cos 2\Delta\theta_e & -L_{df}\sin 2\Delta\theta_e \end{bmatrix}\begin{bmatrix} \bar{i}^e_d \\ \bar{i}^e_q \end{bmatrix} \\
& +(\overline{\omega}_e-\Delta\omega_e)\begin{bmatrix} -L_{df}\sin 2\Delta\theta_e & -L_{av}-L_{df}\cos 2\Delta\theta_e \\ L_{av}-L_{df}\cos 2\Delta\theta_e & L_{df}\sin 2\Delta\theta_e \end{bmatrix}\begin{bmatrix} \bar{i}^e_d \\ \bar{i}^e_q \end{bmatrix} \\
& = L_{df}(2\Delta\omega_e-\overline{\omega}_e)\begin{bmatrix} \sin 2\Delta\theta_e & \cos 2\Delta\theta_e \\ \cos 2\Delta\theta_e & -\sin 2\Delta\theta_e \end{bmatrix}\begin{bmatrix} \bar{i}^e_d \\ \bar{i}^e_q \end{bmatrix} + \overline{\omega}_e L_{av}\begin{bmatrix} -\bar{i}^e_q \\ \bar{i}^e_d \end{bmatrix}.
\end{aligned}
$$

Now, it is obvious that the above derivation yields the same equation as (9.6). For a more compact representation, let

$$
\begin{aligned}
L_\alpha &= L_{av}-L_{df}\cos 2\Delta\theta_e \\
L_\beta &= L_{av}+L_{df}\cos 2\Delta\theta_e \\
L_\gamma &= L_{df}\sin 2\Delta\theta_e.
\end{aligned}
$$

Then, the IPMSM model in a misaligned coordinate is

$$
\overline{\mathbf{v}}^e_{dq} = \mathbf{Z}\,\bar{\mathbf{i}}^e_{dq} + (\overline{\omega}_e-2\omega_e)L_{df}\mathbf{U} - \overline{\omega}_e L_{av}\mathbf{J}\,\bar{\mathbf{i}}^e_{dq} + \mathbf{e} \tag{9.8}
$$

where

$$
\begin{aligned}
\mathbf{Z} &= \begin{bmatrix} r_s-\overline{\omega}_e L_\gamma + L_\alpha p & -\overline{\omega}_e L_\beta + L_\gamma p \\ \overline{\omega}_e L_\alpha + L_\gamma p & r_s+\overline{\omega}_e L_\gamma + L_\beta p \end{bmatrix}, \\
\mathbf{U} &= \begin{bmatrix} \sin 2\Delta\theta_e & \cos 2\Delta\theta_e \\ \cos 2\Delta\theta_e & -\sin 2\Delta\theta_e \end{bmatrix}, \\
\mathbf{e} &= \omega_e\psi_m\begin{bmatrix} \sin\Delta\theta_e \\ \cos\Delta\theta_e \end{bmatrix}.
\end{aligned}
$$

The stationary IMPSM model can be derived from (9.8) by fixing the misaligned (tilted) frame. That is, the stationary IMPSM model is obtained by letting $\overline{\omega}_e = 0$ and $\overline{\theta}_e = 0$:

$$\begin{aligned}
\mathbf{v}_{dq}^s &= \left(\mathbf{Z}|_{\overline{\omega}_e=0}\right)\mathbf{i}_{dq}^s - 2\omega_e L_{df}\ \mathbf{U}|_{\overline{\theta}_e=0} + \omega_e\psi_m\begin{bmatrix}-\sin\theta_e\\ \cos\theta_e\end{bmatrix}\\
&= r_s\mathbf{i}_{dq}^s + \begin{bmatrix}L_s - \frac{3}{2}L_\delta\cos 2\theta_e & -\frac{3}{2}L_\delta\sin 2\theta_e\\ -\frac{3}{2}L_\delta\sin 2\theta_e & L_s + \frac{3}{2}L_\delta\cos 2\theta_e\end{bmatrix}\frac{d}{dt}\mathbf{i}_{dq}^s\\
&\quad -3\omega_e L_\delta\begin{bmatrix}-\sin 2\theta_e & \cos 2\theta_e\\ \cos 2\theta_e & \sin 2\theta_e\end{bmatrix} + \omega_e\psi_m\begin{bmatrix}-\sin\theta_e\\ \cos\theta_e\end{bmatrix}. \qquad (9.9)
\end{aligned}$$

Note that the resulting equation (9.9) is the same as (6.32).

9.2 Sensorless Control for SPMSMs

Two sensorless algorithms for SPMSM are illustrated in the following: One is Ortega's sensorless algorithm utilizing a nonlinear observer for stationary SPMSM model. The other one is Matsui's original sensorless algorithm that is still being used in home appliances.

9.2.1 Ortega's Nonlinear Observer for Sensorless Control

Recall from (6.3) that the P-pole SPMSM dynamics in the stationary frame is

$$\begin{aligned}
L_s\frac{d}{dt}\begin{bmatrix}i_d^s\\ i_q^s\end{bmatrix} &= -r_s\begin{bmatrix}i_d^s\\ i_q^s\end{bmatrix} - \omega_e\psi_m\begin{bmatrix}-\sin\theta_e\\ \cos\theta_e\end{bmatrix} + \begin{bmatrix}v_d^s\\ v_q^s\end{bmatrix} \qquad (9.10)\\
T_e &= \frac{3P}{4}\psi_m(i_q^s\cos\theta_e - i_d^s\sin\theta_e). \qquad (9.11)
\end{aligned}$$

Since the back EMF term contains the information of θ_e, the goal is to estimate $[-\sin\theta_e, \cos\theta_e]^T$ using $\mathbf{i}^s$ and $\mathbf{v}^s$.

Ortega et al. [13] developed a nonlinear observer for (9.10), which involves a coordinate change. A new state variable is defined such that

$$\mathbf{x} = L_s\begin{bmatrix}i_d^s\\ i_q^s\end{bmatrix} + \psi_m\begin{bmatrix}\cos\theta_e\\ \sin\theta_e\end{bmatrix}. \qquad (9.12)$$

Let

$$\mathbf{y} \equiv -r_s\begin{bmatrix}i_d^s\\ i_q^s\end{bmatrix} + \begin{bmatrix}v_d^s\\ v_q^s\end{bmatrix}. \qquad (9.13)$$

Note that $\mathbf{y}$ does not include any unknown terms, and thereby is available for measurement for all time. Then it follows from (9.10) and (9.12) that

$$\begin{aligned}
\dot{\mathbf{x}} &= L_s\frac{d}{dt}\begin{bmatrix}i_d^s\\ i_q^s\end{bmatrix} - \omega_e\psi_m\begin{bmatrix}\sin\theta_e\\ -\cos\theta_e\end{bmatrix}\\
&= \mathbf{y}. \qquad (9.14)
\end{aligned}$$

Define a function $\eta : \mathbb{R}^2 \to \mathbb{R}^2$ as

$$\eta(\mathbf{x}) \equiv \mathbf{x} - L_s \begin{bmatrix} i_d^s \\ i_q^s \end{bmatrix} = +\psi_m \begin{bmatrix} \cos\theta_e \\ \sin\theta_e \end{bmatrix}. \tag{9.15}$$

Then, the Euclidean norm is equal to

$$\|\eta(\mathbf{x})\|^2 = \psi_m^2. \tag{9.16}$$

The nonlinear observer is proposed as

$$\dot{\hat{\mathbf{x}}} = \mathbf{y} + \frac{\gamma}{2}\eta(\hat{\mathbf{x}})[\psi_m^2 - \|\eta(\hat{\mathbf{x}})\|^2], \tag{9.17}$$

where $\hat{\mathbf{x}} \in \mathbb{R}^2$ is the observer state variable and $\gamma > 0$ is the observer gain. Note that the distance, $\psi_m^2 - \|\eta(\hat{\mathbf{x}})\|^2$ from a circle is used as a steering term for observer state, $\hat{\mathbf{x}}$. Let the observation error be defined by

$$\chi \equiv -\frac{1}{\psi_m} e^{\mathbf{J}\theta_e}(\hat{\mathbf{x}} - \mathbf{x}). \tag{9.18}$$

Theorem 9.1 [13]
Consider the SPMSM model, (9.12) and (9.14), and a nonlinear observer, (9.15) and (9.17). The observation error χ defined by (9.18) converges asymptotically to the disk $\{\chi \in \mathbb{R}^2 | \, \|\chi\| \le 2\}$ as $t \to \infty$.

The observer state, $\hat{\mathbf{x}}$, evolves according to (9.17). But it satisfies a condition, $\|\chi\| \le 2$. It carries an important meaning: Temporarily, we let for some $(\xi_1, \xi_2) \in \mathbb{R}^2$

$$\hat{\mathbf{x}} = L_s \begin{bmatrix} i_d^s \\ i_q^s \end{bmatrix} + \psi_m \begin{bmatrix} \xi_1 \\ \xi_2 \end{bmatrix}. \tag{9.19}$$

Since $\|e^{\mathbf{J}\theta_e}\| = 1$, it follows from (9.18), (9.12), and (9.19) that

$$2 \ge \|\chi\| = \frac{1}{\psi_m}\|\hat{\mathbf{x}} - \mathbf{x}\| = \left\| \begin{bmatrix} \xi_1 - \cos\theta_e \\ \xi_2 - \sin\theta_e \end{bmatrix} \right\|.$$

Graphically, $2 \ge \|\chi\|$ forces to satisfy a necessary condition that (ξ_1, ξ_2) is in the unit circle centered at the origin, i.e., $\xi_1^2 + \xi_2^2 = 1$. At this state, we may rewrite $\xi_1 = \cos\hat{\theta}_2$ and $\xi_2 = \sin\hat{\theta}_2$, i.e.,

$$\hat{\mathbf{x}} = L_s \begin{bmatrix} i_d^s \\ i_q^s \end{bmatrix} + \psi_m \begin{bmatrix} \cos\hat{\theta}_e \\ \sin\hat{\theta}_e \end{bmatrix}. \tag{9.20}$$

Then, an angle estimate could be obtained from $\hat{\mathbf{x}}$ such that

$$\hat{\theta}_e = \tan^{-1}\left(\frac{\hat{x}_2 - L_s i_q^s}{\hat{x}_1 - L_s i_d^s}\right). \tag{9.21}$$

Remark

Since the above nonlinear observer is constructed based on the stationary model, it does not require speed information in the construction of an observer. This is an advantage when it is compared with the observer (9.24) constructed on a synchronous frame. See for example [1],[9].

Angle and Speed Estimation

To construct a speed controller or to compensate the cross coupling voltages, $\omega_e L_s i_d^s$ and $\omega_e L_s i_q^s$, it is necessary to estimate the speed. Some observers require the use of speed estimates (see Problem 9). But it is not good to obtain a speed estimate by the numerical differentiation of the position estimates.

In this part, a phase locked loop (PLL) type speed estimator is constructed from angle error, $\theta_e - \overline{\theta}_e$. Fig. 9.2 shows a block diagram of a PLL used for speed estimation [16],[17]. It is basically a tracking controller consisting of a PI regulator and an integrator. Recall from Chapter 1 that PI controllers have the ability of suppressing error under the presence of a disturbance. In the original PLL circuit, the bottom integrator consists of a voltage controlled oscillator (VCO) (voltage/frequency converter) and a pulse counter.

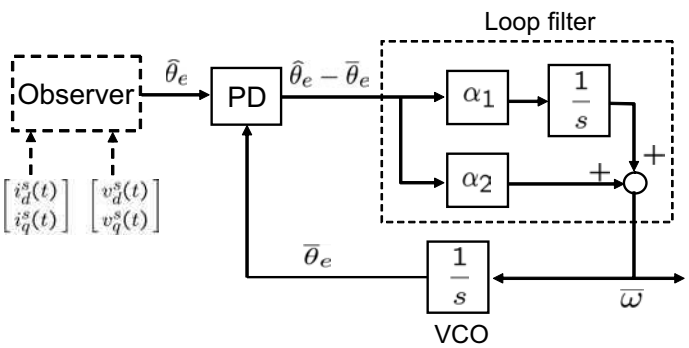

Figure 9.2: PLL type speed estimator utilizing $\theta - \overline{\theta}$.

Assuming $\dot{\theta}_e \approx 0$ and $\dot{\omega}_e \approx 0$, the estimator is described by

$$\begin{aligned} \dot{\overline{\omega}} &= \alpha_1(\hat{\theta}_e - \overline{\theta}_e) + \alpha_2(\hat{\omega}_e - \overline{\omega}_e)\,. \\ \dot{\overline{\theta}}_e &= \overline{\omega}_e\,. \end{aligned} \tag{9.22}$$

The node prior to the integrator, "VCO" signifies a speed information, thereby regarded as speed, i.e., $\overline{\omega}_e = \dot{\overline{\theta}}_e$. Defining errors by $\tilde{\omega}_e = \hat{\omega}_e - \overline{\omega}_e$ and $\tilde{\theta}_e = \hat{\theta}_e - \overline{\theta}$ and assuming $\dot{\hat{\omega}}_e \approx 0$, it follows that

$$\begin{bmatrix} \dot{\tilde{\omega}}_e \\ \dot{\tilde{\theta}}_e \end{bmatrix} = \begin{bmatrix} -\alpha_2 & -\alpha_1 \\ 1 & 0 \end{bmatrix} \begin{bmatrix} \tilde{\omega}_e \\ \tilde{\theta}_e \end{bmatrix}$$

and the characteristic polynomial is equal to $s^2+\alpha_2 s+\alpha_1 = 0$. The PI gains (α_2, α_1) are selected such that the closed-loop bandwidth is larger than the speed bandwidth.

Control Block Diagram

The sensorless control block for a SPMSM, which includes the nonlinear observer, is shown in Fig. 9.3. The nonlinear observer outputs angle estimate $\hat{\theta}$, based on which the field orientation control is synthesized. The conventional PI controller is utilized for d and q axes current control along with the decoupling and the back-EMF compensation. The IP type speed controller is utilizing $\hat{\omega}_e$ that comes out from the speed estimator.

Jansson et al. [19] pointed that injection of d axis current enhanced the robustness of the sensorless system against r_s variation. They applied d–axis current in proportion to q–axis current. But, we inject d–axis current pulses in a low frequency region. To generate such current pulses, we apply a voltage pulse train as shown in Fig. 9.3. In this experiment, the pulse frequency is 200Hz, the peak level is 50 V, and the pulse duty is 0.2msec. Note that no d–axis current is injected if $|\omega| > 100rpm$.

Experimental Results

Experiments were performed with a dynamo test bench that was made with two SPMSMs. The shafts of the two motors are connected via a coupler as shown in Fig. 9.4. All the nonlinear observer and control algorithms were implemented in a TMS320vc33 DSP board. The PWM switching frequency was set to be 8kHz and the dead-time 2μs. The current control algorithm were carried out every 125μs, and the speed control loop was activated every 1.25ms. Dynamo motor controller was constructed with a DSP, PIC30F6015.

Table 9.1: Motor parameters of a SPMSM used for experiments

Parameters [Unit]	Values
Input DC link voltage [V]	200
Rated output power [kW]	0.3
Rated torque [Nm]	3.0
Rated speed [r/min]	1000
Rated phase current [A]	3.0
Number of pole (P)	8
Rotor flux per pole (ψ_m) [Wb]	0.11
Switching frequency [kHz]	8
Stator inductance (L) [mH]	1.14
Stator resistance (R_s) [Ω]	0.675

Fig. 9.5 shows $\sin\hat{\theta}$, $\cos\hat{\theta}$, and $\hat{\theta}$, along with real position θ measured by a 6000 pulses/rev encoder under no-load when (a) $\omega_r = 80$rpm and (b) 300rpm, respectively.

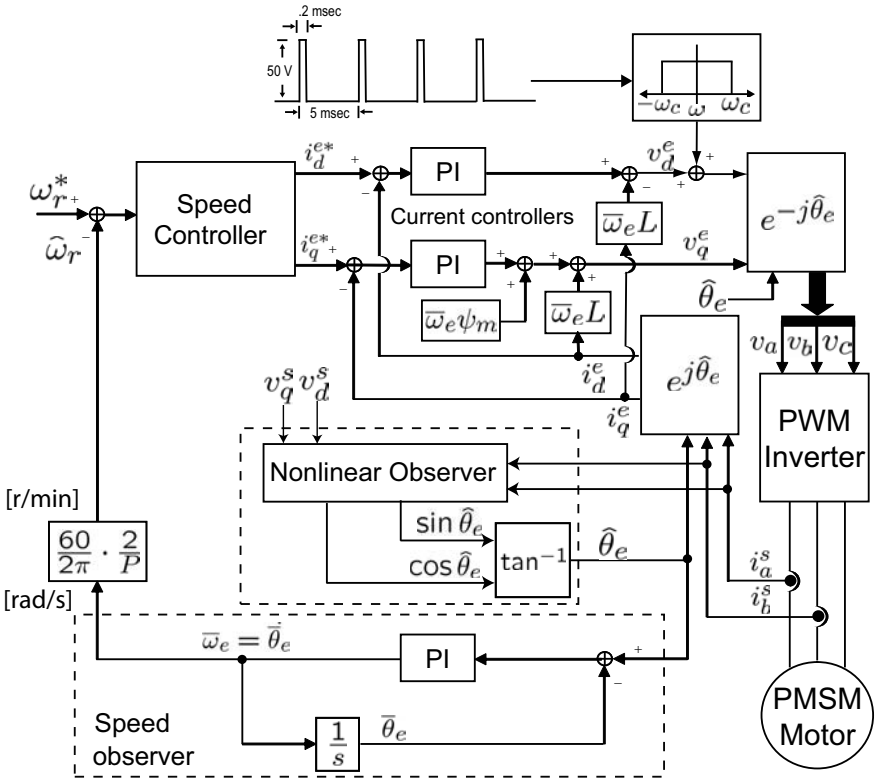

Figure 9.3: The overall sensorless control block diagram with the nonlinear observer and the speed estimator.

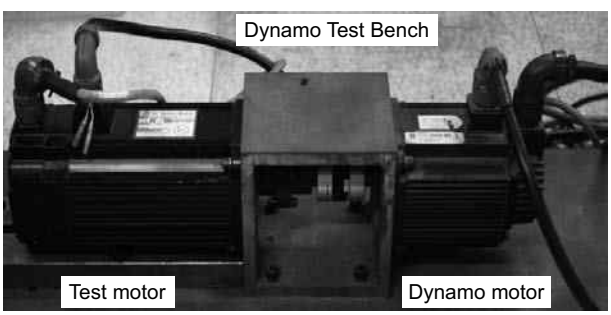

Figure 9.4: Photo of the experiment setup.

Trigonometrical functions as a simple observer output are also shown in Fig. 9.5. Note that the position errors at 300rpm are smaller than those at 80rpm. Fig. 9.6 (a)

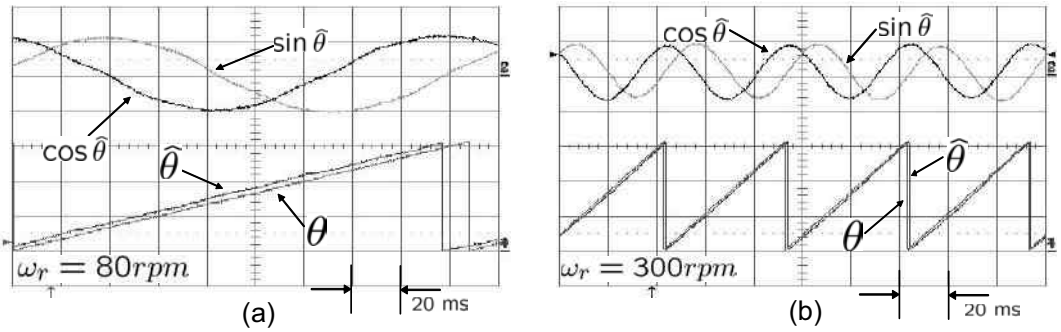

Figure 9.5: Comparison between the real and the estimated position data under no-load condition at (a) 80rpm and (b) 300rpm.

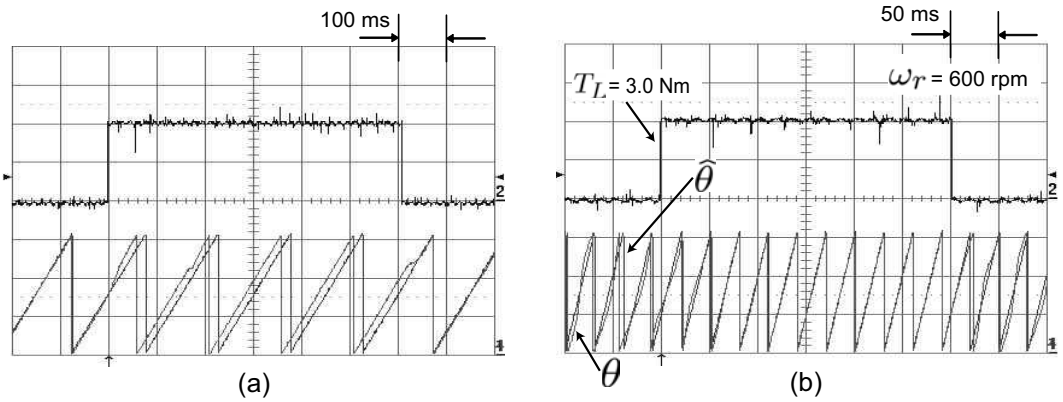

Figure 9.6: Comparison between the real and the estimated position data under a full step load at (a) 100rpm and (b) 600rpm.

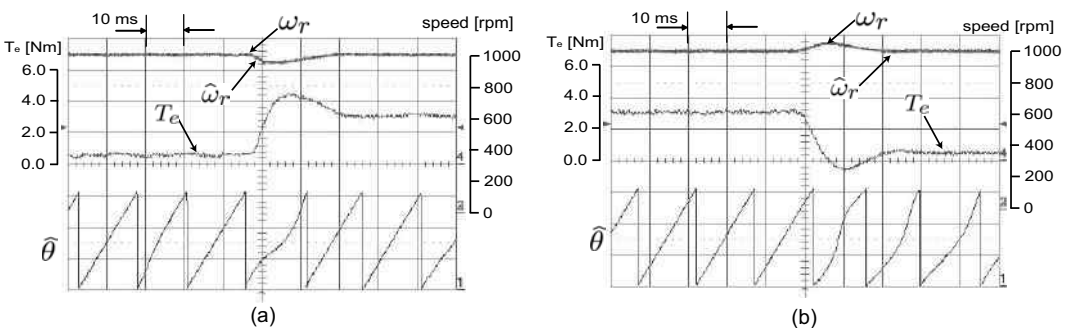

Figure 9.7: Speed and the corresponding torque responses at 1000rpm when a full load torque is (a) applied and (b) removed.

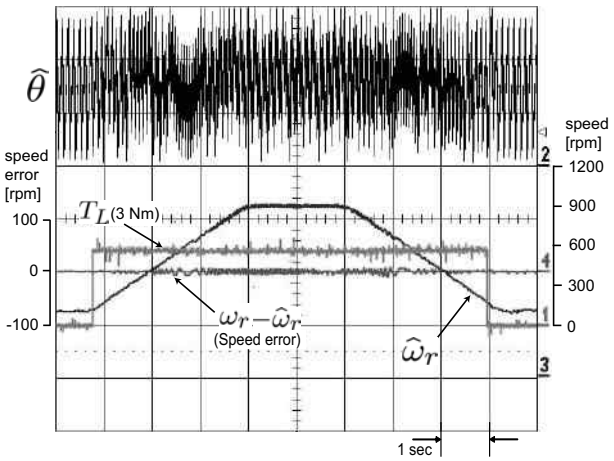

Figure 9.8: A speed control response with a step full load torque.

and (b) show behaviors of the position estimates when full step loads were applied when $\omega_r = 100$rpm and 600rpm, respectively. One can also notice that the steady-state position errors at a higher speed are smaller. Fig. 9.7 (a) and (b) show the responses of the speed estimates and the corresponding torque at the time of full load loading and removal when $\omega_r = 1000$rpm, respectively. Fig. 9.8 shows a macroscopic view of the behaviors of speed and angle estimates when the speed changes from $\omega_r = 100$rpm and 900rpm with a step full load.

Fig. 9.9 shows a stable performance at 10 rpm (0.01pu) with a 1.5Nm (0.5pu) load. Fig. 9.9 (b) is an expanded plot of real and estimated angles shown in Fig. 9.9 (a). Note that the d–axis current has a shape of pulse train and that the q–axis current (2.2A) is flowing for torque production.

Summary

- The nonlinear observer is developed for SPMSMs in the stationary frame.
- One great advantage is that it does not require the speed information, so that a speed estimator can be constructed separately.
- For speed update, the PLL type differentiator is utilized independently.
- Robustness can be enhanced with the d–axis current injection in the low-speed region.
- It has a simple structure and performs well in practical sensorless applications.

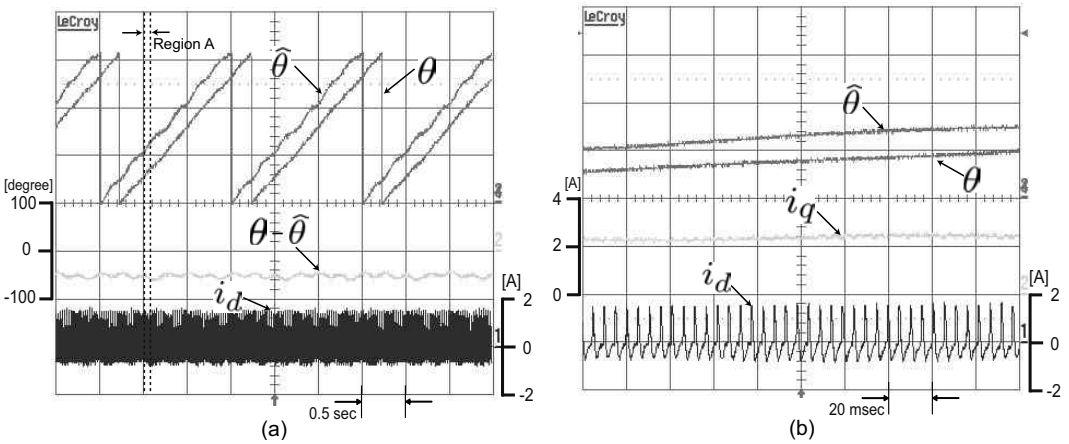

Figure 9.9: (a) Experimental results under half load (1.5 Nm) at 10rpm and (b) an expanded plot of Region A in (a).

9.2.2 Matsui's Current Model-Based Control

Matsui [1] developed a sensorless algorithm for a SPMSM model referenced on a flux angle estimate. Let $\theta_{(k)}$ be a rotor angle estimate at k^{th} step. Let $\Delta\theta_e = \theta_e - \hat{\theta}_{e(k)}$ be the angle deviation from the real angle. The rotor flux vector $\boldsymbol{\psi}_m$ is aligned with the real q–axis, but it is decomposed into

$$\psi_m \begin{bmatrix} -\sin\Delta\theta_e \\ \cos\Delta\theta_e \end{bmatrix}$$

in the misaligned coordinate as shown in Fig. 9.10. Therefore, the SPMSM dynamics seen from the $\theta_{(k)}$-frame is described as

$$\frac{1}{T_s}\left(\begin{bmatrix} i^e_{d(k+1)} \\ i^e_{q(k+1)} \end{bmatrix} - \begin{bmatrix} i^e_{d(k)} \\ i^e_{q(k)} \end{bmatrix}\right) = -\begin{bmatrix} \frac{r_s}{L_s} & -\omega_k \\ \omega_k & \frac{r_s}{L_s} \end{bmatrix}\begin{bmatrix} i^e_{d(k)} \\ i^e_{q(k)} \end{bmatrix} + \frac{\psi_m\omega_k}{L_s}\begin{bmatrix} \sin\Delta\theta_e \\ -\cos\Delta\theta_e \end{bmatrix} + \frac{1}{L_s}\begin{bmatrix} v^e_{d(k)} \\ v^e_{q(k)} \end{bmatrix}, \tag{9.23}$$

where T_s is the sampling period and ω_k is the electrical speed. It is assumed that currents i^e_d and i^e_q are available for measurements. Voltages v_d and v_q are also assumed to be known since they are synthesized in the control processor core.

However, in the controller, the current dynamics is considered as

$$\frac{1}{T_s}\left(\begin{bmatrix} i^m_{d(k+1)} \\ i^m_{q(k+1)} \end{bmatrix} - \begin{bmatrix} i^e_{d(k)} \\ i^e_{q(k)} \end{bmatrix}\right) = -\begin{bmatrix} \frac{r_s}{L_s} & -\hat{\omega}_k \\ \hat{\omega}_k & \frac{r_s}{L_s} \end{bmatrix}\begin{bmatrix} i^e_{d(k)} \\ i^e_{q(k)} \end{bmatrix} - \frac{\psi_m\hat{\omega}_k}{L_s}\begin{bmatrix} 0 \\ 1 \end{bmatrix} + \frac{1}{L_s}\begin{bmatrix} v^e_{d(k)} \\ v^e_{q(k)} \end{bmatrix}, \tag{9.24}$$

where $i^m_{d(k+1)}$ and $i^m_{q(k+1)}$ are the predicted currents when there is no angle error. Defining the differences in the one-step ahead estimates by

$$\begin{bmatrix} \Delta i^e_{d(k+1)} \\ \Delta i^e_{q(k+1)} \end{bmatrix} = \begin{bmatrix} i^e_{d(k+1)} - i^m_{d(k+1)} \\ i^e_{q(k+1)} - i^m_{q(k+1)} \end{bmatrix}, \tag{9.25}$$

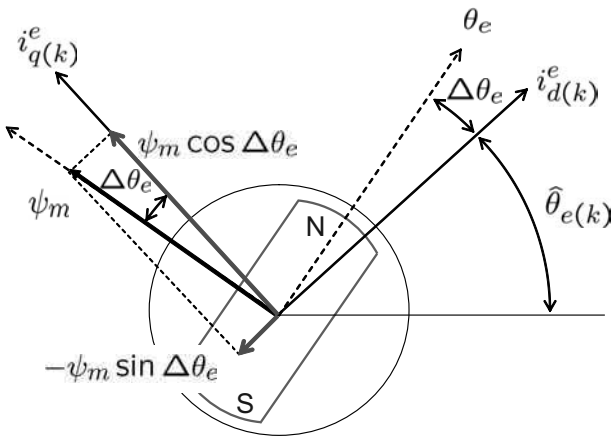

Figure 9.10: Current vector decompositions into $\theta_{e(k)}$ and $\theta_{e(k+1)}$.

we obtain

$$\begin{bmatrix}\Delta i^e_{d(k+1)}\\ \Delta i^e_{q(k+1)}\end{bmatrix} = \frac{T_s\psi_m}{L_s}\begin{bmatrix}\omega_k \sin\Delta\theta_{e(k)}\\ -\omega_k\cos\Delta\theta_{e(k)}+\hat{\omega}_k\end{bmatrix} \approx \frac{T_s}{L_s}\begin{bmatrix}\psi_m\omega_k\Delta\theta_{e(k)}\\ \psi_m\Delta\omega_k\end{bmatrix} \tag{9.26}$$

where $\Delta\omega_k = \hat{\omega}_k - \omega_k$. The observations are:

i) Q–Axis current error is proportional to the speed error;
ii) D–Axis current error is proportional to the angle error.

For correction of speed estimates, the q–axis current error is utilized. Let $J_1 = \frac{1}{2}\Delta i^{e\ 2}_{q(k+1)}$. Then

$$\frac{\partial J_1}{\partial\Delta\omega_k} = \frac{T_s\psi_m}{L_s}\Delta i^e_{q(k+1)}. \tag{9.27}$$

From the gradient method, it follows that

$$\hat{\omega}_{k+1} = \hat{\omega}_k - K_q\Delta i^e_{q(k)}, \tag{9.28}$$

where $K_q > 0$ is an adaptive gain. It is assumed in (9.28) that $\omega_{k+1} = \omega_k$ and that one-step behind value, $\Delta i^e_{q(k)}$ is utilized instead of $\Delta i^e_{q(k+1)}$.

Similarly, let $J_2 = \frac{1}{2}\Delta i^{e\ 2}_{d(k+1)}$. Then

$$\frac{\partial J_2}{\partial\Delta\theta_e} = \frac{T_s\psi_m}{L_s}\omega_k\Delta i^e_{d(k+1)}\,.$$

From the gradient method, it follows that $\Delta\theta_{e(k+1)} = \Delta\theta_{e(k)} - K_{\theta_e}\Delta i^e_{d(k)}$, where K_{θ_e} is an adaptive gain and $\Delta i^e_{d(k)}$ is utilized instead of $\Delta i^e_{d(k+1)}$. Therefore,

$$\hat{\theta}_{e(k+1)} = \hat{\theta}_{e(k)} + K_{\theta_e}\Delta i^e_{d(k)}. \tag{9.29}$$

Extending with the speed update (9.28), the final angle update algorithm is obtained as

$$\hat{\theta}_{e(k+1)} = \hat{\theta}_{e(k)} + K_{\theta_e} \Delta i^e_{d(k)} + \frac{\psi_m T_s}{K_E} \hat{\omega}_{(k+1)}, \tag{9.30}$$

where $K_E > 0$ is a constant gain. Note that the sampling time T_s is multiplied to $\hat{\omega}_{(k+1)}$ in the angle update.

Summary

- The Matsui's sensorless algorithm can be applied to SPMSMs.
- It utilizes an internal model and develops error dynamics.
- Angle and speed update methods can be derived separately by applying the gradient algorithm. The two update methods are glued into a single angle update algorithm.
- It is being used in home appliances.

9.3 Sensorless Controls for IPMSMs

Describing the IPMSM dynamics in the stationary frame is quite complex, as shown in (9.9). Thus, the IPMSM dynamics are hardly treated in the stationary frame. In this part, back EMF based sensorless algorithms for IPMSMs developed by Morimoto et al. [18] and Hong and Nam [21] are illustrated.

9.3.1 Morimoto's Extended EMF-Based Control

As shown in the previous section, the sensorless controls for SPMSM are simpler, since $L_d = L_q$. If $L_d \neq L_q$, the complexity arises with coordinate change. Consider the voltage equation in the aligned synchronous frame:

$$\begin{bmatrix} v^e_d \\ v^e_q \end{bmatrix} = \begin{bmatrix} r_s + pL_d & -\omega L_q \\ \omega L_d & r_s + pL_q \end{bmatrix} \begin{bmatrix} i^e_d \\ i^e_q \end{bmatrix} + \begin{bmatrix} 0 \\ \omega_e \psi_m \end{bmatrix}. \tag{9.31}$$

As shown in the previous section, the model (9.31) becomes complex when it is expressed in the tilted coordinate frame. Morimoto et al. [18] proposed an extended EMF based model in which L_d appears only in the diagonal, whereas L_q in the off-diagonal:

$$\begin{bmatrix} v^e_d \\ v^e_q \end{bmatrix} = \begin{bmatrix} r_s + pL_d & -\omega_e L_q \\ \omega_e L_q & r_s + pL_d \end{bmatrix} \begin{bmatrix} i^e_d \\ i^e_q \end{bmatrix} + \begin{bmatrix} 0 \\ E_{ex} \end{bmatrix} \tag{9.32}$$

where

$$E_{ex} = \omega_e[(L_d - L_q)i_d^e + \psi_m] - (L_d - L_q)(pi_q^e).$$

Note that E_{ex}, called extended EMF, contains the differential operator, p. In the vector form, (9.32) is rewritten as

$$\mathbf{v}_{dq}^e = [(r_s + pL_d)\mathbf{I} - \omega_e L_q \mathbf{J}]\, \mathbf{i}_{dq}^e + \boldsymbol{\zeta} \tag{9.33}$$

where

$$\mathbf{v}_{dq}^e = \begin{bmatrix} v_d^e \\ v_q^e \end{bmatrix}, \qquad \mathbf{i}_{dq}^e = \begin{bmatrix} i_d^e \\ i_q^e \end{bmatrix}, \qquad \boldsymbol{\zeta} = \begin{bmatrix} 0 \\ E_{ex} \end{bmatrix}.$$

In order to describe vectors in the misaligned coordinate ($\overline{\theta}_e$), the vectors in the real coordinate (θ_e) need to be multiplied by

$$e^{\mathbf{J}(\overline{\theta}_e - \theta_e)} = \begin{bmatrix} \cos(\overline{\theta}_e - \theta_e) & \sin(\overline{\theta}_e - \theta_e) \\ -\sin(\overline{\theta}_e - \theta_e) & \cos(\overline{\theta}_e - \theta_e) \end{bmatrix}.$$

Let

$$\overline{\mathbf{v}}_{dq}^e \equiv e^{\mathbf{J}(\overline{\theta}_e - \theta_e)} \mathbf{v}_{dq}^e \qquad \text{and} \qquad \overline{\mathbf{i}}_{dq}^e \equiv e^{\mathbf{J}(\overline{\theta}_e - \theta_e)} \mathbf{i}_{dq}^e. \tag{9.34}$$

Then the dynamics in the misaligned coordinate is given as

$$\overline{\mathbf{v}}_{dq}^e = e^{\mathbf{J}(\overline{\theta}_e - \theta_e)}\, [(r_s + pL_d)\mathbf{I} - \omega_e L_q \mathbf{J}]\, e^{-\mathbf{J}(\overline{\theta}_e - \theta_e)} \overline{\mathbf{i}}_{dq}^e + e^{\mathbf{J}(\overline{\theta}_e - \theta_e)} \boldsymbol{\zeta}, \tag{9.35}$$

Rearranging (9.35), it follows that

$$\begin{bmatrix} \overline{v}_d^e \\ \overline{v}_q^e \end{bmatrix} = \begin{bmatrix} r_s + pL_d & -\omega_e L_q \\ \omega_e L_q & r_s + pL_d \end{bmatrix} \begin{bmatrix} \overline{i}_d^e \\ \overline{i}_q^e \end{bmatrix} + \begin{bmatrix} \xi_d^e \\ \xi_q^e \end{bmatrix} \tag{9.36}$$

where

$$\begin{bmatrix} \xi_d^e \\ \xi_q^e \end{bmatrix} = E_{ex} \begin{bmatrix} \sin(\overline{\theta} - \theta) \\ \cos(\overline{\theta} - \theta) \end{bmatrix} + (\overline{\omega}_e - \omega_e) L_d \begin{bmatrix} -\overline{i}_q^e \\ \overline{i}_d^e \end{bmatrix}, \tag{9.37}$$

and $\overline{\omega}_e = \frac{d}{dt}\overline{\theta}_e$. It is interesting to see that the dynamic model is simple even in misaligned frame with the extended EMF.

Estimation of Extended EMF via Disturbance Observer

Dynamic model (9.36) is a linear system with the disturbance $[\xi_d^e, \xi_d^e]^T$. It is further assumed that $\overline{\omega}_e = \omega_e$. Then, the angle error is obtained by

$$\overline{\theta}_e - \theta_e = \tan^{-1}\left(\frac{\xi_d^e}{\xi_q^e}\right). \tag{9.38}$$

This method eliminates the need for calculating E_{ex}. To obtain the angle error using (9.38), it is necessary to estimate disturbance terms, ξ_d and ξ_q. For this purpose,

two disturbance observers are constructed for ξ_d and ξ_q assuming that they are constants. A disturbance observer for ξ_d is shown in Fig. 9.11. Recall that the disturbance observer contains a differentiator functionally, but a filter is combined to prevent signal differentiation. Note that the low-pass filter in Fig. 9.11 approaches to unity with a large $\alpha > 0$.

Most commonly, the disturbance observer is used in the speed loop for unknown load torque estimation. But in this particular example, the disturbance observers are used in the current loop to estimate unknown voltage terms that are caused by the coordinate misalignment. Note also that the current loop bandwidth is larger than that of the speed loop. Thereby, the observer filter bandwidth should be sufficiently large.

The estimates are denoted by $\hat{\xi}_d$ and $\hat{\xi}_q$. Using $\hat{\xi}_d$ and $\hat{\xi}_q$, the angle difference is obtained such that

$$\widehat{\Delta\theta}_e = \widehat{\overline{\theta}_e - \theta_e} = \tan^{-1}\left(\frac{\hat{\xi}_d}{\hat{\xi}_q}\right). \tag{9.39}$$

Speed $\overline{\omega}$ is estimated by utilizing the PLL type filter (9.22).

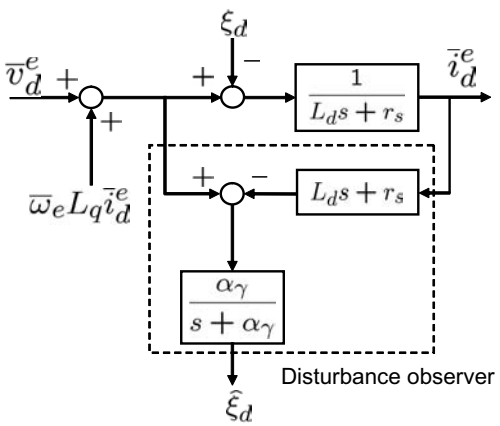

Figure 9.11: Block diagram of a disturbance observer in the current loop.

Experimental Results

Experiments were performed with an IPMSM developed for an air conditioner compressor. The specifications were listed in Table 9.2. The control algorithms were implemented in a TMS320vc33 DSP board. The PWM switching frequency was set to be 5kHz and the dead-time $2\mu s$. The current control and speed/position estimation were carried out every 0.2ms, and the speed control loop was activated every 2ms.

Fig. 9.12 shows the responses of θ_e, $\hat{\theta}_e$, $\theta_e - \hat{\theta}_e$, and $\hat{\omega}_r$ at 500 and 6000rpm (field-weakening region). Note that the angle error is less than $\pm 5^\circ$ at 500 rpm and $\pm 2^\circ$

Table 9.2: Motor parameters of an IPMSM used for experiments.

Parameters [Unit]	Values
Input DC link voltage [V]	540
Rated output power [kW]	11
Rated speed [r/min]	5000
Rated torque [Nm]	21
d–axis inductance (L_d) [mH]	3
q–axis inductance (L_q) [mH]	6.2
Stator resistance (r_s) [Ω]	0.151
Rotor flux per pole (ψ_m) [Wb]	0.09486
Rated current [A_{rms}]	25
Rated voltage [V_{rms}]	220
Number of poles (P)	6

at 6000 rpm. Fig. 9.13 shows a transient response to a step speed command from 3000 to 4000rpm. At the point of abrupt speed change, the angle error develops, but settles down within 0.15 sec. To make the transient response better, α needs to be increased as much as possible. In this experiment, $\alpha = 3450$. Fig. 9.14 shows speed control responses: 500rpm → 6000rpm → 500rpm. This shows that the field-weakening control with the Morimoto's algorithm is also stable.

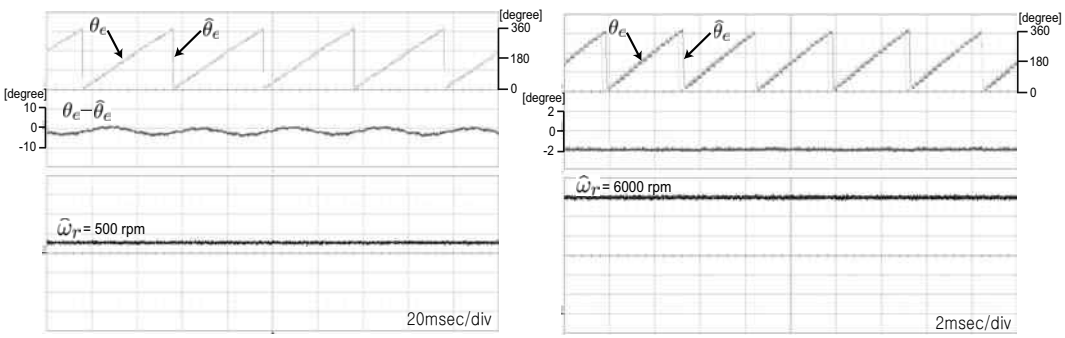

Figure 9.12: Angle estimation with the disturbance observer: θ, $\hat{\theta}$, $\theta - \hat{\theta}$, and $\hat{\omega}_r$ at (a) 500rpm and (b) 6000rpm.

Summary

- The Morimoto's sensorless algorithm can be applied to IPMSMs.
- The essential part is to make L_d appear in the diagonal part and L_q in the off-diagonal part of the voltage equation while driving out the remaining terms

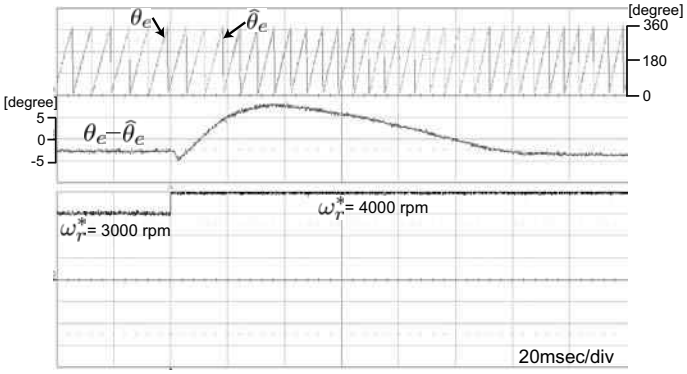

Figure 9.13: Transient response for a step speed change from 3000rpm to 4000rpm.

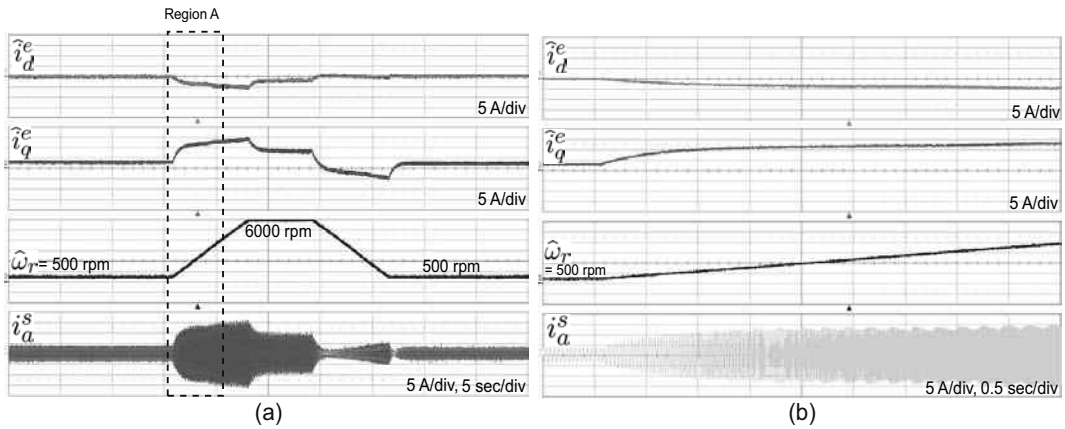

Figure 9.14: Speed control responses with the Morimoto's sensorless algorithm: (a) 500rpm → 6000rpm → 500rpm and (b) a magnified plot of region A.

to the extended EMF term.

- The extended EMF based model has a simple structure in the misaligned coordinate.
- Utilizing the disturbance observer, voltage disturbances are detected which carry angle information.
- The structure is simple and has less tuning parameters than the Matsui's sensorless algorithm.

9.3.2 Sensorless Control Using Adaptive Observer

In this section, the IPMSM dynamic model in a misaligned frame is derived and approximated as precisely as possible when the angle error is small. An adaptive observer is constructed and the rotor angle is estimated by a parameter adaptive law.

The IPMSM model, (9.6), in the misaligned frame is rewritten as

$$\begin{aligned}\overline{v}_d^e &= \left(r_s - \frac{3}{2}L_\delta \overline{\omega}_e \sin 2\Delta\theta_e\right)\overline{i}_d^e + \left(L_s - \frac{3}{2}L_\delta \cos 2\Delta\theta_e\right)(p\overline{i}_d^e) + \omega_e \psi_m \sin\Delta\theta_e \\ &\quad -\overline{\omega}_e\left(L_s + \frac{3}{2}L_\delta \cos 2\Delta\theta_e\right)\overline{i}_q^e + 3L_\delta \Delta\omega_e \overline{i}_q^e \cos 2\Delta\theta_e + E_D \qquad (9.40)\\ \overline{v}_q^e &= \left(r_s + \frac{3}{2}L_\delta \overline{\omega}_e \sin 2\Delta\theta_e\right)\overline{i}_q^e + \left(L_s + \frac{3}{2}L_\delta \cos 2\Delta\theta_e\right)(p\overline{i}_q^e) + \omega_e \psi_m \cos\Delta\theta_e \\ &\quad +\overline{\omega}_e\left(L_s - \frac{3}{2}L_\delta \cos 2\Delta\theta_e\right)\overline{i}_d^e + 3L_\delta \Delta\omega_e \overline{i}_d^e \cos 2\Delta\theta_e + E_Q, \qquad (9.41)\end{aligned}$$

where

$$\begin{aligned}E_D &= \frac{3}{2}L_\delta \sin 2\Delta\theta_e (p\overline{i}_q^e) + 3L_\delta \Delta\omega_e \overline{i}_d^e \sin 2\Delta\theta_e \\ E_Q &= \frac{3}{2}L_\delta \sin 2\Delta\theta_e (p\overline{i}_d^e) - 3L_\delta \Delta\omega_e \overline{i}_q^e \sin 2\Delta\theta_e.\end{aligned}$$

Assume that $\Delta\omega_e$ and $\Delta\theta_e$ are small. Then,

$$\Delta\omega_e \sin\Delta\theta_e \approx \Delta\omega_e \Delta\theta_e \in \mathcal{O}^2,$$

where $\mathcal{O}^2 \equiv \{f(x) : \mathbb{R}^n \to \mathbb{R} \mid \lim_{\|x\|\to\infty} |f(x)|/\|x\|^2 < \infty\}$. Further, $p\overline{i}_d^e \approx 0$ and $p\overline{i}_q^e \approx 0$ in the steady-state. Then, E_D and E_Q are small enough to be neglected, i.e., $E_D \approx 0$ and $E_Q \approx 0$.

An Approximate Model

One can approximate

$$\frac{3}{2}L_\delta \overline{\omega}_e \sin 2\Delta\theta_e = 3L_\delta \overline{\omega}_e \sin\Delta\theta_e \cos\Delta\theta_e \approx 3L_\delta \overline{\omega}_e \sin\Delta\theta_e.$$

Therefore, the voltage equations (9.40) and (9.41) turn out to be

$$\overline{v}_d^e = (r_{ds} - 3L_\delta \overline{\omega}_e \sin\Delta\theta_e)\overline{i}_d^e + L_{dv}(p\overline{i}_d^e) - \overline{\omega}_e L_{qv}\overline{i}_q^e + \omega_e \psi_m \sin\Delta\theta_e + 3L_\delta \Delta\omega_e \overline{i}_q^e \qquad (9.42)$$

$$\overline{v}_q^e = (r_{qs} + 3L_\delta \overline{\omega}_e \sin\Delta\theta_e)\overline{i}_q^e + L_{qv}(p\overline{i}_q^e) + \overline{\omega}_e L_{dv}\overline{i}_d^e + \omega_e \psi_m \cos\Delta\theta_e + 3L_\delta \Delta\omega_e \overline{i}_d^e, \qquad (9.43)$$

where

$$\begin{aligned} L_{dv} &= L_s - \frac{3}{2}L_\delta \cos 2\Delta\theta_e, \\ L_{qv} &= L_s + \frac{3}{2}L_\delta \cos 2\Delta\theta_e\,. \end{aligned}$$

For simplicity, we let

$$\begin{aligned} L_{dv} &\approx L_s - \frac{3}{2}L_\delta \equiv L_d, \\ L_{qv} &\approx L_s + \frac{3}{2}L_\delta \equiv L_q. \end{aligned}$$

Substituting L_d and L_q for L_{dv} and L_{qv} and utilizing

$$\omega_e\psi_m \cos\Delta\theta_e \approx \overline{\omega}_e\psi_m \cos\Delta\theta_e - \psi_m\Delta\omega_e,$$

it follows that

$$\frac{d}{dt}\bar{i}_d^e = -\frac{r_s}{L_d}\bar{i}_d^e - \overline{\omega}_e\frac{\psi_m - 3L_\delta\bar{i}_d^e}{L_d}\sin\Delta\theta_e + \overline{\omega}_e\frac{L_q}{L_d}\bar{i}_q^e - \frac{3L_\delta}{L_d}\Delta\omega_e\bar{i}_q^e + \frac{1}{L_d}\overline{v}_d, \tag{9.44}$$

$$\begin{aligned} \frac{d}{dt}\bar{i}_q^e &= -\frac{r_s}{L_q}\bar{i}_q^e - \overline{\omega}_e\frac{3L_\delta\bar{i}_q^e}{L_q}\sin\Delta\theta_e - \overline{\omega}_e\frac{L_d}{L_q}\bar{i}_d^e - \frac{\overline{\omega}_e\psi_m}{L_q}\cos\Delta\theta_e \\ &\quad + \frac{\psi_m}{L_q}\Delta\omega_e - \frac{3L_\delta}{L_q}\Delta\omega_e\bar{i}_d^e + \frac{1}{L_q}\overline{v}_q. \end{aligned} \tag{9.45}$$

$$\frac{d}{dt}\Delta\theta_e = \Delta\omega_e\,. \tag{9.46}$$

Further, letting $\sin\Delta\theta_e \approx \Delta\theta_e$ and $\cos\Delta\theta_e \approx 1$, it follows in the matrix form that

$$\frac{d}{dt}\begin{bmatrix}\bar{i}_d^e \\ \bar{i}_q^e \\ \Delta\theta_e\end{bmatrix} = \mathbf{A}_s(t)\begin{bmatrix}\bar{i}_d^e \\ \bar{i}_q^e \\ \Delta\theta_e\end{bmatrix} + \mathbf{b}_s(t)\Delta\omega_e + \begin{bmatrix}\overline{\omega}_e\frac{L_q}{L_d}\bar{i}_q^e \\ -\overline{\omega}_e\frac{L_d\bar{i}_d^e + \psi_m}{L_q} \\ 0\end{bmatrix} + \begin{bmatrix}\frac{1}{L_d}\overline{v}_d \\ \frac{1}{L_q}\overline{v}_q \\ 0\end{bmatrix}, \tag{9.47}$$

where

$$\mathbf{A}_s(t) = \begin{bmatrix} -\frac{r_s}{L_d} & 0 & \overline{\omega}_e\frac{3L_\delta - \psi_m\bar{i}_d^e}{L_d} \\ 0 & -\frac{r_s}{L_q} & -\overline{\omega}_e\frac{3L_\delta}{L_q}\bar{i}_q^e \\ 0 & 0 & 0 \end{bmatrix} \quad \text{and} \quad \mathbf{b}_s(t) = \begin{bmatrix} -\frac{3L_\delta}{L_d}\bar{i}_q^e \\ \frac{\psi_m - 3L_\delta\bar{i}_d^e}{L_q} \\ 1 \end{bmatrix}.$$

Note here that $\mathbf{A}_s$ and $\mathbf{b}_s$ contain $\bar{i}_d^e$ and $\bar{i}_q^e$, so that they depend on t. If the axes are aligned, $\theta_e = \overline{\theta}_e$ and $\omega_e = \overline{\omega}_e$. In such a case, the approximate model (9.47) reduces to the model of synchronous frame (6.39).

Note that $\frac{-3L_\delta}{L_d}$ and $\frac{-3L_\delta}{L_q}$ originated from the rotor saliency. The above model is regarded more precise than the models in the previous works, for example (9.23), since it accounts $\frac{-3L_\delta}{L_d}$ and $\frac{-3L_\delta}{L_q}$ in $\mathbf{A}_s$ and $\mathbf{b}_s$, and reflects the dynamics of the speed error, $\Delta\omega_e$.

Adaptive Observer

Adaptive observer is constructed for a system with unknown parameters. It is accompanied by a parameter adaptive law. Hence, the goal of an adaptive observer is not only to estimate the state but also to identify the unknown parameters. In this particular problem, the unknown parameter to be identified is $\Delta\omega_e$. In the following adaptive observer, $\Delta\omega_e$ is tracked by $\hat{p}(t)$. On the other hand, $\Delta\theta_e$ is estimated as a state variable.

An adaptive observer for (9.47) is constructed such that

$$\dot{\mathbf{x}} = \mathbf{A}_s\mathbf{x} + \mathbf{b}_s\hat{p}(t) + \begin{bmatrix} \overline{\omega}_e \frac{L_q}{L_d} \overline{i}_q^e \\ -\overline{\omega}_e \frac{L_d \overline{i}_d^e + \psi_m}{L_q} \\ 0 \end{bmatrix} + \begin{bmatrix} \frac{1}{L_d}\overline{v}_d \\ \frac{1}{L_q}\overline{v}_q \\ 0 \end{bmatrix} + \mathbf{K}\begin{bmatrix} \overline{i}_d^e - x_1 \\ \overline{i}_q^e - x_2 \end{bmatrix}, \tag{9.48}$$

where $\mathbf{x} = [x_1, x_2, x_3]^T$, $\hat{p}(t) \in \mathbb{R}$ is a parameter for tuning and $\mathbf{K} \in \mathbb{R}^{3\times 2}$ is an observer gain. Let the observation error be defined by

$$\mathbf{e}(t) \equiv \begin{bmatrix} \overline{i}_d^e(t) - x_1(t) \\ \overline{i}_q^e(t) - x_2(t) \\ \Delta\theta_e - x_3(t) \end{bmatrix}.$$

Then, the error obeys

$$\frac{d}{dt}\mathbf{e} = (\mathbf{A}_s - \mathbf{KC})\mathbf{e} + \mathbf{b}_s\Delta p(t), \tag{9.49}$$

where $\Delta p(t) = \Delta\omega_e - \hat{p}(t)$ and

$$\mathbf{C} = \begin{bmatrix} 1 & 0 & 0 \\ 0 & 1 & 0 \end{bmatrix}.$$

The gain matrix $\mathbf{K}$ is chosen such that all the eigenvalues of $(\mathbf{A}_s - \mathbf{KC})$ lie in the left half plane of $\mathbb{C}$. If the gain is high enough, the observer error dynamics behave much faster than the rate of the parameters change. Normally, real parts of the poles are chosen to be less than -1000 for several kW range PMSMs.

$\mathbf{A}_s$ contains time-varying variables, $\overline{i}_d^e$, $\overline{i}_q^e$, and $\overline{\omega}_e$. But, they can be regarded as constants for short time intervals. Then the solution for (9.49) is given as

$$\mathbf{e}(t) = e^{(\mathbf{A}_s - \mathbf{KC})t}\mathbf{e}(0) + \int_0^t e^{(\mathbf{A}_s - \mathbf{KC})(t-\tau)}\mathbf{b}_s(\tau)\Delta p(\tau)d\tau. \tag{9.50}$$

Let

$$\boldsymbol{\beta}(t) \equiv \int_0^t e^{(\mathbf{A}_s - \mathbf{KC})(t-\tau)}\mathbf{b}_s(\tau)d\tau \in \mathbb{R}^3 \tag{9.51}$$

$$\boldsymbol{\varepsilon}(t) \equiv -\boldsymbol{\beta}(t)\hat{p}(t) + \int_0^t e^{(\mathbf{A}_s - \mathbf{KC})(t-\tau)}\mathbf{b}_s(\tau)\hat{p}(\tau)d\tau\,. \tag{9.52}$$

An equivalent expression for $\boldsymbol{\beta}$ is

$$\dot{\boldsymbol{\beta}}(t) = (\mathbf{A}_s - \mathbf{KC})\boldsymbol{\beta}(t) + \mathbf{b}_s(t), \qquad \boldsymbol{\beta}(0) = \mathbf{0}. \tag{9.53}$$

Adding $\boldsymbol{\varepsilon}(t)$ to the both sides of (9.50), it follows that

$$\mathbf{e}(t) + \boldsymbol{\varepsilon}(t) = e^{(\mathbf{A}_s - \mathbf{KC})t}\mathbf{e}(0) + \boldsymbol{\beta}(t)\Delta p(t)\,. \tag{9.54}$$

It should be noted that

$$\boldsymbol{\varepsilon}(t) = \int_0^t e^{(\mathbf{A}_s - \mathbf{KC})(t-\tau)}\mathbf{b}_s(\tau)(\hat{p}(\tau) - \hat{p}(t))d\tau\,. \tag{9.55}$$

and that $\boldsymbol{\varepsilon}(t)$ is an available term, i.e., something that is obtained through a calculation. This is a normal practice in the adaptive systems used for extracting $\hat{p}(t)$ out of the integral operation [22], [23].

Parameter Update Law

Note from the error equation (9.54) that $e^{(\mathbf{A}_s - \mathbf{KC})t}\mathbf{e}(0)$ vanishes exponentially. Neglect the initial error and we let

$$\check{\mathbf{e}}(t) \equiv \mathbf{C}(\mathbf{e}(t) + \boldsymbol{\varepsilon}(t)) \approx \mathbf{C}\boldsymbol{\beta}(t)\Delta p(t)\,. \tag{9.56}$$

Let the cost $J = \frac{1}{2}\boldsymbol{\beta}^T(t)\mathbf{C}^T\mathbf{C}\boldsymbol{\beta}(t)(\Delta p)^2$. Note that

$$\frac{\partial J}{\partial \Delta p} = -\boldsymbol{\beta}^T(t)\mathbf{C}^T\mathbf{C}\boldsymbol{\beta}(t)\Delta p(t) = -\boldsymbol{\beta}^T(t)\mathbf{C}^T\check{\mathbf{e}}(t)\,. \tag{9.57}$$

Then applying the gradient law, it follows that

$$\dot{\Delta p} = -\frac{\gamma_0}{\epsilon_0 + \boldsymbol{\beta}^T(t)\mathbf{C}^T\mathbf{C}\boldsymbol{\beta}(t)}\boldsymbol{\beta}^T(t)\mathbf{C}^T\check{\mathbf{e}}(t), \tag{9.58}$$

where $\epsilon_0 > 0$ is a small number introduced to prevent the denominator from being zero, and $\gamma_0 > 0$ is an adaptive gain.

Assume that the speed change is slow enough to let $\frac{d}{dt}\Delta\omega_e \approx 0$. It follows from (9.58) that

$$\dot{\hat{p}} = \frac{\gamma_0}{\epsilon_0 + \boldsymbol{\beta}^T(t)\mathbf{C}^T\mathbf{C}\boldsymbol{\beta}(t)}\boldsymbol{\beta}^T(t)\mathbf{C}^T\check{\mathbf{e}}(t). \tag{9.59}$$

If the whole adaptive system is stable, then $\hat{p}$ converges to $\omega_e - \overline{\omega}_e$, and x_3 converges to $\theta_e - \overline{\theta}$.

Overall Sensorless Control Block Diagram

The adaptive observer based sensorless control algorithm is summarized as:

$$
\begin{aligned}
\dot{\mathbf{x}} &= \mathbf{A}_s\mathbf{x} + \mathbf{b}_s\hat{p}(t) + \begin{bmatrix} \overline{\omega}_e \frac{L_q}{L_d}\bar{i}_q^e \\ -\overline{\omega}_e \frac{L_d\bar{i}_d^e + \psi_m}{L_q} \\ 0 \end{bmatrix} + \begin{bmatrix} \frac{1}{L_d}\overline{v}_d \\ \frac{1}{L_q}\overline{v}_q \\ 0 \end{bmatrix} + \mathbf{K}\begin{bmatrix} \bar{i}_d^e - x_1 \\ \bar{i}_q^e - x_2 \end{bmatrix}, \\
\dot{\boldsymbol{\beta}}(t) &= (\mathbf{A}_s - \mathbf{KC})\boldsymbol{\beta}(t) + \mathbf{b}_s(t), \\
\boldsymbol{\varepsilon}(t) &= -\boldsymbol{\beta}(t)\hat{p}(t) + \int_0^t e^{(\mathbf{A}_s - \mathbf{KC})(t-\tau)}\mathbf{b}_s(\tau)\hat{p}(\tau)d\tau\,, \\
\dot{\hat{p}} &= \frac{\gamma_0}{\epsilon_0 + \boldsymbol{\beta}^T(t)\mathbf{C}^T\mathbf{C}\boldsymbol{\beta}(t)}\boldsymbol{\beta}^T(t)\mathbf{C}^T\begin{bmatrix} \bar{i}_d^e(t) - x_1(t) - \varepsilon_1(t) \\ \bar{i}_q^e(t) - x_2(t) - \varepsilon_2(t) \end{bmatrix}.
\end{aligned}
$$

Note that x_3 is an estimate of $\theta_e - \overline{\theta}_e$. Using x_3, a new angle estimate is obtained such as $\hat{\theta}_e = x_3 + \overline{\theta}_e$ i.e., a new angle is updated by

$$\overline{\theta}_e(t_{k+1}) = x_3(t_k) + \overline{\theta}_e(t_k) \tag{9.60}$$

and the field-oriented control is synthesized based on this new angle repeatedly. The speed is estimated through the PLL type filter, (9.22).

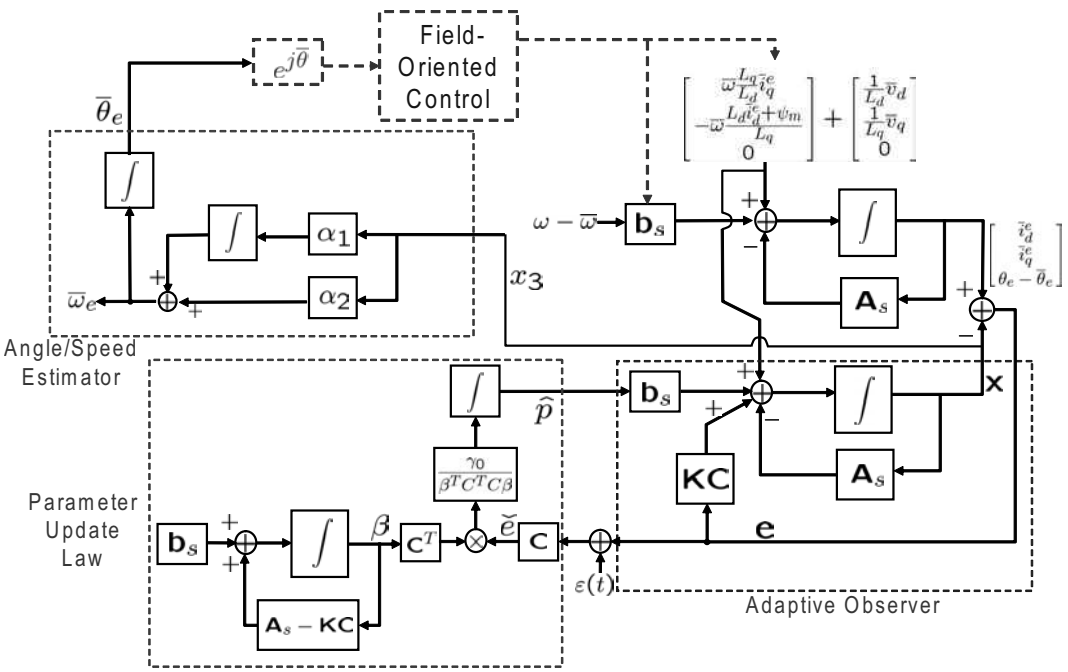

Figure 9.15: Overall sensorless control block diagram.

Note from (9.55) that

$$\dot{\boldsymbol{\varepsilon}}(t) = (\mathbf{A}_s - \mathbf{KC})\boldsymbol{\varepsilon}(t) - \left(\int_0^t e^{(\mathbf{A}_s - \mathbf{KC})(t-\tau)} \mathbf{b}_s(\tau) d\tau \right) \dot{\hat{p}}(t)\,. \tag{9.61}$$

Therefore, if $|\dot{\hat{p}}(t)|$ is not large, then $\boldsymbol{\varepsilon} \approx 0$. In such a case, it is possible to neglect $\boldsymbol{\varepsilon}(t)$. An overall sensorless control block diagram is shown in Fig. 9.15. Note that the voltage vectors, $(\overline{v}_d^e,\ \overline{v}_q^e)$, are synthesized based on the angle estimate $\overline{\theta}_e$. Such loop is depicted by dotted line in Fig. 9.15.

Experimental Results

The experiment was performed with an IPMSM drive for FCEV, and its specifications are listed in Table 7.3. The control algorithms were implemented using a MPC5554 floating-point DSP. The PWM switching frequency was 8kHz and the dead-time of PWM was 2μs. Current control routine was carried out every 125μs, and torque control loop was activated every 1.25ms. The dynamo consists of PMSM and induction motor with a water cooling system. The PMSM under test was controlled in a torque mode by an inverter, and the induction motor of dynamo was controlled in a speed control mode.

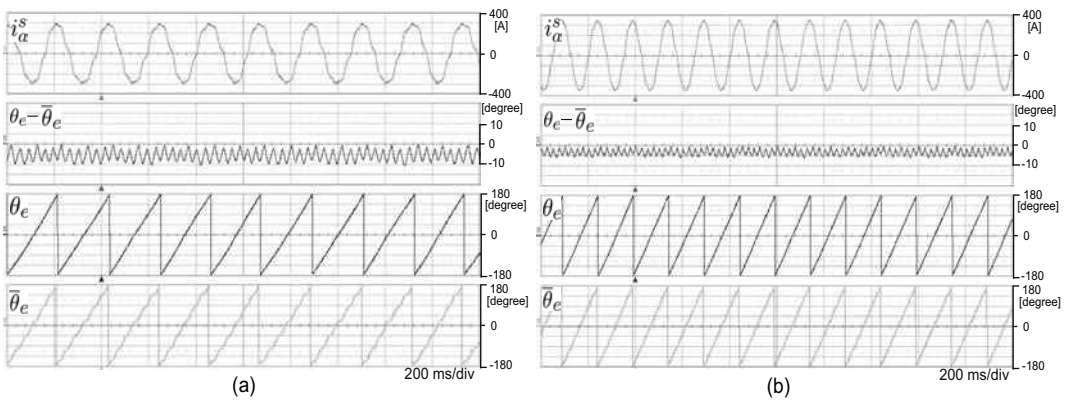

Figure 9.16: Steady state performance of the adaptive observer based sensorless control with 50% load at (a) 70rpm and (b) 100rpm.

Fig. 9.16 shows the steady-state responses at 70rpm and 100rpm with 50% of a rated load. Fig. 9.17 shows a transient response at 100rpm when the load was increased from 5% to 25%. Fig. 9.18 shows the responses of phase current and angle estimation error when the load torque changes to 50% in a step manner. Finally, Fig. 9.19 shows the maximum torque performances versus speed. Note that the adaptive observer based sensorless control performs well along the maximum power curve. Good performance in the high-speed region is attributed firstly to an accurate modeling with the state augmentation (9.47): $\overline{\omega}_e$-dependent term is not omitted in $\mathbf{A}_s$.

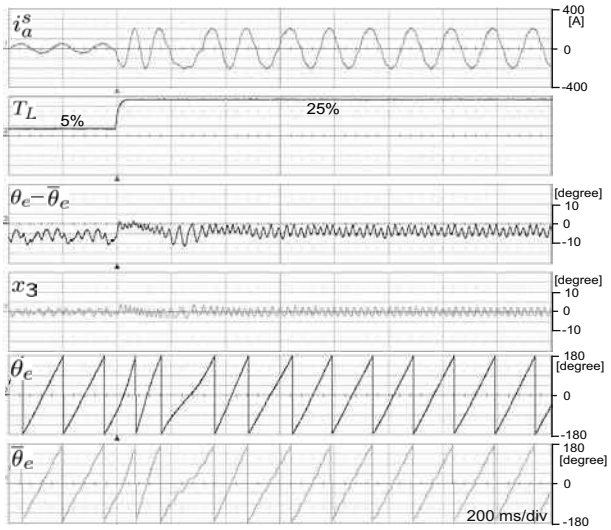

Figure 9.17: Transient response for step change of load torque (5% → 25%) at 100rpm.

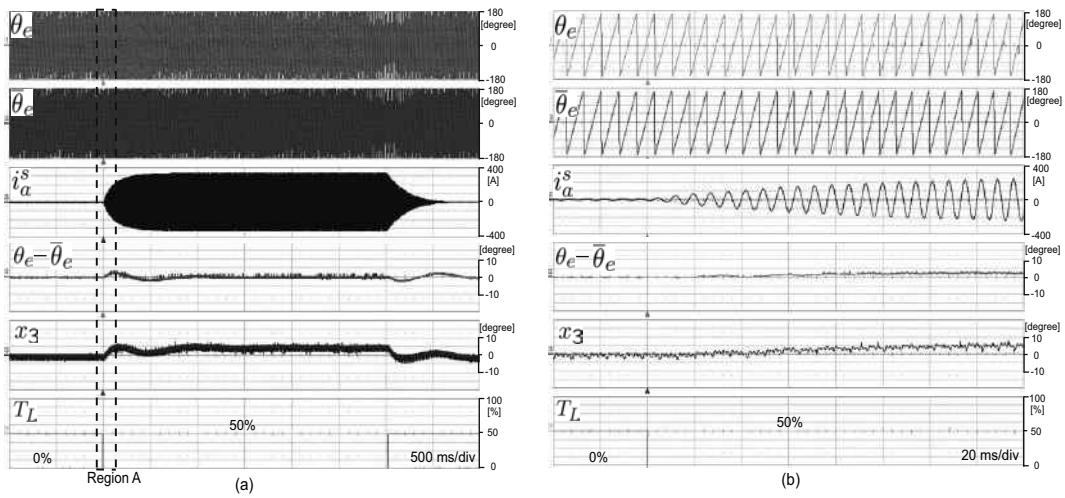

Figure 9.18: (a) Response for step change of load torque (0% → 50% → 0%) and (b) a magnified plot of region A.

Summary

- A best effort was exercised to approximate accurately the IPMSM dynamic model in a misaligned coordinate.
- An approximate model was derived with a state augmentation: Angel error $\theta_e - \overline{\theta}_e$ was treated as a state variable together with $\bar{i}_d^e$ and $\bar{i}_q^e$.

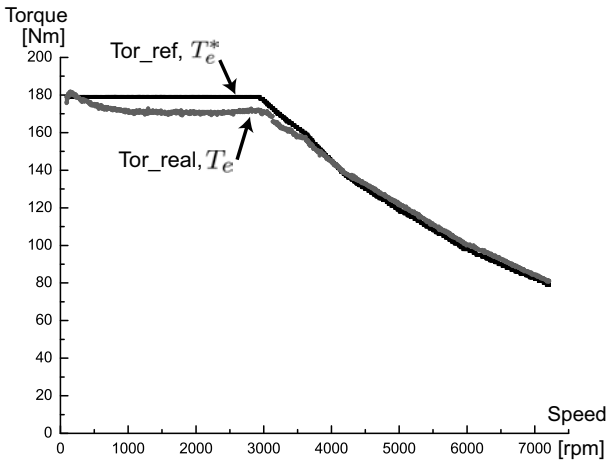

Figure 9.19: Torque-speed characteristic when the motor speed increases from 100rpm to 7200rpm with a 60% load.

- An adaptive observer was constructed with a speed error update law. Speed error estimate $x_3 = \hat{\omega}_e - \overline{\omega}_e$ is integrated to give angle error $\hat{\theta}_e - \overline{\theta}_e$, based on which the coordinate frame is updated.

- Experiments were done with a FCEV motor, and showed superior performances compared with the other ones. But, the algorithm requires a high computational load.

9.4 Starting Algorithm by Signal Injection Method

The back EMF can be estimated by applying a certain pattern of voltage and detecting the current response. However, it is well known that the back EMF estimation method does not work well in the low-speed region since the back EMF is as low as the noise levels. Specifically, the forward voltage drop of switching devices and the dead-time voltage error of the inverter are as big as the back EMF in the low-speed environments. This is an inherent problem since the back EMF is developed in proportion to the speed. Therefore, a back EMF based sensorless algorithm must be used with a separate starting algorithm [24]. In this section, a typical method of starting IPMSM is presented [25]-[27]. Since the IPMSM has a rotor saliency, its inductance differs depending on the rotor position. To estimate the rotor position and speed, a probing signal, which is a periodic voltage pulse, is applied to the motor. By analyzing the current responses, the rotor position can be estimated roughly.

9.4.1 Position Error Estimation Algorithm

In the low-speed region, it can be assumed that $\overline{\omega}_e \approx 0$ and $\omega_e \approx 0$. Then, (9.8) is reduced to

$$\overline{\mathbf{v}}_{dq}^{e} = \mathbf{Z}\overline{\mathbf{i}}_{dq}^{e} + \mathbf{e}. \tag{9.62}$$

Since the back EMF term is rotor position dependent, the current response to an injected probing voltage is different according to the rotor position. The pulse is injected intermittently, such as every 20 or 30 current samplings. In [24], the following probing voltage was used:

$$\Delta\mathbf{v} = \begin{cases} \begin{bmatrix} V_p \\ 0 \end{bmatrix}, & t_k \le t < t_k + T_p \\ \text{zero}, & t_k + T_p \le t < t_{k+1}, \end{cases} \tag{9.63}$$

where V_p is a constant. Note that the probing signal is injected only in the d–axis. If there is no angle error, the d–axis voltage pulse would cause a change only in the d–axis current when $\omega_e \approx 0$. That is, no coupling exists between the d and q dynamics if the speed is equal to zero and there is no angle error. However, if the two axes are not aligned, the d–axis voltage pulse will also affect the q–axis current.

The probing voltage is superposed on the reference voltage, and let $\Delta\mathbf{i}$ be the response to $\Delta\mathbf{v}$. It follows from (9.62) that

$$\Delta\mathbf{v} = \mathbf{Z}|_{\overline{\omega}_e=0}\,\Delta\mathbf{i}. \tag{9.64}$$

Therefore, the current response will be

$$\begin{aligned} \Delta\mathbf{i}(s) &= \left(\mathbf{Z}|_{\overline{\omega}_e=0}\right)^{-1}(s)\Delta\mathbf{v}(s) \\ &= \frac{1}{(L_d s + r_s)(L_q s + r_s)} \begin{bmatrix} r_s + L_\beta s & -L_\gamma s \\ -L_\gamma s & r_s + L_\alpha s \end{bmatrix} \Delta\mathbf{v}(s). \end{aligned} \tag{9.65}$$

Solving (9.65) for $\Delta\mathbf{v}(s) = \left[\frac{V_s}{s},\, 0\right]^T$, it follows that

$$\begin{bmatrix} \Delta i_d \\ \Delta i_q \end{bmatrix}(T_p) = \begin{bmatrix} I_0 + I_1 \cos 2\Delta\theta_e \\ -I_1 \sin 2\Delta\theta_e \end{bmatrix}, \tag{9.66}$$

where

$$\begin{aligned} I_0 &= \frac{V_p}{r_s}\left[1 - \frac{1}{2}\left(e^{-\frac{r_s}{L_q}T_p} + e^{-\frac{r_s}{L_q}T_p}\right)\right] \\ I_1 &= \frac{1}{2}\frac{V_p}{r_s}\left(e^{-\frac{r_s}{L_q}T_p} - e^{-\frac{r_s}{L_q}T_p}\right). \end{aligned}$$

Using (9.66), an angle error estimate is calculated as

$$\Delta\theta_e = \frac{1}{2}\tan^{-1}\left(\frac{-\Delta i_q}{\Delta i_d - I_0}\right). \tag{9.67}$$

It should be noted that $I_1 = 0$ if there is no saliency. Thus, (9.67) cannot be used for SPMSMs.

Experimental Results

Experiments were performed with the IPMSM whose specifications are listed in Table 9.2. The control algorithms were implemented in a TMS320vc33 DSP board. The PWM switching frequency was set to be 5kHz. The probing voltage (50V, 125μs) was injected every 20 current samplings.

Fig. 9.20 shows Δi_d and Δi_q for repeated d–axis rectangular voltage pulses, while the motor shaft rotated from zero to 360°. As predicted by (9.66), Δi_d is a cosine function with a DC offset, and Δi_q is a sine function with negative sign. Fig. 9.20 also shows the zoomed-in current responses for $\Delta\theta_e = 0$, $\frac{\pi}{4}$, $\frac{\pi}{2}$, and $\frac{3\pi}{4}$.

Fig. 9.21 (a) shows an angle estimate and the real angle when the motor speed was increased from standstill to 100rpm. Fig. 9.21 (b) shows a moment of transition from the starting algorithm to a back EMF based sensorless algorithm at 350rpm.

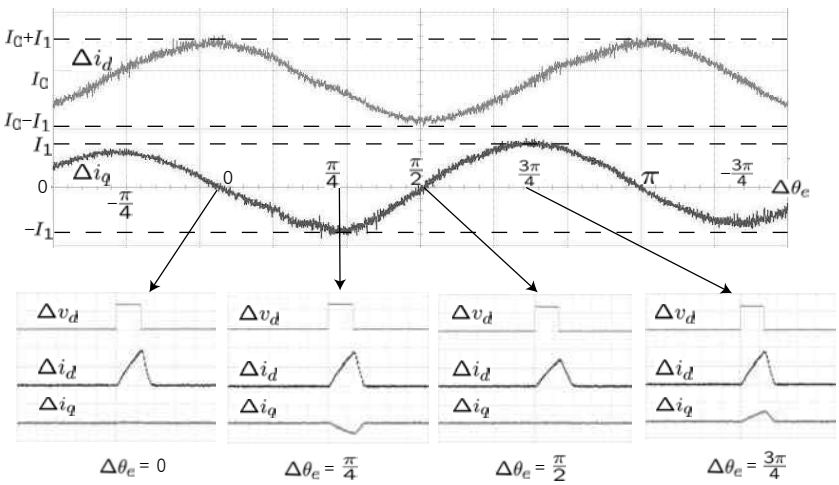

Figure 9.20: Δi_d and Δi_q for a d–axis rectangular voltage pulse, (50V, 125μs), when $\Delta\theta_e$ changes from zero to 360°.

Summary

- Back EMF based sensorless algorithms require to use a starting algorithm, since the back EMF based methods are incompetent at zero speed. Once the motor speed is increased to a certain level (300∼500rpm) by a starting algorithm, then the control is switched to a sensorless algorithm.

- Voltage pulses are injected periodically to the d–axis for IPMSMs. If the reference frame is misaligned, then the response is also monitored in q–axis current. By analyzing the relative magnitudes of the dq currents, the real rotor flux angle is estimated.

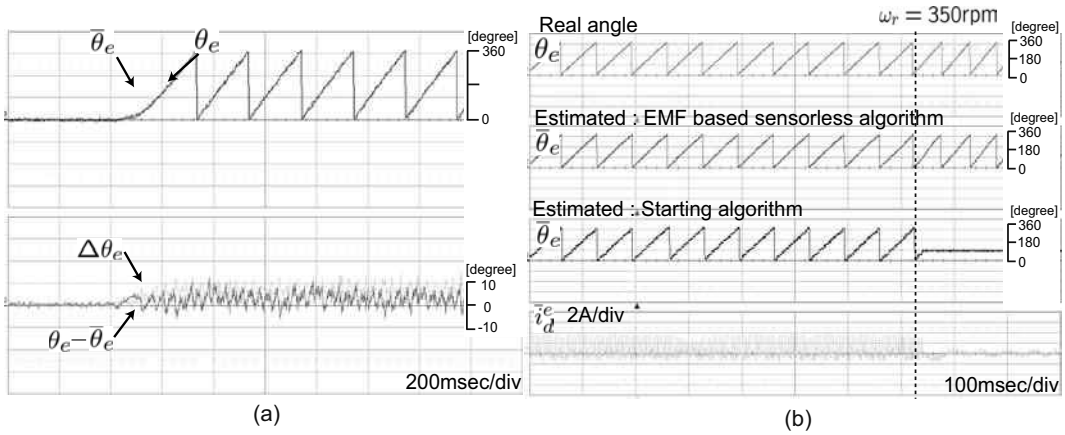

Figure 9.21: Experimental results of the starting algorithm: (a) angle estimate and real angle when the speed increases from 0rpm to 100rpm and (b) algorithm transition from the starting algorithm to a back EMF based sensorless algorithm at 350rpm.

- Although the angle estimation error is large, the above method works satisfactorily in starting the motor. It is widely used in many applications such as home appliances.

9.5 High-Frequency Signal Injection Methods

Back-electromotive-force (EMF) estimation-based sensorless methods have critical drawback in the low frequency area. To overcome such a low-speed sensing problem, signal injection methods were developed: High frequency probing signals are injected into the motor terminal with the main driving power. The high frequency probing signal does not affect the motor motion, but it yields different responses in the d and q axes currents depending on the angle misalignments. The difference is caused by rotor saliency, based on which the true rotor angle is estimated. Since it does not depend on the back EMF, it could be used in the zero speed area. However, the injection methods cannot be applicable to SPMSMs that do not have saliency. In the following, two kinds of signal injection methods are described.

9.5.1 Rotating Voltage Vector Signal Injection

Recall from (9.68) that the IPMSM model in the stationary frame is obtained as

$$\mathbf{v}_{dq}^s = r_s \mathbf{i}_{dq}^s + \frac{d}{dt}(L_{av}\mathbf{i}_{dq}^s - L_{df}e^{j2\theta_e}\mathbf{i}_{dq}^{s*}) + j\omega_e\psi_m e^{j\theta_e}.$$

Note also that the saliency effect is condensed in the term, $L_{df}e^{j2\theta_e}\mathbf{i}_{dq}^{s*}$. In the matrix formalism, it is written as

$$L_{df}\begin{bmatrix}\cos 2\theta_e & \sin 2\theta_e \\ \sin 2\theta_e & -\cos 2\theta_e\end{bmatrix}\begin{bmatrix}i_d^s \\ i_q^s\end{bmatrix}.$$

One may neglect the resistive voltage drop and the back EMF in the high frequency model:

$$\mathbf{v}_{dq}^s = \frac{d}{dt}(L_{av}\mathbf{i}_{dq}^s - L_{df}e^{j2\theta_e}\mathbf{i}_{dq}^{s*}). \tag{9.68}$$

Assume that a high frequency rotating voltage vector is injected into the IPMSM:

$$\mathbf{v}_{dq}^s = V_h e^{j\omega_h t}. \tag{9.69}$$

Substituting (9.69) into (9.68), the current solution has the following form:

$$\mathbf{i}_{dq}^s = I_{cp}e^{j(\omega_h t-\pi/2)} + I_{cn}e^{-j(\omega_h t-2\theta_e-\pi/2)}, \tag{9.70}$$

where

$$I_{cp} = \frac{V_h}{\omega_h}\frac{L_{av}}{L_{av}^2 - L_{df}^2} \quad \text{and} \quad I_{cn} = \frac{V_h}{\omega_h}\frac{L_{df}}{L_{av}^2 - L_{df}^2}.$$

Note that the resulting high frequency current contains both positive and negative sequences. It is emphasized here that only the negative sequence component carries θ_e. Lorenz et al. [3],[4],[5] applied a signal processing technique to extract the θ_e information from the negative sequence as shown in Fig. 9.22:

i) Map the current into the synchronous frame by multiplying $e^{-j\omega_e t}$.
ii) Apply a high pass filter to eliminate the fundamental component.
iii) Shift the spectrum to the right by multiplying $e^{j\omega_h t}$.
iv) Apply a low-pass filter.
v) Apply a PLL type tracking filter to get an angle estimate $\hat{\theta}_e$.

9.5.2 Voltage Signal Injection into D-Axis

In this part, a sinusoidal signal is injected only into the d–axis, and the current solution is obtained from the high frequency model of the IPMSM.

High-Frequency Model of IPMSM

Suppose that a high frequency signal, $[v_{dh}^e,\ v_{qh}^e]^T$ is added to the main driving voltage, $[v_{dh}^e,\ v_{qh}^e]^T$, in the aligned coordinate frame. Then by the superposition law, the current responses can be separated such that

$$\begin{bmatrix}v_d^e + v_{dh}^e \\ v_q^e + v_{qh}^e\end{bmatrix} = \begin{bmatrix}r_s + pL_d & -\omega_e L_q \\ \omega_e L_d & r_s + pL_q\end{bmatrix}\begin{bmatrix}i_d^e + i_{dh}^e \\ i_q^e + i_{qh}^e\end{bmatrix} + \begin{bmatrix}0 \\ \omega_e\psi_m\end{bmatrix}, \tag{9.71}$$

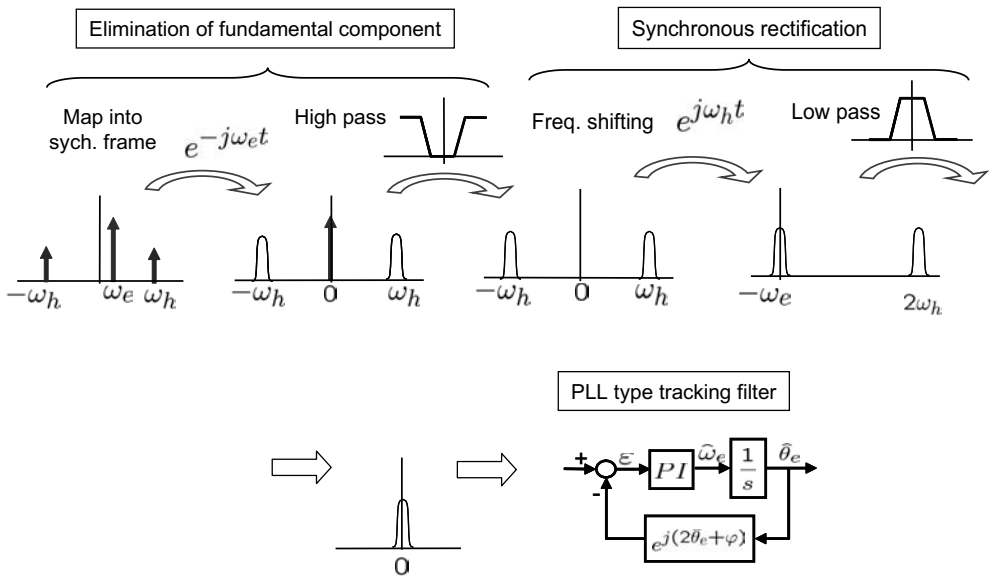

Figure 9.22: Signal processing block diagram in which the rotor position information is extracted from the negative sequence.

where i^e_{dh}, i^e_{qh} are the high frequency responses. The high frequency part can be extracted such that

$$\begin{bmatrix} v^e_{dh} \\ v^e_{qh} \end{bmatrix} = \begin{bmatrix} r_s + pL_d & -\omega_e L_q \\ \omega_e L_d & r_s + pL_q \end{bmatrix} \begin{bmatrix} i^e_{dh} \\ i^e_{qh} \end{bmatrix} \approx \begin{bmatrix} r_s + pL_d & 0 \\ 0 & r_s + pL_q \end{bmatrix} \begin{bmatrix} i^e_{dh} \\ i^e_{qh} \end{bmatrix}. \tag{9.72}$$

The last approximation in (9.72) is based on the observation that $\omega_h L_d \gg \omega_e L_q$ since $\omega_h \gg \omega_e$, where ω_h is a frequency of the probing signal. Writing (9.72) for current vector, we obtain

$$\begin{bmatrix} i^e_{dh} \\ i^e_{qh} \end{bmatrix} = \begin{bmatrix} \frac{1}{r_s+pL_d} & 0 \\ 0 & \frac{1}{r_s+pL_q} \end{bmatrix} \begin{bmatrix} v^e_{dh} \\ v^e_{qh} \end{bmatrix}. \tag{9.73}$$

Suppose that the estimated angle $\overline{\theta}_e$ is different from the real angle, θ_e by $\Delta\theta_e = \theta_e - \overline{\theta}_e$. Like the method shown in (9.7), the dynamics in the misaligned coordinate are given as

$$\begin{aligned} \begin{bmatrix} \bar{i}^e_{dh} \\ \bar{i}^e_{qh} \end{bmatrix} &= \begin{bmatrix} \cos\Delta\theta_e & -\sin\Delta\theta_e \\ \sin\Delta\theta_e & \cos\Delta\theta_e \end{bmatrix} \begin{bmatrix} \frac{1}{r_s+pL_d} & 0 \\ 0 & \frac{1}{r_s+pL_q} \end{bmatrix} \begin{bmatrix} \cos\Delta\theta_e & \sin\Delta\theta_e \\ -\sin\Delta\theta_e & \cos\Delta\theta_e \end{bmatrix} \begin{bmatrix} \overline{v}^e_{dh} \\ \overline{v}^e_{qh} \end{bmatrix} \\ &= \begin{bmatrix} \frac{\cos^2\Delta\theta_e}{r_s+pL_d} + \frac{\sin^2\Delta\theta_e}{r_s+pL_q} & \frac{\cos\Delta\theta_e\sin\Delta\theta_e}{r_s+pL_d} - \frac{\cos\Delta\theta_e\sin\Delta\theta_e}{r_s+pL_q} \\ \frac{\cos\Delta\theta_e\sin\Delta\theta_e}{r_s+pL_d} - \frac{\cos\Delta\theta_e\sin\Delta\theta_e}{r_s+pL_q} & \frac{\sin^2\Delta\theta_e}{r_s+pL_d} + \frac{\cos^2\Delta\theta_e}{r_s+pL_q} \end{bmatrix} \begin{bmatrix} \overline{v}^e_{dh} \\ \overline{v}^e_{qh} \end{bmatrix}. \end{aligned}$$

We assume that a high frequency signal is injected only to d–axis, i.e., we let

$$\begin{bmatrix} \overline{v}^e_{dh} \\ \overline{v}^e_{qh} \end{bmatrix} = \begin{bmatrix} V_h \cos\omega_h t \\ 0 \end{bmatrix}. \tag{9.74}$$

Then, it follows that

$$\begin{bmatrix} \bar{i}^e_{dh} \\ \bar{i}^e_{qh} \end{bmatrix} = \begin{bmatrix} \frac{\cos^2 \Delta\theta_e}{r_s+pL_d} + \frac{\sin^2 \Delta\theta_e}{r_s+pL_q} \\ \frac{\cos \Delta\theta_e \sin \Delta\theta_e}{r_s+pL_d} - \frac{\cos \Delta\theta_e \sin \Delta\theta_e}{r_s+pL_q} \end{bmatrix} V_h \cos \omega_h \, . \tag{9.75}$$

Let

$$A \equiv \frac{V_h}{r_s + pL_d} \cos \omega_h t \qquad \text{and} \qquad B \equiv \frac{V_h}{r_s + pL_q} \cos \omega_h t \, .$$

The steady-state solutions of A and B are

$$A = \frac{V_h}{\sqrt{r_s^2 + \omega_h^2 L_d^2}} \cos \left(\omega_h t - \tan^{-1}(\frac{\omega_h L_d}{r_s}) \right), \tag{9.76}$$

$$B = \frac{V_h}{\sqrt{r_s^2 + \omega_h^2 L_q^2}} \cos \left(\omega_h t - \tan^{-1}(\frac{\omega_h L_q}{r_s}) \right). \tag{9.77}$$

The solution for (9.75) is written as

$$\begin{bmatrix} \bar{i}^e_{dh} \\ \bar{i}^e_{qh} \end{bmatrix} = \begin{bmatrix} \frac{A+B}{2} + \frac{A-B}{2} \cos 2\Delta\theta_e \\ \frac{A-B}{2} \sin 2\Delta\theta_e \end{bmatrix}. \tag{9.78}$$

Simplified Angle Error Estimation Method [25]

Now consider a limiting case where $\omega_h L_d \gg r_s$ for a high $\omega_h > 0$. Then,

$$A \approx \frac{V_h}{\omega_h L_d} \sin \omega_h t \qquad \text{and} \qquad B \approx \frac{V_h}{\omega_h L_q} \sin \omega_h t.$$

Then, (9.78) reduces to

$$\begin{bmatrix} \bar{i}^e_{dh} \\ \bar{i}^e_{qh} \end{bmatrix} = \frac{V_h}{\omega_h L_d L_q} \begin{bmatrix} L_{av} + L_{df} \cos 2\Delta\theta_e \\ L_{df} \sin 2\Delta\theta_e \end{bmatrix} \sin(\omega_h t) \tag{9.79}$$

where

$$L_{av} = \frac{L_d + L_q}{2} \qquad \text{and} \qquad L_{df} = \frac{L_q - L_d}{2}.$$

To obtain an estimate of $\Delta\theta_e$, $\sin(\omega_h t)$ should be eliminated. For this purpose, a synchronous rectification method is utilized: First, multiply a signal by $\sin(\omega_h t)$. Then, remove the high frequency term by a low-pass filter (LPF). We let

$$X_{dh} = \frac{2\omega_h L_d L_q}{V_h} \times \mathrm{LPF}(i_{dh} \times \sin \omega_h t) \tag{9.80}$$

$$X_{qh} = \frac{2\omega_h L_d L_q}{V_h} \times \mathrm{LPF}(i_{qh} \times \sin \omega_h t), \tag{9.81}$$

where LPF(r) represents the filtered signal of $r(t)$. Note that

$$\begin{aligned} X_{dh} &\approx L_{av} + L_{df}\cos 2\Delta\theta_e \\ X_{qh} &\approx L_{df}\sin 2\Delta\theta_e. \end{aligned}$$

Therefore, an angle error estimate is obtained such that

$$\widehat{\Delta\theta}_e = \frac{1}{2}\tan^{-1}\left(\frac{X_{qh}}{X_{dh} - L_{av}}\right).$$

Fig. 9.23 shows the signal processing block diagram.

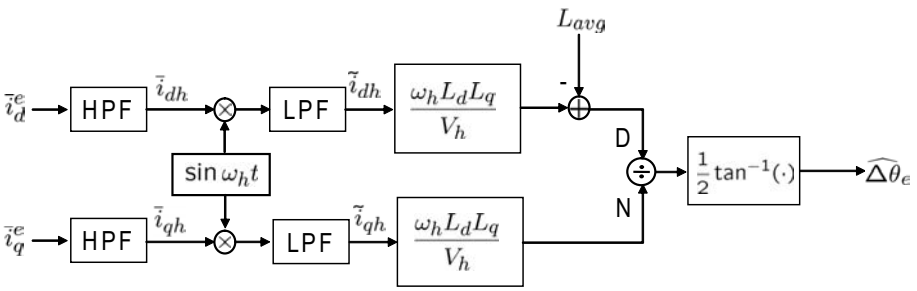

Figure 9.23: Signal processing block diagram of a signal injection-based sensorless algorithm.

If the rotor position estimation error is small, then (9.81) is approximated as

$$X_{qh} \approx 2L_{df}\Delta\theta_e. \tag{9.82}$$

The PLL type estimator shown in Fig. 9.2 can be used to obtain $\hat{\theta}_e$ from the error, $\Delta\theta_e$. It is redrawn as Fig. 9.24 for this case. Jang et al.[25], [27] utilized a bang-bang controller instead of the PI controller. A low-pass filter may be used in order to reduce the ripples contained in the output of the bang-bang controller.

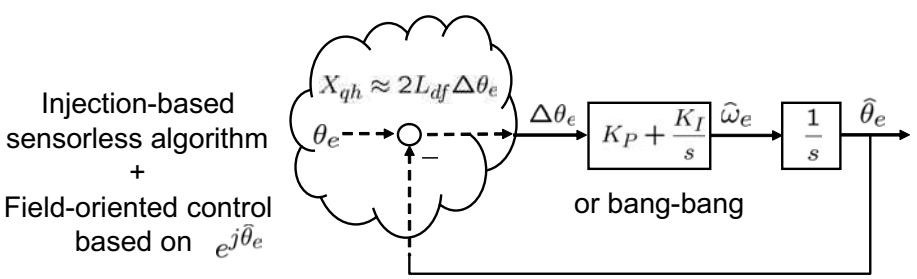

Figure 9.24: Block diagram illustrating the concept of rotor position estimator using PI or bang-bang controller.

Summary

- With the signal injection method, it is possible to control the motor at zero speed.
- A high frequency probing signal is injected to detect the rotor angle by exploiting the salient feature of IPMSMs. For angle detection, the synchronous rectification method is utilized.
- Signal injection methods are applied in practical systems such as elevators, etc.
- The high frequency signal makes audible noise and core saturation.

Bibliography

[1] N. Matsui, "Sensorless PM brushless DC motor drives," *IEEE Trans. on Ind. Electron.,* vol. 43, no. 2, pp. 300 – 308, Apr. 1996.

[2] M. Tomita, T. Senjyu, S. Doki, and S. Okuma, "New sensorless controls for brushless dc motors using disturbance observers and adaptive velocity estimations," *IEEE Trans. on Ind. Electron.,* vol. 45, no.2, pp. 274 – 282, Apr. 1998.

[3] M. J. Corley and R. D. Lorenz, Rotor position and velocity estimation for a salient-pole permanent magnet synchronous machine at standstill and high speeds, *IEEE Trans. on Ind. Appl.,* vol. 34, no 4, pp. 784 – 789, Jul./Aug. 1998.

[4] Y.S. Jeong, R. D. Lorenz, T. M. Jahns, and S. K. Sul, Initial rotor position estimation of an interior permanent-magnet synchronous machine using carrier-frequency injection methods, *IEEE Trans. Ind. Appl.*, vol. 41, no. 1, pp. 38 – 45, Jan./Feb. 2005.

[5] S. Wu, D. D. Reigosa, Y. Shibukawa, M. A. Leetmaa, R. D. Lorenz, and Y. Li, Interior permanent-magnet synchronous motor design for improving self-sensing performance at very low speed, *IEEE Trans. Ind. Appl.*, Vol. 45, No. 6, pp. 1939 – 1945, Nov./Dec. 2009.

[6] Z.Q. Zhu, Y. Li, D. Howe, C.M. Bingham, and D. A. Stone, Improved rotor position estimation by signal injection in brushless AC motors, accounting for cross-coupling magnetic saturation, *IEEE Trans. Ind. Appl.*, Vol. 45, No. 5, pp. 1843 – 1849, Sept./Oct. 2009.

[7] T. Aihara, A. Toba, T. Yanase, A. Mashimo, and K. Endo, "Sensorless torque control of salient-pole synchronous motor at zero-speed operation," *IEEE Trans. on Power Elec.,* vol 14, no 1, pp. 202 – 208, Jan. 1999.

[8] Z. Chen, M. Tomita, S. Doki, and S. Okuma, "New adaptive sliding observers for position- and velocity-sensorless controls of brushless DC motors," *IEEE Trans. on Ind. Electron.,* vol. 47, no. 3, pp. 582 – 591, Jun. 2000.

[9] B. Nahid-Mobarakeh, F. Meibody-Tabar, and F. M. Sargos, "Back EMF estimation-based sensorless control of PMSM: robustness with respect to mea-

surement errors and inverter irregularities," *IEEE Trans. on Ind. Appl.,* vol. 43, no. 2, pp. 485 – 494, Mar./Apr. 2007.

[10] Z. Xu and M. F. Rahman, "An adaptive sliding stator flux observer for a direct-torque-controlled IPM synchronous motor drive," *IEEE Trans. on Ind. Electron.,* vol. 54, no. 5, pp. 2398 – 2406, Oct. 2007.

[11] Y. Liu, Z. Q. Zhu, and D. Howe, "Instantaneous torque estimation in sensorless direct-torque-controlled brushless DC motors," *IEEE Trans. on Ind. Appl.,* vol. 42, no. 5, pp. 1275 – 1283, Sep./Oct. 2006.

[12] S. Bolognani, L. Tubiana, and M. Zigliotto, "Extended Kalman filter tuning in sensorless PMSM drives," *IEEE Trans. on Ind. Appl.,* vol. 39, no. 6, pp. 1741 – 1747, Nov./Dec. 2003.

[13] R. Ortega, L. Praly, A. Astolfi, J. Lee, and K. Nam, "A Simple observer for permanent magnet synchronous motors with guaranteed stability properties," *LSS Internal Report*, Dec. 2008.

[14] G. Zhu, A. Kaddouri, L. A. Dessaint, and O. Akhrif, "A nonlinear state observer for the sensorless control of a permanent-magnet AC machine," *IEEE Trans. on Ind. Electron.,* vol. 48, no. 6, pp. 1098 – 1108, Dec. 2001.

[15] J. Solsona, M. I. Valla, and C. Muravchik, "On speed and rotor position estimation in permanent-magnet AC drives," *IEEE Trans. on Ind. Electron.,* vol 47, no. 5, pp. 1176 – 1180, Oct. 2000.

[16] L. Harnefors and H.-P. Nee, A general algorithm for speed and position estimation of ac motors, *IEEE Trans. Ind. Electron.*, vol. 47, no. 1, pp. 77 – 83, Feb. 2000.

[17] O. Wallmark and L. Harnefors, Sensorless control of salient PMSM drives in the transition region, *IEEE Trans. Ind. Electron.*, vol. 53, no. 4, pp. 1179 – 1187, Aug. 2006.

[18] S. Morimoto, K. Kawamoto, M. Sanada, and Y. Takeda, "Sensorless control strategy for salient-pole PMSM based on extended EMF in rotating reference frame," *IEEE Trans. on Ind. Appl.,* vol. 38, no 4, pp. 1054 – 1061, Jul./Aug. 2002.

[19] M. Jansson, L. Harnefors, O. Wallmark, M. Leksell, "Synchronization at startup and stable rotation reversal of sensorless nonsalient PMSM drives" *IEEE Trans. on Ind. Electron.,* vol. 53, no. 2, pp. 379 – 387, Apr. 2006.

[20] J. Lee, J. Hong, K. Nam, R. Ortega, L. Praly, and A. Astolfi, Sensorless control of surface-mount permanent magnet synchronous motors based on a nonlinear observer, *IEEE Trans. on Power Elec.*, Vol. 25, No.2, pp. 290 – 297, 2010.

[21] J. Hong and K. Nam, Sensorless control of IPMSM based on an adaptive Observer, submitted for review, 2010.

[22] S. Morese, Adaptive control of single-input, single-output linear systems, *IEEE Trans. on Automat. Contr.*, Vol. AC-23, No. 4, pp. 557 – 569, Aug., 1978.

[23] G. Kreisselmeier, Adaptive observers with exponential rate of convergence, *IEEE Trans. on Automat. Contr.*, Vol. AC-22, No. 1, pp. 2 – 8, Feb., 1977.

[24] R. Mizutani, T. Takeshita, and N. Matsui, Current model-based sensorless drives of salient-pole PMSM at low speed and standstill, *IEEE Trans. Ind. Appl.*, Vol. 34, No. 4, pp. 841 – 846, Jul./Aug. 1998.

[25] J. H. Jang, J. I. Ha, M. Ohto, K. Ide, and S. K. Sul, Analysis of permanent-magnet machine for sensorless control based on high-frequency signal injection, *IEEE Trans. Ind. Appl.*, Vol. 40, No. 6, pp. 1595 – 1604, Nov./Dec. 2004.

[26] M. Linke, R. Kennel, and J. Holtz, Sensorless speed and position control of synchronous machines using alternating carrier injection, *Proc. Int. Elect. Mach. Drives Conf.* (IEMDC 03), Madison, pp. 1211 – 1217, Jun. 2003.

[27] J.H. Jang, S.K. Sul, J.I. Ha, K. Ide, and M. Sawamura, Sensorless drive of surface-mounted permanent-magnet motor by high-frequency signal injection-based on magnetic saliency, *IEEE Trans. Ind. Appl.,* Vol. 39, No. 4, pp. 1031 – 1039, 2003.

Problems

9.1 Define the observation error by $\tilde{\mathbf{x}} \equiv \hat{\mathbf{x}} - \mathbf{x}$. Show that the error dynamics directly follows from (9.12)-(9.17) such that

$$\begin{aligned} \dot{\tilde{\mathbf{x}}} &= -\gamma a(\tilde{\mathbf{x}}, t) \left\{ \tilde{\mathbf{x}} + \psi_m \begin{bmatrix} \cos\theta_e(t) \\ \sin\theta_e(t) \end{bmatrix} \right\} \\ a(\tilde{\mathbf{x}}, t) &\equiv \frac{1}{2}\|\tilde{\mathbf{x}}\|^2 + \psi_m[\tilde{x}_1 \cos\theta_e(t) + \tilde{x}_2 \sin\theta_e(t)]. \end{aligned}$$

9.2 Using the MATLAB® Simulink, construct a speed controller based on the Ortega's sensorless algorithm for a SPMSM listed in Table 9.1 following the instructions below:

a) Use a PLL type speed estimator:

$$\begin{aligned} \dot{z}_1 &= K_p(\hat{\theta}_e - z_1) + K_i z_2 \\ \dot{z}_2 &= \hat{\theta}_e - z_1 \\ \hat{\omega} &= K_p(\hat{\theta}_e - z_1) + K_i z_2, \end{aligned}$$

where K_p and K_i are proportional and integral gains, respectively.

b) Use PI controllers for current control and compensate the cross coupling voltages, $\omega L i_d$ and $\omega L i_q$.

c) Use a PI controller for the speed control.

d) Refer to the control block diagram shown in Fig. 9.3. But neglect the d–axis voltage pulse injection shown on the top.

Obtain a comparable result (300rpm, no load) with the experimental one shown in Fig. 9.5 (b).

9.3 Derive

$$\dot{\boldsymbol{\varepsilon}}(t) = (\mathbf{A}_s - \mathbf{KC})\boldsymbol{\varepsilon}(t) - \left(\int_0^t e^{(\mathbf{A}_s - \mathbf{KC})(t-\tau)} \mathbf{b}_s(\tau) d\tau \right) \dot{\hat{p}}(t)$$

from

$$\begin{aligned} \dot{\boldsymbol{\beta}}(t) &= (\mathbf{A}_s - \mathbf{KC})\boldsymbol{\beta}(t) + \mathbf{b}_s(t), \\ \boldsymbol{\varepsilon}(t) &= -\boldsymbol{\beta}(t)\hat{p}(t) + \int_0^t e^{(\mathbf{A}_s - \mathbf{KC})(t-\tau)} \mathbf{b}_s(\tau)\hat{p}(\tau) d\tau \,. \end{aligned}$$

9.4 Derive from (9.35) the following:

$$\begin{bmatrix} \overline{v}_d^e \\ \overline{v}_q^e \end{bmatrix} = \begin{bmatrix} r_s + pL_d & -\omega_e L_q \\ \omega_e L_q & r_s + pL_d \end{bmatrix} \begin{bmatrix} \bar{i}_d^e \\ \bar{i}_q^e \end{bmatrix} + \begin{bmatrix} \xi_d^e \\ \xi_q^e \end{bmatrix}$$

where

$$\begin{bmatrix} \xi_d^e \\ \xi_q^e \end{bmatrix} = E_{ex} \begin{bmatrix} \sin(\overline{\theta} - \theta) \\ \cos(\overline{\theta} - \theta) \end{bmatrix} + (\overline{\omega}_e - \omega_e) L_d \begin{bmatrix} -\bar{i}_q^e \\ \bar{i}_d^e \end{bmatrix}.$$

9.5 Show that if $\overline{\omega}_e \neq \omega_e$ then

$$\begin{aligned} & e^{\mathbf{J}\Delta\theta_e} \begin{bmatrix} pL_d & 0 \\ 0 & pL_q \end{bmatrix} e^{-\mathbf{J}\Delta\theta_e} \bar{\mathbf{i}}_{dq}^e \\ = \; & (\overline{\omega}_e - \omega_e) \begin{bmatrix} L_{df} \sin 2\Delta\theta_e & -L_{av} + L_{df} \cos 2\Delta\theta_e \\ L_{av} + L_{df} \cos 2\Delta\theta_e & -L_{df} \sin 2\Delta\theta_e \end{bmatrix} \begin{bmatrix} \bar{i}_d^e \\ \bar{i}_q^e \end{bmatrix} \\ & + \begin{bmatrix} L_{av} - L_{df} \cos 2\Delta\theta_e & L_{df} \sin 2\Delta\theta_e \\ L_{df} \sin 2\Delta\theta_e & L_{av} + L_{df} \cos 2\Delta\theta_e \end{bmatrix} \begin{bmatrix} p\bar{i}_d^e \\ p\bar{i}_q^e \end{bmatrix}. \end{aligned}$$

9.6 a) Show that

$$\begin{aligned}\Delta\mathbf{i}(s) &= \begin{bmatrix} r_s + sL_\alpha & sL_\gamma \\ sL_\gamma & r_s + sL_\beta \end{bmatrix}^{-1} \Delta\mathbf{v}(s) \\ &= \frac{1}{(L_d s + r_s)(L_q s + r_s)} \begin{bmatrix} r_s + L_\beta s & -L_\gamma s \\ -L_\gamma s & r_s + L_\alpha s \end{bmatrix} \Delta\mathbf{v}(s).\end{aligned}$$

b) Derive (9.66) for $\Delta\mathbf{v} = [\frac{V_p}{s}, 0]^T$.

Chapter 10

Pulse-Width Modulation and Inverter

A three-phase voltage source inverter consisting of six switches and a common DC rail is shown in Fig. 10.1. The pulse-width modulation (PWM) is a technique that provides an arbitrary shape of voltage by adjusting the ratio of on and off duties. With the PWM techniques, the semiconductor switches are not allowed to operate in the active region. Only on and off modes are used like an ideal switch. Otherwise, large heat losses will take place in the switches. Note that the ideal switches do not consume power in cut-off mode, as well as in conduction mode, since either cut-off current or on-drop voltage is zero.

As physical switching devices, IGBTs are most widely used. But, power MOSFETs are suitable for low voltage, low power applications where fast switching (e.g., above 30kHz) is required. For high-power applications (6000V, 6000A), IGCTs are utilized. Note that each switch has an anti-parallel diode in the voltage source inverter to provide commutation paths for inductive loads.

However, practical semiconductor switches show non-ideal behavior: During the

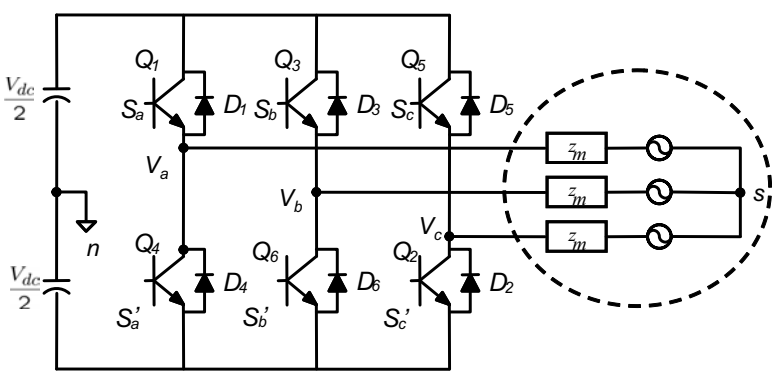

Figure 10.1: A voltage source inverter with six switching devices.

turn on transient, the (collector-emitter) voltage that a switch bolsters drops only after the switch (collector) current builds up. Since the collector current flows while the collector-emitter voltage remains high, power loss takes place in the switch. During the turning off transient, the current begins to drop after the collector-emitter voltage rises. For the same reason, the switch loss takes place. Fig. 10.2 (a) shows plots of nonzero-voltage turn on and nonzero current turn off. Fig. 10.2 (b) shows voltage-current contours during the switching transitions. Theses switching losses heat up the switch and are directly proportional to the switching frequency.

Besides, physical switches cause conduction losses due to the switch on-drop voltage during the conduction stage. As the voltage blocking capability increases, the on-drop voltage increases. The semiconductor switches should be cooled off so that the junction temperature is below 150°C.

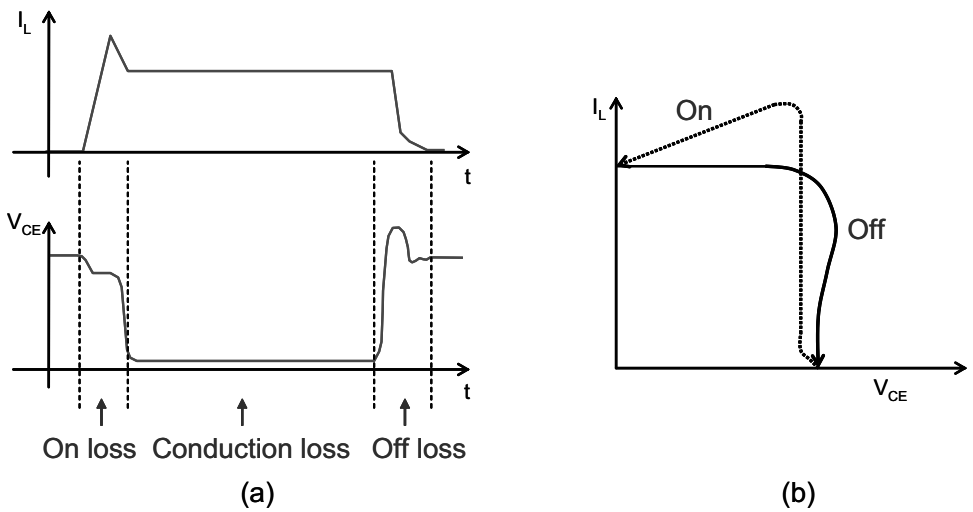

Figure 10.2: (a) Typical current and voltage profiles of a semiconductor switch and (b) turn on and off contours in the voltage-current plane.

10.1 Switching Functions and Six-Step Operation

Three-phase voltage source inverters consist of six switches and DC link capacitors, as shown in Fig. 10.1. The switches are grouped by arm such that (S_a, S'_a), (S_b, S'_b), and (S_c, S'_c). In each switching arm, both upper and lower switches should not be turned on concurrently to avoid arm shorting.

Note that the middle point of the DC link capacitor is denoted n. We also denote by $S_a = 1$ if switch S_a is turned on, otherwise $S_a = 0$. The same rule is applied to

S_b and S_c. Consider the switching pattern for $n = 0, 1, 2, \cdots$:

$$\begin{cases} S_a = 1, & n\pi \le \omega t < (n+1)\pi \\ S_a = 0, & (n+1)\pi \le \omega t < (n+2)\pi, \end{cases}$$
$$\begin{cases} S_b = 1, & (n+2/3)\pi \le \omega t < (n+5/3)\pi \\ S_b = 0, & (n+5/3)\pi \le \omega t < (n+8/3)\pi, \end{cases}$$
$$\begin{cases} S_c = 1, & (n-2/3)\pi \le \omega t < (n+1/3)\pi \\ S_c = 0, & (n+1/3)\pi \le \omega t < (n+4/3)\pi. \end{cases}$$

This switching pattern is called "six-step operation", since it utilizes six switchings per period. Using the switching function, the pole voltages with reference to n are $\pm\frac{V_{dc}}{2}$. More specifically,

$$v_{an} = \frac{V_{dc}}{2}(2S_a - 1), \tag{10.1}$$
$$v_{bn} = \frac{V_{dc}}{2}(2S_b - 1), \tag{10.2}$$
$$v_{cn} = \frac{V_{dc}}{2}(2S_c - 1). \tag{10.3}$$

Hence, the line-to-line voltage is obtained such that

$$\begin{aligned} v_{ab} &= v_{an} - v_{bn}, \\ v_{bc} &= v_{bn} - v_{cn}, \\ v_{ca} &= v_{cn} - v_{an}. \end{aligned}$$

The pole voltages and line-to-line voltages versus time are shown in Fig. 10.3. Note that the peak value of the line-to-line voltage is V_{dc}. The fundamental component of the line-to-line voltage is calculated as

$$v_{ab[1]} = \frac{2}{\pi}\int_0^{\pi} v_{ab}\sin\omega t \; d(\omega t) = \frac{2}{\pi}\int_{\pi/6}^{5\pi/6} V_{dc}\sin\omega t \; d(\omega t) = \frac{2\sqrt{3}V_{dc}}{\pi}.$$

This is the maximum output voltage that an inverter can produce for a given DC link V_{dc}. Some higher order spectral coefficients are listed in Table 10.1.

Table 10.1: Harmonic coefficients of the six-step line-to-line voltage.

Harmonic number (n)	1	-5	7	-11	12
$v_{ab[n]}/v_{ab[1]}$	1	-0.2	0.14	-0.1	0.08

Note that

$$v_{an} = v_{as} + v_{sn}, \tag{10.4}$$
$$v_{bn} = v_{bs} + v_{sn}, \tag{10.5}$$
$$v_{cn} = v_{cs} + v_{sn}. \tag{10.6}$$

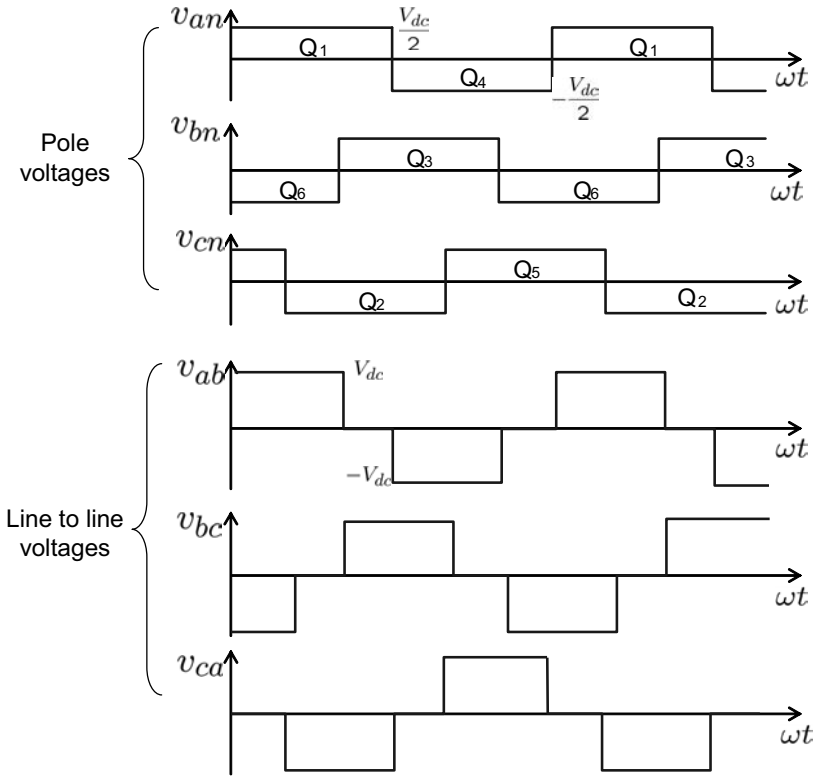

Figure 10.3: Pole and line-to-line voltages with the six-step operation.

With the assumption that $v_{as} + v_{bs} + v_{cs} = 0$, it follows that

$$v_{sn} = \frac{v_{an} + v_{bn} + v_{cn}}{3} = \frac{V_{dc}}{6}(2S_a + 2S_b + 2S_c - 3)\,. \tag{10.7}$$

Note again that v_{sn} is the voltage difference between the neutral point, s of the motor and the DC link center tap, n. Then, the motor phase voltages follow from (10.4)-(10.7) as:

$$v_{as} = \frac{V_{dc}}{3}(2S_a - S_b - S_c), \tag{10.8}$$

$$v_{bs} = \frac{V_{dc}}{3}(2S_b - S_c - S_a), \tag{10.9}$$

$$v_{cs} = \frac{V_{dc}}{3}(2S_c - S_a - S_b). \tag{10.10}$$

The motor phase voltages and v_{sn} are depicted in Fig. 10.4. Obviously, the sum of (10.8), (10.9), and (10.10) is equal to zero. But, v_{sn} is changing its level six times per period, producing a sixth harmonic component. The fluctuation of v_{sn} is a source of the common mode noise, which causes bearing current.

The phase voltages shown in Fig. 10.4 are the typical voltage patterns of the six-step inverter operation. The rms of the fundamental component of the phase

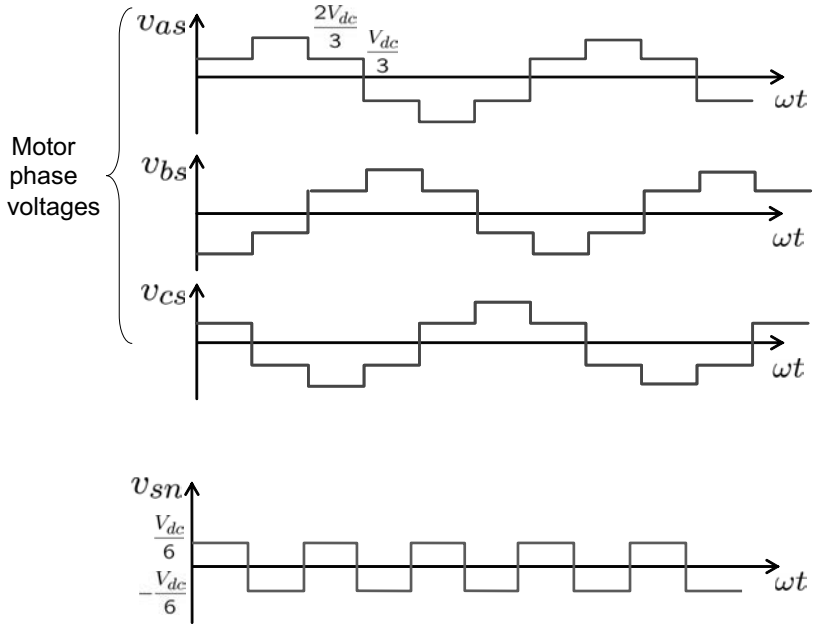

Figure 10.4: Phase voltages and the motor neutral voltage with the six-step operation.

voltage is equal to

$$v_{as(rms)[1]} = \frac{\sqrt{2}}{\pi} V_{dc}.$$

It should be noted that the six-step operation requires the minimum number of switchings whereas it produces the maximum rms voltage under a given DC link voltage. Therefore, it is utilized in some high-power machine drives where the fast switching is not feasible. But, it causes large current harmonics, as shown in Fig. 10.5.

Exercise 10.1
Show that the rms value of the fundamental component of the six-step phase voltage, v_{as} is equal to $v_{as(rms)[1]} = \frac{\sqrt{2}}{\pi} V_{dc}$.

10.2 PWM Methods

The pulse-width modulation (PWM) is a DC voltage modulation method that provides an arbitrary intermediate voltage by adjusting the on and off ratio in each period. Numerous PWM methods were investigated by many researchers [4], [5], [6], but sinusoidal PWM and space vector PWM are the two most popular methods. The sinusoidal PWM can be realized by analog circuits, whereas the space vector

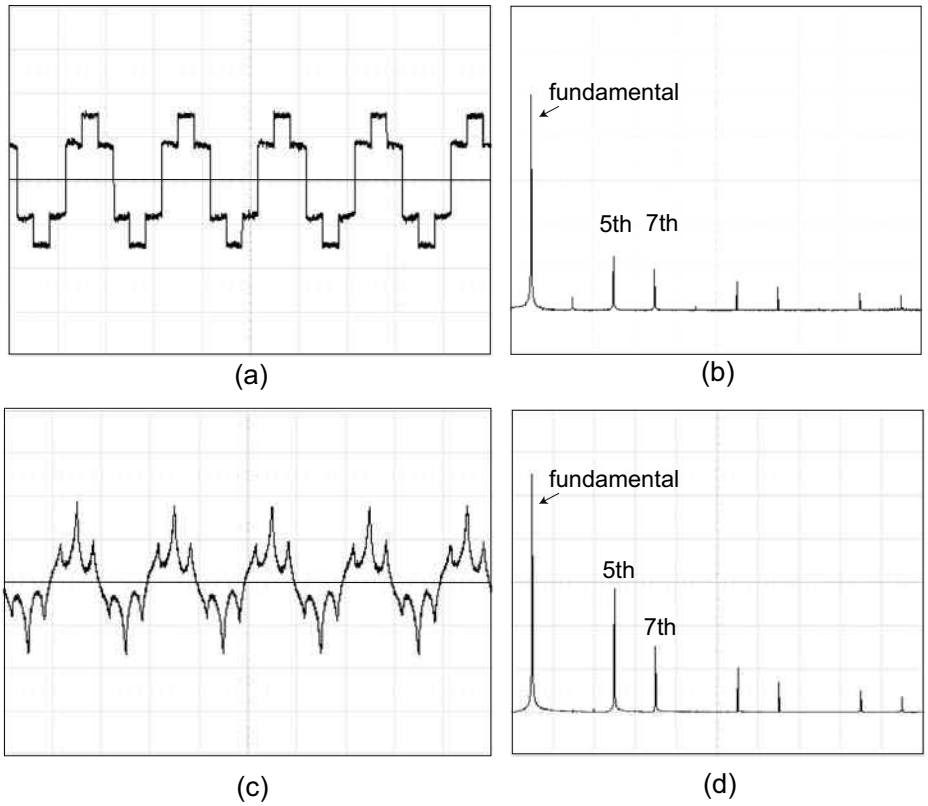

Figure 10.5: Six-step operation: (a) phase voltage, (b) phase voltage spectrum, (c) current, and (d) current spectrum.

PWM consumes a DSP computing power since PWM duties are calculated by a partitioning method in each PWM period.

10.2.1 Sinusoidal PWM

Sinusoidal PWM is obtained by comparing a triangular wave with a sinusoidal wave, as shown in Fig. 10.6: Turn-on signal of the high-side switch is determined according to

$$S_a = \begin{cases} 1, & \text{if } V_{sine} \geq V_{tri} \\ 0, & \text{if } V_{sine} < V_{tri} \end{cases},$$

where V_{sine} and V_{tri} are sinusoidal and triangular waves, respectively. A schematic drawing of the sinusoidal PWM and the corresponding output voltage is shown in Fig. 10.6. The maximum peak voltage is equal to $V_{dc}/2$. Thus, the ratio of the maximum sinusoidal PWM to the six-step operation is equal to

$$\frac{\max V_{rms}(\text{sinusoidal})}{V_{rms}(\text{six–step})} = \frac{\frac{1}{2\sqrt{2}}}{\frac{\sqrt{2}}{\pi}} = 0.785.$$

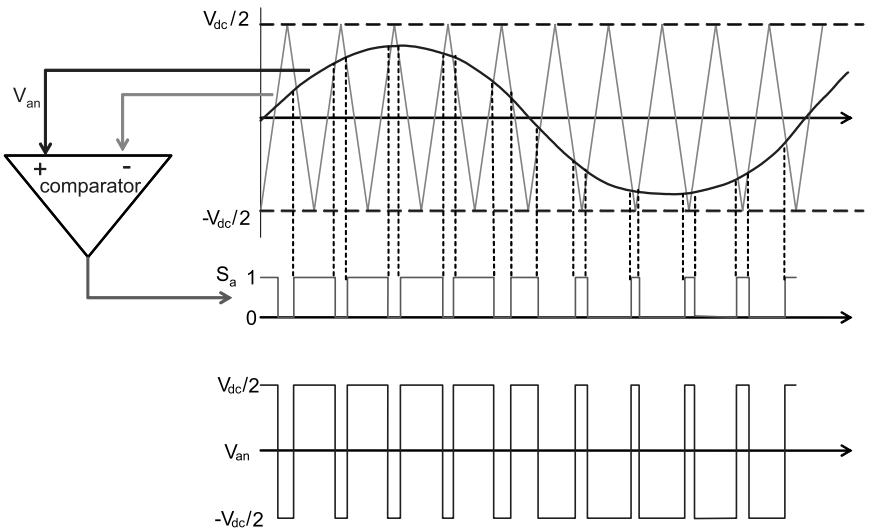

Figure 10.6: Sinusoidal PWM method by comparing with triangular wave.

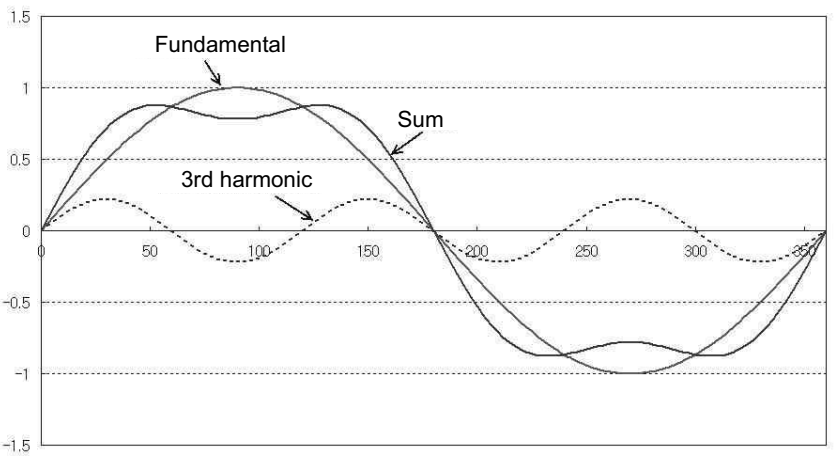

Figure 10.7: Addition of a 3^{rd}-order harmonics.

Note that the simple sinusoidal PWM yields a low voltage utilization. It is possible to increase the rms voltage within $V_{dc}/2$ by adding some higher-order harmonics. These methods are referred to as overmodulation. Fig. 10.7 shows how the 3^{rd}-order harmonics lowers down the peak value of the fundamental, providing room to increase further the fundamental component. On the other hand, since the 3^{rd}-order harmonics are identical in a, b, and c phases, they are canceled out in the line-to-line voltages. Therefore, the line-to-line voltage level can be increased without any distortion by adding 3^{rd}-order harmonics. A simple overmodulated waveform and

the overmodulation regions are shown in Fig. 10.8.

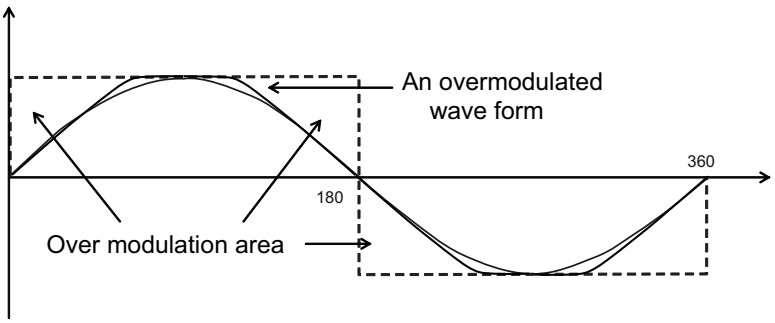

Figure 10.8: Over modulation region.

10.2.2 Space Vector PWM

The six-inverter switching status can be mapped into the vertices of a regular hexagon. With zero (0,0,0) and seven (1,1,1) switching vectors, the eight vectors are defined by

$$
\begin{aligned}
V_1 &: (S_a, S_b, S_c) = (1, 0, 0);\\
V_2 &: (S_a, S_b, S_c) = (1, 1, 0);\\
V_3 &: (S_a, S_b, S_c) = (0, 1, 0);
\end{aligned}
$$

$$
\begin{aligned}
V_4 &: (S_a, S_b, S_c) = (0, 1, 1);\\
V_5 &: (S_a, S_b, S_c) = (0, 0, 1);\\
V_6 &: (S_a, S_b, S_c) = (1, 0, 1);\\
V_7 &: (S_a, S_b, S_c) = (1, 1, 1);\\
V_0 &: (S_a, S_b, S_c) = (0, 0, 0).
\end{aligned}
$$

Fig. 10.9 shows the directions of the flux vectors that correspond to the switching vectors $V_1, \cdots, V_6$. The direction of a space vector is chosen to be identical with that of the resulting flux vector. For example, the direction of $V_1 = (1, 0, 0)$ is the same as that of the flux (or current) vector that resulted from the switching state, $(S_a, S_b, S_c) = (1, 0, 0)$. In the similar methods, space vectors $V_2, \cdots, V_6$ are defined as shown in Fig. 10.10. Based on $V_0, \cdots, V_6$, sectors are named Sector 1, $\cdots$, Sector 6. Note that V_0 and V_7 are the zero vectors that are located at the origin.

An arbitrary space vector can be represented as a sum of the decomposed vectors. Consider a vector V_a in Sector 1 shown in Fig. 10.11. Note that $V_a = V_{a1} + V_{a2}$, where V_{a1} and V_{a2} are the decomposed vectors into the lines of V_1 and V_2, respectively.

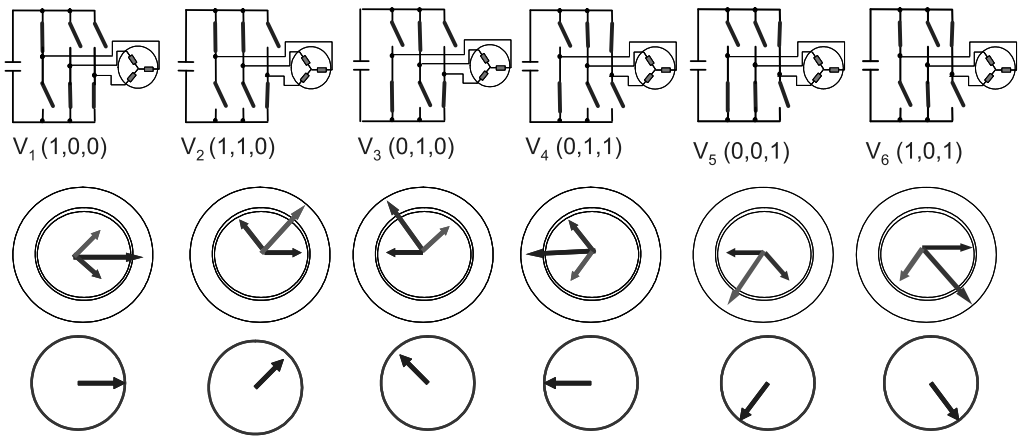

Figure 10.9: Directions of the flux vectors for the switching vectors $V_1, \cdots, V_6$.

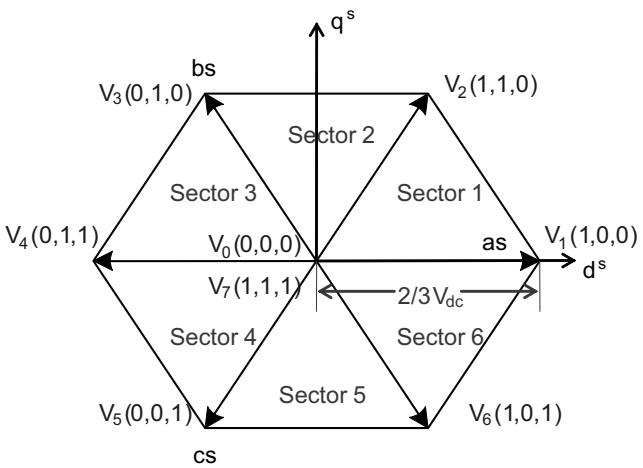

Figure 10.10: Space vector diagram.

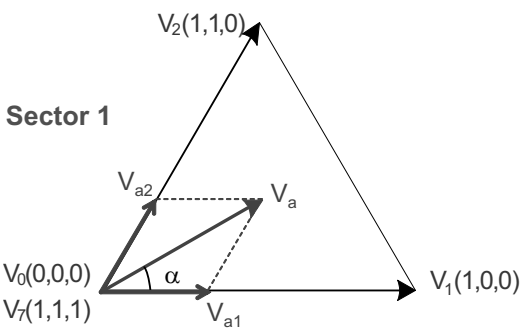

Figure 10.11: Calculation of on-times for v_1 and v_2 (partitioning by parallelogram).

Let T_s be the PWM switching interval. Decomposed vector, V_{a1}, is synthesized

by turning on $V_1(1,0,0)$ during a fractional time interval, T_1, which is proportional to the magnitude of V_{a1}. Specifically, T_1 and T_2 are determined as

$$\frac{V_{a1}}{(2/3)V_{dc}} = \frac{T_1}{T_s}, \tag{10.11}$$

$$\frac{V_{a2}}{(2/3)V_{dc}} = \frac{T_2}{T_s}. \tag{10.12}$$

On the other hand, it follows from the geometrical relationship that

$$\begin{aligned} \begin{bmatrix} v_d^s \\ v_q^s \end{bmatrix} \equiv V_a \begin{bmatrix} \cos(\alpha) \\ \sin(\alpha) \end{bmatrix} &= \frac{T_1}{T_s}\frac{2}{3}V_{dc}\begin{bmatrix} 1 \\ 0 \end{bmatrix} + \frac{T_2}{T_s}\frac{2}{3}V_{dc}\begin{bmatrix} \cos\frac{\pi}{3} \\ \sin\frac{\pi}{3} \end{bmatrix} \\ &= \frac{2}{3}\frac{V_{dc}}{T_s}\begin{bmatrix} 1 & \cos\frac{\pi}{3} \\ 0 & \sin\frac{\pi}{3} \end{bmatrix}\begin{bmatrix} T_1 \\ T_2 \end{bmatrix}. \end{aligned} \tag{10.13}$$

Therefore,

$$\begin{bmatrix} T_1 \\ T_2 \end{bmatrix} = \frac{\sqrt{3}T_s}{V_{dc}}\begin{bmatrix} \sin\frac{\pi}{3} & -\cos\frac{\pi}{3} \\ 0 & 1 \end{bmatrix}\begin{bmatrix} v_d^s \\ v_q^s \end{bmatrix}. \tag{10.14}$$

This gives a relation between d, q voltage components and PWM duties in Sector 1. Generalizing (10.14) in the other sectors, we obtain

$$T_1 = \frac{\sqrt{3}T_s}{V_{dc}}\left[\sin(\frac{\pi}{3}m)v_d^s - \cos(\frac{\pi}{3}m)v_q^s\right], \tag{10.15}$$

$$T_2 = \frac{\sqrt{3}T_s}{V_{dc}}\left[-\sin(\frac{\pi}{3}(m-1))v_d^s + \cos(\frac{\pi}{3}(m-1))v_q^s\right], \tag{10.16}$$

where $m = 1, 2, \cdots, 6$ denotes a sector number. Equations (10.15) and (10.16) enable us to calculate directly the switching duties from d, q voltage components.

Exercise 10.2
It is desired to calculate a voltage vector $|V_a|e^{j\alpha}$ in Sector 1. Show that

$$\begin{aligned} T_1 &= T_s\frac{|V_a|}{2V_{dc}/3}\frac{\sin(\frac{\pi}{3}-\alpha)}{\sin\frac{\pi}{3}} \\ T_2 &= T_s\frac{|V_a|}{2V_{dc}/3}\frac{\sin(\alpha)}{\sin\frac{\pi}{3}} \\ T_0 &= T_s - (T_1+T_2). \end{aligned}$$

To use the polar coordinate representation, arctangent function should be used, i.e., $\alpha = \tan^{-1}(v_q^s/v_d^s)$. This can be a drawback. But, the arctan values can be obtained through a look-up table or Taylor series expansion.

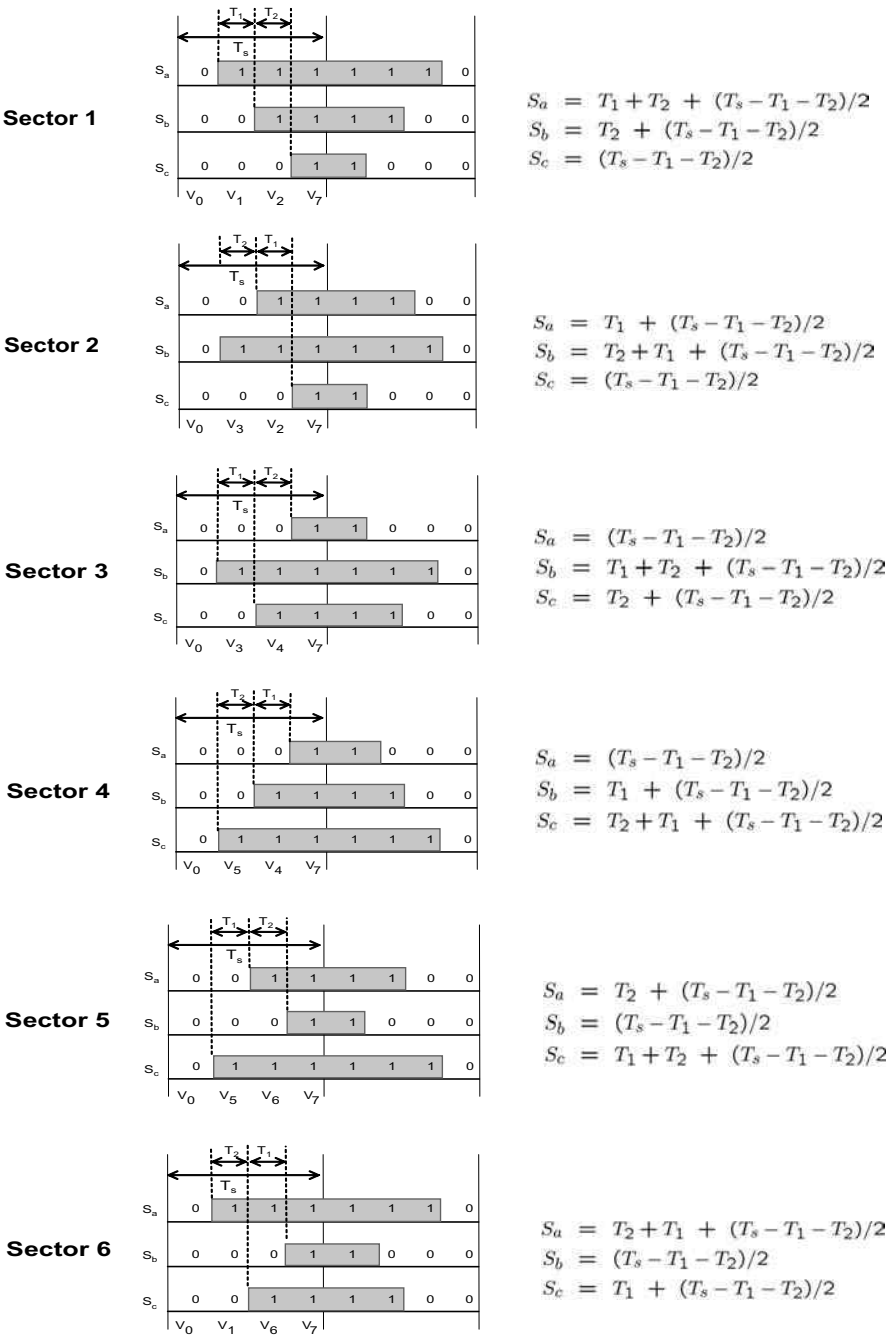

Figure 10.12: PWM waveforms and gating signals.

10.2.3 Space Vector PWM Patterns

A vector V in Sector m can be obtained in an average concept such that for $m = 1, 2, ..., 6$,

$$\int_0^{T_s} V\,dt = \int_0^{T_m} V_m dt + \int_{T_m}^{T_m+T_{m+1}} V_{m+1} dt + \int_{T_m+T_{m+1}}^{T_s} V_0 dt$$

i.e.,

$$V = V_m \frac{T_m}{T_s} + V_{m+1} \frac{T_{m+1}}{T_s}.$$

Zero voltage can be applied to the terminals by shorting either lower or upper switches. All inverter output terminals are tied to the negative side of the DC link in case of V_0, whereas they are shorted to the positive rail of the DC link in case of V_7. With the symmetric PWM method, the zero vector intervals are partitioned evenly between V_0 and V_7, i.e,

$$T_0 = T_7 = \frac{T_s - (T_m + T_{m+1})}{2}.$$

Fig. 10.12 shows the method of synthesizing S_1, S_2, and S_3 from T_1 and T_2 and the corresponding symmetric PWM patterns.

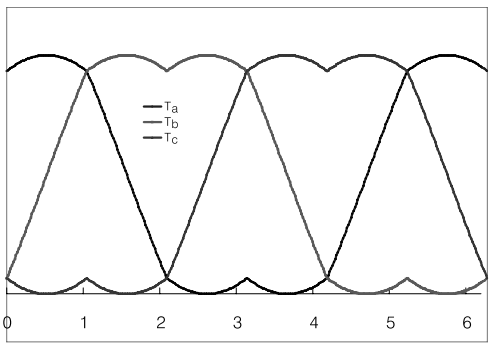

(a)

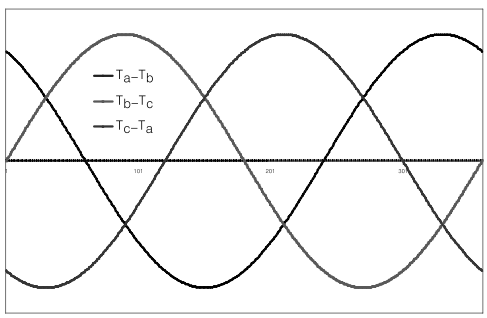

(b)

Figure 10.13: (a) Space vector PWM output (S_a, S_b, S_c) and (b) line to line voltage of the space vector PWM ($S_a - S_b$, $S_b - S_c$, $S_c - S_a$).

Fig. 10.13 (a) shows the phase voltages represented by S_1, S_2, and S_3. Note that each phase voltage is not sinusoidal wave. Each phase voltage contains 3^{rd}-order harmonics, so that the rms value is higher than that of the sinusoidal wave. In other words, the wave looks more like a trapezoidal wave. For this reason, the space vector PWM produces higher voltage than the sinusoidal PWM. But, the line to line voltage appears sinusoidal as shown in Fig. 10.13 (b). Note from (10.14) that the

space vector wave can be decomposed as the sum of a perfect sinusoidal wave and a triangular wave (3^{rd}-order harmonics). Since the 3^{rd}-order harmonics are identical in a, b, and c phases, they are canceled out when taking the line-to-line voltage.

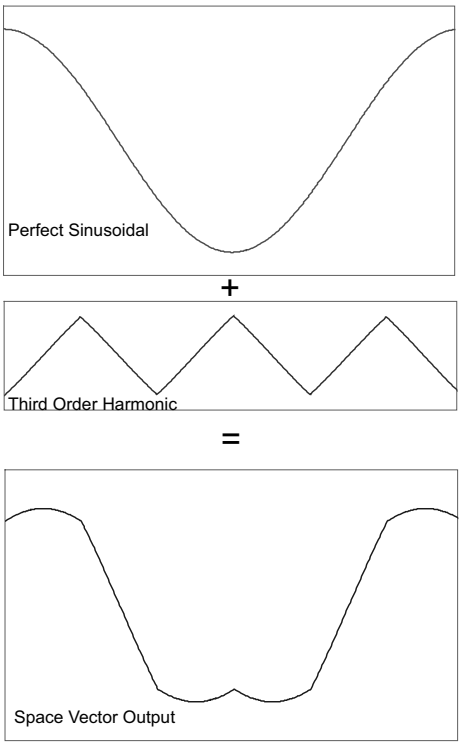

Figure 10.14: Space vector wave decomposition.

10.2.4 Sector-Finding Algorithm

As shown in the above, duty computing equations, (10.15) and (10.16), are different depending on sectors. To compute the on-duties of a given vector, $V^* = (v_d^s, v_q^s)$, the first step is to find a sector to which V^* belongs. In finding a sector, the signs of v_d^s and v_q^s are utilized firstly. Note that $v_q^s > 0$ for Sectors 1, 2, and 3, and $v_q^s < 0$ for Sectors 4, 5, and 6. Further to distinguish between Sector 1 or Sector 2, $|v_q|$ and $\sqrt{3}|v_d|$ are compared. Similarly, we have

$$\begin{cases} \text{Sector 2, 5,} & \text{if } |v_q^s| > \sqrt{3}|v_d^s| \\ \text{Sector 1, 3, 4, 6,} & \text{if } |v_q^s| < \sqrt{3}|v_d^s|. \end{cases}$$

Fig. 10.15 shows the sector-finding rule from (v_d^s, v_q^s), and Fig. 10.16 shows a complete sector-finding algorithm.

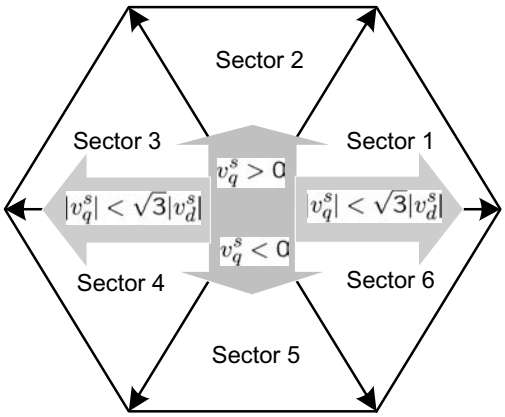

Figure 10.15: Finding sectors from (v_d^s, v_q^s).

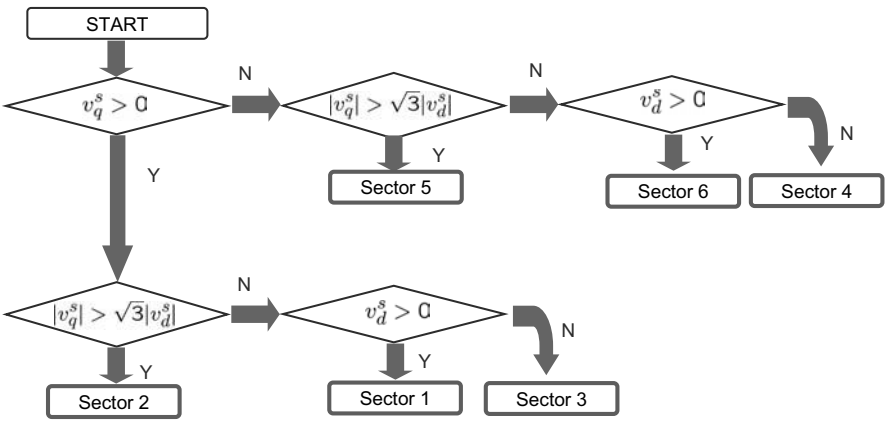

Figure 10.16: Sector finding flow chart.

10.2.5 Overmodulation

The maximum three-phase sinusoidal voltages are obtained if the space vectors are synthesized along the periphery of the inscribed circle in the hexagon, as shown in Fig. 10.17. Therefore, the maximum rms voltage obtainable through the space vector PWM is

$$v_{max} = \frac{1}{\sqrt{2}} \frac{\sqrt{3}}{2} \frac{2}{3} V_{dc} = \frac{1}{\sqrt{6}} V_{dc}. \tag{10.17}$$

But this is a case without harmonics. With some harmonic distortion, the rms voltage can be increased further. For example, if we use the shaded region of Fig. 10.17, higher voltage can be produced at the price of harmonic distortion. The PWM generation method utilizing the shaded region is called overmodulation. Overmodulation techniques were studied by many researchers [7],[3],[8]. In high-speed applications, the overmodulation plays an important role, since the back EMF grows steadily with the shaft speed while the source voltage is fixed.

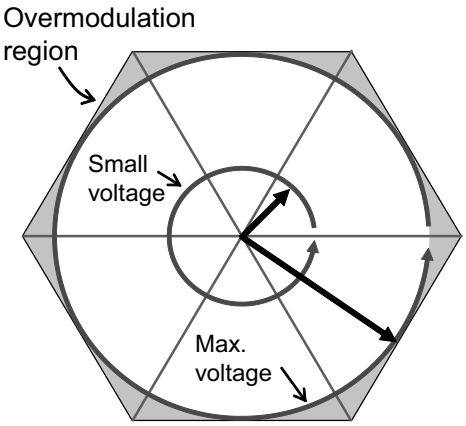

Figure 10.17: A maximum voltage and overmodulation region in the space vector PWM.

10.2.6 Comparision of Sinusoidal PWM and Space Vector PWM

We denote by v_{o1} and i_o the rms values of line to line voltage (fundamental component) and current, respectively. The inverter switch utilizing factor (SUF) is defined by

$$SUF = \frac{\sqrt{3} v_{o1} i_o}{6 V_T I_T},$$

where V_T and I_T are the maximum voltage and current applied to the switches, respectively [1]. Note that the maximum rms voltages are

$$v_{o1} = \begin{cases} \frac{\sqrt{3}}{2\sqrt{2}} V_{dc}, & \text{Sinusoidal PWM} \\ \frac{1}{\sqrt{2}} V_{dc}, & \text{Space vector PWM.} \end{cases}$$

Note also that $V_T = V_{dc}$ and $I_T = \sqrt{2} I_0$. Therefore,

$$SUF = \begin{cases} \frac{1}{8} = 0.125, & \text{Sinusoidal PWM} \\ \frac{\sqrt{3}}{12} = 0.144, & \text{Space vector PWM.} \end{cases}$$

Note that the SUF for the space vector PWM is higher than that of the sinusoidal PWM, since the former utilizes 3^{rd} order harmonics.

10.2.7 Current Sampling in the PWM Interval

To implement the vector control, it is necessary to sample the current. However, the current changes even in a PWM interval. Therefore, the sampled value must be the average value of the PWM interval. Fig. 10.18 shows a symmetric PWM and an asymmetric PWM with a current sampling point. In case of the symmetric PWM, the center value represents the average value. Therefore, current sampling at the center guarantees an average current in the symmetric PWM. However, the average value is not taken at the center with the asymmetric PWM.

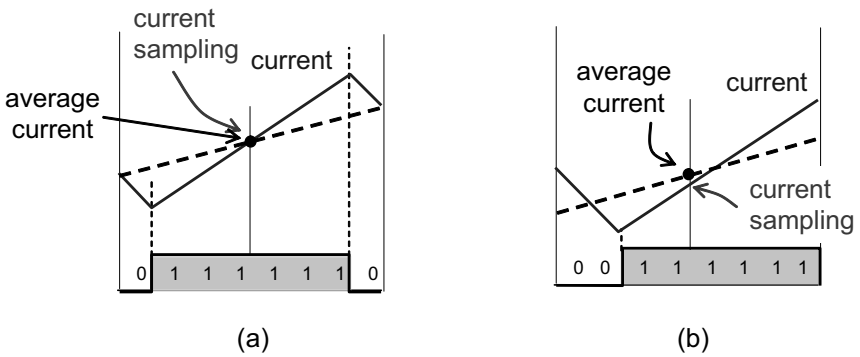

Figure 10.18: Current sampling points and points representing the average value: (a) symmetric PWM and (b) asymmetric PWM.

10.2.8 Dead Time

As shown in Fig. 10.2 (a), the switch conduction current does not fall down to zero immediately after the gating signal becomes low. This is because IGBTs have long tail current and the switching circuit has stray inductance. Therefore, the complementary switch should turn on after the current tail disappears. Otherwise, the shoot-through phenomenon takes place. To prevent such a shoot-through, a dead interval, in which both upper and lower switches are low, should be provided for each signal transition. In case of IGBTs, the dead-time is typically 2μsec. The dead-time is made by putting off all rising edges of gating signals. Fig. 10.19 shows a method of generating the dead-time and the voltage error caused by the dead-time.

In most cases, especially when the load is inductive, the load current continues to flow through an anti-parallel (free wheeling) diode during the dead-time even though the two gating signals are low: Therefore, the pole voltage (inverter terminal voltage) is determined to be either $V_{dc}/2$ or $-V_{dc}/2$ depending on the current direction: If the current flows into the load ($i_{as} > 0$), the load current flows through the anti-parallel diode of low arm. Thus, $-V_{dc}/2$ appears at the terminal during the dead-time, i.e., a negative error voltage is made, as shown in Fig. 10.19 (a). On the other hand, if current flows out from the load ($i_{as} < 0$), the load current flows through the anti-parallel diode of the upper arm. Thus, $V_{dc}/2$ appears at the terminal during the dead-time, i.e., a positive error voltage is made as shown in Fig. 10.19 (b).

When the current level is low, the pole voltage during the dead-time tends to be clamped zero since the pole voltage is not determined definitely. Distorted voltage current waveforms are depicted in Fig. 10.20. It is obvious from Fig. 10.20 that the percentage of distortion is large when the current level is low. The distortion caused by dead-time can be corrected by adding or subtracting the dead-time interval, T_d, depending on the current polarities: To compensate the dead-time error, on-duty of high-side switch is increased by T_d, if $i_a < 0$. Conversely, if $i_a < 0$, then on-duty is

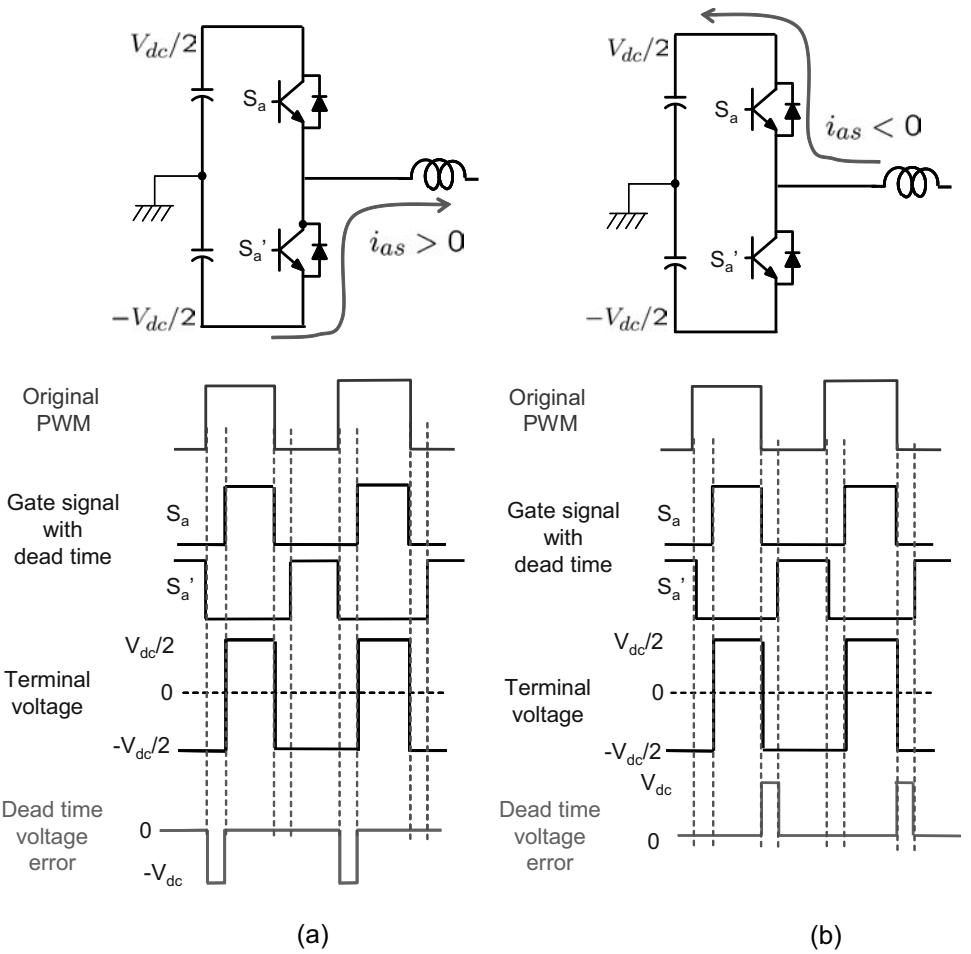

Figure 10.19: Dead-time effects depending on current direction: (a) $i_{as} > 0$ and (b) $i_{as} < 0$.

decreased by T_d:

$$\begin{cases} T_a + T_d, & \text{if } \; i_a > 0, \\ T_a - T_d, & \text{if } \; i_a < 0, \end{cases}$$

where T_a is on-duty of the upper switch before compensation. Fig. 10.21 shows the dead-time compensation method.

Fig. 10.22 shows experimental current waveforms before and after the dead-time correction. It is observed that the dead-time also causes a reduction in the fundamental component of the output voltage, apart from distortion. In an extreme case, the distorted output voltage produces subharmonics, resulting in torque pulsation and instability at low-speed and light-load operation [10], [11]. In the sensorless vector control, the voltage error caused by the dead-time has a significant negative impact on the low-speed performance [12]. Some dead-time compensation schemes are found in [10],[11],[9].

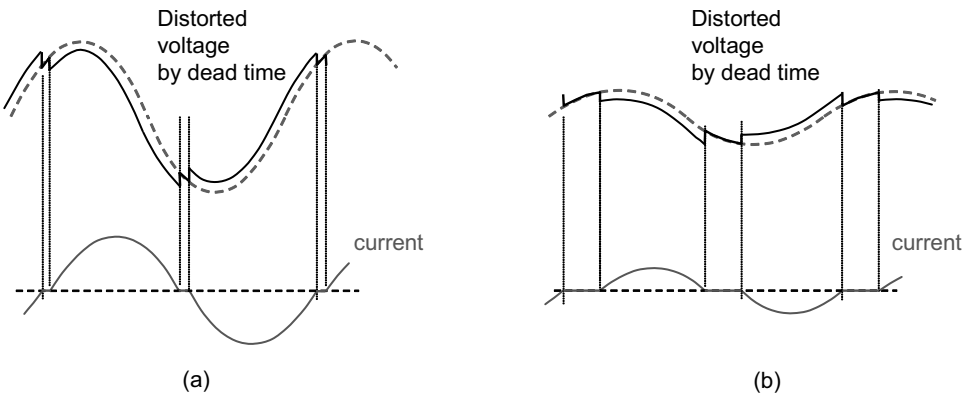

Figure 10.20: Voltage distortion due to the dead-time when the current level is (a) high and (b) low.

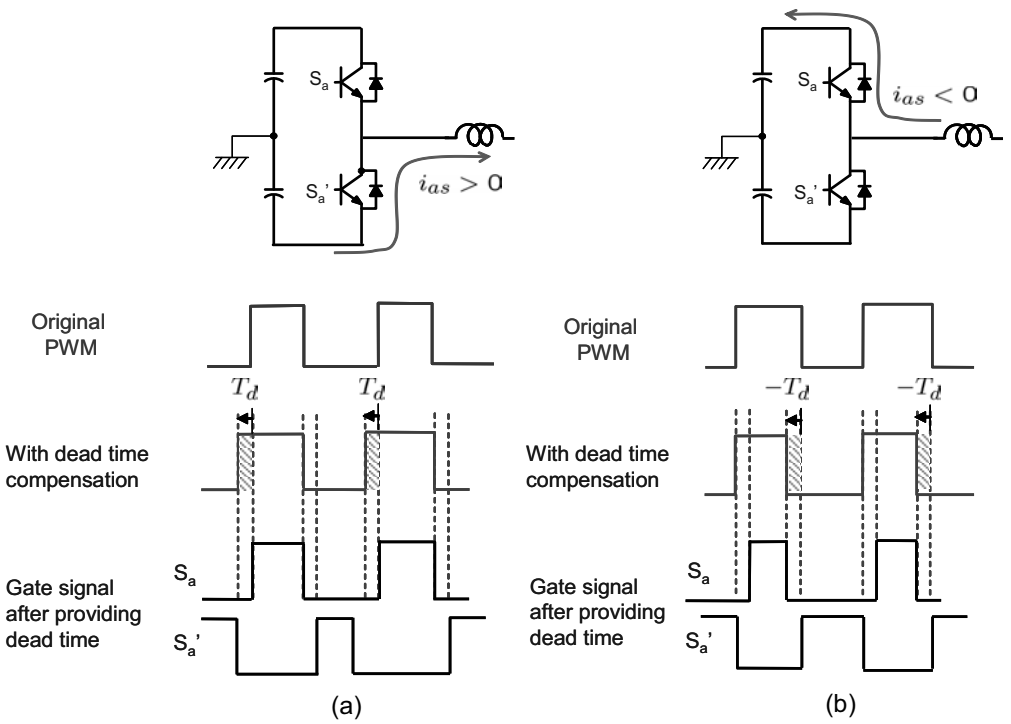

Figure 10.21: Dead-time compensation depending on the current polarities: (a) $i_{as} > 0$ and (b) $i_{as} < 0$.

10.3 Speed/Position and Current Sensors

In order to construct a current controller in the reference frame, the measured current vector should be mapped into the reference frame. Therefore, the rotor angular position and phase currents need to be measured. For position sensing, the absolute

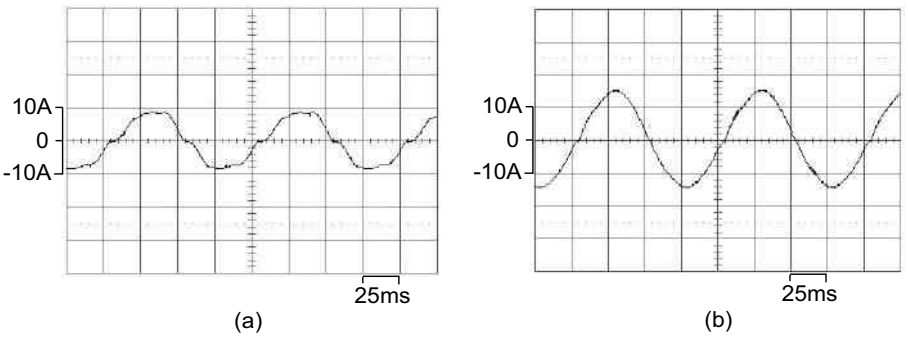

Figure 10.22: Current distortion due to the dead-time: (a) before compensation and (b) after compensation.

encoder or resolver is utilized. Since absolute encoders are normally expensive, incremental encoders are used with some starting methods in some applications. For current sensing, Hall sensors are most popularly used.

10.3.1 Encoder

An incremental rotary encoder generates electrical pulses when the shaft rotates. By counting the pulses, angular position or speed is measured. Fig. 10.23 shows the structure of an encoder consisting of LEDs, photo transistors, and a disk with slits. Normally, the disk is made of glass with the slits created by etching. As the disk rotates, flickering light is monitored at the photo transistors and transformed into electrical pulses. The voltage or current pulses are transmitted outside after being shaped. Incremental encoders output three pairs of signals: A, $\overline{A}$, B, $\overline{B}$, and Z, $\overline{Z}$. The A and B phase signals are 90° out of phase, as shown in Fig. 10.23. The signal states are summarized in Table 10.2. The direction is determined based on which signal comes first after resetting, $(A, B) = (0, 0)$. If the rising edge of B comes first, then the device is determined to rotate in the clockwise (CW) direction. Alternatively if the rising edge of A comes first, then it is determined to rotate in the counterclockwise (CCW) direction.

Table 10.2: State diagram for encoder pulses.

Direction	CW			CCW		
	Phase	A	B	Phase	A	B
	1	0	0	1	1	0
	2	0	1	2	1	1
	3	1	1	3	0	1
	4	1	0	4	0	0

The disk has one slot for Z-phase, so that the Z-phase pulse arises once per

revolution. The Z-phase signal is used for resetting the data with an absolute position.

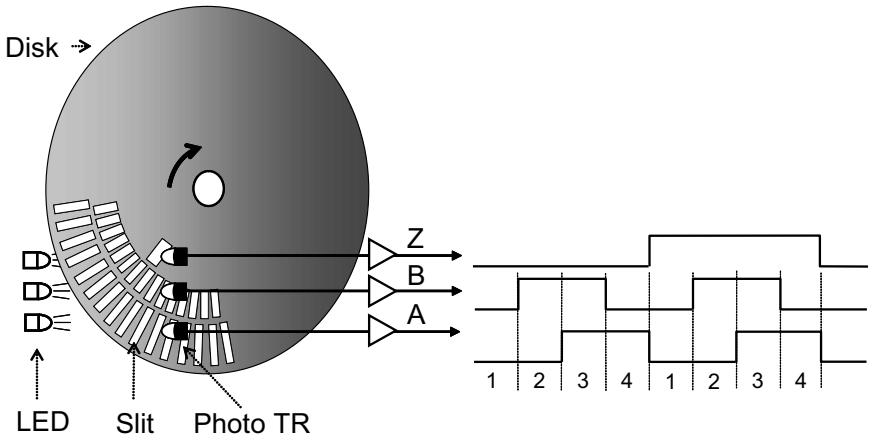

Figure 10.23: Incremental encoder and its signal patterns.

M/T-methods

There are two speed measuring methods: M-method and T-method. With the M-method, the speed is measured by the number of encoder pulses, m_m for a given fixed time interval, T_s. Suppose that an encoder resolution is P_{pr} pulses per revolution (PPR). Then, the number of pulses per second is $\frac{m_m}{T_s}$. Therefore, the shaft speed, N_f, in rpm is calculated as

$$N_f = \frac{60}{T_s}\frac{m_m}{P_{pr}} \text{ (rpm)}.$$

Note however that the encoder pulse-width increases wider and wider as the speed decreases, while T_s is fixed. Finally, m_m will be a fractional number at a low speed. The truncation error of m_m/T_s becomes serious in a low speed. Correspondingly, the M-method error increases as the speed decreases.

The T-method utilizes high frequency reference pulses internally. An encoder pulse period is measured by counting the number of reference pulses captured between the rising edges of encoder pulses. Denote by f_t the frequency of reference pulses and by m_t the number of reference pulses in an encoder period. Then, m_t/f_t is the encoder period, and f_t/m_t is the number of encoder pulses per second. Therefore, the shaft speed, N_f in rpm is calculated as

$$N_f = \frac{60 f_t}{P_{pr} m_t} \text{ (rpm)}.$$

The T-method is more accurate in a low-speed region, but becomes less accurate as the speed increases, m_t being small. Thus, it is not appropriate for high-speed measurements.

Fig. 10.25 compares the measurement errors of the M-method and T-method. An integrated method that combines both M and T methods is called the M/T-method. A synchronous speed measurement method was proposed in [13].

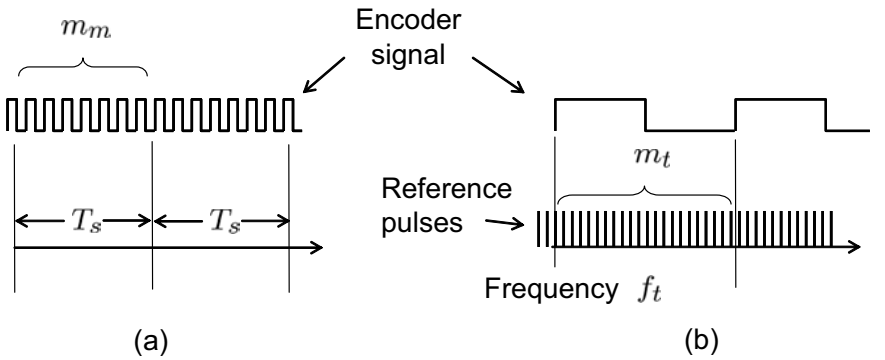

Figure 10.24: Speed measuring methods: (a) M-method and (b) T-method.

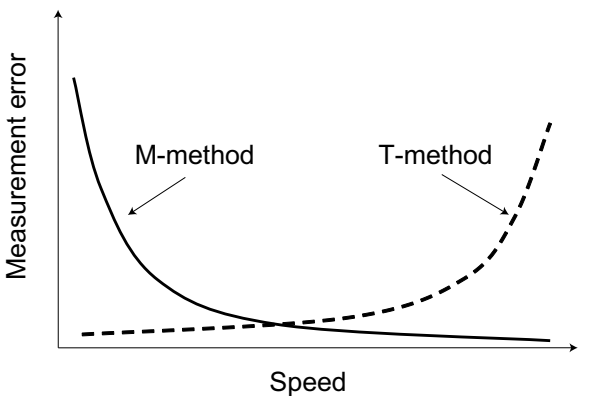

Figure 10.25: Measurement errors versus speed.

10.3.2 Resolver and R/D Converter

Resolver is a type of angular position sensor that yields the absolute position [2]. Basically, it looks like a small synchronous generator. Fig. 10.26 shows a type of resolver having one input coil and two output coils. But, the two stator windings are 90 degrees apart; therefore, the coil currents are independent. It has a rotary transformer on the rotor shaft so that the rotor coil is excited by an external stationary power source ($2 \sim 8$V, $1 \sim 20$kHz). Depending on the rotor position, the coupling coefficients between the rotor and stator windings change. As a result, induced voltage levels of the two stator windings are different.

Specifically, a carrier signal is injected to the rotor winding through the rotary transformer. Then, the induced voltage is modulated by the stator angle as the

rotor rotates. The output voltages are expressed as sine and cosine functions of the rotor angle, θ_r:

$$\begin{aligned} V_d &= V_0 \sin\theta_r \sin\omega_{rs}t \\ V_q &= V_0 \cos\theta_r \sin\omega_{rs}t. \end{aligned}$$

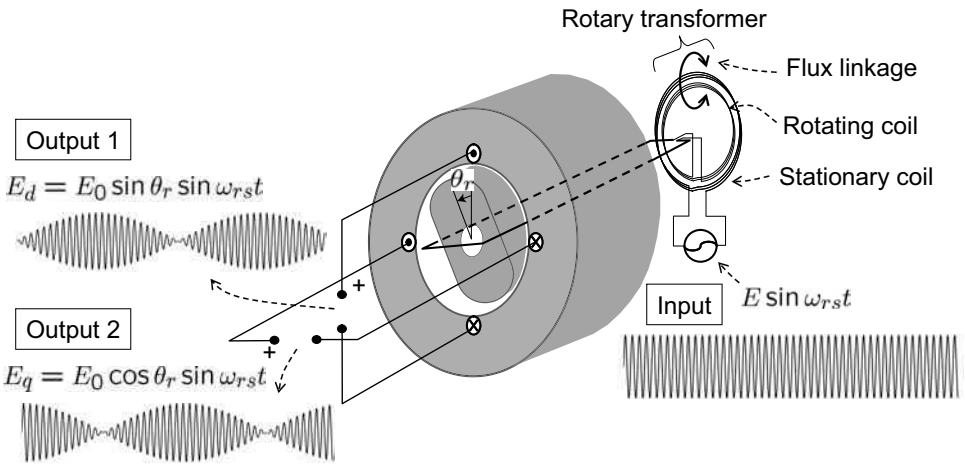

Figure 10.26: Schematic diagram of a 1-input, 2-output resolver.

The rotor angle is measured by processing the output signals. The signal processing module is called the resolver-to-digital converter (RDC). In a RDC, demodulation and PLL circuits are normally employed, as shown in Fig. 10.27. First, V_d and V_q are multiplied by $\cos\varphi$ and $\sin\varphi$, respectively. Note that φ is an internal variable which is desired to track θ_r. Then, we have

$$V_0 \sin\theta_r \cos\varphi \sin\omega_{rs}t - V_0 \cos\theta_r \sin\varphi \sin\omega_{rs}t = V_0 \sin(\theta_r - \varphi)\sin\omega_{rs}t.$$

Second, the carrier signal is eliminated by the synchronous rectification: Multiply the signal by $\sin\omega_{rs}t$ and pass through a low-pass filter:

$$V_0 \sin(\theta_r - \varphi)\sin^2\omega_{rs}t = V_0 \sin(\theta_r - \varphi)\frac{1 - \cos 2\omega_{rs}t}{2} \quad \overset{\text{LPF}}{\Rightarrow} \quad \frac{V_0}{2}\sin(\theta_r - \varphi).$$

As shown in Fig. 10.27 (a), the PI controller is required for the tracking performance of the loop. The voltage-to-frequency (V/F) converter generates pulses in proportion to the input voltage level. Thus, a pulse counter yields digital values. Note that the V/F converter along with the pulse counter functions as an integrator. Note also that $\sin(\theta_r - \varphi) \approx \theta_r - \varphi$ if φ is close to θ_r. Then, the RDC makes a closed-loop with the resolver, as shown in Fig. 10.27 (b). Note further that φ converges to θ_r due to the tracking ability of the PI controller.

Since the resolvers provide absolute angle, it is suitable in the PMSM control. Another advantage is that resolvers are more robust mechanically than encoders, since they do not use a fragile piece such as a glass disk.

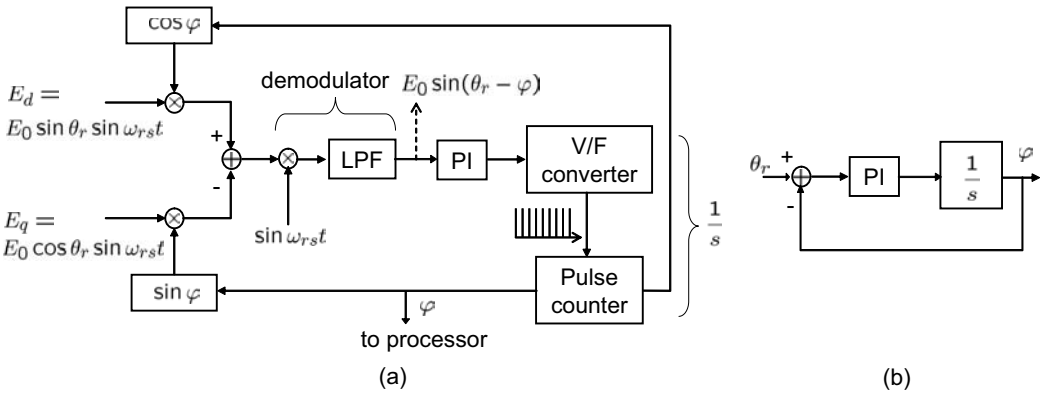

Figure 10.27: RDC block diagram: (a) functional blocks and (b) simplified equivalent block diagram.

10.3.3 Current Sensors

When the current flows through a semiconductor piece that is laid in a magnetic field, the carriers (holes and electrons) experience a force in an orthogonal direction. That force makes a carrier concentration gradient, so that a voltage appears across the device width. The voltage is proportional to the magnet field, and this effect is called the Hall-effect. Hall sensors are most widely used for current measurements, since they provide natural isolation between the measured line and the sensing circuit.

Fig. 10.28 shows two types of current sensors. The voltage type directly utilizes the Hall-sensor voltage, v_h as a measured current. But, the core material shows nonlinear characteristics as the B field increases. Further, this method contains an offset error due to the hysteresis loop. Thus, the voltage type current sensors have a relatively large error (typically $\pm 1\%$).

The current type Hall-current sensor employs an extra winding and a current servo amplifier. The Hall sensor is used for detecting the air gap flux. If the gap field is not equal to zero, then the servo amplifier forces current, i_{sv}, to flow in the opposite direction until the air gap field is nullified. Since the closed-loop is formed with a PI controller, the air gap field remains zero. In this case, i_{sv} is proportional to I. Here, resistor, r_{sv}, is inserted to measure i_{sv}. That is, I is detected by measuring $v_{sv} = r_{sv} i_{sv}$. Since the current type sensor maintains the core field equal to zero, it is less affected by the material properties of the core. Therefore, it yields more accurate measurements (0.1% offset error).

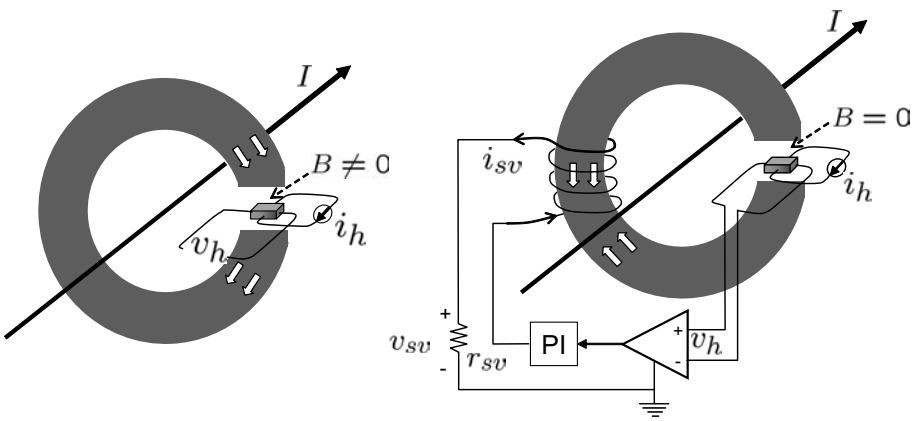

Figure 10.28: Hall-effect current sensors: (a) voltage type and (b) current type.

Bibliography

[1] N. Mohan, T. M. Undeland, and W.P. Robbins, Power Electronics, Converters, Applications, and Design, John Wiley & Sons. Inc., 1995.

[2] C.W de Silva, Sensors and Actuators : Control Systems Intrumentation, CRC Press, 2007.

[3] J. Holtz, W. Lotzkat, and A. Khambadkone, On continuous control of PWM inverters in the overmodulation range including the six-step mode, *IEEE Conf. Ind. Electron.*, pp. 307 – 312, 1992.

[4] J. Holtz, Pulsewidth modulation. a survey, *IEEE Trans. Ind. Electron.*, Vol. 39, No. 5, pp. 410 – 420, Dec. 1992.

[5] J. Holtz, Pulsewidth modulation for electronic power conversion, *Proc. IEEE*, Vol. 82, No. 8, pp. 1194 – 1214, Aug. 1994.

[6] D. G. Holmes and T. A. Lipo, *Pulse Width Modulation for Power Converters: Principles and Practice*, Hoboken, NJ: Wiley, 2003.

[7] A. M. Hava, R. J. Kerkman, and T. A. Lipo, Carrier-based PWM-VSI overmodulation strategies: Analysis, comparison, and design, *IEEE Trans. Power Electron.*, Vol. 13, no. 4. pp. 674 – 689, July 1998.

[8] G. Narayanan and V. T. Ranganathan, Extension of operation of space vector PWM strategies with low switching frequencies using different overmodulation algorithms, *IEEE Trans. Power Electron.*, Vol. 17, No. 5, Sep. 2002.

[9] N. Hur, K. Nam, and S. Won, A two degrees of freedom current control scheme for dead-time compensation, *IEEE Trans. Ind. Electron.*, Vol. 47, pp. 557 – 564, June 2000.

[10] R. C. Dodson, P. D. Evans, H. T. Yazdi, and S. C. Harley, Compensating for dead-time degradation of PWM inverter waveforms, *IEE Proc. B, Electr. Power Appl.*, Vol. 137, No. 2, pp. 73 – 81, Mar. 1990.

[11] D. Leggate and R. J. Kerkman, Pulse-based dead-time compensator for PWM voltage inverters, *IEEE Trans. Ind. Electron.*, Vol. 44, pp. 191 – 197, Apr. 1997.

[12] J. Lee, T. Takeshita, and N. Matsui, Optimized stator-flux-oriented sensorless drives of IM in low speed performance, *in Conf. Rec. IEEE IAS Annu. Meeting*, 1996, pp. 250 – 256.

[13] T. Tsuji, T. Hashimoto, H. Kobayashi, M. Mizuochi, and K Ohnishi, A wide-range velocity measurement method for motion control, *IEEE Trans. on Ind. Electron.*, 56, 510 – 519, 2009.

Problems

10.1 Calculate $v_{as[5]}/v_{as[1]}$ and $v_{as[7]}/v_{as[1]}$ for six-step inverter operation.

10.2 Suppose that the DC link voltage is $V_{dc} = 300$V and that the switching frequency is 8kHz. Calculate T_1 and T_2 in the symmetric PWM to synthesis a voltage vector, $100\angle 30°$V.

10.3 Determine the sector where the voltage vector $(v_d^s,\, v_q^s) = (-100\text{V}, -77\text{V})$ belongs according to the sector-finding algorithm.

10.4 It is desired to synthesize 10V and 100V using an inverter whose DC link is 300V. Assume that the PWM frequency is 8kHz and that current polarity is positive. If the dead-time is 2μs, calculate the relative voltage errors, $\Delta V/V$ for both cases.

10.5 Consider a 1000 pulse/rev encoder. Calculate the maximum speed error $(\Delta N_f/N_f)$ when the M-method is utilized with 100Hz sampling ($T_s = 20$ ms) for $N_f = 10$ and 100 rpm.

10.6 Consider a 2 input, 1 output resolver shown in Fig. 10.29. Determine the output function.

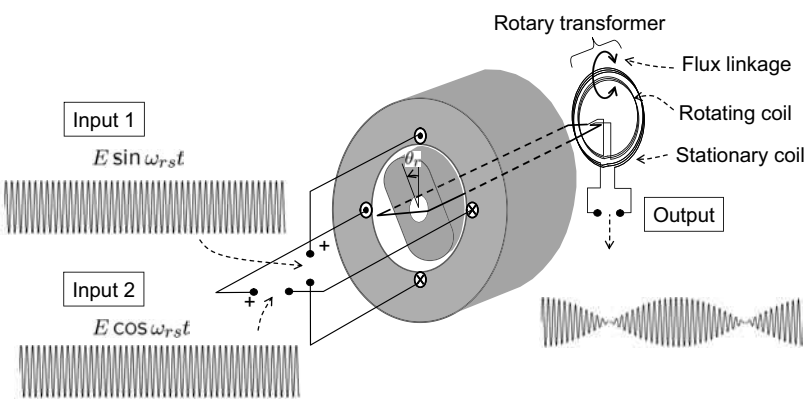

Figure 10.29: A 2-input, 1-output resolver (Problem 10.6).

Chapter 11

Vehicle Dynamics

Since the land vehicles are designed to move primarily in one direction, only single dimensional lateral dynamics are considered. There are five lateral force components: inertial force, longitudinal traction force, air drag, tire rolling resistance, and gravity when the vehicle is moving up or down a hill.

11.1 Longitudinal Vehicle Dynamics

Fig. 11.1 shows the lateral force components for a vehicle moving on an inclined road. Air drag, F_{aero}, rolling resistance, F_{roll}, and gravity constitute the road load. Traction force, F_x, is provided via the slip between tire and road, and the engine or electric motor is the real power source for the slip generation. The difference between the sum of road loads and the traction force is used for acceleration or deceleration:

$$m_v \frac{d}{dt} V_x = F_x - F_{aero} - F_{roll} - m_v g \sin\alpha \tag{11.1}$$

where V_x is the vehicle velocity along the longitudinal x-direction, m_v is the vehicle mass including passenger loads, g is the acceleration of gravity, and α is the incline angle of the road.

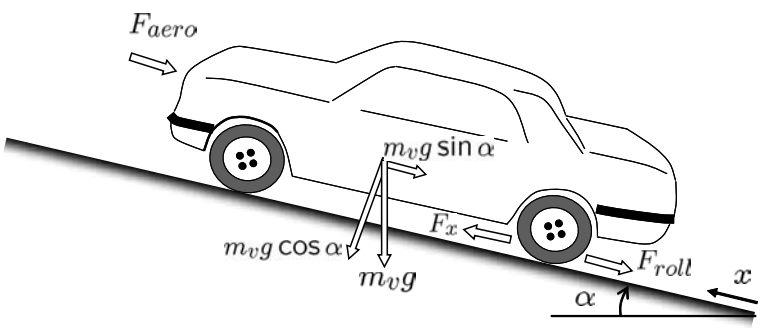

Figure 11.1: Lateral force components of a vehicle.

11.1.1 Aerodynamic Drag Force

When a headwind blows at a speed of V_{wind} to a moving vehicle, the aerodynamic drag force exerted on a vehicle is calculated as

$$F_{aero} = \frac{\rho C_d A_F}{2}(V_x + V_{wind})^2 \tag{11.2}$$

where ρ is the mass density of air, C_d is the aerodynamic drag coefficient, and A_F is the equivalent frontal area of the vehicle. The mass density of air is equal to $\rho = 1.225\text{kg/m}^3$ at the commonly used standard set of conditions (15°C and a 101.32 kPa). The frontal area A_F is in the range of $79 - 84\%$ of the area calculated from the vehicle width and height for passenger cars [5]. The aerodynamic drag coefficient is typically in the range $0.2 < C_d < 0.4$: $C_d \approx 0.3$ for common passenger cars and $C_d \approx 0.4$ for common sports utility vehicles.

To investigate the aerodynamic effect separately, we assume in the following that a vehicle is traveling a horizontal road when the headwind is equal to zero. Neglecting the rolling resistance, (11.1) reduces to

$$m_v \frac{dV_x}{dt} = -\frac{\rho A_F C_d}{2} V_x^2 + F_x. \tag{11.3}$$

Let $K_1 = \sqrt{\frac{\rho A_F C_d}{2m_v}}$ and $K_2 = \sqrt{\frac{F_x}{m_v}}$. Then it follows from (11.3) that

$$\frac{dV_x}{dt} = -K_1^2 V_x^2 + K_2^2.$$

Separating variables, we obtain

$$\frac{dV_x}{V_x - K_2/K_1} - \frac{dV_x}{V_x + K_2/K_1} = -2K_1 K_2 dt.$$

Thus, integrating over $[0,\ t)$, it follows that

$$\ln \frac{|V_x - K_2/K_1|}{|V_x + K_2/K_1|} = -2K_1 K_2 t.$$

Note however $V_x < K_2/K_1$. Thus, we have

$$-V_x + K_2/K_1 = (V_x + K_2/K_1)e^{-2K_1 K_2 t}.$$

Therefore, the velocity is given as [3]

$$V_x(t) = \frac{K_2}{K_1}\frac{e^{K_1 K_2 t} - e^{-K_1 K_2 t}}{e^{K_1 K_2 t} + e^{-K_1 K_2 t}} = \frac{K_2}{K_1}\tanh\left(K_1 K_2 t\right). \tag{11.4}$$

Since tanh is a monotonically increasing function, the maximum velocity is obtained as

$$\max\ V_x(t) = \lim_{t\to\infty} \frac{K_2}{K_1}\tanh\left(K_1 K_2 t\right) = \frac{K_2}{K_1} = \sqrt{\frac{2F_x}{\rho A_F C_d}}. \tag{11.5}$$

This is a velocity limit caused by the aerodynamic drag force. That is, the maximum velocity is determined mostly by the thrust and aerodynamic coefficients.

Exercise 11.1
Consider a vehicle with parameters: $m_v = 1000\text{kg}$, $A_F = 2.5\text{m}^2$, $\rho = 1.225\text{kg/m}^3$, and $C_d = 0.3$. Assume that the traction force is equal to $2kN$. Considering only the aerodynamic resistance, calculate the maximum velocity. Repeat the calculation when $A_F = 1.5\text{m}^2$.

Solution

$K_1 = \sqrt{\rho A_F C_d/(2m_v)} = 0.0214$ and $K_2 = 1.414$. The maximum velocity is equal to $66.07\text{m/s} = 238\text{km/h}$. When $A_F = 1.5\text{m}^2$, the maximum velocity is 307km/h. ■

11.1.2 Rolling Resistance

As the tire rotates, a part of the tire is continuously depressed at the bottom, and then released back to its original shape after it leaves the contact region. Fig. 11.2 shows a tire depression. These depressing and releasing processes are not totally elastic. That is, due to the damping action, energy is consumed during the deforming and recovering processes. Such a loss of energy in the tire is reflected as a rolling resistance that opposes the motion of the vehicle.

Obviously, the amount of deformation depends on the vehicle's weight. Typically, the rolling resistance is modeled to be proportional to the normal force, F_z, on the tire, i.e., the sum of rolling resistance is

$$F_{roll} = f_r F_z = f_r m_v g \cos\alpha, \tag{11.6}$$

where f_r is the rolling resistance coefficient. Typical values for radial tires are in the range of $0.009 \sim 0.015$. The rolling resistance is affected by the vehicle speed, but the contribution of the speed dependent term is very small, so that it is neglected [1]. If the weight distribution between the front and rear wheels is not even, the rolling resistances should be calculated separately.

Exercise 11.2
Suppose that the weight distribution of front and rear wheels is 6:4, and the vehicle mass is 1200kg. Find the rolling resistance force, when $f_r = 0.015$. Assume that the vehicle is running at the speed of 80km/h, while the traction power is equal to $P_x = 30\text{kW}$. Find the percentage of the rolling resistance out of the total traction force.

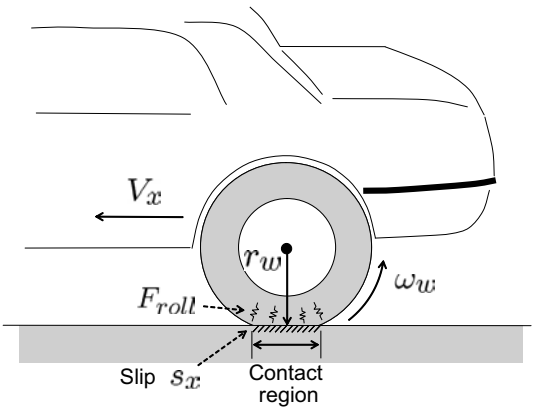

Figure 11.2: Rolling resistance and slip.

Solution

$$\begin{aligned} \text{Front wheels} \quad &: \quad F_{roll} \quad = \quad 0.015 \times 1200 \times 0.6 \times 9.8 = 105.8(\text{N}), \\ \text{Rear wheels} \quad &: \quad F_{roll} \quad = \quad 0.015 \times 1200 \times 0.4 \times 9.8 = 70.6(\text{N}). \end{aligned}$$

The total tire traction force is equal to $F_x = P_x/V_x = 30000/(80000/3600) = 1350$N. Thus, the percentage of the rolling resistance is equal to $(105.8+70.6)/1350 \times 100 = 13\%$. ■

11.1.3 Longitudinal Traction Force

The longitudinal traction force F_x is based on a friction that is proportional to the slip between the tire and road surfaces. The slip speed is defined as the difference between the circumferential speed of the tire, $r_w\omega_w$ and vehicle velocity, V_x, where r_w is the wheel dynamic rolling radius and ω_w is angular speed of wheel. The normalized slip is defined as [2]

$$s_x \quad = \quad \frac{r_w\omega_w - V_x}{r_w\omega_w}. \tag{11.7}$$

Experimental results have shown that the longitudinal traction force increases in proportion to the slip in the low slip range. The force grows almost linearly with the slip, but decays after a certain slip. Fig. 11.3 shows a typical longitudinal friction coefficient versus slip and it is modeled with a nonlinear function, $\mu(\cdot)$, as

$$F_x = \mu(s_x)F_{z(dr)}, \tag{11.8}$$

where $F_{z(dr)}$ is the normal force on the driven axle. However, it depends on the road and tire conditions. On dry concrete or asphalt, the traction force increases

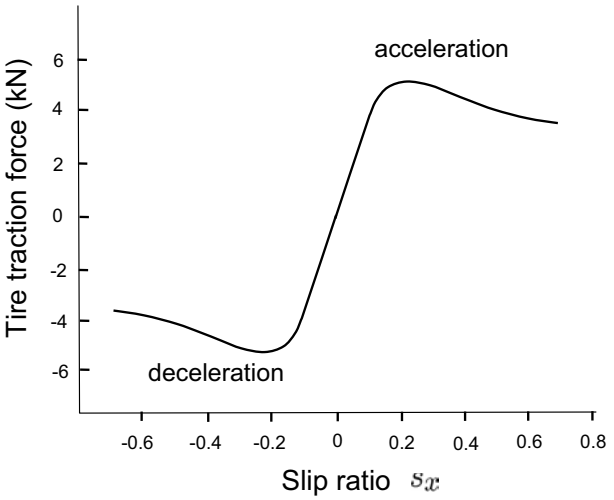

Figure 11.3: Longitudinal traction force as a function of wheel slip.

until the slip reaches 20% [1]. Fig. 11.3 also indicates that slip always takes place whenever the traction force is generated. In the linear region, the traction force is modeled as

$$F_x = \mu_{s0} s_x m_v g \cos\alpha. \tag{11.9}$$

where μ_{s0} is the longitudinal friction coefficient.

Exercise 11.3
Assume that a vehicle of $m_v = 1200$kg is on the horizontal plane. According to the curve shown in Fig. 11.3, the traction force is equal to 4kN at $s_x = 0.1$. Determine μ_{s0}.

Solution

$$\mu_{s0} = \frac{4000}{0.1 \times 1200 \times 9.8} = 3.4.$$

■

11.1.4 Grade

The grade is defined as a percentage, i.e., $\%\,\text{grade} = \frac{\Delta h}{d} \times 100$, where d and Δh are horizontal and vertical lengths of a slope, respectively. Then the grade angle, α is equal to

$$\alpha = \arctan \frac{\%\text{grade}}{100}. \tag{11.10}$$

Typical grade specifications are 7.2% for normal driving and 33% for vehicle launch [1].

Exercise 11.4
Assume that a vehicle of mass 2000kg is moving on a uphill of grade 20%. Calculate the force due to gravity.

Solution
Note that $\alpha = \arctan(20/100) = 11.3°$. Thus, $mg\sin\alpha = 2000 \times 9.8 \times \sin 11.3° = 3841$ N. ■

11.2 Acceleration Performance and Vehicle Power

Vehicle dynamics (11.1) is rewritten as [1]-[4]

$$\frac{dV_x}{dt} = \frac{1}{m_v}\left(F_x - \frac{\rho C_d A_F}{2}V_x^2 - f_r m_v g\cos\alpha - m_v g\sin\alpha\right). \tag{11.11}$$

The difference of tractive force, F_x, from the sum of road loads (gravity, rolling, and aerodynamic resistances) is used for accelerating the vehicle.

Acceleration is an important feature in the vehicle performance evaluation. Most passenger cars have 4∼ 12 second acceleration time from zero to 100km/h. Consider, for example, a car having 10 seconds acceleration time for 0-100km/h. Then, an average acceleration is $0.28g$. Fig. 11.4 shows the inertial force components for $0.28g$ acceleration. Note that the inertial force takes the largest percentage (see Fig. 11.4(a)). The next largest component is the gravity when the grade is 7.5%. The aerodynamic force becomes noticeable when the vehicle speed exceeds 100km/h.

Exercise 11.5
Consider a vehicle with parameters: $m_v = 1500$kg, $A_F = 2\text{m}^2$, $\rho = 1.225\text{kg/m}^3$, $C_d = 0.3$, and $f_r = 0.01$. Suppose that the maximum acceleration is $0.28g$.
a) Calculate the lateral force components; $\frac{\rho}{2}C_d A_F V_x^2$, $m_v\frac{dV_x}{dt}$, $f_r m_v g\cos\alpha$, and $m_v g\sin\alpha$, when the grade is 7.5%.
b) Repeat the same calculation when the vehicle runs at constant speeds when the grade is 20%.

Solution
Fig. 11.4 shows the magnitudes of aerodynamic, gravity, tire rolling, and inertial forces. ■

As indicated by (11.8), the vehicle thrust is generated via the slip between the driving wheels and the load. Note however that the wheel slip is a function of the vehicle speed, V_x, Therefore, the traction force cannot be determined, unless vehicle speed is known, i.e., the complete vehicle dynamics are described by a closed-loop:

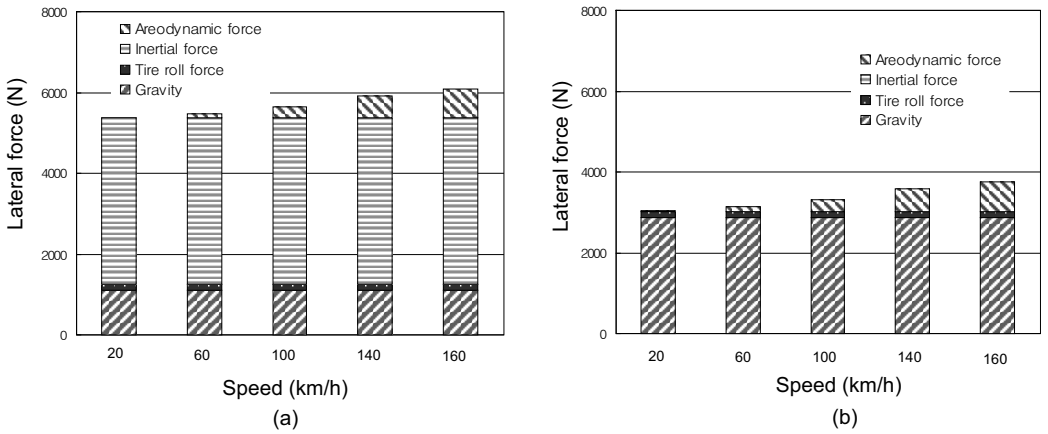

Figure 11.4: Lateral force components versus speeds: (a) acceleration=$0.28g$ and grade=7.5% and (b) zero inertial force with grade=20% (Exercise 11.5).

Substituting (11.9) for F_x, we obtain from (11.11) that

$$\frac{dV_x}{dt} = \frac{1}{m_v}\left(\mu_{s0}\frac{r_w\omega_w - V_x}{r_w\omega_w}m_v g\cos\alpha - \frac{\rho C_d A_F}{2}V_x^2 - f_r m_v g\cos\alpha - m_v g\sin\alpha\right). \tag{11.12}$$

Exercise 11.6 [6]
Simplified longitudinal vehicle dynamics are:

$$J_w\dot{\omega}_w = T_w - r_w F_x \tag{11.13}$$
$$m_v\dot{V}_x = F_x - F_{rl} \tag{11.14}$$
$$F_x = m_v g \times \mu_{s0}\frac{r_w\omega_w - V_x}{r_w\omega_w}, \tag{11.15}$$

where J_w is the wheel inertia, T_w is the wheel shaft torque, and F_{rl} is the road load representing the sum of the rolling resistance, gradient, and aerodynamic drag forces. Draw a block diagram for the longitudinal dynamics based on (11.13)−(11.15) regarding F_{rl} as an external disturbance.

11.2.1 Final Drive

Consider an EV drive-line model, shown in Fig. 11.5. Denote by g_{dr} the whole gear ratio from motor shaft to wheel axle. Also, we denote by η_{dr} the drive-line efficiency, i.e., the efficiency of the gear train between the motor and the axle.

Note that

$$V_x = r_w\omega_w(1 - s_x) = r_w\left(\frac{\omega_r}{g_{dr}}\right)(1 - s_x), \tag{11.16}$$

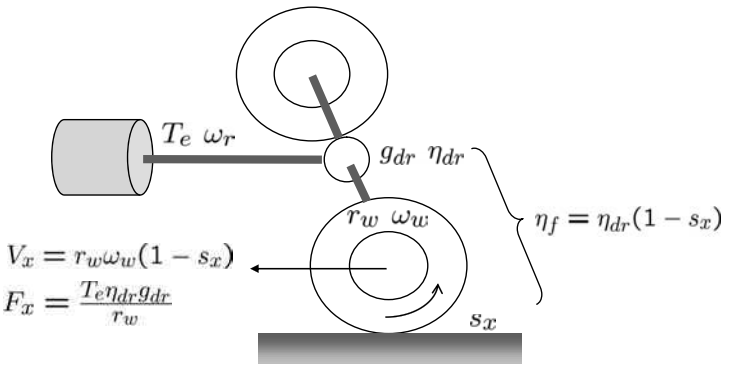

Figure 11.5: EV drive-line model.

where r_w is the effective radius of the driving wheels. Therefore, the vehicle traction power is equal to

$$\begin{aligned} P_x = T_w \frac{V_x}{r_w} &= T_w \left(\frac{\omega_r}{g_{dr}}\right)(1 - s_x) \\ &= T_e\omega_r\eta_{dr}(1 - s_x), \end{aligned} \tag{11.17}$$

where T_w is the torque of the wheel axle. In the second equality of (11.17), the loss in the drive-line is reflected by multiplying η_{dr}, i.e., the motor shaft torque is reduced such that $T_e\eta_{dr} = \frac{T_w}{g_{dr}}$.

We also denote by η_f the whole efficiency from motor shaft power, P_e, to vehicle traction power. Since $P_e = T_e\omega_r$, it follows from (11.17) that

$$\eta_f \equiv \frac{P_x}{P_e} = \eta_{dr}(1 - s_x). \tag{11.18}$$

Thus, the whole efficiency is comprised of the drive-line efficiency and the efficiency in the force conversion between the wheel surface and the road. Note that there is a significant loss mechanism associated with the wheel sleep. Specifically, the power loss caused by the slip is equal to $P_e\eta_{dr}s_x$ or $F_xV_x\frac{s_x}{1-s_x}$. The Sankey diagram for the motor power is depicted in Fig. 11.6.

11.2.2 Speed Calculation with a Torque Profile

The maximum torque curve of a motor is divided into two segments: constant torque and constant power regions. The two regions are separated by the base speed, ω_b, as shown in Fig. 11.7. Therefore, different values of the tractive effort should be used for the maximum acceleration.

Utilizing (11.17) and (11.18), it follows that

$$F_x = \frac{P_x}{V_x} = \frac{T_e\eta_{dr}\omega_r(1 - s_x)}{r_w\omega_w(1 - s_x)} = \frac{T_e\eta_{dr}g_{dr}}{r_w}. \tag{11.19}$$

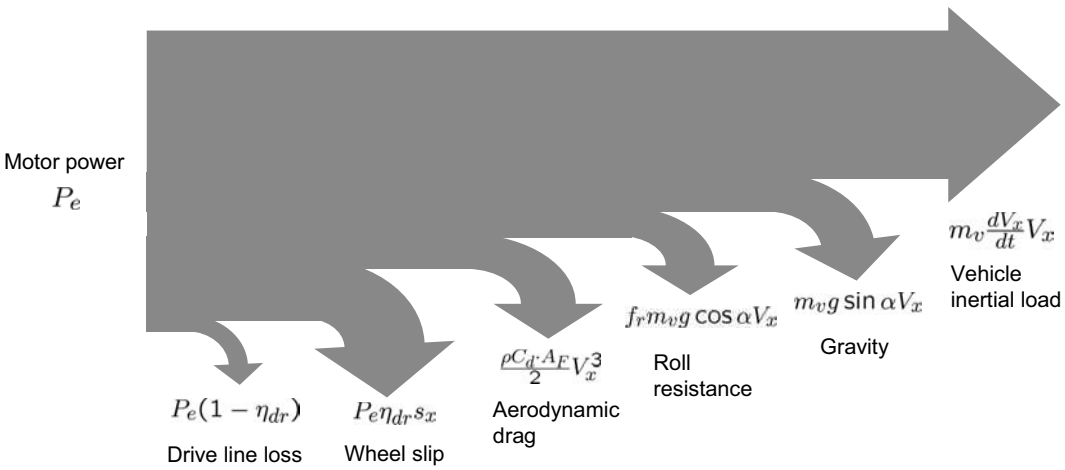

Figure 11.6: Sankey diagram for the EV motor power.

Using the base speed, ω_b, of the traction motor as a pivot value, the maximum tractive effort of EV is set as

$$F_x = \begin{cases} \frac{T_e g_{dr}\eta_{dr}}{r_w}, & \omega_r \le \omega_b \\ \frac{P_e\eta_f}{V_x}, & \omega_r > \omega_b. \end{cases}$$

Then, the governing equations for the maximum acceleration are

$$\frac{dV_x}{dt} = \frac{1}{m_v}\left(\frac{T_e g_{dr}\eta_{dr}}{r_w} - f_r m_v g - \frac{\rho C_d A_F}{2}V_x^2\right) \quad \text{for constant torque region.} \tag{11.20}$$

$$\frac{dV_x}{dt} = \frac{1}{m_v}\left(\frac{P_e\eta_f}{V_x} - f_r m_v g - \frac{\rho C_d A_F}{2}V_x^2\right) \quad \text{for constant power region.} \tag{11.21}$$

Exercise 11.7
Consider an EV with the parameter listed in Table 11.1.

a) Assume that $g_{dr} = 4.1$ and $\eta_{dr} = 0.95$. Calculate the maximum tractive effort. Draw the tractive effort versus speed for 50kW constant power.

b) Assume that the vehicle mass with a load is 1500kg. Compute road loads according to

$$F_{rl} = \frac{\rho C_d A_F}{2}V_x^2 + f_r m_v g\cos\alpha + m_v g\sin\alpha$$

when the grades are 0, 10, 20, 30, and 35%. Draw the load lines versus speed.

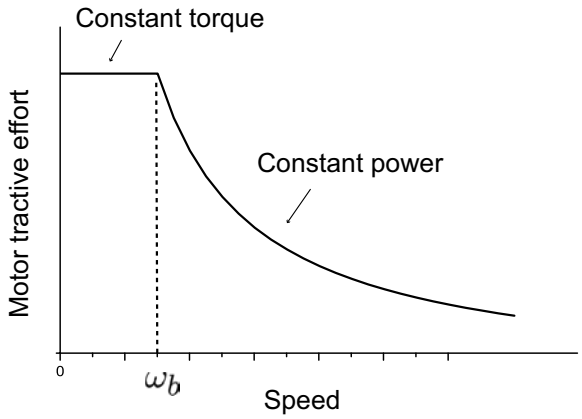

Figure 11.7: An EV motor tractive effort.

Table 11.1: Example EV parameters

Vehicle		Motor	
Curb weight	1313kg	Max. torque	400Nm
Drag Coeff., C_d	0.3	Base speed	1200rpm
Frontal area, A_F	1.746m^2	Max. speed	6400rpm
Rolling resistance, f_r	0.009	Max. power	50kW
Dynamic tire radius, r_w	0.29m		

Solution

$$F_x = \frac{T_e g_{dr} \eta_{dr}}{r_w} = \frac{400 \times 4.1 \times 0.95}{0.29} = 5372\text{N}.$$

The vehicle speed corresponding to the motor base speed (with zero slip) is

$$\frac{1200}{60} \times 2\pi \times \frac{1}{4.1} \times 0.29 \times \frac{3600}{1000} = 32\text{km/h}.$$

Calculation results are shown in Fig. 11.8. ■

Exercise 11.8
Consider an EV with parameters: $m_v = 1598$kg, $A_F = 2$m^2, $\rho = 1.225$kg/m^3, $C_d = 0.3$, $f_r = 0.015$, $r_w = 0.284$m, $g_{dr} = 9$, $\eta_{dr} = 0.9$, $\eta_f = 0.8$, and $\alpha = 0$. The motor has the constant maximum motor torque of 270 Nm under a base speed. Assume that the vehicle speed corresponding to the motor base speed is $V_{xb} = 30$ km/h.

a) Calculate the time elapsed before the vehicle speed reaches 30km/h. Neglect the aerodynamic force, since it is small in a low speed range.

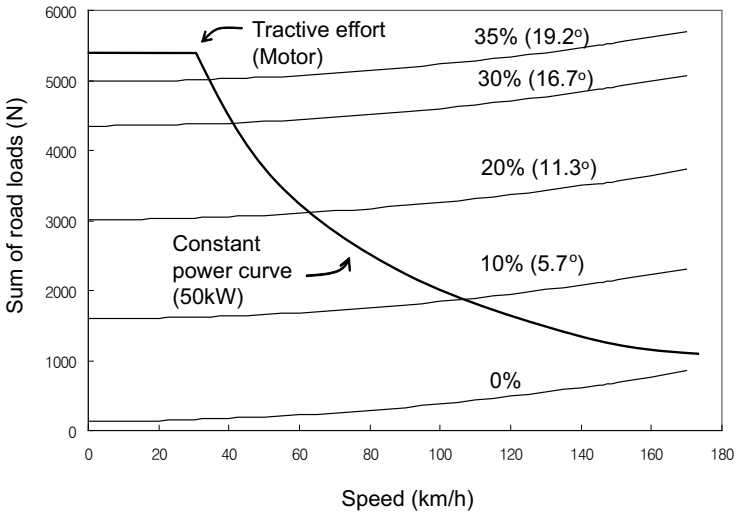

Figure 11.8: Motor tractive force and sum of lateral road loads of an EV listed in Table 11.1. (Exercise 11.7).

b) Calculate the maximum motor power at the time vehicle speed reaches V_x = 30km/h.

c) Compute the acceleration performance utilizing Rounge−Kutta 4th method based on (11.20) and (11.21).

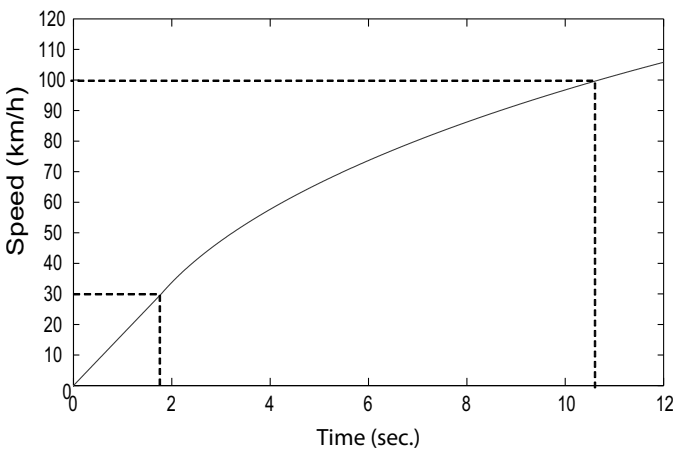

Figure 11.9: Acceleration performance (Exercise 11.8).

Solution.
a) Neglecting the aerodynamic force, we have

$$\frac{dV_x}{dt} = \frac{1}{1598}\left(\frac{270 \times 9 \times 0.9}{0.284} - 0.015 \times 1598 \times 9.8\right) = 4.67\text{m/s}^2.$$

Therefore, the elapsed time for $V_x = 30$km/h is equal to

$$\frac{30 \times 1000}{3600} \times \frac{1}{4.67} = 1.78\text{s}.$$

b) The motor power is equal to

$$P_e = T_e \frac{\eta_{dr} g_{dr}}{\eta_f} \frac{V_x}{r_w} = 270 \times \frac{9 \times 0.95}{0.8} \times \frac{30000}{3600 \times 0.284} = 80.2\text{kW}.$$

c) Fig. 11.9 shows a simulation result based on (11.20) and (11.21) according to the maximum torque and constant power curves shown in Fig. 11.7. Note that 0-100km/h acceleration time is 10.7 s. The simulation result shows that the acceleration time up to 30km/h is 1.8 s, which is quite close to the approximate solution (1.78 s) obtained in a). ■

Exercise 11.9
Consider an EV with $m_v = 1500$kg and $f_r = 0.015$. Assume that the drive-line efficiency is $\eta_f = 0.82$. Neglecting the aerodynamic force, calculate the road load, F_x when the road grade is 7.5%. Calculate the required motor power to maintain a vehicle speed at 36km/h.

Solution.
Note that $\alpha = \tan^{-1}(0.075) = 4.3°$. The required force at steady-state is equal to

$$\begin{aligned} F_x &= f_r m_v g \cos\alpha + m_v g \sin\alpha \\ &= 0.015 \times 1500 \times 9.8 \times \cos 4.3° + 1500 \times 9.8 \times \sin 4.3° = 1319.5\text{N}. \end{aligned}$$

Thus,

$$P_e = F_x V_x \times \frac{1}{\eta_f} = 1319.5 \times \frac{36000}{3600} \times \frac{1}{0.82} = 16091\text{W}.$$

■

11.3 Driving Cycle

A driving cycle is a standardized driving pattern developed to test the efficiency of vehicle engines or drive trains. The pattern is a velocity-time table which represents

urban stop and go driving or relatively smooth highway cycles. The US Environmental Protection Agency (EPA) developed the Federal Test Procedure (FTP75) to assess the performance of vehicles, such as fuel consumption and polluting emissions. The urban portion of the FTP75 is taken as the urban dynamometer driving schedule (UDDS). The UDDS, often called LA-4 or FTP72 cycle, has high percentage of stop time and acceleration/deceleration, and the maximum speed is less than 30km/h. A hybrid power-train may demonstrate a noticeable gain in fuel economy with the UDDS.

NYCC is the most representative of urban driving that includes signals and congestion, with an average speed of only 11.4 km/h. US 06 cycle is an EPA highway cycle representing a high-speed traffic flow. The average speed is 77.2 km/h, but the maximum acceleration is 3.8m/s^2. New European driving cycle (NEDC) consists of four repeated ECE-15 driving cycles and an Extra-Urban driving cycle. But, the maximum velocity is lower than the real vehicles speed on European trunk road. Fig. 11.10 shows the speed plots of EPA UDDS, US06 Hwy, and NEDC, whose average speeds are 34, 77.2, and 32.2 km/h.

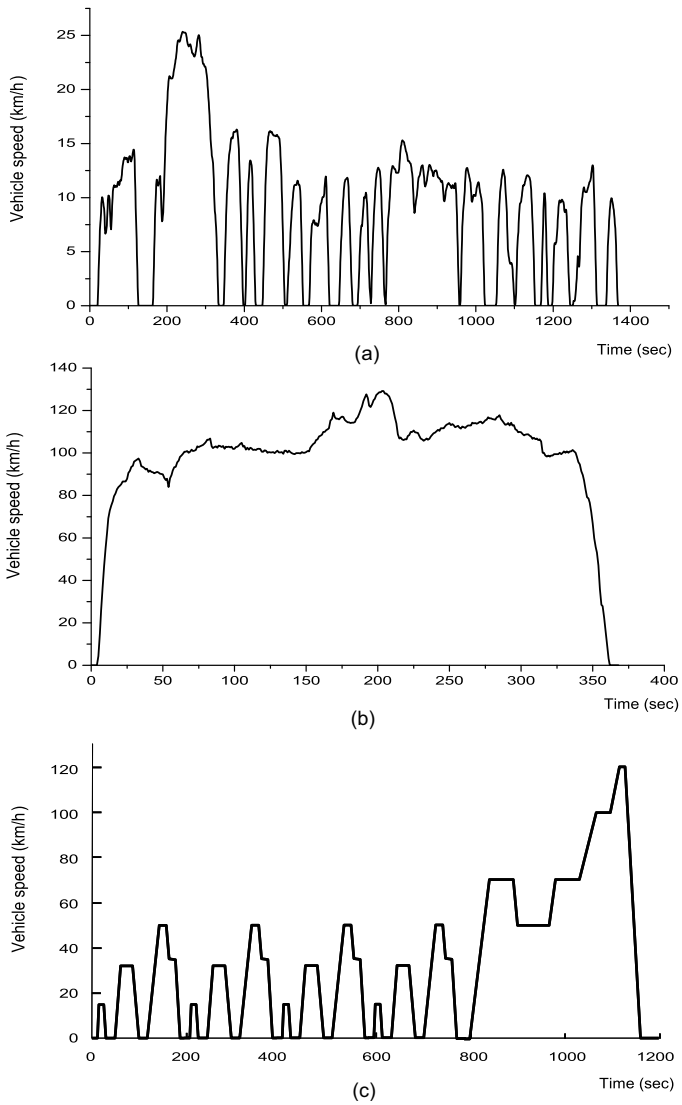

Figure 11.10: (a) EPA urban dynamometer driving schedule (UDDS), (b) highway driving cycle (US06 Hwy), and (c) NEDC.

Bibliography

[1] J. M. Miller, *Propulsion Systems for Hybrid Vehicles,* IEE, London, 2004.

[2] R. Rajamani, *Vehicle Dynamics and Control,* Springer, 2006.

[3] I. Husain, *Electric and Hybrid Vehicles, Design Fundamentals*, CRC Press, 2003.

[4] W. Gao, Performance comparison of a fuel cell-battery hybrid powertrain and a fuel cell-ultracapacitor hybrid powertrain, *IEEE Trans. on Vehicular Techonology*, Vol. 54, No. 3, May 2005.

[5] J.Y. Wong, *Theory of Ground Vehicles*, Wiley-Interscience, 3rd. Ed., 2001.

[6] D. Yin and Yoichi Hori, A novel traction control of EV based on maximum effective torque estimation, *IEEE VPPC*, Sep. $3-5$, 2008, Harbin, China.

[7] K. Muta, M. Yamazaki, and J. Tokieda, Development of new-generation hybrid system THS II - Drastic improvement of power performance and fuel economy, *Proc. of SAE World Congress* Detroit, Michigan, Mar., 2004.

Problems

11.1 Consider a vehicle with parameters: $m_v = 1200\text{kg}$, $A_F = 1.5\text{m}^2$, $\rho = 1.225\text{kg/m}^3$, and $C_d = 0.35$. Assume that the traction force is equal to $4kN$.

a) Calculate the acceleration time for $0-100\text{km/h}$ considering only the aerodynamic drag and inertial force.

b) Calculate the theoretical speed limit.

c) Calculate the acceleration time again for $0-100\text{km/h}$ when the wind blows at 10m/s in the opposite direction.

11.2 Obtain the solution of the following in an explicit form:

$$s(t) = \int_0^t V_x(\tau)d\tau = \int_0^t \frac{K_2}{K_1}\tanh(K_1K_2\tau)d\tau.$$

Calculate the distance traveled during $0 - 100$km/h acceleration under the conditions of Problem 11.1.

11.3 Consider an EV listed in Table 11.1. Assume $s_x = 0.1$ and $g_{dr} = 4.1$. Utilizing $V_x = \frac{\omega_r r_w}{g_{dr}}(1-s_x)$, determine the maximum vehicle speed when the motor runs at 6400rpm.

11.4 Consider a driving pattern shown in Fig. 11.11.

a) Calculate the rolling resistance, gravity, and inertial force using the data listed in Table 11.1 when the vehicle mass with a load is 1350kg and the grade is 10%.

b) Draw the corresponding power plot.

c) Calculate the motor torque and speed for $7 \leq t < 15$ sec when the wheel slip is $s_x = 0.1$, the drive-line gear ratio is $g_{dr} = 4.1$, and the drive-line efficiency is $\eta_{dr} = 0.95$.

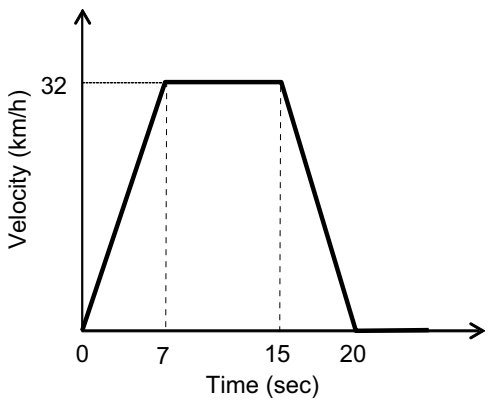

Figure 11.11: A driving pattern (Problem 11.4).

11.5 Consider an EV with parameters: the vehicle mass is $m_v = 1500$kg, the maximum motor torque is $T_e = 250$Nm, the drive-line gear ratio is $g_{dr} = 4.1$, the drive-line efficiency is $\eta_{dr} = 0.95$, and the wheel radius is $r_w = 0.29$m

a) Calculate the maximum grade of an EV at launching. Neglect the roll force.

b) Calculate the base speed of the motor when the rated power is equal to 55kW and the rated torque 250Nm.

c) Assuming $s_x = 0.1$, calculate the vehicle speed when the motor operates at the base speed.

11.6 Consider an electric bus with parameters: $m_v = 4500$kg, $r_w = 0.35$m, and $f_r = 0.01$.

a) Assuming the slip, $s_x = 0.15$, calculate wheel shaft speed when the bus runs at 60km/h.

b) The motor speed needs to be 7500rpm when the bus runs at 60km/h with the slip 0.15. Determine the gear ratio.

c) The required thrust is $F_x = 4000$N at $V_x = 60$km/h. Determine the motor power assuming that the drive-line efficiency with slip is 0.8.

d) When the base speed is 3600rpm, determine the rated torque.

e) Calculate the roll force according to $F_{roll} = f_r mg$. Suppose that the motor starting torque is 330Nm. Determine the maximum grade at launching.

11.7 Consider EV parameters listed in Table 11.1 and refer to the motor tractive effort shown in Fig. 11.8. Calculate the vehicle $0-100$ km/h acceleration time with the following instructions:

For (0, 32)km/h range, the maximum torque is applied. Neglect the aerodynamic drag in calculating the road load.
For (32, 100)km/h, let $\eta_f = \eta_{dr}(1 - s_x) = 0.8$.

Obtain the solution by solving (11.20) and (11.21) with the Rounge–Kutta method.

Chapter 12

Hybrid Electric Vehicles

Hybrid electric vehicles (HEVs), as the name stands for, have two kinds of power sources. An electric power source is added to the conventional internal combustion engine (ICE), which helps to improve the fuel economy through load sharing and regenerative braking.

Note that common ICEs have the optimum fuel efficiency in the middle speed and high torque range. But, the efficiency is low in the low-speed/low-torque region. Therefore, the ICEs have relatively inferior performances in urban driving where there are many stop-go situations. On the other hand, electric motors produce high torque naturally in the low-speed region and have a fairly high-efficiency in overall operating region. If the vehicle is propelled by a motor in a low-speed region, the overall fuel economy will be improved significantly. Furthermore, the motor can force the engine to operate in an optimal condition independently of the road load. The motor also enables the regenerative braking, i.e., vehicle's kinetic energy can be retrieved into the battery when the vehicle is decelerating. But, ICEs provide sustainable power over long driving periods and have the advantage of short refueling times.

12.1 HEV Basics

Typical driving patterns include start, acceleration/incline, cruise, decline, and deceleration/stop, as shown in Fig. 12.1. Direct benefits of HEVs can be summarized as follows:

Idle Off: Idle off means that the engine shuts down during even brief stops. Its functionality is designed so as not to be noticeable by the driver. As soon as a driver releases the brake pedal, the vehicle is initially propelled by the motor, and engine cranking follows soon afterwards. Idle off is particularly advantageous for urban traffic situations; taxis and buses are ideal candidates for idle off application. According to the tests undertaken by Tokyo Metropolitan authorities, idling-stopping improved fuel economy as much as 14%.

Regenerative Braking: Regenerative braking is an important feature of the hybrid systems. Electric motors can retrieve the vehicle's kinetic energy in the form of electrical energy, while applying a deceleration torque to the wheel. That is, the regenerative braking saves the energy that would normally dissipate as waste heat. In the LA-4 driving mode, about 25% of the total efficiency improvement gained by hybridization is attributed to regenerative braking [15] out of the total efficiency improvement gained by hybridization. But the regeneration capacity is limited mainly by the battery power rating, i.e., it is limited by the maximum acceptable charge rate of the battery. For example, the maximum power of the Prius II battery is 21kW, whereas the required braking power is larger than 50kW. In order to improve the fuel economy through regeneration, the battery power rating should be increased.

Power Assist or Power Split: Conventional ICEs are relatively inefficient at low speeds (efficiency: $5-10\%$). Hence, it is better to use the electric power-train at low speeds, and shift to the ICE at high speeds. In the series power-train architecture, the ICE, being devoted to electric power generation, is decoupled from the wheel power demand. The ICE operates at an optimal operating point, or stops. In the parallel power architecture, the motor assists the ICE while managing surges and deficits of power to the wheels. Of course, surplus engine power is saved in the battery, and used later at the time of high-power demand. Separating the ICE operation from the direct wheel power demand is termed "power split." Efficiency enhancement of HEVs is mostly attributed to this power split.

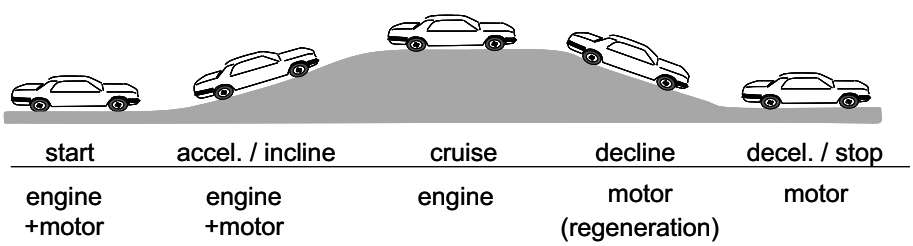

Figure 12.1: A driving cycle.

12.1.1 Types of Hybrids

HEVs are typically grouped into five categories according to the following criteria [1],[2]:

1) Idle-off capability
2) Regenerative braking capacity (up to step 2 : "micro" hybrid)
3) Power assist and engine downsizing (up to step 3 : "mild" hybrid)

4) Electric-only drive (up to step step 4 : "full" hybrid)
5) Extended battery-electric range (up to step 5 : "plug-in" hybrid)

i) Micro Hybrid: Micro hybrid systems have only the idle off function. A conventional ICE vehicle can be converted into a micro hybrid car by replacing the starting motor and alternator by an integrated alternator starter (IAS). Fuel efficiency gain is about $5-15\%$. Toyota "Crown" is an example of micro hybrid vehicle.

ii) Mild Hybrid: An electric motor is incorporated in the power-train, but the ICE plays a dominant role. Mild hybrid systems offer major HEV functions such as idle off, regenerative braking, and power assisting. However, the engine power split is imperfect and fuel efficiency gain is about $50\%-60\%$. Honda "Civic Hybrid" is a typical mild hybrid vehicle.

iii) Full Hybrid: Full hybrids have the power split feature, i.e., the electrical power-train enables the vehicle to operate its engine more time at its most efficient operating point. Further, the electrical power rating is large so that the vehicle can be driven solely by the electric motor, though the range and speed are limited. In a low-speed region, the electric motor drives the vehicle, but at a high speed the engine cuts in. Efficiency gain is about $50\%-100\%$. Toyota "Prius" and Ford "Escape" are the full hybrid vehicles.

iv) Plug-In Hybrid: In the plug-in hybrid electric vehicles (PHEVs), the battery capacity is enlarged, so that the vehicles can run for a significant range fully by electric mode. Since the vehicle battery can be charged from the power grid, a PHEV does not use a drop of gasoline if it is used for commuting on the daily basis. Depending on the all electric range (AER) in miles, they are sorted as PHEV 10, PHEV 40, and PHEV 60. For example, PHEVs with the energy storage capacity for 10 miles of driving are denoted as PHEV10. The PHEV is a viable solution to reduce the emission of CO_2 and toxic gases in urban areas. Plug-in hybrids are favored by potential customers due to low operation costs. Chevrolet "Volt," which is planned for roll out in 2011, is a PHEV.

Fig. 12.2 shows various types of EVs ranked according to the power-train electrification. The conventional ICE vehicle is located on the left end, while the battery electric vehicle (BEV) is on the right end. HEVs and PHEVs lie in between, but PHEVs have greater reliance on the electric power. Plug-in hybrid vehicles (PHEV) carry bigger batteries than HEVs. The battery size of a PHEV determines the commuting range in the all electric mode.

In some PHEVs, the ICE behaves as a charging power source when the battery is depleted below a predetermined level. Hence, the ICE with such a generator

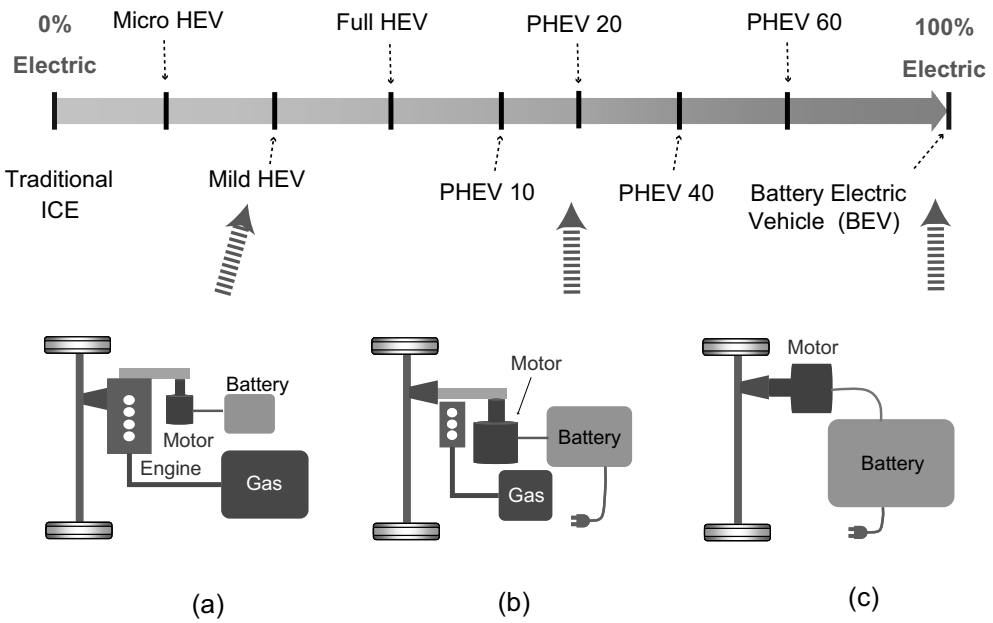

Figure 12.2: Degrees of electrification: (a) HEV (b) PHEV (c) BEV.

is often called a range extender. Further PHEVs carry on-board chargers so that household electricity can be utilized for battery charging. Since the on-board charger is designed to take all the necessary precautions against overcharging, overheating, short circuiting, fire, etc., a user just needs to plug the cord into a receptacle to charge the battery. The use of grid power reduces fuel consumption and greenhouse gas emission. Characteristics of hybrid systems are summarized in Table 12.1.

Table 12.1: Hybrid systems characteristics.

	Micro Hybrid	Mild Hybrid	Full Hybrid	Plug-in Hybrid
Elec. power	ISG	Motor	Motor-Gen.	Motor-Gen.
Motor power	5kW	16kW	60kW	100∼120kW
Engine power split	no	no	yes	yes
Batt. voltage	42V	200-300V	200-300V	>300V
Batt. capacity		1kWh	1kWh	4∼16kWh
Fuel eff. gain	5∼15%	50∼60%	50∼100%	50∼100%
AER	no	no	< 1km	16∼64 km
Gas emission	yes	yes	yes	no/yes

12.1.2 HEV Power Train Components

HEV power-trains consist of an ICE, a motor, a generator, a battery, and a power-control unit. The battery stores and supplies energy from and to the motor and generator. Another key component is the power split device, which splits the engine power to the motor, generator, and wheels.

a) ICE:
The efficiency of an engine is based on the fuel flow rate per useful power output, and brake specific fuel consumption (BSFC) is a measure of fuel efficiency: If the measured power at the crankshaft is denoted by P_o and the fuel (mass) flow rate denoted by $\dot{m}_f$, then the BSFC is defined as

$$\text{BSFC} = \frac{\dot{m}_f}{P_o}. \tag{12.1}$$

The BSFC map shows the group of contours indicating equi-fuel consumption rate

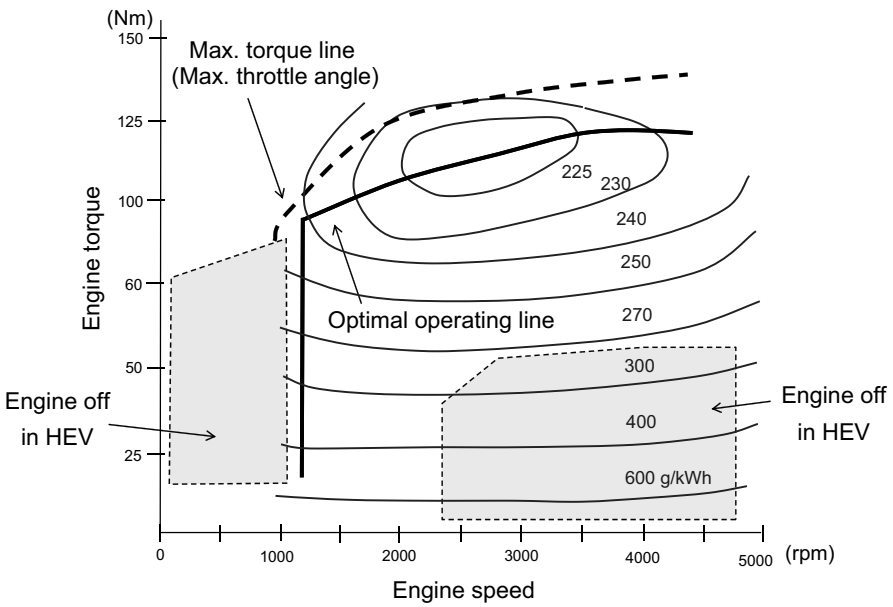

Figure 12.3: Brake specific fuel map of an engine and a basic operating line.

per shaft power production. Fig. 12.3 shows an example BSFC map, in which the units of BSFC is given by gram/kWh. Hence, the smaller number represents the higher efficiency. Note that the highest efficiency (2800rpm, 100Nm) is obtained at a middle point of the speed range and near to the maximum torque line. But, the efficiency is almost halved in the low-torque region (under 20Nm). The optimal operating line represents the trajectory of the most efficient operating points when the power and speed increase. To achieve the maximum efficiency, it is better to

narrow down the ICE operation area near to (2800rpm, 100Nm), or to stop the operation. A (dual) hybrid power-train enables the ICE to operate at its maximum efficiency, while allowing wheels to roll at independent speeds. The maximum torque is obtained when the throttle angle is fully open (90°). The top dotted line represents the engine maximum torque.

b) Motor and Generator:
The motor and generator are the same devices functionally. But depending on the power flow, they act in either motoring or generating modes. They are named according to the major usage. As for the motor and the generator, permanent magnet synchronous machines are normally utilized for high-efficiency. The motor power rating is normally bigger than that of the generator, since the motor has to take care of peak power demands while the generator responds to more or less the average power. The maximum speeds of the Prius III motor and generator are above 10,000 rpm.

c) Power Control Unit:
The power-control unit refers to an electronic circuit system that includes two inverters for motor and generator, DC-DC converter for battery voltage boosting, and an electronic control unit (ECU). One inverter controls the motor shaft torque, and the other inverter controls the generator current, so that proper battery charging or discharging takes place. The DC-DC converter boosts up the battery voltage to the required DC link level. The ECU handles sensor signals and command signals from a higher level ECU.

d) Battery:
The battery is the most typical energy storage system for EVs, and should be evaluated according to energy density, power density, life time, safety, and cost. Nickel-metal hydrid batteries or lithium-ion batteries are utilized for HEVs.

e) Power Split Device:
The power split device is required in the series/parallel hybridization. With the planetary gear, the engine power is split into a direct mechanical path and an electrical path.

12.2 HEV Power Train Configurations

The major design targets of HEVs are

- maximum fuel economy,
- minimum emissions,
- minimum system costs,
- good driving performance.

The power-control strategies for HEVs involve the following considerations:

Optimal engine operation: Restricting the engine operation to the optimal area brings not only fuel savings, but also emission reduction. As shown in Fig. 12.3, there are low efficiency regions in the engine fuel map. In the low efficiency regions, it is better to turn off the engine and run the vehicle only by motor. Engine turn-off regions are marked by the shaded areas in Fig. 12.3.

Safe battery operation: The battery should be protected from overcharging and excessive dissipation. Overcharging may lead to battery explosion, and excessive charge depletion shortens the battery life time. During battery operation, the current should be limited so that the maximum power rating is not exceeded.

According to the power flow, HEVs are divided into three categories: parallel hybrids, series hybrids, and series/parallel hybrids, as shown in Fig. 12.4 [5], [1]. Dotted lines indicate electrical power flow, whereas solid lines show mechanical power flow. The series HEV topology is described in Fig. 12.4 (a): The engine, operating in the on-off modes, is devoted to generating electricity. The battery charging current is regulated by the converter. The motor delivers power to the wheel, utilizing the stored energy in the battery. Since the engine operation is independent of the vehicle speed and road load, it can operate at its optimal condition. But a disadvantage lies in the cascaded structure: Suppose that efficiencies of generator, converter, inverter, and motor are 0.95, 0.97, 0.97, and 0.92, respectively. Then, the compound efficiency is equal to their product, 0.82, which is much lower compared with that of the direct mechanical path. Furthermore since each power conversion unit has the full power rating, the mass and volume are large, and the cost is correspondingly high. Thus, this configuration was not used in passenger cars, but has been adopted in some electric locomotive propulsion systems or in electric propulsion ships. Since the series power-train is simple and enables the engine to operate optimally, it is recently deployed in PHEVs.

In the parallel configuration, shown in Fig. 12.4 (b), both mechanical and electrical paths coexist. Therefore, the engine and motor can drive the wheels individually or collaboratively. It does not employ a separate generator. But, the motor, behaving as a generator, retrieves excess engine power when the engine operates in the vicinity of an optimum operation point. The parallel configuration is not so efficient, since the engine power split is imperfect.

The series/parallel hybrid employs a power split device so that the engine power can be delivered via two paths, as shown in Fig. 12.4 (c). Various power flow control modes are feasible, and the configuration varieties are coordinated for engine optimal operations.

12.3 Planetary Gear

A planetary gear together with a motor and a generator plays a key role in the engine power splitting in the series/parallel hybrid configuration. The planetary

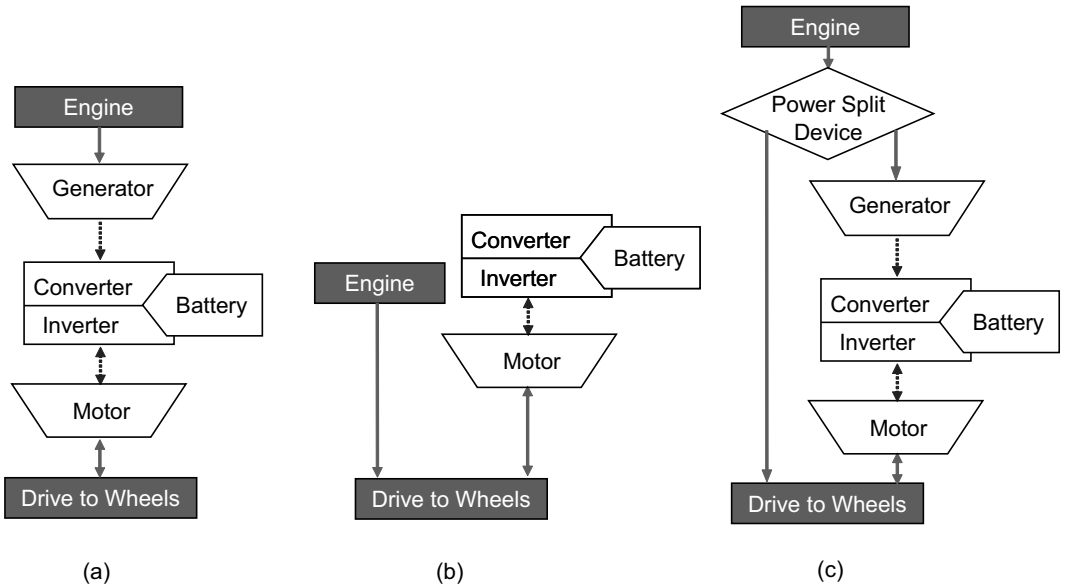

Figure 12.4: HEV power-train topologies. (solid line : mechanical power, dotted line : electric power) : (a) series, (b) parallel, (c) series/parallel.

gear consists of sun gear, planetary gear, and ring gear, as shown in Fig. 12.5. The sun gear is located in the center, the ring gear is positioned in the outer shell, and the planetary carrier is made by clustering the pinions in the middle. Based on the schematic shown in Fig. 12.5 (a), it follows that

$$R_r\omega_r - R_c\omega_c \;=\; R_c\omega_c - R_s\omega_s, \tag{12.2}$$

where R_s, R_p, and R_r are the radii of sun gear, carrier, and ring gear, and ω_s, ω_c, and ω_r are the speeds of sun gear, carrier, and ring gear, respectively. Let the gear ratio be defined by $R_r/R_s = k_p$. Then, dividing the right-hand side by the left-hand side of (12.2), it follows that

$$\frac{R_r\omega_r - \frac{R_r+R_s}{2}\omega_c}{\frac{R_r+R_s}{2}\omega_c - R_s\omega_s} = \frac{2\omega_r k_p - (k_p+1)\omega_c}{(k_p+1)\omega_c - 2\omega_s} = 1\,. \tag{12.3}$$

This is the fundamental equation of the planetary gear (i.e., epicyclic gearing), indicating that the gear rotation must maintain a fixed ratio, k_p, of angular velocity relative to the carrier body. After rearranging, (12.3) reduces to the more general form [5]:

$$\omega_s + k_p\omega_r - (k_p+1)\omega_c = 0. \tag{12.4}$$

Note that there is one constraint equation, (12.4) among three independent variables, ω_s, ω_c, and ω_r. Therefore, the planetary gear has two degree of freedom, i.e., it accommodates two independent shaft speeds. This illustrates the inherent speed

summing nature of the planetary gear and the reason it is used in power split. Equation (12.4) of planetary gear is rearranged such that

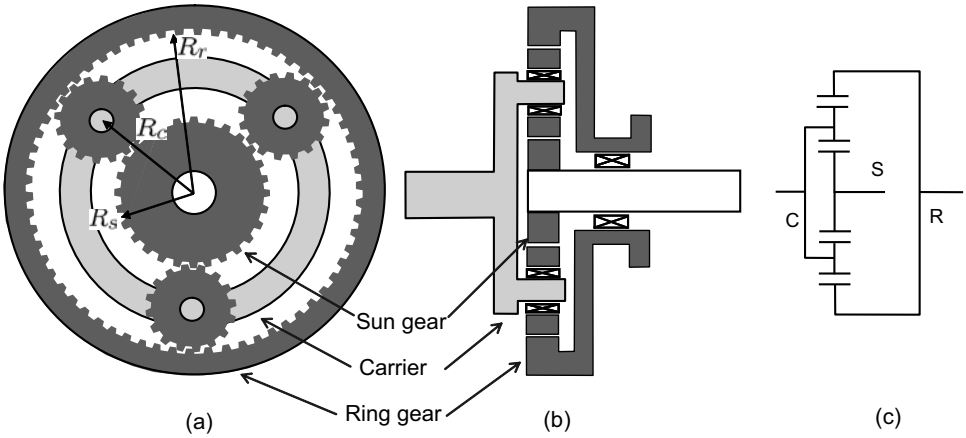

Figure 12.5: Planetary gear: (a) front view, (b) side view, (c) symbol.

$$\omega_c = \frac{1}{k_p + 1}\omega_s + \frac{k_p}{k_p + 1}\omega_r \,. \tag{12.5}$$

Geometrically, (12.5) appears to be a straight line as shown in Fig. 12.6, and it is called a lever diagram. The planetary gear of the Prius II has the following individual gears:

sun gear : number of teeth, $N_s = 30$,
ring gear : number of teeth, $N_r = 78$.

Therefore, $k_p = R_r/R_s = N_r/N_s = 78/30 = 2.6$.

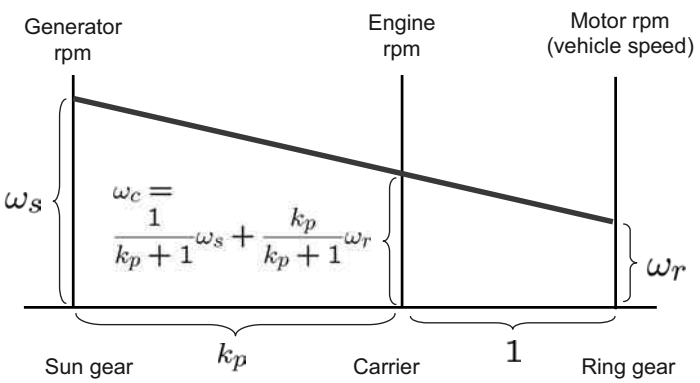

Figure 12.6: Lever diagram for the planetary gear system.

The torque balance and power balance conditions in the steady-state are

$$T_c = T_r + T_s, \tag{12.6}$$
$$T_c\omega_c = T_r\omega_r + T_s\omega_s, \tag{12.7}$$

where T_c, T_r, and T_s are the shaft torques of carrier, ring, and sun gears, respectively. Since (12.6) and (12.7) are the steady-state equations, inertial forces of gears are omitted. Further, the gear efficiency is assumed to be unity. Substituting (12.6) into (12.7), we obtain [6]-[8]

$$T_c = (1 + k_p)T_s, \tag{12.8}$$
$$T_c = \left(1 + \frac{1}{k_p}\right) T_r. \tag{12.9}$$

Exercise 12.1
Consider a planetary gear system, shown in Fig. 12.6. Assume $k_p = 2.6$, $\omega_c = 2500$rpm, and $\omega_s = 3600$rpm.
a) Calculate the speed of ring gear.
b) Assume that the engine produces 60kW and that the generator applies 70Nm load torque to the engine. Calculate the engine power directed to the ring gear.

Solution
a)

$$\omega_r = \left(1 + \frac{1}{k_p}\right)\omega_c - \frac{\omega_s}{k_p} = 1.385 \times 2500 - 0.385 \times 3600 = 2078\text{rpm}$$

b)

$$P_g = \frac{3600}{60} \times 2\pi \times 70 = 26,389\text{W}.$$

Thus, $60 - 26.389 = 33.611$(kW). ■

12.3.1 e-CVT of Toyota Hybrid System

Continuously variable transmissions (CVTs) are devised for continuous changes in the shaft's speed ratio, and are commonly constructed with the V-belt, conical shaped pulleys, and a hydraulic actuator. A CVT allows the driving shaft to maintain a constant speed while the speed of output shaft changes. This improves fuel economy by enabling the engine to run at its most efficient speeds for a range of vehicle speeds. However, the CVTs are friction based devices, resulting in power loss and faults associated with aging.

A planetary gear is used as a power split device in the series/parallel HEVs. Fig. 12.7 shows a schematic diagram of the e-CVT of Toyota Hybrid System (THS)

Table 12.2: Specifications of Prius II and III [15], [16].

		Prius III	Prius II
Engine	Power	73kW	57kW
	Torque	142Nm	115Nm
Motor	Type	IPM	IPM
	Max. power	60kW	50kW
	Max. torque	207Nm	400Nm
	Max. speed	13500rpm	6400rpm
Generator	Type	IPM	IPM
	Max. power		22kW
	Max. speed		11000rpm
Battery	Type	NiMH	NiMH
	Power	21kW	21kW
	Voltage	201.6V	201.6V
	Weight		45kg
	Capacity	1.3	1.3kWh
System voltage		650Vmax	500Vmax
Motor gear ratio		2.636	
Differential gear ratio		3.267	4.113

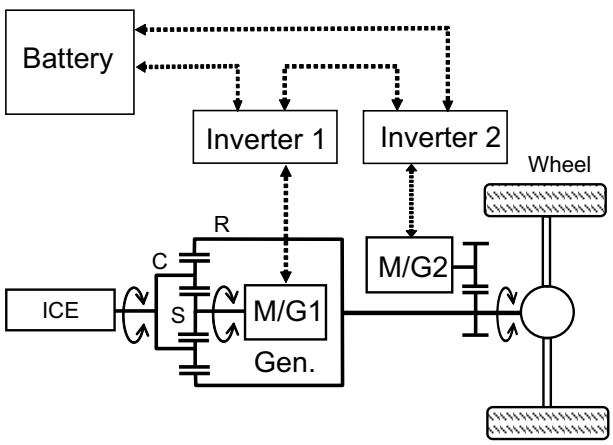

Figure 12.7: Schematic drawing of the THS employing a planetary gear as the input power split device (dotted line : electrical power-train).

in Prius II [15]. In the Prius III, the maximum motor speed was increased to 13500rpm, reducing the mass by about 35% [16]. Major power-train specifications are listed in Table 12.2. Since the power split device is positioned at the input (upstream) side, it is classified as input split. The engine crank shaft is connected to the carrier, The M/G1, labeled "generator," is connected to the sun gear. On the

other hand, the M/G2, labeled "motor," is connected to the ring gear. Note that the ring gear is coupled with the drive axle via the chain, final gear, and differential gear. Thus, the motor has a fixed gear ratio with the axle. Therefore, a part of the engine power is transmitted directly to wheels through the ring gear. The rest of the engine power is taken by the generator. The generated electric power is transmitted to the motor or stored in the battery and may be used later for EV mode or acceleration. A THS schematic diagram is shown in Fig. 12.7. Electrical paths are denoted by dotted lines, whereas mechanical paths are denoted by solid lines. A more detailed diagram and power circuit are shown in Fig. 12.8. Two inverters are connected back to back with a common DC link bus. Note however that the battery voltage is around 200 V, but the DC link voltage is 500V or 650V. Thus, it requires the use of a bi-directional buck-boost converter. The reason for this voltage boosting is to reduce the current rating of cable and M/G coils and to minimize M/G volumes.

The engine is controlled to operate along the optimal operation line (OOL) by controlling the generator speed and motor torque. That is, power flow to wheels is controlled seamlessly while the engine operates in the vicinity of the optimal operating line [9]. This improves the overall vehicle fuel economy. No launch device, such as a torque converter in an automatic transmission, or a clutch in a manual transmission, is necessary. The engine can remain directly connected to the transmission for all speeds.

12.4 Power Split with Speeder and Torquer

It is assumed that the vehicle speed and the load torque do not change during a short time interval due to the large inertia. Here, both T_{dr} and ω_r are treated as fixed numbers.

A power determining procedure consists of the following steps:

i) For a given engine torque, T_c^*, determine ω_c^* such that the engine power is equal to the drive-line power requirement, i.e., $T_c^*\omega_c^* = P_{dr}$.

ii) Choose ω_s so that $\omega_s = (k_p + 1)\omega_c^* - k_p\omega_r$.

The engine speed is selected such that the engine power meets the demand required by the drive-line. Since the ring gear speed, ω_r is fixed by the vehicle speed, the engine speed, ω_c, is passively determined by the sun gear speed, ω_s. In other words, ω_c is determined by ω_s according to the linear equation, (12.4). For this purpose, the generator (M/G1) is controlled in the speed control mode; thereby it is called *the speeder* [3].

Once engine torque, T_c, is fixed, the torques of sun and ring gear shafts are determined according to (12.8) and (12.9). That is, the engine power is split according

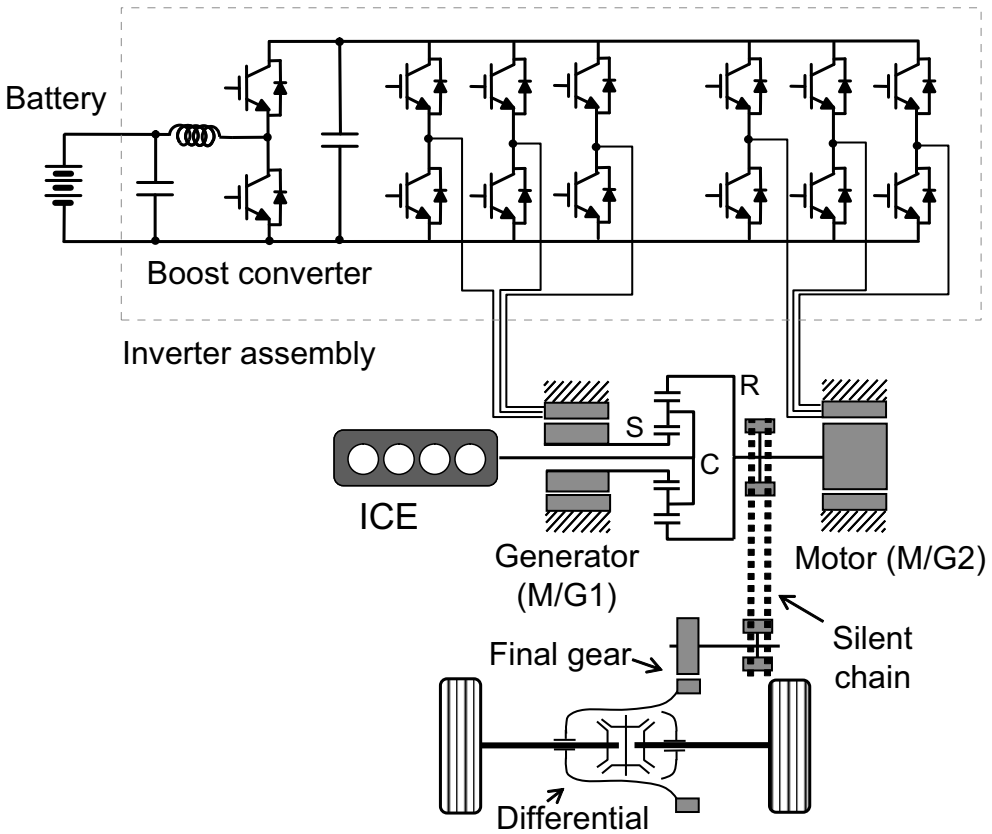

Figure 12.8: THS schematic diagram and power circuit.

to

$$T_c\omega_c = \underbrace{\frac{T_c\omega_s}{k_p+1}}_{=P_{elec}} + \underbrace{\frac{k_pT_c\omega_r}{k_p+1}}_{=P_{mech}}. \tag{12.10}$$

Note that the electrical path consists of sun gear-generator-inverter 1-inverter 2-motor-ring gear, whereas the mechanical path is made by the direct gear coupling – the carrier and ring gear. Note however that the split powers are summed at the drive-line, as shown in Fig. 12.9. The power summation is possible since the motor (M/G2) is controlled in a torque control mode. Specifically, the motor can add/subtract torque at an arbitrary drive-line speed. For this reason, the motor is called *the torquer* [3].

The ratio between the two power flows is equal to

$$\frac{P_{elec}}{P_{mech}} = \frac{\omega_s}{k_p\omega_r}. \tag{12.11}$$

Therefore, as ω_s increase, the electrical path proportion increases. As mentioned in the above, the power transfer efficiency of the electrical path is low compared with

that of the mechanical path.

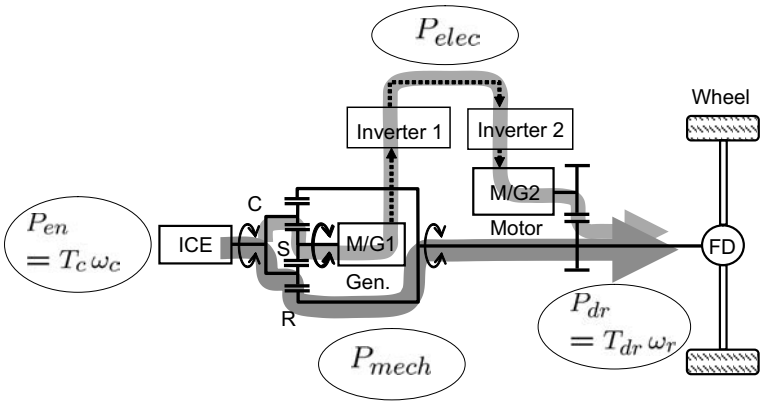

Figure 12.9: Power split consisting of electrical and mechanical paths.

The question is why it is necessary to split the power and sum the splits at the drive-line instead of delivering the whole via the mechanical path. A benefit of the power split is illustrated with the following example: Assume that the drive-line operates at 280 rad/sec with a load of 55.7 Nm. Since $P_{dr} = 15.595$ kW, the same power has to be delivered from the engine. Suppose that the generator speed is forced to down from 208 rad/sec, to 28 and -30 rad/sec by a speed control action, while the throttle angle is controlled to yield constant power, 15.6kW: A: $\omega_s = 280$rad/sec, B: $\omega_s = 28$rad/sec, and C: $\omega_s = -30$rad/sec. The corresponding engine speeds and torque are

A: $(\omega_c,\ T_c) = (2482$ rpm, 60 Nm),
B: $(\omega_c,\ T_c) = (2005$ rpm, 74 Nm),
C: $(\omega_c,\ T_c) = (1853$ rpm, 80.4 Nm).

The engine speed, ω_c, decreases in proportion to ω_s, as shown in Fig. 12.10 (b). Since the engine maintains a constant power mode, the engine operation points migrate from "A" to "B" and "C" along a constant power line as shown in Fig. 12.10 (a). It should be noted that "C" is closer to the OOL than "A" and "B". Specifically, the fuel efficiency is increased to 235 g/kWh from 250 g/kWh.

The power split device makes it possible to move engine operation points near to the OOL while satisfying the wheel power requirements. Specifically, the speeder determines engine speed for a given wheel speed so that the engine operates at its optimal condition. As a result, the engine speed is decoupled from the wheel speed. The power split enhances the system efficiency by letting the engine operate along the OOL, though there is a minor loss along the electrical power flow.

This section is summarized with the following remarks:

1. Since the generator operates commonly in the speed control mode; it is called "speeder." The generator speed is determined to bound the engine operation

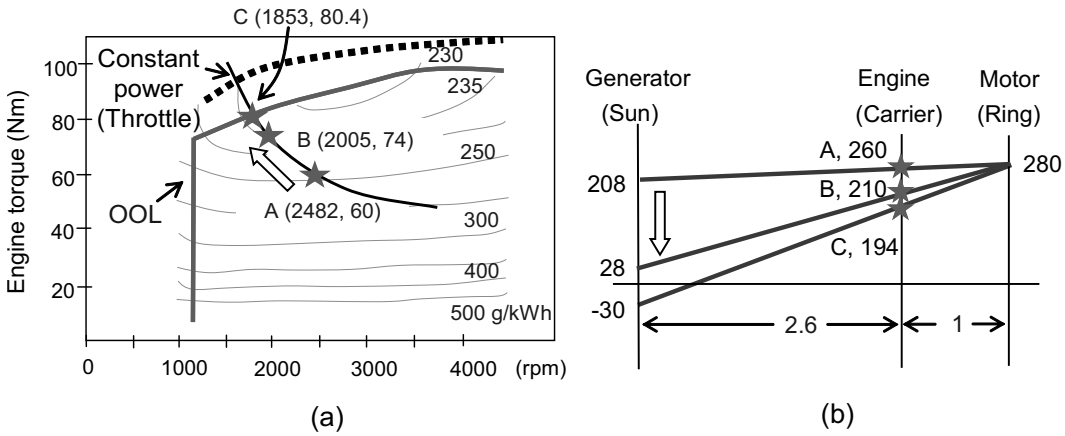

Figure 12.10: Operating point migration toward the OOL as the generator speed is controlled down to −30 rad/sec. (a) operating points in the engine torque-speed plane and (b) lever diagram.

within an optimal operation range. Recall that the engine is efficient when it is highly loaded, i.e., when the operation point is near to the maximum torque line. Thus, the generator, in general, applies an additional load to the engine so that the operation point is near to the OOL when the vehicle road load is light. The generated electric power is transmitted to the motor. But the excess power is used to charge the battery for later use: power-boosting and EV mode operation.

2. Since the motor operates commonly in the torque control mode, it is called "torquer." The motor supplies supplementary torque to the drive shaft utilizing the electric power transmitted from the generator. If the generator power is insufficient during sudden acceleration, the battery power is also utilized.

12.5 Series/Parallel Drive Train

The THS is a typical series/parallel hybrid, in which both the series and parallel features coexist. With a planetary gear, operation is much more flexible compared with the parallel hybrid system. For example, it accommodates "electric mode driving" without utilizing a clutch: The vehicle can be driven by the motor while the engine is stopped. The series/parallel vehicle operates like a series vehicle in a low-speed region, whereas it acts like a parallel HEV in the high-speed region. Extensive researches are being performed regarding the power-train modeling and control optimization [9]-[14].

Various operation modes include:

i) Vehicle launch / EV mode operation

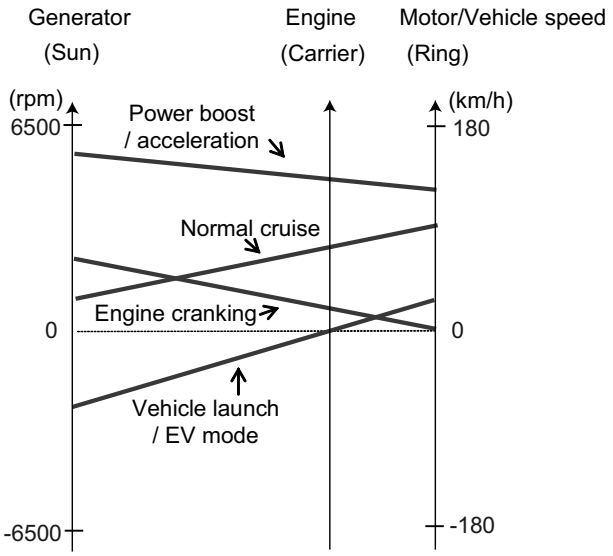

Figure 12.11: Lever diagrams.

ii) Engine cranking

iii) Normal Cruise with battery charging

iv) Power boosting for acceleration

v) Regenerative braking during deceleration

The corresponding lever diagrams are shown in Fig. 12.11. Recall that the motor has a fixed ratio to the vehicle speed (if the wheel slip is constant). During engine cranking, the vehicle speed (ring gear speed) is zero. Note the the engine is kept at a standstill during the EV mode operation. In normal mode operation, the engine power is split and transported to the wheels via mechanical and electrical paths. For sudden acceleration, the battery power is utilized to increase the motor power.

Both M/G1 and M/G2 serve as either a motor or a generator, depending on the driving conditions. For example, the generator (M/G1) normally generates electric power, but acts as a motor during engine cranking. On the other hand, the motor (M/G2) normally generates torque, but acts as a generator during regenerative braking.

1) Vehicle Launch and Battery EV Mode

For vehicle launch and a low-speed operation, the vehicle is propelled only by the battery power. Thus, this mode is called EV mode. Note that the engine is stopped without a clutch mechanism while the vehicle is moving. It is clearly illustrated with the lever diagram: For a given positive ring gear (motor) speed, the sun gear (generator) speed is determined at a negative speed such that the carrier (engine)

speed is zero. It is feasible since the generator is controlled in a speed control mode. Fig. 12.12 shows an example of the battery EV mode.

Exercise 12.2
Planetary gear ratio is equal to $k_p = 2.6$, and the gear ratio of the drive-line is $g_{dr} = 4.1$. The effective tire rolling radius is $r_w = 0.29$m. The vehicle operates in the EV mode with the engine shut off.

a) Determine the ring gear speed in the EV mode when the generator speed is 4500rpm.

b) Assume that the engine cuts in when generator speed reaches 4500rpm. Determine vehicle speed at the time of engine cut-in. Neglect the wheel slip.

Solution
a)

$$\omega_r = \frac{\omega_s}{k_p} = \frac{4500}{60} \times 2\pi \times \frac{1}{2.6} = 181.2\text{rad/sec}.$$

b)

$$\frac{\omega_r}{g_{dr}} \times r_w = \frac{181.2}{4.1} \times 0.29 = 12.8\text{m/sec} = 46\text{km/h}.$$

■

Note that the engine cuts in from 45km/h by gradual acceleration in Prius II.

Exercise 12.3
(Continued from Exercise 12.2) Suppose that the vehicle runs in an EV mode at 40km/h against a 600N road load. Assume that the motor and inverter efficiencies are 0.92 and 0.97, respectively. Assume further that efficiency of the final drive is $\eta_f = 0.82$ including the wheel slip.

a) Calculate speed, torque, and power of the motor when the average slip is $s_x = 0.1$.

b) Calculate the battery output power.

Solution
a) Wheel power is equal to $P_x = -40000/3600 \times 600 = -6667$W. Reflecting the final drive efficiency, motor power is $6667/0.82 = 8130$W. Angular speed of wheel is

$$\omega_w = \frac{V_x}{r_w(1 - s_x)} = \frac{40000}{3600} \times \frac{1}{0.29 \times 0.9} = 42.6\text{rad/sec}.$$

Motor speed is $42.6 \times 4.1 = 174.7$ rad/sec (1668rpm). Motor torque is equal to $8130/174.7 = 46.5$Nm.
b) Battery power is equal to $P_{bat} = 8130/(0.92 \times 0.97) = 9110$(W). The result is depicted in Fig. 12.12. ■

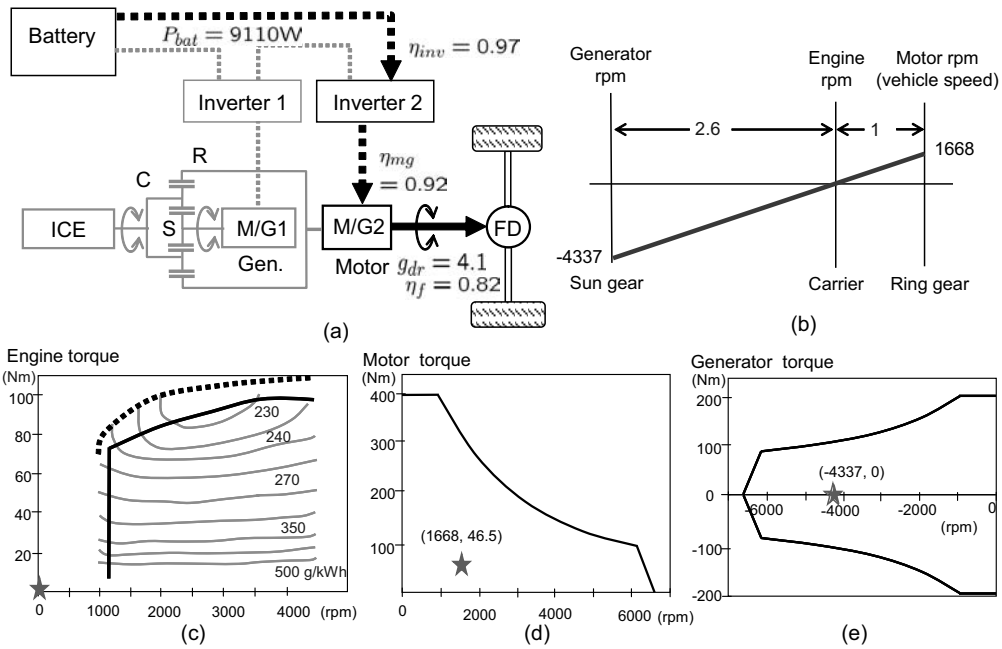

Figure 12.12: Battery EV mode: (a) power flow, (b) lever diagram, (c) engine fuel map, (d) motor torque-speed curve, and (e) generator torque-speed curve (Exercise 12.3).

2) Normal Driving (Cruise) Mode

When the vehicle is cruising at a moderately high speed, the power demand is not so high. The engine power is split by the planetary gear: Through the carrier-ring gears, a portion of engine power is transmitted to wheels mechanically. The other portion is converted into an electrical power and transferred to the motor for torque assist. Fig. 12.13 shows a normal driving mode.

Exercise 12.4

Assume that the vehicle runs at a constant speed, 64.8km/h, bearing a road load, $F_{rl} = 666.7$N. Assume that the M/G and inverter efficiencies are 0.92 and 0.97, respectively, and that the efficiency of the final drive is $\eta_f = 0.82$ including the wheel slip.

a) Calculate the required power at the drive-line, P_{dr}.

b) The effective tire rolling radius is $r_w = 0.29$m and the final drive gear ratio is $g_{dr} = 4.1$. Calculate the motor angular speed, ω_r when the wheel slip is $s_x = 0.1$.

c) Assuming a steady-state, determine the sun gear (generator) speed such that the engine speed is 220 rad/sec (2101rpm).

d) Suppose that the engine output torque is regulated at 67.5Nm. Calculate the power directed to the ring gear, P_r.

e) Calculate the required motor shaft power, $P_e = P_{dr} - P_r$.

f) Calculate the total efficiency of the electrical power-train consisting of generator, inverter 1, inverter 2 and motor, when the inverter efficiency is $\eta_{inv} = 0.97$ and the efficiency of motor and generator is $\eta_{mg} = 0.92$.

g) Calculate the motor shaft power driven by the electric power transferred from the generator.

Solution

a) At constant speeds, there is no inertial force. Therefore, $F_{rl} = F_x$. The vehicle propulsion power is $P_x = -F_x V_x = -666.7 \times 64800/3600 = -12001$W. Since the efficiency of the final drive is $\eta_f = 0.82$, the power at the drive-line should be $P_{dr} = 12001/0.82 = 14636$W.

b)

$$\omega_r = \frac{V_x}{r_w(1 - s_x)} g_{dr} = \frac{64800}{3600 \times 0.29 \times 0.9} \times 4.1 = 282.8\text{rad/sec.}$$

c) Using (12.5), the generator speed is $\omega_s = 3.6 \times 220 - 2.6 \times 282.8 = 56.7$ rad/sec.

d) According to (12.8), generator torque is equal to $67.5/3.6 = 18.75$Nm.
Generator power is $P_s = 56.7 \times 18.75 = 1063$W. Therefore, power of the ring gear shaft is $P_r = P_{en} - P_s = 220 \times 67.5 - 1063 = 13787$W.

e) Amount of power that should be assisted by the motor is
$P_{dr} - P_r = 14636 - 13787 = 849$W.

f) Since there are two M/Gs and two inverters, the efficiency of the electrical path is $(0.97 \times 0.92)^2 = 0.796$.

g) Therefore, the motor power is $P_e = P_s \times \eta_{inv}^2 \eta_{mg}^2 = 1063 \times 0.796 = 847W$. ■

Note from e) and g) that the drive-line lacks 849W, whereas the motor power received from the electric path is 847W. That is, they are almost equal, so that there is no need for battery discharging. The solutions for the above normal mode are summarized in Fig. 12.13.

Fig. 12.14 shows power flow, lever diagram, and operating points of engine, generator, and motor at the normal load of Exercise 12.4. Note that the motor (M/G2) operation point lies in the first quadrant of a torque-speed map. Since the generator applies a load torque to the engine, it produces a negative torque, i.e., the operation point locates in a regeneration region (4th quadrant).

The corresponding Sankey diagram is shown in Fig. 12.14: The engine power, P_{en}, is split into P_s and P_r. The generator power, P_s is used for powering the motor. In the electric power-train, losses of generator, motor, and inverters are considered. Two powers, P_e and P_r, are summed at the drive-line, P_{dr}. Finally, traction power, P_x is obtained bearing the mechanical loss of the final drive.

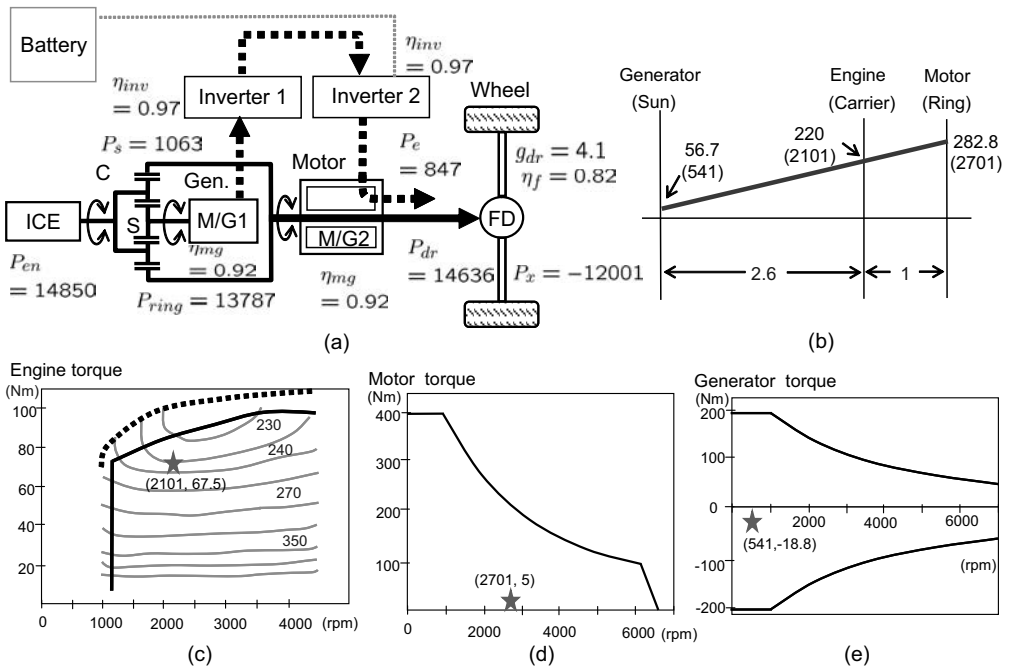

Figure 12.13: Normal driving mode: (a) power flow, (b) lever diagram, (c) engine fuel map, (d) motor torque-speed, and (e) generator torque-speed (Exercise 12.4).

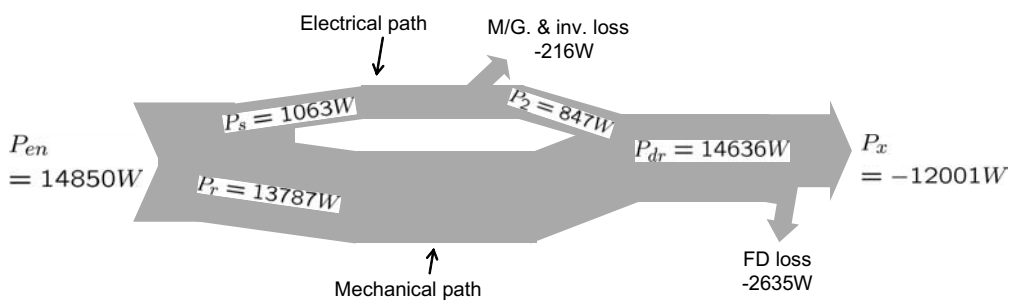

Figure 12.14: Sankey diagram for a normal driving mode (Exercise 12.4).

3) Power-Boost Mode at Sudden Acceleration

When a required road-load torque is higher than the full-throttle torque of the engine, the motor acts as a power-booster utilizing the battery power. That is, in addition to the generator power, more power is drawn from the battery into the motor.

Exercise 12.5

Assume that the vehicle runs at a constant speed, 80km/h bearing a road load of $F_{rl} = 1400$N. The engine speed and torque are regulated at $(T_{en}, \omega_c) = (97$Nm,

314.2rad/sec). Assume that the M/G and inverter efficiencies are 0.92 and 0.97, respectively, and that the efficiency of the final drive is $\eta_f = 0.82$ including the wheel slip.

a) The effective tire rolling radius is $r_w = 0.29$m and the final drive gear ratio is $g_{dr} = 4.1$. Calculate the motor angular speed, ω_r, assuming that the average wheel slip is $s_x = 0.15$.

b) Assuming a steady-state, determine the generator speed, ω_s using the lever diagram of $k_p = 2.6$.

c) Determine the generator torque and calculate the split powers, i.e., P_s and P_r.

d) Calculate the drive-line power, P_{dr} and the battery (discharging) power, P_{bat}.

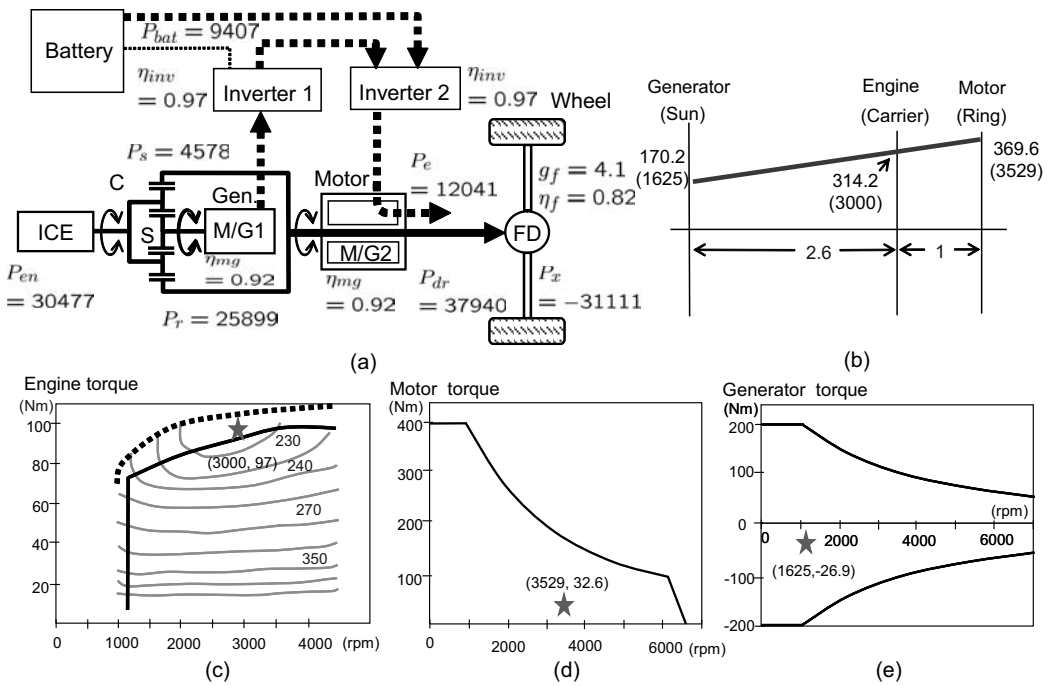

Figure 12.15: Power-boost mode: (a) power flow, (b) lever diagram, (c) engine fuel map, (d) motor torque-speed, and (e) generator torque-speed (Exercise 12.5).

Solution

a) The motor speed is

$$\omega_r = \frac{V_x}{r_w(1-s_x)} \times g_{dr} = \frac{80000}{3600 \times 0.29 \times 0.85} \times 4.1 = 369.6\text{rad/sec}.$$

b) Since the engine speed is 314.2rad/sec, it follows from the level diagram that $\omega_s = 3.6\omega_c - 2.6\omega_r = 3.6 \times 314.2 - 2.6 \times 369.6 = 170.2$ rad/sec (1625 rpm).

c) The engine power is $P_{en} = 97 \times 314.2 = 30477$(W). According to (12.8), the generator torque is equal to $97/3.6 = 26.9$Nm. Thus, the generator power is $P_s = 170.2 \times 26.9 = 4578$W. Therefore, $P_r = P_{en} - P_s = 30477 - 4578 = 25899$W.
d) At constant speeds, $F_x = F_{rl}$. The vehicle power is $P_x = -80000/3600 \times 1400 = -31111$W. Considering the final drive efficiency, the power at the drive-line is $P_{dr} = 31111/0.82 = 37940$W. Thus, the required motor power is $P_e = P_{dr} - P_r = 37940 - 25899 = 12041$W.
A portion of motor power transmitted from the generator is $P_s \times \eta_{inv}^2 \eta_{mg}^2 = 4578 \times (0.92 \times 0.97)^2 = 3646$W.
Additional motor power that should come from the battery is 12041-3646=8395W. Thus, the battery (discharging) power is $P_{bat} = \frac{8395}{0.92 \times 0.97} = 9407$W. ■

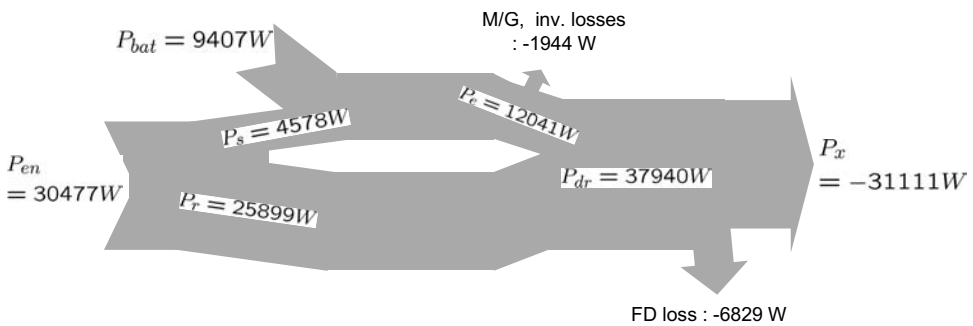

Figure 12.16: Sankey diagram for power-boost mode (Exercise 12.5).

The corresponding Sankey diagram is shown in Fig. 12.16: It is shown that the battery (discharging) power, P_{bat} is added to the electrical power-train so as to make up the lack of engine power, when the drive-line power, P_{dr} exceeds the engine power, P_{en}.

4) Regenerative Braking

While the vehicle is decelerating or declining a hill, the vehicle's kinetic energy can be recovered by operating the motor in the generator mode. At this time, the motor is rotating in the forward direction. But by changing the q-axis current polarity to be negative, the braking power is transformed into electric power and used for recharging the battery. The engine is shut off during the regenerative braking. The regenerative braking is basically the same as the EV mode, but the power flow is reversed.

Exercise 12.6

Assume that the vehicle operates regenerative braking with engine shut off while the speed is regulated at 66.42km/h. The effective tire rolling radius is $r_w = 0.29$ m and the gear ratio of the drive train is $g_{dr} = 4.1$.

a) Assuming that the wheel slip is $s_x = -0.1$. Calculate the motor speed, ω_r.

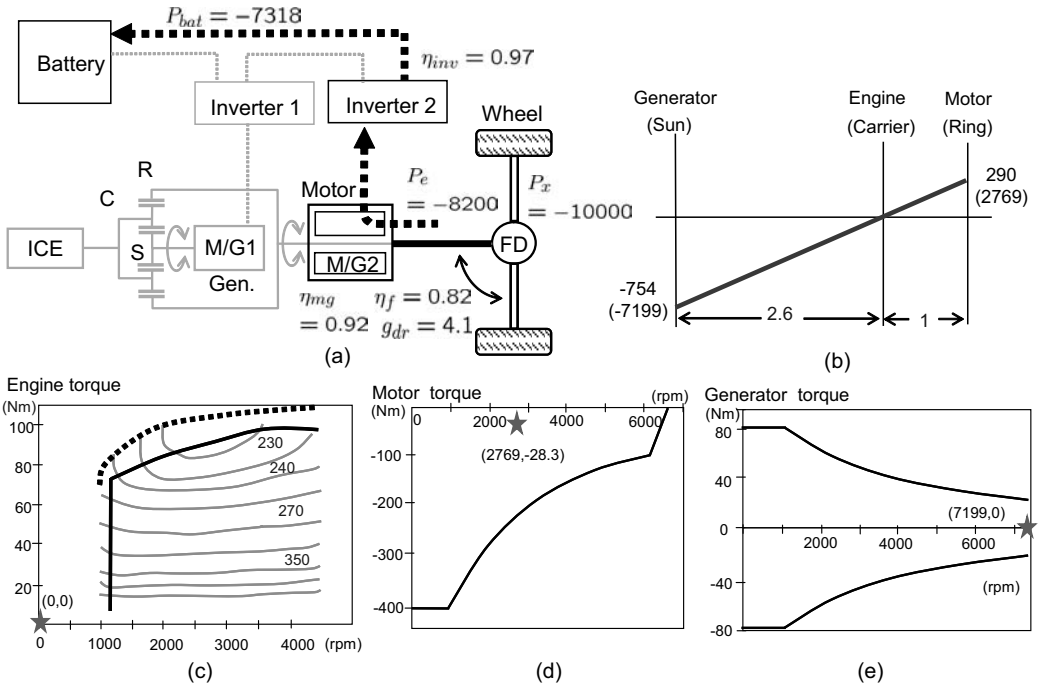

Figure 12.17: Regenerative braking (Exercise 12.6).

b) Assume that the drive-line efficiency is $\eta_f = 0.82$. Determine the motor power, P_e, and the battery recharging power, P_{bat}, when the road load of -542 N.

Solution

a)

$$\omega_r = \frac{V_x}{r_w(1 - s_x)} \times g_{dr} = \frac{66420}{3600 \times 0.29 \times 1.1} \times 4.1 = 237.1 \,\text{rad/sec}.$$

b) The wheel power is equal to $P_x = 66420/(3600) \times (-542) = -10000(\text{W})$. Therefore, the drive-line power is equal to $P_{dr} = -8200\text{W}$. Also, $P_{dr} = P_e = -8200\text{W}$. Considering the motor efficiency, the battery recharging power is $P_{bat} = -8200 \times 0.92 \times 0.97 = -7318(\text{W})$. ■

5) Engine Cranking

During the engine cranking, the vehicle is stationary, so that the motor speed is equal to zero. The generator forces the engine to spin, so that it operates in a motoring mode. The lever diagram for engine cranking is shown in Fig. 12.18. Note also that the lever diagram for stationary battery charging is the same as that of engine cranking. But, the power flow is reversed.

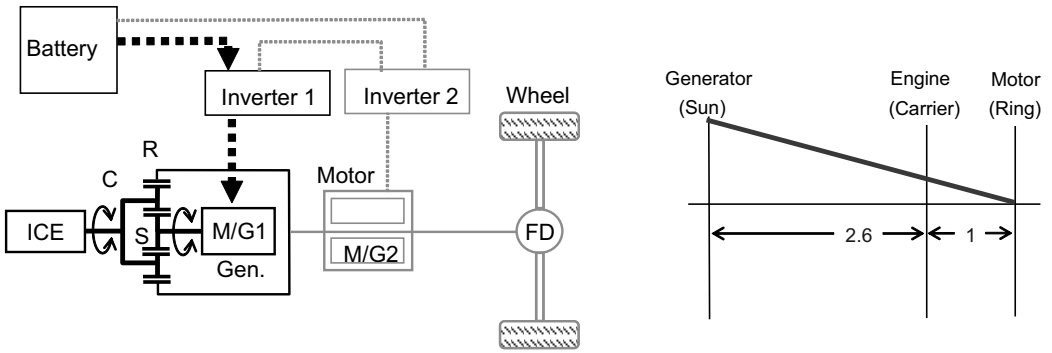

Figure 12.18: Engine cranking mode.

12.5.1 Prius Driving-Cycle Simulation

The simulation was performed with the Prius model using a drive simulation tool, ADVISOR. The vehicle simulation parameters are:

Curb mass with cargo (m_v) = 1398kg,
CD (C_d) = 0.3,
Frontal area (A_F) = 1.746m^2
Rolling coefficient (f_r) = 0.009.

Fig. 12.19 (b) the engine, motor, and generator operation points in the torque-speed plane under simple driving cycles shown in Fig. 12.19 (a). Four driving cycles were repeated to obtain dense operation points. It is shown that the motor produced high torque during the acceleration period especially in a low-speed area. Then, it applied negative torque in the deceleration period, recovering kinetic energy. It should be noted that engine operation points are not spread far from the optimum operating line.

The maximum motor speed is read 2400rpm from Fig. 12.19 (b). Assume that the gear ratio between the wheel and motor shafts is 4.1 and that the effective tire rolling radius is 0.29m. When we neglect the wheel slip, the peak velocity is estimated such that

$$V_x = 2400 \times \frac{2\pi}{60} \times \frac{1}{4.1} \times 0.29 \times \frac{3600}{1000} = 64\text{km/h}.$$

Note that the estimation is close to the peak speed (64km/h), shown in Fig. 12.19 (a).

Fig. 12.20 shows the loci of the engine operation points along a highway driving cycle (US06 Hwy). The operation points were aggregated to the optimum efficiency line, and the engine torque reached the maximum values.

Fig. 12.21 shows the SOC pattern of the Prius II for urbane driving cycle (EPA UDDS). Note the the SOC window of Prius is very narrow (50∼55%), i.e, the battery is cautiously utilized.

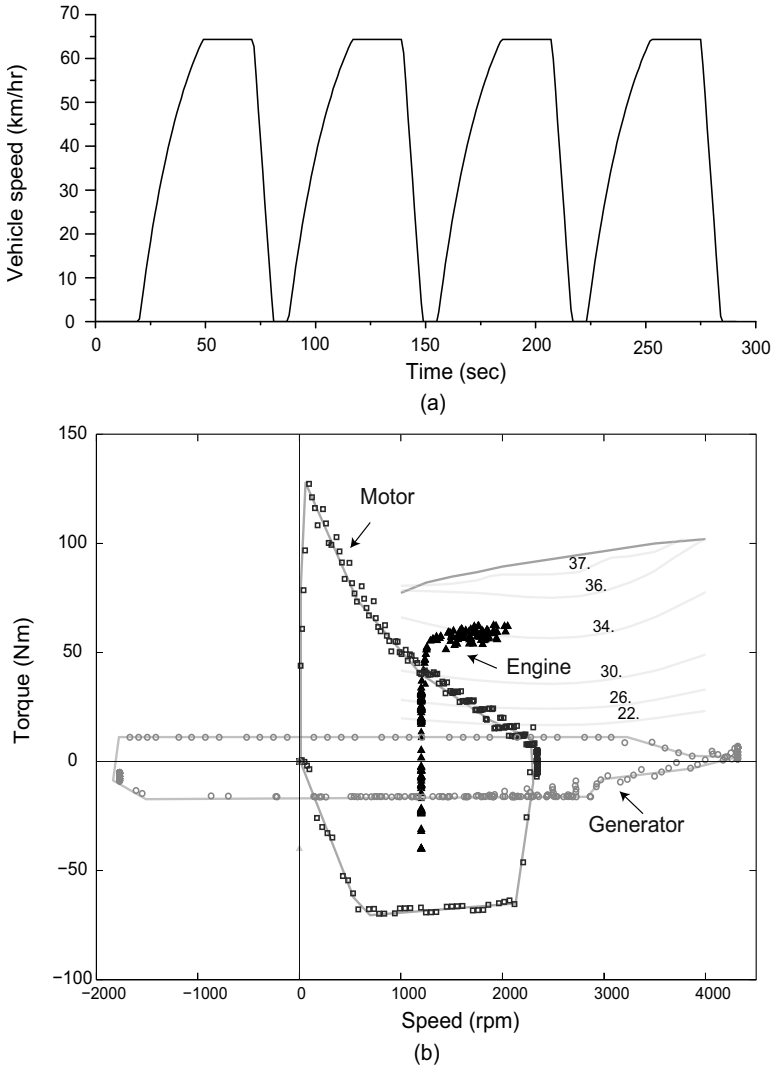

Figure 12.19: Operating points loci of Prius II engine, motor, and generator for a simple driving cycle.

12.6 Series Drive Train

The series drive train includes an ICE, a generator, batteries, and a motor. The engine is devoted to generating electric power by spinning the generator, and only the motor is responsible for satisfying varying power demands of stop-and-go driving. The generated electricity charges the battery, can power the motor directly, or both. Thus, the engine crank shaft is separated from the wheel axle, i.e., engine operation is decoupled from the widely varying power demands of wheels. Therefore, the engine can operate at the optimum efficiency. Specifically, the engine is controlled to either perform an optimal operation, or stop. The engine operates when the

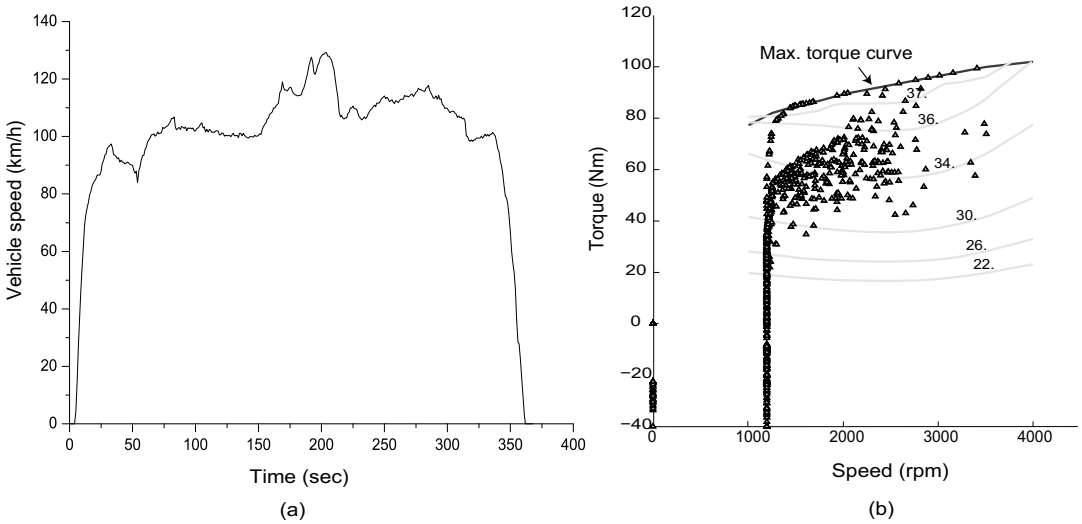

Figure 12.20: Engine operating points for a highway driving cycle (US06 HWY).

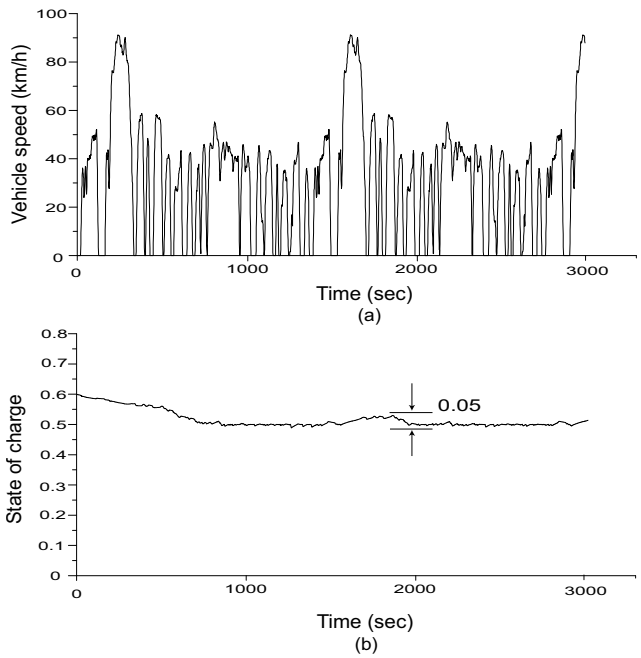

Figure 12.21: The SOC level change of Prius II during UDDS driving cycles: (a) EPA UDDS, (b) SOC.

battery SOC is lower than a predetermined level, or higher power is required from the power bus than the battery can supply. Furthermore, the drive train is simplest among different hybrid architectures since it does not require the use of a clutch, a

multi-speeds transmission, or a power split device. The series power-train topology is shown in Fig. 12.22.

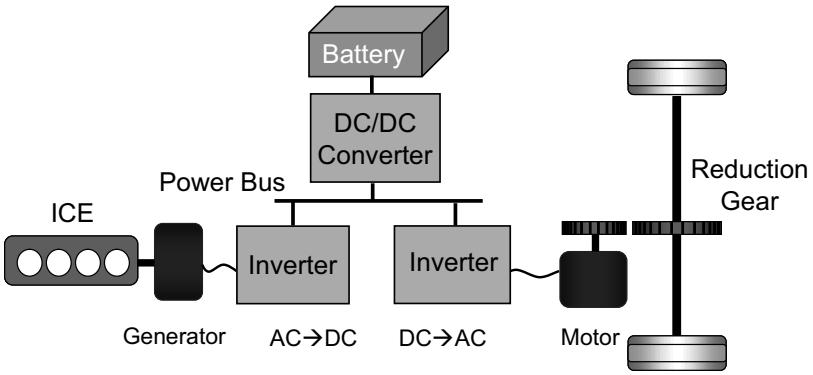

Figure 12.22: Series power-train topology.

One disadvantage of the series connection is that the drive train efficiency is low, since it includes multiple power conversion steps. Suppose that the motor and generator have 92% efficiency and that the inverter and converter have 97% efficiency. Then, the total efficiency, being the product of all efficiencies, is merely 80%. Furthermore, since the power units in the series path have the full power rating, the serial hybrid systems are known to be heavy, expensive, and bulky. Normally, the series drive trains have been used for heavy vehicles, such as buses, trucks, or locomotives. However, the engine size is typically smaller in series hybrid HEVs because it only has to meet the average driving power demand.

A big advantage of the series HEV is that it can be easily converted into a PHEV, if the battery capacity is increased and an on-board charger is attached. In such PHEVs, the ICE acts as a range extender. The series drive train has already been adopted as for a passenger vehicle. Chevrolet Volt is a typical example of series HEV.

Operation modes of the series power-train are classified as the engine on-off mode operation and the blended mode operation. In the engine on-off mode operation, the motor is driven solely by the battery power if the battery charge level is sufficiently high. It is called *EV mode* or *charge-depleting mode*. But the engine turns on when the SOC reaches a prescribed low limit. At this time, the engine operates at the most efficient operating point.

However, in the blended mode operation the engine turns on whenever the power demand from the drive-line exceeds the battery discharging capacity. That is, the engine cooperates with the battery to cover a peak load. It will be discussed again in the PHEV part of Chapter 13.

12.6.1 Simulation Results of Series Hybrids

A driving cycle simulation of a series HEV was performed using the simulation tool, "ADVISOR". In the simulation scenario, the vehicle mass with cargo was 1197kg, and GEO 1l (41kW) SI engine model was used. A 58kW PMSM motor model was adopted as a propulsion motor, and a lead acid battery model consisting of 25 modules with 307V nominal voltage, 3.5kWh capacity, 30kW peak power, and 120kg weight was used.

Fig. 12.23 (a) shows operation points of the motor in the torque-speed plane when the vehicle underwent the UDDS driving cycle. In contrast, Fig. 12.23 (b) shows the operation points when the vehicle underwent the US06 highway driving schedule. Obviously, operation points of the urbane driving cycle clustered in a low-speed area, whereas those of the highway driving are located in a high-speed area. However, differently from ICEs, the efficiency levels of electric motors are fairly even over the whole area. Looking at a typical EV motor efficiency map shown in Fig. 12.24, the motor efficiency ranges from 0.85 to 0.95 except some high-torque low-speed area.

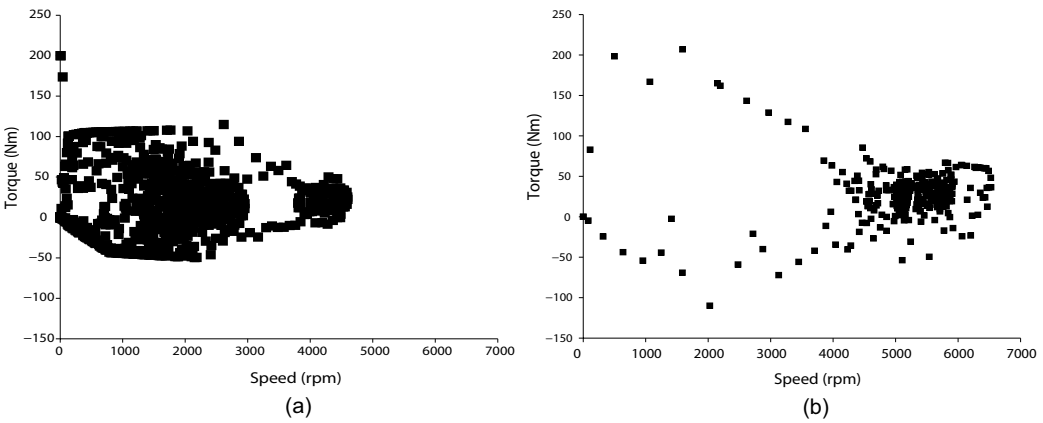

Figure 12.23: (a) Motor operation points for the UDDS and (b) for the US06 Hwy.

Fig. 12.25 shows a characteristic feature of the series hybrid power-train. It is a magnified view of an initial part of the UDDS. As the speed increases, the power requirement grows. Note that the maximum power rating of the battery is 30kW. However, the required peak power by motor is 40kW. Therefore, to make up the deficiency in power, the engine starts to operate at $t = 190$ sec. Fig. 12.25 (d) shows the corresponding operating point, (3300rpm, 58Nm). Note that the engine operates at a point of maximum efficiency (0.33 g/kWh). At this time, the engine power (20kW) is more than sufficient, so that the excess power is used for battery charging. Negative battery power shown in Fig. 12.25 (b) indicates the battery charging.

Fig. 12.26 (b) shows a SOC swing over two UDDS cycles. Note that SOC window is between 0.4 and 0.65, and charging/discharging repeats every 1400 seconds (23

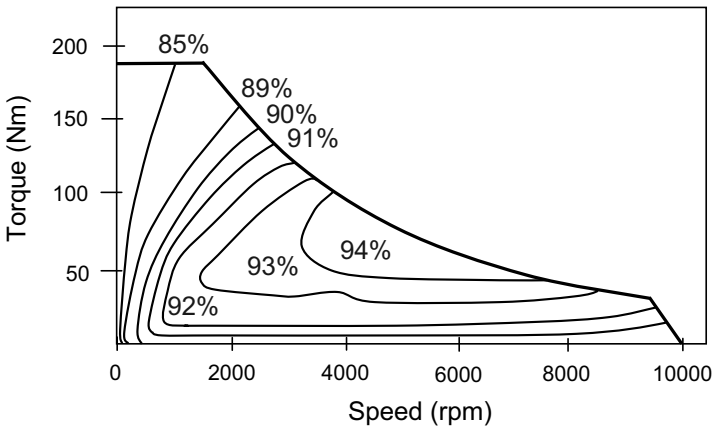

Figure 12.24: Typical EV motor torque-speed efficiency contours.

minutes). One can see from Fig. 12.26 that the engine operates when either power assist is required, or when the battery SOC low limit is reached. Power assist is needed at 190 seconds, and the battery SOC low limit is hit at 1220 seconds. But since the battery SOC high limit was hit at 1480 seconds, the engine stopped.

12.7 Parallel Drive Train

Fig. 12.27 shows the parallel hybrid power-train topology that is utilized in the Hyundai Avante. Generally both the engine and electric motor are coupled to the same drive shaft. Propulsion power to the wheels therefore may be supplied from the engine, the electric motor, or both.

Conceptually, the parallel HEV is inherently an ICE vehicle with electric assistance for lower emissions and fuel consumption. The electric motor can be used as a generator to charge the battery by regenerative braking or absorbing power from the engine when its output is greater than that required to drive the wheels. The parallel architecture does not require a separate full-size generator. Furthermore, the motor power rating is also fractional. For example, the Honda Insight has a 70kW engine, but the motor power rating is only 15kW. In this regard, the size and costs of the electric components of parallel HEVs are generally much less than those of series HEVs.

But since the speed ratio between motor and engine is fixed, the roles of the motor are limited. Honda hybrid cars (Insight, Civic, and Accord) utilize the parallel hybrid architecture.

Also, ICE alone and motor alone operations are feasible. To separate the ICE during the motor alone operation (all electric powering mode), another clutch is provided at the ICE side. However, the ICE and motor motions are not decoupled in general. The parallel assist strategy can be summarized as:

1) The motor alone propels the vehicle with the engine shut off in a low-

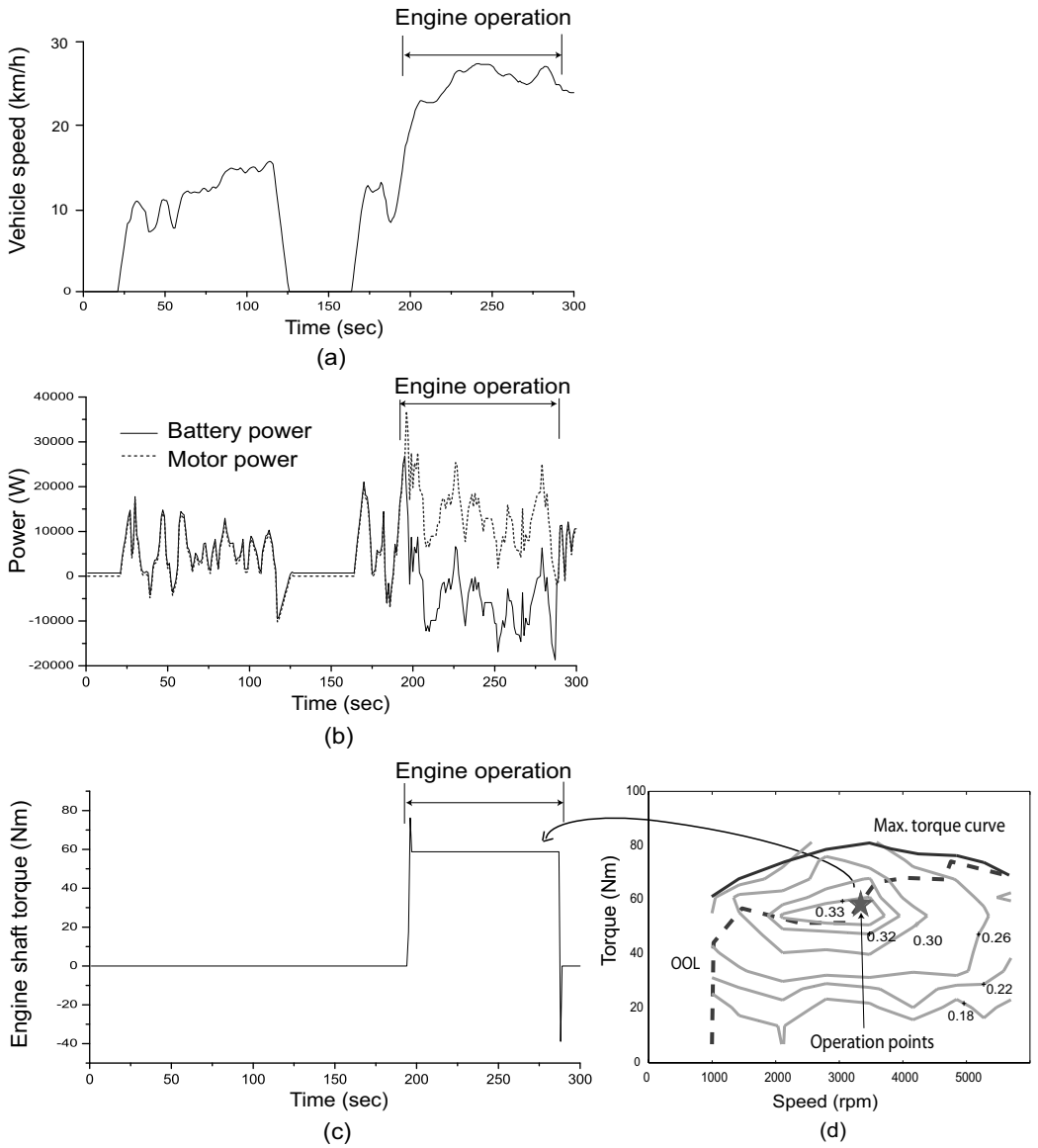

Figure 12.25: Engine involvement in a series HEV: (a) the UDDS driving cycle, (b) motor power and battery power, (c) engine shaft torque, and (d) engine operation point (GEO 1l, 41kW).

speed region, or in the region where the engine would run inefficiently.
2) The motor assists the engine if the required torque is larger than the maximum produceable by the engine.
3) The motor charges the batteries during regenerative braking.
4) When the battery SOC is low, the engine will provide excess torque to charge the battery.

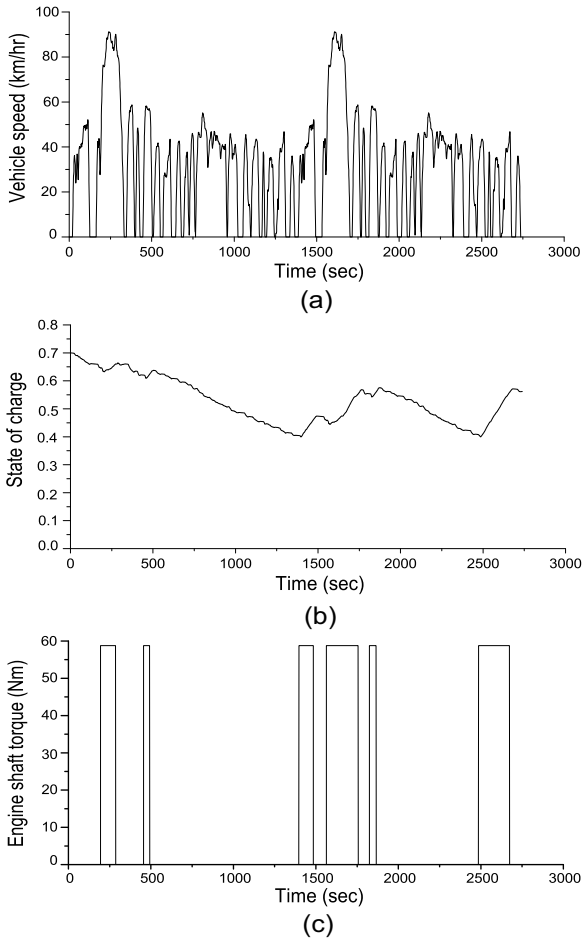

Figure 12.26: SOC swing and engine operation in a series HEV: (a) the UDDS driving cycle, (b) SOC change, and (c) engine shaft torque.

Fig. 12.28 shows a view of the parallel power-train of Hyundai Avante Hybrid. Fig. 12.29 shows an overall control block diagram of a parallel hybrid vehicle. The battery management system (BMS) monitors the cell voltages, temperature, and state of charge, and communicate with the power-control unit via CAN. It also regulates the cell voltages evenly to prevent excessive voltage unbalance. Through the use of a DC-DC converter, the main battery power is transferred to the 14-volt system where conventional electric loads are connected. The isolation is necessary for the safety of human and battery. A typical topology is the full bridge zero-voltage switching (ZVS) circuit. The power rating is 1.6∼2kW. The power-control unit (PCU) receives all necessary sensor signals required for PMSM control and outputs PWM gate signals. It also communicates with the engine controller via CAN. Engine power is controlled by adjusting the throttle angle, and the throttle

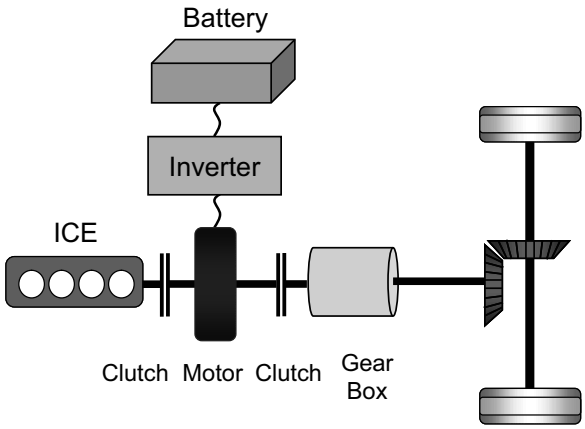

Figure 12.27: Parallel power-train architecture.

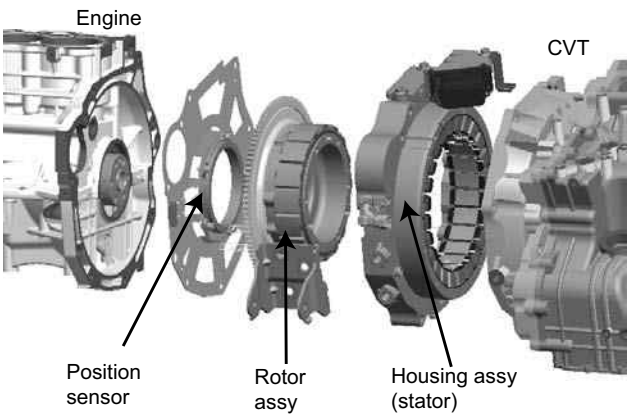

Figure 12.28: Parallel power-train of Hyundai Avante Hybrid.

position sensor (TPS) signal is also monitored by the PCU. Engine/motor shaft power is delivered to the drive wheels via the CVT. Engine control, motor control, and CVT control are coordinated in the PCU to optimize the overall fuel efficiency.

Fig. 12.30 shows the "ADVISOR" [18] simulation results for UDDS and US06Hwy driving cycles. Both engine and motor operation points are shown in a single map. The motor operates mostly in a low-torque region. Note that regenerations took place frequently in the urbane driving cycle. Obviously, engine operation points are widely spread compared with the cases of series and series/parallel hybrids.

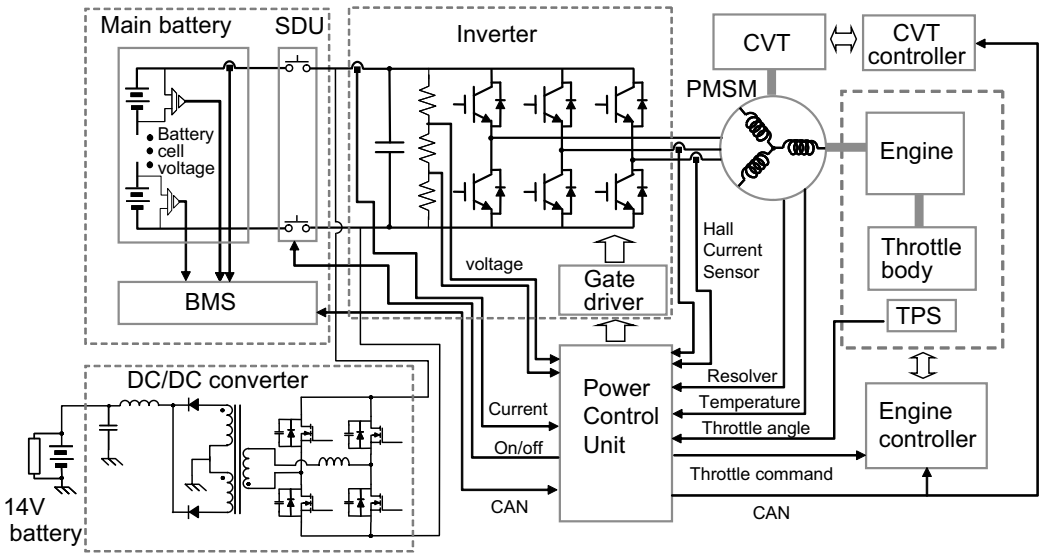

Figure 12.29: Overall control block diagram of a parallel hybrid vehicle.

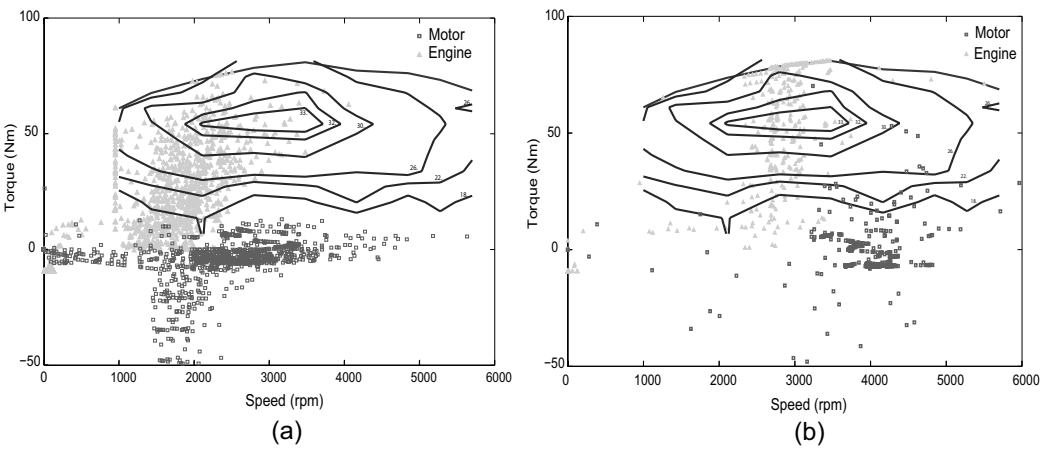

Figure 12.30: Engine and motor operating points of a parallel HEV for (a) UDDS and (b) US06Hwy driving cycles.

Bibliography

[1] K.T. Chau and Y.S. Wong, Overview of power management in hybrid electric vehicles, *Energy Conversion and Management*, Vol. 43 pp.1953 – 1968, 2002.

[2] C. C. Chan, The state of the art of electric, hybrid, and fuel cell vehicles, *Proceedings of IEEE*, Vol. 95, No. 4, pp.704 – 715, Apr. 2007.

[3] J. M. Miller, *Proportion Systems for Hybrid Vehicle,* IEE Power & Energy Series 4, IEEE, London, 2004.

[4] Toyota, Toyota Hybrid System THS II, *Brochure.*

[5] J. M. Miller, Hybrid electric vehicle propulsion system architectures of the e-CVT type, *IEEE Trans. on Power Electronics*, Vol. 21, No. 3, pp. 756 – 767, May 2006.

[6] J. Liu and H. Peng, Control optimization for a power-split hybrid vehicle in *Proceedings of the 2006 American Control Conference* Minneapolis, June, 2006.

[7] Y. Yu, H. Peng, Y. Gao, and Q. Wang, Parametric design of power-split HEV drive train, *IEEE Trans. on Power Electronics*, Vol. 21, No. 3, May 2006.

[8] Z. Chen and C. C. Mi, An adaptive online energy management controller for power-split HEV based on dynamic programming and fuzzy logic, *IEEE VPPC*, Dearborn, Michigan Sep. 2009.

[9] J. Liu, H. Peng and Z. Filipi, Modeling and Analysis of the Toyota Hybrid System *Proceedings of the 2005 IEEE/ASME International Conference on Advanced Intelligent Mechatronics*, Monterey, California, pp. 24 – 28, Jul. 2005.

[10] Y. Cheng, S. Cui, and C.C.Chan, Control strategies for an electric variable transmission based hybrid electric vehicle, *IEEE VPPC*, Dearborn, Michigan Sep. 2009.

[11] Y. Du et al., HEV system based on electric variable transmission, *IEEE VPPC*, Dearborn, Michigan Sep. 2009.

[12] R. Zanasi and F. Grossi, The POG technique for modeling planetary gears and hybrid automotive systems, *IEEE VPPC*, Dearborn, Michigan Sep. 2009.

[13] J. Liu and H. Peng Modeling and control of a power-split hybrid vehicle, *IEEE Trans. on Control Systems Technology*, Vol. 16, No. 6, pp. 1242 – 1251, Nov. 2008.

[14] K. Chen, et al., Comparison of two series-parallel hybrid electric vehicles focusing on control structures and operation modes, *IEEE Trans. on Control Systems Technology*, Vol. 16, No. 6, Nov. 2008.

[15] K. Muta, M. Yamazaki, and J. Tokieda, Development of new-generation hybrid system THS II - Drastic improvement of power performance and fuel economy, *Proc. of SAE World Congress* Detroit, Michigan, Mar., 2004.

[16] Y. Mizuno et al., Development of new hybrid transmission for compact-class vehicles, *Proc. of SAE*, Paper No. 2009-01-0726, 2009.

[17] M. Ehsani, Y. Gao, S.E. Gay, and A. Emadi, *Modern Electric, Hybrid Electric, and Fuel Cell Vehicle, Fundamentals, Theory, and Design*, CRC Press, London, 2004.

[18] AVL ADVISOR (Advanced Vehicle Simulator), www.avl.com.

Problems

12.1 Consider a planetary gear. Derive

$$\begin{aligned} T_c &= (1+k_p)T_s, \\ T_c &= \left(1+\frac{1}{k_p}\right)T_r. \end{aligned}$$

using

$$\begin{aligned} \omega_c &= \frac{1}{k_p+1}\omega_s + \frac{k_p}{k_p+1}\omega_r, \\ T_c &= T_r + T_s, \\ T_c\omega_c &= T_r\omega_r + T_s\omega_s. \end{aligned}$$

12.2 Consider a planetary gear system, shown in Fig. 12.31. For the carrier, the dynamics is represented by

$$T_{en} - (J_{carr} + J_{en})\dot{\omega}_c = T_{sun} + T_{ring}.$$

Derive the rest of equations for the sun and ring.

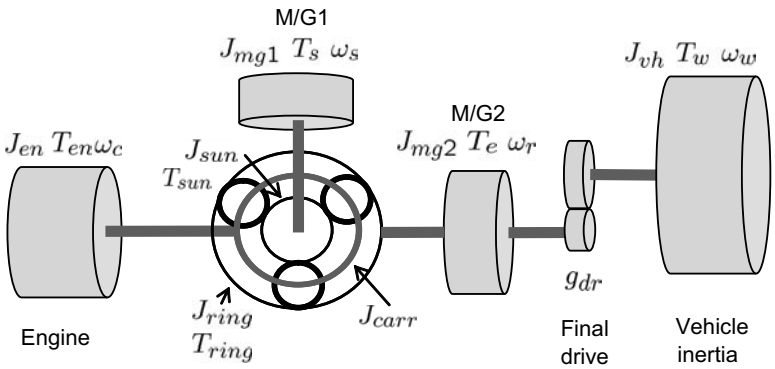

Figure 12.31: A planetary gear system (Problem 12.2).

12.3 Consider the engine torque-speed chart shown in Fig. 12.10. The motor speed is fixed at 280 rad/sec.

a) Obtain the generator speed, ω_s so that the engine operation point moves to (1750 rpm, 82 Nm).
b) Calculate the generator power.

12.4 (Normal driving mode : Low load) Assume that a series/parall HEV of the THS type runs at 80km/h against load road of 270 N. The gear ratio of the drive-line is $g_{dr} = 4.1$ and the effective tire rolling radius is $r_w = 0.29$. The engine speed and torque are regulated at $(T_{en}, \omega_{en}) = (84\text{Nm}, 150\text{rad/sec})$ while the generator torque is 24Nm. Assume that the M/G and inverter efficiencies are 0.92 and 0.97, respectively, and that the efficiency of the final drive is $\eta_f = 0.82$.

a) Calculate the motor speed when the wheel slip is $s_x = 0.1$.
b) Determine the generator speed and draw the lever diagram.
c) Calculate the power that should be provided by the motor.
d) Calculate the battery charging power.

12.5 Consider a series HEV drive train. Assume that 15kW power is being used by the drive-line while the engine operates with the full throttle at (60 Nm, 3400 rpm). The battery voltage is 307 V. Calculate the battery charging current when the efficiencies of motor and generator are 0.92 and those of their inverters are 0.97.

Chapter 13

Battery EVs and PHEVs

Future vehicles will be powered by cleaner and more efficient energy conversion systems. Since the oil price has been shown to fluctuate dramatically in recent years, there are many incentives to switch to a new alternative fuel. Further, considering the depletion rate of the world's oil resources, it is difficult to predict the available oil quantities as a fuel for vehicles beyond 50 years. Another motivation for advanced vehicular technologies is environmental concerns. Recently, CO_2 has been drawing special attention since it is known that cumulative CO_2 increase causes the greenhouse effects leading to global warming. To achieve stabilization of greenhouse gas (GHG) concentrations in the atmosphere, the Kyoto Protocol was established in June 1992 and entered into force on 16 February 2005. Under Kyoto, industrialized countries agreed to reduce their collective greenhouse gas emissions by 5.2% compared to the year 1990. Transportation is responsible for around 20% of the total CO_2 emissions. European automobile manufacturers' association (ACEA) set the CO_2 regulation target that would reduce average car emissions down to 130 grammes CO_2/km by 2012. With emissions regulations tightening, car manufacturers have begun to develop vehicles with alternative power sources.

13.1 Electric Vehicles Batteries

Zero emission vehicles (ZEV) are inevitable for car manufacturers to satisfy the ACEA 2020 commission target level of 95gCO_2/km. Battery electric vehicles (BEV) and hydrogen vehicles are regarded as feasible ZEV solutions. But hydrogen vehicles require infrastructures for creating, distributing, and storing hydrogen, which is costly. Thus, most players conclude that hydrogen power-trains will not be available in a foreseeable future, i.e., before 2020 [15].

The key concern for BEVs is the availability of a battery that can provide an acceptable driving range with cost targets competitive with gasoline cars. Properties of high-power batteries and supercapacitors are summarized in Table 13.1.

Table 13.1: High power battery and ultracapcitor characteristics

Parameter	VRLA	NiMH	Li Ion	Ultracap
Nominal cell voltage (V)	2	1.2	3.6	1.8
Battery electrolyte	Acid	Alkaline	Organic	Organic
Specific energy (Wh/kg)	25	40	60-180	5
Specific power (W/kg,10sec)	400	1300	1500	>3000
Energy efficiency	Good	Moderate	Good	Very good
Thermal mng. requirements	Moderate	High	Moderate	Light

13.1.1 Battery Basics

Rechargeable batteries, in general, consist of negative electrode, positive electrode, electrolyte, and separator. During discharge, oxidation takes place at the negative electrode, yielding metallic ions and electrons. The ions dissolve into the electrolyte and migrate to the positive electrode, while the separated electrons are transferred to the positive electrode via an external circuit. At the positive electrode, the migrated metal ions combine with the transported electrons. The separator prevents the ohmic contact between cathode and anode material, but allows selective penetration for ions. The discharging procedure is illustrated in Fig. 13.1. The nominal voltage of a galvanic cell is fixed by the electrochemical characteristics of the active chemicals used in the cell.

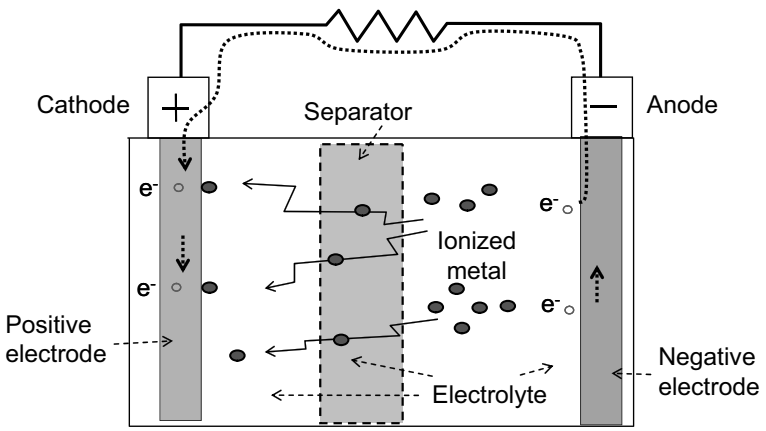

Figure 13.1: Battery schematic drawing.

The no-loss (open circuit) cell voltage is determined by the Nernst potential. Fig. 13.2 shows a typical bipolar curve of a cell. The actual cell voltage appearing at the terminals depends on the load current. The voltage drop from the no-loss cell voltage is counted as the loss. In the low current region, the activation loss is dominant. The activation loss is an intrinsic electrochemical property of electrode, and its magnitude is predicted by Tafle's empirical equation.

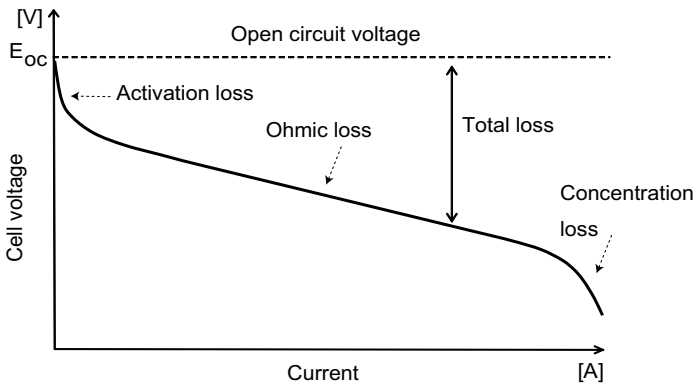

Figure 13.2: Polarization curve.

The ohmic loss due to the internal impedance increases linearly as the current density increases. The internal impedance is mainly affected by the physical characteristics of the electrolyte. Finally, the concentration loss prevails in the high current region.

13.1.2 Lithium-Ion Batteries

Since the commercial release of the Li-ion battery in 1991, lithium-ion battery technology has progressed significantly in safety, power, and energy densities. A typical lithium-ion battery structure is shown in Fig. 13.3. Most commonly, the anode is made from carbon (graphite) containing lithium-ions. This replaces metallic lithium anode, which causes severe safety issues. Layered oxide materials with porous structure are used as cathode material. Common lithium-ion battery electrolytes are derived solutions of $LiPF_6$ salt in a solvent blend of ethylene carbonate and other various carbonates such as dimethyl carbonate [5]. Metal current collectors (copper at anode and aluminum at cathode) press the electrode materials providing low resistance conductive paths.

Electro chemistry of lithium-ion cell is

$$\mathrm{LiCoO_2} \rightleftharpoons \mathrm{Li_{1-x}CoO_2 + xLi^+ + xe^-} \tag{13.1}$$

$$\mathrm{xLi^+ + xe^- + 6C} \rightleftharpoons \mathrm{Li_xC_6}, \tag{13.2}$$

where (13.1) is the cathode reaction, and (13.2) is the anode reaction. Note that the left-hand side direction indicates discharging operation. Therefore, the overall reaction is

$$\mathrm{LiCoO_2 + 6C} \rightleftharpoons \mathrm{Li_{1-x}CoO_2 + Li_xC_6}. \tag{13.3}$$

During discharge, lithium-ions are dissociated from the anode and migrate across the electrolyte and are inserted into the crystal structure of the cathode. At the same

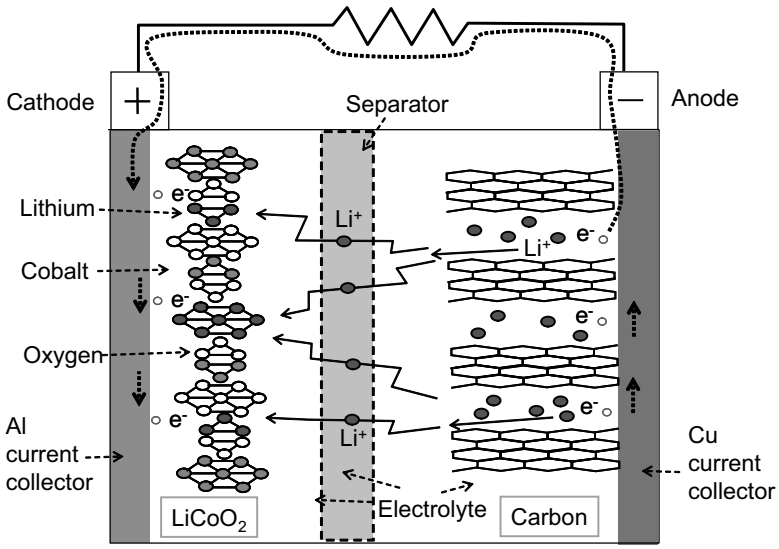

Figure 13.3: Li-ion battery.

time the compensating electrons travel in the external circuit and are accepted by the cathode to balance the reaction. The process is completely reversible [2].

Lots of efforts were made to reduce or substitute the use of expensive cobalt in the cathode fabrication. Four different cathode chemistries are being considered by the industry: $Li(Ni, Co)O_2$, $Li(Ni, Co, Mn)O_2$, $LiMn_2O_4$, and $LiFePO_4$. The layered nickel cobalt oxide, $Li(Ni, Co)O_2$, has the highest energy density, but is not safe. The manganese spinel, $LiMn_2O_4$, is relatively safe and has a high-power density, but the energy density is low. The iron phosphate, $LiFePO_4$, is completely stable since it shows no exothermal behavior in charged state [6]. Further, the lithium iron phosphate battery has longer life time and high peak power rating compared with other lithium-ion batteries. But the conductivity is low, thereby the energy density is the lowest.

A123Systems claimed that their proprietary nanostructure increased the surface area of electrodes 100 times, thereby the energy and power densities of their battery were improved significantly [4]. The properties of some cathode materials are shown in Table 13.2.

13.1.3 High-Energy versus High-Power Batteries

Battery designs can be optimized for high-capacity or high-power rating. For example, in BEV applications, the driving range per charge is most important, so that high-capacity batteries are required for BEVs. HEVs, on the other hand, require high-power ratings. The battery requirements are summarized in Table 13.3. As the battery dependence increases (HEV→PHEV→BEV), the vehicle requires higher energy density and larger depth of discharge.

Table 13.2: Properties of cathode materials for lithium-ion battery

Layered Oxide	
$LiCoO_2$	used in most lithium batteries high-performance, high stability high price due to Co active material limited safety
$LiNiO_2$	high capacity advantageous in price bad safety
Spinel Structured Oxide	
$LiMn_2O_4$	highly safe low cost active material Mn dissolution, unstable structure short life time especially in high temperature
Lithium Metal Phosphate with Ovline Structure	
$LiFePO_4$	very low cost superior safety long life time due to stable structure low energy density due to low discharge voltage (3.4V) low power capacity due to low conductivity

In the cell construction, the design trade-offs are involved. Fig. 13.4 shows a schematic view comparing high-power density with high energy density batteries. Note that high energy batteries utilize thick electrodes, whereas high-power batteries utilize thin electrodes. Thus, high-power batteries, retaining larger surface area under the same volume, react fast at high-power demands. But, they have lower energy density since current collectors and separators take relatively larger volume proportion.

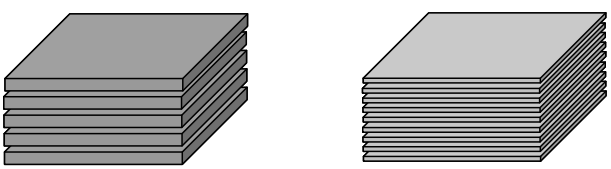

Figure 13.4: Battery structures: (a) energy (intensified) battery and (b) power (intensified) battery.

The specific energy (SE) and specific power (SP) of batteries are depicted in Fig. 13.5. The bottom labels denote product names of Saft batteries (www.saftbatteries.com). It shows that the energy density is traded with the power

Table 13.3: Battery requirements for passenger vehicles.

	Mild HEV	Full HEV	PHEV	BEV
Key performance	High power	High power	Mid-power and energy	High energy
Life time	15 years	15 years	> 8 years	> 8 years
Pack voltage	42-144V	> 144V	> 200V	> 330V
Power	5-10 kW	25-75 kW	25-100 kW	50-100 kW
Battery capacity	<1 kWh	1-2 kWh	4-15 kWh	40-100 kWh
SOC window	5%	5-20%	20-60%	20-80%
Chemistry	NiMH, Li-ion	Li-ion	Li-ion	Li-ion

density. For example, $LiFePO_4$ batteries can be designed to have either SE=180Wh/kg, SP=174W/kg or SE=54Wh/kg, SP=4375W/kg.

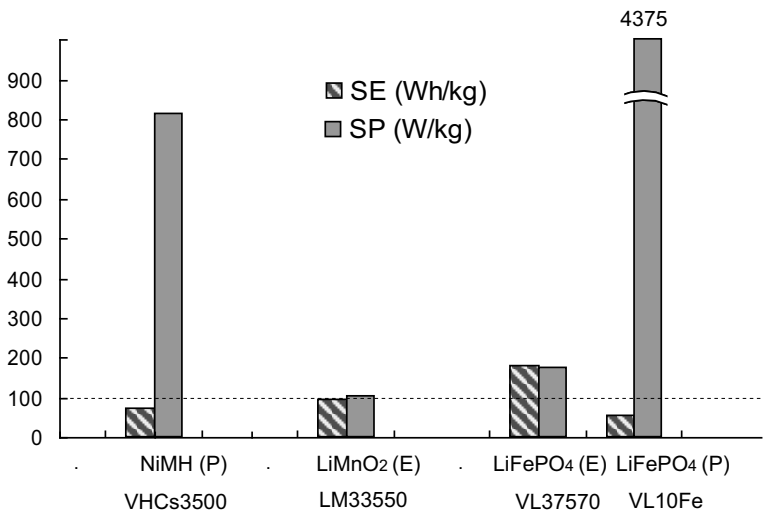

Figure 13.5: SP and SE of batteries. (E): energy intensified and (P): power intensified.

13.1.4 Discharge Characteristics

The discharge characteristics depend on temperature, discharge rate (current), and the age of the cell. Fig. 13.6 (a) and (b) show typical discharge curves for different currents and temperatures. After initial quick voltage drop, the voltage level maintains a fairly constant level. But, as the charge empties out, the voltage drops drastically. End of discharge voltage (EDV) is defined as the minimal voltage acceptable for a battery, and battery capacity, Q_{max} is defined as the total charge when the battery voltage drops to EDV.

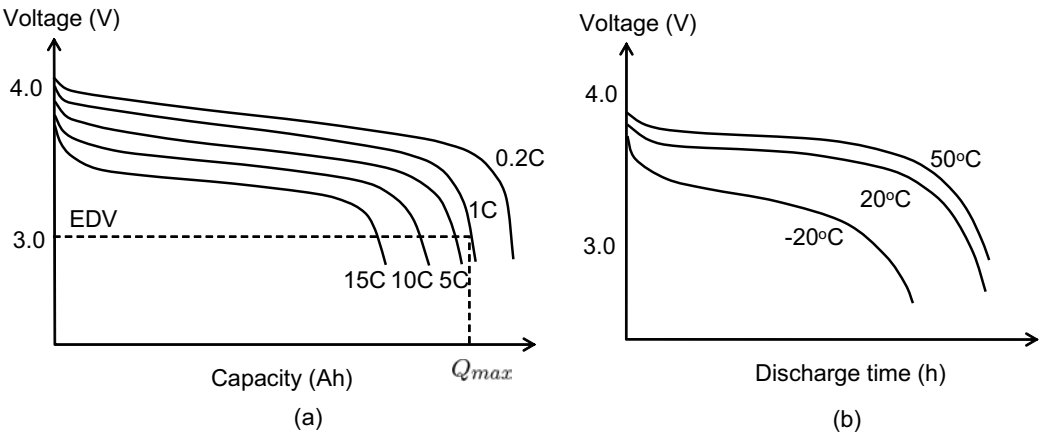

Figure 13.6: Battery discharge characteristics under (a) different discharging rates (currents) and (b) different temperatures.

Dependence on Current Magnitude

Fig. 13.6 (a) shows the voltage drop as the cell discharge proceeds. However, the drop curves are different depending on the discharge rate. Discharge rate is defined to be 1C if a fully charged battery depletes the total capacity in an hour. For example, 1C rate of a 2000mAh battery is equal to 2000mA. According to a simple calculation, it should take five hours if a battery depletes in 0.2C rate. However, the effective capacity is increased more if discharge takes place over a long period with a low C rate (0.2C). Conversely, if discharge current is high, the effective capacity falls off dramatically. It is mainly due to the internal resistance since the battery operation is accompanied by the Joule loss, I^2R.

Dependence on Temperature

Fig. 13.6 (b) shows the cell voltage variation with temperatures. The lithium-ion battery performance declines steeply as the operating temperature dips below $-10°$C. At a low extreme temperature, the electrolyte may freeze. Thus, EV cold starting is a problem in a very cold region. The reasons for poor performance are: Electrolytes tend to be highly viscous and the reaction rate drops at low temperatures. But once battery operation starts, the Joule losses, I^2R heats up the battery cell. It is called *battery self heating*. As the temperature increases, the resistance of the electrolyte decreases and the reaction rate increases. These synergic effects accelerate the exothermic electrode reaction, which, in turn, escalates the temperature.

At high temperatures, the electrode reaction rate and ion mobility are high. But unwanted self-discharge rate also high with temperature. Furthermore, the active chemicals expand causing the cell structural changes at high temperatures. More seriously, the anion, PF_6^-, of electrolyte is unstable above 60°C. It leads to a rapid degradation of the electrode material. The operation temperature window of

lithium-ion batteries is 0∼ 20°C [11].

Overcharging Problem

The level of current flowing into the battery during charging is controlled by the electrical battery charging system and may well exceed the natural redox reaction capacity of the battery cell electrodes. The imposition of excess current results in electrolysis of the aqueous electrolyte away from the electrodes. This electrolysis frees gaseous oxygen which reduces the effective electrode surface area. It also causes a pressure buildup that may result in leakage of oxygen gas and aqueous electrolyte solution [13]. Further, the overcharging causes a temperature hike and may lead to an explosion.

13.1.5 State of Charge

The state of charge (SOC) is defined as the available capacity expressed as a percentage of some reference. The SOC is written as

$$SoC(t) = \frac{Q_{max} - \int_{t_0}^{t} i(t)dt}{Q_{max}} \times 100. \tag{13.4}$$

The SOC measurement is particularly important in EV applications, since it indicates how farther the vehicle can go. One SOC estimation method is to use the voltage level of the battery cell. But this method is useful when the voltage versus SOC has a certain steepness. Unfortunately, this method cannot be applied for lithium-ion batteries, since they have fairly flat discharge curves. Other method is to take the integral of current over time according to (13.4). This method, known as Coulomb counting, provides higher accuracy than most other SOC measurements since it measures the charge flow directly [2].

13.1.6 Peukert's Equation

The Peukert's equation gives a relation between the discharge current and the cut off time:

$$C_k = t_{cut} I^n, \tag{13.5}$$

where C_k is a constant representing the theoretical capacity of the battery, n is also an intrinsic constant of the battery called the Peukert's number, I is the discharging current, and t_{cut} is the cut off time (time of discharge) expressed in hours. The Peukert's equation is an empirical formula showing the battery performance under constant discharge currents. Note that $n \approx 1.3 - 1.4$ for lead acid batteries and $n \approx 0.95$ for lithium batteries [4]. The higher n, the more capacity is lost during high current discharge. Two constants $\log C_k$ and n satisfy a linear relationship:

$$\log_{10} C_k = \log_{10} t_{cut} + n \log_{10} I. \tag{13.6}$$

Thus, it is used for determining n and C_k from experimental data.

Exercise 13.1
When a fully charged battery dissipated energy at a constant rate, $I = 80$A, the cut off time was 2h. The same experiment was done but with a different load current, $I = 20$A. At this time the cut off time was 9h. Find n and C_k.

Solution

$$\begin{aligned} \log_{10} C_k &= \log_{10}(2) + n \log_{10} 80 \\ \log_{10} C_k &= \log_{10}(9) + n \log_{10} 20. \end{aligned}$$

Thus, $n = 1.085$, $\log_{10} C_k = 2.365$, and $C_k = 232$Ah. ■

13.1.7 Ragone Plot

Ragone plot shows the energy storage capacity of an energy storage device for constant active power request. Fig. 13.7 shows a Ragone plot for various types of batteries and supercapacitors, in which the vertical axis represents the specific power (W/kg) and the horizontal axis the specific energy (Wh/kg) in the log scale. Two extreme points, A and B, may be explained with water storage tanks with different orifices. The former has a large orifice, but the tank size is small. On the other hand, the latter can store a large volume of water. But since the orifice is small, a large amount of water cannot be filled or drained in a short time. Capacitors are typical high-power and low energy density devices.

For BEV applications, the specific energy is obviously important for a large driving range. However, the specific power is particularly important in HEVs since the required vehicle power is peaky. Hence, a parallel use of battery and supercap is sometimes recommended. Based on the Ragone plot shown in Fig. 13.7, the lithium-ion batteries are superior to the others both in the energy and power densities.

13.1.8 Automotive Applications

A typical small electric car will use 90∼160Wh per kilo meter on the average. Thus, to drive 160km at a rate of 125Wh/km, a 20kWh battery will be required. As of now, the battery cost is about 1,000 US$/kWh including cooling and management systems on a small scale order. Then, the total battery package cost would be 20,000US$ for 20kWh capacity. This cost barrier is a major impediment that retards the EV spread on the market. On the other hand, in an automotive application, the batteries are under harsh environments. Other than vibration and wide temperature range, the discharging/charging current pattern is wild and peaky: The current demands are very high during hard acceleration or hill climbing, whereas

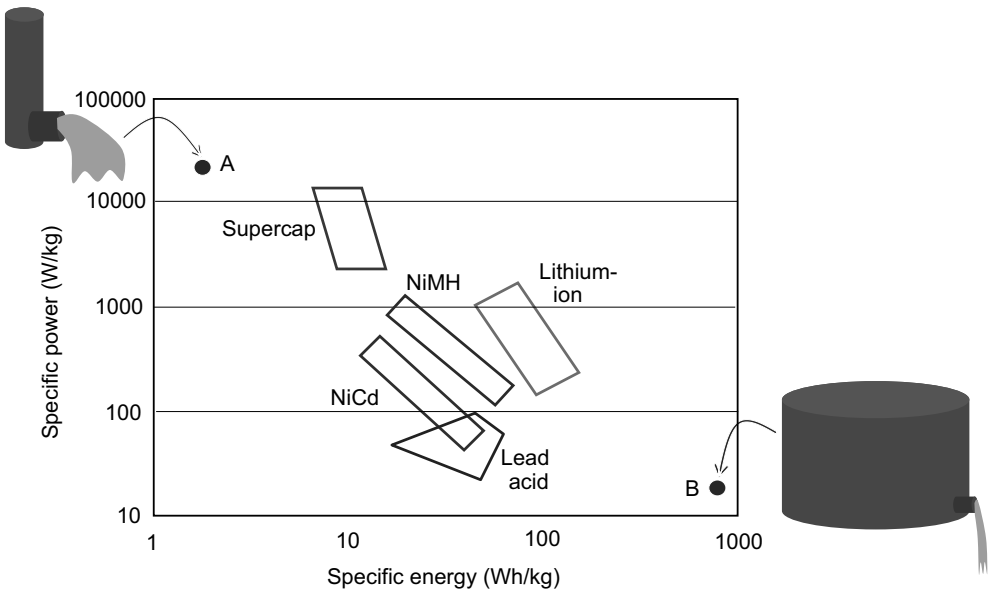

Figure 13.7: Ragone plot of batteries.

almost no current is necessary during coasting. Conversely, to accommodate a high acceptance of regenerating power, the battery charging current rate should be high correspondingly.

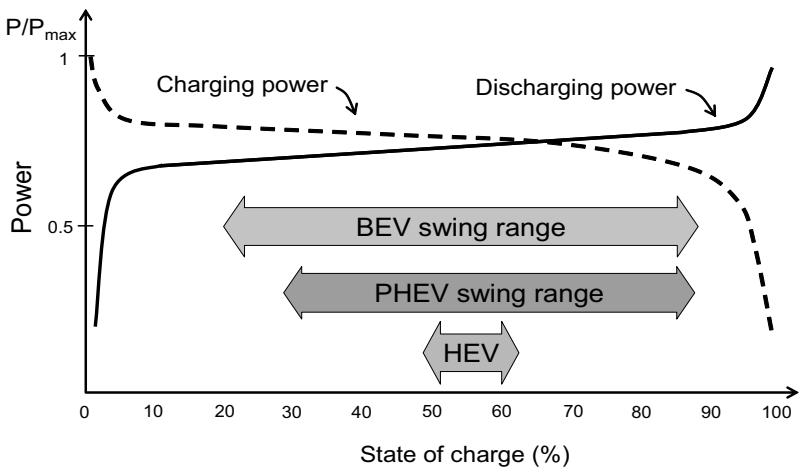

Figure 13.8: Charging and discharging power versus SOC.

Fig. 13.8 shows the charging and discharging rates versus SOC. The acceptance capability of charging power drops drastically above 80%, so that it takes a very long time to charge beyond 80%. Further, special care has to be taken not to overcharge a cell in a high SOC range.

Note also that the discharging power decreases steadily as the SOC level reduces,

and it drops drastically below 10% SOC. The lithium-ion batteries should not be discharged below 2.5V cell voltage, under which the cathode breaks down and the copper current collector is dissolved into the electrolyte [2]. Thus, if a battery is depleted to below a minimum point, then the life time shortens drastically.

The SOC swing range of HEVs is managed to be very shallow in order to satisfy the required specifications regarding the battery life time. But deep charge-discharge cycles are inevitable in the BEVs. The BEVs' SOC ranges from 20% to 90%. In the case of PHEVs, the SOC range is 30 to 90%.

13.2 BEV and PHEV

For all these progresses, battery package costs are still too high (US$1,000/kWh), and energy density is still too low (80∼100Wh/kg) for vehicle applications. Therefore, the battery takes a dominant portion in the cost of the electric power-train. For example, the battery takes about 47% in the cost of electric power-train of HEVs. In the BEVs, the battery proportion is larger than triple times the rest in the components cost breakdown. The PHEVs are functionally the same as BEVs when the daily driving pattern is restricted to a commuting range and the battery is recharged overnight. Therefore, availability of a robust battery at a competitive price remains a big challenge for the market spread of PHEVs and BEVs. Even in the year 2020, no BEV is expected to have the same driving range as ICE cars. Thereby, the BEV use will be limited to city or near-city driving [15].

Characteristics of HEV, PHEV, and BEV are summarized in Table 13.4. A main differences is that HEVs utilize power (intensified) batteries, whereas PHEVs and BEVs energy (intensified) batteries.

Table 13.4: Characteristics of HEV, PHEV and HEV.

	HEV	PHEV	BEV
Battery capacity	small (1kWh)	large (∼16kWh)	very large (16∼20kWh)
All electric range	very small	sizable distance (16∼64km)	entire range (160∼200km)
Power/energy battery	power battery (1500∼3000W/kg)	energy battery (150Wh/kg)	energy battery (150Wh/kg)
On-board charger	no	yes	yes

According to the USA VMT study results [14], 60% of American drivers' daily driving range is less than 60 miles. Considering the EV milage of 90∼160Wh/km, a typical energy estimate used daily by a BEV is about 15kWh. Regarding the utility rate as 11 cents per kWh, the EV's electricity cost would be less than two dollars a day. Since the electric energy cost is much lower than the corresponding gas cost,

the vehicle operation cost reduces as the AER expands. But due to the battery, the up-front cost of a BEV is a burden to customers and it increases as the AER grows.

13.3 BEVs

Fig. 13.9 shows a schematic block diagram of a BEV. The power-train consists of a pack of a battery, an inverter, a battery charger, and a propulsion motor. Also, it contains a DC to DC converter to provide power to a 14-volt DC bus for powering conventional electric loads such as lights, wipers, power windows, and fans.

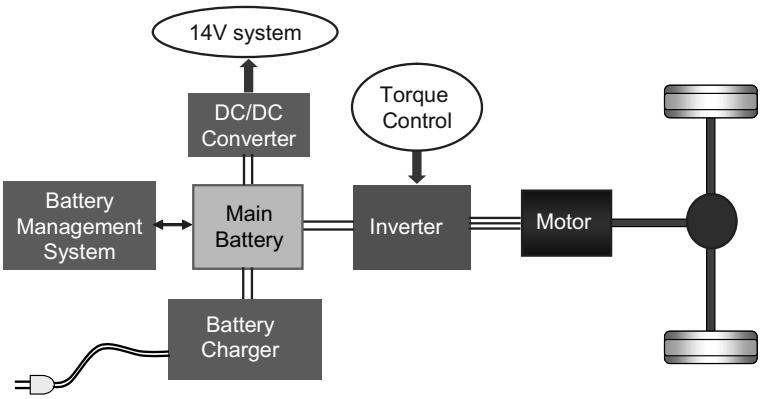

Figure 13.9: BEV block diagram.

To economize the cable size, a trend is to increase the battery voltage. In the passenger EVs, the continuous current rating is normally less than 200A to reduce the size and cost of cable, sockets, and terminals [4]. For example, a 200A cable should be used to deliver 60kW power if the battery voltage is 300V.

BEVs have a 3kW on-board charger for home charging. Since the BEV battery capacity is 16 $\sim$ 20kWh and the maximum power rating of household electricity is about 3kW, it takes 6 $\sim$ 7 hours to fully charge a BEV battery at home. BEVs can be recharged from the grid overnight when the overall electric demand is at its lowest. Further, BEVs have an extra receptacle for a fast charge (16 $\sim$ 32kW) at a charging station. Since there is no engine and transmission, the structure of the power-train is simple compared with HEVs.

Further, the battery's internal resistance increases as the charging-discharging cycle repeats. Normal battery life time is 1000$\sim$2000 cycles in the case of deep discharge. Therefore, if they are utilized on a once-a-day charge-discharge cycle, most current batteries would be replaced within five years. This expensive replacement offsets the advantages of using low-cost energy source (electricity). Therefore, the battery life and cost are the key issues in accelerating the market penetration of the commercial BEVs.

13.3.1 Battery Capacity and Driving Range

For a BEV to be acceptable in the market, the driving range needs to be 300 km per charge with a battery life of 10 years. Adding more battery packs is not the way of extending the EV driving range, since increasing battery weights adds more vehicle load. This is illustrated with a simple example: Consider a BEV with the following parameters: curb mass without a battery : 980kg, drag coefficient (C_d) : 0.308, rolling resistance (f_r) : 0.009, frontal area (A_F) : 2.22m^2, accessory electric load (P_{el}) : 700W.

We calculate the driving range with different battery capacities (weights) with the assumption that the vehicle runs at a constant speed, V_x=60km/h. The driving range is calculated according to

$$\begin{aligned} d_x &= V_x \times \frac{E_b}{P}, \\ P &= \left(m_v g f_r + \frac{\rho C_d A_F}{2} V_x^2 + m_v g \sin\alpha \right) V_x + P_{el}\,, \end{aligned}$$

where E_b is the usable battery capacity. Computed results are plotted in Fig. 13.10, where the battery capacity is scaled linearly with the battery modules (200kg, 16kWh). It is obvious that the travel distance is not proportional to the battery capacity, since the battery weight, correspondingly the rolling resistance and gravity, increases.

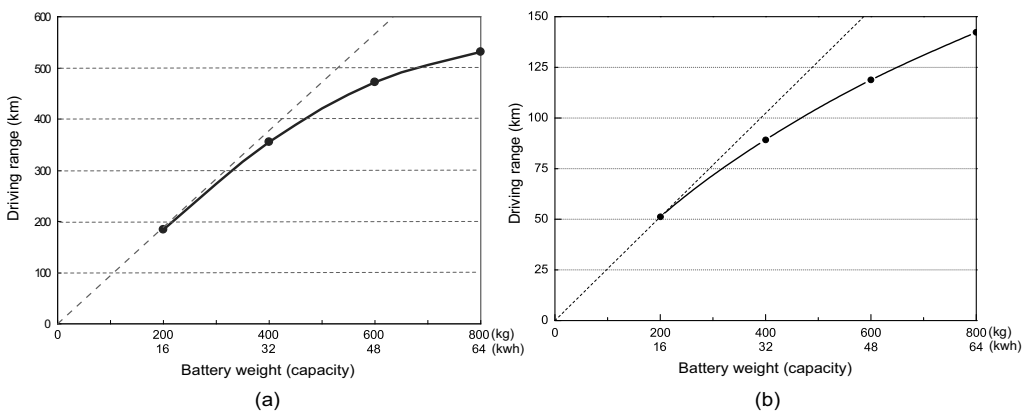

Figure 13.10: Driving range for different number of battery units: (a) zero grade and (b) 7.5% grade.

In midsize cars, it is not easy to accommodate a battery whose weight is higher than 200kg. Additionally, cost and space are other discouraging factors for the battery capacity increase. Hence, a fundamental solution for the driving range extension is to increase the battery energy density. Fig. 13.11 shows an expectation on the energy density growth of Li-ion battery and the corresponding range extension

[15]. This says that the battery energy density will be doubled by 2020, and the battery capacity will be tripled so that driving range will be extended to 300 km. However, the battery weights remain around 200 kg. According to the California Air Resources Board, the target specifications of EV batteries are:

Life time : 10years,
Total mileage: 240,000km,
Number of charging/discharging: 5000 cycles,
Target price: US$300/kWh.

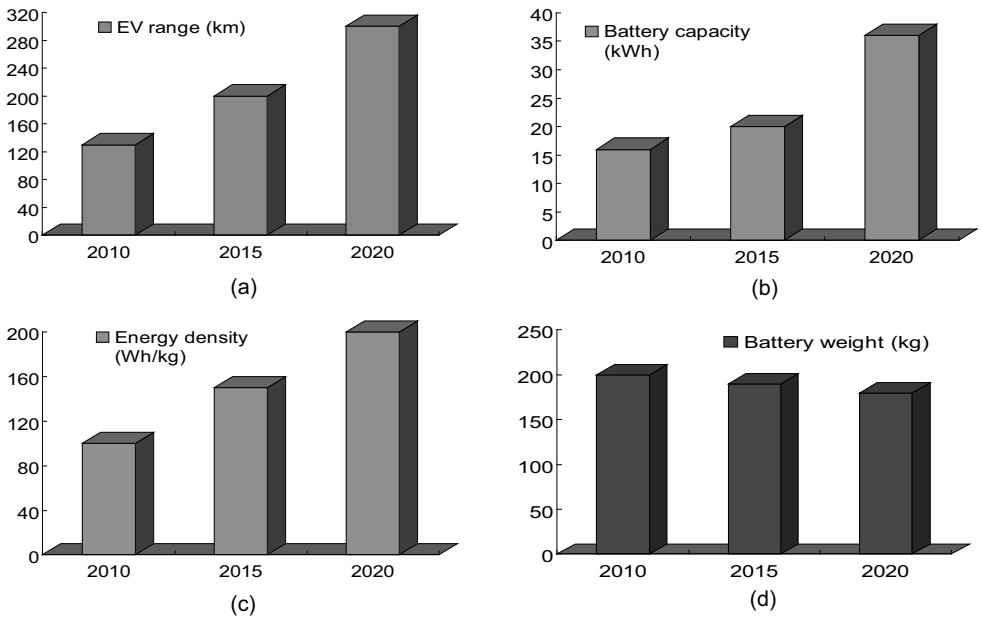

Figure 13.11: Expectation on the energy density growth of Li-ion battery and the range extension: (a) EV range, (b) battery capacity, (c) energy density, and (d) battery weight.

13.3.2 BEVs on the Market

There were many EV development programs. EV1 was developed by GM under the collaboration with Hughes and produced in 1997 with lead-acid battery. The second model was released with nickel metal hydride battery in 1999. But the EV1 program was terminated in 2003. Among many reasons for the short termination of EV1, poor driving range, long charging times, and a complex infrastructure of chargers were the main technical problems.

Mitsubishi announced an EV named "MiEV" which will be commercially available in world market in 2010 [10]. By plug-in charge at home, it takes 7 hours. But at a charging station, it takes 30 minutes for 80% charging. Toyota plans to launch an urban commuter BEV by 2012. Toyota's FT-EV is targeted to an urban dweller, driving up to 50 miles between home, work and other forms of public transportation. Tesla Roadster is a sports car-type BEV. It utilizes an induction motor, which has a better efficiency in the high-speed region. Specifications of MiEV and Roadster are summarized in Table 13.5.

Table 13.5: Major specifications of Mitsubishi's MiEV and Tesla Roadster

Maker	Mitsubishi Motors (MiEV)	Tesla Motors (Roadster)
Vehicle dimension	3395×1475×1600 mm	3946×1851×1126 mm
Curb weight	1080 kg	1238 kg
No. of passengers	4 persons	2 persons
Max. speed	130 km/hr	200 km/hr
Max. driving range/charge	160 km	350 km
Motor type	PMAC	Induction
Max. power	47 kW	185 kW
Max. torque	180 Nm	375 Nm
Driving	rear wheels	rear wheels
Battery type	Li-Ion	Li-Ion
Battery voltage (peak)	330 V	370 V
Battery capacity	16 kWh	53 kWh
Battery weight	157 kg	450 kg
Charging time (at station)	0.5 hrs	3.5 hrs

13.4 Plug-In Hybrid Electric Vehicles

The operation mode of PHEVs and BEVs is characterized by a deep cycling between full charge and intense depletion. The depth of depletion ranges 70∼80%. Therefore, the batteries should be robust against deep discharge and tolerable to a high number of charge/discharge cycles.

Fig. 13.12 shows the fuel consumption versus travel distance. The PHEV depletes the battery energy first. Once the SOC decreases down to the predetermined level, then the power source is switched to the ICE. The benefit of PHEV is apparent when the driving range is short. With a PHEV 40 a driver is not supposed to use a drop of fuel if the daily mileage is less than 40 miles. Many studies show that the use of PHEVs will reduce the fuel consumption significantly, contributing to reducing the petroleum import and the GHG emission.

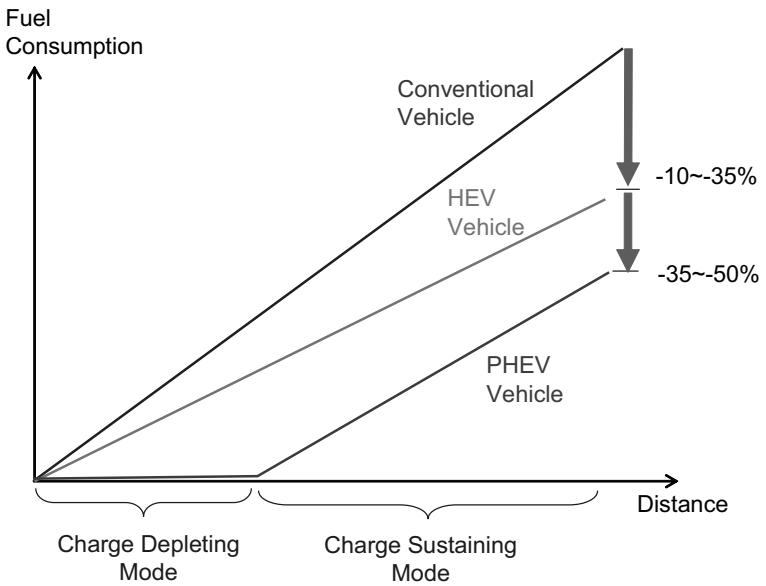

Figure 13.12: Fuel consumptions over travel distance [12].

13.4.1 PHEV Operation Modes

Two typical operation modes are continuous discharge (charge-depleting) mode and high-power cycling (charge sustaining) mode.

Charge-depleting (CD) mode: In this mode, the vehicle is driven exclusively by an electric motor with the combustion engine off. The state-of-charge (SOC) may fluctuate but, on the average, decreases until the SOC lowers down to a predetermined level. From that time, the ICE turns on. The maximum CD mode range is AER.

Charge-sustaining (CS) mode: The ICE and the electrical motor cooperate in a most efficient manner. The SOC is confined in a predetermined band while the vehicle operates. This is the common operating mode of commercial HEVs. Once the SOC level drops down to a lower bound, it is switched into the CS mode automatically. The power plots for the CD and CS mode operations are shown in Fig. 13.14.

Blended mode: This is basically a CD mode; thus the SOC decreases, on the average, while the vehicle operates. However, the engine turns on when the required power is larger than the battery power capability. That is, the engine is engaged to cover up the peak power demand that exceeds the battery power capability, as shown in Fig. 13.13. A vehicle design on the basis of the blended mode operation requires a less battery

(power) capacity. Thus, it reduces the proportion of battery cost.

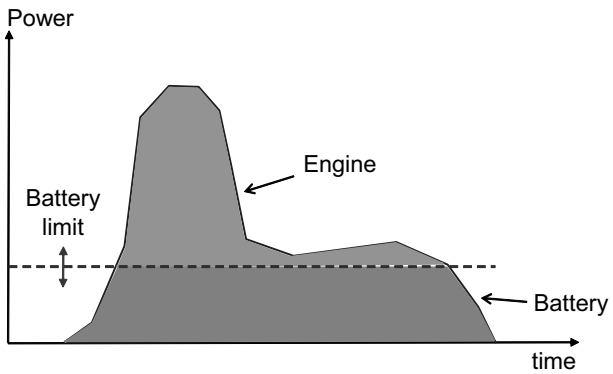

Figure 13.13: Peak power is covered by engine in blended mode operation [18].

Fig. 13.14 is a simulation result of a power plot for the CD and CS mode operations [16]. On the other hand, Fig. 13.15 shows a power plot for the blended and CS mode operations [16]. It needs to be checked that the engine cuts in operation frequently in the blended mode. Komatsu et al.[17] claimed that the blended mode design was beneficial on the basis of driving cycle simulations [17].

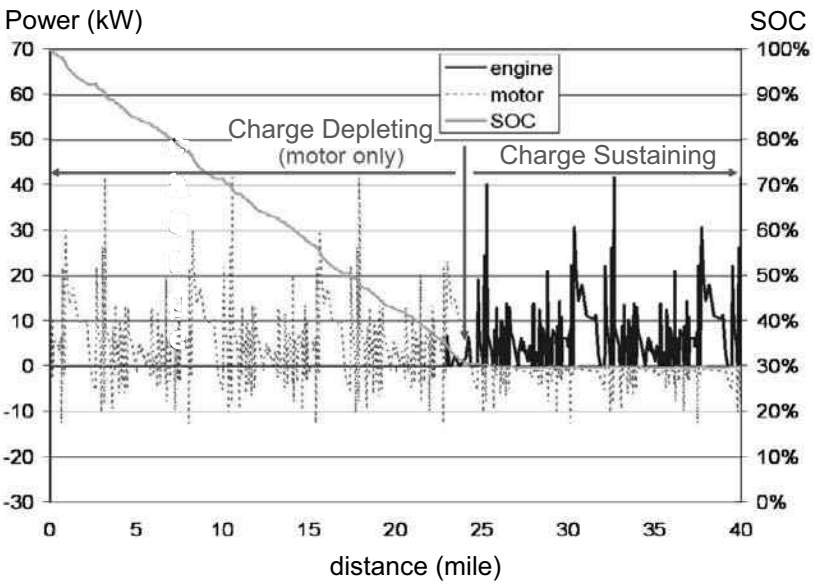

Figure 13.14: Power plots for the CD and CS mode operations [16].

13.4.2 A Commercial PHEV, Volt

Volt is a first serious PHEV that a major car manufacturer (Chevrolet, GM) will produce. Volts will be available in the market in 2011. Wheels are connected to a

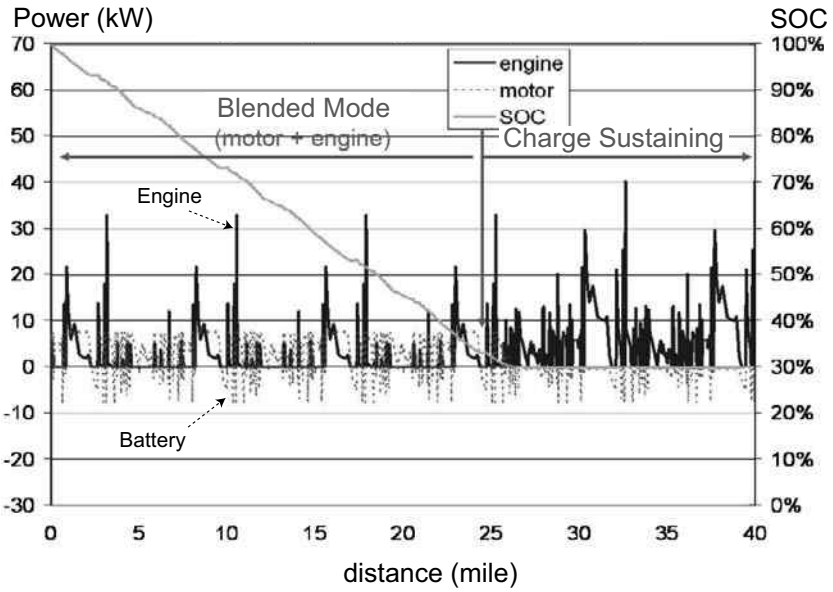

Figure 13.15: Power plots for the blended and CS mode operations [16].

120kW motor, while the ICE is devoted to driving a generator to charge the battery. Hence it has a serial hybrid structure. The ICE is a 53kW, three-cylinder gasoline (1400cc) engine. Since the engine operates after the battery is depleted, the engine is called "range extender." The AER of Volt is 64km (40 miles), but with the gasoline its driving range can be extended to 480km. Since the batteries are packed under the T-shape frame, the vehicle's center of mass is lowered, thereby the cornering work is expected to be excellent. A photo of Volt is shown in Fig. 13.16, and major parameters are listed in Table 13.6.

Table 13.6: Major specifications of Chevrolet's Volt

Battery capacity	16kWh
Battery weight	180kg
EV Driving range	64km
Cell structure	80 × 4V cells
Battery volume	100L
Battery life time	10 years (or 4000 charge/discharge)
Engine size	1.4-liter
No. of cylinders	3
Engine power	53-kW
Motor power (max.)	120 kW
Motor torque (max.)	320 Nm

Figure 13.16: Photo of Volt

Bibliography

[1] Green Car Congress, www.greencarcongress.com/2008/05/the-battery-pac.html.

[2] Electropaedia, Battery and Energy Technologies, http://www.mpoweruk.com/index.htm.

[3] European Automobile Manufacturer's Association, www.acea.be.

[4] J. Voelcker, Lithium batteries for hybrid cars, *IEEE Spectrum,* Jan., 2007.

[5] K. Tikhonov and V. R. Koch, Li-ion battery electrolytes for a wide temperature range, *Covalent Associates, Inc.*

[6] X.Q. Yang, Lithium batteries − The next generation power sources for vehicles, *VPPC 2009*, Dearborn, MI 2009.

[7] J. M. Miller, *Proportion Systems for Hybrid Vehicle,* IEE Power & Energy Series 4, IEE, London, 2004.

[8] R. Ridley, The future of the electric car, *APEC Conf.,* 2006.

[9] B. Moor, Power electronics for electric drive, *EDTA 08 Conference*, Washington, Dec. 2 − 4, 2008.

[10] www.mitsubishi-motors.com/special/ev/

[11] John M. Miller, Energy storage system technology challenges facing strong hybrid, plug-in and battery electric vehicles, *VPPC 09 Conference*, Dearborn, Michigan, Sep., 2009.

[12] A. Pesaran and T. Markel, Battery requirements and cost-benefit analysis for plug-in hybrid vehicles, *24th International Battery Seminar & Exhibit*, Mar., 2007.

[13] S. T. Hung, D. C. Hopkins, and C. R. Mosling, Extension of Battery Life via Charge Equalization Control, *IEEE Trans. on Industrial Electronics*, Vol. 40, No. 1 pp.96 − 104, Feb. 1993.

[14] Nancy Gioia, Realizing the power of plugging-in can we commercialize PHEVs? *EVS23*, Anaheim, Dec. 2007.

[15] R. Berger, Automotive insights, powertrain 2020−the future drives electric, *Automotive Competence Center*, June 2008.

[16] A. Pesaran, Battery choices for different plug-in HEV configurations, *Plug-in HEV Forum and Technical Roundtable* Diamond Bar, CA, Jul. 12, 2006.

[17] M. Komatsu et al., Study on the potential benefits of plug-in hybrid systems, *SAE technical paper*, Paper No. 2008-01-0456, MI April 14 − 17, 2008.

[18] T. Markel and A. Pesaran, PHEV Energy Storage and Drive Cycle Impacts, *7th Advanced Automotive Battery Conference*, Long Beach, CA May 17th, 2007.

Problems

13.1 Suppose that a 18650 battery has 1.66Ah capacity and its weight is 46 gram. When the nominal voltage is 3.8V, calculate the specific energy density.

13.2 Consider battery discharging curves shown in Fig. 13.17.

a) Determine the capacity in Wh for 1C rate discharge.

b) Suppose that the battery weight is 0.9 kg. Determine the specific energy.

c) The dotted curve shows the discharge characteristics at 48C rate. Determine specific power.

d) Determine the capacity in Wh for 48C rate. Explain why it is low compared with the nominal capacity.

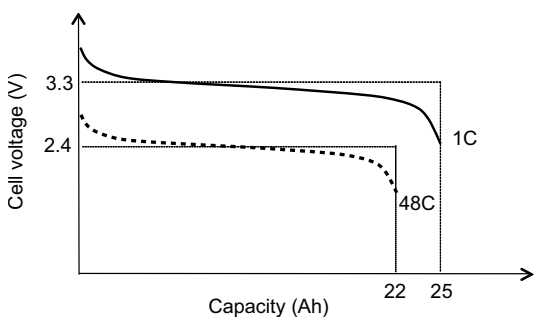

Figure 13.17: Battery discharge curves (Problem 13.2).

13.3 Battery capacity was measured while draining current at constant rates. The experimental results are

Exp. 1 : $t_{cut} = 10$h for $I = 15$A,
Exp. 2 : $t_{cut} = 1$h for $I = 100$A.

Utilizing the above data, predict cut off time, t_{cut} when $I = 200$A.

13.4 Cathode materials and the properties are listed below: Make relevant pairs from left and right columns.

a) $LiCoO_2$	1) Good cycle life time, thermally and chemically stable
b) $LiNiO_2$	2) Low cost, high-power density, unstable at high temp.
c) $LiMn_2O_4$	3) Expensive, high capacity
d) $LiFePO_4$	4) High capacity, low cost, unsafe

13.5 Calculate the driving ranges for different numbers of battery modules, (120kg, 16kWh) when the road grade is 7.5%. Use the same vehicle parameters used for Fig. 13.10.

13.6 Explain

a) Why do the Li-ion batteries show poor performance below $-20°$?

b) Why is high temperature operation not desirable?

c) Why is overcharging not good for the battery life time and dangerous?

d) Why is silicon not used as an anode material though it has a potential of very high energy density?

13.7 Discuss the main benefits of the blended mode operation.

Chapter 14

EV Motor Design Issues

The operation ranges of ICEs are limited compared with electric motors. To cover wide speed range, the use of clutch and transmission gear box is necessary. Further, ICEs do not produce starting torque; thereby a slip mechanism should be used for vehicle starting. Note, however, that electric motors inherently have large starting torque, and can cover a wide speed range without a gear shift. Simplicity in the drive train is an attractive feature of EVs. Fig. 14.1 shows the torque-speed curves of a typical ICE for various gear shifts, along with that of an EV motor.

Induction motors, being very rugged and inexpensive, are considered as propulsion motors for EVs. But the overall efficiency is low compared with PMSMs. The difference is pronounced more in the low-speed area. The low efficiency enforces EV to increase the battery capacity to meet a driving range requirement. Therefore, motor cost saving may result in battery cost increase, which is undesirable. Thus, the recent trend is not to use induction motors for passenger vehicles.

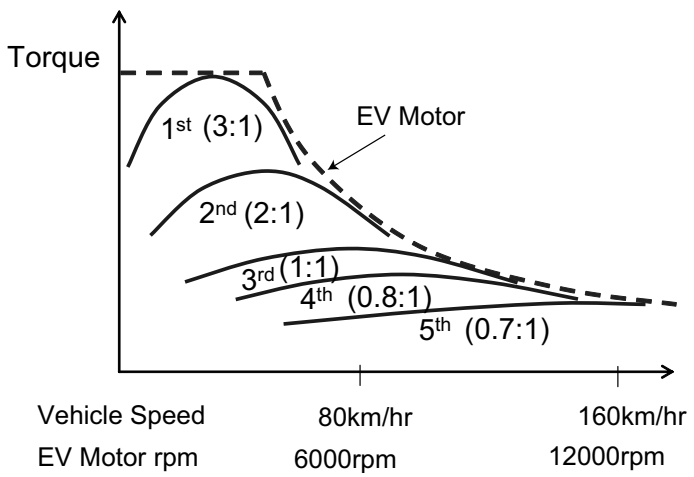

Figure 14.1: Torque-speed curves of an internal combustion engine with gear shifts along with an electric motor torque-speed curve (dotted line).

14.1 Types of Synchronous Motors

Fig. 14.2 shows cross-sectional views of typical 4-pole synchronous motors. PMs are marked by dark areas. The first four utilize PMs, but the last two do not use any PM: Fig. 14.2 (a) shows a typical SPMSM. Fig. 14.2 (b) shows an inset type PMSM, where the PMs are set in the grooves. Note in this case that $L_d < L_q$. Fig. 14.2 (c) shows a typical IPMSM, in which the saliency ratio. $\xi = L_q/L_d$, is maximized with the use of bridges and flux barriers. Fig. 14.2 (d) shows a flux-concentrating (or flux-squeezing) arrangement, which enables the air gap field density to be higher than the remnant field density of the PM. If the torque is generated purely by reluctance, then it is called reluctance motor. Fig. 14.2 (e) shows a switched reluctance motor, whereas Fig. 14.2 (f) shows a synchronous reluctance motor, in which the rotor is constructed by stacking laminated steel sheets in the radial direction.

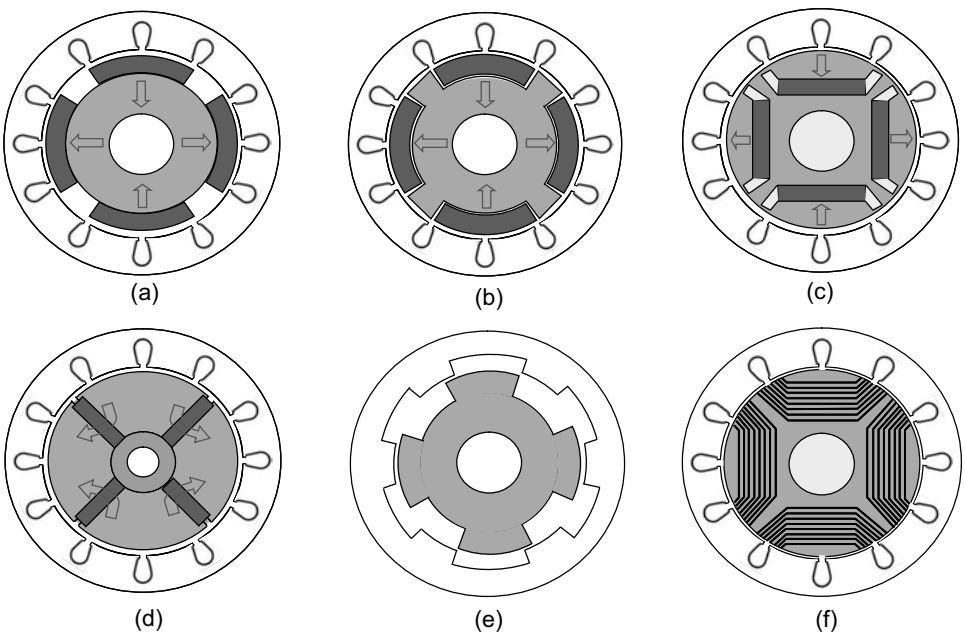

Figure 14.2: Cross-sectional views of 6 synchronous motors (a) surface mounted PMSM, (b) inset PMSM, (c) interior PMSM, (d) flux-concentrating PMSM, (e) switched reluctance motor, and (f) synchronous reluctance motor.

14.1.1 SPMSM

PMs are normally bonded on the surface of the rotor back iron by some epoxy glues. In some applications, stainless steel band or glass fiber band is used to fix the PMs, since glue bonding is not strong enough to endure high centrifugal force. If a stainless steel band is used for fixing the PMs, then eddy current loss takes place by the field harmonics. Therefore, care should be taken not to heat up the PMs by the

loss of stainless steel band.

Since the permeability of PM materials is close to that of air ($\mu_r = 1.05$ for Nd-Fe-B and Ferrite), PMs look like air in the view of magnetic reluctance. Therefore, the reluctance is uniform along any radial directions in SPMSMs (see Section 6.2). In other words, SPMSMs do not have rotor saliency.

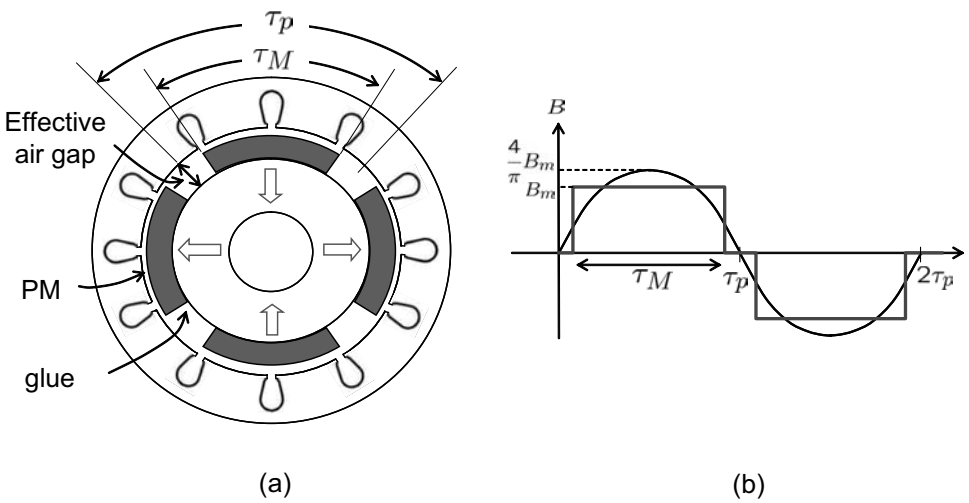

Figure 14.3: (a) Schematic view of SPMSM and (b) fundamental component of air gap field.

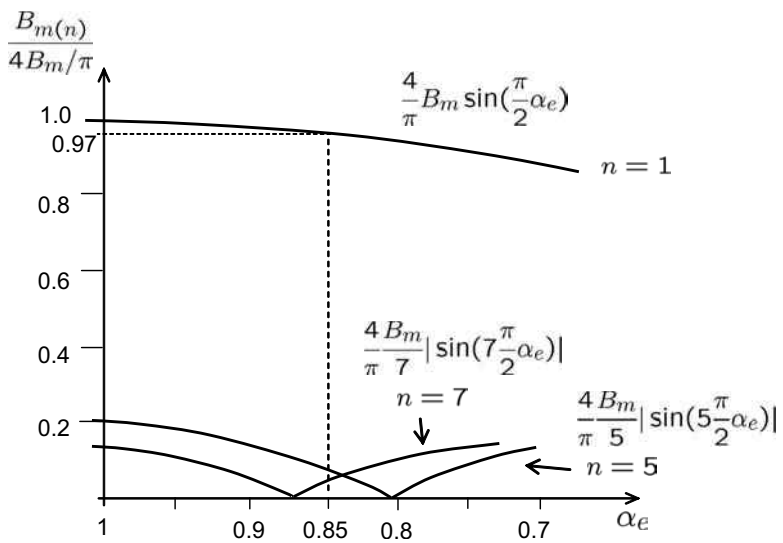

Figure 14.4: Harmonics of air gap field versus PM coverage (α_e): Air gap field harmonics versus PM coverage α_e [1].

PM Coverage Ratio

To make air gap field sinusoidal, the PM coverage over the rotor surface should be considered. The pole coverage ratio is defined as the ratio of PM arc length, τ_M, to pole pitch, τ_p, i.e., $\alpha_e = \tau_M/\tau_p$. Then, $\alpha_e = 1$ implies that the whole rotor surface is covered completely by PMs. Fig. 14.3 (a) and (b) shows a PM coverage and the corresponding air gap field density, respectively. Similarly to (2.4), harmonic coefficients of the air gap field density are obtained as

$$B_{m(n)} = \frac{4}{\pi}\frac{B_m}{n}\sin(n\alpha_e\frac{\pi}{2}), \qquad n = 1, 3, 5, \cdots . \tag{14.1}$$

Based on (14.1), computed results of the fundamental, 5^{th} and 7^{th}-order harmonics versus α_e are shown in Fig. 14.4. For $\alpha_e = 0.85$, 5^{th} and 7^{th}-order harmonics reduce significantly, whereas the fundamental component is decreased only by 3% [1]. Hence, 85% PM coverage is good for reducing the harmonic contents of the air gap field.

Inset PMSM

In some SPMSMs, PMs are inserted on the grooves of the rotor surface, as shown in Fig. 14.5. Those types of motors are called inset PMSM. It was reported that the reluctance torque gained by an inset configuration amounted to 38% of the peak magnet torque [2]. The hook shown in Fig. 14.5 plays a role not only as a PM holder, but also as a shield to demagnetizing field.

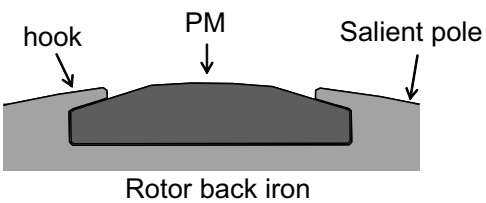

Figure 14.5: A hook design of an inset motor.

14.1.2 IPMSM

Since PMs are inserted in the cavities of the rotor core, no fixation device is necessary in IPMSMs. Since PMs are surrounded by soft silicon steel ($4000\sim5000\mu_0$), PMs are partially protected from the stator harmonic fields.

The foremost advantage of IPMSM is the capability of utilizing reluctance torque. As was discussed in Section 6.2, the d–axis reluctance is greater than the q–axis reluctance, i.e., $L_d < L_q$. This inductance asymmetry leads to generating the reluctance torque.

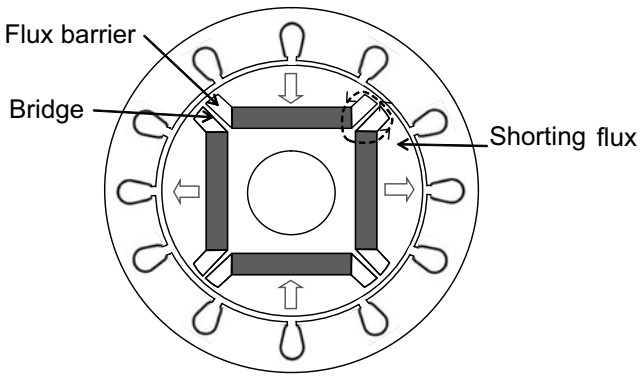

Figure 14.6: Bridge and flux barrier of IPMSM.

The PM flux is valid for torque production when it makes a flux linking with the stator windings. Specifically, the PM flux needs to cross the air gap and encircle the stator windings through the back iron of stator core. But a certain amount of flux does not make such a flux linking: Some flux makes a closed path inside the rotor, called the flux shorting [3]. This leakage flux just wastes the PM potential. To minimize the flux shorting, flux barrier and bridge need to be used. The flux barriers are formed by air holes that penalize flux passing. The bridge is nothing but a narrow ridge of thickness 1∼2 mm that holds the rotor structure. The tensile strength of the bridges should be large enough to endure the centrifugal force of rotor segments in the outer layer. Therefore, there should be design compromise between minimizing the shorting flux and increasing the mechanical rigidity. Fig. 14.6 shows a cross-sectional view of an IPMSM having typical flux barriers and bridges.

14.1.3 Flux-Concentrating PMSM

Flux-concentrating configuration is shown in Fig. 14.7. PMs are set in the radial direction. But, they are magnetized in the circumferential direction and the same poles face each other. Further, flux path around the rotor shaft is blocked by non-ferromagnetic material such as stainless steel. As a consequence, the fields are squeezed toward the rotor surface. By this method, air gap field density can be made higher than the remnant field density of the PM.

Fig. 14.8 shows an example design of 8-pole ferrite flux-concentrating PMSM. Note from Fig. 14.8 (a) that most flux lines pass through the air gap. Fig. 14.8 (b) shows the air gap field density: Note that the maximum field density is about 0.6T, which is much higher than the ferrite remnant field density (0.39T).

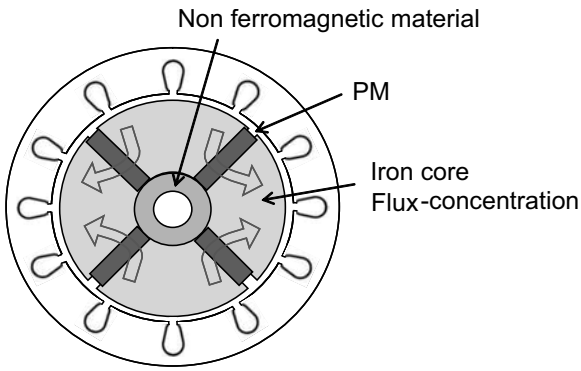

Figure 14.7: Flux-concentrating PMSM.

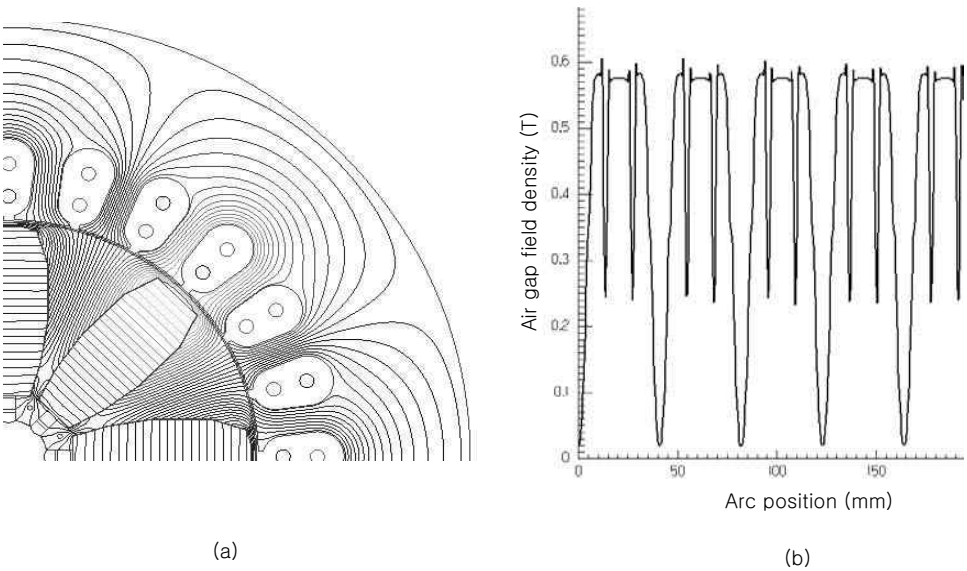

Figure 14.8: A design example of 8-pole ferrite flux-concentrating PMSM: (a) flux lines and (b) air gap field density.

14.1.4 Reluctance Motors

Variable reluctance motors utilize purely the reluctance torque. Since expensive PMs are unnecessary, reluctance motors were favored as a candidate for EV traction motors. There are two kinds of reluctance motors, as shown in Fig. 14.2 (e) and (f): The former is the switched reluctance motor, the latter is the synchronous reluctance motor. In the switched reluctance motors, typical stator and rotor pole numbers are 6-4 or 12-8. Only one-pole pair is aligned at each phase current excitation in the 6-4 switched reluctance motor. If phase currents are switched sequentially, the rotor keeps rotating.

With the synchronous reluctance motor, the torque is governed by

$$T_e = \frac{3}{2}\frac{P}{2}(L_d - L_q)i_d^e i_q^e . \tag{14.2}$$

In order to make the torque density comparable with that of an induction motor, the inductance variation should be sufficiently large. For example, $L_d : L_q = 8 : 1$ [4]. Further, the air gap has to be less than 0.3mm in order to have comparable power density. But, it requires precise machining for brackets and precise rotor assembly. This increases manufacturing cost, which offsets the cost advantage gained from PM elimination. The manufacturing costs of the axially laminated rotors are particularly high, since they require different sizes of lamination sheets. Reluctance motors are not widely used for EV propulsion.

14.2 Distributed and Concentrated Windings

Coil span is counted by the number of teeth encircled by a phase winding. If the coil span is larger than one, that winding is called distributed winding. However, if the coil span is equal to one, then the phase coil surrounds a single tooth, i.e., a coil coming out of a slot goes into an adjacent slot. This winding is called concentrated winding. Obviously, the length of coil is minimized with the concentrated winding. The number of slots per pole per phase is denoted by

$$q = \frac{Q}{m \times P}, \tag{14.3}$$

where m is the number of phases and Q is the number of slots. Using the value of q, one can easily determine whether the winding is distributed or concentrated:

If $q \geq 1$, then the winding is distributed.
If $q < 1$, then the winding is concentrated.

Feasible slot/pole combinations for distributed and concentrated windings are listed in Table 14.1 [1], [5], [6], [7].

14.2.1 Distributed Winding

If $q = 1$ and the air gap field density is rectangular, then the resultant MMF will be also rectangular. However, if multiple slots are used per phase per pole ($q > 1$), then the MMF will have multiple steps, approaching a sinusoidal wave. For example, consider double-layer windings for $q = 2$. Fig. 14.9 (a) shows MMF of the full pitch winding. On the other hand, Fig. 14.9 (b) shows MMF of a fractional pitch winding ($W/\tau_p = 5/6$). Obviously, fractional pitch windings yield less MMF harmonics than the full pitch winding. Fig. 14.10 shows Toyota Camry motor and generator that have distributed windings.

Table 14.1: Slot/pole combinations for three-phase motors.

Distributed Windings									
Number of slots	6	9	12	15	18	21	24	36	48
Pole Numbers	2	2	2	2	2	2	2	2	2
		4	4	4	4	4	4	4	4
				10	6	8	8	6	8
					8		10	8	10

Concentrated Windings									
Number of slots	6	9	12	15	18	21	24	36	48
Pole Numbers	4	6	8		12		20	30	38
	8	8	10		14		22	32	40
		12	14		16		26	38	44
			16		20			42	52

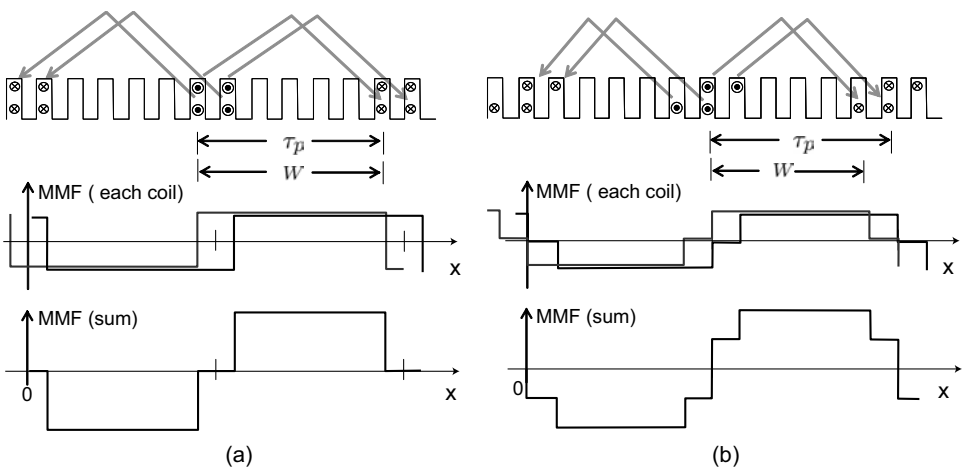

Figure 14.9: MMFs of double layer windings ($q = 2$): (a) full pitch ($W/\tau_p = 1$) and (b) $W/\tau_p = 5/6$ [1].

14.2.2 Concentrated Winding

Note that concentrated windings have fractional slot numbers. Among many slot/pole combinations listed in Table 14.1, practically reasonable combinations are

$$Q = P \pm 2. \tag{14.4}$$

For example, $(Q, P) = (8, 6)$, $(12, 10)$, and $(24, 22)$ are frequently used, since they offer performance advantages in terms of a higher torque capability and reduced torque ripple [12], [8], [15].

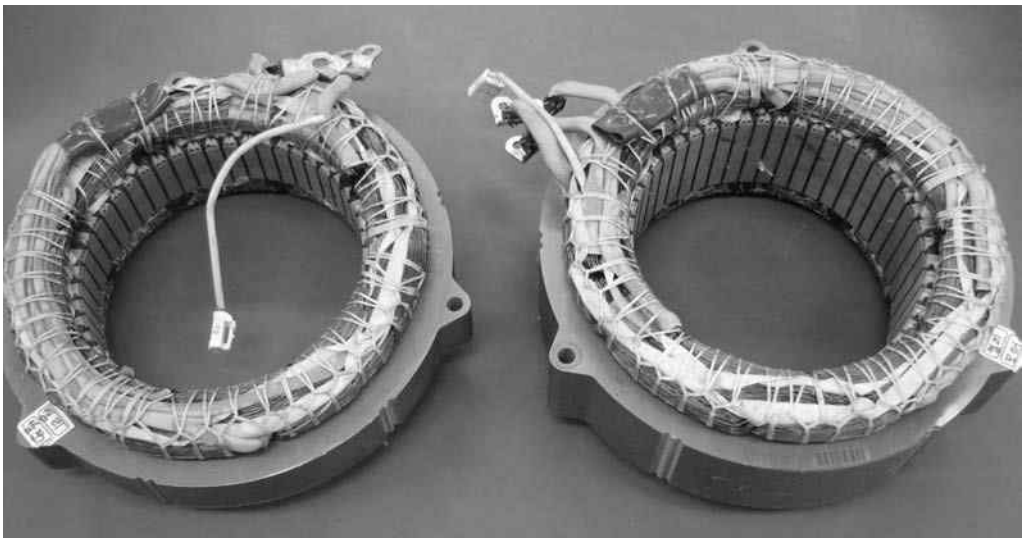

Figure 14.10: Toyota Camry motor and generator.

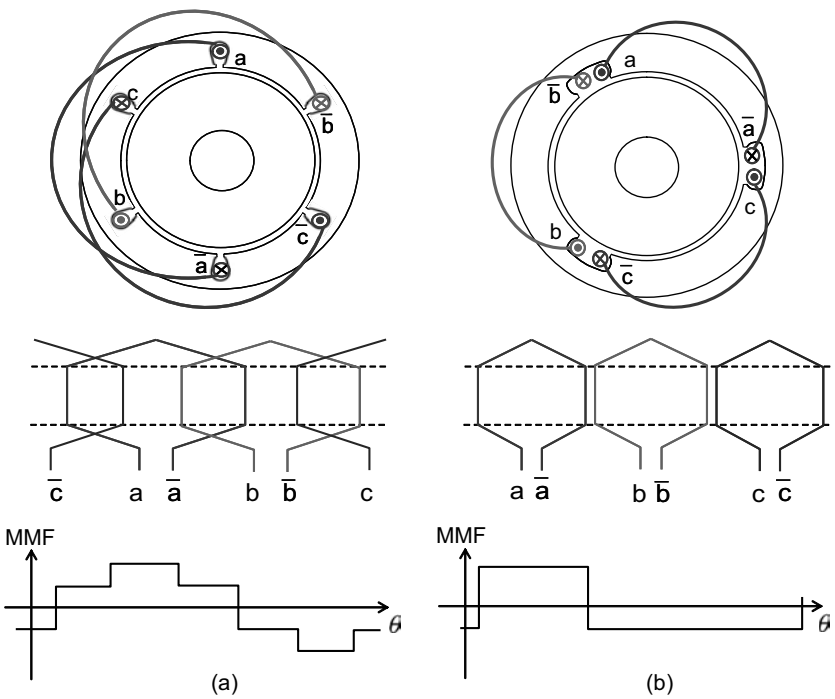

Figure 14.11: Winding and MMF patterns for 6-slot and 3-slot motors (2-pole, 3-phase): (a) distributed winding ($q = 1$) and (b) concentric winding ($q = 1/2$).

For the purpose of illustration, consider two 2-pole three-phase motors having 6-slots and 3-slots. In the former case, $q = 1$ and thus the winding is distributed. However, since $q = 1/2$ in the latter case, the winding is concentrated. Note from Fig. 14.11 that the end turn of the concentrated winding is short and does not intersect with other phase windings. Therefore, the concentrated winding has a shorter pitch, and does not make a flux linking among the phase windings, i.e., the mutual inductance is equal to zero.

The resultant MMFs for $(i_a,\, i_b,\, i_c) = (I,\, -\frac{1}{2}I,\, -\frac{1}{2}I)$ are also shown in Fig. 14.11. It should be noted that MMF of the distributed winding is symmetric over pole periods, but that of the concentred winding is not symmetric. Due to this asymmetry, the concentrated winding generates even MMF harmonics along with odd harmonics (see Problem 14.1):

$$\begin{aligned} \nu &= 1, -2, 4, -5, 7, -8, 10, \cdots \quad \text{for concentrated winding,} \\ \nu &= 1, -5, 7, -11, 13, \cdots \qquad\quad \text{for distributed winding.} \end{aligned}$$

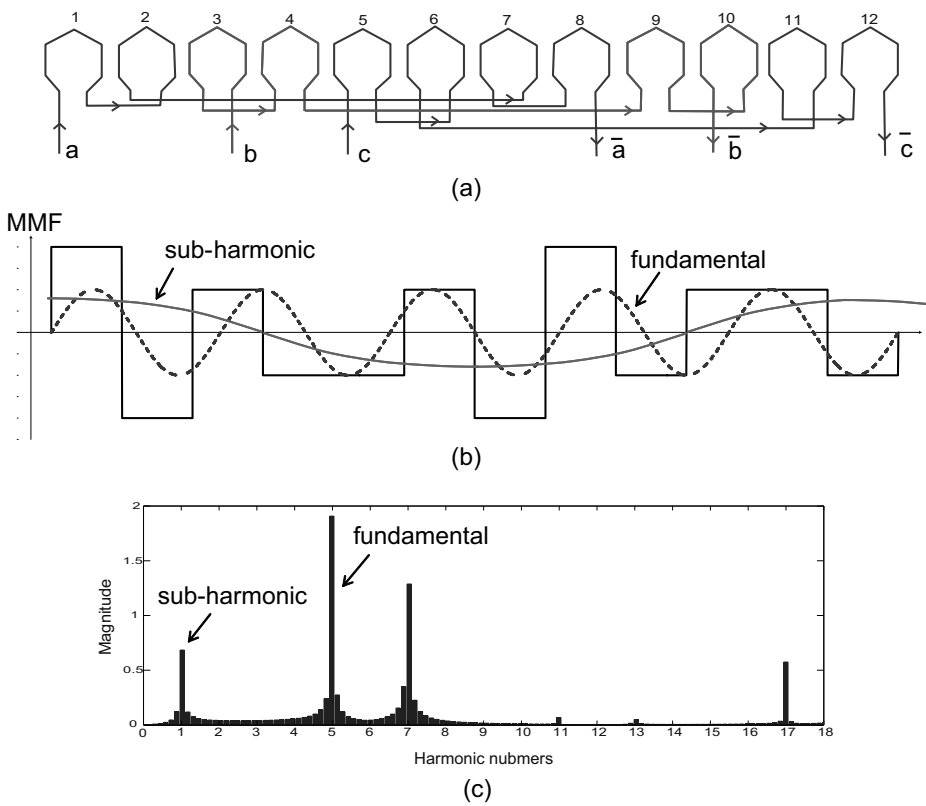

Figure 14.12: 10-pole, 12-slot motor : (a) fractional pitch (concentrated) winding, (b) MMF for $(i_a,\, i_b,\, i_c) = (I,\, -\frac{1}{2}I,\, -\frac{1}{2}I)$, and (c) spectrum of the MMF.

Aside from even harmonics, fractional-slot windings also produce MMF sub-harmonics [8]. As an example, consider 10-pole, 12-slot, three-phase motor shown

in Fig. 14.12 [12]. A winding pattern and the corresponding MMF are shown in Fig. 14.12 when $(i_a, i_b, i_c) = (I, -\frac{1}{2}I, -\frac{1}{2}I)$ [1]. To show graphically how 10-pole is made with 12 teeth, the fundamental component is denoted by dotted lines. The result of square MMF harmonic analysis is shown in Fig. 14.12 (c). Note that $\nu = 5$ is the fundamental component for the 10-pole motor. It should be noted that it has a big subharmonic at $\nu = 1$.

Fig. 14.13 shows a 10-pole, 12-slot motor with an exterior rotor and its back EMF. Note that the back EMF patterns look like perfect sinusoids, i.e., harmonic contents are quite low in the back EMF wave. This is a common phenomenon found in fractional slot winding motors. The reason is that each pole segment experiences different harmonics, and that the harmonics cancel each other within a phase winding since the pole segment windings are connected in series.

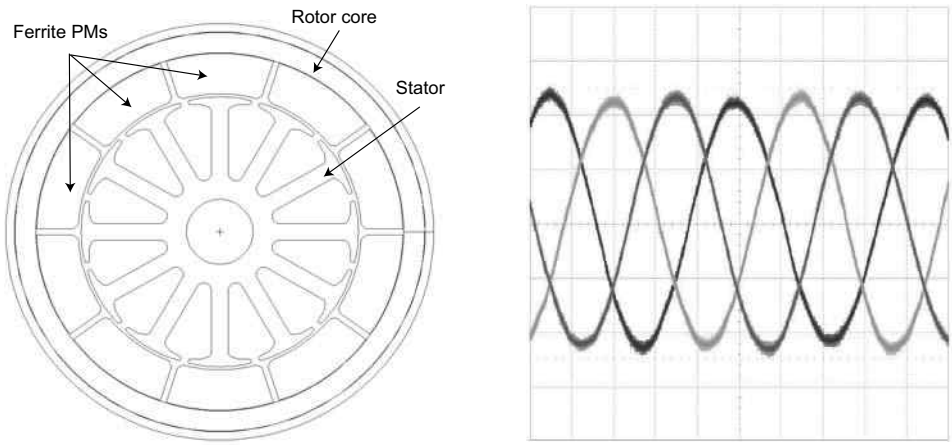

Figure 14.13: 10-pole, 12-slot motor with an exterior rotor: (a) sectional view and (b) back EMFs.

14.2.3 Segmented Motor

In the segmented motor, the stator consists of a multiple number of segmented pieces. Each piece is separately wound, and the wound pieces are assembled together to form a stator core. A schematic diagram of a segmented motor is shown in Fig. 14.14 (a). Since the coils are wound separately before assembly, coil winding is very simple compared with the conventional insertion method. Fig. 14.14 (b) shows an assembled stator of an EV motor. The segmented motors are suitable for automation and thereby for mass production.

Another advantage of the segmented motors is that the copper usage is reduced significantly along with the concentrated winding. In most distributed winding motors, the coil end turn lengths are as long as the coil segments in the stator slot,

i.e., a half of copper is used for the end turns.

But a major disadvantage is that the concentrated winding motors have relatively large MMF harmonics [8]. The stator winding MMF harmonics heat up the rotor PMs by inducing eddy current, which often leads to the PM demagnetization. Another problem is that the segments generate higher audible noise. Hence, the pole segments should be pressed firmly by stator outer ring. Fig. 14.15 shows two types of rotors: (a) surface mounted PM rotor and (b) V-shaped interior PM rotor.

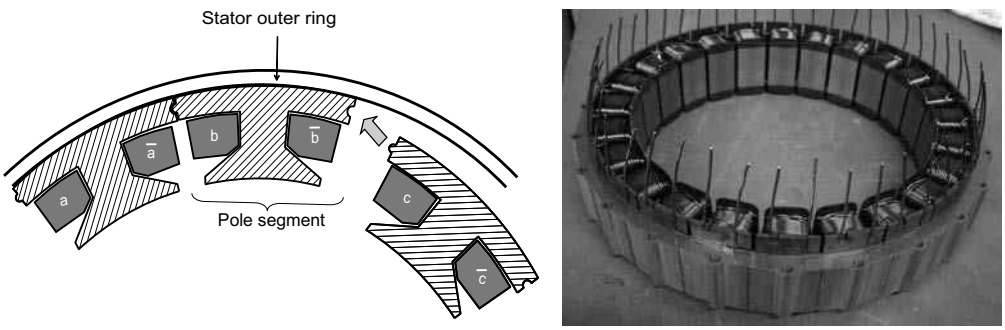

Figure 14.14: (a) Segments assembly with concentrated winding and (b) an assembled stator (Hyundai Motor Company).

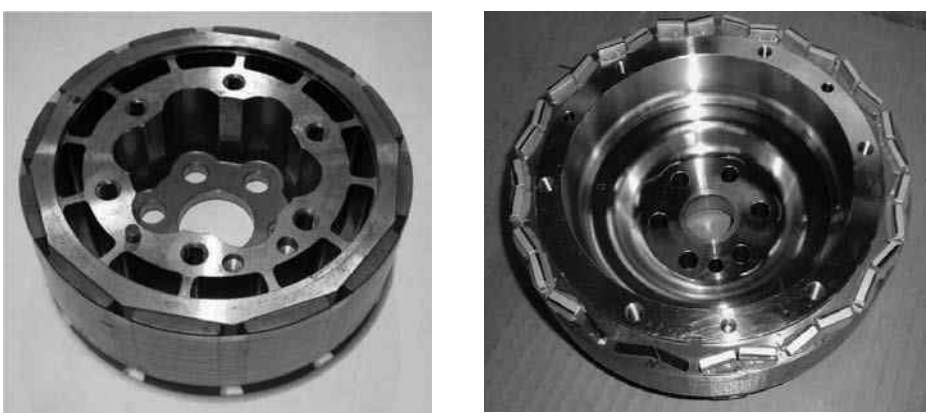

Figure 14.15: Rotors of HEV motor: (a) surface mounted and (b) embedded (V-shape) (Hyundai Motor Company).

14.3 PM Eddy Current Loss and Demagnetization

The B-H curve of a good grade hard magnet material appears as a tilted straight line with a slope in the second quadrant. The normal curve in the second quadrant is called *demagnetization curve*. Fig. 14.16 shows a demagnetization curve with different magnet circuits. Since hard PMs have relative recoil permeability, μ_{rec}, in the range of 1.0−1.1, slope of the demagnetization curve is 45° when the horizontal axis is plotted along with $\mu_0 H$ [13]. The remnant field density, B_r, indicates the field density when an infinitely permeable C-type yoke provides a closed flux path without an air gap.

If a yoke has an open air gap, air gap field density, B_g, is determined from Ampere's law such that $B_g = H_m \frac{\ell_m}{\mu_0 g}$, where g is the air gap height, and H_m and ℓ_m are field intensity and length of the PM, respectively. Geometrically, B_g is determined as intersection point, M between the recoil line and the load line. Note that the recoil line is considered to be the same as the demagnetization curve in the linear analysis. The load line is a line with a slope of Pc, called *permeance coefficient*. The permeance coefficient is normally calculated as the ratio of PM length to air gap height, i.e., $Pc = \ell_m / g$ (see Problem 14.2).

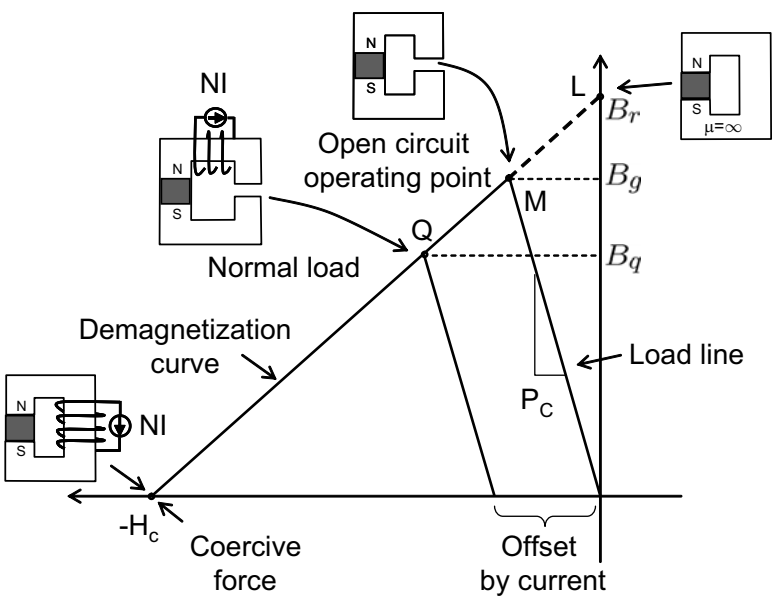

Figure 14.16: B-H characteristic of a hard permanent magnet material.

If current flows in the coil wound around a C-type yoke in the direction that opposes to the PM field, the load line shifts in parallel to the left side. Correspondingly, the air gap field density reduces with the operation point moving down to Q. From Ampere's law, we obtain $H_m \ell_m - \frac{B}{\mu_0} g = NI$, where N is the winding number

and I is current magnitude. Therefore,

$$B_q = \frac{\mu_0}{g} H_m \ell_m - \frac{\mu_0}{g} NI = B_g - \frac{\mu_0}{g} NI. \tag{14.5}$$

When the reversal current is removed gradually, the field density returns to M. Change of operating points along the recoil line is reversible, i.e., if the demagnetization current is removed, then the original state is recovered without a loss of magnetism.

14.3.1 PM Demagnetization

Neodymium Iron Boron (NdFeB) magnets have a high maximum energy product, $(\mathrm{BH})_{\max}$: The remnant field density is high (1.23T), and the coercive force is also high (-1000kA/m) at a room temperature (25°). NdFeB magnets, having a price merit when the energy density is considered, are widely used in commercial products including EV motors.

Fig. 14.17 shows the demagnetization curves of a NdFeB magnet. But at higher temperatures, the demagnetization curve shrinks towards the origin. Further, the knee point moves up into the second quadrant [13], [1].

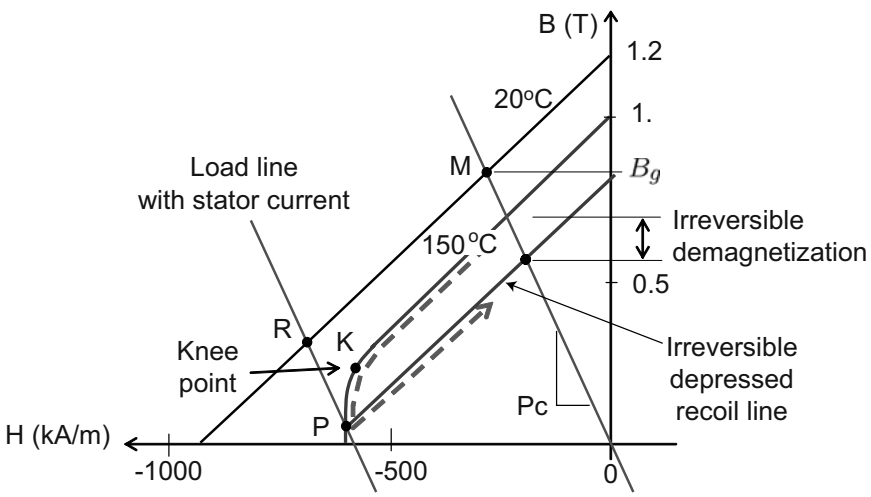

Figure 14.17: NdFeB magnet demagnetization at an elevated temperature.

Consider a specific scenario, where a load line meets the demagnetization curve of 150°C at P, which is below the knee point, K. If the reversal current is released, the operation point follows another depressed recoil line. Therefore, the field density is reduced and the loss is irreversible. That is, a high load current at an elevated temperature may cause a perpetual damage to the PMs. Therefore, motors should be designed such that the operation point does not move after a knee point under various operation environments. Motor heat sources are stator coil Joule loss, iron core loss, mechanical friction loss, etc. But, an important endangering element is

the eddy current loss in the PMs induced by field harmonics. Protective measures to avoid the PM demagnetization include:

1) Increase the PM thickness (height) so that the load line slope, Pc, is sufficiently high.
2) Balance between the heat loading and the cooling capacity: Select a proper value of $A_m J$ for a given cooling system, so that the PM temperature does not exceed a predesignated temperature, where A_m is the current loading and J is the coil current density.
3) Reduce the harmonic field components that would cause eddy current loss on the PMs.

14.3.2 PM Eddy Current Loss due to Harmonic Fields

Although the resistivity of a NdFeB magnet is about 90 times higher than that of copper, a sizable amount of eddy current can be induced in NdFeB magnets by high frequency harmonic fields. Since ferrite magnets have very high resistance, they do not experience eddy current loss. Sources for the field harmonics are [9]-[11]:

a) **MMF harmonics**
Since the fundamental component of stator winding MMF rotates synchronously with the rotor, it is seen as a DC field to PMs. But, the stator space harmonic fields rotates asynchronously with the rotor. Recall from Section 2.1.3 that 5^{th} and 7^{th} space harmonics rotate at the rates of $-\omega_e/5$ and $\omega_e/7$, respectively. Therefore, they are regraded as AC fields rotating at $1.2\omega_e$ and $-0.86\omega_e$ to the PMs.

b) **Slot harmonics**
The stator slot openings make a sequence of dents in the air-gap field density, i.e., a narrow and deep field drop is made at each slot openings (see Fig. 14.8 (b) or Fig. 14.22 (b)). These abrupt field changes induce eddy currents on the PMs. The slotting effect intensifies when the slot openings are large in comparison with air gap height.

c) **Current harmonics**
The PWM inverters cause current harmonics. An extreme example is the six-step operation shown in Section 10.1. Among the current harmonics, the 5^{th} and 7^{th} harmonics are substantial. As shown in (2.25) and (2.26), the 5^{th} harmonics make a negative sequence, whereas the 7^{th} harmonics generate a positive sequence (see Exercise 2.2.1). To PMs, both of them are seen as 6^{th} harmonics that travel six times faster than the electrical frequency. For example, in the Prius II, a 430Hz AC source is fed to the 8-pole motor when it runs at the maximum speed, 6500 rpm. At this time, the 6^{th} harmonics is 2580Hz, which is high enough to induce eddy current on the PMs.

The space harmonic effects are pronounced more in the concentrated (fractional slot) winding motors, since they carry even harmonics and subharmonics additionally. In the perspective of reducing the PM heat loading, distributed windings are better than concentrated windings. In SPMSMs, the PMs are exposed to the air gap, thus they are under direct influence of high-order harmonic fields. Therefore, the PMs of SPMSMs are more vulnerable to demagnetization than those of IPMSMs.

As an effort to decrease the eddy current, PMs are segmented into several pieces and coated with low conductive or non-conductive materials, as shown in Fig. 14.18. Note that the PMs are segmented along the circumferential direction and that the circumferential lamination is slightly better than the axial lamination. Also, the inverter should be controlled so that the current harmonics are low. In some high-speed application, output filters are utilized to reduce the current harmonics.

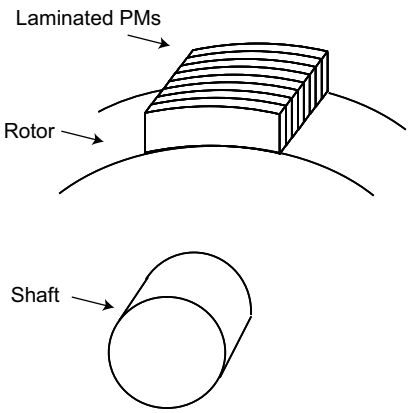

Figure 14.18: PM segmentation along the circumferential direction.

14.3.3 Teeth Saturation and PM Demagnetization

If current flows through the stator winding, the air gap field is generated and superimposed on the PM rotor field (see Problem 14.2). Consider two-pole periods shown in Fig. 14.19. Assume that the MMF of the stator winding is perfect sinusoidal. The PM fields make DC offsets: one upward and the other downward. It should be noted that the field density is high in the leading edge and low in the tailing edge. Specifically, the field density at the leading edge is so high that the rotor core and the stator teeth in that area are saturated. On the other hand, the reverse field generated by the stator MMF acts against the PM field, so that the resulting field density at the tailing edge is attenuated significantly.

If the current loading is strong, a partial demagnetization would take place in the tailing edge especially when the magnet is hot. Fig. 14.20 is a FEM simulation result showing the effects of stator current. The white area indicates high-field density region, and the dark area low-field density region. Note that the PM field is almost nullified by the stator current in the air gap of the tailing edge.

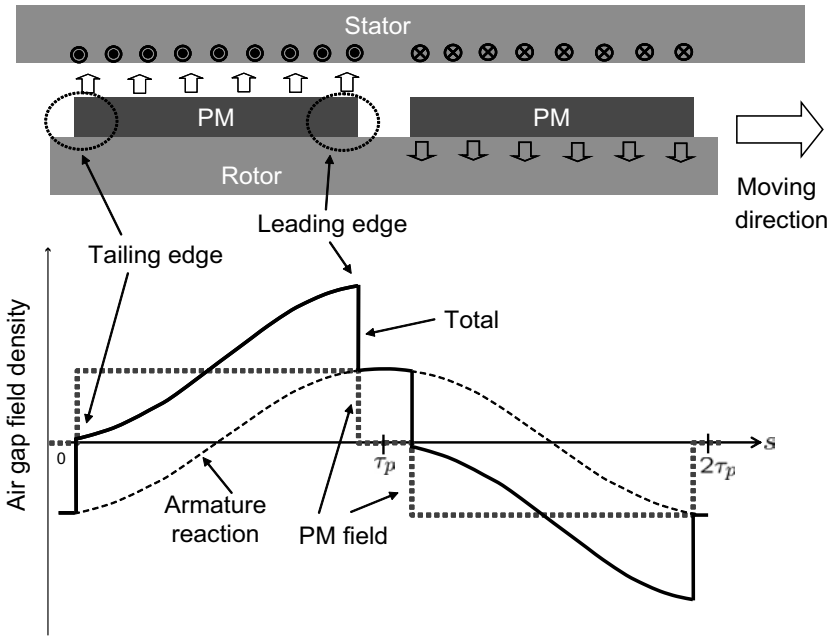

Figure 14.19: Stator current effect (armature reaction) on the leading and tailing edges of PM.

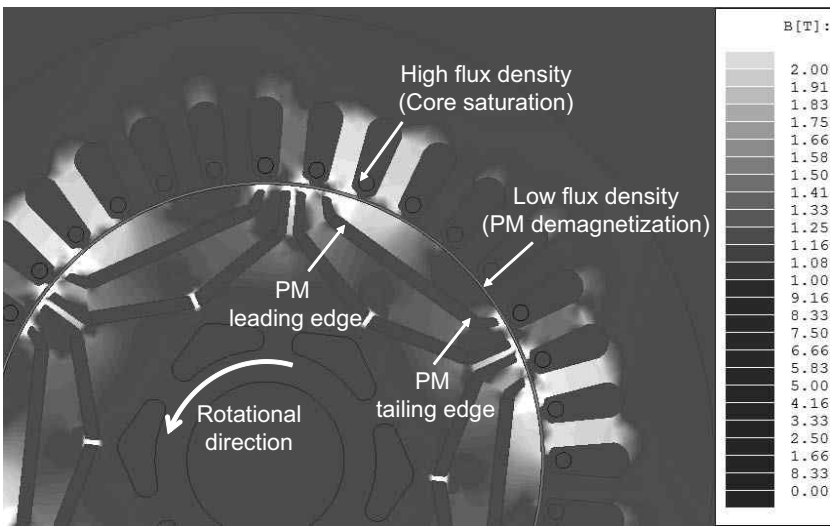

Figure 14.20: FEM results showing the effects of stator current on PMs.

14.4 EV Design Example

The design procedure for a proto-type EV is illustrated in this section. The minimum battery voltage is assumed to be 270V, and the inverter DC link is connected directly without a booster converter. Motor continuous power rating is selected to be 30kW.

Therefore, the maximum phase voltage (rms) is equal to

$$V_a = 270 \times \frac{2}{3} \times \frac{\sqrt{3}}{2} \times \frac{1}{\sqrt{2}} = 110\text{V}.$$

It is the maximum voltage that could be obtained by the space vector PWM in the linear region. The rated speed is chosen as 3600rpm. At the rated operation point, the power factor is assumed to be $\cos\phi = 0.87$. Assuming that the efficiency is equal to $\eta = 0.92$, the rated current is obtained as

$$I_a = \frac{P_e}{3V_a\eta\cos\phi} = \frac{30000}{3 \times 110 \times 0.92 \times 0.87} = 113.6\text{A}. \tag{14.6}$$

The number of pole pair is selected as 3, i.e., $P = 6$. A 36-slot stator is chosen. Thus, the number of slots per pole per phase is equal to $q = 36/(3 \times 6) = 2$. Full pitch winding is assumed, i.e., the pitch factor is equal to $k_p = 1$. Since $q = 2$, the distribution factor is equal to [16]

$$k_d = \frac{\sin(2 \times \frac{30}{2})}{2\sin\frac{30}{2}} = 0.96.$$

Therefore, the winding factor is given as $k_w = k_d \times k_p = 0.96$.

Table 14.2: Specifications for a prototype EV motor.

No. of poles	6	Battery voltage	270V
Base speed	3600rpm	Rated power	30 kW
Rated current	114 A(rms)	Max. current	154 A(rms)
Peak torque	165 Nm	Rated torque	82 Nm
Back EMF constant	$\psi_m = 0.122$V/rad		
Rotor diameter	142.2 mm	Air gap height	0.8 mm
Stack length	135 mm	Stator outer diameter	228 mm
No of slots	36	Coolant	water
Permanent magnet	NdFe (N40SH)	Magnet height	3.3 mm
L_q	1.65 mH	Saliency ratio,	$\frac{L_q}{L_d} = 2.66$
L_d	0.62 mH	No. of PM pieces	18

With the synchronous speed $n_s = \omega_r/(2\pi)$, air gap power, (7.6) becomes

$$P_{gap} = mE_f I_a = \frac{\pi^2}{2} k_w n_s D_r^2 l_{st} B_m A_m. \tag{14.7}$$

The shaft power is set as $P_{shaft} = \frac{1}{\epsilon} P_{gap}\eta\cos\phi$, where $\epsilon = E_f/V_a$ [14]. The peak air gap field is set to be $B_m = 0.8$T, $\epsilon = 1$, and the electric loading is selected as

$A_m = 60000\text{A/m}$. Then, it follows that

$$\begin{aligned} D_r^2 l_{st} &= \frac{\epsilon P_{shaft}}{\frac{\pi^2}{2} k_w n_s B_m A_m \eta \cos\phi} \\ &= \frac{30000}{\frac{\pi^2}{2} \times 0.96 \times \frac{3600}{60} \times 0.8 \times 60000 \times 0.92 \times 0.87} = 2.75 \times 10^{-3}. \end{aligned} \quad (14.8)$$

We choose the rotor diameter and the stack length as $D_r = 0.142\text{m}$ and $l_{st} = 0.135\text{m}$, respectively. Then $D_r^2 \times l_{st} = 2.72 \times 10^{-3}$, which is close to (14.8).

Note that the pole pitch is equal to $\tau_p = \pi D_r / P = 0.0744\text{m}$ and that

$$\Phi_f \equiv \frac{2}{\pi} B_m \tau_p l_{st} = \frac{2}{\pi} \times 0.8 \times 0.0744 \times 0.135 = 5.1 \times 10^{-3}\,\text{Wb}. \quad (14.9)$$

Recall from (7.4) that the rms value of the induced voltage is $E_f = \sqrt{2}\pi f_e N_c k_w \Phi_f$, where N_c the total number of turns per phase. Thus,

$$N_c = \frac{E_f}{\sqrt{2}\pi f_e k_w \Phi_f} = \frac{110}{4.44 \times \frac{3600}{60} \times 3 \times 0.96 \times 5.1 \times 10^{-3}} = 28.1. \quad (14.10)$$

It should be a multiple of 6; therefore $N_c = 24$ was chosen. The full pitch winding is selected for convenience of coil winding and insertion. The motor specifications are summarized in Table 14.2.

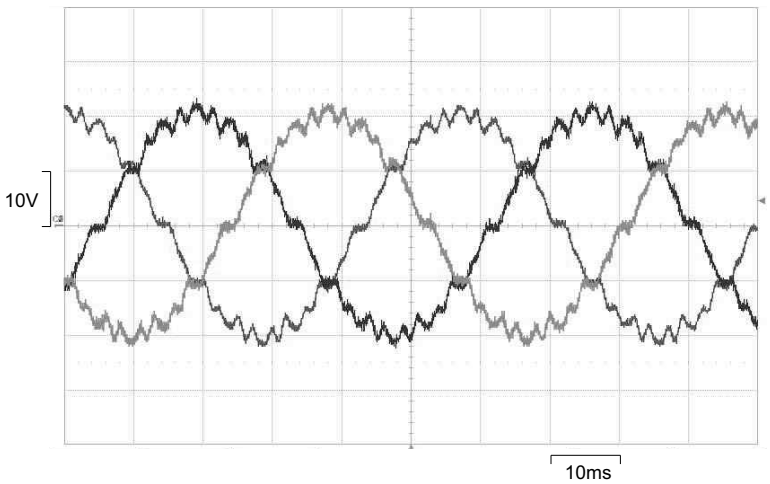

Figure 14.21: Experimental back EMF waveform at 350rpm.

Fig. 14.21 shows an experimental waveform of the back EMF at 350rpm. It is a line-to-line voltage. From the plot, the back EMF constant is read $\psi_m = 0.123\text{V/rad}$ (peak). Fig. 14.22 shows flux lines and the air gap field without stator current. Note

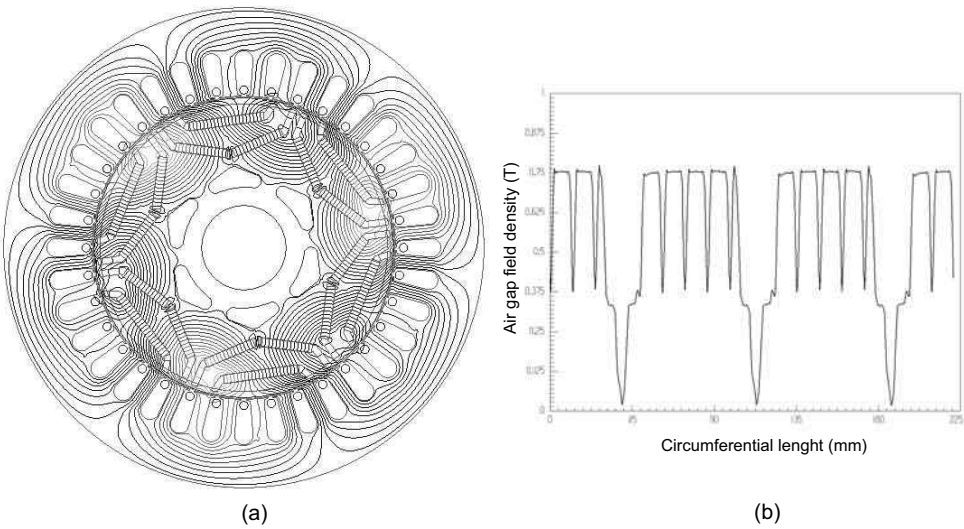

Figure 14.22: (a) Flux lines and (b) air gap field density without stator current.

from Fig. 14.22 (a) that the rotor has double layer cavities. Double layer cavities yield larger saliency than single layer cavities [3]. Fig. 14.22 (b) shows the absolute values of field density. The peak value of the fundamental component is 0.8T.

Fig. 14.23 shows FEM simulation results of torque, current, and power versus speed. Note that the starting torque is 168 Nm with a boosted current 154 A(rms). But above 3000rpm, the current magnitude is kept at 102 A(rms). The shaft power continues to increase until 10000rpm.

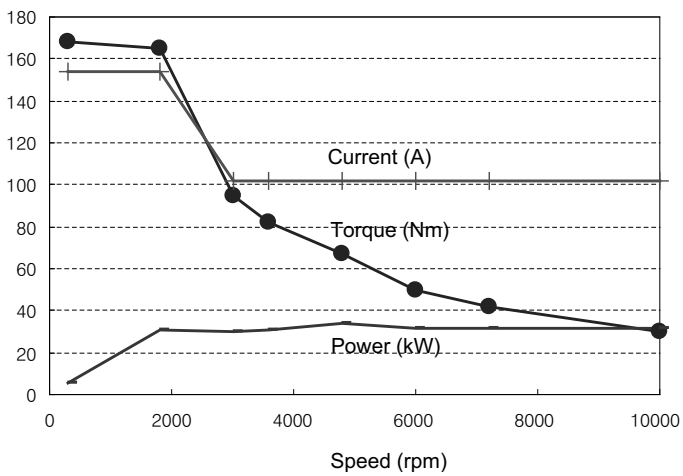

Figure 14.23: Torque, power, current, and current angle versus speed.

Fig. 14.24 shows voltage angle, current angles, and the power factor while the motor speeds up with the maximum power. Note that the current and power angles

approaches to each other as the speed increases. The unity power factor is obtained at 6500rpm. This is because L_dI is larger than the PM flux, $\psi_m = 0.123$V/rad, i.e., $L_dI = 0.00062 \times 102 \times \sqrt{2} = 0.089 < \psi_m$.

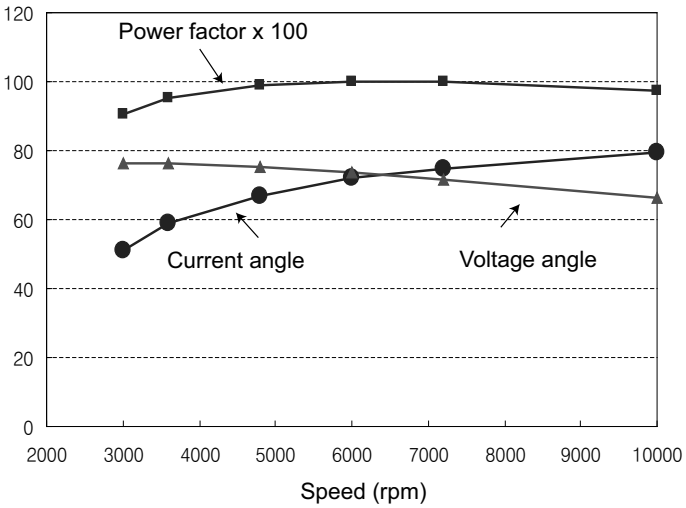

Figure 14.24: Current and voltage angles and power factor along the maximum power operation.

Fig. 14.25 shows the torque components and the sum. Note that the reluctance torque components are larger than the magnetic torque throughout the whole field-weakening range. It is the advantage of IPMSMs that the reluctance torque is gained along with the field-weakening. Fig. 14.26 shows photos of rotor, stator, and their assembly.

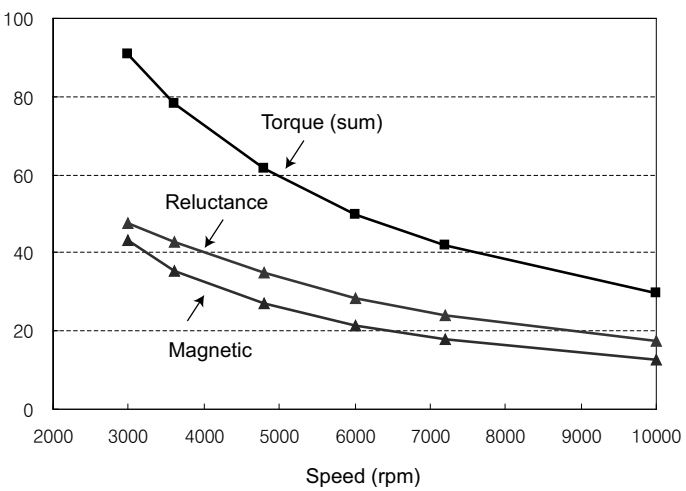

Figure 14.25: Torque components: magnetic torque plus reluctance torque.

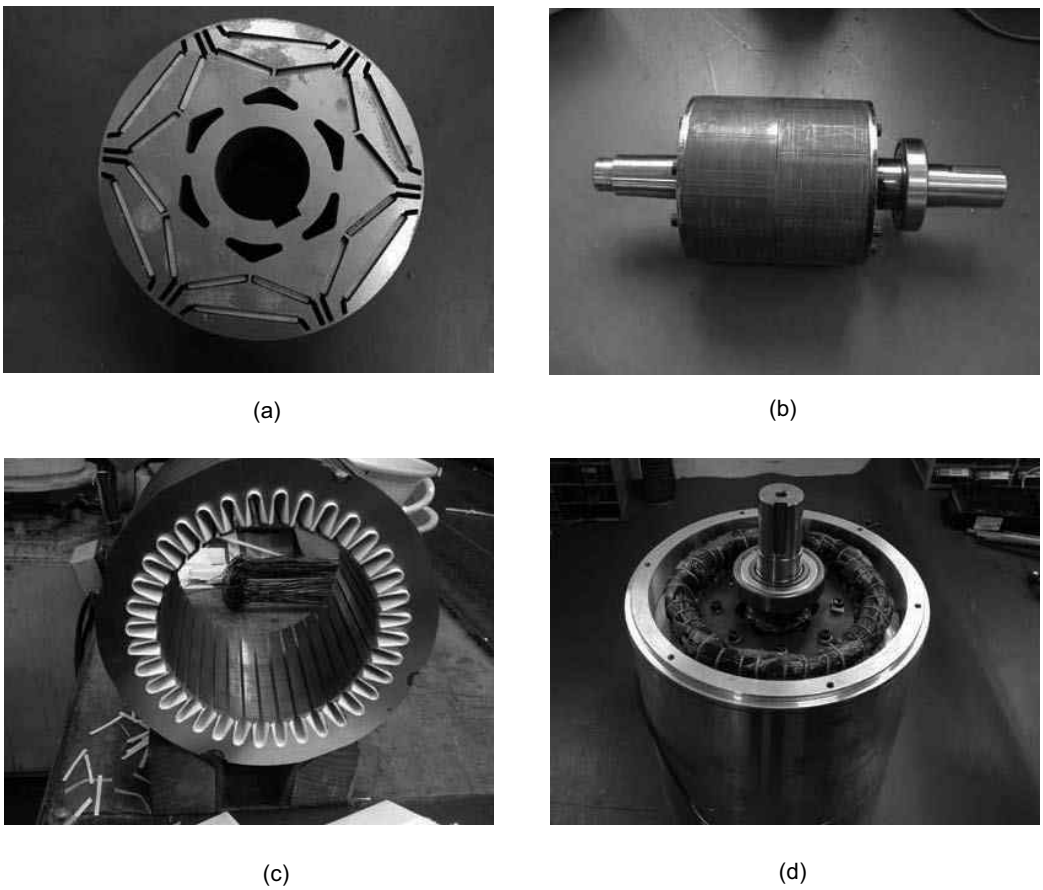

Figure 14.26: Photos of a sample motor: (a) rotor after PM insertion, (b) rotor with shaft, (c) stator core, and (d) their assembly.

Bibliography

[1] A. Binder and K. Reichert, *Permanent Magnet Synchronous Machine Design,* Motor Design Symposium, Pohang, May 2008.

[2] H. Satoh, S. Akutsu, T. Miyamura, and H. Shinoki, Development of traction motor for fuel cell vehicle, *SAE World Congress, Detroit, Michigan* No. 2004-01-0567, Mar. 8 – 11, 2004.

[3] N. Matsui, Y. Taketa, S. Morimoto, Y. Honda, "Design and Control of IPMSM," Ohmsha Ltd. (in Japanese), 2001.

[4] J. M. Miller, *Proportion Systems for Hybrid Vehicle,* IEE Power and Energy Series 4, IEE, London, 2004.

[5] A. J. Mitcham, G. Antonopoulos, and J. J. A. Cullen, Favourable slot and pole number combinations for fault-tolerant PM machines, *IEE Proc.-Electr. Power Appl.*, Vol. 151, No. 5, September 2004.

[6] J. Cros and P. Viarouge, Synthesis of high performance PM motors with concentrated windings, *IEEE Trans. on Energy, Conv.*, Vol. 17, No. 2, pp. 248 – 253, June 2002.

[7] D. Hanselman, *Brushelss Permanent Magnet Motor Design*, 2nd. Ed., The Writers' Collective, Cranston, 2003.

[8] N. Bianchi, S. Bolognani, M. D. Pre, and G. Grezzani, Design Considerations for Fractional-Slot Winding Configurations of Synchronous Machines, *IEEE Trans. on Ind. Appl.*, Vol. 42, No. 4, pp. 997 – 1006, July 2006.

[9] M. Nakano, H. Kometani, M. Kawamura, A study on eddy-current losses in rotors of surface permanent-magnet synchronous machines, *IEEE Trans. on Magnetics*, Vol. 42, No. 2, pp. 429 – 435, Mar. 2006.

[10] D. Ishak, Z.Q. Zhu, D. Howe, Eddy current loss in the rotor magnets of permanent-magnets brushless machines having a fractional number of slots per pole, *IEEE Trans. on Magnetics*, Vol. 41, No. 9, pp. 2462 – 2469, Sep. 2005.

[11] N. Bianchi, S. Bolognani, and F. Luise, Potentials and limits of high-speed PM motors, *IEEE Trans. on Ind. Appl.*, Vol. 40, No. 6, Nov., 2004.

[12] D. Ishak, Z. Q. Zhu, and David Howe, Permanent-magnet brushless machines with unequal tooth widths and similar slot and pole numbers, *IEEE Trans. on Ind, Appl.*, Vol. 41, No. 2, pp. 584 – 590, Mar. 2005.

[13] J.R. Hendershot Jr. and T.J.E Miller, *Design of Brushless Pemanent-Magnet Motors*, Magna Physics Publishing and Clarendon Press, Oxford, 1994.

[14] J. F. Gieras and M. Wing, *Permanent Magnet Motor Technonology, Design Applications*, 2nd. Ed., Marcel, Dekker, Inc., New York, 2002.

[15] P. Salminen, *Fractional Slot Permanent Magnet Synchronous Motors for Low Speed Applications,* Ph. D. Thesis, Lappeenranta University of Technology, Lappeenranta, Finland, 2004.

[16] A. E. Fitzgerlad, C. Kingsley, Jr., and S. D. Umans, *Electric Machinery*, 5th Ed., McGraw Hill, New York, 2003.

Problems

14.1 Consider the MMF of a concentrated winding shown in Fig. 14.27 when $(i_a,\, i_b,\, i_c) = (-\frac{1}{2},\, 1,\, -\frac{1}{2})$. Show that it has nonzero 2^{nd}-order harmonics.

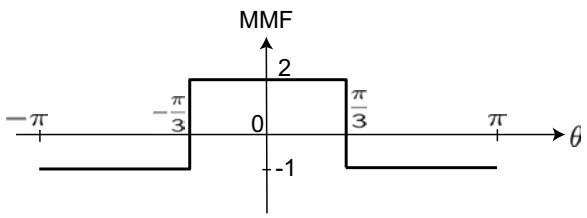

Figure 14.27: MMF of a concentrated winding (Problem 14.1).

14.2 Consider a C-type magnet circuit with a PM in the center, shown in Fig. 14.28. Let B_m denote the field density, H_m the magnetizing force, S_m the cross-sectional area, and ℓ_m the height of the PM. Further, let S_g be the air gap area, g the air gap height, and B_g the air gap field density.

a) Noting that the permeability of the core is much larger than those of air and the PM, derive an equation for B_g from Ampere's law.
b) The permeance coefficient is defined as $P_c = \frac{B_m}{\mu_0 H_m}$. Using approximation, $S_m \approx S_g$, derive a simple expression for the permeance coefficient.

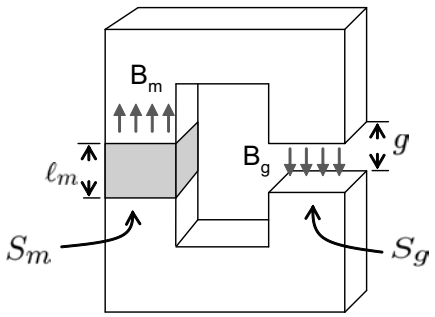

Figure 14.28: A C-type magnet circuit (Problem 14.2).

14.3 Consider Fig. 14.29. The stator current is modeled as a current sheet, A_m, on the stator side, and the PM magnet field directs upward. Let g and h_m be air gap and PM height, respectively.

a) Determine the rotor moving direction.
b) Applying the Ampere's law along a contour indicated by a solid loop, determine the air gap field intensity, H_g, as a function of x caused by the current sheet.

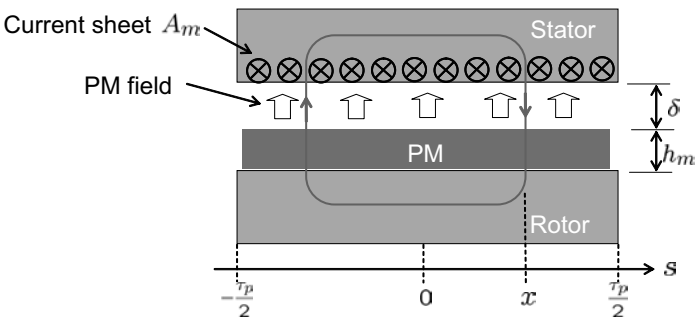

Figure 14.29: Air gap field profile under current sheet (Problem 14.3).

14.4 Consider the magnet circuit shown in Fig. 14.30. The PM (NdFeB) is assumed to be N40SH ($B_r = 1.2$T, $H_c = -950$kA/m). The PM cross-sectional area is $S_m = 10\text{cm}^2$, and its height is 10mm. The air gap area is $S_m = 10\text{cm}^2$ and the air gap height is 1mm.

a) Calculate the air gap field density when $Ni = 0$.

b) Calculate the air gap field density when $Ni = 3000$A turn.

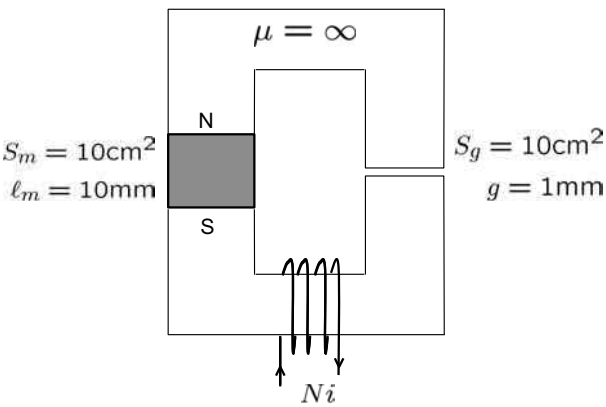

Figure 14.30: Air gap field density under current loading (Problem 14.4).

Solutions

Chapter 1

1.1

a) Since $i_a = 0$A, the torque constant is equal to

$$K_b = K_t = \frac{220\text{V}}{1000\text{rpm}} \times \frac{60\text{rpm}}{2\pi\,\text{rad/sec}} = 2.1\text{V} \cdot \text{sec/rad}.$$

b) At 950rpm,

$$i_a = \frac{220 - 950/60 \cdot 2\pi \times 2.1 - 1}{0.3} = 33.6\text{A}$$

Therefore, $T_e = K_t i_a = 70.56\,\text{Nm}$. The efficiency is equal to

$$\eta = \frac{70.56 \times 950/60 \cdot 2\pi}{220 \times 33.6} \times 100 = 95\%.$$

1.2

a) Since $T_L = T_e = K_t i_a$, $i_a = 8/0.4 = 20$A. Thus,

$$\omega_r = \frac{120 - 0.5 \times 20}{0.4} = 275\text{rad/sec}.$$

b) Since $T_L = T_e = K_t i_a$, $i_a = 8/0.3 = 26.7$A. Therefore,

$$\omega_r = \frac{120 - 0.5 \times 26.7}{0.3} = 355.5\text{rad/sec}.$$

Note that the speed is increased with field reduction.

1.3

a) From $\zeta\omega_n = 1000$ and $2\zeta\omega_n = (r_a + K_p)/L_a$,

$$K_p = 2 \cdot 1000 \cdot 12/1000 - 0.5 = 23.5.$$

K_i can be obtained through simulation.
b)

$$\begin{aligned} \omega_2 &= 1000\text{rad/sec.} \\ \omega_{sc} &= \frac{5}{13}\omega_2 = 385\text{rad/sec.} \\ \omega_1 &= \frac{1}{T_i} = \frac{\omega_{sc}}{5} = 77\text{rad/sec.} \\ K_p &= J\omega_{sc} = 38.5 \end{aligned}$$

c) The (open) loop gain is

$$G(s) = \frac{\omega_{sc}}{s}(1 + \frac{\omega_{sc}}{5\,s})(\frac{1}{1 + \frac{5}{13\omega_{sc}}s}) = \frac{385}{s}(1 + \frac{77}{s})(\frac{1}{1 + \frac{s}{1000}})$$

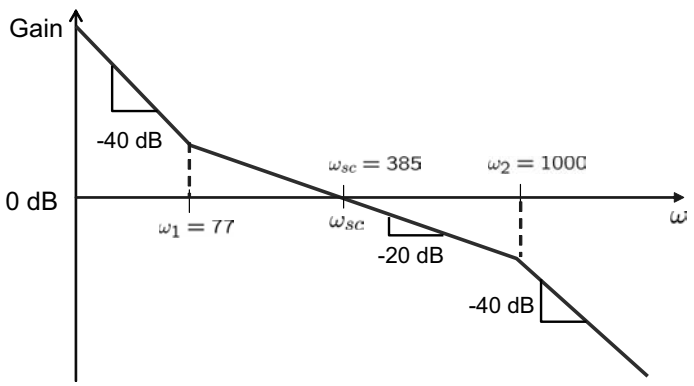

The magnitude of the loop gain is equal to 1 at $\omega_{sc} = 385$rad/sec. Thus, the phase margin is $\angle G(j385) - (-180°) = 57.65°$.

1.4
Fig. 1.17 (b) is rearranged as

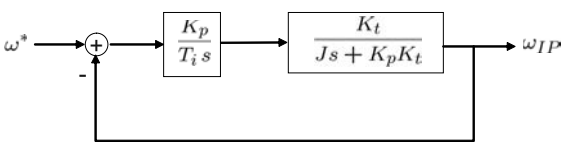

Then (1.17) follows straightforwardly.

1.5
Open loop transfer function is $H(s) = K_p \frac{1}{1+\tau_\sigma s}\frac{1}{Js} = \frac{1/\tau_\sigma}{\tau_\sigma s^2 + s}$. It is necessary to find ω that satisfies $|-\tau_\sigma\omega^2 + j\omega| = \frac{1}{\tau_\sigma}$. The solution is $\omega = \sqrt{\frac{\sqrt{5}-1}{2}}\frac{1}{\tau_\sigma} = 0.786\frac{1}{\tau_\sigma}$. Therefore,

$$\text{phase margin} = \tan^{-1}\left(\frac{1}{-\tau_\sigma\omega}\right) + 180^o = \tan^{-1}\left(\frac{1}{-0.786}\right) + 180^o = 51.8^o.$$

Damping coefficient, $\zeta = 0.5$, follows form the closed loop transfer

$$\frac{1}{\tau_\sigma^2 s^2 + \tau_\sigma s + 1} = \frac{1/\tau_\sigma^2}{s^2 + 1/\tau_\sigma s + 1/\tau_\sigma^2}.$$

1.6

Note that $y = G\left(-Q_d(y - Q_r\hat{G}r) + Q_r r\right) + Gd$. Therefore,

$$A(s) = \begin{bmatrix} \frac{1+\hat{G}Q_d}{1+GQ_d}GQ_r & \frac{G}{1+GQ_d} \\ \frac{1+\hat{G}Q_d}{1+GQ_d}Q_r & \frac{-GQ_d}{1+GQ_d} \end{bmatrix}$$

1.7

a) With the artificial delay, the transfer function is calculated as

$$\left.\frac{\widehat{T}_L(s)}{T_L(s)}\right|_{T_e=0} = \frac{-e^{-\tau_d s}}{1 + \alpha s}$$

b) Without the artificial delay, the transfer function is calculated as

$$\left.\frac{\widehat{T}_L(s)}{T_L(s)}\right|_{T_e=0} = \frac{-e^{-\tau_d s}}{2 + \alpha s - e^{-\tau_d s}} \approx \frac{-1 + \tau_d s}{1 + (\alpha + \tau_d)s}$$

c) With the artificial delay, the pole shifts from $s = -1/(\alpha + \tau_d)$ to $s = -1/\alpha$. That is, the phase margin increases with the artificial delay.

Chapter 2

2.1

The function is the odd function and the period is $2\tau_p$.

$$b_n = \frac{2}{\tau_p}\int_0^{\tau_p} \frac{NI}{2}\sin\left(n\frac{\pi}{\tau_p}\theta\right)d\theta = -\frac{2}{n\pi}\frac{NI}{2}\cos\left(n\frac{\pi}{\tau_p}\theta\right)\Big|_0^{\tau_p} = \frac{2}{n\pi}\frac{NI}{2}(1 - \cos(n\pi))$$

2.2

Three-phase currents are balanced, i.e., $i_a + i_b + i_c = 0$ and $i_c = -v_{sn}/Z = \cos(\omega t)$. Thus,

$$i_a = \cos(\omega t - \frac{2}{3}\pi) \qquad \text{and} \qquad i_b = \cos(\omega t + \frac{2}{3}\pi).$$

Since $v_{an} = Zi_a + v_{sn}$, $v_{bn} = Zi_b + v_{sn}$, v_{an} and v_{bn} are calculated as

$$v_{an} = \sqrt{3}Z\sin(\omega t - \frac{\pi}{3}) \qquad \text{and} \qquad v_{bn} = -\sqrt{3}Z\sin(\omega t + \frac{\pi}{3}).$$

2.3

(a) See Fig. (a).

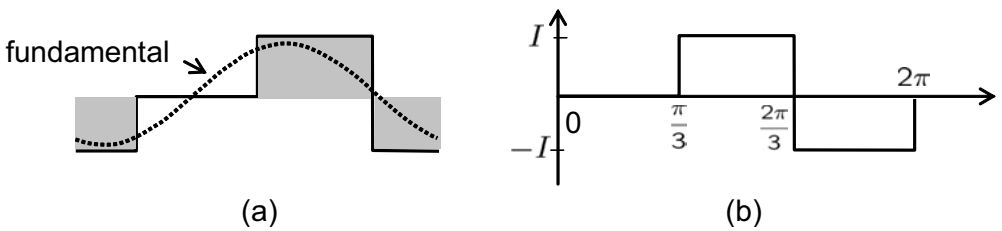

(b) Refer to Fig. (b).

$$a_n = \frac{I}{\pi}\int_0^{2\pi} \text{MMF}\sin(n\theta)d\theta = \frac{I}{\pi}\left(\frac{-1}{n}\cos n\theta|_{\frac{\pi}{3}}^{\frac{2\pi}{3}} + \frac{1}{n}\cos n\theta|_{\frac{2\pi}{3}}^{2\pi}\right)$$
$$= \frac{I}{\pi n}\left(1+\cos\frac{n\pi}{3} - 2\cos\frac{2n\pi}{3}\right)$$
$$b_n = \frac{I}{\pi}\int_0^{2\pi} \text{MMF}\cos(n\theta)d\theta = \frac{I}{\pi n}\left(2\sin\frac{2n\pi}{3} - \sin\frac{n\pi}{3}\right)$$

Thus, $a_2 = \frac{I}{2\pi}\frac{3}{2}$ and $b_2 = -\frac{I}{2\pi}\frac{3\sqrt{3}}{2}$. Therefore, $\sqrt{a_2^2+b_2^2} = \frac{3I}{2\pi}$.
Similarly, $a_4 = \frac{I}{4\pi}\frac{3}{2}$ and $b_4 = \frac{I}{4\pi}\frac{3\sqrt{3}}{2}$. Therefore, $\sqrt{a_4^2+b_4^2} = \frac{3I}{4\pi}$.

2.4

$$v_d^s = \frac{2}{3}(v_a - \frac{1}{2}v_b - \frac{1}{2}v_c) = v_a$$
$$v_q^s = \frac{2}{3}(\frac{\sqrt{3}}{2}v_b - \frac{\sqrt{3}}{2}v_c) = \frac{1}{\sqrt{3}}(v_b - v_c)$$

(v_a, v_b, v_c)	(v_d^s, v_q^s)
$(\frac{1}{2}, -1, \frac{1}{2})$	$(\frac{1}{2}, -\frac{\sqrt{3}}{2})$
$(1, -\frac{1}{2}, -\frac{1}{2})$	$(1, 0)$
$(\frac{1}{2}, \frac{1}{2}, -1)$	$(\frac{1}{2}, \frac{\sqrt{3}}{2})$
$(-\frac{1}{2}, 1, -\frac{1}{2})$	$(-\frac{1}{2}, \frac{\sqrt{3}}{2})$
$(-1, \frac{1}{2}, \frac{1}{2})$	$(-1, 0)$
$(-\frac{1}{2}, -\frac{1}{2}, 1)$	$(-\frac{1}{2}, -\frac{\sqrt{3}}{2})$

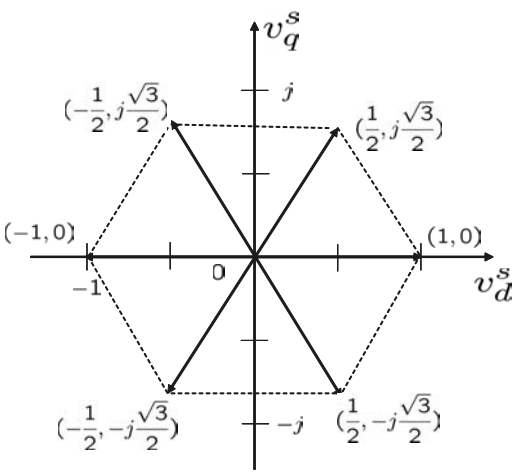

2.5

$$5^{th} \text{ order harmonic} : \mathbf{i}_5^e = \frac{1}{5}e^{-j5\omega t} \cdot e^{-j\omega t} = \frac{1}{5}e^{-j6\omega t}$$
$$7^{th} \text{ order harmonic} : \mathbf{i}_7^e = -\frac{1}{7}e^{j7\omega t} \cdot e^{-j\omega t} = -\frac{1}{7}e^{j6\omega t}$$

Common factor : Both of them appear as 6^{th}-order harmonics.
Difference : The 5^{th}-order harmonic rotates in the clockwise direction.
The 7^{th}-order harmonic rotates in the counterclockwise direction.

2.6
For a unitary matrix,$\mathbf{U}$, $\mathbf{U}\mathbf{U}^T = \mathbf{U}\mathbf{U}^{-1} = I$. Thus,

$$det(\mathbf{U}\mathbf{U}^T) = det(\mathbf{U}) \cdot det(\mathbf{U}^T) = det(\mathbf{U}) \cdot det(\mathbf{U}) = 1$$

2.7

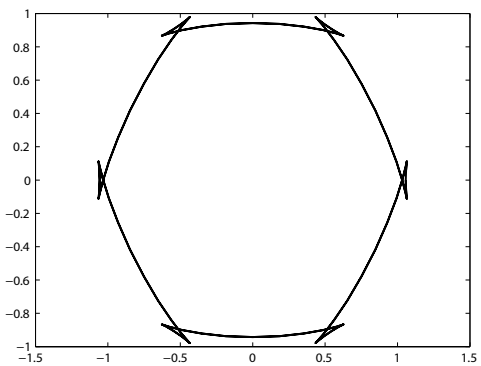

2.8

$$i_a = I\cos(\omega t), \quad i_b = I\cos(\omega t - \frac{2\pi}{5}), \quad i_c = I\cos(\omega t - \frac{4\pi}{5}),$$
$$i_d = I\cos(\omega t + \frac{4\pi}{5}), \quad i_e = I\cos(\omega t + \frac{2\pi}{5}).$$

$$MMF_{sum} = MMF_a + MMF_b + MMF_c + MMF_d + MMF_e = \frac{5NI}{4}\cos(\theta - \omega t)$$

2.9

$$\begin{bmatrix} f_q^s \\ f_d^s \\ f_0^s \end{bmatrix} = \frac{2}{3}\begin{bmatrix} 1 & -\frac{1}{2} & -\frac{1}{2} \\ 0 & -\frac{\sqrt{3}}{2} & \frac{\sqrt{3}}{2} \\ \frac{1}{\sqrt{2}} & \frac{1}{\sqrt{2}} & \frac{1}{\sqrt{2}} \end{bmatrix}\begin{bmatrix} f_a \\ f_b \\ f_c \end{bmatrix}$$

$$\begin{bmatrix} f_q^e \\ f_d^e \\ f_0^e \end{bmatrix} = \begin{bmatrix} \cos(\theta) & -\sin(\theta) & 0 \\ \sin(\theta) & \cos(\theta) & 0 \\ 0 & 0 & 1 \end{bmatrix}\begin{bmatrix} f_q^s \\ f_d^s \\ f_0^s \end{bmatrix}$$

$$\begin{bmatrix} f_q^e \\ f_d^e \\ f_0^e \end{bmatrix} = \frac{2}{3}\begin{bmatrix} \cos(\theta) & \cos(\theta-\frac{2\pi}{3}) & \cos(\theta-\frac{4\pi}{3}) \\ \sin(\theta) & \sin(\theta-\frac{2\pi}{3}) & \sin(\theta-\frac{4\pi}{3}) \\ \frac{1}{\sqrt{2}} & \frac{1}{\sqrt{2}} & \frac{1}{\sqrt{2}} \end{bmatrix}\begin{bmatrix} f_a \\ f_b \\ f_c \end{bmatrix}$$

Chapter 3

3.1

$$P_m = 15+1 = 16\text{kW}, \qquad s = \frac{\omega_e - \frac{P}{2}\omega_r}{\omega_e} = 0.0288$$

$$P_{ag} = \frac{P_m}{1-s} = 16.476\text{kW}$$

$$\text{Copper loss} = P_{ag} - P_m = 476\text{W}$$

3.2

$$P_{ag} = 40\text{kVA} \times 0.9 - 4\text{kW} = 32\text{kW}$$

$$P_m = P_{ag}\cdot(1-s) = 32 \times 0.97 = 31.04\text{kW}$$

$$T_e = \frac{P_m}{\omega_r} = \frac{31040}{2\pi\frac{873}{60}} = 339.5\text{Nm}.$$

3.3

a)

$$s_m = \frac{r_r}{\sqrt{r_s^2 + \omega_e^2(L_{ls}+L_{lr})^2}} = \frac{0.996}{\sqrt{1.6^2 + (2\pi\cdot 60)^2(2\cdot 3.28\times 10^{-3})^2}} \approx 0.338$$

b)

$$\begin{aligned} s &= \frac{s_m}{2.5} \approx 0.135 \\ \omega_r &= \frac{2}{P}\omega_e(1-s) \approx 163 \text{ rad/s} \\ I'_r &= \frac{V_s}{\sqrt{(r_s + \frac{r_r}{s})^2 + \omega_e^2(L_{ls}+L_{lr})^2}} \\ &= \frac{127}{\sqrt{(1.6 + \frac{0.996}{0.135})^2 + (2\pi \cdot 60)^2(2 \cdot 3.28 \times 10^{-3})^2}} \approx 13.64A \\ T_e &= 3I_r'^2 \frac{(1-s)r_r}{s\omega_r} = 3 \cdot 13.64^2 \times \frac{(1-0.135) \times 0.996}{0.135 \times 163} = 21.85\text{Nm} \end{aligned}$$

c) Note that the voltage over the magnetizing inductor is $\sqrt{\left(\frac{r_r}{s}\right)^2 + (\omega_e L_{lr})^2} I'_r$. Thus,

$$I_m = \frac{\sqrt{\left(\frac{r_r}{s}\right)^2 + (\omega_e L_{lr})^2}}{\omega_e L_m} I'_r \approx 4.31\text{A}$$

d) Note that $I_s = I'_r + I_m = 17.95$A and $T_e\omega_r/(1-s) = 3 \cdot V_s I_s \cos\phi$. Thus,

$$\cos\phi = \frac{T_e\omega_r/(1-s)}{3 \cdot V_s I_s} = \frac{21.85 \times 163/0.865}{3 \times \frac{220}{\sqrt{3}} \times 17.95} = 0.6.$$

3.4

$$\begin{aligned} T_{e,rated} &= \frac{P}{2}\frac{3r_r}{s\omega_e}\frac{V_s^2}{(r_s + \frac{r_r}{s})^2 + \omega_e^2(L_{ls}+L_{lr})^2} \approx 112.3Nm \\ T_{e,start} &= \frac{P}{2}\frac{3r_r}{\omega_e}\frac{V_s^2}{(r_s + r_r)^2 + \omega_e^2(L_{ls}+L_{lr})^2} \approx 49Nm \end{aligned}$$

3.5

a) $I_{s0} = \frac{V_s}{\omega_e L_s} = \frac{440/\sqrt{3}}{377 \times 153 \times 10^{-3}}$=4.4A.

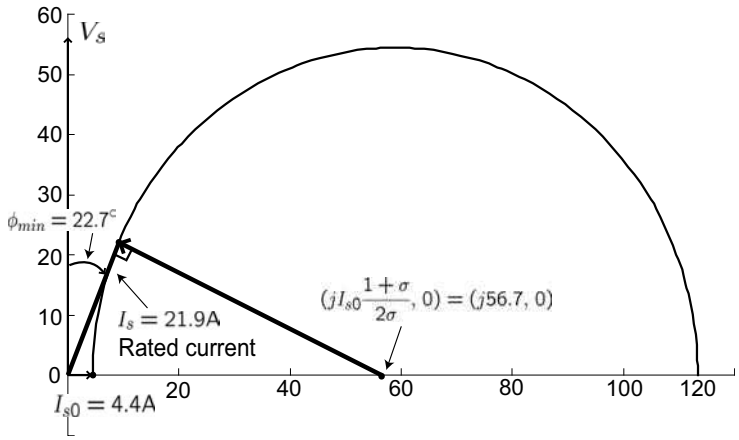

b) $\sigma = \frac{153^2}{150^2} - 1 = 0.0404$. $I_s = I_{s0}/\sqrt{\sigma} = 4.4/0.201 = 21.9\text{A}$.
c)

$$\phi = \cos^{-1}\left(\frac{1-\sigma}{1+\sigma}\right) = 22.7^\circ$$

3.6

$$v_{rms} = \sqrt{\frac{1}{\pi}\int_\alpha^\pi V^2 \sin^2 \omega_e t \; d(\omega_e t)} = \frac{V}{\sqrt{2\pi}}\sqrt{\pi - \alpha + \frac{\sin 2\alpha}{2}}$$

3.7
The slip at 220V is $s = (377 - 2\pi\frac{1750}{60}\frac{P}{2})/377 = 0.0277$. Then at 250V, the slip is equal to

$$s = 0.0277 \times \left(\frac{220}{250}\right)^2 = 0.0215.$$

The speed is equal to $\omega_r = \frac{2}{P}(1-s)\,\omega_e = \frac{1}{2} \times 0.9723 \times 377 = 183.3\text{rad/s}$.

3.8
a) Apparent power is equal to $P_{app} = \sqrt{3} \cdot V_{LL} \cdot I_s = \sqrt{3} \cdot 220 \cdot 2 = 762\text{VA}$. Since the reactive power is $P_{app} \times \sin\alpha = 50\text{W}$, it follows that $\sin(\alpha) = 0.0656$. Therefore, $\alpha = \sin^{-1}(0.0656) = 3.76^\circ$.
b) Assume $s \approx 0$ and $I_r \approx 0$ at no load condition.

$$r_s + j\omega_e L_s = \frac{V_s}{I_s} \quad = \quad 63.5\angle 3.76 = 63.36 + j4.16.$$

Thus, $L_s = 4.16/(2\pi \times 60) = 11mH$.
c) $r_s = 63.36\Omega$.

3.9

a) The apparent power is $P_{app} = \sqrt{3} \cdot V_{LL} \cdot I_s = \sqrt{3} \cdot 90 \cdot 7 = 1091.2\text{W}$. Real power is $P_{app} \cos\phi = 800\text{W}$. Thus, $\cos\phi = 0.733$, i.e., $\phi = 42.85°$.

b)

$$\frac{V_s}{I_s} = \frac{90}{\sqrt{3}} \times \frac{1}{7} (\cos\phi + j \sin\phi) = 5.442 + j5.048.$$

c) $r_r = 5.442 - r_s = 3.342\Omega$.

d) $(L_{ls} + L_{lr}) \times 377 = 5.048$. Thus, $L_{ls} = L_{lr} = 6.7\text{mH}$.

Chapter 4

4.1

Since $\dot{\mathbf{X}}(t) = \mathbf{A}\mathbf{X}(t)$, it follows that $s\mathbf{X}(s) = \mathbf{A}\mathbf{X}(s) - x(0)$.

Thus, $\mathbf{X}(s) = (s\mathbf{I} - \mathbf{A})^{-1} x(0)$, i.e., $x(t) = \mathcal{L}^{-1}\left\{(s\mathbf{I} - \mathbf{A})^{-1}\right\} x(0)$. On the other hand, the solution is $x(t) = e^{\mathbf{A}t} x(0)$. Therefore, $e^{\mathbf{A}t} = \mathcal{L}^{-1}\left\{(s\mathbf{I} - \mathbf{A})^{-1}\right\}$.

4.2

$$\begin{aligned}
\lambda_{ds}^e &= L_s i_{ds}^e + L_m i_{dr}^e = L_s i_{ds}^e + \frac{L_m}{L_r} \lambda_{dr}^e - \frac{L_m^2}{L_r} i_{ds}^e \\
i_{ds}^e &= \frac{1}{\sigma L_s} \left(\lambda_{ds}^e - \frac{L_m}{L_r} \lambda_{dr}^e \right)
\end{aligned}$$

4.3

$$\begin{aligned}
p\lambda_{ds}^e &= v_{ds}^e + \omega_e \lambda_{qs}^e - r_s i_{ds}^e = v_{ds}^e + \omega_e \lambda_{qs}^e - r_s \frac{1}{\sigma L_s} \left(\lambda_{ds}^e - \frac{L_m}{L_r} \lambda_{dr}^e \right) \\
&= -\frac{r_s}{\sigma L_s} \lambda_{ds}^e + \omega_e \lambda_{qs}^e + \frac{r_s L_m}{\sigma L_s L_r} \lambda_{dr}^e + v_{ds}^e \\
p\lambda_{qs}^e &= v_{qs}^e - \omega_e \lambda_{ds}^e - r_s i_{qs}^e = v_{qs}^e + \omega_e \lambda_{ds}^e - r_s \frac{1}{\sigma L_s} \left(\lambda_{qs}^e - \frac{L_m}{L_r} \lambda_{qr}^e \right) \\
&= -\omega_e \lambda_{ds}^e - \frac{r_s}{\sigma L_s} \lambda_{qs}^e + \frac{r_s L_m}{\sigma L_s L_r} \lambda_{qr}^e + v_{qs}^e \\
p\lambda_{dr}^e &= \omega_{sl} \lambda_{qr}^e - r_r i_{dr}^e = \omega_{sl} \lambda_{qr}^e - r_r \frac{1}{\sigma L_r} \left(\lambda_{dr}^e - \frac{L_m}{L_s} \lambda_{ds}^e \right) \\
&= \frac{r_r L_m}{\sigma L_s L_r} \lambda_{ds}^e - \frac{r_r}{\sigma L_r} \lambda_{dr}^e + \omega_{sl} \lambda_{qr}^e \\
p\lambda_{qr}^e &= -\omega_{sl} \lambda_{dr}^e - r_r i_{qr}^e = -\omega_{sl} \lambda_{dr}^e - r_r \frac{1}{\sigma L_r} \left(\lambda_{qr}^e - \frac{L_m}{L_s} \lambda_{qs}^e \right) \\
&= \frac{r_r L_m}{\sigma L_s L_r} \lambda_{qs}^e - \omega_{sl} \lambda_{dr}^e - \frac{r_r}{\sigma L_r} \lambda_{qr}^e
\end{aligned}$$

4.4

$$
\begin{aligned}
v_{ds}^s &= r_s i_{ds}^s + L_s p i_{ds}^s + L_m p i_{dr}^s \\
p i_{dr}^s &= -\frac{1}{L_r}\left(L_m p i_{ds}^s + \omega_r L_m i_{qs}^s + r_r i_{dr}^s + \omega_r L_r i_{qr}^s\right) \\
p i_{ds}^s &= -\frac{r_s}{\sigma L_s} i_{ds}^s + \frac{1-\sigma}{\sigma}\omega_r i_{qs}^s + \frac{L_m r_r}{\sigma L_s L_r} i_{dr}^s + \frac{\omega_r L_m}{\sigma L_s} i_{qr}^s + \frac{v_{ds}^s}{\sigma L_s}
\end{aligned}
$$

$$
\begin{aligned}
v_{qs}^s &= r_s i_{qs}^s + L_s p i_{qs}^s + L_m p i_{qr}^s \\
p i_{qr}^s &= -\frac{1}{L_r}\left(\omega_r L_m i_{ds}^s + p L_m i_{qs}^s - \omega_r L_r i_{dr}^s + r_r i_{qr}^s\right) \\
p i_{qs}^s &= -\frac{1-\sigma}{\sigma}\omega_r i_{ds}^s - \frac{r_s}{\sigma L_s} i_{qs}^s - \frac{\omega_r L_m}{\sigma L_s} i_{dr}^s + \frac{L_m r_r}{\sigma L_s L_r} i_{qr}^s + \frac{v_{qs}^s}{\sigma L_s}
\end{aligned}
$$

$$
\begin{aligned}
0 &= p L_m i_{ds}^s + \omega_r L_m i_{qs}^s + r_r i_{dr}^s + p L_r i_{dr}^s + \omega_r L_r i_{qr}^s \\
p i_{ds}^s &= -\frac{1}{L_s}\left(r_s i_{ds}^s + p L_m i_{dr}^s\right) + \frac{v_{ds}^s}{L_s} \\
p i_{dr}^s &= \frac{L_m}{\sigma L_r L_s} r_s i_{ds}^s - \frac{\omega_r L_m}{\sigma L_r} i_{qs}^s - \frac{r_r}{\sigma L_r} i_{dr}^s - \frac{\omega_r}{\sigma} i_{qr}^s - \frac{L_m}{\sigma L_r L_s} v_{ds}^s
\end{aligned}
$$

$$
\begin{aligned}
0 &= -\omega_r L_m i_{ds}^s + p L_m i_{qs}^s - \omega_r L_r i_{dr}^s + r_r i_{qr}^s + p L_r i_{qr}^s \\
p i_{qs}^s &= -\frac{1}{L_s}\left(r_s i_{qs}^s + p L_m i_{qr}^s\right) + \frac{v_{qs}^s}{L_s} \\
p i_{qr}^s &= \frac{\omega_r L_m}{\sigma L_r} i_{ds}^s + \frac{L_m}{\sigma L_r L_s} r_s i_{qs}^s + \frac{\omega_r}{\sigma} i_{dr}^s - \frac{r_r}{\sigma L_r} i_{qr}^s - \frac{L_m}{\sigma L_r L_s} v_{qs}^s
\end{aligned}
$$

4.5

a) In the rotor field orientation, $\lambda_{qr} = 0$.

$$
\begin{aligned}
0 &= \frac{r_s}{s} i_{dr}^e - \omega_e \lambda_{qr} \Rightarrow i_{dr}^e = 0 \\
\lambda_{qr} &= L_m i_{qs}^e + L_r i_{qr}^e \Rightarrow L_m i_{qs}^e + L_r i_{qr}^e = 0
\end{aligned}
$$

b) From the results of a), $i_{qr}^e = -\frac{L_m}{L_r} i_{qs}^e$.

$$
\lambda_{qs}^e = L_s i_{qs}^e + L_m i_{qr}^e = L_s i_{qs}^e + \frac{L_m^2}{L_r} i_{qs}^e = \sigma L_s i_{qs}^e
$$

Using $i_{dr}^e = 0$,

$$
\lambda_{ds}^e = L_s i_{ds}^e + L_m i_{dr}^e = L_s i_{ds}^e = \sigma L_s i_{ds}^e + \frac{L_m^2}{L_r} i_{ds}^e
$$

c) Using b),

$$\begin{aligned}\mathbf{V}_{dqs} &= r_s\mathbf{I}_{dqs} + j\omega_e\mathbf{\Lambda}_{dqs} \\ &= r_s\mathbf{I}_{dqs} + j\omega_e\left(\sigma L_s + \frac{L_m^2}{L_r}i_{ds}^e + j\sigma L_s i_{qs}^e\right) \\ &= (r_s + j\omega_e\sigma L_s)\,\mathbf{I}_{dqs} + j\omega_e\frac{L_m^2}{L_r}i_{ds}^e\end{aligned}$$

Using $i_{dr}^e = 0$,

$$0 = \frac{r_r}{s}\mathbf{I}_{dqr} + j\omega_e\mathbf{\Lambda}_{dqr} = \frac{r_r}{s}i_{qr}^e + j\omega_e L_m i_{ds}^e$$

d) See Fig. 4.5 (a).

4.6

i) Substituting $i_{dr}^e = \frac{\lambda_{ds}^e - L_s i_{ds}^e}{L_m}$ and $i_{qr}^e = \frac{\lambda_{qs}^e - L_s i_{qs}^e}{L_m}$ into (4.58), then the result follows.

ii)

$$\begin{aligned}T_e &= \frac{P}{2}\cdot\frac{3}{2}L_m\left(i_{qs}^e i_{dr}^e - i_{ds}^e i_{qr}^e\right) \\ &= \frac{P}{2}\cdot\frac{3}{2}\frac{L_m}{L_s L_r}\left(L_s i_{qs}^e L_r i_{dr}^e - L_s i_{ds}^e L_r i_{qr}^e\right) \\ &= \frac{P}{2}\cdot\frac{3}{2}\frac{L_m}{L_s L_r}\left((\lambda_{qs}^e - L_m i_{qr}^e)(\lambda_{dr}^e - L_m i_{ds}^e) - (\lambda_{ds}^e - L_m i_{dr}^e)(\lambda_{qr}^e - L_m i_{qs}^e)\right) \\ &= \frac{P}{2}\cdot\frac{3}{2}\frac{L_m}{L_s L_r}((\lambda_{qs}^e\lambda_{dr}^e - \lambda_{ds}^e\lambda_{qr}^e) - L_m^2(i_{qs}^e i_{dr}^e - i_{ds}^e i_{qr}^e) + L_m(\lambda_{ds}^e i_{qs}^e - \lambda_{qs}^e i_{ds}^e) \\ &\quad + L_m(\lambda_{qr}^e i_{dr}^e - \lambda_{dr}^e i_{qr}^e)) \\ &= \frac{P}{2}\cdot\frac{3}{2}\frac{L_m}{L_s L_r}((\lambda_{qs}^e\lambda_{dr}^e - \lambda_{ds}^e\lambda_{qr}^e) - \frac{4T_e}{3P}L_m + \frac{4T_e}{3P}L_m + \frac{4T_e}{3P}L_m) \\ &= \frac{P}{2}\cdot\frac{3}{2}\frac{L_m}{L_s L_r}(\lambda_{qs}^e\lambda_{dr}^e - \lambda_{ds}^e\lambda_{qr}^e) + \frac{L_m^2}{L_s L_r}\cdot T_e\end{aligned}$$

Therefore, the result follows.

Chapter 5

5.1

a) $\sqrt{3}\cdot V_{LL}I_s\cos\phi\cdot\eta = 7460\text{W}$. Thus, $I_s = \frac{7460}{\sqrt{3}\times 220\times 0.84\times 0.86} = 27.1\text{A}$.

b) $i_{qs}^e = \sqrt{I_s^2 - {i_{ds}^e}^2} = \sqrt{27.1^2 - 10^2} = 25.2\text{A}$.

c) $i_{qr}^e = -\frac{L_m}{L_r}i_{qs}^e = -24.5\text{A}$ and $\lambda_{dr}^e = L_m i_{ds}^e = 0.38\text{Wb}$.

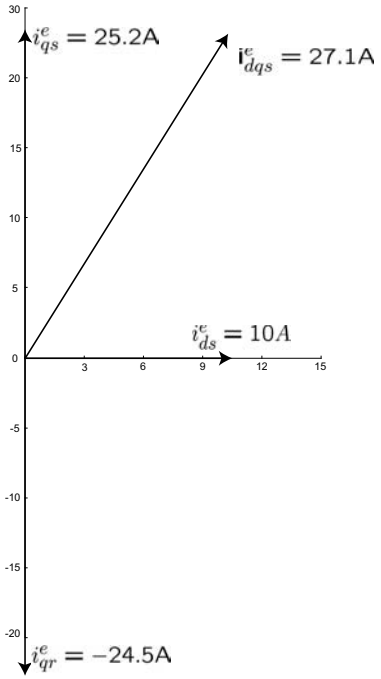

d) From (5.16), $s = \frac{1}{\omega_e} \cdot \frac{r_r}{L_r} \cdot \frac{L_m}{\lambda_{dr}} i^e_{qs} = 0.02$.
e) $T_e = \frac{3P}{4} \cdot \frac{L_m}{L_r} \cdot \lambda^e_{dr} i^e_{qs} = 42.3Nm$.

5.2
a)

$$\Delta\theta_e = \int (\overline{\omega}_{sl} - \omega_{sl})dt = \frac{L_m}{\lambda^e_{dr}} \int \left(\frac{\bar{i}^e_{qs}}{\tau_{rn}} - \frac{i^e_{qs}}{\tau_r} \right) dt.$$

b)

$$\bar{\mathbf{i}}^e_{dqs} - \mathbf{i}^e_{dqs} = (e^{j\bar{\theta}_e} - e^{j\theta_e})\mathbf{i}^s_{dqs} = (e^{j\Delta\theta_e} - 1)\mathbf{i}^e_{dqs} \approx (1 + j\Delta\theta_e - 1)\mathbf{i}^e_{dqs}.$$

c)
If $\tau_r < \tau_{rn}$, then $\Delta\theta_e < 0$. Thus, $\Delta\mathbf{i}^e_{dqs} = e^{-j\frac{\pi}{2}}|\Delta\theta|\mathbf{i}^e_{dqs}$, which implies a reduction in q-axis current. That is, negative angle error enforces torque reduction. As a result, the field-oriented control disallows successive torque increase.

If $\tau_r > \tau_{rn}$, then $\Delta\theta_e > 0$. Thus, $\Delta\mathbf{i}^e_{dqs} = e^{j\frac{\pi}{2}}|\Delta\theta|\mathbf{i}^e_{dqs}$, which implies an increase in q-axis current. That is, positive angle error assists torque production. As a result, the field-oriented control disallows successive torque decrease.

5.3
Note that $i^e_{dr} = \frac{1}{L_m}(\lambda^e_{ds} - L_s i^e_{ds})$ follows from $\lambda^e_{ds} = L_s i^e_{ds} + L_m i^e_{dr}$.

$$\lambda^e_{dr} = L_r i^e_{dr} + L_m i^e_{ds} = \frac{L_r}{L_m}(\lambda^e_{ds} - L_s i^e_{ds}) + L_m i^e_{ds} = \frac{L_r}{L_m}(\lambda^e_{ds} - \sigma L_s i^e_{ds})$$

5.4

a) Note that $i_{ds}^e = \frac{1}{L_s}(\lambda_{ds}^e + \sigma\tau_r L_s i_{qs}^e \omega_{sl})$. Substituting i_{ds}^e into (5.28), it follows that

$$\omega_{sl}^2 - \frac{(1-\sigma)\lambda_{ds}^e}{\sigma^2 L_s \tau_r i_{qs}^e}\omega_{sl} + \frac{1}{(\sigma\tau_r)^2} = 0$$

b) The discriminant should satisfy:

$$\mathbf{D} = \left(\frac{(1-\sigma)\lambda_{ds}^e}{\sigma^2 L_s \tau_r i_{qs}^e}\right)^2 - 4\frac{1}{(\sigma\tau_r)^2} = {\lambda_{ds}^e}^2 - \left(\frac{2\sigma L_s i_{qs}^e}{1-\sigma}\right)^2 \geq 0.$$

Therefore, the stator current should satisfy

$${i_{qs}^e}^2 \leq \left(\frac{\lambda_{ds}^e}{2L_s}(\frac{1}{\sigma} - 1)\right)^2.$$

c) Substituting $i_{qs}^e = \frac{4}{3P}\frac{T_e}{\lambda_{ds}^e}$ into the result of b), it follows that

$$\frac{T_e}{{\lambda_{ds}^e}^2} \leq \frac{3P}{8L_s}\left(\frac{1}{\sigma} - 1\right).$$

5.5

Since $\left(\omega_e \sigma L_s i_{qs}^e\right)^2 + \left(\omega_e L_s i_{ds}^e\right)^2 = V_{max}^2$, we have

$$\begin{aligned} i_{qs}^e &= \sqrt{\frac{{V_{max}}^2 - \left(\omega_e L_s I_s\right)^2}{\omega_e^2 L_s^2\left(\sigma^2 - 1\right)}} = 21.928\text{A} \\ i_{ds}^e &= \sqrt{{I_s}^2 - {i_{qs}^e}^2} = 7.87736\text{A} \\ T_e &= \frac{3}{4}P\frac{L_m^2}{L_r} i_{ds}^e i_{qs}^e = 31.32\text{Nm} \end{aligned}$$

5.6

Derivation of (5.47):

$$\begin{aligned} \Delta\dot{\hat{\mathbf{x}}} &= \left(\mathbf{A}(\omega_r) - \mathbf{GC}\right)\Delta\mathbf{x} + \Delta\omega_r \begin{bmatrix} \frac{L_m}{\sigma L_r L_s}\mathbf{J} \\ -\mathbf{J} \end{bmatrix} \hat{\lambda}_{dqr}^e \\ \dot{\mathbf{p}(t)} &= -\left(\mathbf{A}(t) - \mathbf{GC}\right)^T \mathbf{P}(t) - \mathbf{P}(t)\left(\mathbf{A}(t) - \mathbf{GC}\right) + \mathbf{Q}(t) \\ V &= \Delta\mathbf{x}^T \mathbf{P}(t)\Delta\mathbf{x} + \frac{1}{2\gamma}\Delta\omega_r^2 \end{aligned}$$

$$\begin{aligned}
\dot{V} &= \Delta\mathbf{x}^T\mathbf{P}(t)\Delta\dot{\mathbf{x}} + \Delta\dot{\mathbf{x}}^T\mathbf{P}(t)\Delta\mathbf{x} + \Delta\mathbf{x}^T\dot{\mathbf{P}}(t)\Delta\mathbf{x} + \frac{\Delta\omega_r\Delta\dot{\omega}_r}{\gamma} \\
&= \Delta\mathbf{x}^T\mathbf{P}\Big((\mathbf{A}-\mathbf{GC})\,\Delta\mathbf{x} + \Delta\omega_r\begin{bmatrix}\frac{L_m}{\sigma L_r L_s}\mathbf{J}\\ -\mathbf{J}\end{bmatrix}\hat{\lambda}^e_{dqr}\Big) \\
&\quad +\Big((\mathbf{A}-\mathbf{GC})\,\Delta\mathbf{x} + \Delta\omega_r\begin{bmatrix}\frac{L_m}{\sigma L_r L_s}\mathbf{J}\\ -\mathbf{J}\end{bmatrix}\hat{\lambda}^e_{dqr}\Big)^T\mathbf{P}(t)\Delta\mathbf{x} \\
&\quad +\Delta x^T\Big(-(\mathbf{A}-\mathbf{GC})^T\mathbf{P} - \mathbf{P}\,(\mathbf{A}-\mathbf{GC}) + \mathbf{Q}\Big)\Delta x - \frac{1}{\gamma}\Delta\omega_r\dot{\hat{\omega}}_r \\
&= \Delta\mathbf{x}^T\mathbf{Q}\Delta\mathbf{x} + 2\Delta\omega_r\Delta\mathbf{x}^T\mathbf{P}\begin{bmatrix}\frac{L_m}{\sigma L_r L_s}\mathbf{J}\\ -\mathbf{J}\end{bmatrix}\hat{\lambda}^e_{dqr} - \frac{1}{\gamma}\Delta\omega_r\dot{\hat{\omega}}_r
\end{aligned}$$

Derivation of (5.49):

$$\begin{aligned}
\dot{\hat{\omega}}_r &= 2\gamma\Delta\mathbf{x}^T\mathbf{P}\begin{bmatrix}\frac{L_m}{\sigma L_r L_s}\mathbf{J}\\ -\mathbf{J}\end{bmatrix}\hat{\lambda}^e_{dqr} \\
&= 2\gamma\begin{bmatrix}\Delta i^e_{ds} & \Delta i^e_{qs} & 0 & 0\end{bmatrix}\begin{bmatrix}0 & \frac{L_m}{\sigma L_r L_s}\\ -\frac{L_m}{\sigma L_r L_s} & 0\\ 0 & -1\\ 1 & 0\end{bmatrix}\begin{bmatrix}\lambda^e_{dr}\\ \lambda^e_{qr}\end{bmatrix} \\
&= 2\gamma\frac{L_m}{\sigma L_r L_s}\Big(\Delta i^e_{ds}\lambda^e_{qr} - \Delta i^e_{qs}\lambda^e_{dr}\Big) \\
&= \gamma'\Big(\Delta i^e_{ds}\lambda^e_{qr} - \Delta i^e_{qs}\lambda^e_{dr}\Big)
\end{aligned}$$

Chapter 6

6.1

We have

$$T_e = -\frac{\partial W_{fld}}{\partial\theta} = \frac{\mu_0\pi DL}{2g}\cdot MMF_s\cdot MMF_r\cdot\sin\theta.$$

6.2

Since $L_{ls}=0$ and $i_b=i_c=0$, it follows that

$$\lambda_{as} = (L_{ms} - L_\delta\cos 2\theta_r)\cdot i_{as}.$$

The maximum and minimum values of λ_a are 0.106Wb and 0.065Wb, respectively. Therefore, $L_{ms} = \frac{0.106+0.065}{2\times 40} = 2.14$mH and $L_\delta = \frac{0.106-0.065}{2\times 40} = 0.5$mH. Hence,

$$\begin{aligned}
L_d &= \frac{3}{2}(L_{ms} - L_\delta) = 2.46\text{mH} \\
L_q &= \frac{3}{2}(L_{ms} + L_\delta) = 3.96\text{mH}.
\end{aligned}$$

6.3
a) Note that the back EMF is equal to

$$\omega_e \psi_m \begin{bmatrix} \sin \omega_e t \\ \sin(\omega_e t - \frac{2\pi}{3}) \\ \sin(\omega_e t + \frac{2\pi}{3}) \end{bmatrix}$$

Since the number of poles is 4,

$$\psi_m = \frac{220}{2\pi \times \frac{4}{2} \times \frac{6000}{60}} = 0.175 \; Wb.$$

b)

$$\begin{aligned} V_s &= \sqrt{(\omega_e \psi_m + \omega_e L_d i_d^e)^2 + (\omega_e L_q^e i_q^e)^2} = \sqrt{(220 - 9.95)^2 + (108.33)^2} \\ &= 236.36 \; V. \end{aligned}$$

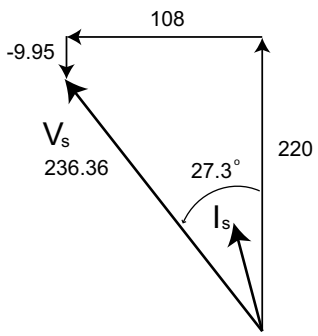

c)

$$\begin{aligned} T_e &= \frac{3P}{4}(\psi_m i_q^e - (L_q - L_d) i_d^e i_q^e) \\ &= \frac{3 \times 6}{4}(0.175 \times 37.5 - (2.3 - 1.2) \times 10^{-3} \times (-6.6) \times 37.5) = 30.8\text{Nm}. \end{aligned}$$

d) Voltage angle $= \tan^{-1}(\frac{108.33}{220-9.95}) = 27.29°$,
Current angle $= \tan^{-1}(\frac{6.6}{37.5}) = 9.98°$,
Power factor $= \cos(27.29° - 9.98°) = 0.955$.

6.4
(a) $L_d = L_q$, (b) $L_d < L_q$, (c) $L_d < L_q$, (d) $L_d < L_q$.

Chapter 7

7.1
$T_e = \frac{36000}{3000/60 \times 2\pi} = 114.6\text{Nm}$. Since $T_e = k_w B_m A_m \text{Vol}$, it follows that

$$l_{st} = \frac{114.6(\text{Nm})}{0.96 \times 0.8(\text{T}) \times 55000(\text{A/m}) \times \pi/4 \times 0.11^2(\text{m}^2)} = 0.285\text{m}.$$

7.2

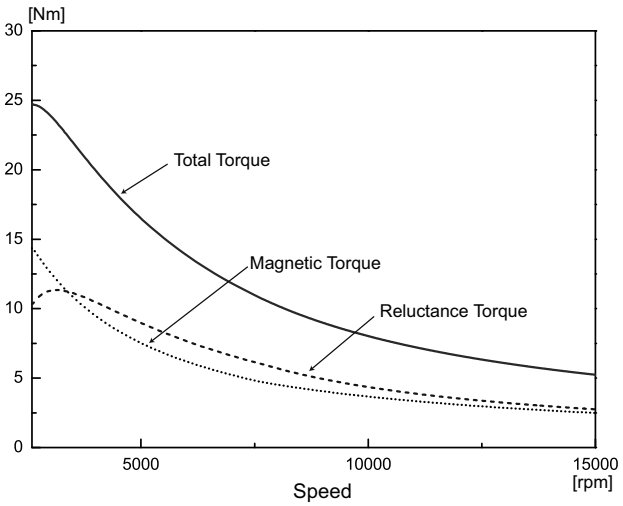

7.3

Let $L(i_d^e, i_q^e) = \frac{3P}{4}(\psi_m i_q^e + L_d(1-\xi) i_d^e i_q^e) + \mu_1(\xi i_q^{e2} + i_d^{e2} + i_d^e i_f)$. Then,

$$\begin{aligned} \frac{\partial L}{\partial i_d^e} &= \frac{3P}{4}(L_d(1-\xi) i_q^e) + \mu_1(2i_d^e + i_f) = 0 \\ \frac{\partial L}{\partial i_q^e} &= \frac{3P}{4} L_d(i_f + (1-\xi) i_d^e) + 2\mu_1 \xi i_q^e = 0. \end{aligned}$$

Then substituting $\mu_1 = \frac{-\frac{3P}{4} L_d(1-\xi) i_q^e}{2i_d^e + i_f}$ into $\frac{\partial L}{\partial i_q^e} = 0$, we obtain

$$i_f + (1-\xi) i_d^e - \frac{2\xi i_q^{e2}(1-\xi)}{2i_d^e + i_f} = 0.$$

Utilizing $\frac{\partial L}{\partial \mu} = \xi i_q^{e2} + i_d^e(i_d^e + i_f) = 0$, we obtain a second-order equation for i_d^e:

$$4(1-\xi) i_d^{e2} + (2 + 3(1-\xi)) i_d^e i_f + i_f^2 = 0.$$

Then, the solutions are

$$\begin{aligned}
i_d^e &= \frac{-(2+3(1-\xi))+\sqrt{9(1-\xi)^2-4(1-\xi)+4}}{8(1-\xi)} \times i_f \\
i_q^e &= \sqrt{\frac{-i_d^e(i_d^e+i_f)}{\xi}} \\
T_e &= \frac{3P}{4}(\psi_m i_q^e - (L_q - L_d) i_d^e i_q^e) \\
\xi &= \frac{L_q}{L_d} = 2.03, \quad i_f = \frac{\psi_m}{L_d} = 31.08\text{A}. \\
i_d^e &= -20\text{A}, \quad i_q^e = 10.45\text{A}. \\
T_e &= 7.42\text{Nm}.
\end{aligned}$$

7.4

$$\begin{aligned}
\xi &= \frac{0.0062}{0.00305} = 2.03 \\
\psi_b &= \sqrt{(\psi_m + L_d i_{db})^2 + (L_q i_{qb})^2} = 0.21\text{Wb}. \\
V_b &= \omega_b \psi_b = \frac{2600}{60} \times 2\pi \times \frac{6}{2} \times 0.21 = 171.53\text{V}. \\
L_{dn} &= \frac{\omega_b L_d I_b}{V_b} = \frac{816.8 \times 0.00305 \times 40}{171.53} = 0.581 \\
L_{qn} &= \frac{\omega_b L_q I_b}{V_b} = \frac{816.8 \times 0.0062 \times 40}{171.53} = 1.181 \\
\psi_n &= \frac{\psi_m}{\psi_b} = \frac{0.0948}{0.21} = 0.451. \\
V_{dn} &= -\omega_n \xi L_{dn} i_{qn} = -1.18 \omega_n i_{qn} \\
V_{qn} &= \omega_n L_{dn} i_{qn} + \omega_n \psi_n = 0.581 \omega_n i_{dn} + 0.451 \omega_n \\
T_n &= 0.451 i_{qn} - 0.6 i_{dn} i_{qn}
\end{aligned}$$

7.5
a)

$$\begin{aligned}
\xi &= \frac{0.0035}{0.001} = 3.5 \\
I_b &= 500\text{A} \\
\psi_b &= \sqrt{(\psi_m + L_d i_{db})^2 + (L_q i_{qb})^2} = 0.137\text{Wb.} \\
V_b &= \omega_b \psi_b = \frac{2600}{60} \times 2\pi \times \frac{8}{2} \times 0.137 = 149\text{V.} \\
L_{dn} &= \frac{\omega_b L_d I_b}{V_b} = \frac{1089 \times 0.0001 \times 500}{149} = 0.365 \\
\psi_n &= \frac{\psi_m}{\psi_b} = \frac{0.052}{0.137} = 0.38. \\
V_{dn} &= -\omega_n \xi L_{dn} i_{qn} = -1.278 \omega_n i_{qn} \\
V_{qn} &= \omega_n L_{dn} i_{dn} + \omega_n \psi_n = 0.365 \omega_n i_{dn} + 0.38 \omega_n \\
T_n &= 0.38 i_{qn} - 0.913 i_{dn} i_{qn}
\end{aligned}$$

b)

$$V_{dn}^2 + V_{qn}^2 = (1.278 \times \frac{388}{500})^2 + (0.38 - 0.365 \times \frac{314}{500})^2 = 1$$

c)

$$\begin{aligned}
\omega_{cn} &= \frac{1}{\psi_n - L_{dn}} = \frac{1}{0.38 - 0.365} = 66.67 \\
\omega_c &= 66.67 \times 2600 = 173,342\text{rpm.}
\end{aligned}$$

Chapter 8

8.1
(a) The flux through the loop area $4xy$ is equal to $\Phi_{xy} = -4xyB(t)$. Then, the EMF around the loop is

$$v = -\frac{d\Phi_{xy}}{dt} = \frac{4L}{W/N} x^2 \frac{dB}{dt}.$$

(b) The resistance of the loop is

$$r_x = \frac{4y}{\sigma D dx} = \frac{4}{\sigma D} \frac{L}{W/N} \frac{x}{dx}.$$

(c) The dissipated power in each incremental loop is equal to

$$dP_{xy} = \left(\frac{4L}{W/N}x^2\frac{dB}{dt}\right)^2 \frac{1}{r_x} = \frac{4\sigma LD}{W/N}x^3dx\left(\frac{dB}{dt}\right)^2.$$

(d) The power loss in each sheet is then found by integrating dP_{xy}:

$$P_{sheet} = \int_0^{\frac{W}{2N}} dP_{xy} = \int_0^{\frac{W}{2N}} \frac{4\sigma LD}{W/N}x^3dx\left(\frac{dB}{dt}\right)^2 = \frac{L\sigma DW^3}{16N^3}\left(\frac{dB}{dt}\right)^2$$

(e) The total eddy current loss of the stack is equal to

$$P_{st} = N \times P_{sheet} = \frac{\pi^2\sigma LDW^3}{4N^2}f^2B_m^2\cos^2(2\pi ft).$$

(f) The average value of $\cos^2(2\pi ft)$ is equal to $\frac{1}{2}$. Therefore, the average eddy current loss is equal to

$$P_{ed} = \frac{\pi^2\sigma LDW^3}{8N^2}f^2B_m^2.$$

8.2
Substituting $i_{ds}^{e2} + i_{qs}^{e2} = I_{max}^2$ into (5.34), it follows that

$$i_{ds}^{e2} = \frac{1}{\sigma^2-1}\left(\sigma^2I_{max}^2 - \left(\frac{V_{max}}{\omega_{ps}\ L_s}\right)^2\right) \quad \text{and} \quad i_{qs}^{e2} = \frac{1}{\sigma^2-1}\left(\left(\frac{V_{max}}{\omega_{ps}\ L_s}\right)^2 - I_{max}^2\right).$$

Note from (5.36) that

$$\left(\frac{V_{max}}{\omega_{ps}\ L_s}\right)^4 = 4\sigma^2 i_{ds}^{e2}i_{qs}^{e2}$$

Replacing i_{ds}^{e2} and i_{qs}^{e2}, it follows that

$$\omega_{ps}^4\left(4(L_s\sigma I_{max})^4\right) - \omega_{ps}^2\left(4(L_s\sigma V_{max}I_{max})^2(\sigma^2+1)\right) + V_{max}^4(\sigma^2+1)^2 = 0$$

Using the quadratic formula, the solution is obtained.

8.3
Note that $T_{m2} = K_t i_{ds}^e i_{qs}^e$. Substituting i_{ds}^{e2} and i_{qs}^{e2} by the solutions obtained in (**8.2**), the result follows.

Chapter 9

9.1
Note that

$$\eta(\hat{\mathbf{x}}) = \hat{\mathbf{x}} - \mathbf{x} + \mathbf{x} - L_s \begin{bmatrix} i_d^s \\ i_q^s \end{bmatrix} = \tilde{\mathbf{x}} + \psi_m \begin{bmatrix} \cos\theta_e(t) \\ \sin\theta_e(t) \end{bmatrix}.$$

Therefore,

$$\begin{aligned}
\dot{\tilde{\mathbf{x}}} &= \frac{\gamma}{2}\eta(\hat{\mathbf{x}})[\psi_m^2 - \|\eta(\hat{\mathbf{x}})\|^2] \\
&= \frac{\gamma}{2}\left(\tilde{\mathbf{x}} + \psi_m \begin{bmatrix} \cos\theta_e(t) \\ \sin\theta_e(t) \end{bmatrix}\right)\left(\psi_m^2 - \left\| \begin{bmatrix} \tilde{x}_1 + \psi_m \cos\theta_e(t) \\ \tilde{x}_2 + \psi_m \sin\theta_e(t) \end{bmatrix} \right\|^2\right) \\
&= -\gamma\left(\tilde{\mathbf{x}} + \psi_m \begin{bmatrix} \cos\theta_e(t) \\ \sin\theta_e(t) \end{bmatrix}\right)\left(\frac{1}{2}\|\tilde{\mathbf{x}}\|^2 + \psi_m \tilde{x}_1 \cos\theta_e(t) + \psi_m \tilde{x}_2 \sin\theta_e(t)\right)
\end{aligned}$$

9.2
The solution is omitted.

9.3
Let $\mathbf{m}(t) = \int_0^t e^{(\mathbf{A}_s - \mathbf{KC})(t-\tau)}\mathbf{b}_s(\tau)\hat{p}(\tau)d\tau$. Then, an equivalent expression for $\mathbf{m}(t)$ is

$$\dot{\mathbf{m}}(t) = (\mathbf{A}_s - \mathbf{KC})\mathbf{m}(t) + \mathbf{b}_s(t)\hat{p}(t).$$

Thus,

$$\begin{aligned}
\dot{\boldsymbol{\varepsilon}}(t) &= -\dot{\boldsymbol{\beta}}(t)\hat{p}(t) - \boldsymbol{\beta}(t)\dot{\hat{p}}(t) + (\mathbf{A}_s - \mathbf{KC})\mathbf{m}(t) + \mathbf{b}_s(t)\hat{p}(t) \\
&= (\mathbf{A}_s - \mathbf{KC})\big(\mathbf{m}(t) - \boldsymbol{\beta}(t)\hat{p}(t)\big) - \boldsymbol{\beta}(t)\dot{\hat{p}}(t) \\
&= (\mathbf{A}_s - \mathbf{KC})\boldsymbol{\varepsilon}(t) - \left(\int_0^t e^{(\mathbf{A}_s - \mathbf{KC})(t-\tau)}\mathbf{b}_s(\tau)d\tau\right)\dot{\hat{p}}(t).
\end{aligned}$$

9.4

$$\begin{aligned}
\overline{\mathbf{v}}_{dq}^e &= e^{\mathbf{J}(\overline{\theta}_e - \theta_e)}\left[(r_s + pL_d)\mathbf{I} - \omega_e L_q \mathbf{J}\right] e^{-\mathbf{J}(\overline{\theta}_e - \theta_e)}\overline{\mathbf{i}}_{dq}^e + e^{\mathbf{J}(\overline{\theta}_e - \theta_e)}\boldsymbol{\zeta} \\
&= e^{\mathbf{J}(\overline{\theta}_e - \theta_e)} \begin{bmatrix} r_s + pL_d & -\omega_e L_q \\ \omega_e L_q & r_s + pL_d \end{bmatrix} \begin{bmatrix} \cos(\overline{\theta}_e - \theta_e) & -\sin(\overline{\theta}_e - \theta_e) \\ \sin(\overline{\theta}_e - \theta_e) & \cos(\overline{\theta}_e - \theta_e) \end{bmatrix} \begin{bmatrix} \overline{i}_d^e \\ \overline{i}_q^e \end{bmatrix} \\
&\quad + \begin{bmatrix} \cos(\overline{\theta}_e - \theta_e) & \sin(\overline{\theta}_e - \theta_e) \\ -\sin(\overline{\theta}_e - \theta_e) & \cos(\overline{\theta}_e - \theta_e) \end{bmatrix} \begin{bmatrix} 0 \\ E_{ex} \end{bmatrix}
\end{aligned}$$

$$
\begin{aligned}
&= e^{\mathbf{J}(\overline{\theta}_e-\theta_e)}\begin{bmatrix} r_s & -\omega_e L_q \\ \omega_e L_q & r_s \end{bmatrix}\begin{bmatrix} \cos(\overline{\theta}_e-\theta_e) & -\sin(\overline{\theta}_e-\theta_e) \\ \sin(\overline{\theta}_e-\theta_e) & \cos(\overline{\theta}_e-\theta_e) \end{bmatrix}\begin{bmatrix} \bar{i}_d^e \\ \bar{i}_q^e \end{bmatrix} \\
&\quad + e^{\mathbf{J}(\overline{\theta}_e-\theta_e)}\begin{bmatrix} pL_d & 0 \\ 0 & pL_d \end{bmatrix}\begin{bmatrix} \cos(\overline{\theta}_e-\theta_e) & -\sin(\overline{\theta}_e-\theta_e) \\ \sin(\overline{\theta}_e-\theta_e) & \cos(\overline{\theta}_e-\theta_e) \end{bmatrix}\begin{bmatrix} \bar{i}_d^e \\ \bar{i}_q^e \end{bmatrix} \\
&\quad + E_{ex}\begin{bmatrix} \sin(\overline{\theta}_e-\theta_e) \\ \cos(\overline{\theta}_e-\theta_e) \end{bmatrix} \\
&= \begin{bmatrix} r_s & -\omega_e L_q \\ \omega_e L_q & r_s \end{bmatrix}\begin{bmatrix} \bar{i}_d^e \\ \bar{i}_q^e \end{bmatrix} + E_{ex}\begin{bmatrix} \sin(\overline{\theta}_e-\theta_e) \\ \cos(\overline{\theta}_e-\theta_e) \end{bmatrix} \\
&\quad + (\overline{\omega}_e-\omega_e)L_d e^{\mathbf{J}(\overline{\theta}_e-\theta_e)}\begin{bmatrix} -\sin(\overline{\theta}_e-\theta_e) & -\cos(\overline{\theta}_e-\theta_e) \\ \cos(\overline{\theta}_e-\theta_e) & -\sin(\overline{\theta}_e-\theta_e) \end{bmatrix}\begin{bmatrix} \bar{i}_d^e \\ \bar{i}_q^e \end{bmatrix} \\
&\quad + L_d e^{\mathbf{J}(\overline{\theta}_e-\theta_e)}\begin{bmatrix} \cos(\overline{\theta}_e-\theta_e) & -\sin(\overline{\theta}_e-\theta_e) \\ \sin(\overline{\theta}_e-\theta_e) & \cos(\overline{\theta}_e-\theta_e) \end{bmatrix}\begin{bmatrix} p\bar{i}_d^e \\ p\bar{i}_q^e \end{bmatrix} \\
&= \begin{bmatrix} r_s & -\omega_e L_q \\ \omega_e L_q & r_s \end{bmatrix}\begin{bmatrix} \bar{i}_d^e \\ \bar{i}_q^e \end{bmatrix} + E_{ex}\begin{bmatrix} \sin(\overline{\theta}_e-\theta_e) \\ \cos(\overline{\theta}_e-\theta_e) \end{bmatrix} \\
&\quad + \begin{bmatrix} 0 & -(\overline{\omega}_e-\omega_e)L_d \\ (\overline{\omega}_e-\omega_e)L_d & 0 \end{bmatrix}\begin{bmatrix} \bar{i}_d^e \\ \bar{i}_q^e \end{bmatrix} + \begin{bmatrix} pL_d & 0 \\ 0 & pL_d \end{bmatrix}\begin{bmatrix} \bar{i}_d^e \\ \bar{i}_q^e \end{bmatrix} \\
&= \begin{bmatrix} r_s + pL_d & -\omega_e L_q \\ \omega_e L_q & r_s + pL_d \end{bmatrix}\begin{bmatrix} \bar{i}_d^e \\ \bar{i}_q^e \end{bmatrix} + E_{ex}\begin{bmatrix} \sin(\overline{\theta}_e-\theta_e) \\ \cos(\overline{\theta}_e-\theta_e) \end{bmatrix} + (\overline{\omega}_e-\omega_e)L_d\begin{bmatrix} -\bar{i}_q^e \\ \bar{i}_d^e \end{bmatrix}.
\end{aligned}
$$

9.5

$$
\begin{aligned}
& e^{\mathbf{J}\Delta\theta_e}\begin{bmatrix} pL_d & 0 \\ 0 & pL_q \end{bmatrix} e^{-\mathbf{J}\Delta\theta_e}\bar{\mathbf{i}}_{dq}^e \\
&= \begin{bmatrix} \cos\Delta\theta_e & \sin\Delta\theta_e \\ -\sin\Delta\theta_e & \cos\Delta\theta_e \end{bmatrix}\begin{bmatrix} pL_d & 0 \\ 0 & pL_q \end{bmatrix}\begin{bmatrix} \cos\Delta\theta_e & -\sin\Delta\theta_e \\ \sin\Delta\theta_e & \cos\Delta\theta_e \end{bmatrix}\begin{bmatrix} \bar{i}_d^e \\ \bar{i}_q^e \end{bmatrix} \\
&= \Delta\omega_e\begin{bmatrix} \cos\Delta\theta_e & \sin\Delta\theta_e \\ -\sin\Delta\theta_e & \cos\Delta\theta_e \end{bmatrix}\begin{bmatrix} -L_d\sin\Delta\theta_e & -L_d\cos\Delta\theta_e \\ L_q\cos\Delta\theta_e & -L_q\sin\Delta\theta_e \end{bmatrix}\begin{bmatrix} \bar{i}_d^e \\ \bar{i}_q^e \end{bmatrix} \\
&\quad + \begin{bmatrix} \cos\Delta\theta_e & \sin\Delta\theta_e \\ -\sin\Delta\theta_e & \cos\Delta\theta_e \end{bmatrix}\begin{bmatrix} L_d\cos\Delta\theta_e & -L_d\sin\Delta\theta_e \\ L_q\sin\Delta\theta_e & L_q\cos\Delta\theta_e \end{bmatrix}\begin{bmatrix} p\bar{i}_d^e \\ p\bar{i}_q^e \end{bmatrix} \\
&= \Delta\omega_e\begin{bmatrix} (L_q-L_d)\sin\Delta\theta_e\cos\Delta\theta_e & -(L_d\cos^2\Delta\theta_e + L_q\sin^2\Delta\theta_e) \\ L_q\cos^2\Delta\theta_e + L_d\sin^2\Delta\theta_e & (L_d-L_q)\sin\Delta\theta_e\cos\Delta\theta_e \end{bmatrix}\begin{bmatrix} \bar{i}_d^e \\ \bar{i}_q^e \end{bmatrix} \\
&\quad + \begin{bmatrix} L_d\cos^2\Delta\theta_e + L_q\sin^2\Delta\theta_e & (L_q-L_d)\sin\Delta\theta_e\cos\Delta\theta_e \\ (L_q-L_d)\sin\Delta\theta_e\cos\Delta\theta_e & L_q\cos^2\Delta\theta_e + L_d\sin^2\Delta\theta_e \end{bmatrix}\begin{bmatrix} p\bar{i}_d^e \\ p\bar{i}_q^e \end{bmatrix}
\end{aligned}
$$

$$
\begin{aligned}
&= (\overline{\omega}_e - \omega_e)\begin{bmatrix} \frac{L_q - L_d}{2}\sin 2\Delta\theta_e & -\frac{L_q+L_d}{2} + \frac{L_q-L_d}{2}\cos 2\Delta\theta_e \\ \frac{L_q+L_d}{2} + \frac{L_q-L_d}{2}\cos 2\Delta\theta_e & -\frac{L_q-L_d}{2}\sin 2\Delta\theta_e \end{bmatrix}\begin{bmatrix} \bar{i}_d^e \\ \bar{i}_q^e \end{bmatrix} \\
&\quad + \begin{bmatrix} \frac{L_q+L_d}{2} - \frac{L_q-L_d}{2}\cos 2\Delta\theta_e & \frac{L_q-L_d}{2}\sin 2\Delta\theta_e \\ \frac{L_q-L_d}{2}\sin 2\Delta\theta_e & \frac{L_q+L_d}{2} + \frac{L_q-L_d}{2}\cos 2\Delta\theta_e \end{bmatrix}\begin{bmatrix} p\bar{i}_d^e \\ p\bar{i}_q^e \end{bmatrix} \\
&= (\overline{\omega}_e - \omega_e)\begin{bmatrix} L_{df}\sin 2\Delta\theta_e & -L_{av} + L_{df}\cos 2\Delta\theta_e \\ L_{av} + L_{df}\cos 2\Delta\theta_e & -L_{df}\sin 2\Delta\theta_e \end{bmatrix}\begin{bmatrix} \bar{i}_d^e \\ \bar{i}_q^e \end{bmatrix} \\
&\quad + \begin{bmatrix} L_{av} - L_{df}\cos 2\Delta\theta_e & L_{df}\sin 2\Delta\theta_e \\ L_{df}\sin 2\Delta\theta_e & L_{av} + L_{df}\cos 2\Delta\theta_e \end{bmatrix}\begin{bmatrix} p\bar{i}_d^e \\ p\bar{i}_q^e \end{bmatrix}.
\end{aligned}
$$

9.6

(a)

$$
\begin{aligned}
\det(\mathbf{Z}(s)) &= (r_s + L_\alpha s)(r_s + L_\beta s) - L_\gamma^2 s^2 \\
&= r_s^2 + r_s(L_\alpha + L_\beta)s + (L_\alpha L_\beta - L_\gamma^2)s^2 \\
&\quad \left(\because L_\alpha L_\beta - L_\gamma^2 = L_d L_q,\ L_\alpha + L_\beta = L_d + L_q\right) \\
&= r_s^2 + r_s(L_d + L_q)s + L_d L_q s^2 \\
&= (L_d s + r_s)(L_q s + r_s).
\end{aligned}
$$

Thus,

$$
\mathbf{Z}^{-1}(s) = \frac{1}{(L_d s + r_s)(L_q s + r_s)}\begin{bmatrix} r_s + L_\beta s & -L_\gamma s \\ -L_\gamma s & r_s + L_\alpha s \end{bmatrix}.
$$

(b)

$$
\begin{aligned}
\begin{bmatrix} \Delta i_d(s) \\ \Delta i_q(s) \end{bmatrix} &= \frac{1}{(L_d s + r_s)(L_q s + r_s)}\begin{bmatrix} r_s + L_\beta s & -L_\gamma s \\ -L_\gamma s & r_s + L_\alpha s \end{bmatrix}\begin{bmatrix} \frac{V_p}{s} \\ 0 \end{bmatrix} \\
&= \frac{V_p}{(L_d s + r_s)(L_q s + r_s)}\begin{bmatrix} \frac{r_s}{s} + L_\beta \\ -L_\gamma \end{bmatrix}.
\end{aligned}
$$

$$
\begin{aligned}
\Delta i_d(s) &= \frac{-\frac{V_p L_d}{2r_s}(1 + \cos 2\Delta\theta_e)}{L_d s + r_s} + \frac{-\frac{V_p L_q}{2r_s}(1 - \cos 2\Delta\theta_e)}{L_q s + r_s} + \frac{V_p}{r_s s}, \\
\Delta \bar{i}_q(s) &= \frac{\frac{V_p L_d}{2r_s}\sin 2\Delta\theta_e}{L_d s + r_s} + \frac{-\frac{V_p L_q}{2r_s}\sin 2\Delta\theta_e}{L_q s + r_s},
\end{aligned}
$$

$$
\begin{aligned}
\Delta i_d(T_p) &= \frac{V_p}{r_s}\left[1 - \frac{1}{2}\left(e^{-(r_s/L_q)T_p} + e^{-(r_s/L_d)T_p}\right)\right. \\
&\quad \left. + \frac{1}{2}\left(e^{-(r_s/L_q)T_p} - e^{-(r_s/L_d)T_p}\right)\cos 2\Delta\theta_e\right], \\
\Delta i_q(T_p) &= -\frac{V_p}{2r_s}\left[e^{-(r_s/L_q)T_p} - e^{-(r_s/L_d)T_p}\right]\sin 2\Delta\theta_e.
\end{aligned}
$$

Chapter 10

10.1
$v_{as[5]}/v_{as[1]} = 1/5$ and $v_{as[7]}/v_{as[1]} = 1/7$.

10.2
$v_d^s = 100\cos(\frac{\pi}{6}) = 50 \times \sqrt{3}$V and $v_q^s = 100\sin(\frac{\pi}{6}) = 50$V. According to (10.14),

$$\begin{bmatrix} T_1 \\ T_2 \end{bmatrix} = \frac{\sqrt{3} \times 125(\mu s)}{300\text{V}} \begin{bmatrix} \frac{\sqrt{3}}{2} & -\frac{1}{2} \\ 0 & 1 \end{bmatrix} \begin{bmatrix} 50\sqrt{3} \\ 50 \end{bmatrix} = \begin{bmatrix} 36 \\ 36 \end{bmatrix} (\mu s). \tag{14.11}$$

$T_0 = 125 - 72 = 53\mu$s.

10.3

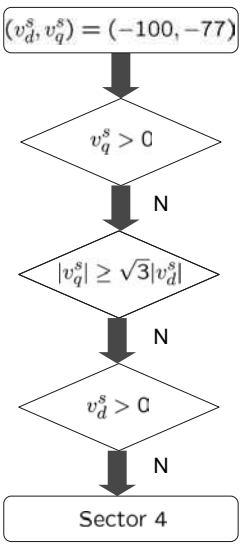

10.4

$$\begin{aligned} \frac{\Delta V}{V} &= -\frac{\frac{2}{125} \times 300}{10} = -0.48 \\ \frac{\Delta V}{V} &= -\frac{\frac{2}{125} \times 300}{100} = -0.048. \end{aligned}$$

Therefore, the relative voltage error is large when the output voltage is small.

10.5
For $N_f = 10$, 3.33 pulses are in 20ms. But, the fractional part (0.33 pulse) is not counted. Hence, $\Delta N_f/N_f = 0.33/3.33 = 0.099$.
Similarly, 33.33 pulses are in 20 ms for $N_f = 100$. $\Delta N_f/N_f = 0.33/33.33 = 0.0099$.

10.6
When $E\sin(\omega_{rs}t)$ and $E\cos(\omega_{rs}t)$ are applied to the resolver, the output is calculated as

$$E\cos(\omega_{rs}t)\cos\theta_r + E\sin(\omega_{rs}t)\sin\theta_r = E\cos(\omega_{rs}t - \theta_r)$$

Chapter 11

11.1
a) We need to use $V_x(t) = \frac{K_2}{K_1}\tanh(K_1K_2t)$.
Note that $K_1 = \sqrt{\frac{1.225\times1.5\times0.35}{2400}} = 0.01637$ and $K_2 = \sqrt{\frac{4000}{1200}} = 1.826$.
Thus, we have

$$\tanh(0.0299t) = 0.00896 \times \frac{100000}{3600} = 0.249.$$

Therefore $t = 8.5$s.
b) max $V_x = \frac{K_2}{K_1} = 111.5$m/s $= 400.8$km/h.
c)

$$m_v\frac{dV_x}{dt} = m_v\frac{d(V_x+10)}{dt} = -\frac{\rho A_F C_d}{2}(V_x+10)^2 + F_x.$$

$$\ln\frac{|(V_x+10) - K_2/K_1|}{|(V_x+10) + K_2/K_1|} - \ln\frac{|10 - K_2/K_1|}{|10 + K_2/K_1|} = -2K_1K_2t.$$

$$V_x(t) + 10 = \frac{K_2}{K_1}\tanh(K_1K_2t + 0.09).$$

Thus,

$$\tanh(0.0299t + 0.09) = 0.00896 \times \left(\frac{100000}{3600} + 10\right) = 0.338.$$

Therefore $t = 8.76$s.

11.2

$$s(t) = \int_0^t V_x(\tau)d\tau = \int_0^t \frac{K_2}{K_1}\tanh(K_1K_2\tau)d\tau = \frac{1}{K_1^2}\ln[\cosh(K_1K_2t)]$$

$s(8.5) = 117.5$m.

11.3

$$V_x = \frac{\frac{6400}{60}\times 2\pi\times 0.29}{4.1}\times 0.9 = 42.66\text{m/s} = 154\text{km/h}$$

11.4
a) $\alpha = \tan^{-1}(0.1) = 5.71^\circ$

The tire rolling resistance:

$$F_{roll} = f_r m_v g \cos\alpha = 0.009 \times 1350 \times 9.8 \times \cos 5.71^\circ = 118.5\text{N}.$$

The gravity:

$$m_v g \sin\alpha = 1350 \times 9.8 \times \sin 5.71^\circ = 1316.5\text{N}.$$

The inertial force:

$$m_v \frac{dV_x}{dt} = 1350 \times (32000/3600) \times (1/7) = 1714.3\text{N} \quad \text{for} \quad 0 \le t < 7;$$
$$m_v \frac{dV_x}{dt} = 1350 \times (-32000/3600) \times (1/5) = -2400\text{N} \quad \text{for} \quad 15 \le t < 20.$$

Time	Rolling resistance	Gravity	Inertial force	Sum	Power
[0, 7)	118.5	1316.5	1714.3	3149.3	$3149.3 \times 1.27t$
[7, 15)	118.5	1316.5	0	1435	1435×8.89
[15, 20)	118.5	1316.5	-2400	-965	$-965 \times (8.89 - 1.788t)$

b)

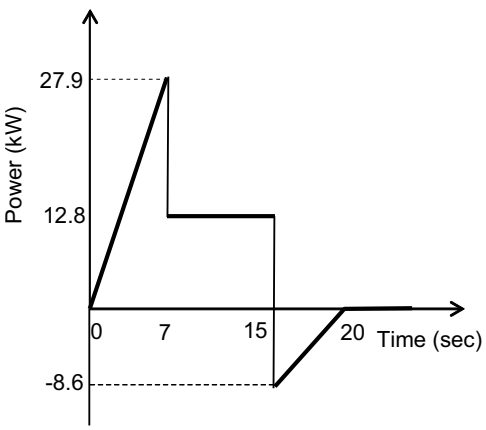

c) The motor speed is equal to

$$\frac{8.89}{0.29 \times 0.9} \times 4.1 \times \frac{60}{2\pi} = 1334\text{rpm}.$$

The motor torque is equal to

$$T_e = \frac{F_x r_w}{g_{dr}\eta_{dr}} = \frac{1435 \times 0.29}{4.1 \times 0.95} = 107\text{Nm}.$$

11.5

a) Note that $F_x = T_e \eta_{dr} g_{dr}/r_w = 250 \times 0.95 \times 4.1/0.29 = 3358\text{N}$. Since $F_x = m_v g \sin\alpha$ at launching,

$$\alpha = \sin^{-1}\left(\frac{3358}{1500 \times 9.8}\right) = 13.2^\circ \quad \Rightarrow \quad \text{grade} = \tan\alpha \times 100 = 23.5\%$$

b) The motor base speed is

$$\omega_r = \frac{P_e}{T_e} = \frac{55000}{250} = 220\text{rad/sec} = 2100\text{rpm}.$$

c)

$$V_x = \frac{\omega_r}{g_{dr}} r_w (1 - s_x) = \frac{220}{4.1} \times 0.29 \times (1 - 0.1) = 14\text{m/s} = 50.4\text{km/h}.$$

11.6

a) Wheel shaft speed is

$$\omega_w = \frac{V_x}{r_w(1 - s_x)} = \frac{60000}{3600 \times 0.35 \times 0.85} = 56\text{rad/sec}.$$

b) The motor speed is 785 rad/sec. The gear ratio is $g_{dr} = \frac{\omega_r}{\omega_w} = \frac{785}{56} = 14$.

c) The motor power is

$$P_e = F_x V_x \frac{1}{\eta_f} = 4000 \times \frac{60000}{3600} \times \frac{1}{0.8} = 83333\text{W}.$$

d) The rated torque at the base speed, $\omega_r = 376.8$rad/s is

$$T_e = \frac{P_e}{\omega_r} = \frac{83333}{376.8} = 221.2\text{Nm}.$$

e) At the launching, $F_x = F_{roll} + m_v g \sin\alpha$. Thus,

$$\sin^{-1}\left(\frac{\frac{330\times14}{0.35} - 4500 \times 9.8 \times 0.01}{4500 \times 9.8}\right) = 16.9^\circ \;\Rightarrow\; \text{grade} = \tan(16.9^\circ) \times 100 = 17.4\%$$

11.7 The solution is omitted.

Chapter 12

12.1

$$\begin{aligned} T_r &= T_c - T_s \\ T_c\omega_c &= (T_c - T_s)\omega_r + T_s\omega_s \\ T_c &= \frac{\omega_s - \omega_r}{\omega_c - \omega_r} T_s = \frac{\omega_s - \omega_r}{\frac{1}{k_p+1}\omega_s + \frac{k_p}{k_p+1}\omega_r - \omega_r} T_s = (k_p + 1)T_s \\ T_r &= T_c - T_s = T_c - \frac{1}{k_p+1} T_c = \frac{k_p}{k_p+1} T_c. \end{aligned}$$

12.2

For the sun

$$T_{sun} - (J_{mg1} + J_{sun})\dot{\omega}_s = T_s.$$

For the ring

$$T_{ring} - (J_{mg2} + J_{ring})\dot{\omega_r} = (T_w + J_{vh}\dot{\omega}_v)g_{dr} - T_e.$$

12.3
a) The speed of engine has to move at $\omega_c = 1750 \times \frac{2\pi}{60} = 183.2$rad/sec. The corresponding generator speed is

$$\omega_s = (k_p + 1)\omega_c - k_p\omega_r = 3.6 \times 183.2 - 2.6 \times 280 = -68.48\text{rad/sec.}$$

b) The generator torque is

$$T_s = \frac{T_c}{k_p + 1} = \frac{82}{3.6} = 22.78\text{Nm.}$$

Therefore, the generator power is

$$P_s = T_s\omega_s = 22.78 \times (-68.48) = -1560\ W.$$

12.4
a)

$$\omega_r = g_{dr}\omega_w = g_{dr}\frac{V_x}{(1 - s_x)r_w} = 4.1 \times \frac{80000}{3600} \times \frac{1}{0.9 \times 0.29} = 349\text{rad/sec.}$$

b) Since the engine speed is 150 rad/sec, it follows from the level diagram that

$$\omega_s = 3.6\omega_c - 2.6\omega_r = 3.6 \times 150 - 2.6 \times 349 = -367.4(\text{rad/sec}).$$

c) The engine power is $P_{en} = T_{en} \times \omega_{en} = 84 \times 150 = 12600$W. The generator torque is $T_s = 84/3.6 = 23.33$Nm. Thus, the generator power is $P_s = -23.33 \times 367.4 = 8571$W. the rest $P_r = 12600 - 8571 = 4029$W is transmitted through the mechanical path. The vehicle power is equal to $P_x = (80000/3600) \times 270 = 6000$W. Since the drive-line efficiency is $\eta_f = 0.82$, power at the upstream of the drive-line is $6000/0.82 = 7317$W. Therefore, $P_e = 7317 - 4029 = 3288$(W) should be provided from the electrical path (motor).
d) Considering the efficiencies of M/Gs and inverters, the electrical power transmitted from the generator to the DC link is $8571 \times 0.92 \times 0.97 = 7649$(W). However, $3288/(0.97 \times 0.92) = 3684$W should go to the motor. Therefore, the battery charging power is equal to $P_{bat} = 7649 - 3684 = 3965$W.

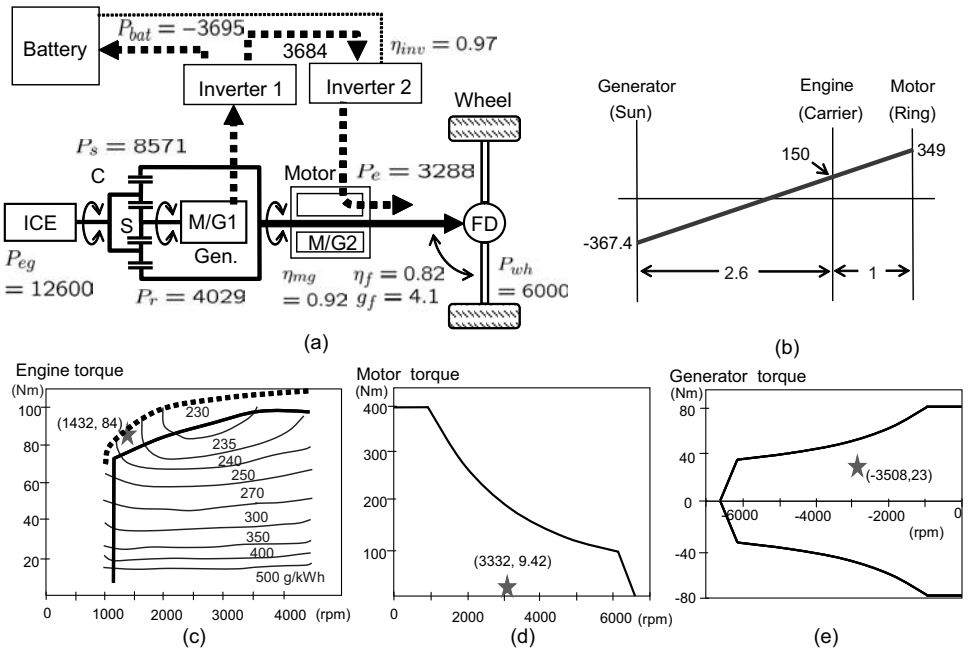

12.5

The engine power is $P_{en} = T_{en}\omega_{en} = 60 \times 3400 \times \frac{2\pi}{60} = 21352$W. The electrical power at the DC link side is $21352 \times 0.97 \times 0.92 = 19054$W. The battery charging power is $P_{bat} = 19054 - 15000 = 4054$W. Therefore, the charging current is $I_{bat} = \frac{P_{bat}}{V_{bat}} = \frac{4054}{307} = 13$A.

Chapter 13

13.1

$\frac{1.66 \times 3.8}{0.046} = 137$Wh/kg.

13.2

a) $3.3 \times 25 = 82.5$Wh.

b) $\frac{82.5}{0.9} = 91.7$Wh/kg.

c) Since the battery delivers 25Ah during 1 hour (at 1C rate), the current at 1 C rate is 25A. Therefore, 48C rate means that the discharging current is $48 \times 25 = 1200$A. Hence, the specific power at 48C rate is $1200 \times 2.4 = 2880$W.

d) $2.4 \times 22 = 52.8$Wh. The battery ohmic loss increases with current density, i.e., the ion conductance rate decreases. Further, the concentration loss also takes place at a very high discharging current. Refer to the polarization curve shown in Fig. 13.2.

13.3
Using the Peukert's equation, it follows that

$$\begin{aligned} \log_{10} C_k &= \log_{10} 10 + n \log_{10} 15 = 1 + n \log_{10} 15 \\ \log_{10} C_k &= \log_{10} 1 + n \log_{10} 100 = 2n \end{aligned}$$

Therefore, $n = 1.2137$ and $\log_{10} C_k = 2.4275$. Thus, $C_k = 267.6$. Since $267.6 = t_{cut} 200^{1.2137}$, $t_{cut} = 0.43$h.

13.4
a)-3), b)-4), c)-2), d)-1).

13.5

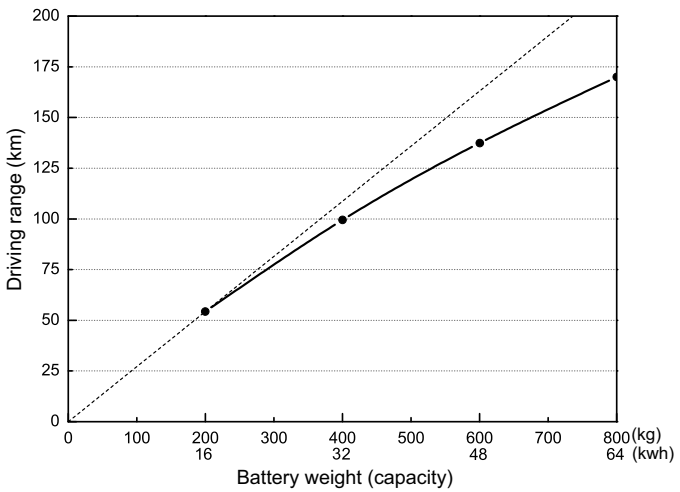

13.6
a) Electrolyte is highly viscous and may be freezed. The reaction rate is low at low temperatures.
b) Self discharge rate is high. Cell structure changes. Electrolyte is unstable.
c) Excess charging current may results in electrolysis of the electrolyte, producing gaseous oxygen. The pressure build up leads to leakage of gas and electrolyte.
d) Silicon takes up lithium with the volume increase (as many as four times). Thus, during the charge, a great mechanical strain is exerted on the brittle material, so that silicon anodes tend to crack only after a few cycles.

Chapter 14

14.1

$$\frac{1}{\pi}\int_{-\pi}^{\pi}(\text{MMF})\cos 2\theta\, d\theta = \frac{3\sqrt{3}}{2\pi} \neq 0.$$

14.2

a) $B_g = \mu_0 H_m \frac{\ell_m}{g}$.

b)

$$P_c = \frac{S_m B_m}{S_m \mu_0 H_m} = \frac{S_g B_g}{S_m \mu_0 H_m} = \frac{S_g B_g}{S_m \mu_0 H_g (g/\ell_m)} \approx \frac{\ell_m}{g}.$$

14.3

a) To the left.

b)

$$\oint_C H \cdot ds = 2H_g(\delta + h_m) = 2A_m x\,,$$

Then, the resulting field intensity by the current sheet is a function of x:

$$H_g = \frac{A_m}{\delta + h_m} x.$$

14.4

a) The $B_m - \mu_0 H_m$ curve is a straight line of 45° degree in the second quadrant. Note that $P_c = \ell_m/g = 10$. From the the intersection between P_c and the demagnetization curve, $B_g = 1.2 - 1.2/11 = 1.09$T.

b) The load line is shifted to the left by $-3000/0.011 = -273$kA/m. The solution is obtained from the intersection of the two curves: $y = x + 1.2$ and $y = -10(x + 273/950)$. The solution is $B_g = 0.83$T.

Index

Power Electronics

AC Motor Control *and* Electric Vehicle Applications

Motor control technology continues to play a vital role in the initiative to eliminate or at least decrease petroleum dependency and greenhouse gas emissions around the world. Increased motor efficiency is a crucial aspect of this science in the global transition to clean power use in areas such as industrial applications and home appliances—but particularly in the design of vehicles.

Summarizes the evolution of motor-driving units toward high efficiency, low cost, high power density, and flexible interface with other components

AC Motor Control and Electric Vehicle Applications addresses the topics mentioned in its title but also elaborates on motor design perspective, such as back EMF harmonics, loss, flux saturation, reluctance torque, etc. Maintaining theoretical integrity in AC motor modeling and control throughout, the author focuses on the benefits and simplicity of the rotor field-oriented control, describing the basics of PWM, inverters, and sensors. He also clarifies the fundamentals of electric vehicles and their associated dynamics, motor issues, and battery limits. A powerful compendium of practical information, this book serves as an overall useful tool for the design and control of high-efficiency motors.

K11033

CRC Press
Taylor & Francis Group
an **informa** business
www.crcpress.com

6000 Broken Sound Parkway, NW
Suite 300, Boca Raton, FL 33487
270 Madison Avenue
New York, NY 10016
2 Park Square, Milton Park
Abingdon, Oxon OX14 4RN, UK

ISBN: 978-1-4398-1963-0
90000
9 781439 819630